N° d'enregistrement

THESE de Doctorat

Pour l'obtention du grade de

DOCTEUR DE L'UNIVERSITE DE PAU ET DES PAYS DE L'ADOUR

Spécialité: Géophysique

U.F.R. des Sciences et Techniques de Pau

Diplôme National - Arrêté du 7 août 2006

ECOLE DOCTORALE DES SCIENCES EXACTES ET LEURS APPLICATIONS

Présentée par

Myriam KARS

Calibration and Application of the MagEval geothermometer in sedimentary rocks

Calibration et Application du géothermomètre magnétique MagEval dans les roches sédimentaires

Soutenue le 5 Janvier 2012

A l'Ecole Normale Supérieure de Paris

Devant la Commission d'Examen présidée par Jean-Noël ROUZAUD

JURY

M. Charles AUBOURG	Professeur d'Université	Directeur de thèse
M. Jean-Paul CALLOT	Professeur d'Université	Examinateur
M. Michel CATHELINEAU	Directeur de Recherche CNRS	Rapporteur
M. Jean-Pierre GIRARD	Chef Géochimie Minérale ISS/RGM	Superviseur TOTAL
Mme. France LAGROIX	Chargé de Recherche CNRS	Examinatrice
M. Jean-Pierre POZZI	Directeur de Recherche Emerite CNRS	Co-directeur de thèse
M. Pierre ROCHETTE	Professeur d'Université	Rapporteur
M. Jean-Noël ROUZAUD	Directeur de Recherche CNRS	Examinateur

"La seule vraie science est la connaissance des faits"
Georges-Louis Leclerc, comte de BUFFON (1707-1788)

"L'observation scientifique est toujours une observation polémique"
Gaston BACHELARD (1884-1962)

Abstract

To evaluate the burial temperature experienced by sedimentary rocks, a wide range of geothermometers is available, based on both organic and inorganic constituents of these rocks. Like all experimental techniques, they show limitations. In this thesis, we used a magnetic approach to estimate burial temperature. In a first part, we studied the magnetic assemblage of selected boreholes over the world to better characterize the magnetic geothermometer MagEval. Two calibrations were established. To assess the relationship between the peak burial temperature experienced by the rocks and their constitutive magnetic minerals, we conducted laboratory heating experiments from 50 to 130°C on unmetamorphosed claystones. The experimental heating showed that nano magnetic minerals are continuously produced with temperature. In a second part, we investigated rock magnetic properties of sedimentary rocks from two geological plays of petroleum interest : the Grès d'Annot basin in SE France (burial temperature 60-250°C) and the fold-and-thrust belts of the Valley & Ridge Province in the Appalachians, USA (burial temperature ∼120-200°C). These studies suggested an evolution of the main magnetic minerals with temperature. Magnetite, nanogoethite and pyrrhotite are mainly formed. All the conducted analyses lead us to propose an evolution of the magnetic minerals as a function of the maturity of the rocks and temperature.

Key words : MagEval geothermometer, magnetic assemblage, magnetite, maturity of rocks, heating experiments

---

Résumé

Pour évaluer la température d'enfouissement subie par les roches sédimentaires, une large gamme de géothermomètres est disponible, basés sur les constituants organiques ou minéralogiques de ces roches. Comme pour toutes les techniques expérimentales, elles présentent des avantages et des inconvénients. Dans cette thèse, nous utilisons une approche magnétique pour estimer la température d'enfouissement. Dans une première partie, nous avons étudié l'assemblage magnétique de puits sélectionnés à travers le monde pour mieux caractériser le géothermomètre magnétique MagEval. Deux calibrations ont pu être établies. Pour décrire la relation entre la température maximale d'enfouissement subie par les roches et leur assemblage magnétique, nous avons réalisé des expériences de chauffe en laboratoire de 50 à 130°C sur des argilites non métamorphosées. Les chauffes expérimentales ont montré que des nanominéraux magnétiques sont continuellement produits avec la température. Dans une deuxième partie, nous avons étudié les propriétés magnétiques des roches sédimentaires dans deux sites géologiques analogues pétroliers : le bassin des Grès d'Annot dans le SE de la France (température d'enfouissement 60-250°C) et les chaînes plissées de la Valley & Ridge Province dans les Appalaches, Etats-Unis (température d'enfouissement ∼120-200°C). Ces études suggèrent une évolution des principaux minéraux magnétiques avec la température. Magnétite, nanogoethite et pyrrhotite sont principalement formées. Les différents résultats obtenus dans cette thèse nous ont permis de proposer une évolution des minéraux magnétiques en fonction de la maturité des roches et de la température.

Mots clefs : géothermomètre MagEval, assemblage magnétique, magnétite, maturité des roches, expériences de chauffe

Remerciements

Je tiens à remercier mes directeurs de thèse, Charles Aubourg et Jean-Pierre Pozzi, et mon superviseur au sein de Total, Jean-Pierre Girard, de m'avoir donné l'occasion de réaliser cette thèse. Un tel travail n'aurait pas été possible sans les nombreuses discussions qui ont eu lieu au cours de ces trois années.

Je remercie les membres du jury de m'avoir fait l'honneur de juger ce travail.

Je suis reconnaissante envers les différents laboratoires et équipes qui m'ont accueillie au sein de leur structure pour le bon déroulement de la thèse. Je remercie mes collègues du service Roche et Géochimie Minérale du Centre Scientifique et Technique de Total à Pau pour leur accueil chaleureux et leur contribution à un moment donné ou l'autre. Merci également au service Fluide et Géochimie Organique et plus particulièrement à Eric Legendre pour la modélisation GENEX.

Une place spéciale est réservée au laboratoire de Géologie de l'Ecole Normale Supérieure de Paris dont j'ai partagé les murs une grande partie de la thèse. Je remercie chaleureusement Dominik Janots pour sa précieuse aide, notamment dans la partie chimie-RX. Les expériences en capsules d'or n'auraient pas été réalisables sans Fabrice Brunet ; un grand merci. Merci à Nathaniel Findling, Bertrand Doumert et Damien Deldicque pour la diffraction RX et les observations MEB de lames minces.

Une grande partie du travail analytique n'aurait pas été envisageable sans la collaboration de France Lagroix du laboratoire de Paléomagnétisme de l'Institut de Physique du Globe à Paris. Je tiens particulièrement à la remercier pour m'avoir permis d'utiliser le MPMS et pour nos différentes discussions.

Je n'oublie pas l'Institute for Rock Magnetism de Minneapolis qui m'a accueillie trois fois dans

le cadre des Visiting Fellowship. Ces différents séjours m'ont permis d'engendrer une grande quantité de données qui ont eu un impact certain sur l'avancement de mes travaux. Je remercie Mike Jackson, Julie Bowles et Peat Solheid pour leur aide technique, Thelma Berquò pour les mesures Mössbauer et l'ensemble de l'équipe pour les nombreuses discussions fructueuses autour de cafés, cookies et bagels. Je leur suis également reconnaissante de m'avoir permis de participer à leur première université d'été d'une qualité exceptionnelle.

Je remercie Mark Evans de la Central Connecticut State University, New Britain, pour son inestimable aide apportée en amont et en aval dans l'étude des Appalaches. Je remercie également Pierre Labaume de l'Université de Montpellier pour nous avoir fourni des échantillons et des documents pour une meilleure compréhension du bassin des Grès d'Annot.

Merci également à Martiane Cabié et Christian Dominici du Centre Pluridisciplinaire de Microscopie et de Microanalyse à Marseille pour la réalisation de coupes FIB et d'observations MET et MEB.

Je remercie enfin le laboratoire des Fluides Complexes et leur Réservoir de l'Université de Pau et des Pays de l'Adour et le laboratoire Géosciences et Environnement Cergy de l'Université de Cergy-Pontoise pour la partie administrative et leur accueil lors de mes passages plus ou moins occasionnels.

Les remerciements ne seraient pas complets sans mentionner famille et amis pour leur soutien inconditionnel. A Alexandra et Djamila qui m'ont conseillée et soutenue à tout instant (y compris soir et weekend), je leur suis indéfiniment redevable. Un grand merci à Laureen et Emeline pour leur soutien et nos bons et moins bons moments de thèse partagés autour de petits pains, cafés et muffins. Merci à Eva pour avoir partagé notre petit coin magnéticien du 3ème et qui m'a appris, par son expérience, à approcher la thèse différemment. Merci à Florian et Sebastien pour leur présence. A ceux que je n'ai pas cités et qui se reconnaîtront, merci.

Ce travail a bénéficié d'un financement dans le cadre d'une convention CIFRE ANRT-TOTAL.

Contents

Version française abrégée

La reconstitution de l'histoire thermique dans les roches sédimentaires est importante dans la compréhension des bassins et de la génération des hydrocarbures. Au-delà des analyses de routine utilisées dans l'industrie pétrolière, comme la pyrolyse RockEval ou la réflectance de la vitrinite Ro, l'étude des propriétés magnétiques des roches peut également apporter des informations.

Certaines transformations chimiques, comme l'altération de la pyrite, impliquent le fer, et d'une certaine manière, vont aussi modifier les assemblages magnétiques.

Depuis deux décennies, plusieurs études ont montré l'existence d'assemblages magnétiques diagnostiques de la température atteinte par la roche (e.g. Rochette, 1987 ; Dunlop *et al.*, 2000 ; Schill *et al.*, 2002 ; Aubourg & Pozzi, 2010). C'est dans ce contexte que s'inscrit cette thèse. Dans une première partie, nous discuterons des principaux résultats obtenus dans la calibration du géothermomètre MagEval. Dans une deuxième partie, nous présenterons les résultats expérimentaux de chauffe en laboratoire qui suggèrent que les minéraux magnétiques sont continuellement produits/détruits avec l'augmentation de la température. Enfin, dans une troisième partie, nous montrerons les résultats de deux études de terrain dans le bassin des Grès d'Annot (SE de la France) et dans les chaînes plissées des Appalaches (Virginie Occidentale, Etats-Unis). Ces études montrent que les assemblages minéralogiques magnétiques évoluent avec la température. Nous terminerons en proposant un modèle d'enfouissement des minéraux magnétiques.

1 Géothermomètre MagEval

Le géothermomètre MagEval a été proposé par Aubourg & Pozzi (2010) à la suite d'observations et de travaux expérimentaux sur l'effet de l'enfouissement sur les argilites naturelles. Son principe est supposé fondé sur la thermodépendance du couple pyrrhotite/magnétite. Le signal magnétique type MagEval, révélé par une étude expérimentale à basse température (inférieure à la température ambiante), se présente comme suit :

– La courbe de refroidissement d'une rémanence acquise en laboratoire à température ambiante (300 K/27°C ; RT-SIRM [1]) présente une transition de Verwey (∼120 K) correspondant à une magnétite stoechiométrique et un "P-behavior" en dessous de 70 K (Aubourg & Pozzi, 2010 ; Kars *et al.*, 2011a)
– La courbe de réchauffement d'une rémanence acquise à 10 K (ZFC [2]) présente une allure en deux paliers (Figure 1) : une diminution de la rémanence entre 10 et 35 K et la transition de Verwey de la magnétite.

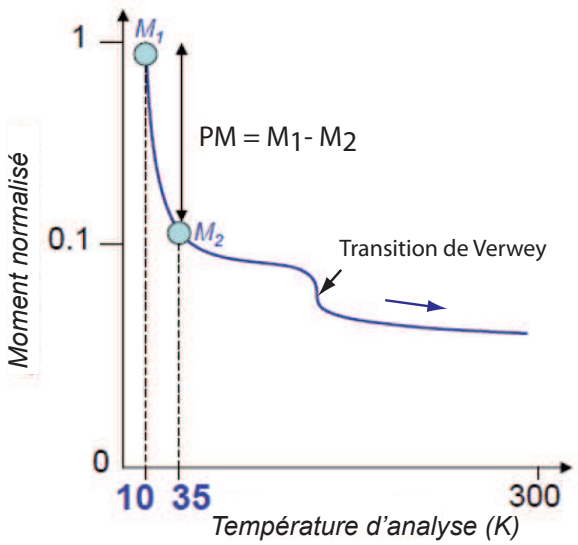

Figure 1 – Allure en deux paliers de la courbe de réchauffement ZFC permettant de calculer le paramètre PM

Nous proposons que la température d'enfouissement d'une roche peut être estimée par le paramètre PM [3] correspondant à la chute de la rémanence entre 10 et 35 K (Figure 1) :

$$PM = \frac{LTSIRM_{10K} - LTSIRM_{35K}}{LTSIRM_{10K}}$$

where LT-SIRM stands for Low Temperature-Saturation Isothermal Remanent Magnetization.

Aubourg & Pozzi (2010) ont proposé en première approche que ce paramètre avait une évolution en deux pentes : tout d'abord une augmentation des valeurs (PM-Up), puis une diminution des PM (PM-Down), le tout dans une gamme de température de 50 à 250°C, la valeur maximale PM max se situant autour de 80-90°C. De façon à mieux caractériser le géothermomètre MagEval, une large étude de forages de par le monde a été réalisée. Le signal type MagEval a été retrouvé dans une très grande

1. Room Temperature Saturation Isothermal Remanent Magnetization
2. Zero Field Cooling
3. Pyrrhotite-Magnétite

majorité des puits sélectionnés. Les ressemblances/différences observées ont permis de déterminer des critères de sélection des échantillons valides pour la calibration du géothermomètre MagEval d'une part, et pour l'estimation de la température d'enfouissement d'autre part. Ceci peut se résumer selon le schéma de la Figure 2. Des analyses statistiques ont montré que la mesure du PM est reproductible et est définie à ± 0,02. Sur les 7 puits investigués, deux ont retenus notre attention pour l'établissement de la calibration du géothermomètre MagEval : Girassol-1 (Angola) et 22/30C-10 (Mer du Nord, Royaume-Uni). Après application des critères de sélection, l'évolution des valeurs des PM en fonction de la température calculée à partir d'une modélisation GENEX est conforme au modèle d'Aubourg & Pozzi (2010) (Figure 3).

Les tendances PM-Up et PM-Down passant par un maximum PM-max sont vérifiées dans les deux puits sélectionnés pour l'établissement du géothermomètre MagEval. L'étude montre que le signal est peu dépendant thermiquement pour Girassol-1 dans la branche PM Up, comparé à la branche PM-Up de 22/30C-10. Il est à noter que ces deux calibrations ont été obtenues sur des déblais et différentes lithologies. Quelques facteurs semblent altérer la valeur de PM (vieillissement des échantillons, mélange de faciès...). A l'instar de la réflectance de la vitrinite qui repose sur une étude statistique, nous proposons qu'à terme, une valeur moyenne du PM par tranche de profondeur soit réalisée pour mieux contraindre la variabilité, plutôt que de considérer des échantillons isolés. Les calibrations obtenues ont été appliquées sur les autres puits investigués présentant un signal MagEval. Il semblerait que la calibration obtenue à partir de 22/30C-10 donne de meilleurs résultats que celle établie à partir de Girassol-1.

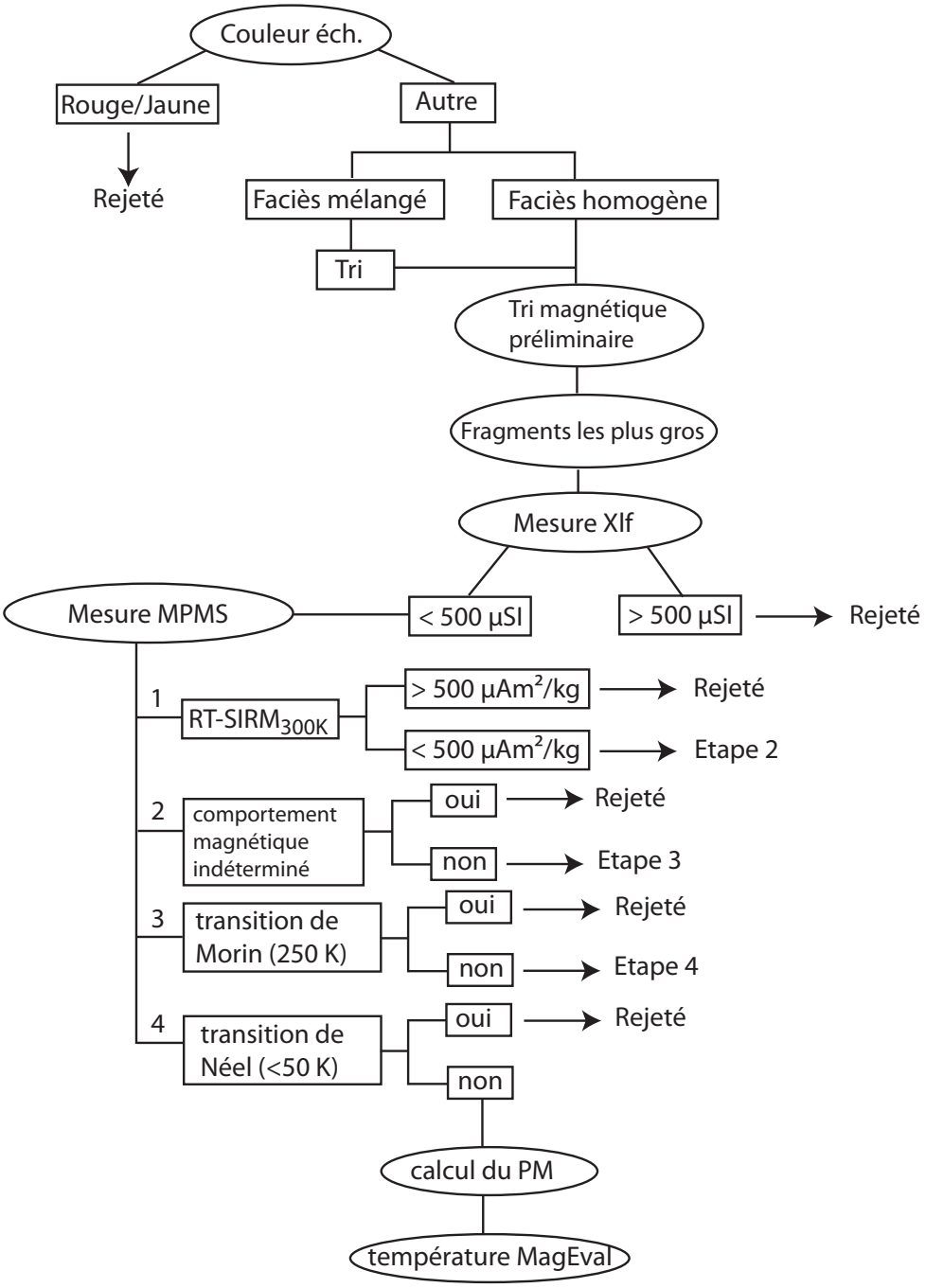

Figure 2 – Protocole d'étude et utilisation du géothermomètre MagEval. Xlf : susceptibilité magnétique à champ faible, MPMS : Magnetic Properties Measurement System (magnétomètre cryogénique SQUID), RT-SIRM : aimantation à saturation à température ambiante

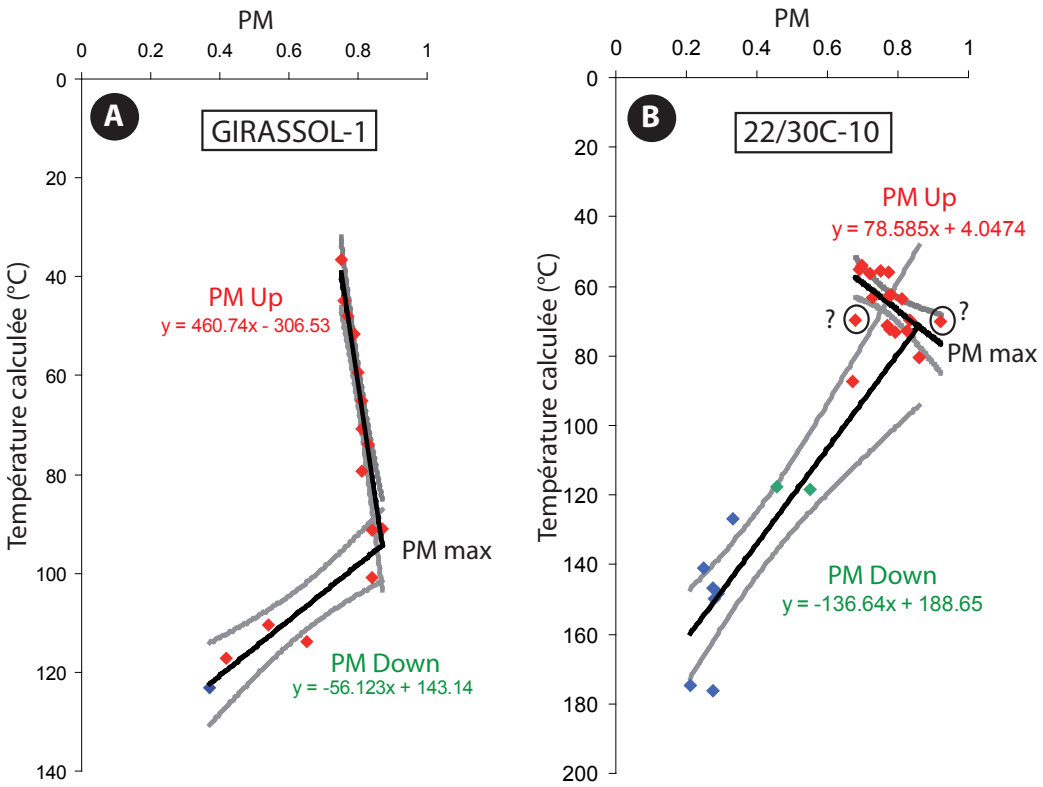

Figure 3 – Calibrations du géothermomètre MagEval obtenues pour A) Girassol-1 (Angola) et B) 22/30C-10 (Mer du Nord) en fonction des températures calculées à partir de la modélisation GENEX. Les courbes grisées représentent l'intervalle de confiance à 95%. Points rouges : argiles, points verts : grès, points bleues : calcaires.

2 Expériences de chauffe en laboratoire

2.1 Expériences sous champ magnétique à pression ambiante (0.1 MPa)

En suivant le protocole initialement proposé par Cairanne *et al.* (2004) et repris par Aubourg *et al.* (2008), nous avons réalisé des séries de chauffe, en présence d'un champ magnétique de 2 mT, sur des argilites immatures : les argilites de Boom (Oligocène, Belgique) et de Bure (Callovo-Oxfordien, Bassin Parisien). Le but est de simuler en laboratoire les conditions d'enfouissement se produisant dans la nature. La technique utilisée présente deux caractéristiques fondamentales :

1. L'application du champ magnétique permet de suivre l'évolution des minéraux magnétiques néoformés pour des concentrations aussi faibles que quelques dizaines de ppbv ;

2. L'analyse des aimantations stable (CRM [4]) et instable (TVRM [5]) permet de distinguer deux fractions de nano minéraux néoformés.

Dans ce qui suit, seule la série de chauffe de 50 à 130°C sur les argilites immatures de Bure (Callovo-Oxfordien, Bassin de Paris) est présentée (Kars *et al.*, en révision, annexe 2).

Lorsque placés à une température stabilisée, l'aimantation des échantillons augmente très rapidement dès les premières heures avant d'atteindre un plateau qui présente une valeur moyenne plus élevée à chaque palier de température (Figure 4). Cette aimantation est la somme d'une aimantation rémanente chimique et d'une aimantation thermovisqueuse.

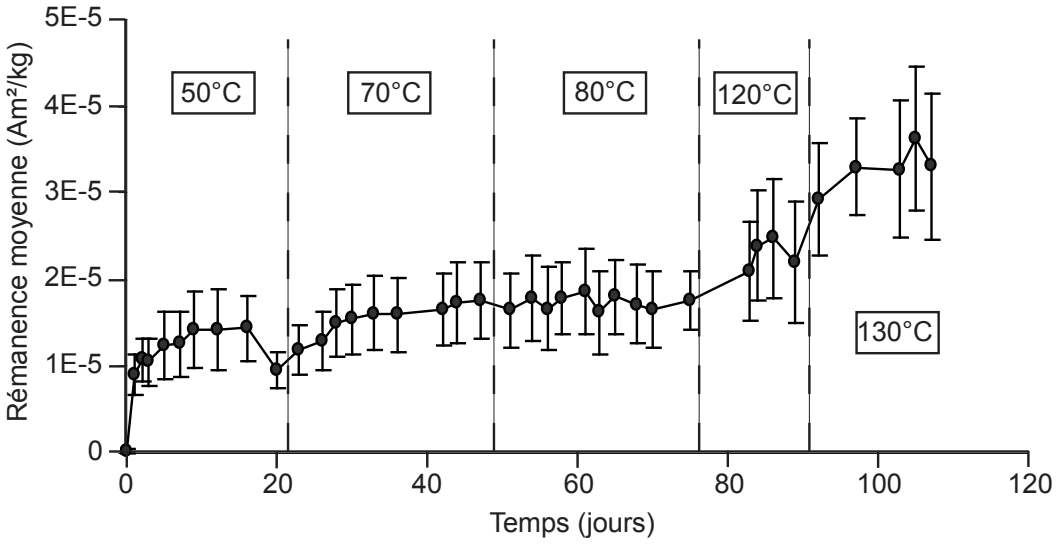

Figure 4 – Evolution de l'aimantation rémanente moyenne pendant la chauffe (50-130°C) pour les différents paliers de température. La déviation standard ($\pm 1\sigma$) est également reportée (Kars *et al.*, en révision, annexe 2).

Les CRMs créées au cours de l'expérience augmentent de 5 ± 1 à 19 ± 6 $\mu Am^2/kg$ avec la température. Pour tous les paliers de chauffe, sauf celui à 130°C, la TVRM est supérieure à la CRM (Figure 5).

Pour préciser la nature des minéraux néoformés, on peut caractériser les températures de déblocage par le biais de la désaimantation thermique des CRMs. Ces températures de déblocage évoluent vers de plus hautes valeurs (Figure 6A). Plus la température de chauffe de l'expérience est grande, plus la température de déblocage est élevée. Ce déplacement vers les valeurs plus élevées peut être attribué à une distribution de la taille des grains. Plus la taille des minéraux néoformés est grande, plus la

4. Chemical Remanent Magnetization / Aimantation rémanente chimique
5. Thermo Viscous Remanent Magnetization / Aimantation rémanente thermovisqueuse

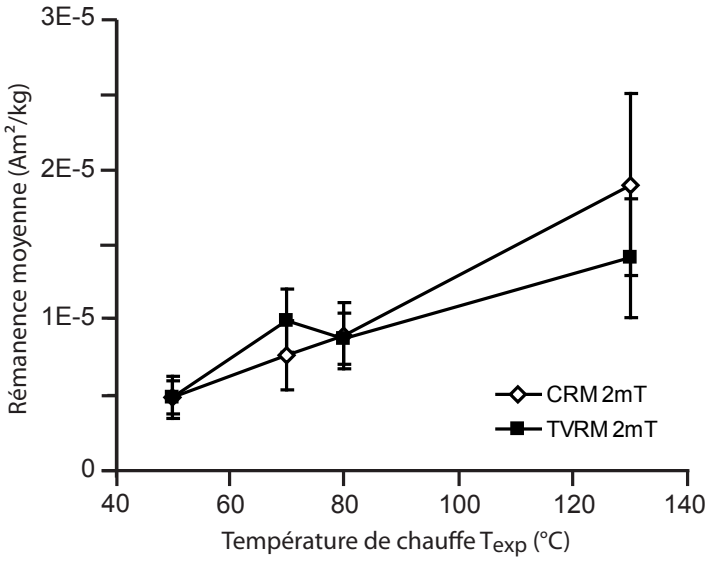

Figure 5 – Evolution de la CRM et de la TVRM créées au cours de l'expérience de chauffe de 50 à 130°C. La déviation standard ($\pm$ 1σ) est également reportée (Kars *et al.*, en révision, annexe 2).

température de déblocage sera élevée. Du fait des températures maximales de déblocage situées entre 400 et 500°C, l'hypothèse la plus simple (et la plus logique) est de supposer que seule la magnétite est formée. La taille des grains évolue de 30 à 35 nm pour des températures comprises entre 250 et 500°C. Toujours dans l'hypothèse que le porteur de la CRM est une magnétite, nous proposons que la CRM traduit une population de grains $>$ 20 nm, tandis que la TVRM représente les grains superparamagnétiques de taille $<$ 20 nm et les grains multidomaines de taille $>$ 0,1 μm. L'augmentation de la fraction superparamagnétique est confirmée par des mesures basse température (10-300 K ; Figure 6B). Le paramètre PM augmente lorsque la température de chauffe de l'expérience augmente.

Ces expériences sous champ magnétique ont apporté des résultats très importants pour la compréhension du géothermomètre MagEval :

- des argilites différentes (Boom et Bure, voir chapitre V) présentent un comportement remarquablement similaire lorsque placées dans les mêmes conditions expérimentales. Ceci permet d'expliquer pourquoi le comportement magnétique des argilites semble être similaire d'un environnement géologique à l'autre ;
- à température donnée, dès 50°C, les minéraux magnétiques sont très rapidement créés, puis s'ensuit une période de stabilisation. L'élévation de température conduit à nouveau au même schéma. Transposé à l'histoire d'enfouissement, cela soutient l'hypothèse d'une création continue de minéraux magnétiques ;

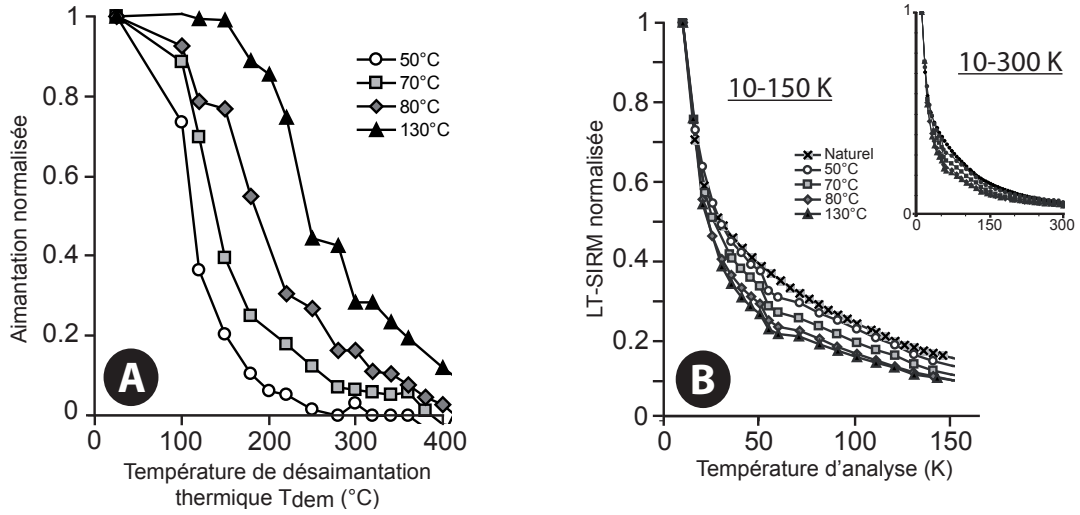

Figure 6 – A) Désaimantation thermique des CRMs créées au cours de l'expérience de 50 à 130°C et B) évolution de la rémanence à saturation acquise à 10 K de 10 à 150 K (de 10 à 300 K en insert ; Kars *et al.*, en révision, annexe 2).

– l'évolution continue d'une fraction superparamagnétique et monodomaine à polydomaine est sans doute un élément clef dans la compréhension de l'évolution du paramètre PM, dont une large partie est contrôlée par la fraction ultra-fine des minéraux.

2.2 Expériences de chauffe en capsules d'or sous pression de 100 MPa

Dans l'expérience de chauffe précédente, la pression n'était pas considérée. Pour nous rapprocher des conditions d'enfouissement, les échantillons sont placés, dans cette expérience, dans des capsules d'or, puis le tout dans des autoclaves à 100 MPa. Cependant, le champ magnétique ne peut être contrôlé et l'évolution des minéraux magnétiques nouvellement formés ne peut être suivie. Pour suivre l'évolution de l'assemblage magnétique, au sens large, nous utilisons les mesures à basse température (< 300 K).

Une première expérience à 80 jours montre qu'un échantillon naturellement chauffé à $\sim$40°C voit sa valeur de PM augmenter lorsqu'il est chauffé à 80°C (Figure 7A-1). Lorsqu'ensuite chauffé à 110°C, la valeur de PM diminue (Figure 7A-2). Les résultats encourageants de cette première série de chauffe nous ont conduit à utiliser le même échantillon initial pour une deuxième série. L'échantillon est placé dans 4 capsules d'or chauffées à 80, 90, 110 et 130°C pendant 110 jours. Contrairement à l'expérience précédente, les échantillons sont laissés à l'intérieur des capsules d'or pour les mesures au MPMS. La capsule C3 n'est pas interprétable. Le PM mesuré après chauffe montre une augmentation avec la température que l'on interprète comme étant liée à la formation de grains superparamagnétiques (Figure 7B). Cependant, le signal de basse température traduit à la fois les minéraux néoformés, mais aussi,

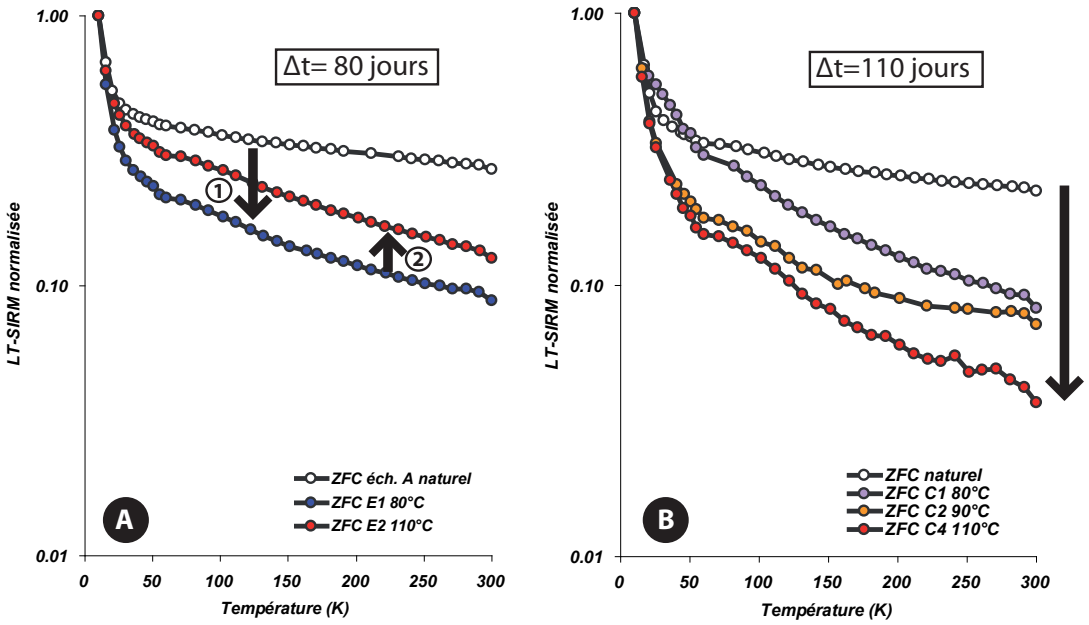

Figure 7 – Evolution de la rémanence acquise à 10 K de 10 à 300 K pour les capsules d'or de A) l'expérience à 80 jours et de B) l'expérience à 110 jours

probablement, celui des minéraux altérés. La diminution de ∼50 à 90% de l'aimantation à saturation acquise à température ambiante (RT-SIRM$_{300K}$) des échantillons après la chauffe souligne sans doute l'altération des minéraux magnétiques pendant la chauffe.
A la suite de ces résultats, nous avons réalisé une série de chauffe supplémentaire sur ces mêmes capsules d'or en augmentant de 30°C leur température seuil précédente. Malgré des problèmes de pollution et de distribution non homogène du sédiment à l'intérieur de la capsule, les résultats obtenus laissent suggérer cette fois une augmentation de l'aimantation RT-SIRM$_{300K}$.

Les expériences sous pression, par rapport à l'expérience sous champ magnétique, ne permettent pas de visualiser la nature des nouveaux minéraux formés pendant la chauffe. Cependant, dans la perspective du géothermomètre MagEval, nous obtenons des informations précieuses :

- une fraction de minéraux ultrafins est formée, ce qui se traduit par une augmentation du paramètre PM ;
- on assiste au développement de la transition de Verwey qui indique la formation de magnétites > 20 nm ;
- une fraction magnétique semble s'altérer dès les premières chauffes. Transposée à l'enfouissement, cela traduit l'existence de mécanismes propices à la dégradation des minéraux magnétiques.

3 Evolution de l'assemblage magnétique : études de terrain

3.1 Le Bassin des Grès d'Annot (SE de la France)

Le bassin des Grès d'Annot est un bassin turbiditique éocène-oligocène d'avant-pays de la chaîne alpine (e.g. Apps *et al.*, 2004). La séquence lithostratigraphique du bassin reflète son histoire depuis sa formation jusqu'à l'arrêt de la sédimentation (voir chapitre VI). Les sédiments à l'origine des Grès d'Annot proprement dits proviennent de l'érosion du massif élevé corso-sarde au sud. La mise en place des Schistes à Blocs et des nappes alpines ont provoqué l'arrêt de l'apport des sédiments.

L'histoire thermique du bassin, établie par Labaume *et al.* (2008) à partir de données thermochronologiques et pétrologiques, montre l'existence d'un gradient d'enfouissement de < 2 km au SW à $\sim$8-10 km au NE en supposant un gradient géothermique de 30°C/km (chapitre VI). Trois secteurs tectoniques/diagénétiques ont pu être établies :

- La secteur externe caractérisé par une paléotempérature inférieure à 65°C et un enfouissement de 2-2,5 km
- Le secteur intermédiaire représenté par des paléotempératures de 65-70°C à 110°C
- Le secteur interne avec des températures supérieures à 200°C, voire à 250°C dans certaines zones près du Front Pennique, caractérisé par un enfouissement jusqu'à 10 km

45 échantillons ont été prélevés essentiellement dans les niveaux argileux/marneux de la Trilogie Nummulitique. Les mesures basse température ont permis de distinguer 4 types de signaux magnétiques répartis selon les 3 secteurs tectoniques/diagénétiques (Figure 8 ; Kars *et al.*, 2011b).
Dans le secteur externe, la transition de Verwey de la magnétite autour de 120 K est facilement identifiable sur les courbes de basse température (Figure 8A ; Muxworthy & McClelland, 2000). La désaimantation thermique d'un échantillon de cette zone (Figure 8D) montre une chute autour de 300 et de 450°C correspondant respectivement à un sulfure de fer (greigite, pyrrhotite) et à la magnétite.
Le secteur intermédiaire est quant à lui caractérisé par une courbe ZFC présentant un point d'inflexion autour de 200-250 K (Figure 8E). Des nanoparticules de goethite sont supposées être responsables de ce comportement magnétique (e.g. Guyodo *et al.*, 2003).
Magnétite et sulfures de fer sont également présents comme l'indiquent le changement de pente dans la désaimantation thermique à 340°C et la disparition totale de la rémanence à 600°C (Figure 8H).
Le secteur interne présente deux signaux magnétiques différents : le premier présente une "transition" de type Néel à 24 K (Figure 8I), dont l'origine reste inconnue, et le second est typique d'une pyrrhotite > 1 μm (Figure 8M ; Rochette *et al.*, 1990). La magnétite est également présente (Figures 8N et 8P) mais disparaît progressivement en faveur de la pyrrhotite. La magnétite qui est présente dans les 3 zones diagénétiques est néoformée et de taille monodomaine.

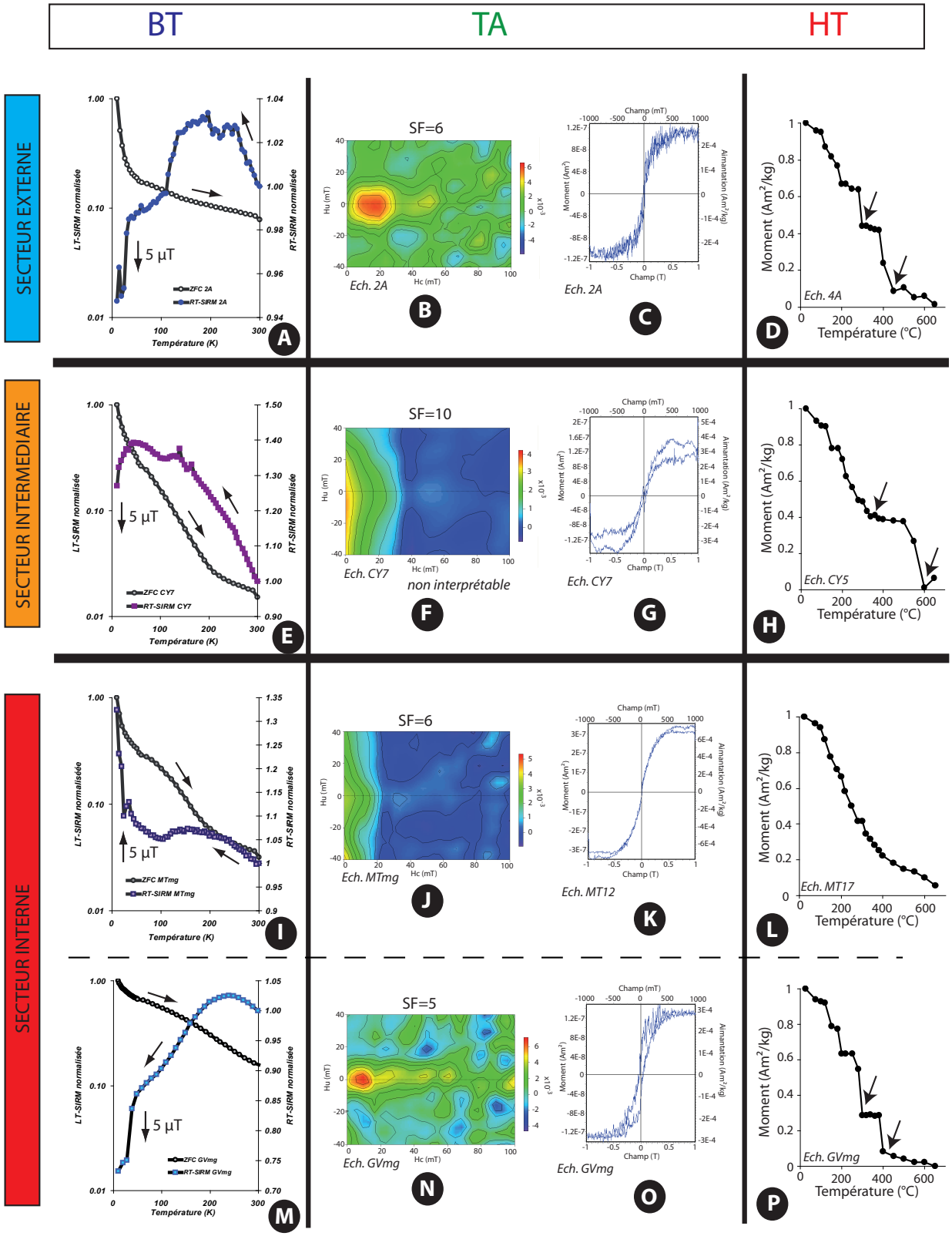

Figure 8 – Signaux magnétiques identifiés dans les trois secteurs tectoniques/diagénétiques. BT : basse température, TA : température ambiante, HT : haute température. Les flèches noires indiquent les changements de pente ; SF = smoothing factor

En replaçant nos observations magnétiques dans le contexte géologique de la zone d'étude, il apparaît que l'assemblage magnétique évolue dans un transect SW-NE concordant avec les données thermiques disponibles. Magnétite et sulfures de fer sont dominants pour une gamme de température < 90°C. Autour de 110-120°C, des nanoparticules de goethite apparaissent dont l'origine est encore mal déterminée (circulation de fluides ? altération ? enfouissement ?). Enfin pour des températures supérieures à 200°C, à l'approche des nappes alpines et du Front Pennique, la pyrrhotite > 1 μm se forme au détriment de la magnétite.

La reconnaissance des assemblages magnétiques pourrait donc être utilisée comme marqueur du métamorphisme de bas degré (< 250°C). Nous avons appliqué le géothermomètre MagEval dans cette zone d'étude. Les résultats obtenus à partir des calibrations donnent des températures inférieures à 75°C pour le secteur externe et supérieures à 85°C pour le secteur intermédiaire (jusquà 110°C). Ceci est cohérent avec les autres indicateurs thermiques disponibles dans le bassin des Grès d'Annot (AFTA, Ro).

3.2 Les chaînes plissées des Appalaches, Etats-Unis

Pour confirmer la thermodépendance du signal/assemblage magnétique identifiée dans le bassin des Grès d'Annot, une étude complémentaire a été réalisée dans la chaîne plissée de la Valley and Ridge Province en Virginie Occidentale (USA) qui s'est formée au cours de l'orogenèse alléghanienne (dernière phase orogénique de la formation des Appalaches). Cette zone a été très largement étudiée d'un point de vue paléomagnétique du fait de l'enregistrement de la réaimantation permienne Kiaman dans les carbonates paléozoïques (McCabe & Elmore, 1989 pour une revue). Le porteur de cette réaimantation est une magnétite superparamagnétique à monodomaine (e.g. Jackson, 1990) dont l'origine est encore débattue mais probablement liée à la circulation de fluides orogéniques (e.g. Oliver, 1986).

La séquence stratigraphique étudiée reflète les épisodes de transgression-régression liés aux phases orogéniques (chapitre VII). Notre échantillonnage en Virginie Occidentale couvre les formations Clinton (Silurien) à Pocono (Carbonifère), incluant la formation Marcellus (Dévonien) très étudiée du fait de son potentiel pétrolier (schistes à gaz). L'échantillonnage peut être divisé en 2 sections :

- La section A de faciès essentiellement carbonaté, des formations Tonoloway à Oriskany, caractérisée par une susceptibilité magnétique χ de 241 $\pm$ 146 μSI et une RT-SIRM$_{300K}$ de 131 $\pm$ 113 μAm^2/kg ;
- La section B de faciès silto-argileux, des formations Needmore à Chemung, caractérisée par une χ de 287 $\pm$ 88 μSI et une RT-SIRM$_{300K}$ de 95 $\pm$ 272 μAm^2/kg

.

Les mesures de basse température réalisées sur les échantillons montrent également une répartition selon les sections considérées. La section A montre deux types de signaux S1 et S2 que l'on

peut comparer à ce que l'on trouve dans le bassin des Grès d'Annot dans les zones du Ruch et de la Moutière respectivement (Figure 9). Ainsi, la section A est représentée par un assemblage magnétique goethite + magnétite (signal S1) avec parfois de la pyrrhotite > 1 μm à proximité du Front Structural Alléghanien (signal S2). La section B montre un troisième type de signal supplémentaire S3. Il est caractérisé par une chute très importante de l'aimantation rémanente entre 10 et 35 K sur la courbe ZFC et une augmentation de la rémanence très importante de la RT-SIRM en dessous de 50 K (Figure 10).

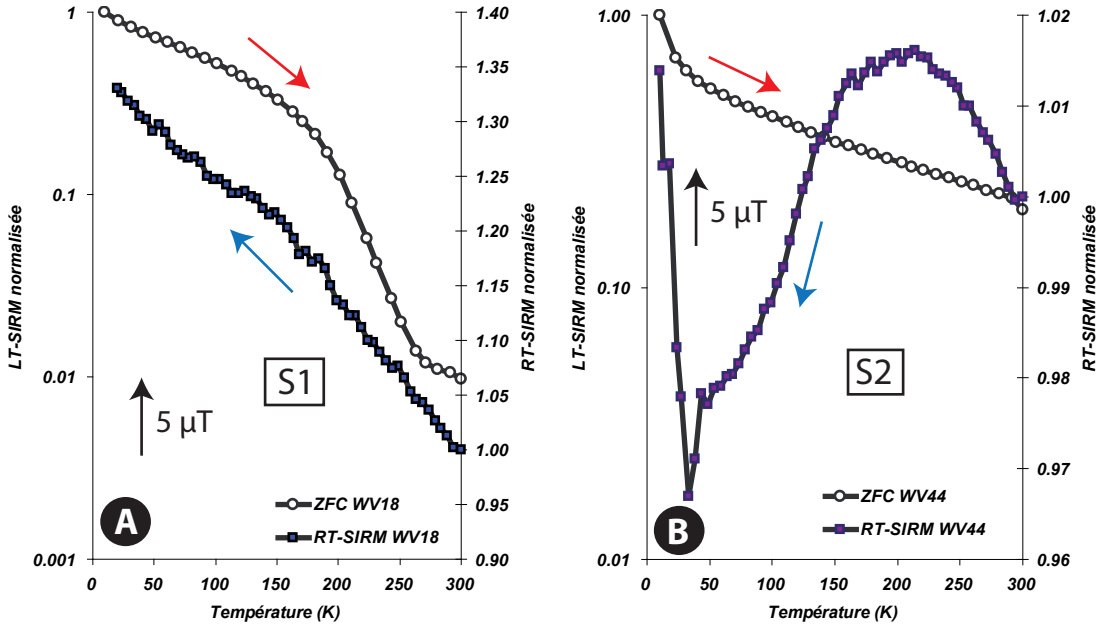

Figure 9 – Exemples des signaux magnétiques : A) S1 et B) S2 identifiés dans l'intervalle Tonoloway-Oriskany

Les signaux magnétiques identifiés en Virginie Occidentale sont stratigraphiquement distribués ce qui suggère un effet lithologique et/ou thermique. L'intervalle Tonoloway-Oriskany est caractérisé par la présence de goethite dont l'origine est certainement liée à la circulation de fluides météoriques (Evans & Elmore, 2006). D'autre part, en comparaison avec le bassin des Grès d'Annot, le signal S1 pourrait caractériser une température d'enfouissement d'au moins 100-120°C. Du fait de la présence de pyrrhotite > 1 μm, l'intervalle stratigraphique concerné a pu atteindre localement des températures jusqu'à 250°C. Enfin le signal S3 caractéristique de l'intervalle Needmore-Chemung pourrait représenter un chemin de migration des hydrocarbures qui aurait provoqué des conditions réductrices favorisant la formation de magnétite et de sulfures de fer. D'autre part, il pourrait être caractéristique de roches post-matures et riches en matière organique.

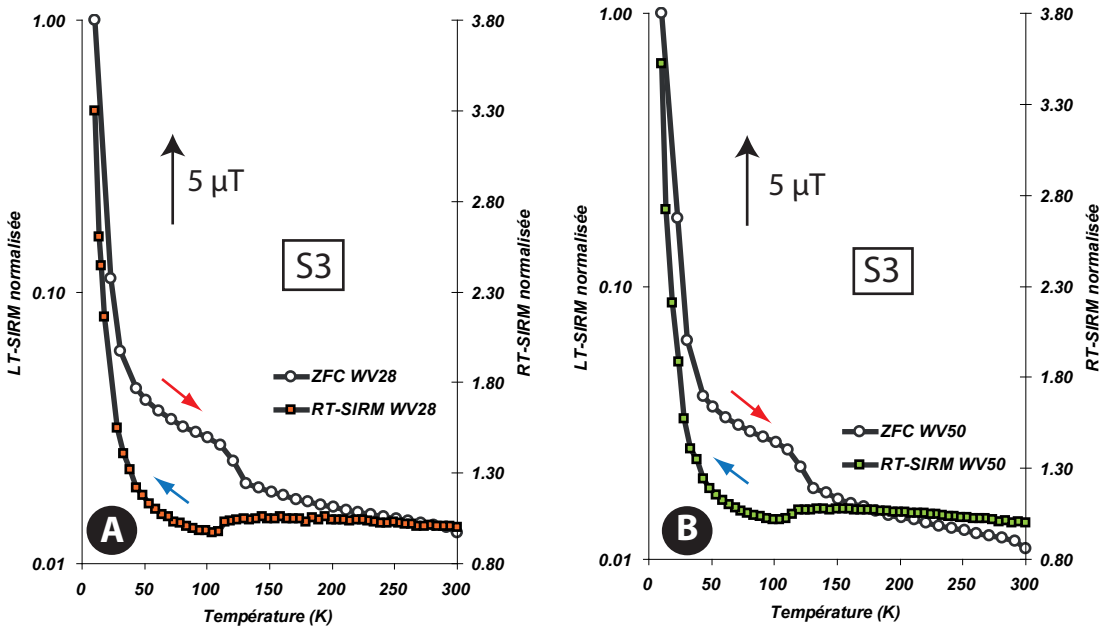

Figure 10 – Exemples du signal magnétique S3 identifié dans l'intervalle Needmore-Chemung

4 Conclusion

Dans cette thèse, nous avons proposé une approche magnétique pour l'estimation des températures des roches sédimentaires en contexte d'enfouissement. Les expériences de chauffe en laboratoire ont montré que les grains magnétiques, principalement la magnétite, sont continuellement formés et détruits/transformés avec l'augmentation de la température. Poursuivant les travaux d'Aubourg & Pozzi (2010), nous avons étudié l'assemblage magnétique de plusieurs forages dans le but de mieux caractériser le géothermomètre MagEval. Deux calibrations ont pu être établies et appliquées aux différents sites étudiés. D'autre part, les études de terrain dans le bassin des Grès d'Annot et des chaînes plissées des Appalaches ont montré une évolution des assemblages magnétiques avec la température. Ces résultats combinés avec des études antérieures ont permis de suggérer un modèle d'enfouissement des minéraux magnétiques (Figure 11) (Aubourg *et al.*, en révision, annexe 3).

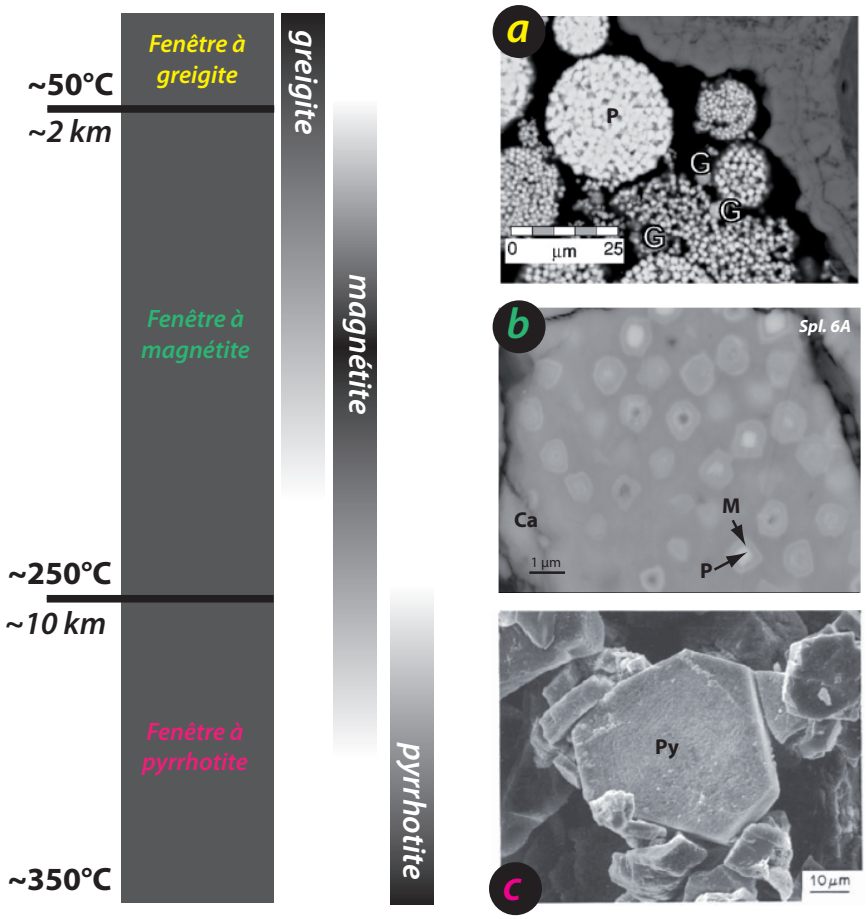

Figure 11 – Modèle d'enfouissement des minéraux magnétiques à 3 fenêtres magnétiques(d'après Aubourg *et al.*, en révision, annexe 3). Images MEB : a) extrait de Horng *et al.* (1998), b) échantillon 6A du bassin des Grès d'Annot (notre étude) et c) extrait de Sassen *et al.* (1989) (P : pyrite, G : greigite, M : magnétite, Ca : calcite, Py : pyrrhotite)

Pour approfondir le travail amorcé dans la thèse, une approche statistique du calcul du PM serait à envisager (moyenne de PM à des profondeurs rapprochées assortie d'un écart-type). La vérification de la thermodépendance du signal MagEval pourrait également s'avérer une mesure clef. D'un point de vue expérimental, des expériences de chauffe en laboratoire sous champ magnétique sur une gamme plus large de température (jusqu'à 250°C) seraient à envisager. Une étude similaire sur d'autres faciès lithologiques, comme les carbonates, pourrait également être réalisée. Comme l'on traite de petites concentrations de grains magnétiques, des méthodes en vue de concentrer ces mêmes grains seraient à prévoir. Des modélisations thermodynamiques pourraient également être effectuées dans le but de mieux comprendre les mécanismes chimiques à l'origine des transformations minéralogiques magnétiques observées.

Introduction

Reconstruction of the thermal history of sedimentary rocks is a critical part in the understanding of basin history and hydrocarbon generation. In addition to analyses commonly performed in oil and gas exploration programs (vitrinite reflectance Ro, RockEval pyrolysis, fluid inclusions...), paleomagnetic and rock magnetic properties could bring valuable information to the reconstruction of thermal regimes and fluid migration.

Paleomagnetism and hydrocarbons

Hydrocarbon circulation within a sedimentary rock leads to mineralogical transformations as a result of changes in redox conditions. Authigenic magnetic minerals may form and cause a chemical remagnetization of the rock. Recognition and dating of such phenomenon in the sedimentary rocks may provide an indication of the timing of hydrocarbon migration (e.g. Elmore *et al.*, 1993). In such instances, identification of neoformed magnetic minerals may be of major interest.

In the late 80's - early 90's, many studies established links between hydrocarbons and authigenic magnetic minerals (e.g. magnetite). The study by Elmore *et al.* (1987) about the Permian speleothems in SW Oklahoma showed a correlation between the presence of crude oil and the precipitation of authigenic magnetite. Indeed, the dark layers in the studied speleothems were enriched in hydrocarbons and showed a stronger magnetization than the light-colored (HC poor) layers. However, there was no distinct relationship between hydrocarbons and magnetization. Kilgore & Elmore (1989) showed in red-bed formations of Montana that hydrocarbon circulations dissolved hematite leading to a decrease in the rock magnetization. In order to explain the neoformation (authigenesis) of magnetite in relation with hydrocarbons, different propositions were made. McCabe *et al.* (1987) suggested that magnetite was a by-product mineral formed as a result of crude oil biodegradation by bacterial activity. Elmore *et al.* (1993) showed that the magnetic intensity seemed to increase with the extractable organic matter (EOM) content, but no relationship appeared between the percentage of asphaltenes which represent the majority of the EOM and the intensity of the natural remanent magnetization. In addition to

hydrocarbon biodegradation by bacteria, a number of other mechanisms have been proposed as possible ways to produce neoformed authigenic magnetite :

- Magnetotactic bacteria which form superparamagnetic to single domain magnetite grains but with a different shape with respect to the spherical hydrocarbon-linked authigenic magnetite (Elmore *et al.*, 1987 ; McCabe *et al.*, 1987)
- Iron sulfides oxidation such as the replacement of pyrite by magnetite (Suk *et al.*, 1990 ; Suk *et al.*, 1991)
- Basinal fluids (e.g. McCabe & Elmore, 1989)
- Inorganic processes such as siderite or Fe-rich silicates alteration (Elwood *et al.*, 1988)
- Thermal maturity or removal of organic compounds (Banerjee *et al.*, 1997)

However, the influx of hydrocarbons does not necessarily lead to the precipitation of magnetite. If reducing conditions prevail, iron sulfides such as pyrrhotite (Sassen, 1980 ; Sassen *et al.*, 1989 ; Reynolds *et al.*, 1991), greigite (Reynolds *et al.*, 1991) and pyrite (Reynolds *et al.*, 1993 and references therein) may be preferentially neoformed. Pyrrhotite and greigite are of equal importance to magnetite regarding changes in rock magnetic properties following hydrocarbon circulation (Reynolds *et al.*, 1993).

Magnetic minerals and temperature

It is well known that magnetic mineralogical changes occur when heating a rock in the laboratory. In Figure 1, the magnetic susceptibility of an immature claystone from Taiwan changes with increasing temperature. At ∼400°C, the susceptibility increases drastically as a result of the formation of a new magnetic phase. Susceptibility reaches a maximum at ∼500°C and finally decreases to zero at ∼580°C which is the Curie temperature of magnetite. The irreversible behavior of the curve comforts the mineralogical transformation with production of magnetite grains upon 1-hour heating.

The formation of a given mineral is governed by the thermodynamics and fluids composition (Machel & Burton, 1991). Seven geochemical parameters govern the stability of magnetic mineral species : temperature, pressure, dissolved sulfur, dissolved inorganic carbon, dissolved iron, pH and Eh (Burton *et al.*, 1993 ; Machel, 1995). Overall, mineral stability diagrams show enhanced formation and preservation of the magnetic minerals with increasing temperature and pressure (burial). Due to kinetic and microbial effects, magnetic assemblages may be transient in thermodynamic equilibrium. This may be particularly true during early diagenesis where bacterial activity is a key factor.

In any case, the use of magnetic properties to estimate burial temperature infers that the original (detrital) magnetic signal was removed during early diagenesis. This assumption may not be fulfilled systematically.

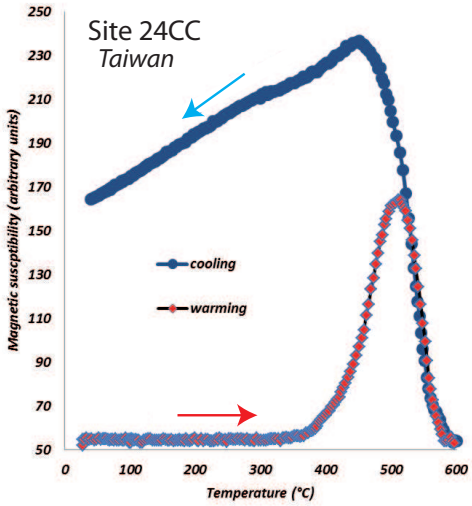

Figure 1 – Evolution of the magnetic susceptibility during heating (from 25 to 600°C) and cooling of an immature claystone from Taiwan. Note the irreversible behavior suggesting magnetic transformation : herein formation of magnetite.

Magnetic minerals and early diagenesis

Under anoxic conditions, iron-bearing minerals such as magnetite will react with H_2S, produced by bacterial activity (reduction of sulfate during the decomposition of organic matter). This leads eventually to the formation of pyrite FeS_2 with intermediate precursors such as greigite Fe_3S_4 and pyrrhotite Fe_7S_8 (Figure 2 ; e.g. Berner, 1984 ; Karlin, 1990).

During early diagenesis, in anoxic sedimentary environments, pyritization of detrital iron-bearing minerals leads to a decrease in magnetic properties of the sediments. Studies realized on anoxic marine sediments of the California continental borderland (Leslie *et al.*, 1990 and references therein) show a decay of the natural remanent magnetization NRM, carried by detrital magnetite, to 10% of its surface value. Rock magnetic measurements show differences in the rate and degree of magnetic intensity loss with depth. This is accompanied by a shift to softer coercivity component related to a coarsening of the magnetite grain sizes with depth. All are related to a dissolution process (Figure 3B), finest-grained magnetic minerals being preferentially dissolved (e.g. Bloemendal *et al.*, 1993).

The degree of dissolution is a function of several factors : surface area of the magnetite, concentration of dissolved sulfides and the time which magnetite is in contact with sulfidic pore fluids (Canfield & Berner, 1987). These parameters will depend on source rock and predepositional history of the sediment, sedimentation rate, sulfate reduction rate, depth and intensity of bioturbation, and finally reactivity of iron minerals contained in the sediment (Canfield & Berner, 1987). Much higher dissolution rates are observed in highly-sulfidic pore waters.

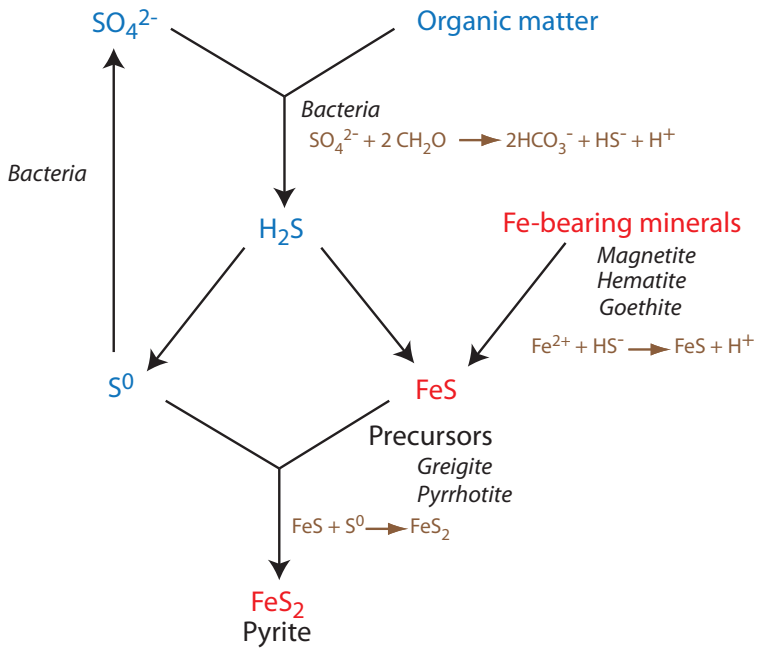

Figure 2 – Pyritization process in reductive environments during early diagenesis (after Berner, 1984)

Ferric Fe^{3+} ions dissociated from dissolved iron oxides are reduced into the ferrous divalent state Fe^{2+}. Then, ferrous ions react with hydrogen sulfide H_2S. Reduction of dissolved sulfate is driven by bacteria that use organic matter as a reducing agent. Formation of iron sulfides follows in a specific order : mackinawite ($FeS_{0.9}$), greigite or pyrrhotite and finally pyrite (e.g. Berner, 1984).

The formation of magnetic iron sulfides in anoxic environments results in a chemical remanent magnetization (CRM) which contributes to the NRM of the sediments together with a detrital remanent magnetization (DRM) carried by any magnetite that survives dissolution. This may have some importance in paleomagnetic studies, especially for the Earth's magnetic field recording and remagnetization issues (e.g. Horng *et al.*, 1998 ; Rowan & Roberts, 2005, 2006 ; Rowan *et al.*, 2009).

Laboratory experiments carried in conditions close to those of anoxic environments suggest that the formation of pyrite is not influenced by the nature of the iron-bearing precursor mineral (oxide or oxyhydroxide), but rather by pH and content in organic matter (Morse & Wang, 1997).

The dominant iron sulfide species formed during early diagenesis will thus depend on the respective amounts of reactants in presence. Organic carbon, dissolved sulfide and reactive iron are the principal controlling factors (Berner, 1984 ; Roberts & Turner, 1993 ; Kao *et al.*, 2004).

In marine environments, sulfates and detrital iron minerals are generally unlimited. Thus organic matter constitutes the limiting factor. In the case where little organic carbon is available, the increasing iron activity in fine-grained sediments may lead to the delay, even the arrest, of the pyriti-

zation process. This favors the preservation of the intermediate iron sulfides phases (Kao *et al.*, 2004). Mackinawite is unstable under natural conditions and then it is rapidly transformed into other iron sulfides such as greigite or pyrrhotite. Environmental conditions will control the formation of either mineral. Relative abundance of the reactive iron over the organic matter content seems to be the factor controlling formation of greigite or pyrrhotite (Kao *et al.*, 2004). Greigite preservation is favored by a combination of limited organic carbon, which limits microbial production of dissolved sulfide, and high concentrations of reactive iron. Greigite growth begins with the nucleation of nanoparticles at the sulfate-methane transition (Figures 3A and C ; Rowan *et al.*, 2009). The formation of pyrrhotite is favored by more reducing environments (low Eh) with higher H_2S concentration and more important organic matter consumption. On the other hand, occurrence of these iron sulfides depends also on the sediment grain size. Greigite occurs mainly in fine-grained sediments, whereas pyrrhotite is present in coarser-grained sediments (Horng *et al.*, 1998). This infers that formation of pyrrhotite and greigite occurs at different depths. Pyrrhotite would be formed at shallower depths than greigite.

In the case where organic carbon and dissolved sulfide are abundant, dissolved reactive iron will be completely sulfidized and pyrite will be the dominant authigenic sulfide formed (Rowan *et al.*, 2009). Laboratory experiments suggest that the formation of pyrite is more rapid in the presence of greigite. The pyritization of metastable iron sulfide minerals follows a dissolution-precipitation pathway (Wang & Morse, 1996).

Three main factors may eventually limit the formation of pyrite : 1) the amount and reactivity toward sulfate reduction of organic matter, 2) the amount and reactivity toward H_2S of detrital iron minerals and 3) the availability of dissolved sulfate (Berner, 1984).

The iron sulfides formed at an early burial stage are then altered at higher temperature (50-100°C). In late diagenesis stage, alteration of pyrite can lead to the formation of magnetite (e.g. Suk *et al.*, 1990 ; Suk *et al.*, 1993 ; Brothers *et al.*, 1996) and pyrrhotite in low-grade metamorphic conditions (Gillett, 2003 ; Horng & Roberts, 2006). Pyrrhotite and greigite can be oxidized and form iron oxides (Bina & Daly, 1994 ; Belzile *et al.*, 2004).

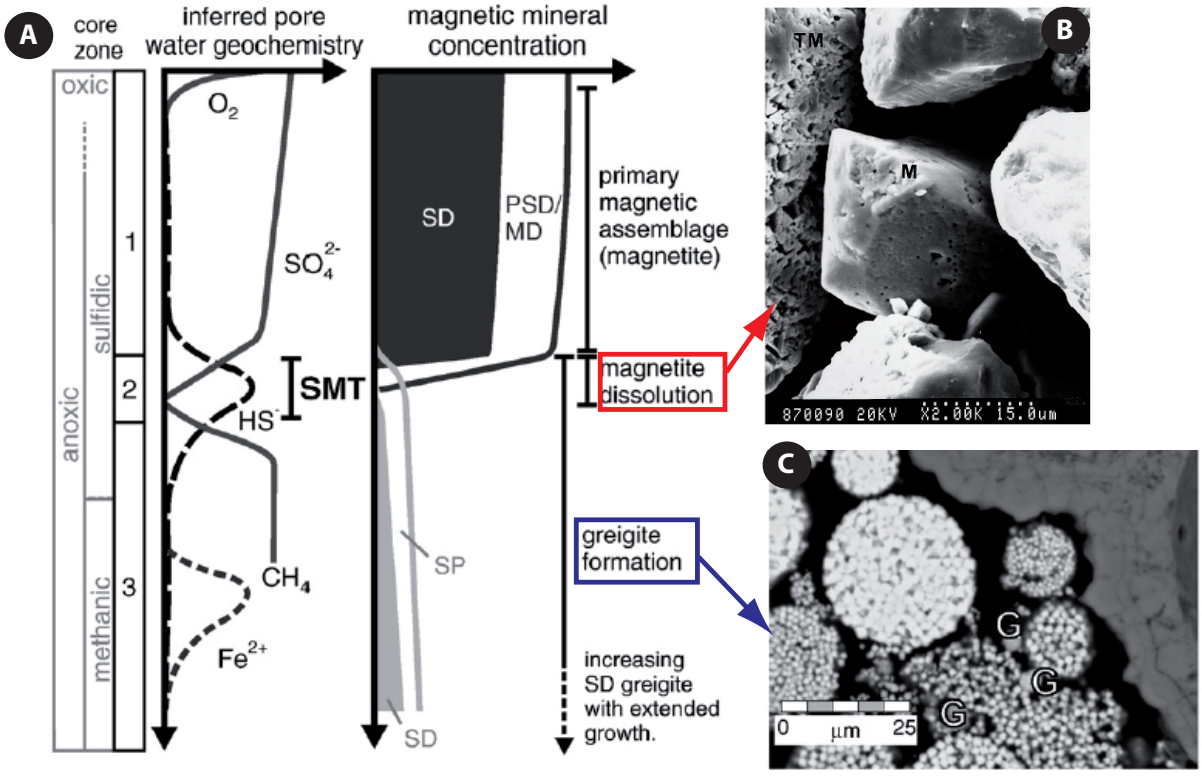

Figure 3 – A) Simplified model of magnetic mineral content in cores (Rowan *et al.*, 2009), B) SEM image of a magnetite grain M with dissolution pits on the surface (Horng *et al.*, 1998), C) SEM image of an early pyrite framboid surrounded by later space-filling pyrite and greigite G (Rowan *et al.*, 2009). SMT is the sulfate-methane transition. SP : superparamagnetic, SD : single domain, PSD : pseudo single domain, MD : multidomain

Some proposed magnetic geothermometers

In the last two decades, attempts have been made to correlate the development of magnetic minerals and the burial temperature experienced by the rocks.

Rochette (1987) was one of the first to establish the so-called "magnetic isograde" which separate areas of occurrence of a given magnetic mineral based on magnetic susceptibility measurements. In Swiss Alps metamorphic units whose experienced temperature is > 250°C, Rochette (1987) determined two isograde based on the breakdown of magnetite Fe_3O_4, and the breakdown of pyrite FeS_2 into monoclinic pyrrhotite Fe_7S_8 (Figure 4). These reactions are produced by the progressive maturation of the organic matter that yields increased reducing conditions. The two isograde characterize the boundary between the anchizone and the epizone (∼250°C), and the middle epizone (∼320-350°C) respectively.

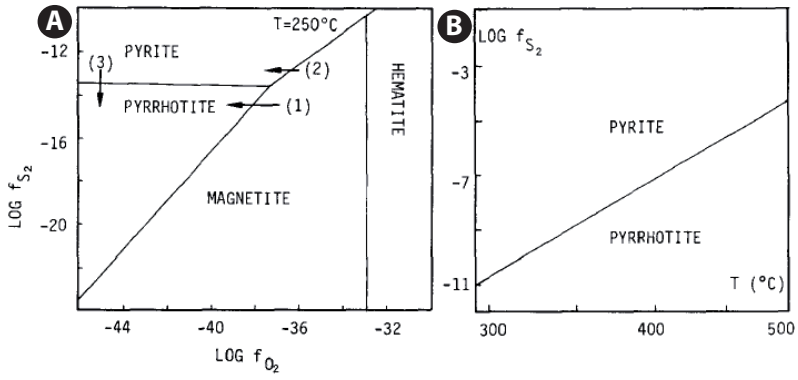

Figure 4 – A) Phase diagram of iron at 250°C as a function of sulfur and oxygen fugacity (after Crerar *et al.*, 1978) and B) Pyrite-pyrrhotite equilibrium as a function of temperature and sulfur fugacity (after Barker & Parks, 1986) (extracted from Rochette, 1987)

A pretty spectacular example of the entire consumption of magnetite is provided by the Dauphinoise Zone from the French Western Alps. There, the natural remanent magnetization NRM of Jurassic limestones is carried only by single domain pyrrhotite formed at the expense of magnetite, with cooperation of organic matter (Rochette *et al.*, 1992 ; Crouzet *et al.*, 1997). This NRM is a thermo remanent magnetization (TRM) as cooling of these rocks from ∼350°C (peak metamorphism) started above the Curie temperature of pyrrhotite (Tc∼320°C). Using this TRM record of exhumation of metamorphic rocks, Crouzet *et al.* (1999) estimated a vertical geothermal gradient based on unblocking temperatures of pyrrhotite in a vertical transect at a given Earth's magnetic reversal (∼20 Ma). By using thermopaleomagnetic method, a reconstruction of the cooling history of the Dauphinoise Zone can be realized (Crouzet *et al.*, 2001).

Interestingly, two potential magnetic geothermometers, based on the presence of pyrrhotite and magnetite respectively, have been proposed. One is related to the record of a thermoviscous remagnetization (Dunlop *et al.*, 2000) and the second one is based on the relative consumption of magnetite, monitored by the record of the NRM (Schill *et al.*, 2002).

At a given burial temperature, the rocks will be remagnetized by a process of thermo-viscous remagnetization. As Curie temperatures of pyrrhotite and magnetite are different, there is the potential to retrieve the peak burial temperature by characterizing the spectrum of unblocking temperatures of rocks carrying pyrrhotite and magnetite. This technique requires that pyrrhotite and magnetite are present before the burial and that NRM is either carried by pyrrhotite and magnetite without superimposition of the two. In practical, this technique cannot be used in sedimentary rocks and may be limited to plutonic rocks. Thermal overprinting of NRM can occur in any rock type over broad temperature ranges : up to 580°C for magnetite and up to 320°C for monoclinic pyrrhotite. This "remagnetization geothermometer" (Pullaiah *et al.*, 1975) is based on the Néel theory of magnetic single domain grains which links temperature, time and grain size (Néel, 1949). This was applied by Dunlop

et al. (2000) in the Triassic Milton Monzonite in the Sydney Basin, Australia (Figure 5). Their temperature estimate of the remagnetization is comparable to the value calculated from vitrinite reflectance data.

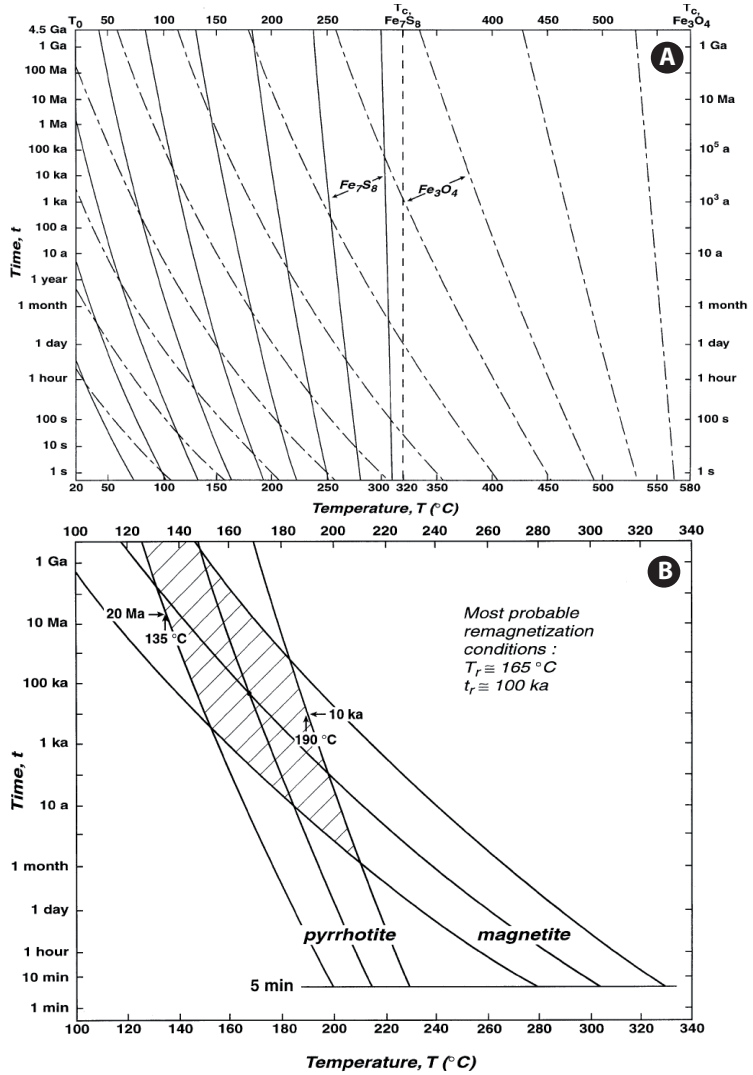

Figure 5 – A) Monograms showing the time vs. temperature contours for the acquisition of a thermoviscous magnetization for magnetite and pyrrhotite and B) determination of the remagnetization conditions in the Milton Monzonite (Dunlop *et al.*, 2000). The burial temperature is here estimated at 165 ± 30°C.

Another thermal dependence of pyrrhotite/magnetite ratio was investigated by Schill *et al.* (2002) in the Mesozoic metacarbonates of the Thethyan Himalayas in Nepal. Two characteristic remanent magnetizations (ChRM) were found. ChRM1 is carried by pyrrhotite and ChRM2 is carried by ma-

gnetite which is of detrital origin. Pyrrhotite is formed at the expense of magnetite and its formation is temperature-dependent in carbonates during low-grade metamorphism (Rochette, 1987). During the thermal demagnetization of the NRM and the SIRM (saturation isothermal remanent magnetization), they observed a variation of the content of pyrrhotite and magnetite. The ratios of remanence intensities of both minerals in the NRM and SIRM were used for the determination of thermal gradients in low-grade metamorphic carbonates for temperature < 300°C.

Very recently, another pyrrhotite/magnetite geothermometer, called MagEval (Aubourg & Pozzi, 2010), was proposed based on the evolution of the remanence between 10 and 35 K. This new geothermometer is described in detail in chapter IV and calls upon the progressive development of fine-grained pyrrhotite with burial/temperature.

The objective of this thesis is to better characterize the MagEval geothermometer in order to help to the reconstruction of the thermal history of sedimentary basins. More precisely, the aim was specifically to calibrate and evaluate the applicability of this new geothermometer. This new tool, complementary to the standard geothermometers, would be particularly useful in cases where the latter show limitations.

To first verify that the MagEval signal was commonly observed in nature in sedimentary basins, measurements of magnetic properties in a number of selected wells were carried out. This first step also permitted to establish selection criteria for identifying samples suitable for MagEval geothermometry. Two wells exhibiting a well-defined evolution of the MagEval signal were studied in greater details in order to establish the temperature calibration of the geothermometer.

In a second step, the established calibration was applied in two test areas where thermal history was known : 1) the Grès d'Annot basin, SE France and 2) the Appalachians thrust belts, West Virginia, USA. This was done to confront the MagEval geothermometer calibration and evaluate the soundness of this magnetic approach.

In parallel, laboratory heating experiments have been conducted in order to constrain the empirically defined calibration. Two types of procedures were used : 1) open conditions under magnetic field to follow the formation of magnetic minerals during temperature increase and 2) confined conditions in gold capsules to better approach conditions occurring during burial in nature.

The present manuscript is organized as follows :

- Introduction
- Part A : Background and Methods
  - Chapter I : Frequently used geothermometers in basin thermal history reconstitution
  - Chapter II : Elements of Rock Magnetism
  - Chapter III : Methods
- Part B : MagEval Geothermometry

  - Chapter IV : The MagEval Geothermometer
  - Chapter V : Laboratory Heating Experiments
- Part C : Field Case Studies
  - Chapter VI : Magnetic Assemblage in the Grès d'Annot Basin, SE France
  - Chapter VII : Magnetic Assemblage in the Appalachians, West Virginia, USA
- Synthesis
- Conclusion and Perspectives

A list of symbols and abbreviations frequently used in the text is added at the end of the manuscript.

Part A

Background and methods

Chapter I

FREQUENTLY USED GEOTHERMOMETERS IN BASIN THERMAL HISTORY RECONSTITUTION

Reconstructing thermal history of sedimentary rocks is an important part in understanding basin history and hydrocarbons generation. One particular key information is the determination of the maximum temperature reached by sediments during vertical movements associated with basin-fill. However, this reconstitution is not always easy. For instance, in sedimentary basins where erosion was significant, the maximum temperature reached in the past by sediments may be very different (higher) from the present day maximum temperature. Similarly, in basins with essentially no erosion, where rocks are considered to be at maximum burial, variations of paleogeothermal gradient might have occurred related to the basin geodynamic evolution and/or to the development of isolated thermal events (e.g. magmatic intrusion, changes in heat flux ...).

Nevertheless, a range of geothermometers based on minerals and organic matter properties in sediments is available to estimate the maximum temperature experienced by a rock and its maturity.. The geothermometers are based on specific physical and/or chemical parameters of inorganic and organic components which vary with temperature. Their thermal dependence is calibrated, with variable accuracy, on the basis of theoretical, experimental or empirical grounds. In this chapter, the most commonly used geothermometers are presented, with greater emphasis for those used in the thesis.

1 Organic geothermometers

No organic parameter can be directly converted in terms of paleotemperature. The evolution of organic matter depends on its initial type/composition and on the integrated time/temperature history it experienced.

Chapter I. FREQUENTLY USED GEOTHERMOMETERS IN BASIN THERMAL HISTORY RECONSTITUTION

1.1 Composition of organic matter

Hydrocarbons, in a broad sense, result from transformation of buried organic matter. At the surface (marine or terrestrial environments), vegetal organisms such as plants, algae, phytoplankton, absorb 90% of carbon and hydrogen by photosynthesis. The remaining 10% are used by animals. All is not released into the atmosphere : a part is trapped in sediments and transforms in carbon-bearing products during diagenesis/burial. Organic matter transportation, recycling by other organisms, chemical alteration and deposit environment are among factors which play a role in the preservation and the concentration of organic matter in sediments. On average, organic matter content of sedimentary rocks is around 0.5%. Sediments with organic content in the range of 4 to 12%, are considered potential source rocks capable of generating hydrocarbons. According to the type of organic matter, source rocks yield different types of kerogen and so different kinds of deposit. Three initial types of kerogen are identified according to the origin and sedimentation conditions. They are differentiated on the basis of H/C and O/C ratios (Tissot *et al.*, 1974), conventionally plotted in a so-called Van Krevelen diagram (Van Krevelen, 1961) (Figure I.1) :

- Type I : high H/C, low O/C. This type of kerogen is formed in lacustrine environments and comes from algal and bacterial lipid products. A typical example is the Green River Shale, Cretaceous, USA. This type of kerogen is rare ;
- Type II : intermediate H/C and O/C. Type II is characteristic of anoxic marine environments. It is mainly planktonic in origin, with sometimes some detrital materials. Toarcian argillites (Early Jurassic) of the Paris Basin, France, constitute a typical example of type II kerogen ;
- Type III : low H/C, high O/C. This kerogen is generally associated with proximal deltaic environments. It is derived from vegetation products of continental origin. A typical example is the Miocene argillites from the Mahakam Delta, Indonesia.

A forth type was later defined by Tissot (1984) as type IV, characterized by a very low H/C and high O/C. This type of kerogen (not shown in Figure I.1) consists of highly reworked organic matter with no hydrocarbon generative potential.

Evolution of organic matter is a function of burial and time. In the first stage of burial, sediments and organic matter undergo early diagenesis. This leads to the formation of kerogen and bitumen. Kerogen is the insoluble fraction of the organic matter (80 to 95% of organic content), while bitumen is the soluble fraction. At this stage, bacteria release methane (bacterial or biogenic gas). During further burial, kerogen and sediments experienced temperature increase. Kerogen begins to loose its oxygen components as H_2O and CO_2. Decrease of O/C is therefore faster than that of H/C. At greater depths, catagenesis processes occur which produce oil and light hydrocarbons (condensate gas). Decrease of O/C ratio is slowed down, while the H/C ratio decreases rapidly. Thermal cracking is efficient. The depth interval at which hydrocarbon generation occurs is called the oil window, and corresponds to temperatures varying from about 60 to about 120°C (Biju-Duval, 1999). The last step of evolution is

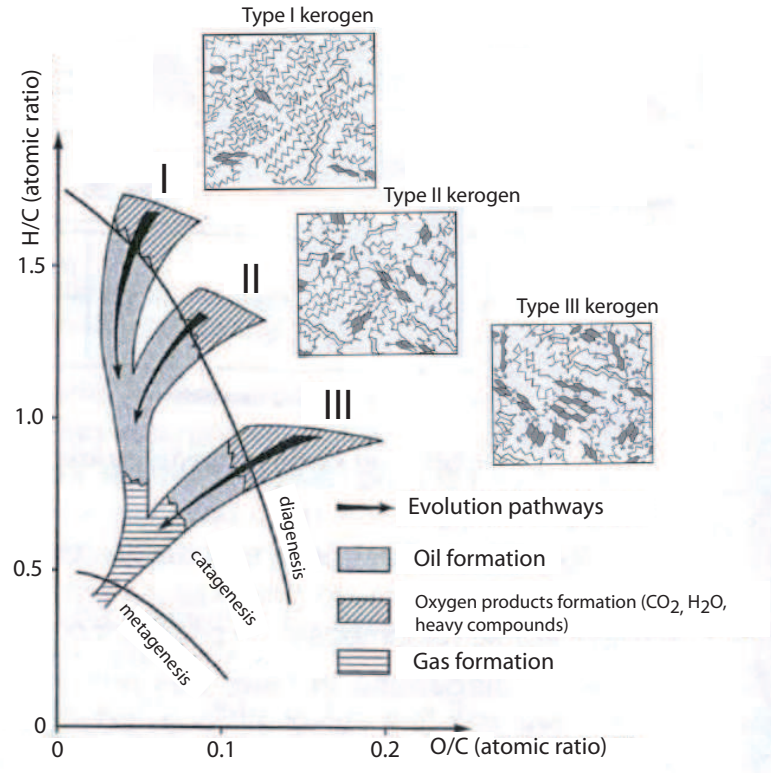

Figure I.1 – Evolution pathways of the three main kerogen types plotted in a Van Krevelen (H/C vs. O/C) diagram (after Bordenave, 1993)

metagenesis, which is characterized by formation of dry gas (thermogenic methane). This corresponds to the gas window, occurring from about 120 to 200°C.
The three main types of kerogen experienced different evolution pathways during burial and temperature increase, in relation with their different initial compositions, leading to the formation of somewhat different products. CO_2 content release depends on O/C ratio and decreases from type III to type I. Hydrocarbons quantity depends on H/C ratio and increases from type III to type I. Type III is said to be gas prone kerogen, while type I is said to be oil prone.

1.2 Vitrinite Reflectance Ro

The most common geothermometer used in oil industry is vitrinite reflectance, expressed as Ro or VRo (o stands for oil), because of its sensitivity to temperature in the range corresponding to hydrocarbons generation (60-120°C) although it was initially developed for coal classification. Vitrinite is a maceral and a microscopic component of kerogen (Figure I.2A). It is abundant in organic matter of continental origin. Vitrinite forms by thermal alteration of lignin and cellulose from cell membranes of plants. With increasing maturity, chemical composition and structure of vitrinite change leading to an increase of its reflectance (Figure I.2B). These transformations are irreversible.

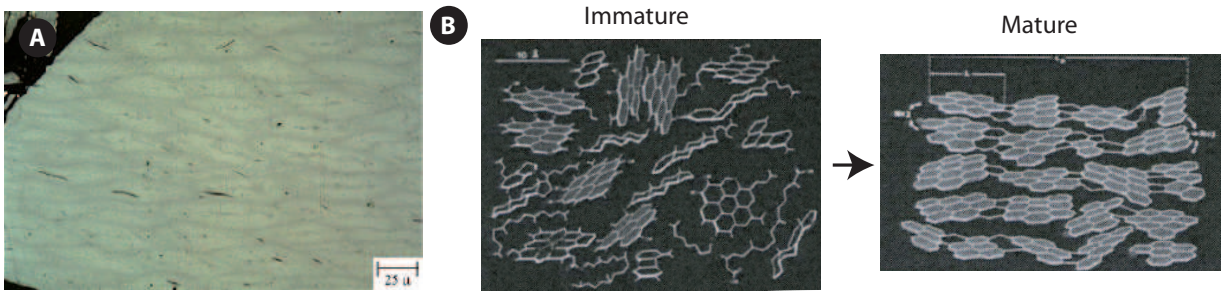

Figure I.2 – A) Vitrinite (microscopic image) and B) its structure evolution as a function of maturity

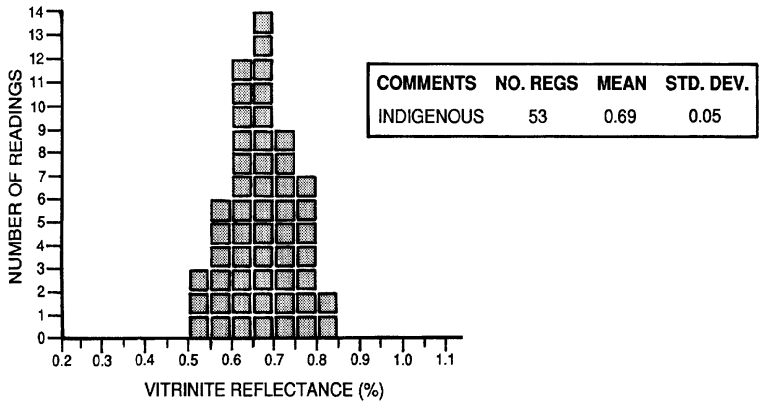

Figure I.3 – Typical histogram of vitrinite reflectance measurements showing a normal distribution (Senftle & Landis, 1991)

Vitrinite reflectance is defined as the proportion of reflection of a white light incident ray normal to the polished surface of a vitrinite sample. Number of measurements performed on a single sample must be sufficiently high (between 30 and 100) to yield a reliable estimate of sample maturity. Measurements are reported as histograms (Figure I.3). Measured Ro values must theoretically exhibit a normal distribution, and Ro is thus reported as the average value associated to the 1σ standard deviation. Oil window is defined as the Ro interval going from 0.5-0.6 to 1.2% and gas window from 1.2 to 3%. These limits may vary slightly according to authors and oil companies.

The Ro method has some limitations. As vitrinite reflectance can only be measured on samples bearing vitrinite, it implies that it cannot be applied to geological formations free of vitrinite, i.e. formations older than Silurian. Vitrinite is fairly common in organic matter-rich sedimentary rocks (e.g. shales). In contrast, carbonates and evaporites are usually devoid of vitrinite. Because of the origin of this maceral, this method is well adapted for type III kerogen, but not for type I. Moreover, vitrinite is absent in pre-Silurian rocks (before 440 Ma) because terrestrial plants had not developed yet. Identification of vitrinite under the optical microscope requires an expert eye. The operator must

be experimented to distinguish vitrinite from the other macerals, or significant errors may arise. Core and outcrop samples are preferred from cuttings which can be contaminated by drilling material. In spite of the above listed limitations, the VRo method has many advantages which overcome disadvantages.

This method, applicable on a broad range of temperature of interest, allows a fairly accurate estimate of paleotemperature of a sedimentary basin. However, correlation between vitrinite reflectance and maximum paleotemperature is not direct. Indeed, vitrinite maturity reflects integrated evolution of time and temperature. Generally, the thermal history of a rock can be considered to be described as a succession of discrete intervals of temperature. Kerogen maturity in rocks can therefore be estimated using the following equation (Lopatin, 1971, 1976 ; Waples, 1980) :

$$\mathrm{TTI} = \sum(\Delta t_i)(2^{n_i})$$

in which Δt_i is the time (Ma) spanned by kerogen in the i^{th} temperature interval, n_i is an integration weighting factor for the i^{th} interval and TTI stands for time-temperature index. A TTI value alone does not make sense because it is based entirely on an arbitrary system of temperature intervals and weighting factors. It therefore needs to be calibrated using other maturity indicators. Some authors proposed a calibration between TTI and vitrinite reflectance. The calibration is quasi-linear in a log-log diagram and it can be written as follows :

$$\ln\,(\mathrm{TTI}) = \mathrm{A} \times \ln\,(\mathrm{Ro}) + \mathrm{B}$$

for TTI values calculated from the previous equation. A and B are constants with variable values depending on authors.
Barker & Pawlewicz (1986) compiled more than 600 vitrinite-temperature couple data in basins with well known thermal history. They proposed the following relationship :

$$\ln\,(\mathrm{Ro}) = 0.0078 \times \mathrm{Tmax} - 1.2$$

(Ro in % and Tmax in °C where Tmax represents the maximum burial temperature). This relation, however, is a significant approximation as it does not take time into consideration (Beardsmore & Cull, 2001).

Development of chemical kinetic models allows modeling of the evolution of vitrinite reflectance as a function of integrated time and temperature (Burnham & Sweeney, 1989). The most commonly used method is the one developed by Sweeney & Burnham (1990) from LLNL (Lawrence Livermore National Laboratory, California, USA) called Easy%Ro. Easy%Ro is a kinetic model of vitrinite evolution based on a first order Arrhenius law with energy distribution. In this model, vitrinite reflectance %Ro is

expressed as :

$$\%\mathrm{Ro} = \exp(-1.6 + 3.7\mathrm{F})$$

in which F = 1-$\frac{w}{w_0}$ with $\frac{dw}{dt}$ = -kw and k = A exp(Ea\RT). w represents the amount of non reactant component, w_0 the initial concentration of total reactants, A the pre-exponential factor, Ea the activation energy (kJ/mol), R the ideal gas constant and T the temperature (K).

This first order Arrhenius law governs also the kerogen transformation into hydrocarbons. This model is used for Ro values ranging between 0.3 and 4.5%, by considering heating rate between laboratory (1°C/week) and slowly subsiding basin rates (1°C/10Ma) (Figure I.4). Sweeney & Burnham (1990) model supposes that pressure is high enough, so that time and temperature are the sole important variables. They noticed previously that pressure is not of particular importance in type I and type II kerogens, but could be a key parameter for type III (Burnham & Sweeney, 1989). The model was then modified by Dalla Torre *et al.* (1997) and Carr (1999) in order to take into consideration the effect of pressure. Pressure may delay vitrinite maturation by retaining volatile products inside solid vitrinite, thereby preventing vitrinite reorganization and slowing down increase of reflectance.

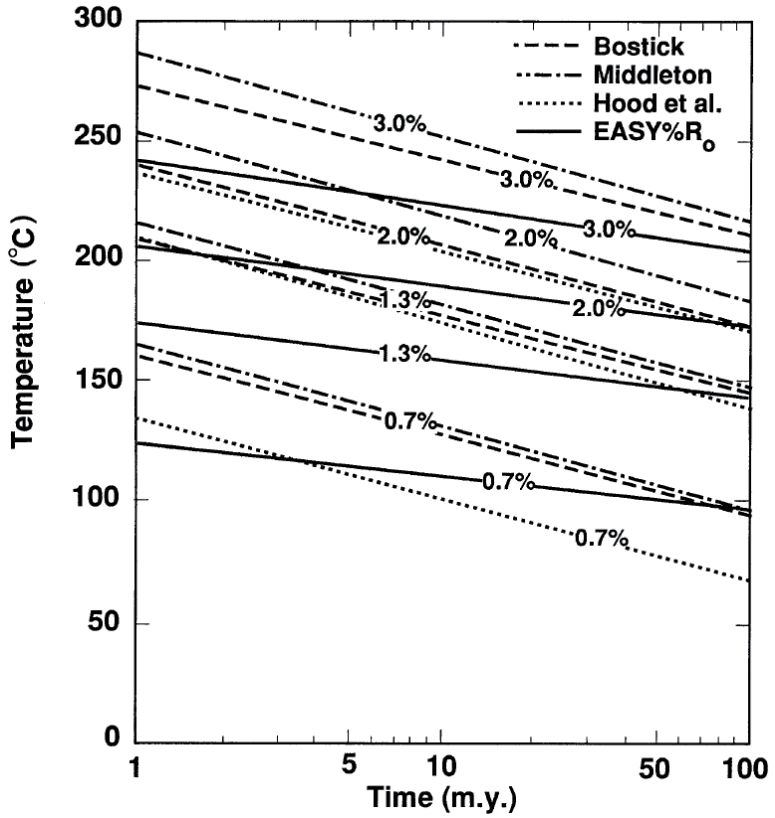

Figure I.4 – Monogram of reflectance vitrinite as a function of time and temperature (Sweeney & Burnham, 1990 and references therein)

A model equivalent to that of the LLNL was developed by IFP [1] (Tissot *et al.*, 1987). The main difference resides in the choice of the entry parameters, such as the pre-exponential factor and the activation energies (Waples & Marzi, 1998; Waples *et al.*, 1992). In general, the LLNL model predicts faster kinetics of oil and gas generation than the IFP model, even though minor oil generation does occur earlier in the IFP model (Figure I.5 ; Waples *et al.*, 1992).

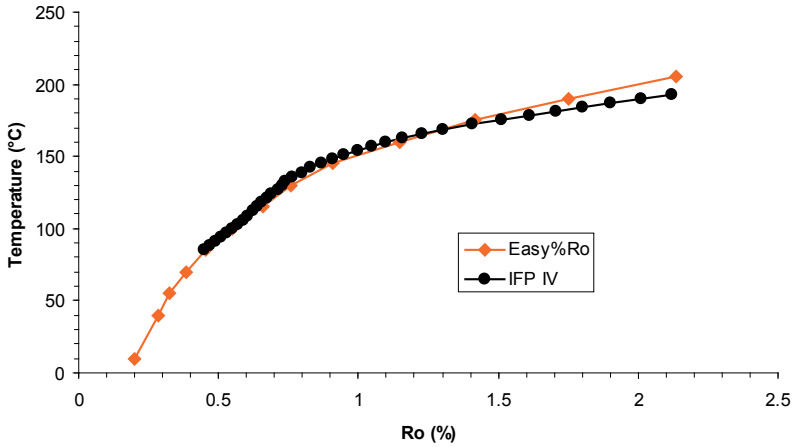

Figure I.5 – Comparison of the evolution of vitrinite reflectance Ro as a function of temperature in the LLNL (Easy%Ro) and IFP models, based on a constant heating rate of 3°C/Ma

In the absence of vitrinite, reflectance measurements can be performed on other particles of organic matter, such as bitumen or graptolites (Bertrand, 1990). These measurements can then be converted in equivalent vitrinite reflectance (%eq.Ro) using appropriate conversion factors. For instance, Jacob (1985) related bitumen reflectance (BR) and vitrinite reflectance (VR) by the following equation :

$$\mathrm{VR} = 0.618 \times \mathrm{BR} + 0.4$$

The maturity range of a sample can also be estimated from observations of organic particles in transmitted light. In this case, color, transparence and morphology of some microfossils such as spores, pollens, algae, conodonts, are the parameters of interest. Several indices can be defined based on changes in color, opacity of these fossils with respect to temperature.

1.3 Thermal Alteration Index TAI

Thermal Alteration Index (TAI) of Staplin (1969) is an arbitrary scale which ranks progressive change in color and opacity of liptinite with temperature. Liptinite is a maceral derived from spores, pollens and leaves cuticles.

Palynomorphs change color when thermally altered. They become darker with maturity increase

1. Institut Français du Pétrole, now IFP-En Energies Nouvelles, France

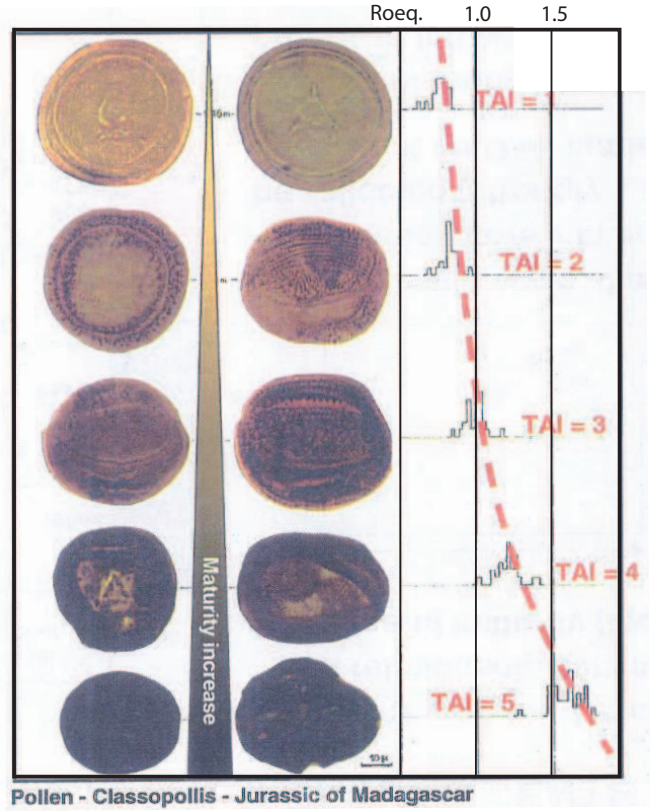

Figure I.6 – Thermal Alteration Index (TAI) compared with %eq.Ro for different pollens maturities

(Figure I.6). TAI varies from 1 for strictly immature spores and pollens (light yellow color) to 5 for a strong thermal evolution corresponding to dry gas zone and beyond (black color). Below TAI = 2, no oil is expected, whereas above TAI = 3.5 thermal conditions are identical to that of gas zone. Oil window is restricted to a narrow range of values (between 2 and 2.7).

Although this technique, widely used, provides a general indication of organic matter maturity, its application is quite limited. It is necessary to have a significant biological diversity of palynomorphs to improve reliability of the results. In addition this method is laboratory-specific and somewhat subjective because one must define the observed color with respect to a standard scale (appreciation of color matching may be different from one analyst to the other). Low resolution of this index limits precision of paleotemperatures estimation by ± 20°C.

1.4 Conodont Alteration Index CAI

Conodont Alteration Index (CAI) is, like TAI, an arbitrary scale with 8 levels related to progressive changes in color and opacity of conodonts with temperature (Epstein *et al.*, 1977). Conodonts are extinct chordates looking like eels. CAI is performed on conodonts teeth (Figure I.7), which are composed of apatite.

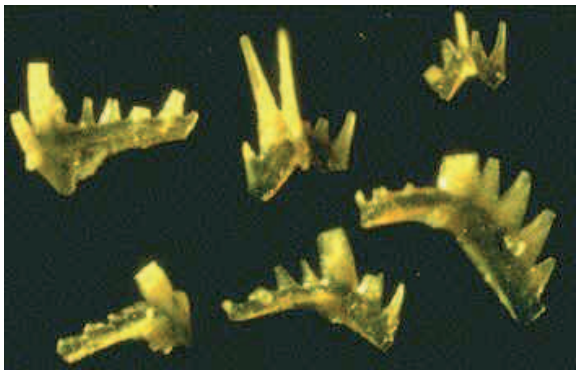

Figure I.7 – Conodonts elements (0.1-1 mm)

Determining CAI is quite fast because this method does not require any sophisticated protocol. However, this index is valid only for Paleozoic and Triassic (before 200 Ma). In addition, CAI suffers the same limitations as TAI. Color assignment may vary from one operator to another due to subjectivity of color determination. One CAI value may reflect a wide temperature range (Table I.1). Uncertainty on the maximum temperature is comprised between ± 20 and ± 50°C. This is too high to allow detailed reconstitutions of thermal history.

CAI	Colour	Paleotemperature (°C)	Thermal Maturity
1.0	Pale yellow	50-80	Immature
1.5	Very pale brown	50-90	Early mature
2.0	Brown to dark brown	60-140	Mature
2.5		85-180	Late mature
3.0.	Very dark grey	110-200	Overmature
3.5		150-260	Overmature
4.0	Light black	190-300	Partially carbonized
4.5		230-240	Partially carbonized
5.0	Dense black	300-400	Carbonized
5.5	Dark grey-black	310-420	Early volatilization of carbon
6.0	Grey	350-435	Volatilization of carbon
6.5	Grey-white	425-500	Late volatilization of carbon
7.0	Opaque white	480-610	Carbon fully volatilized
7.5	Semi-translucent	>530	Partially recrystallized
8.0	Transparent	>600	Recrystallized

Table I.1 – Conodont Alteration Index (CAI) and corresponding paleotemperature (Helsen *et al.*, 1995)

Other color indices can be found in literature, which are not developed here. One can cite Spore Coloration Index (SCI, Barnard *et al.*, 1976) based on spores color variations and Acritarch Alteration Index (AAI, e.g. Tyson, 1995) based on phytoplanktonic algae color. Several approaches were tested in order to eliminate human-related errors by correlating such color indices with more objectively

measured/observed optical characteristics, such as fluorescence, but they did not reveal successful.

1.5 Fluorescence

Fluorescence is a physical property of atoms and molecules that absorb light at a given wavelength and emit light at a higher wavelength after some time. Fluorescence of organic materials is measured in white light after UV excitation.

Some exinite-rich biological particles such as spores, pollens, algae show generally the strongest fluorescence whereas their reflectance is the lowest. Exinite is a maceral derived from the resistant lipid part of certain plants. In contrast, samples containing vitrinite show an important reflectance and a medium fluorescence.

Evolution of fluorescence spectrum varies with thermal alteration, hence with maturity (Figure I.8). This method can be used in complement to vitrinite reflectance measurements. Nevertheless, its resolution and applicability domain are more limited than Ro.

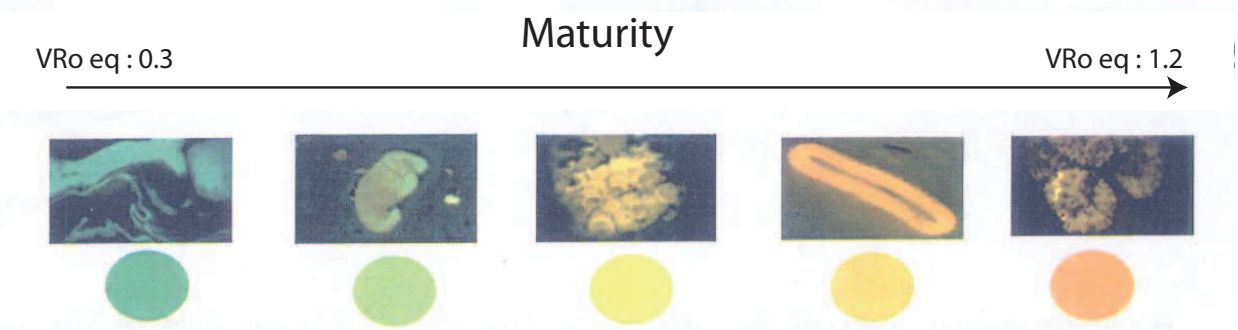

Figure I.8 – Fluorescence as a function of degree of maturity expressed in terms of %eq.Ro

1.6 Rock Eval pyrolysis

This is the most comprehensive method to characterize petroleum evolution (Espitalié *et al.*, 1977 ; Lafargue *et al.*, 1998). This technique consists in thermally cracking bulk rock samples (not kerogen extracts) allowing determination of free hydrocarbons, oxygen and carbon components (CO_2) and total organic carbon content (TOC) in the sample, in order to characterize type, potential and maturity of the source rock.

A small quantity of rock (∼100 mg) is heated under helium atmosphere at 300°C for 3 minutes, then temperature is increased by 25°C step every minute until it reaches 600°C. The residue of this pyrolysis is then oxidized by air introduction.

Parameters measured chronologically during heating are (Figure I.9) :

– S1 peak : quantity of free hydrocarbons (oil and gas) volatilized at 300°C for 3 minutes (in mgHC/g of rock). Free hydrocarbons are then S1/g rock

– S2 peak : quantity of hydrocarbon products from kerogen cracking (but also from extractable heavy compounds such as resins and asphaltenes) between 300 and 600°C (in mgHC/g of rock). This is the expression of petroleum potential (PP = S2/g rock)
– Maximum temperature Tmax reached at the top of S2 peak. This temperature does not necessarily correspond to maximal burial temperature experienced by the organic matter (rock) in natural conditions. Tmax measured by Rock Eval is an analytical parameter which provides information on the maturity
– S3 peak : quantity of CO_2 resulting from decomposition of oxygen components between 300 and 390°C (in mgCO_2/g of rock)
– Content in residual organic carbon (%weight) obtained by combustion at 600°C. Resulting CO_2 corresponds to the S4 peak (in mgCO_2/g of rock).

From the different measurements, several parameters can be calculated as follows :

– Total Organic Carbon (TOC) content : residual organic C + organic C from pyrolysis deduced from S1 and S2 peaks
– Hydrogen Index : HI = S2/TOC
– Oxygen Index : OI = S3/TOC
– Transformation Ratio : TR = S1/(S1+S2)

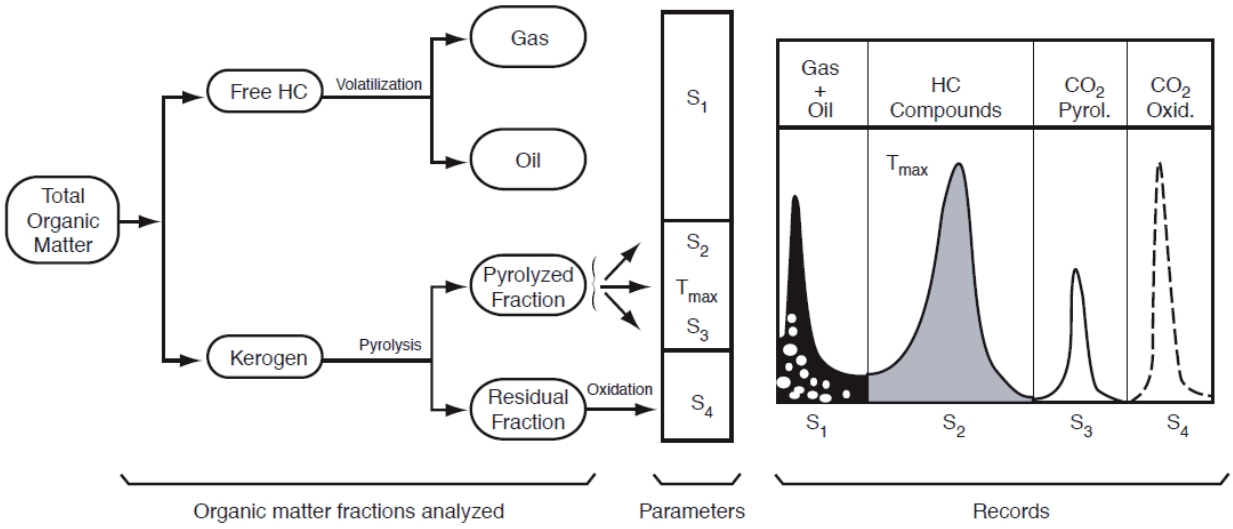

Figure I.9 – Rock Eval principle (Lafargue *et al.*, 1998). See text for explanation.

The greater the thermal maturity of the original rock, the lower the amount of potential hydrocarbons still contained within the kerogen. Two aspects of the pyrolysis plot (Figure I.9) are related to the effects of increasing maturity. Firstly, the location of S2 peak moves progressively to the right (leading to increasing Tmax values) and secondly the amplitude of the S1 peak increases relatively to the S2 peak.

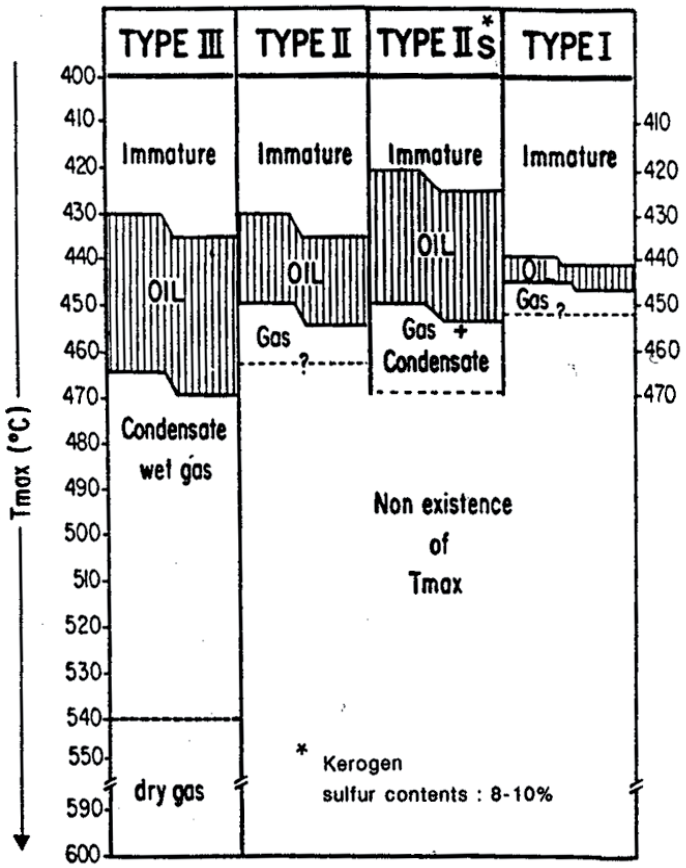

Figure I.10 – Relation between maturity and Tmax values for the different kerogen types (Bordenave, 1993)

Among the different Rock Eval parameters, Tmax is the one used to assess the thermal maturity of a rock. Tmax value is function of the organic matter maturity. Mature organic matter being more condensed is more difficult to pyrolyse due to greater activation energy, i.e. a higher temperature to initiate reaction. It therefore displays higher Tmax values. Tmax evolution depends on the type of organic matter and it is mainly used for types II and III kerogens. Tmax values for oil and gas windows vary according to the kerogen type (Figure I.10). Types I and II kerogens exhibit less complex molecular structures than type III (Figure I.10). This induces a narrower distribution of activation energies and a faster kinetics of cracking for types I and II.

For type I, oil generation starts when Tmax is 440°C and Ro is closed to 0.7%. Cracking is rapid and all kerogen is transformed when Ro reaches 1%, whereas Tmax is roughly constant. For type II, the beginning of oil generation seems to occur for Tmax = 435°C (Ro∼0.6-0.65%). The most part of kerogen is transformed for Tmax = 445°C (Ro = 1%). Gas and condensate areas correspond to a range of Tmax values between 455 and 470°C. For type III, hydrocarbons are formed for Tmax higher than 435°C (Ro∼0.6%). Condensate gas zone corresponds to Tmax = 470°C. Dry gas are generated for

Tmax > 540°C (Bordenave, 1993). A correspondence between Tmax and Ro is represented in Figure I.11 for type III.

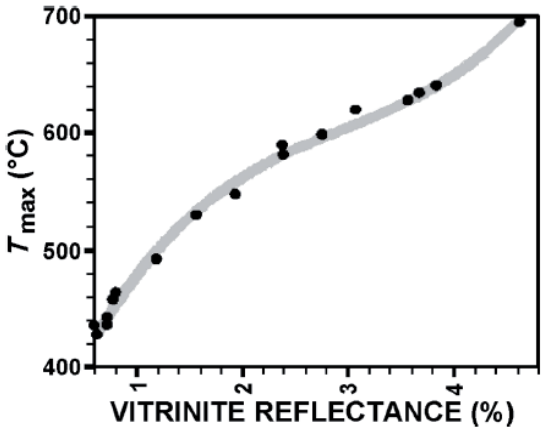

Figure I.11 – Correlation between Tmax and Ro for type III kerogen (Deville & Sassi, 2006)

Due to the strong influence of kerogen type on Tmax values, the latter should only be compared for samples containing the same kerogen type.

Rock Eval pyrolysis results have little significance for samples depleted in organic matter. Moreover, influence of pollution by drilling mud and natural impregnation by hydrocarbons may dominate, or even overwhelm the contribution of organic matter within the sample to the Rock Eval signal. This kind of pollution is characterized by Tmax values abnormally low, generally less than 400°C. Tmax measurements for overmature kerogen are not very reliable because of the rather flat morphology of the S2 peak (Bordenave, 1993).

1.7 Molecular biomarkers

The chemical reactions that take place during the thermal evolution of kerogen are many and complex. Molecular biomarkers are geochemical fossils and they are found in sediments, source rocks and liquid hydrocarbons (Peters *et al.*, 2005). No biomarker is found in gas. They have structures inherited from once-living organisms. They are deriving from molecules constitutive of cell membranes of plants (chlorophyll) or animals. The effect of temperature on reactions involving biomarkers can be investigated if there is a strong relationship between two molecules : one parent-reactant, the other daughter-product. The relative concentrations of such two molecules can then yield information about the sample maturity.

Several processes occurring during maturation lead to changes in biomarkers (Beardsmore & Cull, 2001) :

- Cracking : large molecules break into smaller ones
- Isomerization : changes in 3D arrangements of atoms in molecules

– Aromatization : formation of aromatic rings - loss of hydrogen

Some biomarker families are commonly studied in the oil industry, in particular steranes and hopanes from animals and phytanes and pristanes from plants (Figure I.12).
These biomarkers differ from their C atoms and aromatic cycle numbers. Because of the tetravalent structure of carbon, molecules may have different spatial configurations but a same chemical composition. They are called isomers R and S.

Let's consider steranes as an example. In nature, sterane 20R is produced. During hydrocarbon formation, sterane molecules are chemically excited and tend toward the thermodynamic equilibrium. This equilibrium is reached when sterane 20S amounts for 60% of total sterane. 20S/20R ratio increases with maturity. On the other hand, progressive aromatization of molecules which increases with maturity can also be used like biomarker. Several considerations must be kept in mind when assessing source rock maturity by use of molecular biomarkers (Beardsmore & Cull, 2001) :

– Relationship between biomarker and source maturity is function of heating rate, source lithofacies and kerogen type
– Biomarkers are applicable only over a specific maturity range
– Concentrations of biomarkers decreases with thermal maturity

More detailed information about biomarkers can be found in Peters *et al.* (2005).

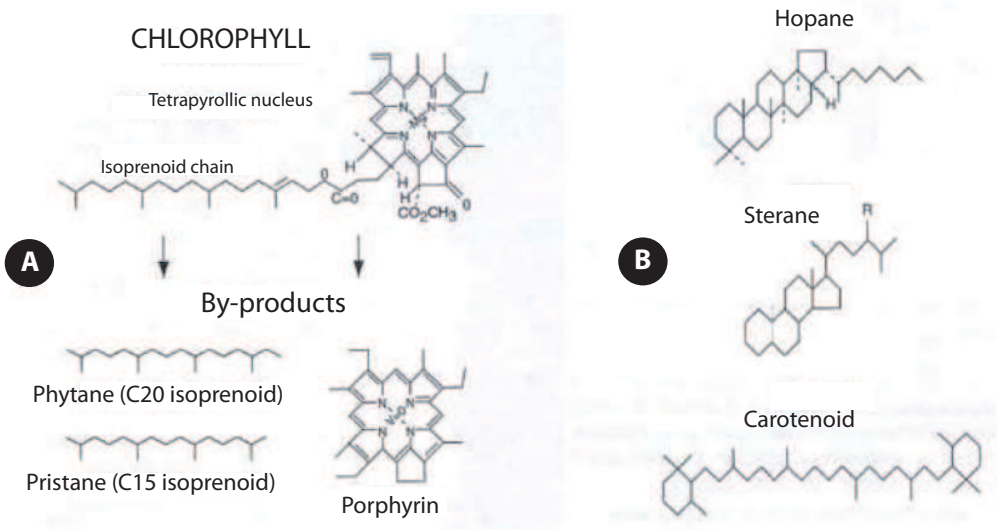

Figure I.12 – Some biomarkers. A) chlorophyll and B) animals cell membranes by-products (Biju-Duval, 1999)

2 Inorganic geothermometers

2.1 Fluid Inclusions Microthermometry (FIM)

Fluid inclusion analysis is generally used in oil industry to constraint temperature, time and duration of hydrocarbons migration in relation with inorganic diagenesis (Goldstein, 2001). It also allows determination of pressure fluid regime and the composition of the original fluid in some cases. Fluid inclusions (<20 nm) are considered to be unchanged in volume and composition with time. They are pore fluids trapped during crystallization of diagenetic cement like calcite and quartz and/or during healing of microfractures inside detrital grains (Figure I.13). In sandstones, they commonly found along the irregular contact between detrital quartz grains and diagenetic quartz overgrowth developed around the grains (Goldstein & Reynolds, 1994).

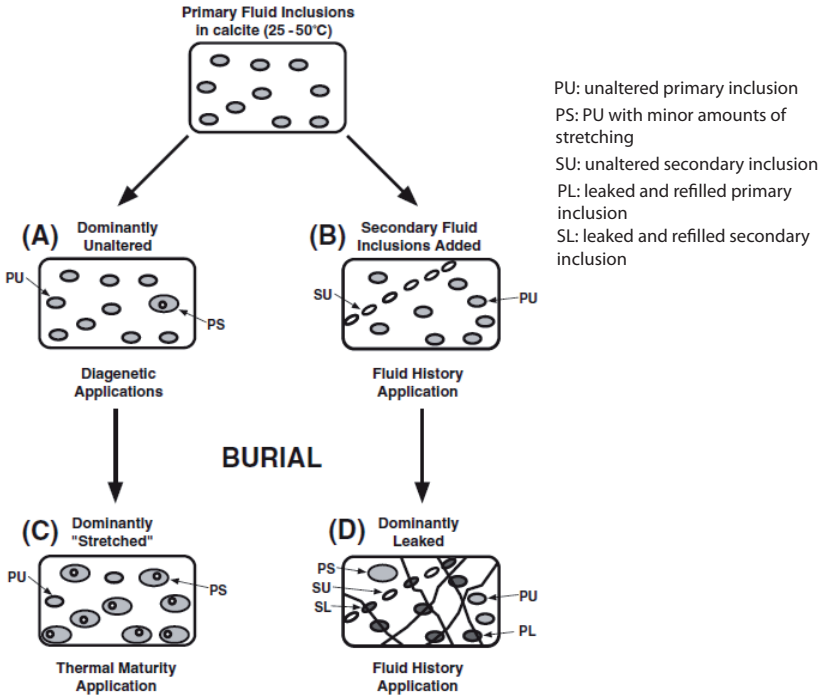

Figure I.13 – Fluid inclusions petrography as a function of burial history (Tobin & Claxton, 2000)

At the time of trapping, they can be filled by aqueous solutions (pore water), or by hydrocarbons such as liquid oil and/or gases if present in the pore space. At the surface (room) conditions, inclusions are frequently observed in petroleum reservoirs and may be one-phase (liquid or vapor), two-phase (vapor bubble in a liquid phase), or multi-phase (vapor, liquid and solid phases) (Figure I.14). The number of phases present at room temperature reflects the nature of the fluid trapped, the PVT conditions at the time of trapping and phase demixing occurring during cooling (from downhole to

surface PT conditions). The demixing process is usually reversible and constitutes the principle of fluid inclusion microthermometry.

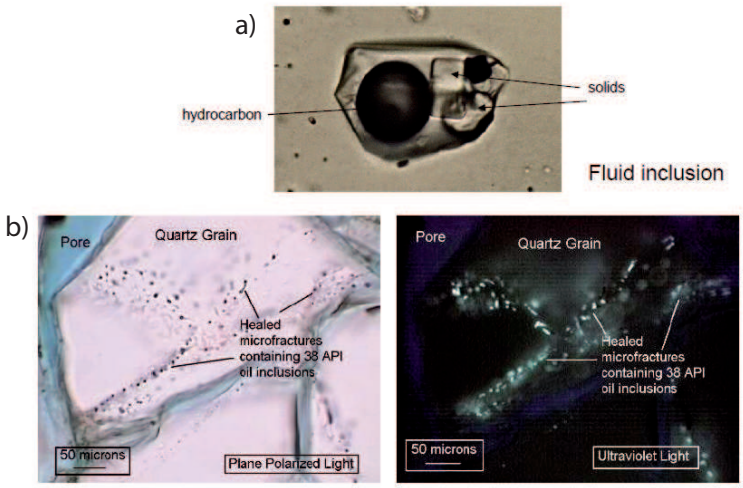

Figure I.14 – a) Fluid inclusion containing solids and hydrocarbons and b) Oil inclusions in microfractures seen in polarized and ultraviolet lights

In practice, inclusions are often diphasic at room temperature, containing for instance a gas bubble in a liquid inclusion. The inclusion is heated in the laboratory. At a certain temperature, the gas bubble disappears and the inclusion becomes homogenous. Inclusion behavior with temperature is isochoric (same density). This temperature corresponds to the homogenization temperature Th (Roedder, 1984). This is the minimum temperature at which the inclusion was formed.

There exist different approaches in applying this method (Tobin & Claxton, 2000). The first one is to use Th of fluid inclusions present in cements to get a minimum estimate of the maximum diagenetic temperature reached during burial. The precision of such an estimate is ± 1°C below 100°C and ± 2°C above. Homogenization temperature of aqueous inclusions yields the closest estimate of the true trapping temperature. For PVT consideration, homogenization temperature of hydrocarbons and gas are generally lower than the true trapping temperature. In most cases, Th of hydrocarbons inclusions is less than Th of aqueous inclusions. This first approach is of limited use particularly if inclusions are situated in cements not formed at maximum burial temperature.
A second approach is to study systematically all subsets of fluid inclusions based on physical and chemical criteria. Use of homogenization temperatures of each subset allows establishing a quite whole thermal history of diagenetic fluids. Short heating event can be recognized (e.g. magmatic or hydrothermal events) from fluid inclusions observations.
A third method is to estimate the maximum burial temperature by correcting Th data of fluid inclusions formed close to the burial temperature peak of the pressure effect. However, this approach is

limited by the low probability to find enough inclusions formed at this time and by error sources related to pressure correction (need to know the chemical composition of the fluid and trapping pressure).

Fluid inclusion microthermometry also allows the measurement of melting temperature, Tm, which characterizes disappearance of the last solid (ice) present in an inclusion previously frozen (liquid nitrogen) upon warming. In aqueous inclusions, Tm can be converted in terms to salinity expressed in %wt eq.NaCl.

FIM analysis requires to first perform a very careful study of the fluid inclusion petrography, i.e., document the type and localization of the different populations of fluid inclusions in a sample. Different populations may relate to different diagenetic events of different ages, but they may also result from post-entrapment modifications (leaking, necking, stretching...) or from heterogeneous trapping (trapping in the two-phase domain, with coexisting gas+liquid). Th values are reported as Th histograms, which may exhibit unimodal or polymodal distributions, therefore recording one or multiple events. Uncertainty on temperature measurements is on the order of ± 1°C. However, much of the uncertainty on temperature reconstruction based on fluid inclusions microthermometry lie particularly in the inclusion choice (size, shape, localization), hence inclusions representativeness, as well as data statistics and treatment. In ideal situation, diagenetic temperatures can be reconstructed from homogenization temperatures to about ± 5-10°C.

2.2 Fission Track Thermochronology (FTT)

Fission Track Thermochronology is based on the fact that natural uranium (half life = 4.5×10^9 years), present in many minerals such as apatite, sphene and zircon, undergoes fission phenomenon. Fission is characterized by ejection of heavy particles, called fission fragments, in opposite directions following a linear pathway (Figure I.15A). These fragments lose their energy by ionizing the materials they travel across. Thus, they create a narrow damaged zone within the host mineral called latent track which is a sub-continuous linear structure defect (Figure I.15B). ^{238}U is considered to be responsible for fission tracks in minerals because it is present in greater quantity with respect to ^{235}U and ^{232}Th. Number of fission tracks observed on the mineral surface is a function of both grain uranium concentration and time spent by the grain at a given temperature. A high uranium concentration generates a high number of spontaneous tracks, but a long time period at low temperature creates also a high density of tracks because old tracks do not anneal.

In order to be observed under the microscope, tracks must undergo a preferential etching leading to the formation of fission tracks. This process is called tracks revelation.
To identify latent tracks, some criteria must be satisfied (Laslett *et al.*, 1984) :

– Tracks have to be random trajectories : probability for two tracks being parallel is near zero ;

– Tracks are linear ;
– Tracks length is < 20 μm (16.3 μm) for apatite which is the most widely used mineral for FTT because of its capacity to record temperatures between 60 and 120°C (encompassing the oil window) ;
– Tracks must cut surface for acid penetration.

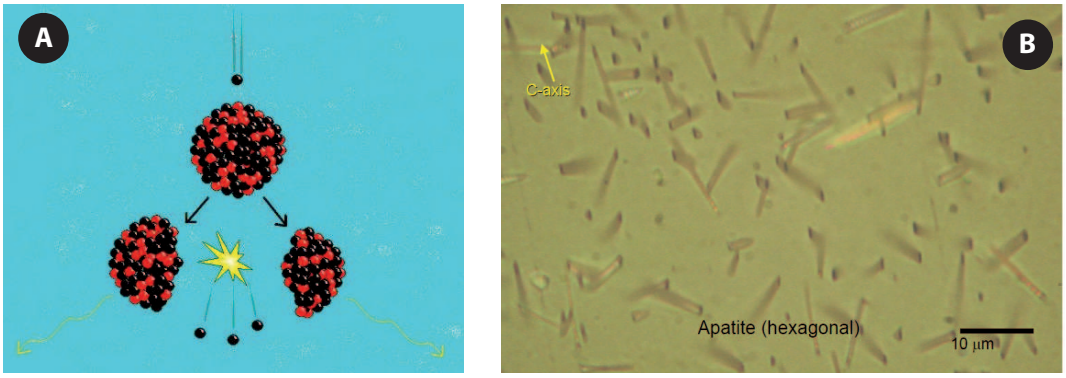

Figure I.15 – A) Fission phenomenon at the origin of the AFTA method and B) Fission tracks observed with a microscope

Analysis of fission tracks provides information about paleotemperatures and "age" of temperature events. In the following, only the thermometry aspect is treated.

Initial length of fission tracks is relatively constant for a given mineral ($\sim$ 20 μm for apatite). Latent tracks are mainly temperature sensitive. Only thermal energy can reactive damages and latent tracks anneal progressively. This phenomenon leads to typical tracks shortening. Annealing begins at the extremities towards interior at a rate depending on temperature (e.g. Green, 1986). Degree of annealing is then a marker of past temperatures. Crystallographic orientation of hexagonal apatite grains influences the track length (Wagner & Van den Haute, 1992). Tracks parallel to the c-axis would be thinner and longer than tracks perpendicular to the axis. Annealing is faster for perpendicular tracks (e.g. Green *et al.*, 1989). This is due to the fact that apatite dissolution is controlled by the atomic structure. In addition, annealing rate varies with apatite chemical composition. Cl-enriched apatites are more resistant to annealing than F-enriched apatites (Green *et al.*, 1986), making it important to determine the chemical composition of apatite samples to interpret thermal history.
Kinetic analysis of fission tracks annealing yields that final tracks length corresponds to the highest temperature experienced. With increasing temperature, tracks become shorter. If temperature drops after a certain time, tracks still present at this time are frozen and record the maximum temperature. Tracks formed after the sudden cooling are longer than those formed before and during the heating phase (prior to cooling). Laboratory experiments (e.g. Green *et al.*, 1986 ; Barbarand *et al.*, 2003) showed that annealing rate is not linear with temperature. Tracks annealing is slow at low temperatures,

but more rapid at higher temperature especially for track length of ∼7 μm.

For a reliable interpretation of tracks size, their lengths are measured on horizontal confined tracks situated inside the mineral and revealed by etching by their connection with other tracks (Figure I.16).

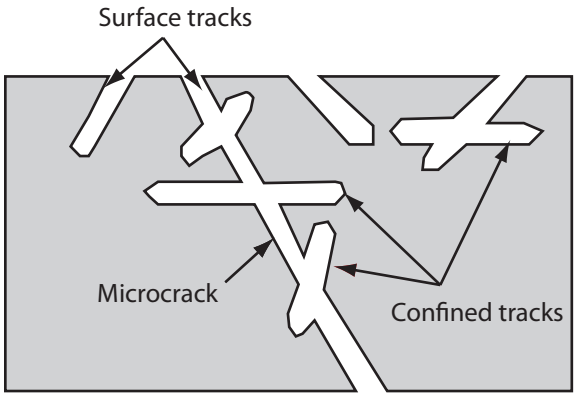

Figure I.16 – Different tracks shape

AFTA (Apatite Fission Tracks Analysis) data are reported in histograms representing tracks length distribution (Figure I.17). About 100 tracks have to be counted on one grain and this has to be repeated on at least 20 grains for a reliable statistic.
In rocks which were not heated to temperature higher than 50°C after a rapid and permanent cooling (e.g. volcanic rocks), mean tracks length ranges typically between 14 and 15 μm with a standard deviation of 1 μm, and exhibit a narrow and symmetric distribution (Figure I.17 ; Gleadow *et al.*, 1986). In most cases, length distribution is more complex and dispersion is less important. Above 50°C, fission tracks start annealing. Tracks are shorter with a weaker density leading to a decrease of the apparent age. Beyond a critical temperature which depends on the mineral considered (110-120°C for apatite), fission tracks anneal completely and apparent age is reduced to zero. On Figure I.18, a complete set of AFTA data from the Otway Basin, Australia, is presented.

Three causes can explain widening of fission tracks dispersion with increasing temperature (Naeser & McCulloh, 1989) :

- Anisotropy of annealing process in apatite ;
- Variation in annealing properties in apatite of different composition : shorter tracks may correspond to grains more susceptible to annealing, longer tracks to more resistant grains ;
- Continuous production of tracks : some tracks exist since the beginning of the thermal history, others are formed more recently.

AFTA can be applied to rocks of all ages (Precambrian to Recent). Lithologies containing enough apatite grains for AFTA are medium to coarse grained sand units and acidic igneous bodies. Clayish and fine grained sediments, carbonates and basalts are apatite-poor rocks. From an experimental

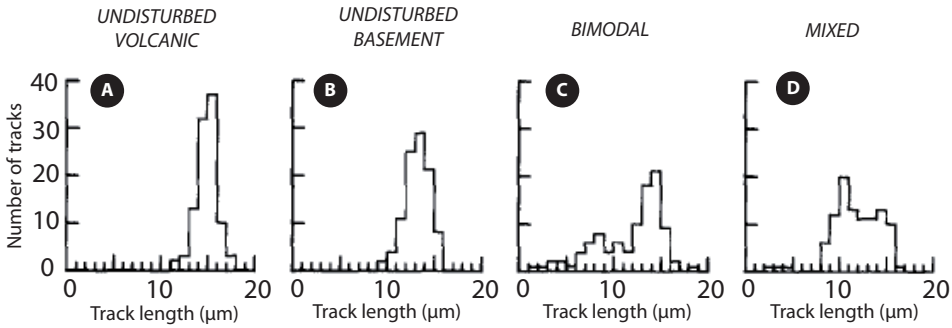

Figure I.17 – Typical tracks length distribution for apatite in volcanic rocks. A) rapid cooling volcanic rock, B) undisturbed basement, C) bimodal distribution, D) mixed distribution (two separate components) (Gleadow *et al.*, 1986)

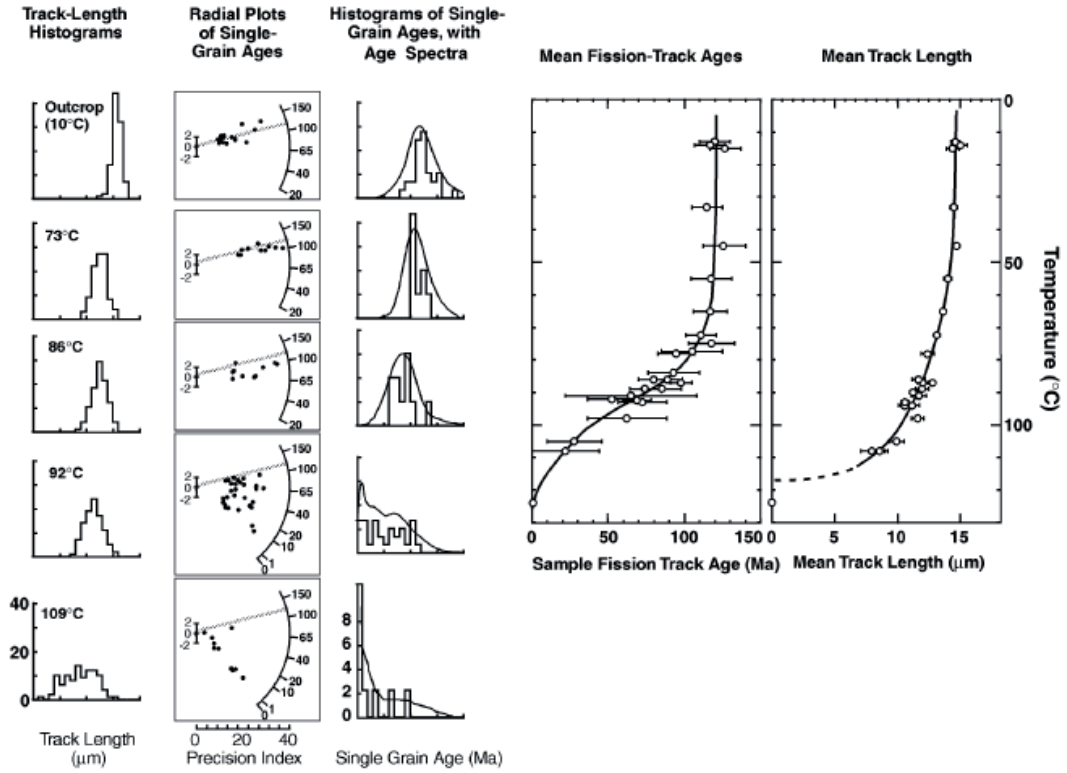

Figure I.18 – Apatite fission tracks data from the Otway Basin, Australia (Gallagher *et al.*, 1998)

point of view, samples must contain enough apatite grains which origin is known. Cores and outcrops samples are better than cuttings. Required quantity of bulk material depends on apatite concentration within the sample, but generally at least 5-10 kg are necessary. Like many other methods, sampling in a given depth interval is not really interesting, it is preferable to analyze series of samples from different locations in the stratigraphic sequence (Figure I.18).

2.3 Clay Mineralogy

Clay minerals are closely associated with basins history (Figure I.19). They are capable to "record" past conditions from deposition (e.g. interaction with solution) to late diagenesis, and they can provide information about fluid migration inside the basin. They are responsive to changes in thermodynamic conditions, but their reactions are very much controlled by kinetics (time-temperature effect). Clays are classified in 4 main groups : smectite, illite, kaolinite and chlorite.

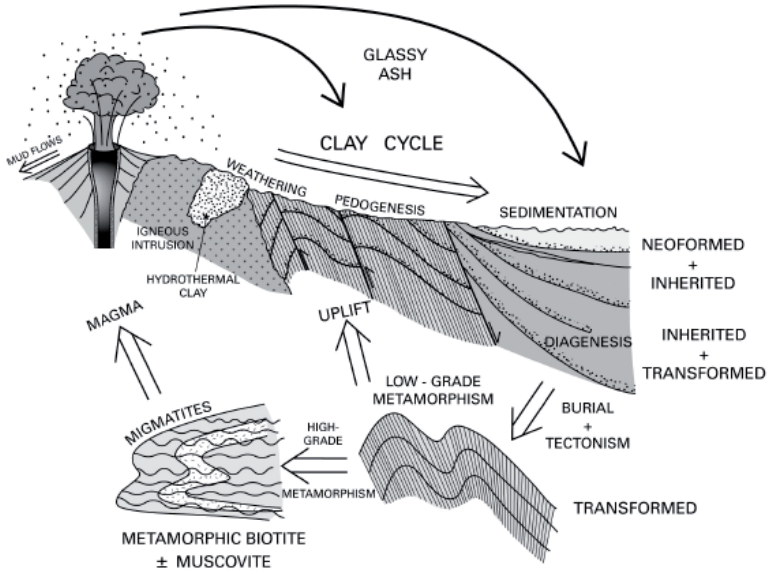

Figure I.19 – Clay cycle (Merriman, 2005)

After deposition detrital clay minerals in sediments are destabilized as a result of increasing temperature and pressure, and changes in pore fluid composition. They are progressively transformed and/or replaced by clay minerals more stable in deep conditions, which are illite, dickite and chlorite. These three latter minerals are the last step of complex mineral transformations. Indeed, there exist many possible reactions and associated mechanisms with creation of metastable minerals (Figure I.20).

In typical argillites, clay mineral assemblage is constituted of reactants and products of several chemical reactions which give some indications on the advancement of the reactions and on the rock maturity. Because of the reactants-products interlocking, it is impossible to bound stability of a given clay mineral to a specific zone. Generally, presence of smectite and kaolinite in clays is an indication of immature basin, whereas an illite-chlorite-mica assemblage rather indicates an overmature basin (Merriman, 2005).

Among the different reactions involving clays occurring in sedimentary basins, one of particular interest is the illitization of smectite : Smectite ⇒ Interlayered Illite/Smectite (I/S) ⇒ Illite

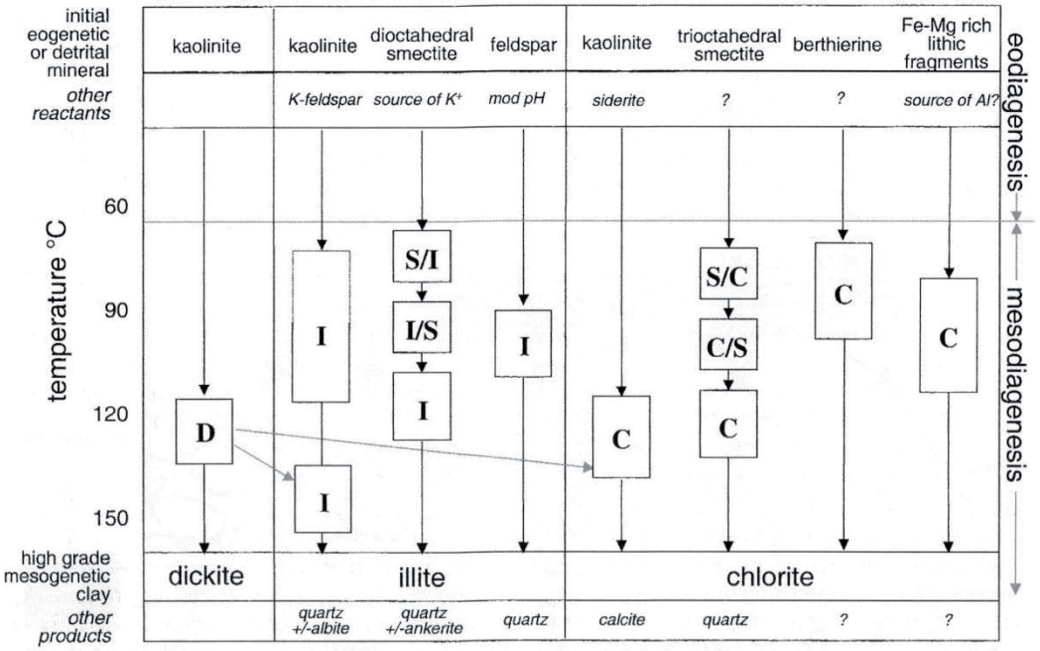

Figure I.20 – Typical reaction pathways for dickitization, illitization and chloritization in diagenetic conditions (Worden & Morad, 2003)

Interlayered I/S are constituted of two components : a swelling component of smectitic origin and a non-swelling component related to illite. The relative proportion of smectite with respect to illite in clayey rocks decreases with increasing time and temperature. I/S clays progressively loose their swelling layers and the thickness of illite sheets in I/S increases. This leads to increase of the clay minerals size being more isometric with increasing temperature. As temperature increases, the degree of order within the illite crystal lattice also increases. The measure of I/S ratio (expressed as a percentage of smectite layers %S) and degree of order R are used to estimate the maturity of sedimentary rocks. Moore & Reynolds (1997) defined three different interstratifications forms in I/S, using the notation "Reichweite" (R). A random, disordered arrangement is characterized by R=0 (smectite-rich) and an ordered one by R>1 (illite-rich). Pollastro (1993) tried to correlate ordering characteristics of I/S mixed-layered clays with temperature in shales, using a model by Hoffmann & Hower (1979) (Figure I.21). The transition from I/S R=0 to I/S R=1 occurs at about 100-110°C which roughly corresponds to the temperature of hydrocarbons generation peak. The transition from I/S R=1 to I/S R=3, at about 175-180°C, may represent the upper boundary of hydrocarbons generation for a potential source-rock.

Hillier *et al.* (1995) proposed to express the percentage of expandable layers in mixed-layer I/S (%Exp) with respect to %Ro for different geothermal gradients (Figure I.22). Clay minerals and vitri-

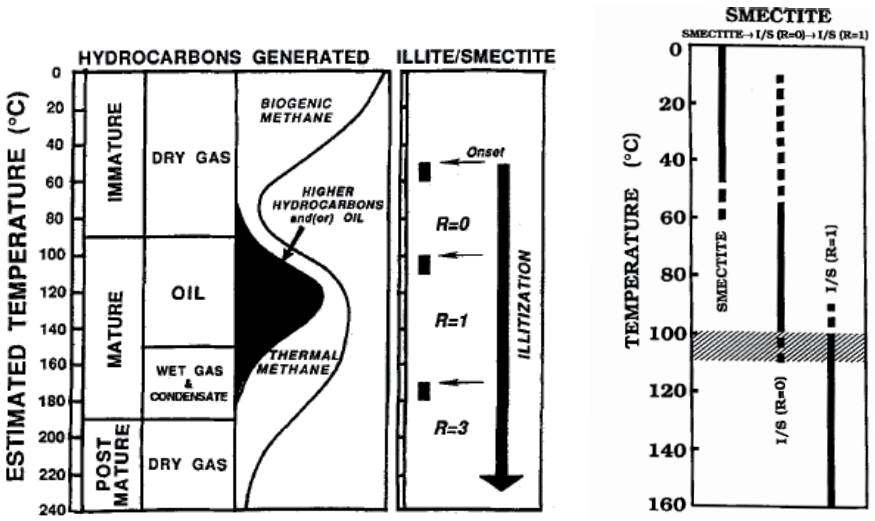

Figure I.21 – Relationship between temperature hydrocarbon generation and I/S transitions (Pollastro, 1993)

nite reflectance evolve at different rates. Smectite-illite reaction would be more advanced than vitrinite maturation for 25°C/km geothermal gradient and delayed for higher heating rate (e.g. 55°C/km).

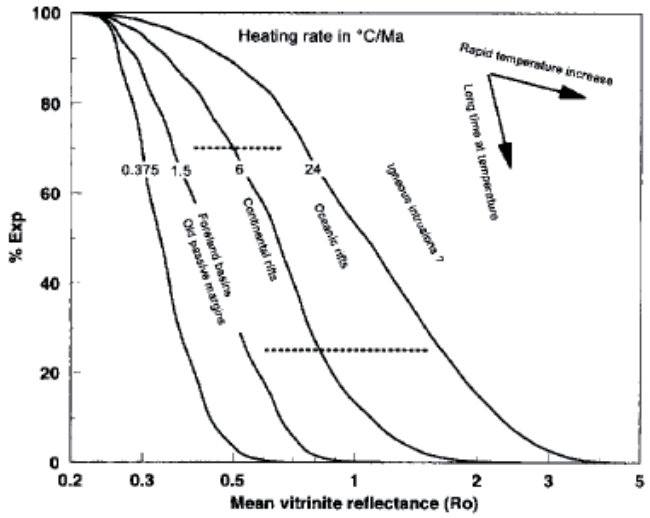

Figure I.22 – Correlation between vitrinite reflectance %Ro and I/S percentage of expansibility %Exp for different geothermal gradients (Hillier *et al.*, 1995)

However, the main difficulty with this method is that clay mineralogy is also affected by chemical conditions (water and rock chemistry), paleogeography, in addition to temperature and time. Chemical parameters may change simultaneously to the illitization process leading to difficulties to constrain

the smectite-illite reaction rate (Velde & Vasseur, 1992). Fluid interactions also play a role in altering clay chemistry (Beardsmore & Cull, 2001).

Kübler index (e.g. Kübler & Jaboyedoff, 2000 for a review) of illite crystallinity, KI, is used to indicate the progression of smectite-illite reaction. In general, burial appears to favor the formation of illite, and both relative abundance and degree of ordering in the illite crystal lattice increase with depth.

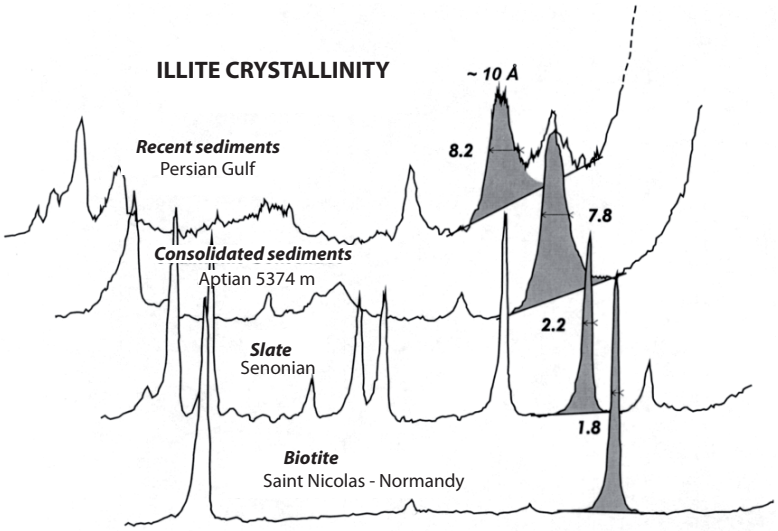

Figure I.23 – Illite diffraction peak (°(Δ 2Θ Cu Kα)) for different lithologies with increasing metamorphism degree downward (Kübler & Jaboyedoff, 2000)

From a technical point of view, Kübler index is measured on the XRD (X-Ray Diffraction) spectrum of the < 2 μm grain-sized fraction. KI depends upon grain-size fraction studied and instrumental factors (e.g. size and shape of sample holder, diffractometer geometry...). KI estimates changes in the full width at half maximum (FWHM) of the 10 Å XR diffraction peak which is inversely related to illite crystals thickness (Figure I.23). As temperature increases, the 10 Å FWHM becomes progressively narrower. Actually, KI is an indirect measurement of the average thickness of stacks of consecutive illite sheets in interlayered I/S : 24 layers in I/S would correspond to the diagenesis-anchizone boundary and 56 layers to the anchizone-epizone transition (Kübler & Jaboyedoff, 2000). Absence of swelling layers (Meunier & Velde, 1989 ; Srodon *et al.*, 1992), a weak percentage of smectitic layers up to 5%S (Moore & Reynolds, 1997) and mica-chlorite assemblage would be also characteristic of anchizone. Epizone is represented by other mineralogical assemblage and a chlorite-like mineral is considered to be the beginning of the epizone.

Interpreting results only on the basis of KI values is tricky. For accuracy, one should compare KI values with other maturity indicators (either organic or inorganic) and with the tectono-sedimentary

history of the basin. Kübler index remains commonly for studies dealing with rocks from deep diagenesis and anchizone settings, and, therefore, burial-temperature conditions often beyond the oil-gas window. At lower temperatures, the characterization of illitic I/S relies more on the decomposition of XRD diagnostic peaks in individual clay components.

Another process occurring in sedimentary basins is dickitization which is the transformation of kaolinite into dickite (e.g. Beaufort *et al.*, 1998). This is characterized by a change in morphology from vermicular crystals (kaolinite) to coarser and isometric crystals (dickite) (Figure I.24). Kaolinite-dickite transition is controlled by kinetics. However, there is no strict and simple dependence with burial depth and temperature because other factors such as reaction time/duration, water/rock ratio, nature of mineral precursor, etc. . .also influence the advancement and reaction rate of the dickitization process.
In petroleum reservoirs lying at similar temperature, dickitization may vary strongly, in particular with respect to porosity and hydrocarbons saturation. The dickitization process therefore does not appear as a reliable geothermometer.

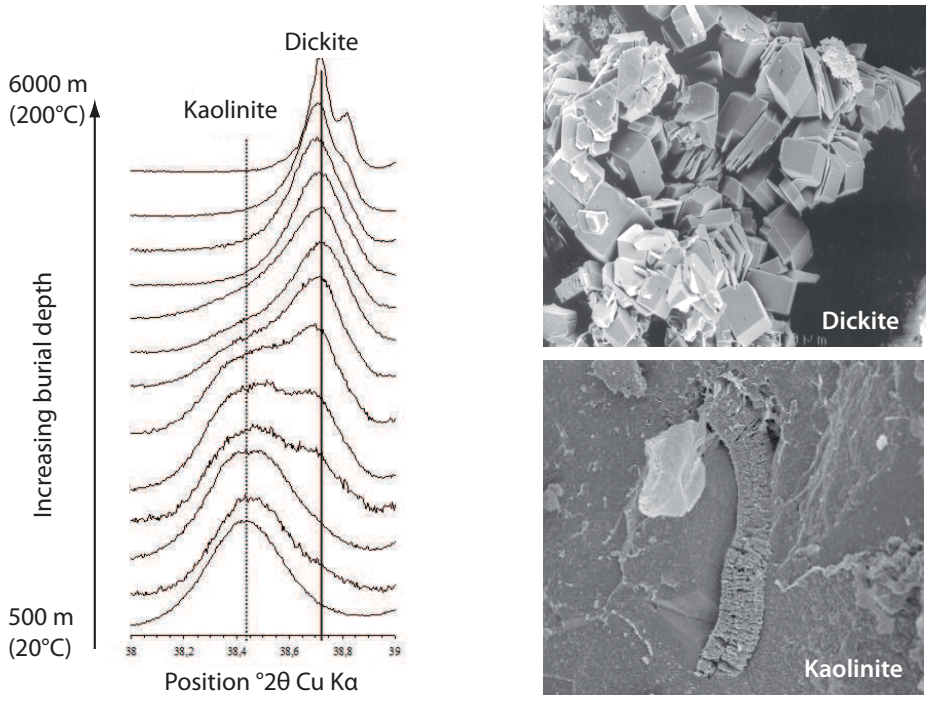

Figure I.24 – Dickitization process seen by X-Ray diffraction (Beaufort *et al.*, 2009)

Another mineral transformation series is chloritization. This leads to the formation of chlorite for temperature range between 60 and 120°C depending on the precursor mineral (e.g. berthierine, smectite, corrensite). In sandstones reservoirs, chlorite appears as grains coating usually formed during

early diagenesis, or as pore-filling cement usually formed later. There has been considerable work and debate about to the possibility of using the chemical composition and/or the polytype of chlorites as temperature indicators (Cathelineau & Nieva, 1985 ; De Caritat *et al.*, 1993). Up to now, there is no general consensus on the use of chlorites as geothermometers, largely because chlorites exhibit very variable chemical compositions and rather complex solid solutions. In addition, there are many different mechanisms by which they evolve and transform, including for some of them precursor minerals. As a consequence, chloritization processes will not be further described here. The reader is referred to Worden & Morad (2003) and references therein for a description.

Clay mineral transformations in sedimentary rocks are kinetic. The general evolution of clay mineral transformations in a given sedimentological setting may therefore provide some information on thermal history, but not the occurrence or absence of any particular clay mineral. However, the mineralogical evolution is influenced by a number of factors which play a role on transformation rate of clay minerals, such as geological factors (cementation, grain size, hydrocarbons migration...) and mechanisms involved in the transformation process (dissolution-crystallization vs. solid-solid reaction...).

2.4 Isotopic geothermometers

Stable isotopes do not decay naturally and thus are good tracers of geological processes and their origin. Most commonly used isotopes are hydrogen, carbon, oxygen and sulfur. In paleothermometry, oxygen isotopes (^{16}O, ^{18}O) and, at a lesser extent, those of hydrogen (^{1}H, ^{2}H) are used. Sulfur (^{32}S, ^{34}S) and carbon (^{12}C, ^{13}C) isotopes are used to define their origin (biogenic or inorganic processes). The isotopic composition of a mineral is expressed by use of the delta notation as :

$$\delta_A = (\frac{R_A}{R_{std}} - 1) \times 1000$$

with R_A isotopes ratio of the same element A and R_{std} standard ratio of two isotopes of the same element (reference ratio).

The isotopic composition of a mineral is controlled by the isotopic composition of the circulating fluid by fluid/mineral interaction and temperature by fractionation.
Before isotope exchange reaction used as geothermometers, some conditions must be satisifed :

- Isotopes of the element considered must coexist in two different compounds
- Isotopic equilibrium between these two compounds is attained
- Isotope exchange rate has to be fast enough to allow equilibrium
- Temperature has to be the dominant factor for fractionation
- Fractionation degree is linear with temperature and detectable

Generally, equations for isotope geothermometry are expressed as :

$$\Delta = 10^3 \ln\alpha = \frac{\mathrm{A} \times 10^6}{\mathrm{T}^2} + \frac{\mathrm{B} \times 10^3}{\mathrm{T}} + \mathrm{C}$$

Constant values (A, B, C) are derived from experimental determinations of the fractionation factors α (dependent on temperature).
If one knows the isotopic composition of a given mineral and that of the parent fluid (e.g. water) independently, then it is possible to determine the temperature of the formation of that mineral by using the above equation (Figure I.25).

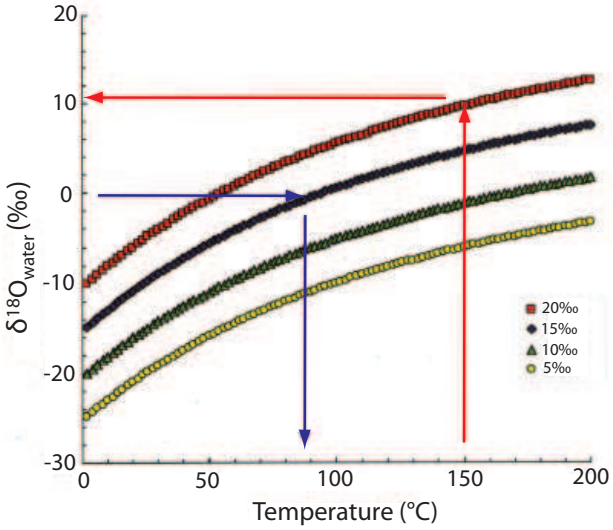

Figure I.25 – Temperature coordinates of the possible forming conditions for 4 kaolinites whose $\delta^{18}O_{kaolinite}$ values are 5, 10, 15 and 20‰ (Girard & Fouillac, 1995)

Then, there exist many methods to qualify or quantify thermal maturity (Figure I.26). Each of them is based on chemical and/or physical specific process which is non reversible, temperature dependent and acting on one or many sediments components. Each method above has limitations and none is universally applicable (Table I.2). In the case of the organic geothermometers, rocks older than Cambrian cannot be thermally estimated as a result of the absence of the considered organic matter. Moreover, the organic geothermometers are quite subjective. By contrast, the inorganic geothermometers, though more quantitative, depend on many geological factors. In order to face their various limitations, we develop in the following a new geothermometer called MagEval. It is based on the magnetic assemblage of the sedimentary rocks which evolve with temperature/burial. The previous work by Aubourg & Pozzi (2010) suggested that this geothermometer could be applied on a wide range of temperature (50-250°C) and a priori independent of the lithology (claystone, limestone, sandstone). It is thought to record the maximum temperature experienced by a rock (time-independent). The

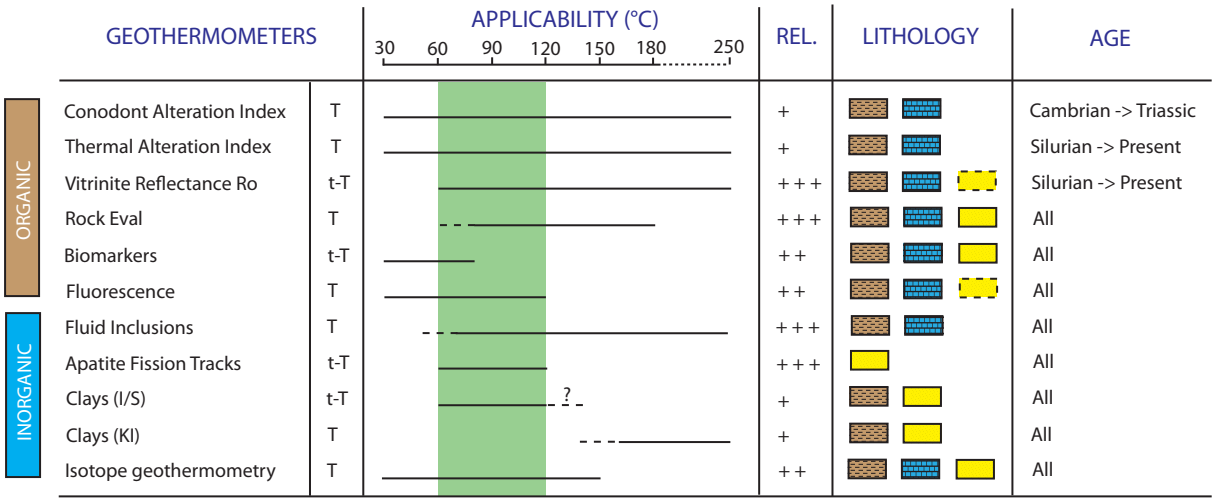

Table I.2 – Applicability of some geothermometers. REL : reliability from less (+) to more (+++) reliable, t : time, T : temperature.

geothermometer is based on low temperature measurement (10-300 K) which is rather fast (2h30 for a standard sequence).

It is strongly recommended to estimate thermal maturity by using several techniques. To know those most appropriated, many factors have to be considered : lithology, present temperature, required precision for paleotemperature estimate, geodynamic history of the basin...Ideally, it is best to get converging results by use of several independent geothermometers, thereby providing higher confidence in the temperature reconstructions.

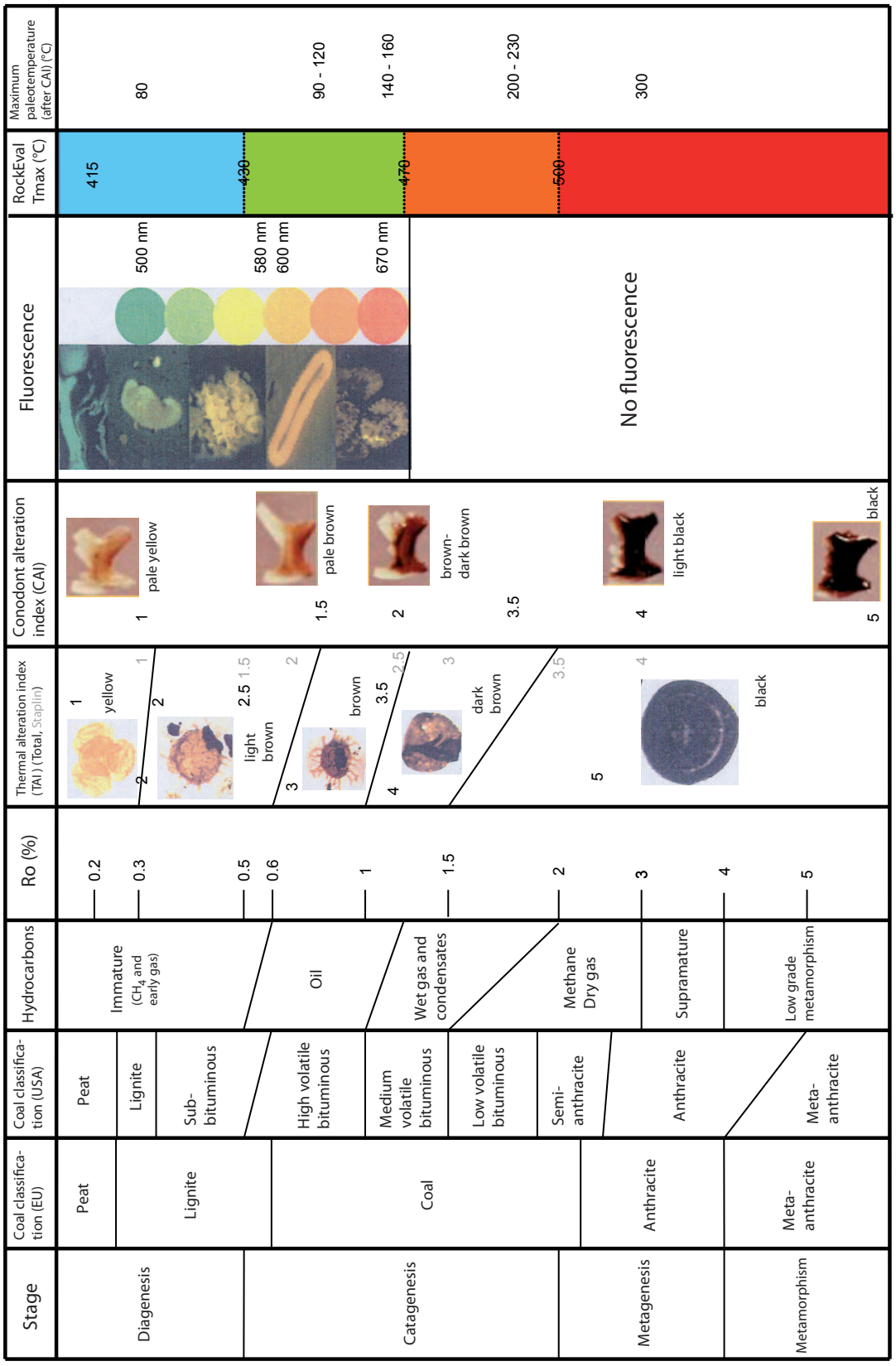

Figure I.26 – Correlation chart between different maturity indicators

Chapter I. FREQUENTLY USED GEOTHERMOMETERS IN BASIN THERMAL HISTORY RECONSTITUTION

Chapter II

ELEMENTS OF ROCK MAGNETISM

Rock magnetism is a science which aims at studying magnetic properties of rocks and minerals from atomic to terrestrial - even universal - scale. Reconstructing the variations of the Earth's magnetic field and its reversals, determining plate motions and past climatic changes, studying ancient extraterrestrial magnetic fields, are among the common applications of rock magnetism.

In nature, not all atomic elements are magnetic. Only four have magnetic properties at ambient temperature and the most common being iron (Fe) (Figure II.1).

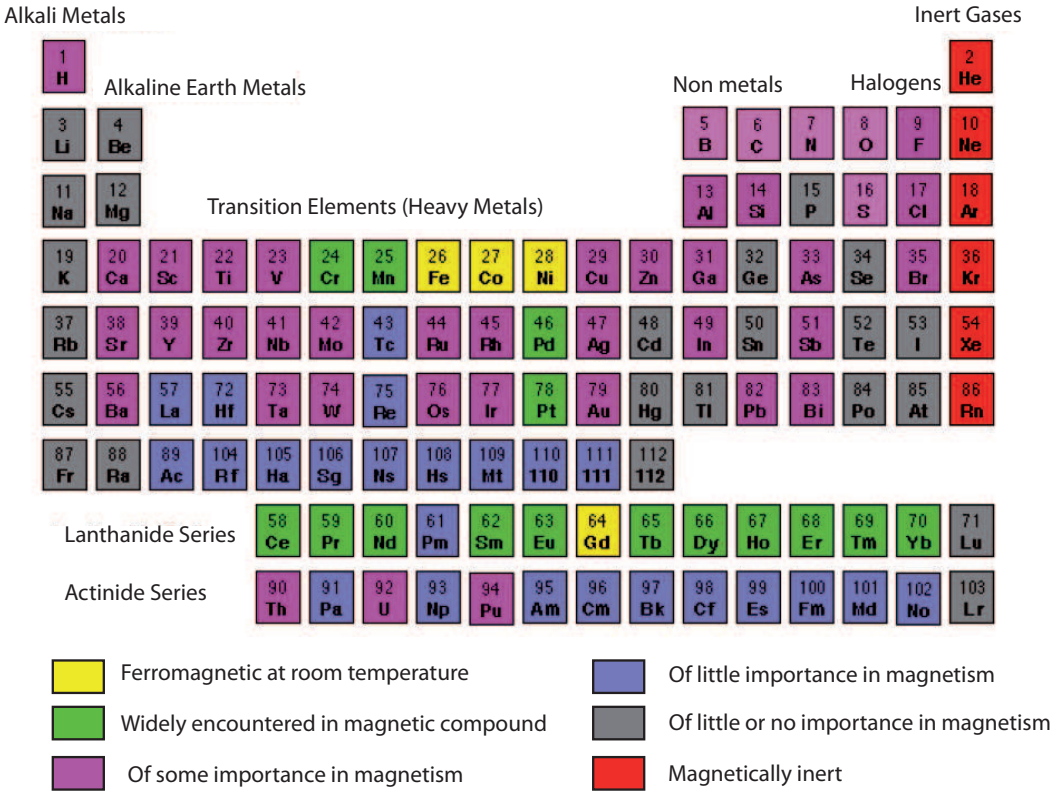

Figure II.1 – Magnetic periodic table of elements (IRM lecture notes)

Fe- and Ti- oxides (e.g. magnetite, hematite, titanomagnetite) are the most important magnetic minerals on Earth. Iron oxyhydroxides (e.g. goethite) and iron sulfides (e.g. pyrrhotite) are also important magnetic minerals in rock and environmental magnetism.
In the following, fundamentals of rock magnetism are first reminded. Then, the low temperature magnetic properties of the magnetic minerals encountered during the course of this thesis are presented.

1 Fundamentals of rock magnetism

When a material (e.g. mineral) is submitted to a magnetic field, it acquires a magnetization generally constituted of two components :

- The induced magnetization which is created by the applied magnetic field and removed when the field is switched off
- The remanent magnetization (or remanence) which is the magnetization remaining in the absence of a magnetic field.

The resulting magnetization $\mathbf{M}$ of a rock is then expressed as :

$$\mathbf{M} = \mathbf{M_i} + \mathbf{M_r}$$

where $\mathbf{M_i}$ is the induced magnetization and $\mathbf{M_r}$ the remanent magnetization.

In isotropic materials, the induced magnetization $\mathbf{M_i}$ is parallel to the direction of the applied magnetic field $\mathbf{H}$ and proportional to its intensity :

$$\mathbf{M_i} = \chi \times \mathbf{H} = \chi \times \frac{\mathbf{B}}{\mu_\mathbf{0}}$$

with $\mathbf{B} = \mu_0 \ (\mathbf{H} + \mathbf{M})$ and $\mathbf{H}$ the magnetic field (A/m), $\mathbf{M}$ the macroscopic magnetization (A/m) and $\mathbf{B}$ the induced field in Tesla ($\mu_0 = 4\pi.10^{-7}$ H/m).
χ is a quantity called magnetic susceptibility (dimensionless) characterizing the capacity of a material to magnetize under the action of a magnetic field. χ can be expressed as the sum of specific susceptibilities characterizing magnetic states :

$$\chi = \chi_{dia} + \chi_{para} + \chi_{ferro}$$

1.1 Magnetic states

When a mineral is magnetized under the influence of a magnetic field, it displays one of the following magnetic behaviors : diamagnetism, paramagnetism, ferromagnetism (Figure II.2).

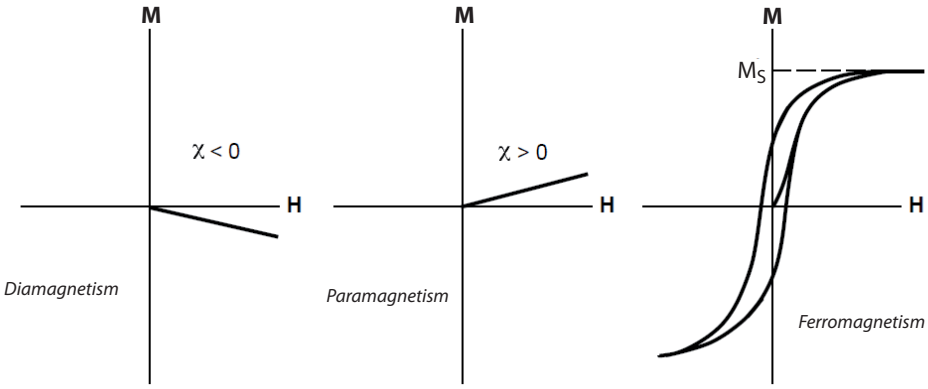

Figure II.2 – Magnetic states. Magnetization M vs. magnetic field H. χ is the magnetic susceptibility and Ms the magnetization at saturation (Butler, 1992).

1.1.1 Diamagnetism

In a presence of a magnetic field H, all moving charges experience a Lorentz force qvH where q is the electric charge and v the velocity. The Lorentz force causes a movement of electron precession equivalent to an electric current. This produces an induced magnetic moment in opposite direction to H (Figure II.3). This is called diamagnetism which is the property of all materials. Diamagnetism is temperature independent.
Most non-iron-bearing minerals such as quartz, calcite and feldspars are purely diamagnetic. Their magnetic susceptibility is negative and very weak ($< 10^{-5}$) (Table II.2). Diamagnetism is overshadowed if any other forms of magnetism are present (Dunlop & Özdemir, 1997).

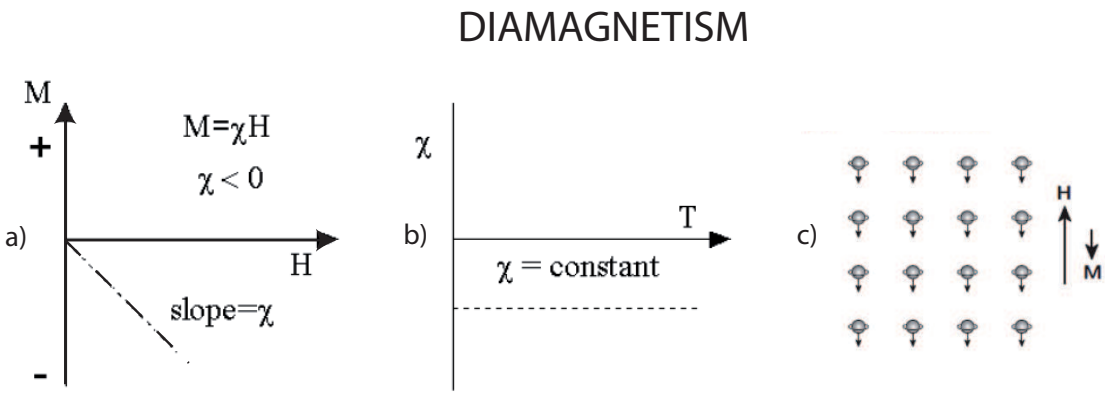

Figure II.3 – Diamagnetism. a) Evolution of magnetization M as a function of the magnetic field H, b) magnetic susceptibility χ as a function of temperature T and c) orientation of the magnetic moments under the application of a magnetic field for diamagnetic materials (IRM lecture notes)

1.1.2 Paramagnetism

If a material has permanent magnetic moments, the application of a magnetic field tends to align these moments in the field direction (Figure II.4). Materials showing such a behavior are called paramagnetic. The induced magnetization is in the same direction as the applied magnetic field (Figure II.4). Magnetic susceptibility is positive comprised between 10^{-3} and 10^{-5} (Table II.2).
Contrary to diamagnetism, paramagnetism is temperature dependent. Thermal perturbations prevent perfect alignment of the magnetic moments with H by favoring random orientation.

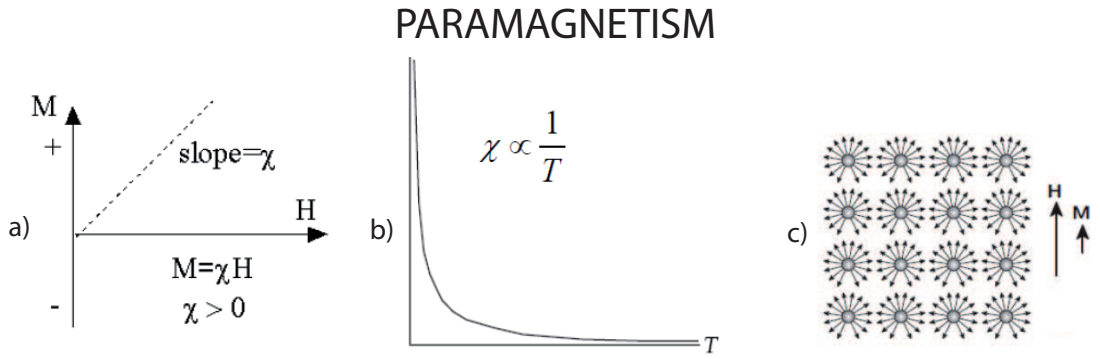

Figure II.4 – Paramagnetism. a) Evolution of magnetization M as a function of the magnetic field H, b) magnetic susceptibility χ as a function of temperature T and c) orientation of the magnetic moments under the application of a magnetic field for paramagnetic materials (IRM lecture notes)

Thus, there exists a competition between thermal energy kT (k is the Boltzmann's constant and T is temperature in Kelvin) and the magnetic energy Em where :

$$\mathrm{Em} = -\mathrm{m}\mu_0\mathrm{H}cos\theta$$

(m is the magnetic moment, θ the angle between **m** and the external magnetic field **H**).
The Langevin theory links the two effects at room temperature :

$$\frac{\mathrm{M}}{\mathrm{Ms}} = \frac{\mathrm{m}\mu_0\mathrm{H}}{3\mathrm{kT}}$$

thus

$$\frac{\mathrm{M}}{\mathrm{H}} = \frac{\mathrm{C}}{\mathrm{T}} = \chi_{para}$$

where M is the magnetization, Ms the magnetization at saturation, C the Curie constant and χ_{para} the paramagnetic susceptibility. This equation is the Curie's law (Figure II.5).

Depending on mineral symmetry, paramagnetic susceptibility in rock-forming minerals can be

anisotropic. χ_{para} is then a function of crystal direction. The anisotropy of magnetic susceptibility (AMS) can be used as a petrofabric tool to reconstruct, for instance, deformation and strain history, paleocurrent directions in sedimentary environments and direction of magma injection.
Most iron-bearing sulfides, carbonates and silicates are paramagnetic.

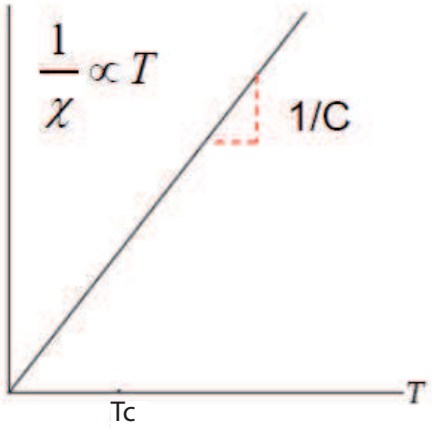

Figure II.5 – Illustration of the Curie's law (IRM lecture notes) : evolution of the inverse of the magnetic susceptibility χ as a function of temperature T. The slope allows the determination of the Curie constant C. Tc is the Curie temperature.

1.1.3 Ferromagnetism

Diamagnetic and paramagnetic magnetizations disappear when the magnetic field is removed. A magnetization can persist which results from electronic interactions. This is called remanent magnetization or remanence which can exist below a certain temperature called Curie temperature Tc dependent of the mineral considered. This phenomenon is known as ferromagnetism (sensu lato). Above Tc, the magnetic material becomes paramagnetic. For such a material, the total magnetic field experienced by the material can be expressed as :

$$\mathrm{H} = \mathrm{Ha} + \mathrm{Hm}$$

where Ha is the applied field and Hm ($= \lambda$m) the molecular field produced by electron interaction (Weiss theory). Above the Curie temperature Tc, there is no internal field hence Hm = 0 (Figure II.6). Ferromagnetic susceptibility obeys to the Curie-Weiss law (Figure II.7) :

$$\chi_f = \frac{\mathrm{C}}{(\mathrm{T} - \mathrm{Tc})}$$

As ferromagnetism (sensu lato) consists of exchanging energy between neighboring atoms, there can be two different spin arrangements (Figure II.8) :

- Ferromagnetism (sensu stricto) : exchange energy minimized when all the spins are parallel
- Antiferromagnetism characterizes spins being perfectly antiparallel

Antiferromagnetism can be subdivided as follows :

– Ferrimagnetism : antiparallel spins of different magnitude
– Canted Antiferromagnetism : antiferromagnetic spins not perfectly aligned in an antiparallel orientation but canted by a few degrees
– Defect moment Antiferromagnetism : spins not perfectly compensated owing to defects in the crystal structure

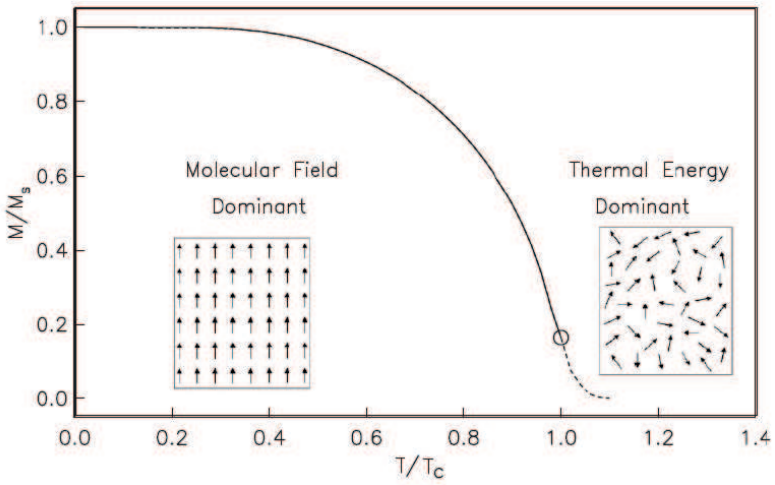

Figure II.6 – Behavior of magnetization (M/Ms) vs. temperature (T/Tc) of a ferromagnetic substance (modified from Tauxe, 2008). At T=Tc, the thermal energy overrides the molecular field.

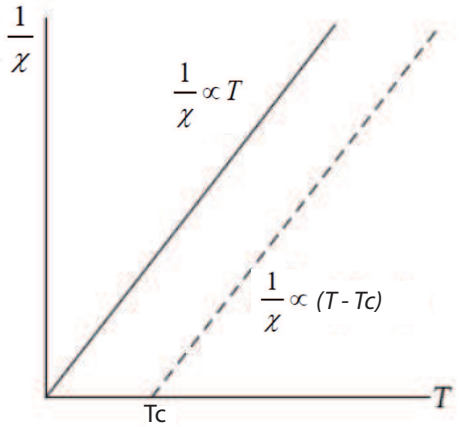

Figure II.7 – Illustration of Curie (black line) and Curie-Weiss (dashed line) laws (IRM lecture notes). See Figure II.5 for legend.

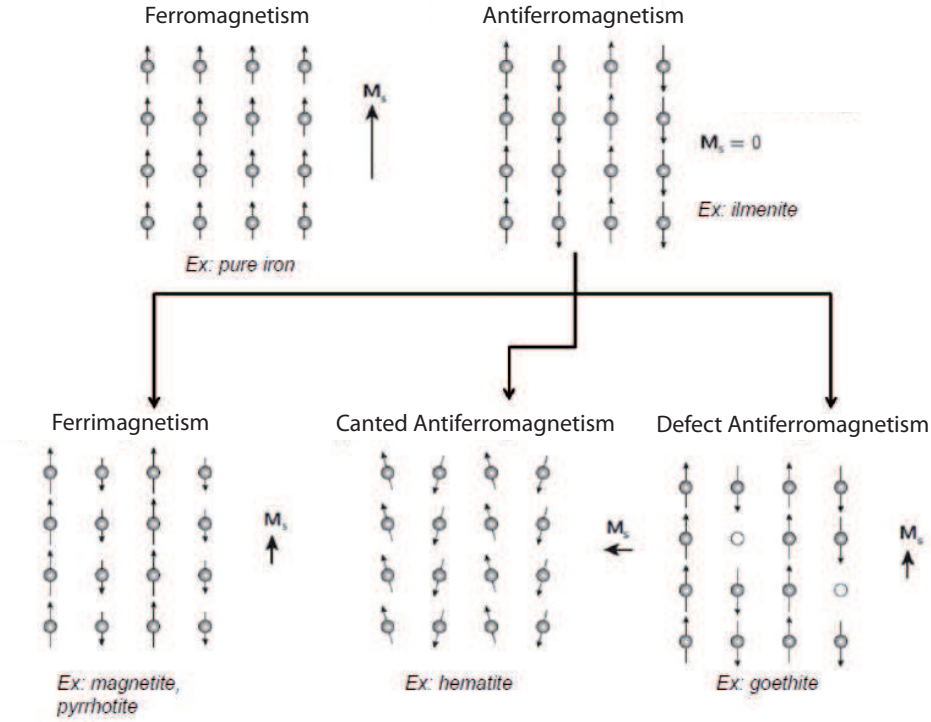

Figure II.8 – Main types of magnetic ordering and resultant magnetization at saturation Ms (IRM lecture notes)

The temperature at which the antiferromagnets become ordered/disordered is called the Néel temperature T_N. At T_N, the magnetization M is equal to 0 and χ is maximum. Below T_N, χ increases due to spins ordering. Above T_N, χ decreases (Figure II.9). $\chi_{antiferro}$ can be expressed as :

$$\chi_{antiferro} = \frac{C}{(T + T_N)}$$

This part was a sketch of what happens in atomic scale for a given mineral. In nature, magnetic minerals occur with different grain sizes presenting different magnetic properties. That is important for paleomagnetic studies to understand why magnetization is fixed in a particular direction.

1.2 Magnetic domains

Within magnetic crystals, some directions exhibit lower energy than others. To shift the magnetization from one called "easy" direction to another, called "hard" direction requires energy. This energy is a measure of the magnetocrystalline anisotropy (Figure II.10). If the barrier energy is high enough, the particle will stay magnetized in the same direction for very long periods of time.

Because electronic interactions depend on interatomic spacing, magnetocrystalline anisotropy constants are a strong function of temperature. They usually change much more rapidly with temperature

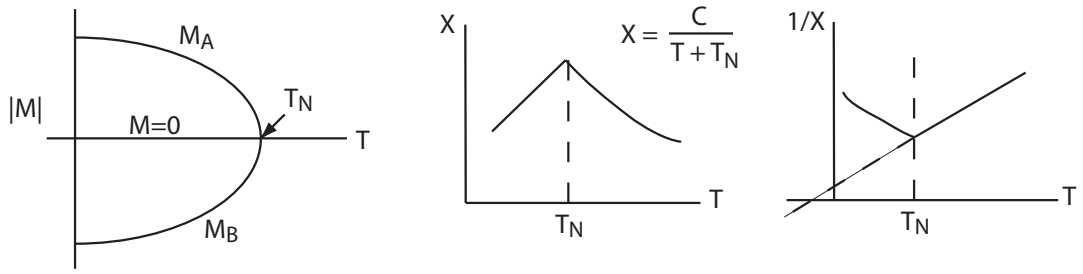

Figure II.9 – Evolution of magnetization M and susceptibility χ below and above the Néel temperature T_N. M_A and M_B are the magnetization for 2 successive sheets (IRM lecture notes)

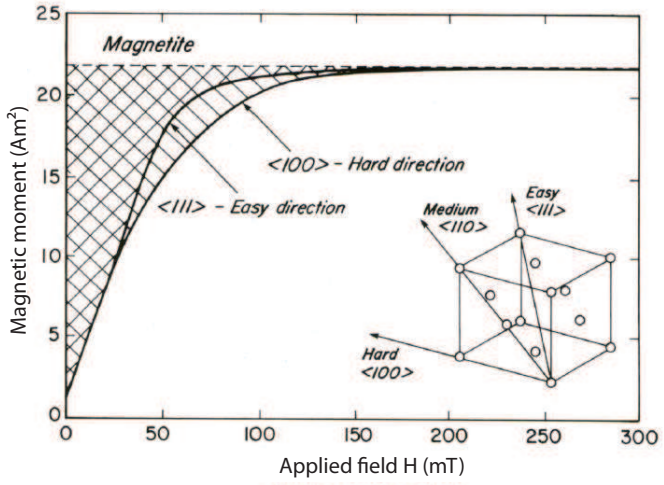

Figure II.10 – Magnetization curves for magnetite along <111> (easy) and <100> (hard) directions. The area between the two curves equals the magnetocrystalline anisotropy energy (Dunlop & Özdemir, 1997 after Moskowitz, 1992)

than does the spontaneous magnetization Ms, particularly in cubic minerals (Figure II.11).

In magnetite, the magnetocrystalline anisotropy constant K_1 changes sign at a temperature known as the "isotropic point". At this point, $K_1 = 0$ and energy barriers are gone. This occurs at $T_K \sim$ 130 K for magnetite (Figure II.12) (Özdemir & Dunlop, 1999).

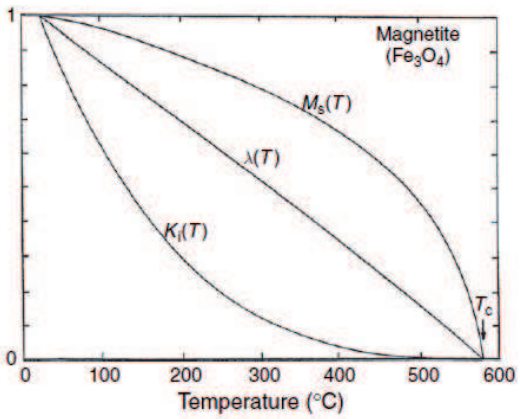

Figure II.11 – Normalized temperature dependences of spontaneous magnetization Ms, direction-averaged magnetostriction λ, and first-order magnetocrystalline anisotropy constant K_1 of magnetite. All three decrease to zero at the Curie point Tc but at very different rates (Dunlop & Özdemir, 2007)

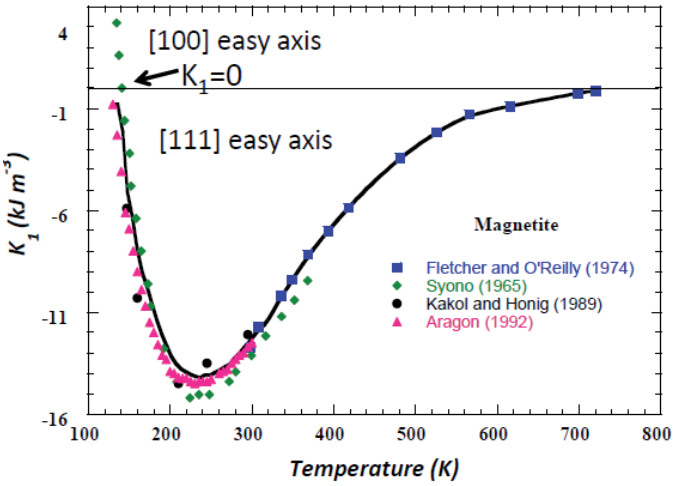

Figure II.12 – Isotropic point of magnetite (Tauxe, 2007 and references therein)

On the other hand, exchange of energy between neighboring atoms also depends strongly on the position of these atoms. In other words, straining a crystal will alter its magnetic behavior and vice versa, changes in the magnetization can change the shape of the crystal. This is magnetostriction. Magnetostriction is positive when crystal expands in the direction of magnetization. In magnetite at room temperature, the magnetostriction depends on directions, being positive for magnetization along a <111> easy axis but negative for a magnetization along a <100> hard axis (Dunlop & Özdemir, 2007).

Another source of magnetic anisotropy is the crystal shape. This is the magnetostatic or shape anisotropy. The direction of the magnetization inside a crystal and the shape of this crystal influence the number of its surface magnetic poles (Figure II.13).

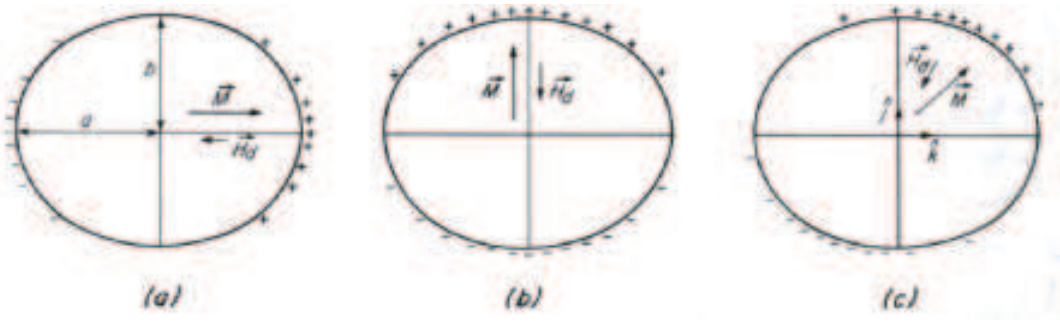

Figure II.13 – Surface poles for a prolate spheroid with an uniform magnetization M a) along the major axis, b) along the minor axis and c) oblique to the major axis (Dunlop & Özdemir, 1997). Hd corresponds to the demagnetization field.

To reduce the magnetostatic energy, Landau & Lifschitz (1935) predicted the existence of ferromagnetic domains. These domains are uniformly magnetized with alternating direction of magnetization (Figure II.14). Domains are small (1-100's μm) but much larger than atomic distances. They are separated by very narrow zones (<1000 nm) in which the magnetization rotates through 90° or 180° between neighboring domains. They are called Bloch domain walls (Figure II.15). The wider the wall, the greater the magnetocrystalline anisotropy energy becomes.

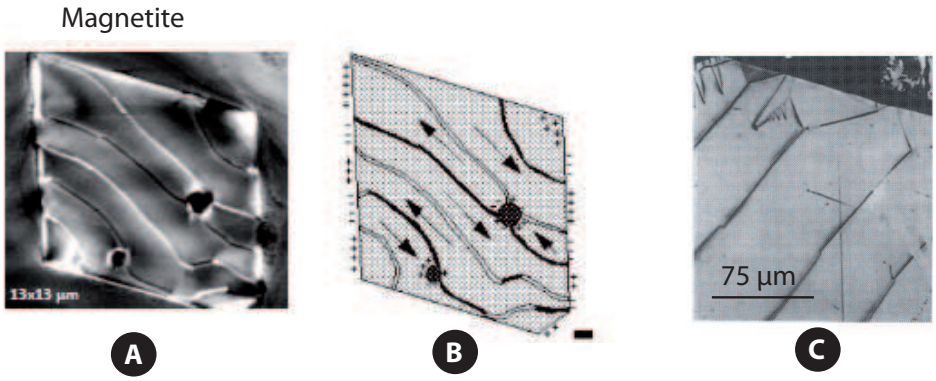

Figure II.14 – A) domains imaged by Magnetic Force Microscopy in magnetite, B) sketch of these domains (Pokhil & Moskowitz, 1997), C) domains imaged by Bitter technique in magnetite (Dunlop & Özdemir, 1997)

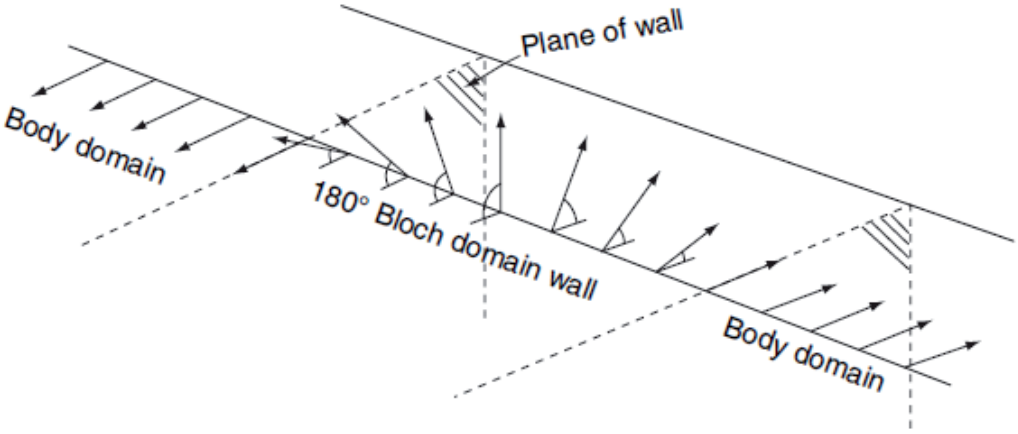

Figure II.15 – Progressive rotation of spins across a 180° wall between two domains (Dunlop & Özdemir, 2007)

If the grain geometry is simple, domains have simple forms. For a 1 domain particle, called single domain (SD), magnetization is uniform and in one direction. There is a high density of surface poles and a large magnetostatic energy associated (Figure II.16a). So they have a very strong remanence which is extremely stable. The maximum size for crystals of a particular mineral to resist subdividing into domains is called the critical single domain size d_0 (Figure II.17 ; Table II.1).

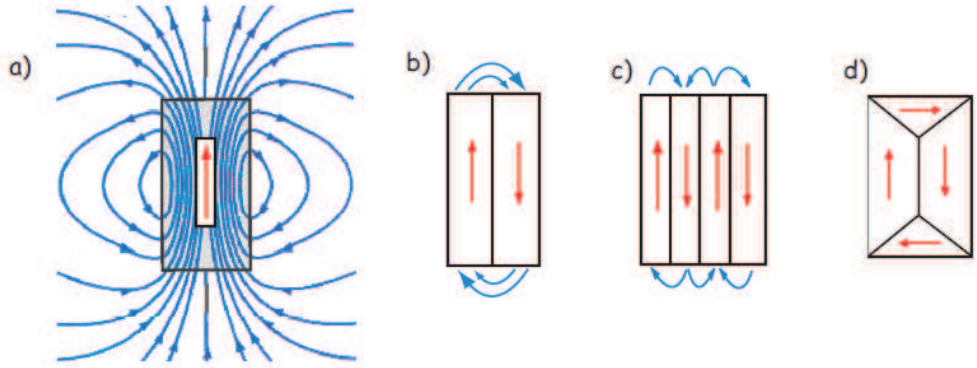

Figure II.16 – Magnetization orientation. A) Uniformly magnetized (SD = 1 domain), B) Two domains, C) Four domains in a lamellar pattern, D) essentially two domains with two closure domains (Tauxe, 2008)

Under ordinary conditions, spontaneous reversals of an SD grain are unlikely because the energy barrier due to crystalline, magnetoelastic (magnetostriction) or shape anisotropy is much larger than the available thermal energy (Dunlop & Özdemir, 1997). In small enough grains, the energy barrier is low and with sufficient thermal energy the magnetic grains become unstable. This thermally acti-

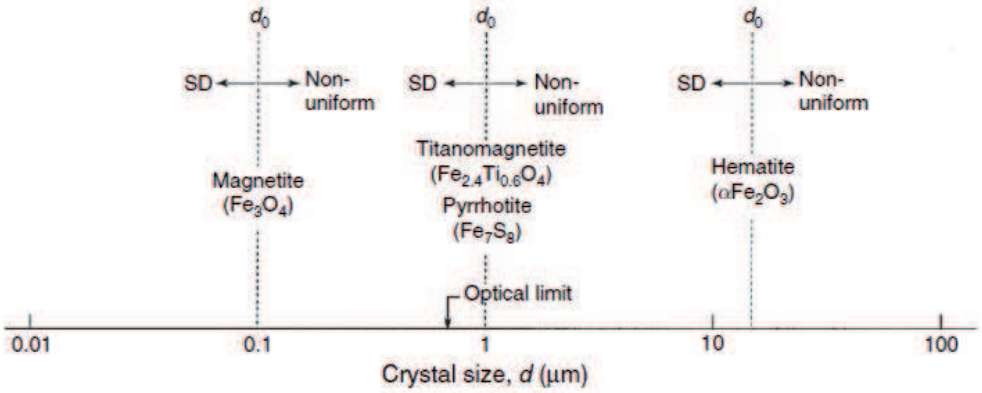

Figure II.17 – Approximate single domain remanence threshold sizes for magnetite, TM60, pyrrhotite and hematite (Dunlop & Özdemir, 2007)

Mineral	Superparamagnetic size d_s (nm)	Single-domain critical size d_0 (nm)
Magnetite (Fe_3O_4)	25-30	50-84
Maghemite (γFe_2O_3)		60
Titanomagnetite TM60	80	200-600
Hematite (αFe_2O_3)	25-30	15000
Pyrrhotite (Fe_7S_8)		1600

Table II.1 – Critical size limits d_0 and d_s for thermally stable single-domain behavior (room temperature, equidimensional grain) (from Dunlop & Özdemir, 2007)

vated condition is called superparamagnetism. There exists a superparamagnetic (SP) threshold size d_s which represents an effective lower limit to the stable SD range (Table II.1). Thus, d_s is strongly dependent on temperature.

As SD particles grow larger, magnetic domains form and these particles are called multidomain (MD). They are not uniformly magnetized. While inside each domain the magnetization is Ms, the entire grain has a net magnetization M lower than Ms. When such a crystal is submitted to an external magnetic field, domain walls move in response to it (Figure II.18). As the field increase, the domain walls move in sudden jerks as each successive local wall energy high is overcome. This process is called Barkhausen jumps. At saturation, all the walls have been flushed out of the crystal and it is uniformly magnetized. When the field decreased, domain walls begin to nucleate. Because the energy of nucleation is larger than the energy of denucleation, there is a net saturation remanence. The walls migrate around as a magnetic field is applied in the opposite direction until there is no net magnetization.

Between SD and MD grains, there are intermediate size grains called pseudo single domain (PSD) grains. They are larger than SD, even MD, but exhibit SD-like magnetic properties.

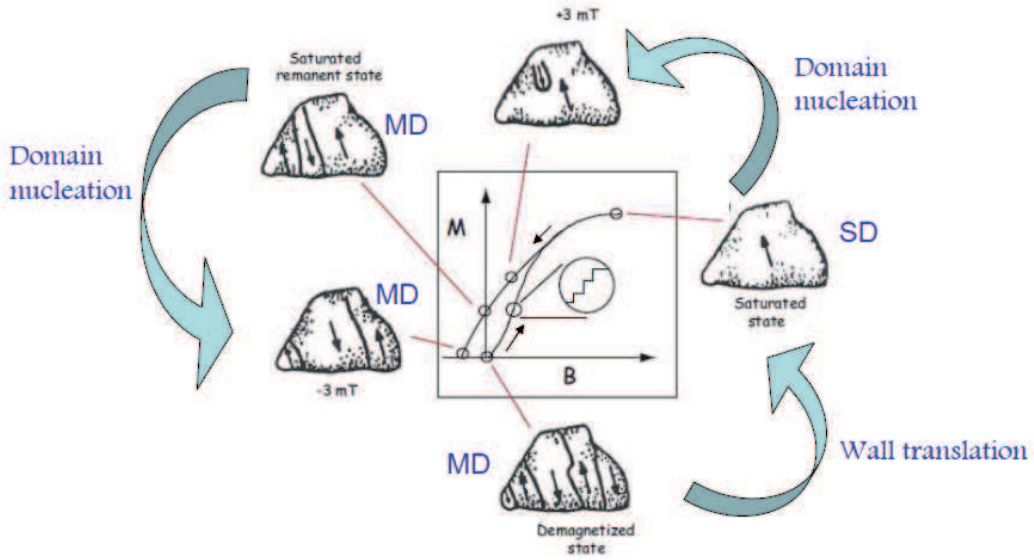

Figure II.18 – Schematic view of the magnetization process in multidomain grain (modified from Tauxe, 2008)

The grain size determines how the magnetic properties of the mineral evolve under magnetic field. This is the principle of the hysteresis loop.
Rocks are an assemblage of ferro/antiferro-magnetic grains dispersed in a dia/para-magnetic matrix. All the particles are randomly oriented. A sample from such a rock would display a hysteresis loop similar to that in Figure II.19. First, a magnetic field is applied and the initial slope of the loop is the low field susceptibility (χ_{lf}). The magnetic field continues to increase to a maximum value (Bmax). All the magnetizations are in the field direction and the net magnetization is the saturation magnetization Ms. It could still exist a slope due to the non-ferromagnetic contribution (dia-or paramagnetism). It is called the high field susceptibility χ_{hf}. The loop must be slope-corrected to determine Ms. When the field is reduced to zero, the moments relax back to their individual easy axes. Some moments are in opposite direction to the magnetic field and cancel each other out. At B = 0 T, the net remanence after saturation is called the saturation remanent magnetization Mr. The field necessary to reduce the net moment to zero defined as the coercive field Bc (= μ_0 Hc). The coercivity of remanence Bcr (= μ_0 Hcr) is the magnetic field required to reduce Mr to zero. Hcr is always greater than or equal to Bc. A mineral is said "soft" (low) when Bc $<$ 10 mT and "hard" (high) when Bc $>$ 100 mT. These hysteresis parameters depend on temperature and grain size. Typical hysteresis loops for different grain sizes are represented in Figure II.20.

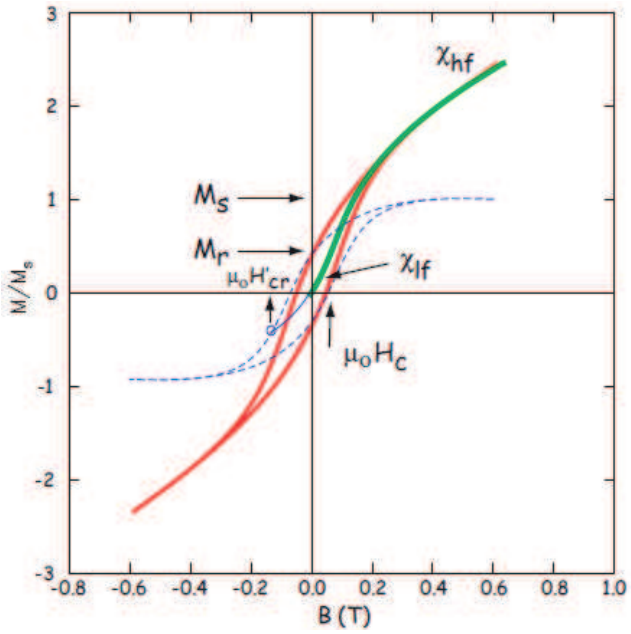

Figure II.19 – Typical hysteresis loop (Tauxe, 2008). In green and red (hard lines) : initial loop, in blue (dashed line) : slope-corrected loop. See text for explanation.

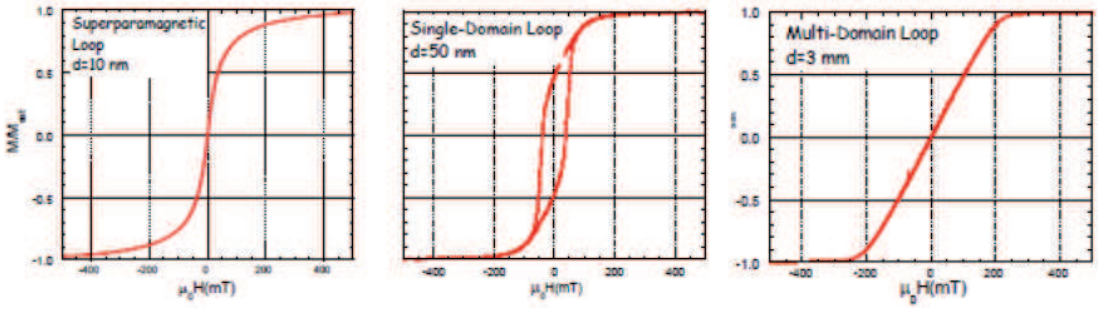

Figure II.20 – Typical hysteresis loops for different grain sizes of magnetite (IRM lecture notes)

To determine domain state and grain size from the hysteresis parameters, Day *et al.* (1977) plotted Mr/Ms with respect to Hcr/Hc and placed the bounds between points which separate the different grain sizes. This is the well-known "Day plot" (Figure VII.14).

SD grains have Mr/Ms $>$ 0.5. PSD grains have Mr/Ms comprised between 0.5 and 0.05 and Hcr/Hc between 1.5 and 5. MD grains have Mr/Ms $<$ 0.5. However, in addition to grain size, other factors do influence the hysteresis parameters. Mixture of magnetic phases like different composition and/or grain sizes yield distorted hysteresis loops (Figure II.22) and so the resulting Mr/Ms and Hcr/Hc ratios do not necessarily represent the specimen grain size (Pick & Tauxe, 1994 ; Tauxe *et al.*, 1996).

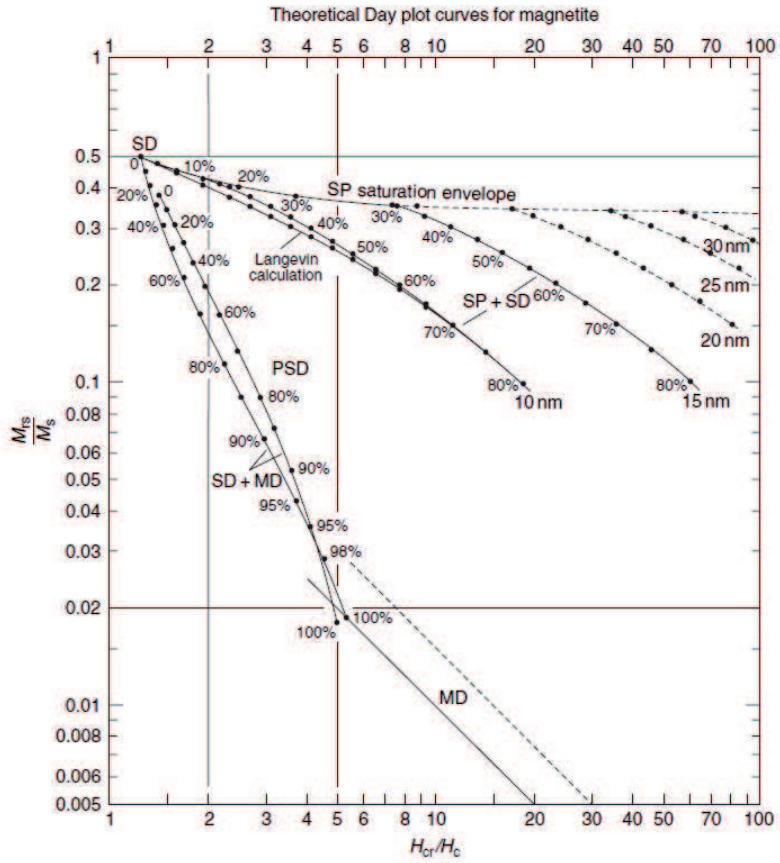

Figure II.21 – Theoretical Day plot curves for magnetite in various domain sates and mixtures of different states (Dunlop & Özdemir, 2007)

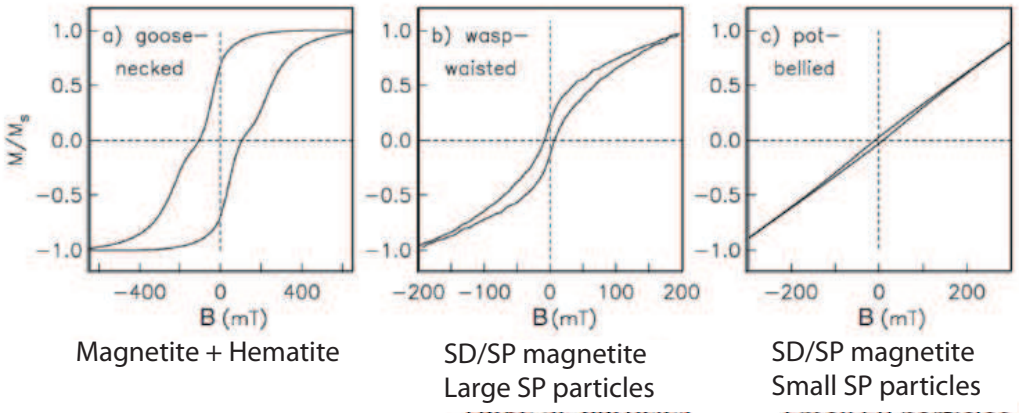

Figure II.22 – Distorted hysteresis loops and their signification (Tauxe *et al.*, 1996)

To represent hysteresis data, Mayergoyz (1986) developed a method known as First Order Reversal Curves or FORCs. The FORC diagrams provide separate representations of the coercivity distribution and the interaction-field distribution In the FORC experiment, like hysteresis, a sample is subjected to a saturating field. The field is lowered to some field H_a, then increased again through some value H_b to saturation. The magnetization curve between H_a and H_b is a FORC. A series of FORCs are generated to the desired resolution (Figure II.23). The FORC distribution is defined by :

$$\rho(H_a, H_b) = -\frac{\partial^2 M(H_a, H_b)}{\partial H_a \, \partial H_b}$$

To transform FORC data in a readily usable format, a regression smoothing technique is used (Harrison & Feinberg, 2008) which permits the calculation of FORC density at a certain point corresponding to arbitrary smoothed data. A FORC diagram is the contour plot of the FORC densities $\rho(H_a, H_b)$ along axes ($Hc = \frac{H_b - H_a}{2}, Hu = \frac{H_b + H_a}{2}$). In Figure II.24, FORCs diagrams for different grain sizes are represented.

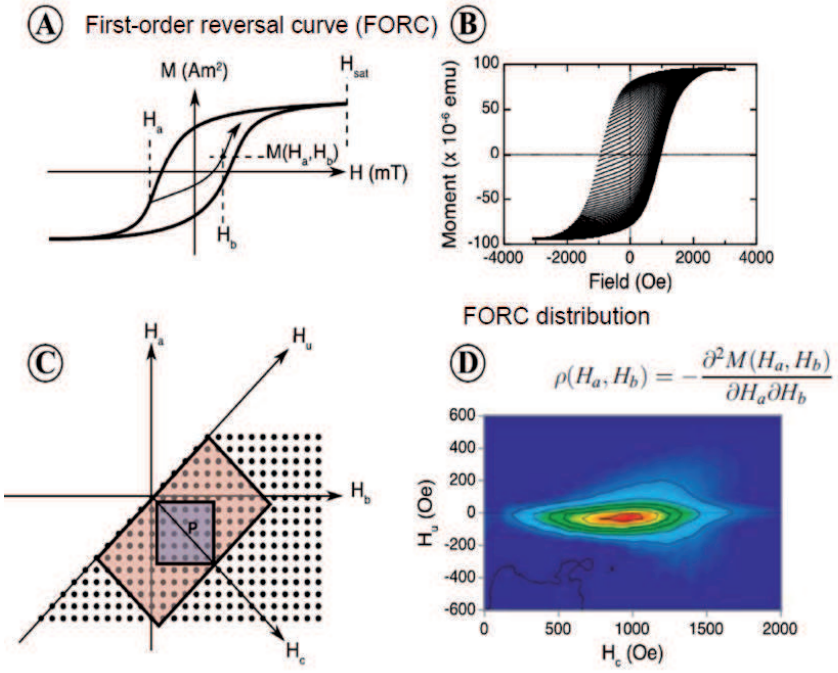

Figure II.23 – Principle of First Order Reversal Curves (IRM lecture notes after Harrison & Feinberg, 2008). See text for explanation.

All these magnetic properties, briefly presented, are responsible for the way the rocks get and stay magnetized for geological time scale. Table II.2 gives some typical magnetic properties of natural minerals at room temperature (e.g. Maher & Thompson, 1999).

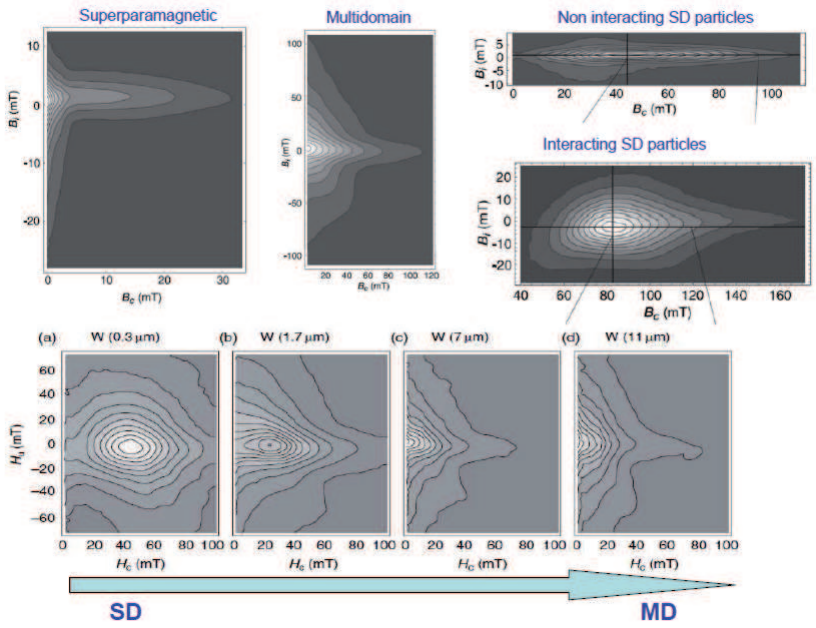

Figure II.24 – FORC diagrams for different grain sizes of magnetite (Muxworthy & Dunlop, 2002 ; Roberts *et al.*, 2006)

Mineral	Formula	X (SI)	Ms(Am²/kg)	Mrs (Am²/kg)	Tc/T_N (°C)
Diamagnetic					
Quartz	SiO_2	-16.4			
Calcite	$CaCO_3$	-13.6			
Paramagnetic					
Troilite	FeS	$0.6\text{-}1.7.10^3$			
Pyrite	FeS_2	$1.5.10^3$			
Siderite	$FeCO_3$	$4.9.10^3$	0.38		-238
Ilmenite	$FeTiO_3$	$4.7\text{-}5.2.10^3$	0		-236
Ulvöspinel	$FeTi_2O_4$	$4.8.10^3$	0		-156
Rhodochrosite	$MnCO_3$		0.46		-242
Clay minerals	Illite-Montmorillonite	$0.33\text{-}0.41.10^3$			
Ferromagnetic					
Iron MD	α-Fe	$3.9.10^6$		80	765
Ferrimagnetic					
Pyrrhotite	Fe_7S_8	$3.2.10^6$		4.5	320
Maghemite MD	$\gamma\text{-}Fe_2O_3$	$2\text{-}2.5.10^6$	74		590-675
Magnetite MD	Fe_3O_4	3.10^6	92	9	580
TM60	$Fe_{2.4}Ti_{0.6}O_4$	$0.13\text{-}0.62.10^6$	24	7	150
Titanomaghemite		$2.8.10^6$			
Greigite	Fe_3S_4		59	11	>350
Antiferromagnetic					
Pyrrhotite	Fe_9S_{10}	$0.17.10^6$	0.4-20		270
Hematite	$\alpha\text{-}Fe_2O_3$	$0.5\text{-}40.10^3$	0.4	0.24	675
Goethite	α-FeOOH	$1.1\text{-}12.10^3$	10^{-3}-1	0.05	120 (70-125)
Lepidocrocite	γ-FeOOH		0.1		-224

Table II.2 – Room temperature magnetic properties of some magnetic minerals. χ is the magnetic susceptibility, Ms the magnetization at saturation, Mrs the remanence at saturation, Tc is the Curie temperature for the ferromagnetic minerals and T_N is the Néel temperature for the ferri/antiferromagnetic minerals (Dunlop & Özdemir, 1997)

1.3 Magnetization in rocks

The minerals magnetization must be in equilibrium with the ambient Earth's magnetic field in order to be preserved. This natural remanent magnetization (NRM) is a function of several important parameters. Consequently, NRM is very often a sum of a primary - component formed during initial rock formation - and a secondary - component(s) formed at some later time - magnetizations (Table II.3).

	Type	**Process**
Primary NRM	Thermo Remanent Magnetization (TRM)	Cooling through Tc
	Detrital Remanent Magnetization (DRM)	Deposition of magnetic grains
	Chemical Remanent Magnetization (CRM)	Growth (alteration) of magnetic grains
Secondary NRM	Viscous Remanent Magnetization (VRM)	Long-term exposure to Ha *(Time)*
	Isothermal Remanent Magnetization (IRM)	Lighting strikes, exposure to large Ha *(Field)*
	Chemical Remanent Magnetization (CRM)	Growth (alteration) of magnetic grains *(Volume)*
	Partial TRM (pTRM)	Reheating below Tc *(Temperature)*

Table II.3 – Different types of NRM and associated processes (IRM lecture notes)

How ancient Earth's magnetic field is recorded and preserved in rocks ? Néel theory is the answer (Néel, 1949, 1955). To "jump over" magnetic anisotropy energy barriers, one mechanism is thermal energy E_T. At some temperature, with no ambient magnetic field, certain grains, having initial magnetization, will have sufficient energy to flip their moments to another easy axis. If there is no preferred direction, the magnetic moments will become random and the magnetization will decay to zero as a function of time (Figure II.25a) :

$$\mathrm{M}(t) = \mathrm{M}_0 \exp(-\mathrm{t}/\tau)$$

where t is time and τ the relaxation time which is the time required for the remanence to decay to 1/e of M_0.

τ depends on the competition between magnetic anisotropy energy and thermal energy (Figure II.26). It is a measure of the probability that a grain will have sufficient thermal energy to overcome the anisotropy energy and switch its moment. Therefore in zero external field :

$$\tau = \frac{1}{\mathrm{C}} \exp\frac{[\text{anisotropy energy}]}{[\text{thermal energy}]} = \frac{1}{\mathrm{C}} \exp\frac{[\mathrm{Kv}]}{[\mathrm{kT}]}$$

with C is a frequency factor $\sim 10^{10}s^{-1}$, K the dominant anisotropy parameter, v the grain volume, T the temperature and k the Boltzmann's constant. Relaxation time is proportional to coercivity and volume and is inversely related to temperature. τ varies rapidly with small changes in v and T.

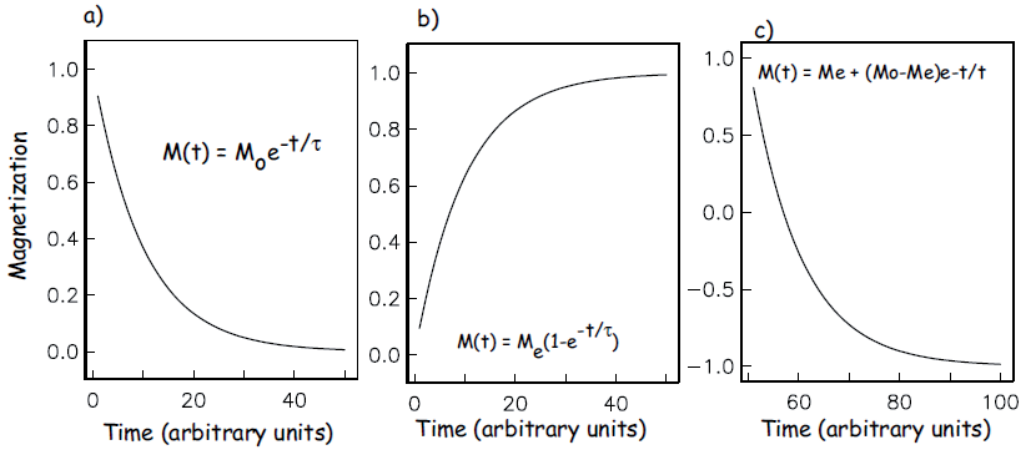

Figure II.25 – Magnetization versus time for a) saturation remanence placed in zero field, b) zero initial magnetization placed in a field and c) magnetization placed in an antiparallel field (Tauxe, 2008)

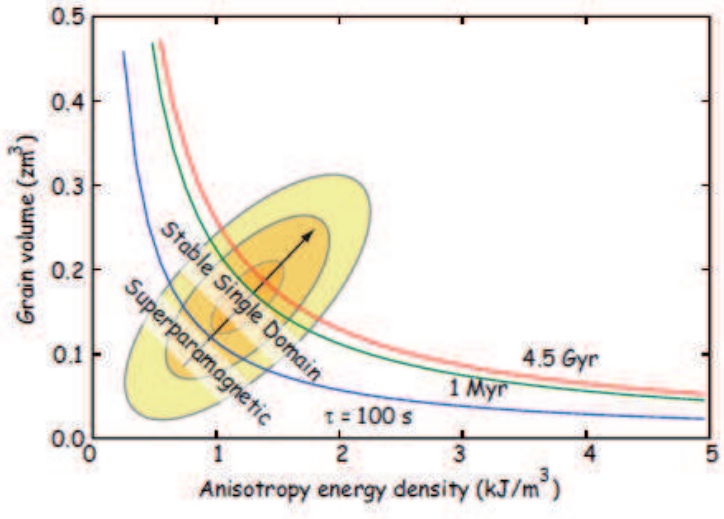

Figure II.26 – Lines of equal blocking energy in plot of grain volume v against the anisotropy energy K. Contours are for a hypothetical population of magnetic grains (Tauxe, 2008)

In a presence of an external magnetic field H_0, it requires less energy for magnetic particles to flip into the direction of the applied field than to flip the other way. So τ is also a function of the applied

field and the equation becomes :

$$\tau = \frac{1}{\tau_0} \exp\frac{[\mathrm{Kv}]}{[\mathrm{kT}]} \left[\frac{1 - \mathrm{H}_0}{\mathrm{H}_k}\right]^2 \text{ and } \mathrm{H}_k = \frac{2\mathrm{K}}{\mu_0 \mathrm{Ms}}$$

with H_k the microscopic coercive force and τ_0 the atomic reorganization time or interval between successive thermal excitations. Thus τ is also a function of magnetization.

1.3.1 Viscous Remanent Magnetization (VRM)

As seen previously, in absence of a magnetic field, magnetization of the sample decreases according to equation

$$\mathrm{M}(t) = \mathrm{M}_0 \exp(-\mathrm{t}/\tau)$$

In an external magnetic field, magnetic particles acquire magnetostatic energy. As inferred previously, a given particle will tend to spend more time with its moment at a favorable angle to the applied field than in the other direction. Then the magnetization would tend to grow to some non-zero equilibrium magnetization M_e such that (Figure II.27) :

$$\mathrm{M}(t) = \mathrm{M}_e[1 - \exp(-\mathrm{t}/\tau)]$$

The magnetization acquired is a viscous remanent magnetization (VRM). VRM will therefore change as a function of time (Figure II.27B), and so the relationship between the remanence vector and the applied field. τ is a strong function of temperature and VRM will grow with increasing temperature (Figure II.27A). Viscous magnetization rises to a dramatic peak 50-100°C below Tc : this is the Hopkinson effect. The cause is rapid decrease in Ms and H_k or Hc. This temperature range corresponds also to the main range of TRM blocking/unblocking temperatures and of enhancement of susceptibility (Dunlop & Özdemir, 1997).

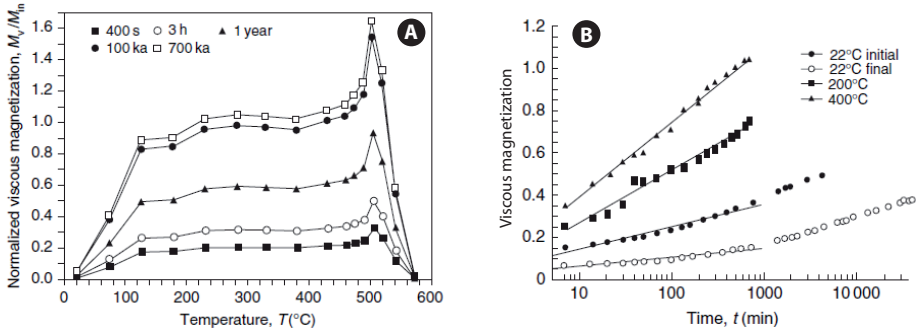

Figure II.27 – Evolution of Viscous Remanent Magnetization (VRM) with a) temperature and b) time (Dunlop & Özdemir, 2007, after Pozzi & Dubuisson, 1992 and Kelso & Banerjee, 1994)

1.3.2 Thermal Remanent Magnetization (TRM)

As said before, τ is a function of temperature and grain size (Figure II.28). For instance at room temperature, a 30 nm particle would have a relaxation time of billions of years, while at 300°C, the grain is superparamagnetic (τ of few 100's seconds).

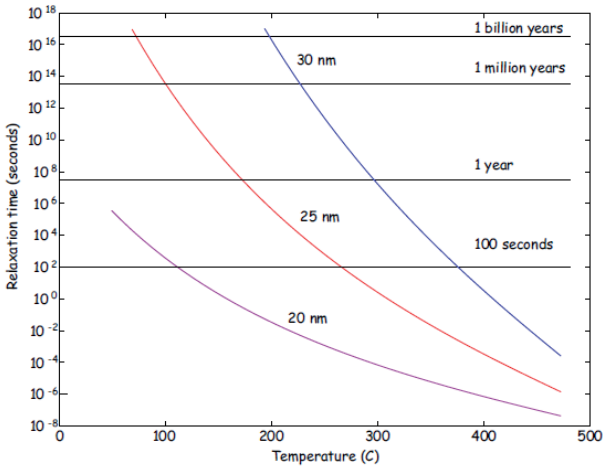

Figure II.28 – Variation of relaxation time versus temperature for magnetite cubes of different lengths (all with length for width ratios of 1 : 3 : 1) (Tauxe, 2008)

It is therefore possible to define a temperature above which a grain is superparamagnetic and able to come into equilibrium with an applied field. This is called the blocking temperature T_B. At or above T_B, but below Tc, a grain will be superparamagnetic. Cooling below T_B increases the relaxation time so the magnetization is effectively blocked and the rock acquires a thermal remanent magnetization or TRM.

The remanence acquired in the presence of a magnetic field is parallel to the orientation of that field and its intensity is proportional to the intensity of the magnetic field applied during cooling for small, uniformly magnetized equant particles (Figure II.29).

For SD particles, the intensity of a weak-field (Earth's magnetic field) TRM is proportional to the applied field strength H_0. Moreover T_B is equal to T_{UB} the unblocking temperature during zero-field reheating. T_{UB} and T_B vary with grain volume v and microcoercivity H_k (Figure II.30). The smaller the grain size, the lower is T_{UB} or T_B. TRM intensity varies strongly with grain size. It increases as v increases : large SD grains should align their moment more efficiently in the direction of H_0 than small grains (Figure II.31). For MD grains, there is no single T_{UB} or T_B. Moreover, TRM intensity is non linear with that of the applied field, except for low values (< 0.1 mT) which is the region of interest in paleointensity determination.

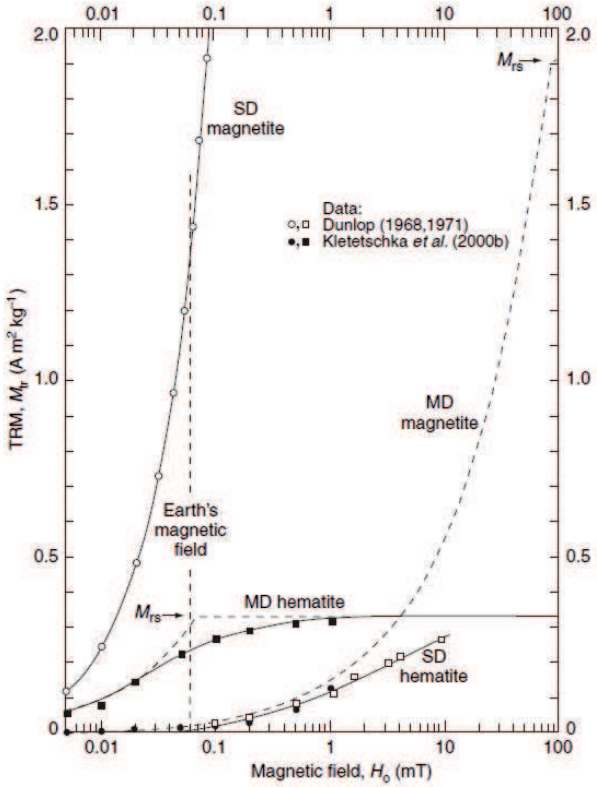

Figure II.29 – Experimental (hard) and theoretical (dashed) dependences of Thermal Remament Magnetization (TRM) intensity on applied magnetic field H_0 (Dunlop & Özdemir, 2007 after Dunlop & Kletetschka, 2000).

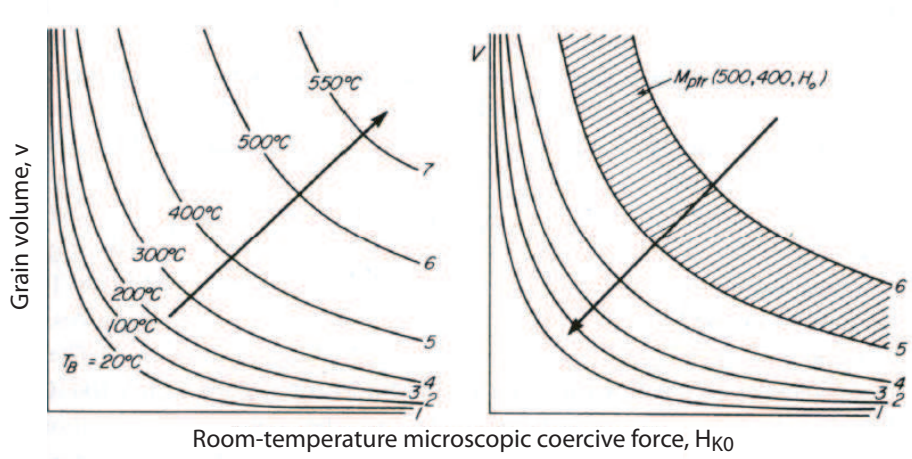

Figure II.30 – Modeling thermal demagnetization of remanence carried by a distribution of SD grains using blocking curves (T_B = constant) on the Néel diagram (Dunlop & Özdemir, 1997)

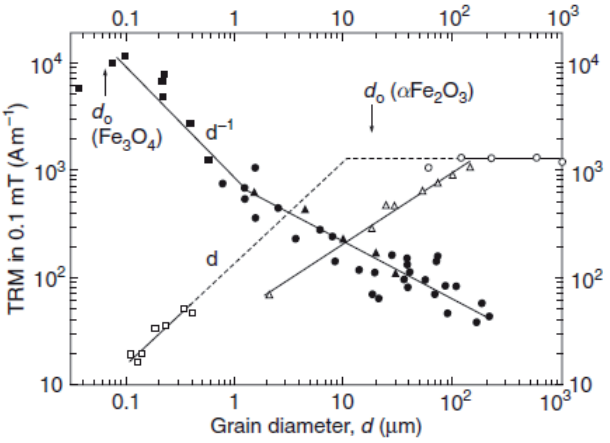

Figure II.31 – Grain-size dependence of Thermal Remanent Magnetization (TRM) intensity for magnetite and hematite (Dunlop & Özdemir, 2007 after Dunlop & Arkani-Hamed, 2005)

1.3.3 ThermoViscous Remanent Magnetization (TVRM)

There exists a strong and narrow relationship between time, temperature and magnetization. Rocks can be exposed to elevated temperature for long periods of time that is the case of deep burial. Grains with relaxation time, at the elevated temperature, shorter than the exposure time may have acquired a thermoviscous remanent magnetization (TVRM). This is important in the case of remagnetization. Considering that the the last grains to acquire remanence are the last to be demagnetized under laboratory heating and assuming that $H_0 << H_k$, Pullaiah *et al.* (1975) stated :

$$\frac{T_L \; ln(t_L/\tau_0)}{Ms(T_L)H_k(T_L)} = \frac{T_A \; ln(t_A/\tau_0)}{Ms(T_A)H_k(T_A)}$$

T_L, t_L, T_A, t_A being laboratory and ancient temperature and time respectively. This allows drawing some time-temperature contours (Figure II.32). T_B is time dependent at low temperature and almost time independent near Tc.

On the Figure II.32, a sample naturally heated at 130°C for 1 Ma shows a blocking temperature of ∼260°C when laboratory heated for 1h.

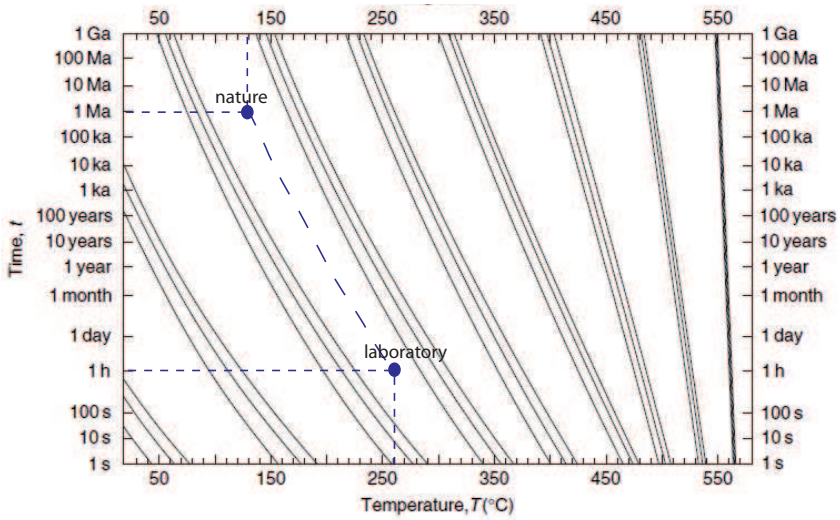

Figure II.32 – Time-temperature blocking contours for SD grains of magnetite (modified after Dunlop & Özdemir, 2007)

1.3.4 Chemical Remanent Magnetization (CRM)

Neoformation of magnetic grains may lead to a chemical remanent magnetization (CRM) also called crystallization remanent magnetization or g-CRM for growth CRM (Dunlop & Özdemir, 1997). New magnetic grains can be formed by nucleation or crystalline growth. This kind of CRM (g-CRM) is by opposition to a-CRM ("alteration", Tauxe, 2008) which is a CRM acquired by alteration of preexisting magnetic minerals (e.g. oxidation, state change...). Formation or removal of magnetic grains may occur at different moments in a sedimentary rock history. Many natural processes can lead to production of magnetic minerals carrying CRM, among which :

- Precipitation from iron-rich solution (Larson *et al.*, 1982)
- Biogenic processes via bacteria (Karlin *et al.*, 1987)
- Inorganic authigenesis (Maher & Taylor, 1988)
- Hydrothermal alteration (e.g. Smith & Banerjee, 1986)
- Fluid circulation (e.g. Oliver, 1986)
- Deformation (Lewchuk *et al.*, 2003)
- Maturation of organic matter (Banerjee *et al.*, 1997)

In the simple case where a magnetic mineral is nucleated in presence of a magnetic field, CRM is acquired when the mineral reaches a certain volume called blocking volume V_b and expressed as (Figure II.33) :

$$V_b = ln(C\tau)\frac{kT}{K} \text{ at constant temperature}$$

where k is the Boltzmann's constant (1.38 x 10^{-6} erg/K), T the temperature (K), K the anisotropy constant, τ the relaxation time (s) and C the frequency factor (10^9).

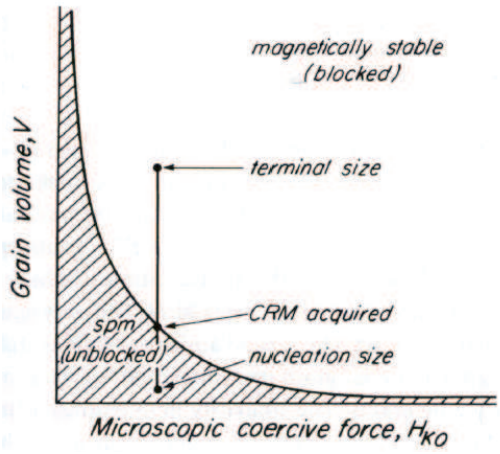

Figure II.33 – Modeling the acquisition of Chemical Remanent Magnetization (CRM) on the Néel diagram (Dunlop & Özdemir, 1997)

Below V_b, grains are in equilibrium with the magnetic field. They behave like SP grains as thermal energy dominates the system. Above V_b, volume becomes sufficient for magnetic anisotropy to overcome thermal energy. The grain moment is blocked and the grain is capable to retain a remanence. The magnetization acquired during grain growth is controlled by the alignment of grain moments at the time that they grew through V_b. So CRM should behave very similarly to TRM.
CRM is the cause of many remagnetizations, especially the widespread remagnetization of rocks in the Appalachian thrust belt in North America in relation with the presence of secondary magnetite (e.g. McCabe & Elmore, 1989).
Experimental studies by Stokking & Tauxe (1987), Stokking & Tauxe (1990) and Pick & Tauxe (1991) showed that the intensity of CRM increases with increasing intensity of the applied magnetic field (Figure II.34).

In addition to natural remanent magnetization produced in nature, artificial magnetizations can also be produced in rocks. In this work, we used Isothermal Remanent Magnetization (IRM). IRM is created by applying a very strong magnetic field on samples in order to align magnetic moments in the direction of the applied field. This principle is beyond the 3D IRM technique of Lowrie (1990) described in chapter III which allows identification of magnetic minerals. Properties of IRMs are also used for determining concentration and grain sizes. However, IRM can be produced naturally by lightning impact.

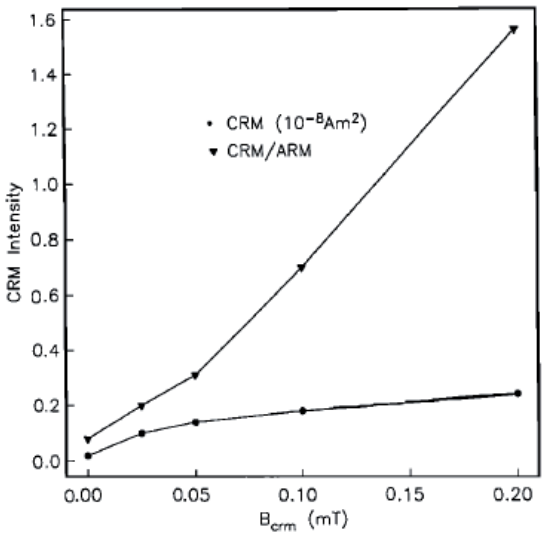

Figure II.34 – CRM intensity as a function of the applied magnetic field Bcrm (Stokking & Tauxe, 1990). ARM is the anhysteretic remanent magnetization which is a laboratory magnetization (a proxy of the magnetic minerals concentration).

2 Magnetic properties at low temperature of current minerals

Over the last two decades, low temperature (< 300 K) magnetic measurements in geosciences have been increasingly used thank to the availability of dedicated devices such as the MPMS (Magnetic Properties Measurement System). These instruments allow the recognition of current magnetic minerals, even in very low concentration (∼ppm-ppb).

Magnetic measurements at low temperature, i.e. below room temperature (< 300 K), against measurements at high temperature, have been developed to prevent chemical alteration due to thermal heating (Van Velzen & Zijderveld, 1992). This is very important in the case of sedimentary rocks which alter rather easily during thermal treatments (e.g. Cairanne *et al.*, 2004).

Many factors control the low temperature behavior of the magnetic minerals. Phase transitions, which occur below room temperature, are the most major factor. Changes in intrinsic properties of the mineral due to temperature variations are also important. Low temperature magnetic properties are also affected by stoichiometry and degree of crystallinity of minerals. Finally, low temperature remanence and magnetic susceptibility evolutions are generally grain size dependent. For instance, ultrafined superparamagnetic grains display a quasi exponential decrease of the remanence on warming because of the progressive unblocking of magnetization due to the thermal activation.

The low temperature magnetic measurement the most commonly used is the thermal demagneti-

zation of a saturation isothermal remanent magnetization (SIRM) acquired most often at 10 K. This allows the detection of magnetic phase transitions, even for a very weak concentration of the magnetic minerals (ppb).

In the following, we will focus on low temperature magnetic properties of some of the magnetic minerals relevant to the work reported in the following chapters.

2.1 Superparamagnetic particles

The superparamagnetic particles are very small (∼10s nm) and are present in very low concentration in rocks (∼ppm-ppb). Magnetic methods are therefore most appropriate to detect them.
As stated before, superparamagnetism (SP) describes the state of SD-sized grain with thermal energy high enough to overcome anisotropy energy barriers. The magnetization of such grains reverses over very short time scales. Hence, the SP grains dot not carry remanence. For a given volume, the grain can be blocked by lowering the temperature (i.e. decreasing the available thermal energy).
A SIRM acquired at 300 K is not typically useful for studying SP particles because they will not block at room temperature. However, many of them will be blocked if the SIRM is imparted at 10 K (LT-SIRM, Figure II.35). SP grains then show a progressive decrease in magnetization from 10 to 300 K due to thermal unblocking. If a sample contains a relatively narrow grain size distribution of SP particles, the LT-SIRM will unblock over a relatively narrow temperature interval. In the case of a wider distribution, the unblocking will be more gradual.

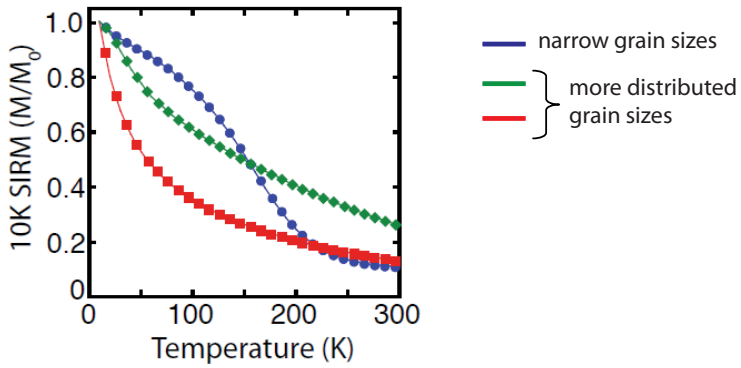

Figure II.35 – Evolution of SIRM acquired at 10 K on warming from 10 to 300 K (Bowles *et al.*, 2009)

On the other hand, in between the fully unblocked state and the fully blocked state, susceptibility will be at a maximum near T_B. Susceptibility (in-phase and out-of-phase) is frequency dependent as the sample goes through the blocking temperature interval. As for LT-SIRM, a very narrow grain size population will result in a relatively narrow temperature range over which frequency dependence is

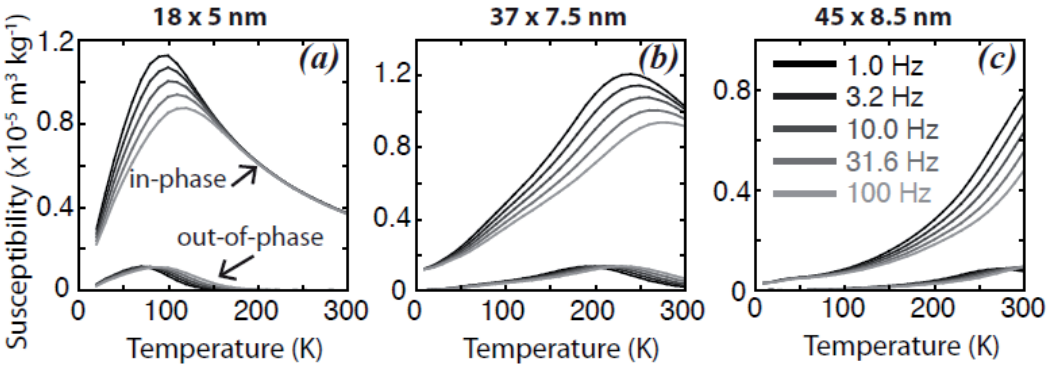

Figure II.36 – Frequency dependence of AC susceptibility for different grain sizes from Tiva Canyon Tuff (Bowles *et al.*, 2009). The average grain size was determined by TEM observation.

observed and in a well-defined maximum in susceptibility (Figure II.36a). This peak shifts to higher temperatures for a larger dominant grain size (Figure II.36b,c). Absence of frequency dependence at room temperature does not preclude the presence of an SP population.

The gradual decrease of LT-SIRM on warming observed in Figure II.35 is not necessarily related to SP unblocking. It may also result from domain-wall reorganization or from partial oxidation (e.g. maghemitization). For the latter, the remanent magnetization decay below 50 K. A phase transition can be also accompanied by a decrease of LT-SIRM below 50-60 K as it is the case for pyrrhotite and siderite for instance. This kind of transition is generally characterized by a frequency dependence of susceptibility. Finally, samples with a large paramagnetic/ferromagnetic ratio may display a marked decrease in the LT-SIRM as a result of an imperfectly-zeroed field (residual field) in the magnetometer (which may enhance the paramagnetic contribution).

2.2 Fe-Ti oxides

The most important magnetic minerals are iron- and titanium oxides. There are three series that can be plotted in a ternary FeO-Fe_2O_3-TiO_2 diagram (Figure II.37) :

- Stoichiometric titanomagnetites with spinel structure varying between two end-members magnetite Fe_3O_4 and ülvospinel Fe_2TiO_4
- Non-stoichiometric (oxidized) titanomagnetites (titanomaghemites)
- Titanohematites (or hemoilmenites) with rhombohedral structure varying between two end-members hematite $\alpha - Fe_2O_3$ and ilmenite $FeTiO_3$

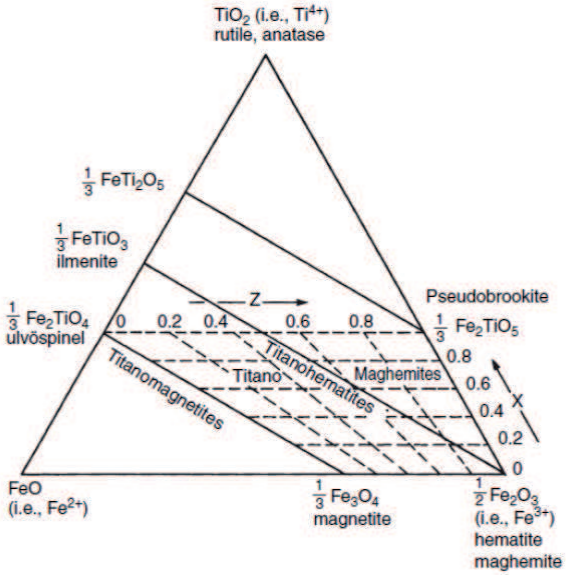

Figure II.37 – Ternary diagram showing the Fe-Ti oxides and their solid solutions (Dunlop & Özdemir, 2007)

2.2.1 Magnetite Fe_3O_4

Magnetite Fe_3O_4 ($Fe^{2+}Fe_2^{3+}O_4$) is the most known and the most common natural magnetic mineral. It is present, in variable concentration, in all kinds of rocks (volcanic, sedimentary and metamorphic rocks). Moreover, magnetite can be produced biologically by a wide variety of organisms like magnetotactic bacteria.

Magnetite is a cubic mineral with inverse spinel structure. Oxygen anions form a face-centered cubic lattice with Fe^{2+} and Fe^{3+} cations in interstitial sites (Figure II.38).

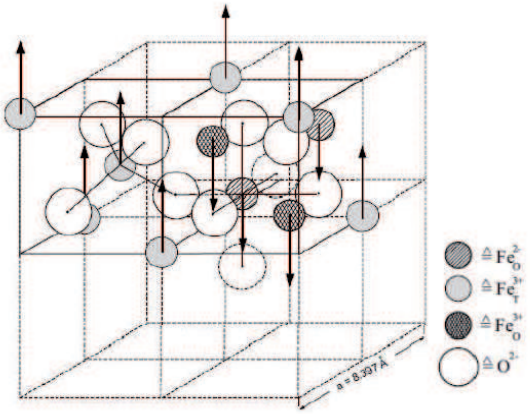

Figure II.38 – Crystal structure of magnetite (Walz, 2002)

Magnetite is ferrimagnetic at room temperature. At low temperature, magnetite is characterized by a phase transition at about T_V ~120 K (Muxworthy & McClelland, 2000). This is the Verwey transition (Verwey, 1935). This transition is due to the lattice distortion from cubic above T_V to monoclinic below T_V because of the ordered arrangement of Fe^{2+} and Fe^{3+} ions. It is easily recognizable in demagnetization curve of a SIRM acquired at 10 or 300 K by a drop of the remanence at T_V (Figure II.39). This drop occurs also in the susceptibility (Figure II.40 ; Muxworthy, 1999). Susceptibility does not display any frequency dependence at low temperature.

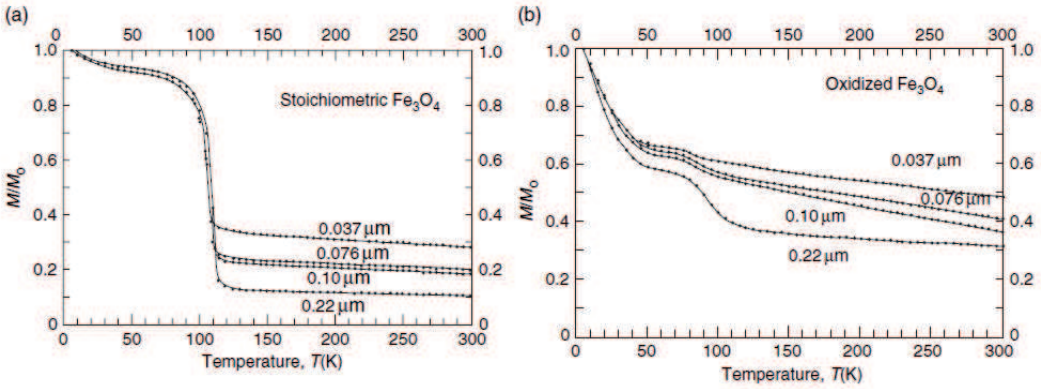

Figure II.39 – Zero field warming curves of a 5 K SIRM for a) stoichiometric SD magnetites and b) oxidized magnetites (Özdemir *et al.*, 1993)

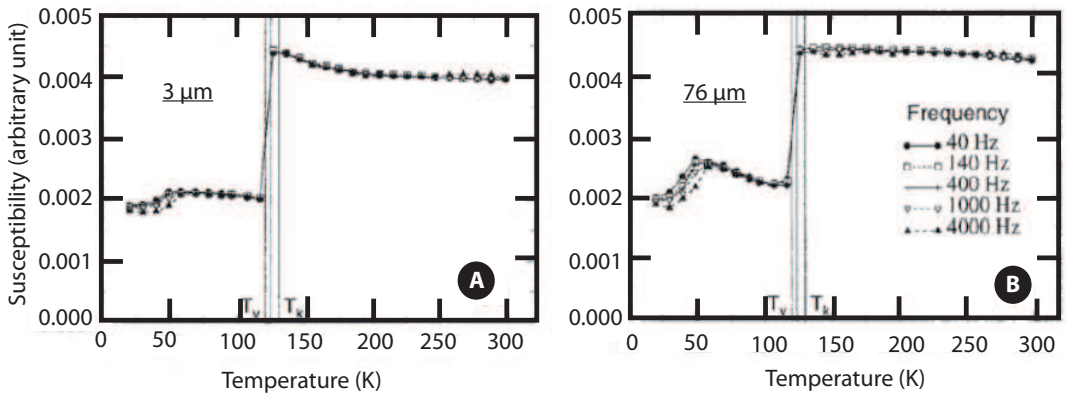

Figure II.40 – Magnetic susceptibility X vs. temperature T for MD magnetites : A) 3 μm and B) 76 μm (Muxworthy, 1999)

When cycling through T_V in zero field, some fraction of the initial remanence is always recovered whatever the size and shape of the magnetite grains. This fraction is called the low temperature memory. Memory is larger for shape-controlled SD grains and decreases as grain size increases (Figure II.41 ; Heider *et al.*, 1992 ; Halgedahl & Jarrard, 1995 ; Özdemir *et al.*, 2002).

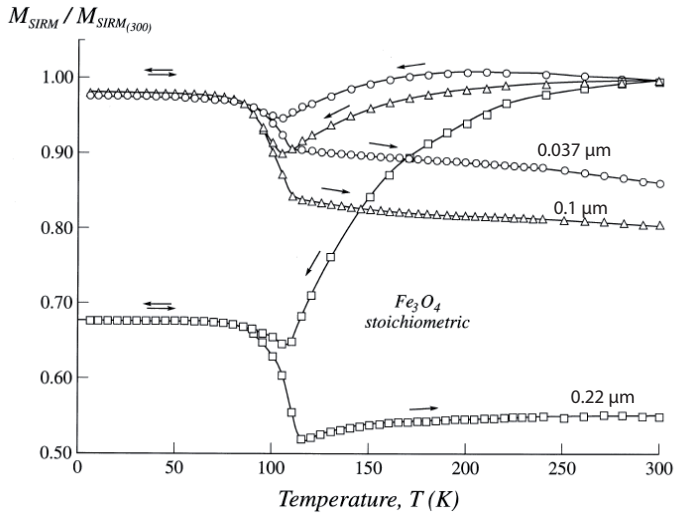

Figure II.41 – Evolution of normalized SIRM of submicron magnetites (Özdemir *et al.*, 2002)

The main magnetic effect is an increase of the magnetocrystalline anisotropy below T_V of about one order of magnitude. At a temperature T_K slightly above T_V (T_K ~130 K), the easy axes switch from <111> to <100>. This is called the isotropic point which corresponds to a change of sign of the first magnetocrystalline anisotropy constant T_K. At T_K , $K_1 = 0$ (Figure II.42).

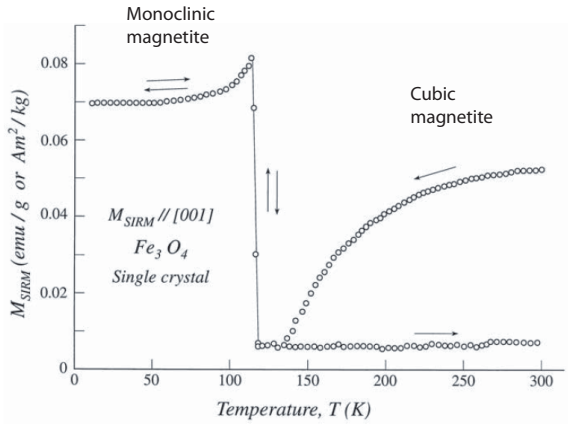

Figure II.42 – Evolution of the magnetization at saturation showing the isotropic point (T_K) and the Verwey transition (T_V) of magnetite (Özdemir & Dunlop, 1999)

Hysteresis parameters change at low temperature (Figure II.43). For submicron magnetite, Hc is almost constant from 300 K to the Verwey transition. At the transition, all magnetites show an increase in Hc. Below T_V, Hc continues to increase but more slowly. The decrease of Hc occurs at T_K rather than T_V because at T_V there is a discontinuous jump in the magnetocrystalline anisotropy energy (Muxworthy, 1999). As with Hc, Mrs/Ms are almost temperature independent between room

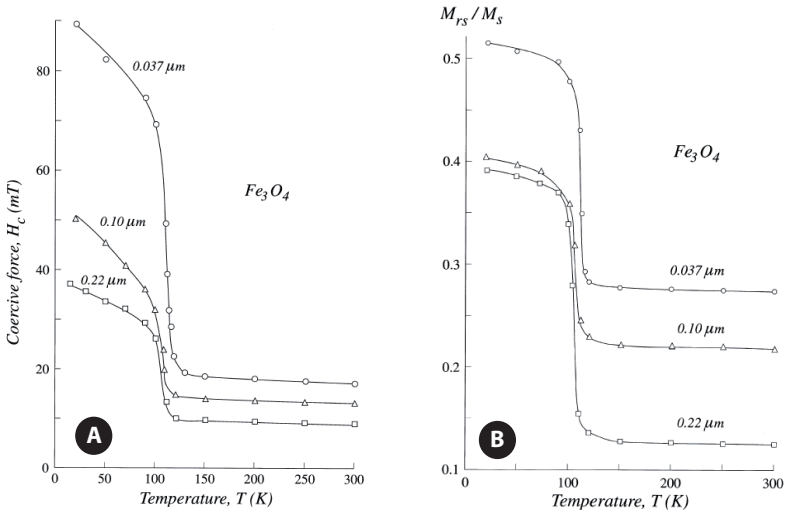

Figure II.43 – A) Coercive force Hc vs. temperature T and B) Mr/Ms vs. T for submicron magnetites (Özdemir *et al.*, 2002)

temperature and T_V. However at the transition point the ratio increases very strongly and rapidly, while it changes very little below T_V.

Fe substitution by Ti, insertion of alien metallic cations (Al, Mg) decrease temperature of the Verwey transition and can even suppress it. Verwey transition is suppressed for Ti < 0.04 (Figure II.45 ; Kakol *et al.*, 1992). Non-stoichiometry of magnetite grains (e.g. Aragòn *et al.*, 1985), oxidation (Figure II.39 ; Özdemir *et al.*, 1993) and stress (Borradaile & Jackson, 1993) have similar effect.
Biogenic magnetite (in form of magnetosome) can be easily distinguished from inorganic magnetite because it displays typical magnetic criteria (Moskowitz *et al.*, 1993).

2.2.2 Titanomagnetites

Titanomagnetites TM are ferrimagnetic Fe-Ti inverse spinels of $Fe_{3-x}Ti_xO_4$ composition. Beyond x$\sim$0.8, oxides are paramagnetic. The replacement of Fe^{3+} on octahedral sites by non magnetic Ti^{4+} causes the magnetization to decrease as Ti content x increases (Figure II.44).

At low temperature, low-Ti titanomagnetites (x < 0.4) have transition temperature below 100 K. There is a drop of SIRM (Figure II.45). For x > 0.4, SIRM is practically temperature independent below 50 K, rapidly decreases with temperature between 50 and 80 K and then continues to decay more gradually with temperature up to 300 K (Moskowitz *et al.*, 1998).
Ti-rich composition (x > 0.5) show the strongest temperature dependence of χ (Figure II.46).

TM compositions near TM20-TM30 have remanence transitions near or below 50 K which could be misidentified as the 34 K pyrrhotite or the 38 K siderite transitions. Compositions near TM40 have isotropic points around 120 K which is the Verwey transition of magnetite. Coarse-grained TM compositions near TM60 exhibit SIRM warming curves which could be misinterpreted as ultrafined

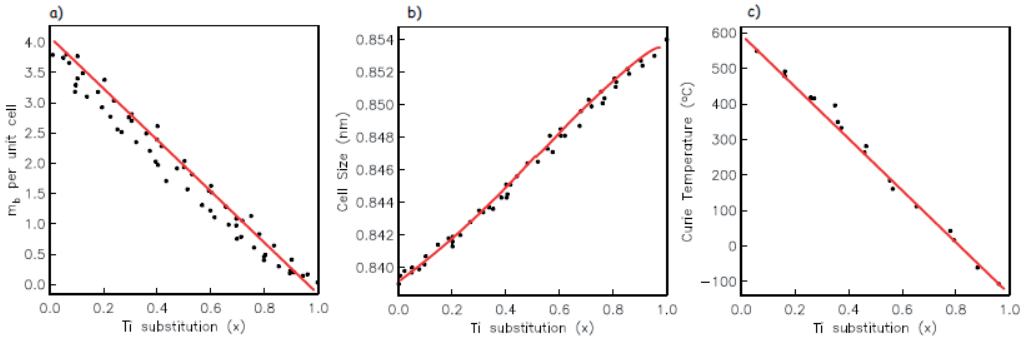

Figure II.44 – Variation of intrinsic parameters with Ti substitution in the titanomagnetite lattice (Tauxe, 2008)

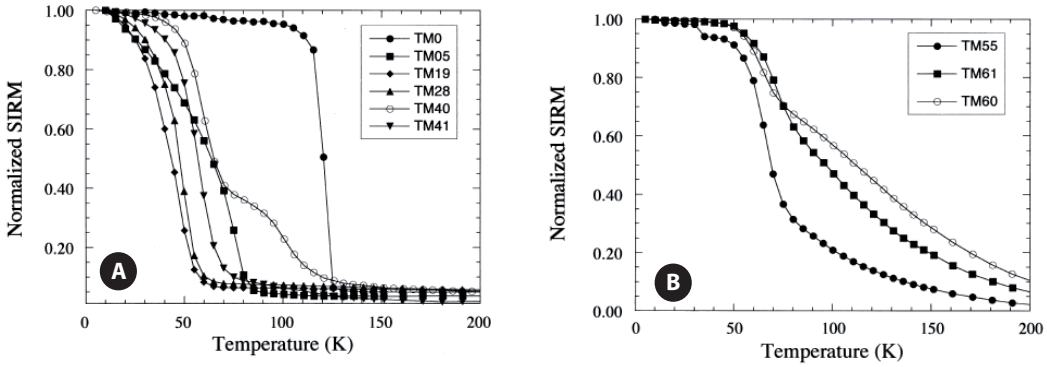

Figure II.45 – Evolution of normalized SIRM curves of synthetic titanomagnetites on warming for different Ti-content (Moskowitz *et al.*, 1998)

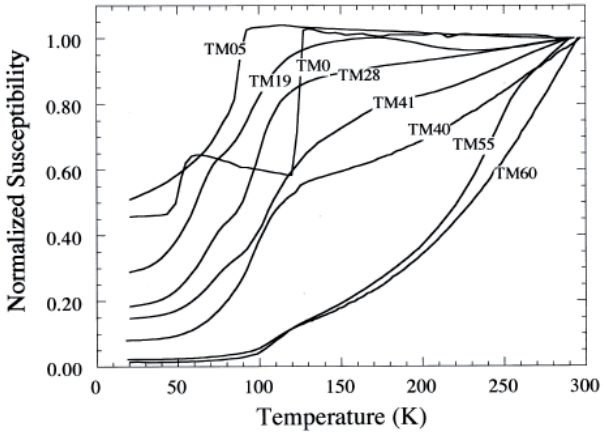

Figure II.46 – Evolution of normalized susceptibility χ for different Ti-content synthetic titanomagnetites on warming (Moskowitz *et al.*, 1998)

SP grains (Moskowitz *et al.*, 1998). In nature, two compositions are commonly found :

- TM60 (x = 0.6, $Fe_{2.4}Ti_{0.6}O_4$) essentially found in MORB (mid-ocean ridge basalt) which composition actually ranges from TM50 to TM70
- TM10-TM30 found in andesitic and dacitic volcanic rocks.

2.2.3 Maghemite ($\gamma - Fe_2O_3$) and titanomaghemites

Maghemite $\gamma - Fe_2O_3$ is the fully low-temperature oxidized equivalent of magnetite. Maghemite is strongly ferrimagnetic with same chemical composition as hematite ($\alpha - Fe_2O_3$) but with a structure essentially similar to that of magnetite (Fe_3O_4). Maghemitization is an iron-leaching process, usually occurring in the presence of water, leading to vacancies in the spinel lattice.
Maghemite has no Verwey transition, nor any transition below room temperature. Remanence acquired by maghemite at low temperature (say 10 K) decreases monotonically upon warming to 300 K (Figure II.47).

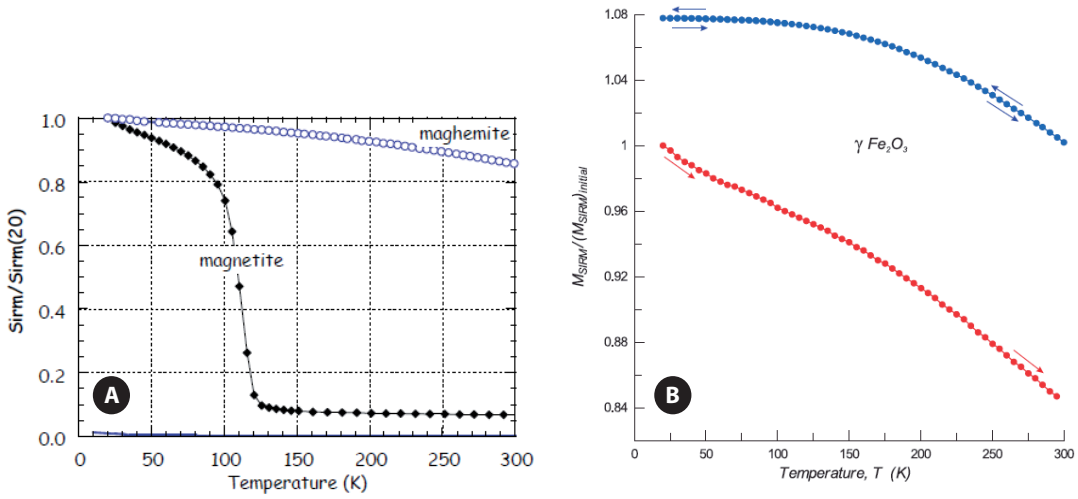

Figure II.47 – A) SIRM curve on warming for maghemite compared to that of magnetite, B) ZFC cooling and rewarming of a 300 K SIRM and 20 K SIRM on warming for maghemite (Özdemir & Dunlop, 2010)

Maghemitization effect leads to (Figure II.48 ; Özdemir & Dunlop, 2010) :

- Lowering Verwey transition temperature when warming a 20 K SIRM
- When cycling a 300 K SIRM, region of the Verwey transition is shifted and broadened
- When cooling and warming a 300 K SIRM, curves are typically humped
- Reducing Verwey transition amplitude

As there exist titanomagnetites, there exist also titanomaghemites which formed by oxidation of TM60. Titanomaghemite structure is metastable and can invert to form hematite, or can be reduced

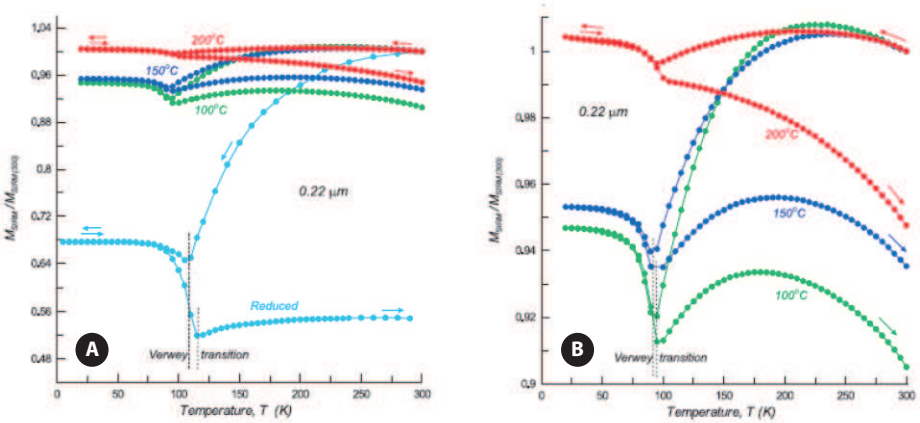

Figure II.48 – ZFC cooling and rewarming of a 300 K SIRM in 22 nm magnetites heating at different temperatures (Özdemir & Dunlop, 2010)

to form magnetite.
Maghemite is commonly found in soils and deep-sea sediments.

2.2.4 Hematite $\alpha - Fe_2O_3$

Hematite $\alpha - Fe_2O_3$ is the fully oxidized end-product of magnetite. It has a corundum (rhombohedral) structure (Figure II.49). At room temperature, it is antiferromagnetic with a weak parasitic ferromagnetism due to spin-canting or defect ferromagnetism. It is canted antiferromagnetic (Lin, 1959).

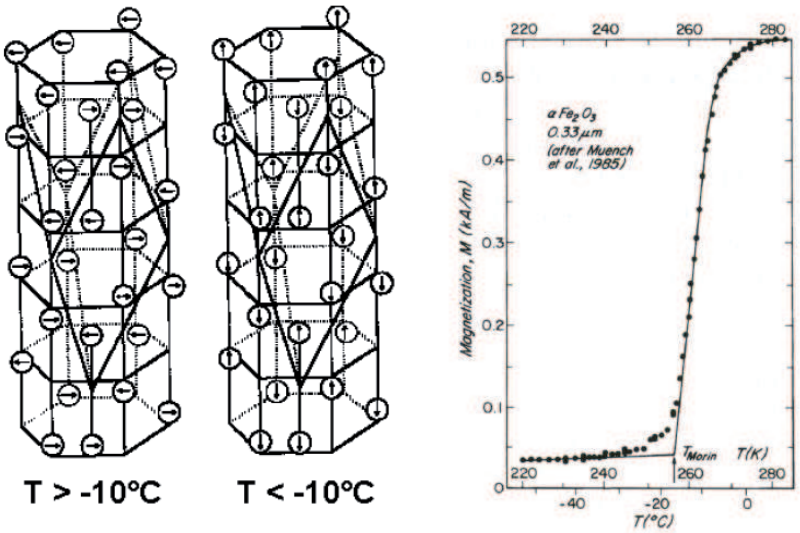

Figure II.49 – Crystal structure of hematite above and below Morin transition T_M (Butler, 1992 ; Dunlop & Özdemir, 1997)

Hematite displays a low temperature magnetic transition due to change in magnetic state rather than change in symmetry as it is the case for magnetite. This transition, called Morin transition, occurs at T_M ∼250 K (Morin, 1950). The Morin transition is (also) the hematite's magnetic isotropic point. At T_M ∼250 K, the net anisotropy changes in sign causing a change in crystallographic easy axis and thus an antiferromagnetic spin flop (Dunlop & Özdemir, 1997). When $T < T_M$, the magnetization M_A and M_B of the two sublattices is pinned along the c-axis and there is no spin-canting. It is a pure antiferromagnetic state. At $T > T_M$, M_A and M_B display a canted resultant moment lying in the c-plane and they are perpendicular to the c-axis (Figure II.50). In addition to the spin canted ferromagnetism that disappears below T_M, hematite possesses a defect moment due to chemical or lattice defects (isotropic ferromagnetism) non affected by the Morin transition.
As for magnetite, when cycling through the Morin transition, hematite recovers a fraction of the initial remanence, the remanence memory during reheating to room temperature (Figure II.50). This is probably due to domain reorganization (de Boer *et al.*, 2001) or to the spin-canted magnetism intrinsic to the crystal structure, rather than the soft defect magnetism (Özdemir & Dunlop, 2002).

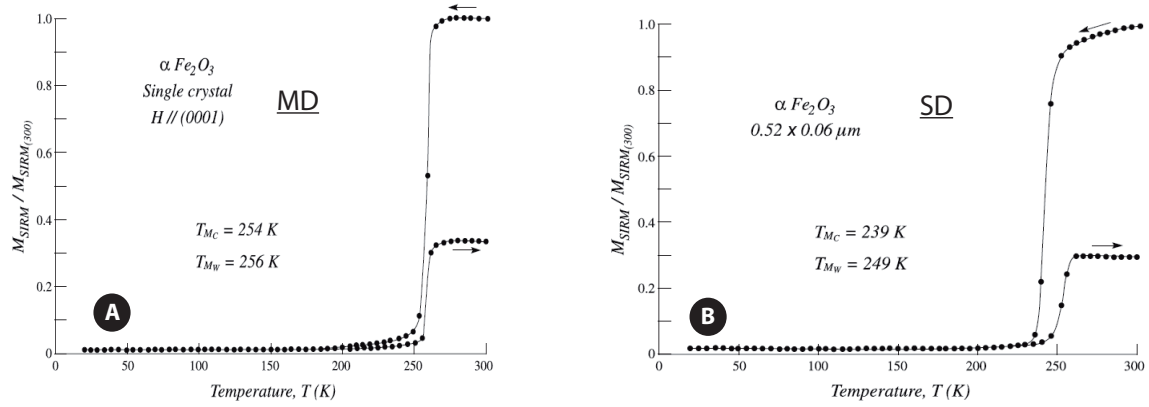

Figure II.50 – Morin transition for A) MD and B) SD grains of hematite (Özdemir *et al.*, 2008)

Temperature of the Morin transition is grain size dependent. This transition tends to be sharp in MD grains and broader in SD grains (Figure II.51 ; Özdemir *et al.*, 2008). Synthetic submicron SD hematites (120-520 nm) have T_M comprised between 241 and 256 K. This variation could be due to crystal morphology, crystallinity and impurities. Natural SD hematites display T_M values between 250 and 261 K. This is due to the fact that natural samples have a variety of crystal imperfections resulting in internal stress which could alter T_M. In the range 100 nm to 10 mm (SD and MD grains), T_M is weakly size dependent, decreasing very gradually with decreasing particle size (Figure II.51). T_M decreases sharply between 100 and 30 nm dropping to ∼90 K. Below 30-20 nm, the transition disappears entirely. As particle size decreases, surface-to-volume ratio increases and surface effects come to dominate the magnetic properties. Lower lattice symmetry gives spin disordering or deviation from antiferromagnetic alignment (Özdemir *et al.*, 2008). Nanoparticles are weakly ferromagnetic at

temperature at least down to 5 K (Bodker *et al.*, 2000).

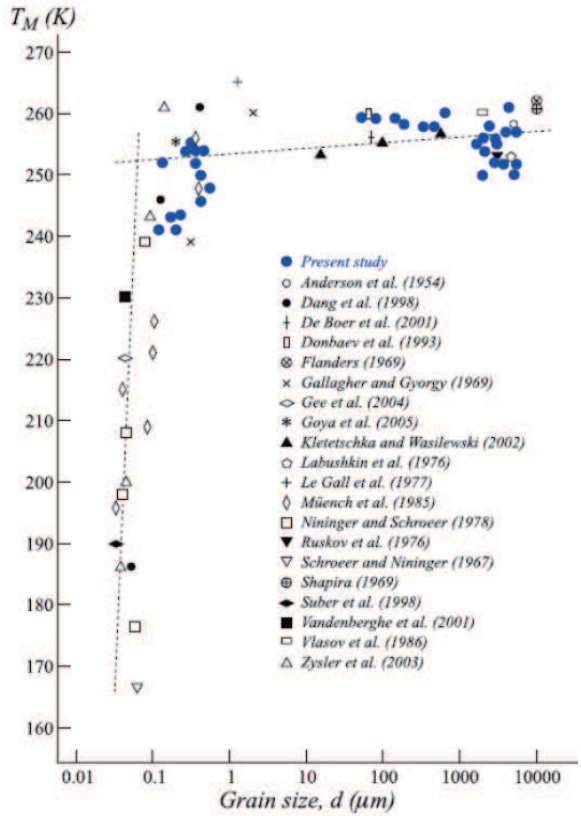

Figure II.51 – Grain size dependence of the Morin transition (Özdemir *et al.*, 2008 and references therein)

Looking at the hysteresis parameters at room temperature, they all are grain size dependent and sensitive to the degree of crystallinity of the grains. They are maximal for SD grains and they decrease in the very fine grained fraction as they approach the hematite superparamagnetic threshold size (Dekkers & Linssen, 1989).

Hematite is the most stable iron oxides. It is both thermally and chemically stable. Hematite can be abundant in sedimentary rocks like red beds or BIF (Banded Iron Formations) (Dekkers & Linssen, 1989) and can be found in many igneous rocks.

Titanohematites or hemoilmenites have formula $Fe_y^{2+}Fe_{2-y}^{3+}Ti_y^{4+}O_3^{2-}$. Substitution of Ti into hematite has consequence more important than for magnetite. y = 0 corresponds to hematite which is canted-antiferromagnetic. When y > 0.45, the magnetization becomes ferromagnetic (Figure II.52). Moreover Ti content with concentration as low as 1% suppresses the Morin transition (Morin, 1950), whereas this latter persists until Al content up to 10% (De Grave *et al.*, 1988).

The second end-member of titanohematites series is ilmenite (y = 1, Fe_2TiO_3). It is antiferromagnetic below its Néel temperature of 57 ± 2 K. Ilmenite contributes only when dealing with an induced magnetization (Senftle *et al.*, 1975).

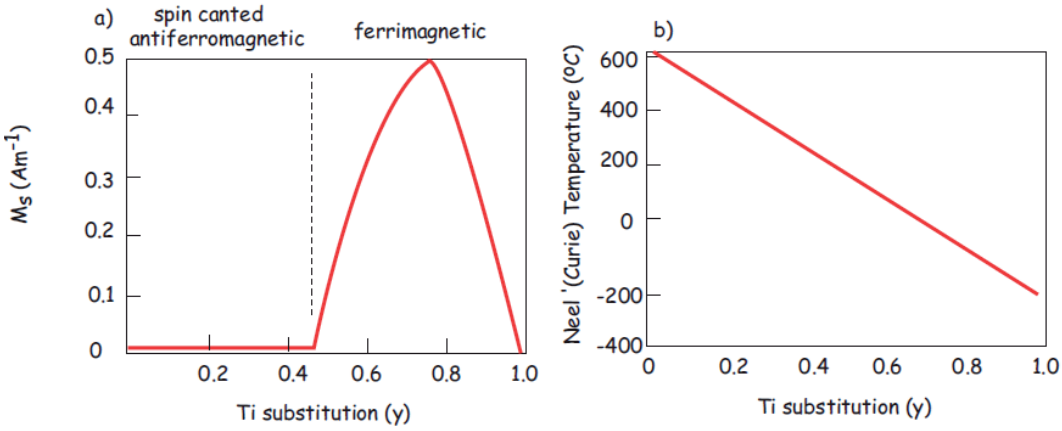

Figure II.52 – Variations of some magnetic properties with Ti substitution in the titanohematite series ; a) variation of saturation magnetization Ms and b) variation of the Néel temperature (Tauxe, 2008)

2.3 Iron oxyhydroxides

Iron oxyhydroxides occur mostly as an alteration by-product of iron-bearing rocks in ambient conditions.

2.3.1 Goethite α-FeOOH

Of all iron oxyhydroxides, orthorhombic goethite α-FeOOH is the most stable at low temperature and is a common mineral of soils (France & Oldfield, 2000) and sediments (Van der Zee *et al.*, 2003). Goethite can be formed by precipitation directly from solution or by conversion of ferrihydrite into goethite (Cornell & Schwertmann, 1996).

At room temperature, goethite is antiferromagnetic associated with a weak ferromagnetism, like hematite. However this ferromagnetism is weaker than that of hematite (Table II.2) and probably due to a defect moment. For a well-crystallized goethite, Néel temperature T_N is ∼120°C which is also Curie temperature Tc (Özdemir & Dunlop, 1996). Impurities, degree of crystallinity can lower T_N considerably (Dekkers, 1989a). Presence of vacancy defects in fine particles of goethite also reduced the Néel temperature up to ∼85°C (Bocquet & Kennedy, 1992).

Some typical magnetic features of goethite are represented in Figure II.54.

Goethite is a highly coercive mineral hardly being saturated (Figure II.54A ; Rochette *et al.*, 2005). At low temperature while cooling to say 10 K, remanence acquired by goethite at room temperature increases (Dekkers, 1989a ; Guyodo *et al.*, 2006). This is a characteristic of goethite (Figures II.53 and II.54B). The remanence increase ratio is determined by the amount of isomorphous substitution, the amount of dispersed elements in the goethite lattice and the temperature range between room temperature and the maximum blocking temperature. The later act simultaneously (Dekkers, 1989a). In Figure II.54C, it is represented the frequency dependence of the susceptibility. There is dependence above 150 K to room temperature corresponding to superparamagnetic behavior. Hopkinson peak and Néel temperature are also observed, characterized by the peak followed by the drop of susceptibility. The small decrease of T_N observed suggest a goethite poorly crystallized, resulting from defects like water excess or isomorphic substitution (Berquò *et al.*, 2007). The Mössbauer spectrum at 300 K shows a doublet (at 0 mm/s) related to superparamagnetism or paramagnetism. At 4.2 K, only one sextet (corresponding to goethite) is present and the doublet is not present anymore. This supports the presence of a superparamagnetic component corresponding to small particles which are blocked only at low temperatures.

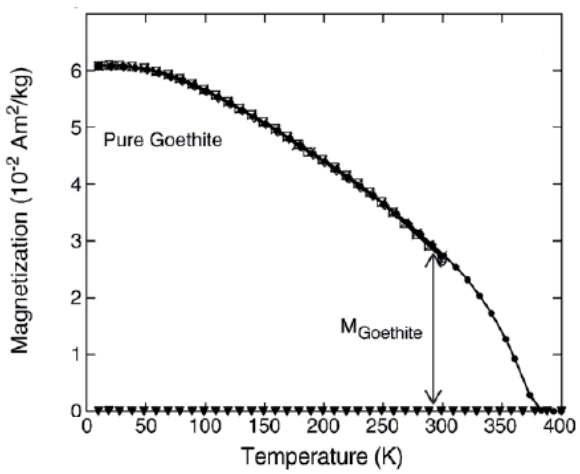

Figure II.53 – Evolution of remanence of a synthetic goethite through measurements cycle of Guyodo *et al.* (2006). $M_{Goethite}$ is a proxy of goethite content in the sample.

In the case of nanoparticles of goethite, decreasing particle size increases the number of surface defects per particle leading to a net increase in magnetization (Figure II.55 ; Guyodo *et al.*, 2003). The peaks in the in-phase and out-of-phase susceptibilities indicate the transition between the thermally blocked state and the superparamagnetic state of the nanoparticles. This transition occurs at a temperature ∼35 K.

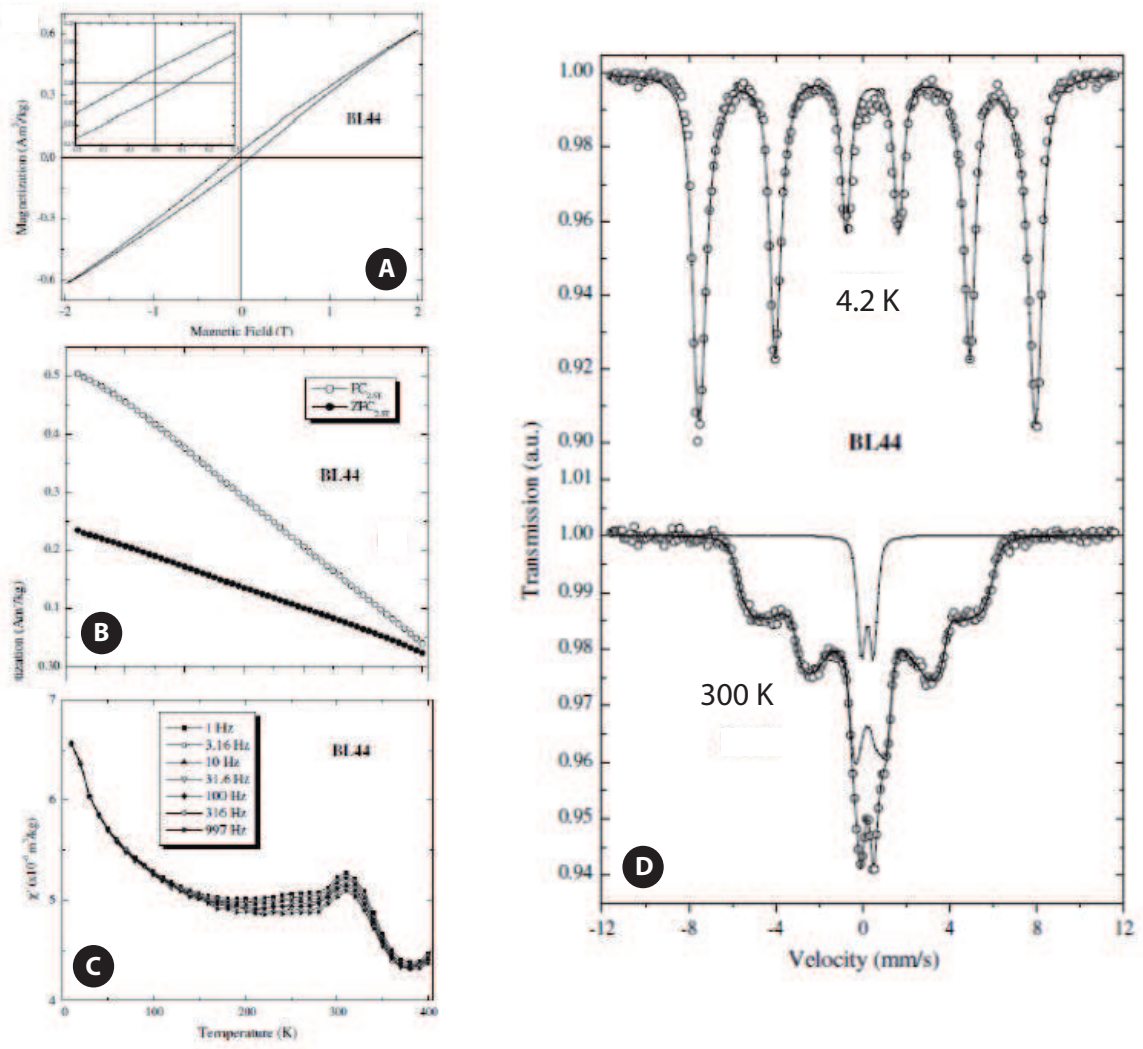

Figure II.54 – Some magnetic properties of goethite sample (Berquò *et al.*, 2007) : A) hysteresis loop at room temperature, B) Field Cooled and Zero Field Cooled (10-300 K), C) Frequency dependence of in-phase susceptibility (10-400 K), D) Mössbauer spectroscopy at 300 and 4.2 K

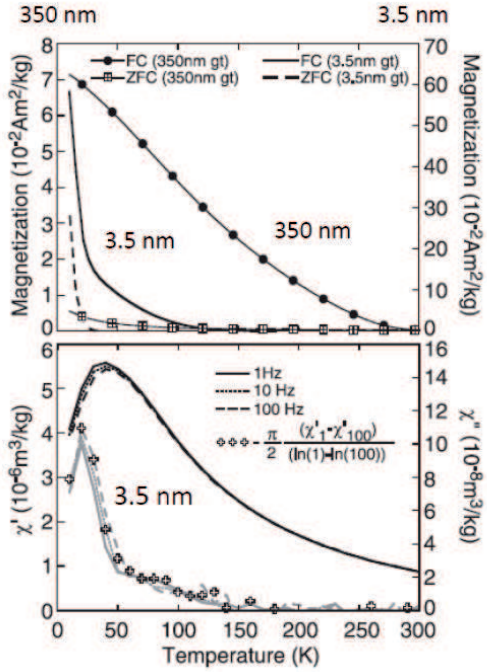

Figure II.55 – Grain size dependence of nanogoethite SIRM and susceptibility (Guyodo *et al.*, 2003)

Goethite can dehydrate to hematite with time (thousands of years or more at room temperature) or elevated temperature (dehydration completed in the range 250-400°C) (Dunlop & Özdemir, 1997). An intermediate spinel phase identified as magnetite can be formed and first appeared at heating temperature of 238°C (Özdemir & Dunlop, 2000). This hematite is generally superparamagnetic and does not carry remanence (Dunlop & Özdemir, 1997).

2.3.2 Lepidocrocite γ-FeOOH

Other iron oxyhydroxides occur in soils and sediments among which lepidocrocite (γ-FeOOH). These minerals are paramagnetic at room temperature and do not contribute to NRM. When moderately heating (< 250°C), lepidocrocite may transform into maghemite thus becoming ferrimagnetic (Gehring & Hofmeister, 1994 ; Dunlop & Özdemir, 1997). Below its arrangement temperature (Néel temperature) which is ∼50-60 K (Hirt *et al.*, 2002), the mineral becomes antiferromagnetic and may acquire a somewhat important remanence (imparted at low temperature) decreasing exponentially during zero-field warming to room temperature (Figure II.56).

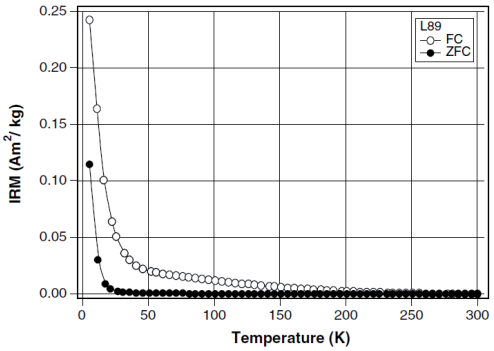

Figure II.56 – Evolution with temperature of a SIRM imparted at 10 K for lepidocrocite (Hirt *et al.*, 2002)

2.4 Iron sulfides

Two iron sulfides are important to paleomagnetism : greigite Fe_3S_4 and pyrrhotite $Fe_7S_8 - Fe_{11}S_{12}$. They both occur in reducing environments (Kao *et al.*, 2004) and both tend to oxidize to various iron oxides leaving paramagnetic pyrite FeS_2 as the sulfide component (Dunlop & Özdemir, 1997).

2.4.1 Pyrrhotite $Fe_7S_8 - Fe_{11}S_{12}$

Pyrrhotite, which the general formula is $Fe_{1-x}S$ with $0 < x < 0.13$, is a common accessory mineral in various rocks, but seldom dominates the remanence. Natural pyrrhotite is actually a mixture of the ferrimagnetic monoclinic Fe_7S_8 and antiferromagnetic hexagonal Fe_9S_{10} and $Fe_{11}S_{12}$ phases (Zapletal, 1993). Structure types of pyrrhotite also evolve with depth from monoclinic in the upper 2-3 km to hexagonal structures (up to 9 km) (Kontny *et al.*, 2000 ; Pósfai *et al.*, 2000).
Pyrrhotite has a NiAs crystal structure, with a c-axis of hexagonal symmetry and Fe and S confined to alternate c-planes (Figure II.57).

Hexagonal pyrrhotite (Fe_9S_{10}) is antiferromagnetic at room temperature. Fe_9S_{10} has a structural transition at ∼200°C, called λ transition (Figure II.58) at which thermally activated vacancy ordering occurs. Hexagonal pyrrhotite becomes ferrimagnetic (Schwarz & Harris, 1970 ; Schwarz, 1975). This magnetic state is maintained till Curie temperature of ∼265°C (Schwarz & Vaughan, 1972).

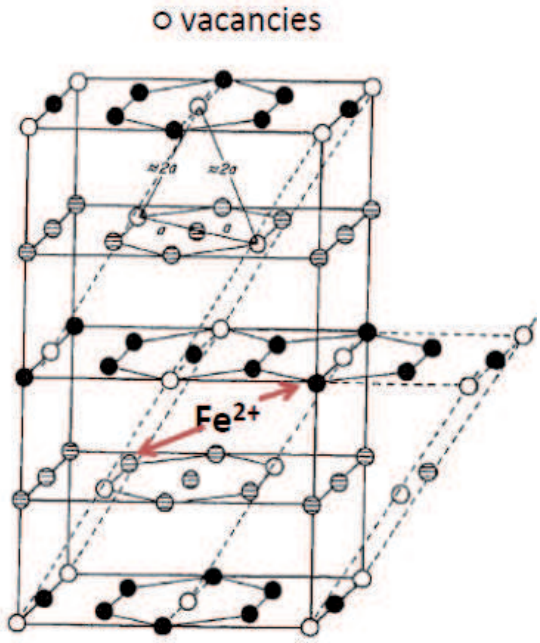

Figure II.57 – Crystal structure of pyrrhotite (black line : hexagonal structure, dashed line : monoclinic lattice) (Dunlop & Özdemir, 1997 after Stacey & Banerjee, 1974).

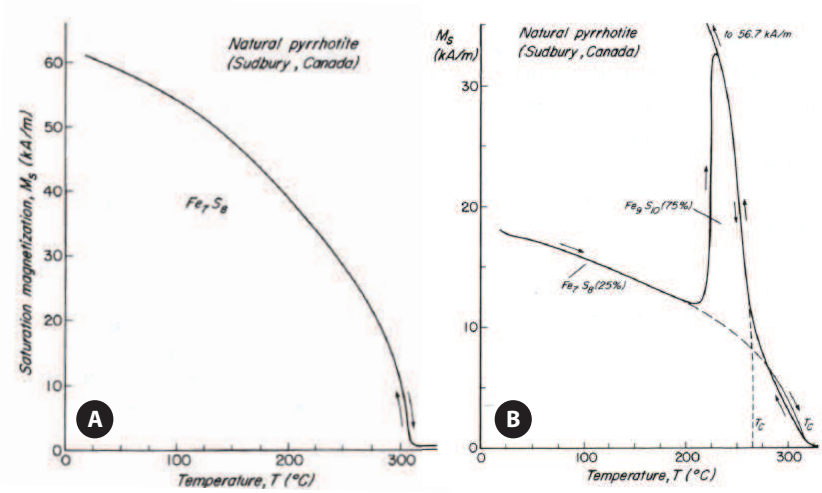

Figure II.58 – Thermomagnetic curves for A) monoclinic pyrrhotite and B) mixture of monoclinic and hexagonal pyrrhotites (Dunlop & Özdemir, 1997 after Schwarz, 1975)

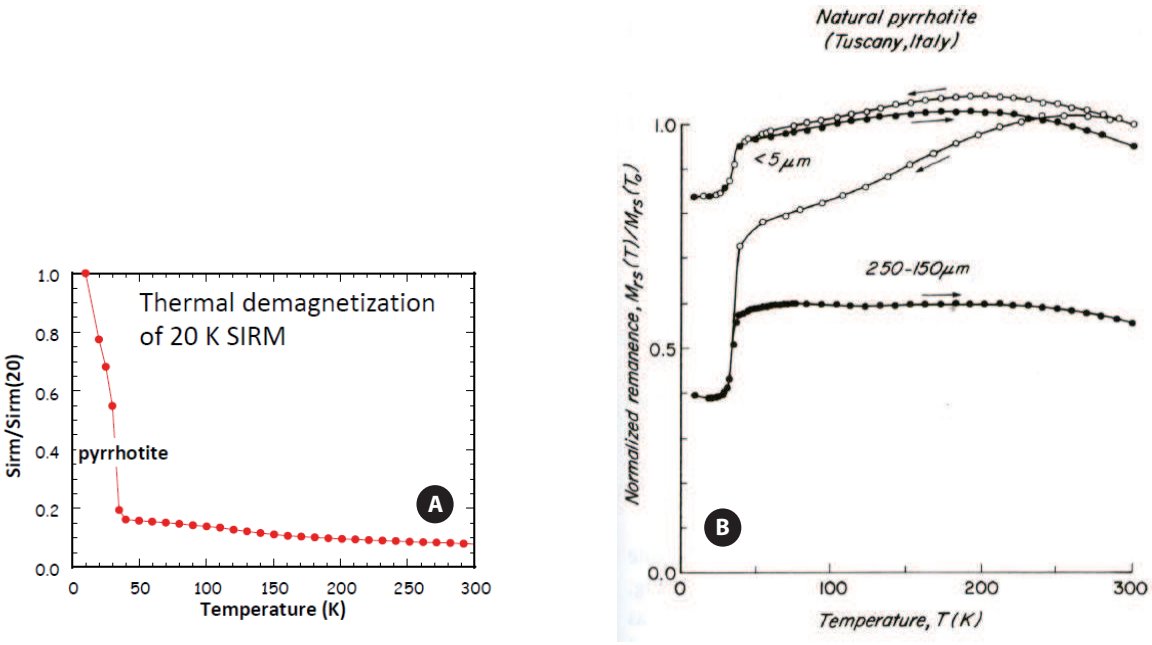

Figure II.59 – A) Thermal demagnetization of a 20 K SIRM of pyrrhotite and B) remanence transition in different grain size of pyrrhotite (Dunlop & Özdemir, 1997 after Dekkers *et al.*, 1989)

Pyrrhotite Fe_7S_8, most depleted in Fe, is monoclinic. The distortion of the hexagonal lattice into the monoclinic one gives rise to a strong ferrimagnetic moment due to cation deficiency and vacancy ordering. Curie temperature is ∼320°C (Dekkers, 1989b). The Fe_7S_8 pyrrhotite does not display λ transition like the hexagonal pyrrhotites. However, Fe_7S_8 has a low temperature transition at about 30-35 K characteristic of this mineral (Figure II.59 ; Dekkers, 1989b ; Rochette *et al.*, 1990). This transition was recently proposed to be named "Besnus transition" after Marie Jeanne Besnus for her work about pyrrhotite (Besnus & Meyer, 1964 ; Besnus, 1966). The origin of this transition is debated. Dunlop & Özdemir (1997) suggested that it corresponds to an isotropic point for the magnetocrystalline anisotropy because MD grains loose, through the transition, more remanence than SD grains and they have also less "memory" to recover initial remanence (Figure II.59B). Recently, it was suggested that this transition may be related to a crystallographic transformation from a room temperature monoclinic structure into a low temperature triclinic structure below the transition (Wolfers *et al.*, 2011).

The Besnus transition is grain size dependent (Figure II.59B) with increasing reversible remanence behavior with decreasing grain size (Dekkers, 1989b ; Dekkers *et al.*, 1989).

At room temperature, variations in hysteresis properties with grain size appear to be gradual, with no evidence of sudden changes associated with domain structure transitions (Clark, 1984).

During thermal heating (> 500°C), pyrrhotite transforms irreversibly into magnetite (Bina & Daly, 1994) and at higher temperature eventually to hematite either directly or by oxidation of magnetite (Dekkers, 1990).

2.4.2 Greigite Fe_3S_4

Greigite (Fe_3S_4) is a thiospinel and is the sulfide counterpart of magnetite having the same inverse spinel structure. It is ferrimagnetic with a magnetization at saturation of about 1/4 that of magnetite (Hoffmann, 1992). Greigite displays a drop of magnetization between 270 and 350°C (Roberts, 1995). The exact Curie point of greigite is still unknown but probably exceeds 350°C (Roberts *et al.*, 2011). Moreover, greigite is chemically unstable until∼200°C.
Contrary to monoclinic pyrrhotite, greigite does not display low temperature transition (Chang *et al.*, 2009). A SIRM acquired at say 10 K decays monotonically in zero field while warming (Figure II.60A). A SIRM acquired at room temperature does not practically changes when cooling. Greigite shows a strong domain-state dependence of low temperature remanence (Figure II.60B). SD grains have relatively stable remanence and magnetic properties while MD grains can undergo significant remanence loss during warming to room temperature (Chang *et al.*, 2009).

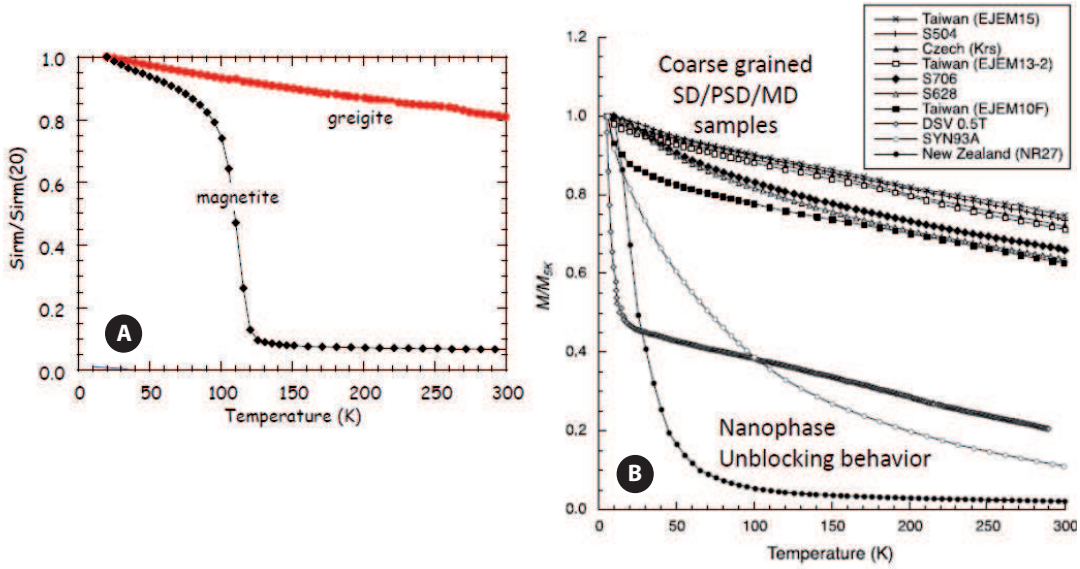

Figure II.60 – A) Evolution of a 20 K SIRM on warming for greigite compared to magnetite and B) grain size dependence of the greigite remanence at low temperature (Roberts *et al.*, 2011)

2.5 Fe-Mn carbonates

Hexagonal Fe-carbonate siderite ($FeCO_3$) and Mn-carbonate rhodochrosite ($MnCO_3$) both precipitate in anoxic sedimentary environments. These two compounds can form solid solution covering a range of intermediate compositions.

Siderite is paramagnetic at ordinary temperatures and carries no NRM. Nevertheless, siderite undergoes low temperature transition at Néel temperature ∼38 K where it becomes antiferromagnetic (Housen *et al.*, 1996). Siderite can acquire remanence below its Néel temperature but this latter is rapidly lost when warming in zero field to room temperature (Figure II.61 ; Frederichs *et al.*, 2003).

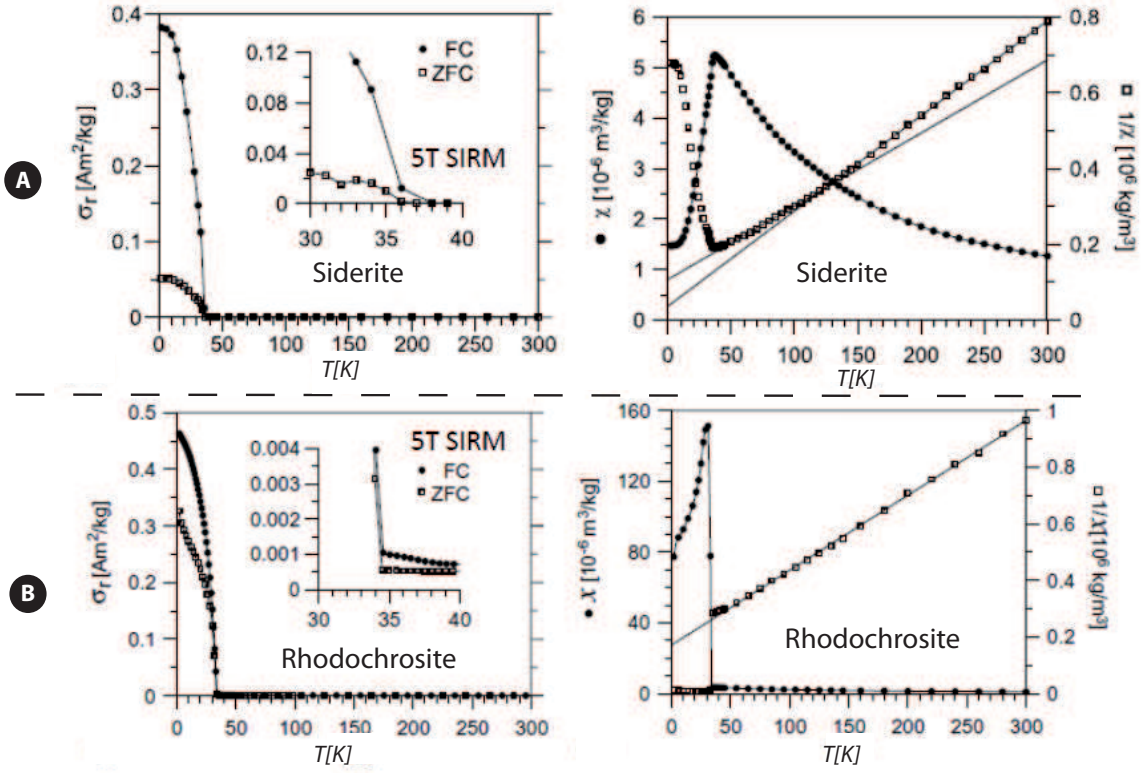

Figure II.61 – Evolution of low temperature remanence and in-phase susceptibility for A) siderite and B) rhodochrosite (Frederichs *et al.*, 2003).

Rhodochrosite is also paramagnetic at room temperature. Like siderite, $MnCO_3$ displays low temperature transition at ∼34 K. Below its Néel temperature, rhodochrosite is canted antiferromagnetic. Remanent magnetization acquired below 34 K is rapidly lost when warming in zero field (Figure II.61 ; Frederichs *et al.*, 2003 ; Kosterov *et al.*, 2006).

Néel temperature for siderite and rhodochrosite are close and in the range 30-40 K. Pyrrhotite Fe_7S_8 has also a transition in this range. These three minerals, on the basis of low temperature remanence shape, can be superimposed (Figure II.62 ; Table II.4). Nevertheless, Fe-Mn carbonates can be distinguished from pyrrhotite because they display a very important difference in the SIRM between FC and ZFC (Housen *et al.*, 1996). Other low magnetic measurements such as FC hysteresis loops can be used to distinct between Fe-Mn carbonates and iron sulfides (Kars *et al.*, 2011a, appendix 1).

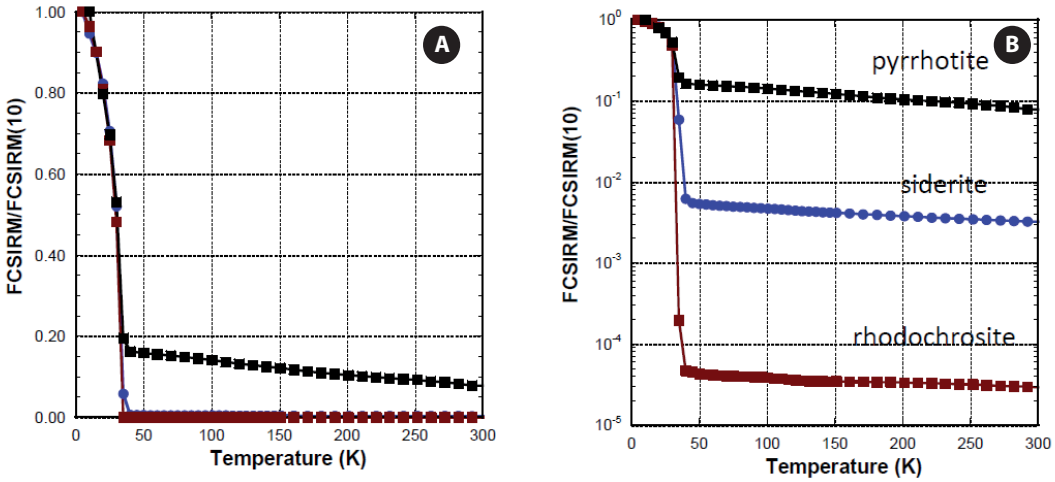

Figure II.62 – Evolution of a low temperature SIRM for pyrrhotite, siderite and rhodochrosite represented in A) a linear scale and B) a log scale (IRM lecture notes)

Mineral	Formula	Low Temperature Characteristic
Magnetite	Fe_3O_4	Verwey transition ∼120 K
Maghemite	γFe_2O_3	Suppression of the Verwey transition
Hematite	αFe_2O_3	Morin transition ∼250 K
Goethite	α-FeOOH	Increase of the RT-SIRM
Pyrrhotite	Fe_7S_8	"Besnus" transition ∼35 K
Siderite	$FeCO_3$	Néel transition ∼38 K
Rhodochorsite	$MnCO_3$	Néel transition ∼32 K

Table II.4 – Low temperature properties of some magnetic minerals

Chapter III

METHODS

1 Mineralogy identification

1.1 Magnetic methods

As stated previously in chapter II, magnetic minerals experienced changes in magnetic moment and/or susceptibility at specific temperatures which are characteristic of a given mineral. This is the recognition of these diagnostic magnetic behaviors which allows the identification of the magnetic mineralogy constitutive of the rock.

Most measurements completed during this 3-year thesis are of magnetic origin. Most of the measurements were done at low temperature (lower than room temperature) to prevent alteration and/or mineralogical transformations which can arise during thermal heating (e.g. Van Velzen & Zijderveld, 1992).

1.1.1 Measurements at low temperature

More than about 80 % of magnetic measurements were carried on with a Magnetic Properties Measurement System (MPMS). It is a SQUID (Superconducting Quantum Interferometric Device) cryogenic magnetometer generating a magnetic field up to 5 T and covering a temperature range from 2 to 400 K. The MPMS measurements were conducted in two different laboratories : the Institut de Physique du Globe de Paris, France, and the Institute for Rock Magnetism, University of Minnesota, Minneapolis, USA. Figure III.1A shows the "Big Red", one of the two MPMS of the Institute for Rock Magnetism. The MPMS sensitivity is up to 10^{-10}Am^2 (from 10^{-10} to 10^{-3}Am^2).

This kind of magnetic measurements requires a specific preparation of the samples prior to analysis. Samples are hand-crushed to very fine powder by use of an agate mortar and pestle. Then the powder is sealed in a gelatin capsule and placed in a plastic straw (Figure III.1B) which is introduced into the magnetometer. During the course of our work, we observed a significant ageing effect of the rock powder (chapter IV). Therefore it is important to perform measurements on powder shortly after

preparation.

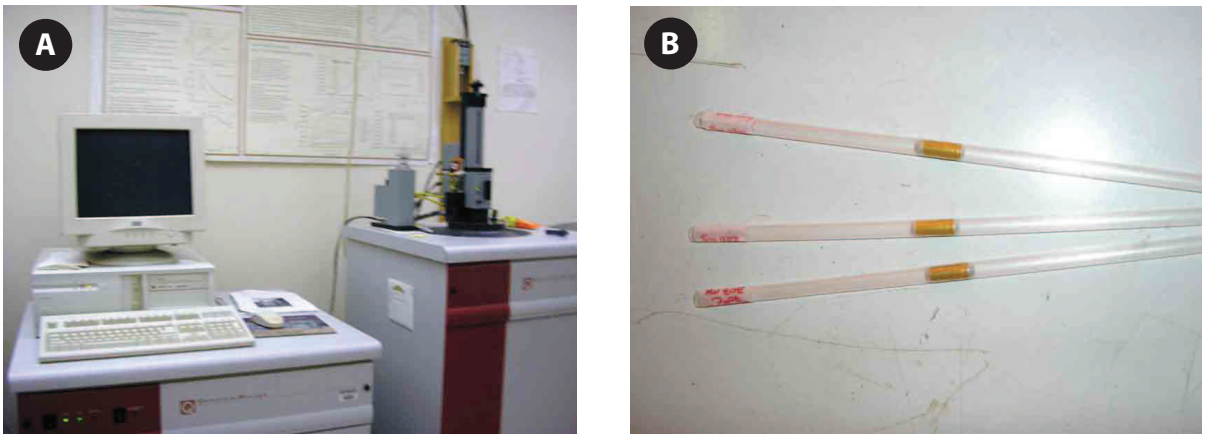

Figure III.1 – A) Magnetic Properties Measurement System (MPMS) at the IRM, B) gelatin capsules in straws then placed inside the MPMS

MPMS measurements were performed with approximately the same measurement sequence which consists in (Figure III.2) :

- At 300 K (27°C, room temperature), a magnetic field of 2.5 T is applied to create a Saturation Isothermal Remanent Magnetization at Room Temperature (called RT-SIRM$_{300K}$). Then the field is switched off.
- The sample is then cooled down to 10 K by 5 K steps under a weak magnetic field of 5 μT inside the MPMS : the acquired curve is called RT-SIRM cooling curve. To avoid possible confusion between the two RT-SIRM acronyms, there will always be a specification. The application of a weak magnetic field during RT-SIRM cooling is not the routine procedure. The latter usually uses a nil magnetic field.
- At 10 K (-263°C), a magnetic field of 2.5 T is applied again to create a LT-SIRM (Low Temperature - SIRM). Then the field is switched off.
- The sample is then warmed up to 300 K under a nil field : the obtained curve is called Zero Field Cooled (ZFC). This ZFC is quite different from the ZFC used by physicists. They applied a magnetic field during warming.

Some variations in the details of this sequence may be allowed for specific purposes. After imparting the RT-SIRM$_{300K}$, the sample may be heated to 400 K (127°C) to remove the goethite contribution which Néel temperature is 120°C (Guyodo *et al.*, 2006). Also, after ZFC completion, the sample may be cooled down to 10 K in a presence of a 2.5 T magnetic field and then warmed up to 300 K in a nil field : the acquired curve is called FC (Field Cooled).
For some specimens, in-phase (K') and out-of-phase (K") AC susceptibility were measured to deter-

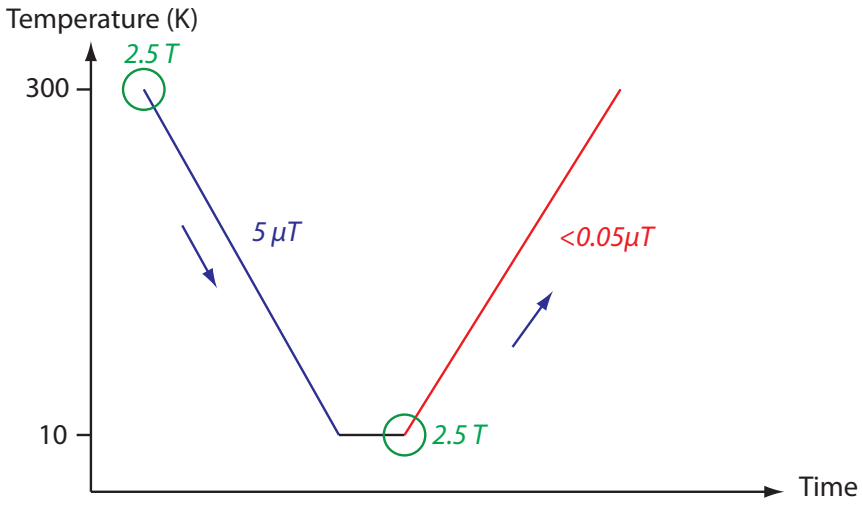

Figure III.2 – Schematic MPMS measurement sequence at low temperature (10-300 K)

mine their field- and/or frequency-dependence (frequency values : 1, 32 and 997 Hz, field values : 20, 239 A/m).

In addition to MPMS measurements, the samples from the Grès d'Annot basin (SE France) and West Virginia folds (Appalachians, USA), which are the subject of chapters VI and VII respectively, were also analyzed with a Princeton Vibrating Sample Magnetometer (VSM, Figure III.3) at the Institute for Rock Magnetism. The VSM sensitivity is 5.10^{-9}Am^2. This permits determination of magnetic grain sizes and coercivities by performing hysteresis loops (e.g. Tauxe *et al.*, 1996) and First Order Reversal Curves (FORC ; Carvallo, 2004; Roberts *et al.*, 2006). The magnetic field applied to saturate the samples is 1 T for hysteresis loops and 1 or 1.5 T for FORC diagrams. The field increment is 5 mT. The average time varies from 200 ms to 2 s. Some hysteresis loops were performed at low temperature from 100 to 10 K after cooling the sample in a 1-1.5 T magnetic field. To interpret FORC measurements, we used FORCInel software (Harrison & Feinberg, 2008).

1.1.2 Measurements at room and high temperatures

The low-field susceptibility χ_{lf} at room temperature was measured for all samples using a KLY3-CS3 Kappabridge susceptometer at Ecole Normale Supérieure, Paris, France (Figure III.4B). This susceptometer is equipped with a furnace which permits measurement of the magnetic susceptibility with temperature (up to 700°C). The sensitivity of the susceptometer is 1.10^{-7}SI and ± 2°C for the furnace.

Even though heating can produce mineralogical transformations, thermal demagnetization using

Figure III.3 – Vibrating Sample Magnetometer (VSM) at the IRM

the protocol by Lowrie (1990) was realized in some samples from the Grès d'Annot basin and West Virginia folds. This protocol consists of imparting an IRM on the three axes X, Y, Z, with a different magnetic field in order to characterize a given magnetic coercivity. X, Y and Z axes represent low, medium and high coercivities respectively. In our case, magnetic fields of 0.1, 0.3 and 1.2 T were applied on X, Y and Z axes respectively. Samples were then thermally demagnetized from 100 to 650°C in an oven isolated from Earth's magnetic field (Figure III.4A). Magnetic moment was measured with a 2G SQUID cryogenic magnetometer which permits the measurement of a magnetization as low as 10^{-11}Am^2 at Ecole Normale Supérieure, Paris, France (Figure III.4C).

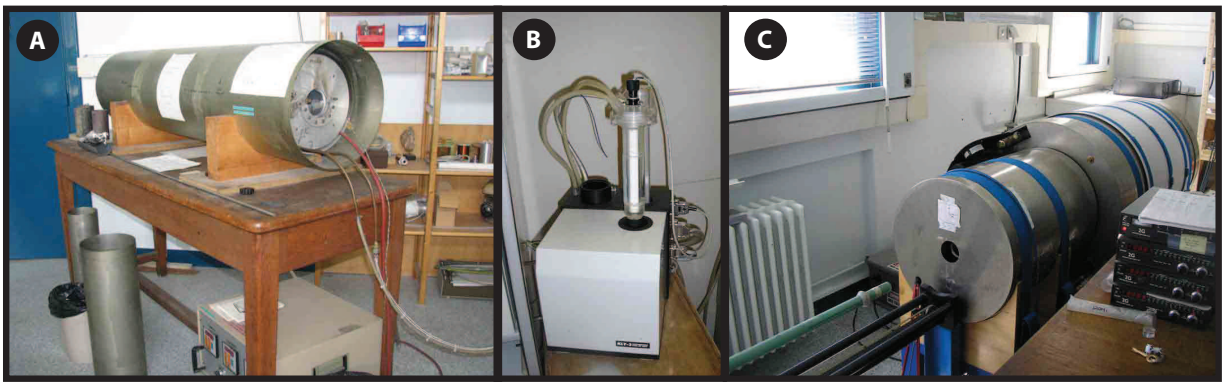

Figure III.4 – A) Oven used for thermal demagnetization, B) KLY3-CS3 susceptometer and C) 2G SQUID magnetometer at ENS

1.2 Non magnetic methods

1.2.1 Electron Microscopy

In order to further investigate magnetic mineralogy derived from magnetic measurements, some samples were examined under electron microscopes. Observations done on samples powders glued on thin polished slices, SEM (Scanning Electron Microscope) images and EDS (X-Ray Energy Dispersive Spectrometry) spectra - to identify and quantify chemical elements present at the sample surface - were performed on a Zeiss Sigma SEM at Ecole Normale Supérieure, Paris, France (Figure III.5).

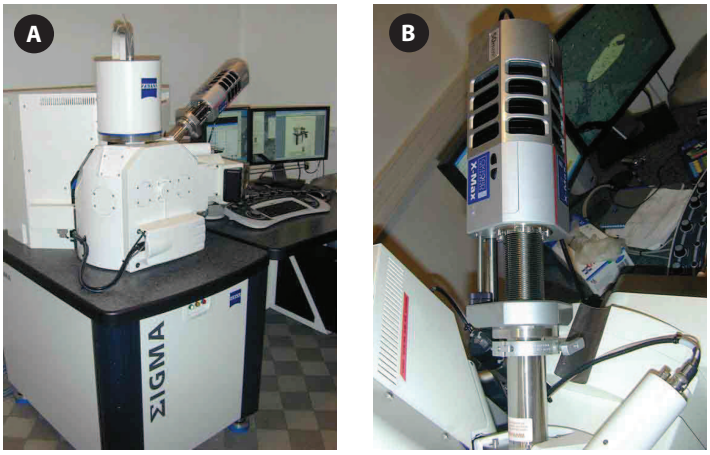

Figure III.5 – A) Scanning Electron Microscope (SEM) and B) EDS (X-ray Energy Dispersive Spectrometry) detector at the ENS

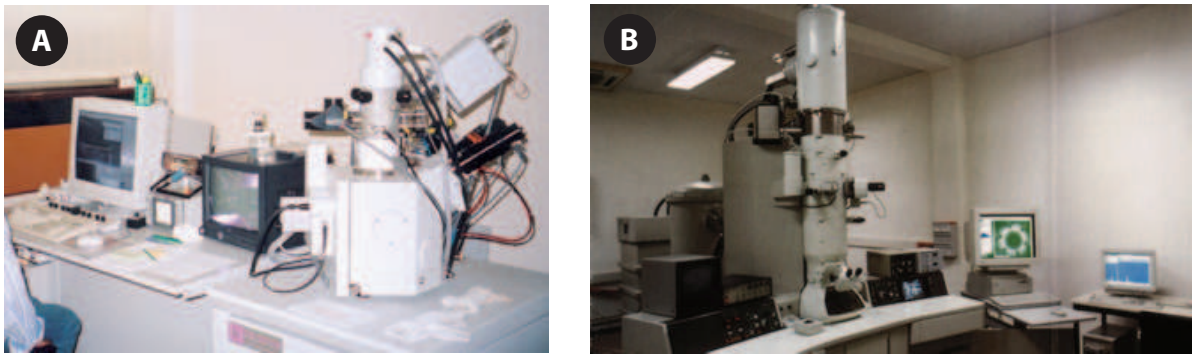

Figure III.6 – A) Focus Ion Beam (FIB) apparatus and B) Scanning Transmission Electron Microscope (STEM) at the CP2M

Specific samples were also studied by the FIB-TEM technique (Focus Ion Beam and Transmission Electron Microscope) at Centre Pluridisciplinaire de Microscopie Electronique et de Microanalyse (CP2M), Université Paul Cézanne, Marseille, France (Figure III.6). FIB sections were prepared on a

Philips FIB200 TEM and TEM observations were done on a JEOL 2010F URP22.

FIB sections were done on pyrite framboids extracted from a set of samples originating from one particular well. The size of the FIB sections was 15 x 5 x 1 μm.

1.2.2 X-ray Diffractometry

X-ray diffraction spectra were acquired for the clay fraction of a number of samples from the Grès d'Annot basin. Analyses were done on a Rigaku X-ray diffractometer at Ecole Normale Supérieure, Paris, France (Figure III.7). Clay fractions were extracted using the protocol established by Bruce Velde, Dominik Janots and Nathaniel Findling at ENS (D. Janots, pers. com.). Main steps are as follows. The sample is crushed very finely in a mortar. The resulting powder is put in a beaker with distilled water and placed in an ultrasonic bath for a few seconds. Then the suspension is decanted for about 8 hours. The supernatant is recovered and put in a test tube. A drop of strontium chloride is added to the supernatant and let sit for one night. A clay precipitate is formed as a result of clays flocculation. The supernatant is disposed of and the clay precipitate is deposited on a thin glass slice and air-dried over night (Figure III.8). The clay covered glass slide is then analyzed by X-ray diffraction.

Figure III.7 – X-ray diffractometer at the ENS

1.2.3 CBD treatment

To determine the occurrence of ultrafine magnetic minerals, CBD treatment (Sodium Citrate-Sodium Bicarbonate-Sodium Dithionite) was realized on Paris Basin samples from the borehole EST-433 near Bure locality (Meuse/Haute-Marne, France). The aim is to chemically remove ultrafine iron oxides.

We used the protocol of Lagroix *et al.* (2005) based on Mehra & Jackson (1960) (Figure III.9).

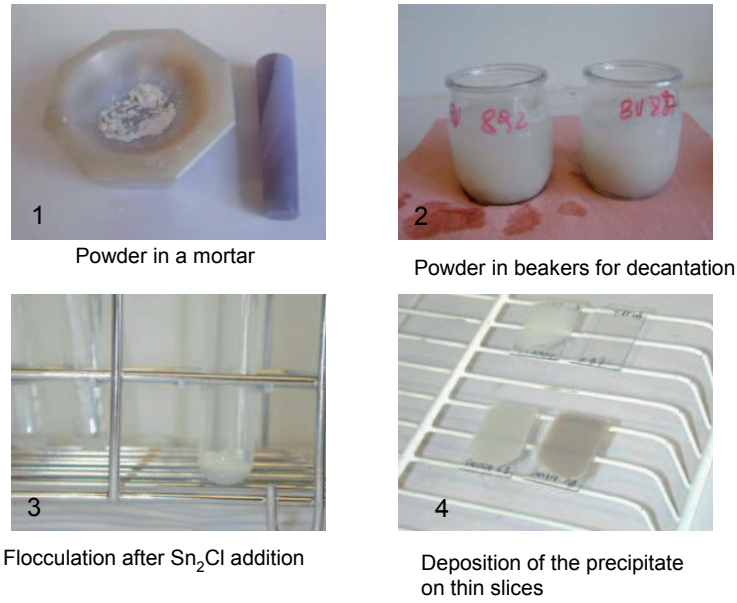

Figure III.8 – Schematic protocol of clays separation used for X-ray diffraction

Samples were crushed and a mass of about 2 g was placed in a beaker. A solution of 20 mL of 0.3 M sodium citrate and 2.5 mL of sodium bicarbonate was added. Then the solution was heated at 80°C for 10 minutes while periodically shaked. 0.5 g of sodium dithionite was added. The mix was let at 80°C for 15 minutes while periodically shaked. Then the solution was placed in centrifuge tubes. Centrifugation lasted 10 minutes. The supernatant was removed and the sediment was washed twice with distilled water. Then the sediment (with distilled water) was centrifuged again for 10 minutes. Finally the supernatant was removed and the sediment was placed in an oven at 45°C for at least 12 hours.

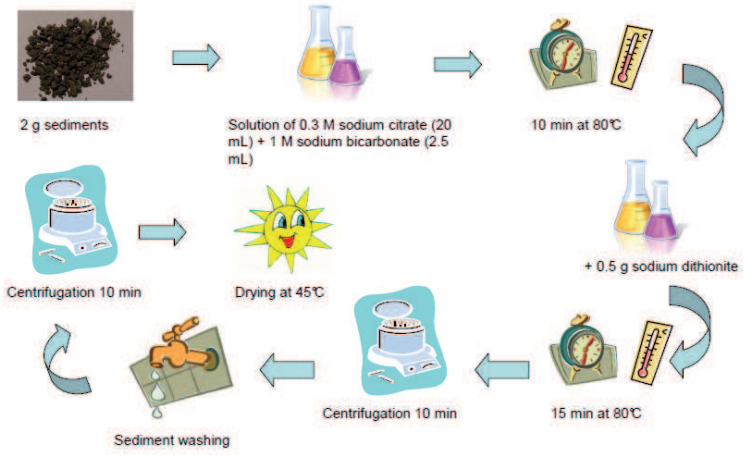

Figure III.9 – Schematic protocol of sodium Citrate-Bicarbonate-Dithionite (CBD) treatment

1.2.4 Quantitative Mineralogy

Detailed mineralogy of some samples was determined by using the quantitative mineralogy procedure of the ISS/RGM laboratory (CSTJF, Pau).
This analysis is based on combining different kinds of data :

- X-Ray diffraction (XRD) analyses on whole rock and clay fraction to identify the minerals present in the samples
- X-Ray fluorescence (XRF) to determine the chemical composition of the sample (major and minor elements)
- Other data : density, CEC (Cation Exchange Capacity), IOC (Insoluble Organic Carbon), IR (Infra-Red), LOI (Loss On Ignition)...

The analyses are realized on ∼10-20 g of samples for representativeness and maximum precision. The method uses calculations routine by using the chemical formula (either theoretical or measured) of the minerals present in the samples. The calculation is iterative so that the best possible fit is obtained between the mineralogical composition derived from the XRD and that from the XRF. The result reliability is controlled by the good agreement between the measured and the theoretical density for a given calculated composition.

2 Laboratory experiments

Two types of heating experiments were conducted in the laboratory in order to simulate heating occurring during natural burial : 1) experiments under open conditions at 0.1 MPa ; 2) experiments under confined conditions at 100 MPa pressure. Protocols are described below.

2.1 Heating experiments in open conditions at 0.1 MPa

Two series of experiments at 0.1 MPa were performed at Ecole Normale Supérieure, Paris, France. These experiments followed those initially conducted by Aubourg *et al.* (2008) and Aubourg & Pozzi (2010). They allowed the monitoring of neoformed magnetic minerals in very small concentration typically on the order of a few ppmv-ppbv. The aim of these experiments was intended to simulate in the laboratory the conditions encountered during burial conditions occurring in nature by progressively increasing temperature. The approach, however, should not be considered as strictly representative of natural conditions because pressure is not considered.

These experiments used claystones from two different localities. Boom clay (Belgium) and Bure claystones (Paris Basin, France) were used for the first series which constitutes experiment A, while only Bure claystones were used for the second experiment corresponding to experiment B.

Samples preparation is the same for the two series. We repeat protocol as defined by Aubourg *et al.* (2008). Fragments of these claystones (∼ 1-2 g) are glued in small glass flasks (one fragment per

flask). The bottles are then filled with glass wool and plugged to create a quasi-confined atmosphere, i.e. the atmosphere is slowly renewed (Figure III.10A). A total of 6 and 14 bottles were prepared for experiment A and B respectively.

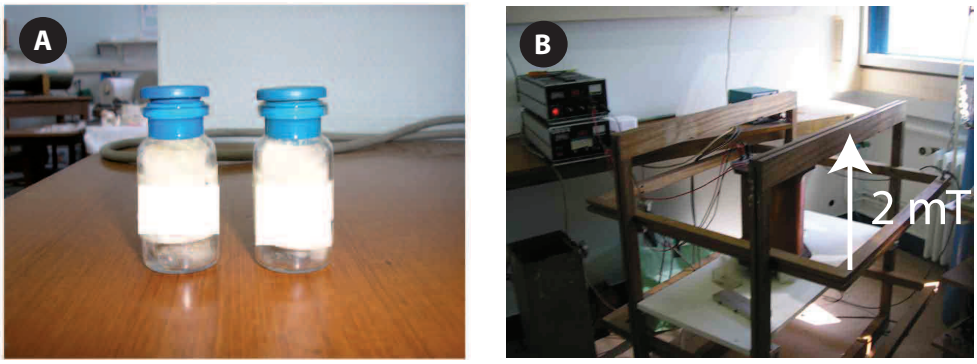

Figure III.10 – A) Samples in glass flasks with glass wool and B) resistance furnace for heating under magnetic field

In these experiments, we focus on the remanent magnetization generated by neoformed grains. In order to highlight this phenomenon, the natural remanent magnetization (NRM) of the samples was initially removed by applying an 80 mT alternating field. The bottles are then placed in the oven. Heating experiments were conducted by progressively increasing temperature T_{exp} at variable rates, in variable time-steps over a variable time duration as shown in Table III.1.

Experiment	Sample	Temperature (°C)	Duration (days)
A	Bure-Boom Bure-Boom	70°C 70-90°C	13 days 29-34 days
B	Bure	50-70-80-120-130°C	20-25-25-10-10 days

Table III.1 – Temperature and duration of the 0.1 MPa experiments

While heating the samples, the Earth's magnetic field is removed and an upward magnetic field of 2 mT is applied. Flasks mass is regularly measured to check for some possible water loss (evaporation). The resulting remanence R is measured repeatedly at room temperature and is expressed as follows : $R = NRM_{AF80} + IRM_{2mT} + CRM_{2mT} + TVRM_{2mT}$, where NRM_{AF80} is the NRM after 80 mT AF demagnetization, IRM_{2mT} the isothermal remanent magnetization imparted at 2 mT, CRM_{2mT} the chemical remanent magnetization acquired by neoformed magnetic minerals above their blocking volume at 2 mT, and $TVRM_{2mT}$ is a thermoviscous remanent magnetization carried by former and neoformed magnetic minerals at 2 mT. NRM_{AF80} and IRM_{2mT} are one to two orders in magnitude less than CRM_{2mT} and $TVRM_{2mT}$, and thus are neglected (Aubourg *et al.*, 2008). The TVRM is by essence time-dependent and thus unstable. Given the duration of the laboratory (tens of days),

it is likely that TVRM is essentially carried by ultra-fined neoformed grains. Finally, the measured remanence can be expressed as : R $\sim$ CRM_{2mT} + $TVRM_{2mT}$. At the end of the heating step, we let the samples at temperature in a nil magnetic field for a few days in order to remove the $TVRM_{2mT}$. This constitutes what we called the TVRM test (Aubourg *et al.*, 2008). The measured magnetization is then a CRM_{2mT} for a given T_{exp} temperature. Then the samples are placed again in the oven at a higher temperature and so on. At the end of the experiment, we obtain several CRM_{2mT} values corresponding to the different temperature steps.

For experiment A, heated samples were then thermally demagnetized from 100 to 650°C. For experiment B, for each temperature step, a couple of samples was removed from the experiment after TVRM test and let settle in a nil field. One set of these samples (set B-1) are measured at low temperature (10-300 K) and the other set (set B-2) were thermally demagnetized from 100 to 650°C.

2.2 Heating experiments under confined atmosphere and pressure conditions (100 MPa)

Two series of experiments were conducted at 100 MPa pressure at Ecole Normale Supérieure, Paris, France. In this case, the goal was also to simulate burial conditions occurring in nature at different temperatures but attempting to take pressure into consideration. The protocol used is that of Aubourg & Pozzi (2010). The magnetic field is not controlled. Thus the CRM can not be monitored.

For these experiments, samples from well were used. Samples were crushed in a mortar and placed in gold capsules with $\sim$5 mL of distilled water. The gold capsules were sealed by electric arc, put in an autoclave (one autoclave per capsule) and heated (Figure III.11). Pressure and temperature were constantly controlled and recorded along the complete duration of the experiments. For the first experiment, called experiment C (two samples 2160 mMD depth) were heated at 80 and 110°C and two others (2975 mMD depth) at 110 and 140°C for 80 days. At the end of the experiment, gold capsules were open and the sediment was dried in an oven over night. Samples were then sealed in gelatin capsules in order to perform low temperature MPMS measurements at Institut de Physique du Globe de Paris (IPGP), France.

The other experiment - experiment D - performed under confined conditions, consisted of heating different aliquots of the 2160 mMD sample. In a first time, four gold capsules are prepared and heated at 80, 90, 110 and 130°C respectively during 110 days each. Once this first experiment was completed, gold capsules were measured at low temperatures (10-300 K) with the MPMS at IPGP. Then the same gold capsules were heated again at 100 MPa at 110, 120, 140 and 160°C respectively for 101 days. At the end of the experiment, low temperature measurements of the gold capsules were performed. Table III.2 summarized the different experiments.

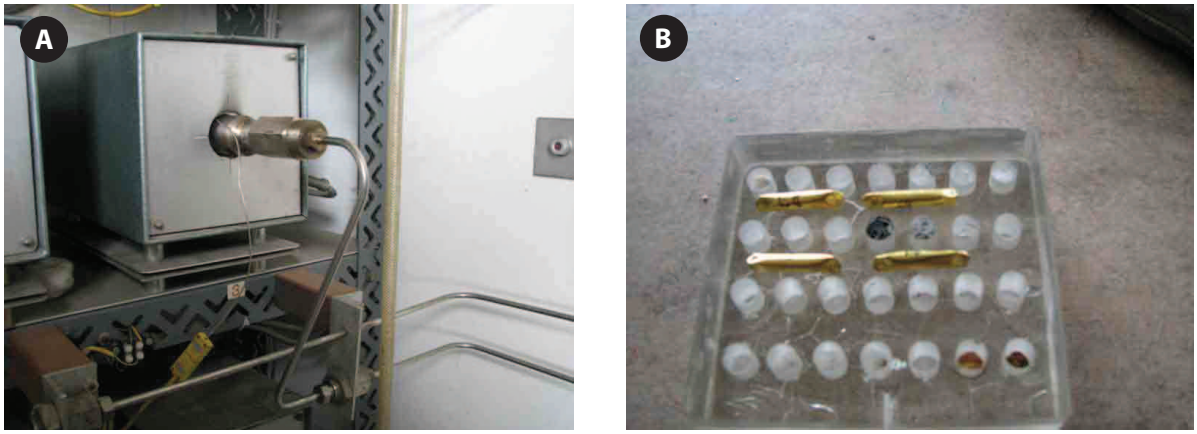

Figure III.11 – A) Autoclaves containing B) gold capsules

Experiment	Sample	Capsule name	Temperature (°C)	Duration (days)
C	A	E1 E2	80 110	80 80
	B	E3 E4	110 140	80 80
D	A	C1	80 110	110 101
		C2	90 120	110 101
		C3	130 160	110 101
		C4	110 140	110 101

Table III.2 – Temperature and duration of the 100 MPa experiment

2.3 Heating experiments under Ar atmosphere

A series of heating under Ar atmosphere was also performed on some powdered samples at the ENS and IPGP at St Maur-des-Fossés. 1 to 2 grams of claystones powders are placed in a tube in the KLY3-CS3 Kappabridge (Figure III.4B). The powders are heated at 100, 110, 120, 130 and 140°C. Then each powder is measured at low temperature (10-300 K) with the MPMS at the IPGP using the standard sequence described before (Figure III.2).

Part B

MagEval Geothermometry

Chapter IV

THE MAGEVAL GEOTHERMOMETER

As seen in the introduction, magnetic minerals evolve with temperature and thus likely during burial. In this part, we discuss a new geothermometer named MagEval (Aubourg & Pozzi, 2010). The calibration and application of this geothermometer are the main goal of this thesis work. In the following, we provide background on the origin and significance of the MagEval geothermometer and present the results of well studies.

1 Presentation of the MagEval geothermometer

1.1 Pioneering work and background

Aubourg & Pozzi (2010) investigated the effects of burial by experimental heating on three different claystones : the Bure Callovo-Oxfordian claystones in the Paris Basin (France, burial temperature ∼40°C), the Opalinus Lower Dogger claystones from the Mont Terri anticline in front of the Jura fold belt (Switzerland, burial temperature ∼85°C) and the Chartreuse Callovian-Oxfordian claystones from Chartreuse Sub-Alpine chains (France, burial temperature < 170°C). They performed different sets of heating experiments documenting the formation of magnetite and iron sulfide with temperature increase. They interpreted this iron sulfide to be fine grained pyrrhotite (< 1 μm) characterized by an increase/decrease of the remanence at ∼35 K which they named P-transition (Aubourg *et al.*, 2008). In Kars *et al.* (2011a), we redefined the P-transition as P-behavior, as the exact mineralogical nature of this comportment remains to be defined. In the following, we use therefore this concept of P-behavior defined in Kars *et al.* (2011a).

In order to simulate burial conditions, Aubourg & Pozzi (2010) performed a heating experiment on Opalinus claystones in gold capsules under a pressure of 100 MPa, and measured the evolution of the remanent magnetization of these samples at low temperature (Figure IV.1). They observed the progressive disappearance of the P-behavior and the development of the Verwey transition with increasing temperature on RT-SIRM [1] curves (Figure IV.1A). To quantify the relative contributions

1. Room Temperature Saturation Isothermal Remanent Magnetization

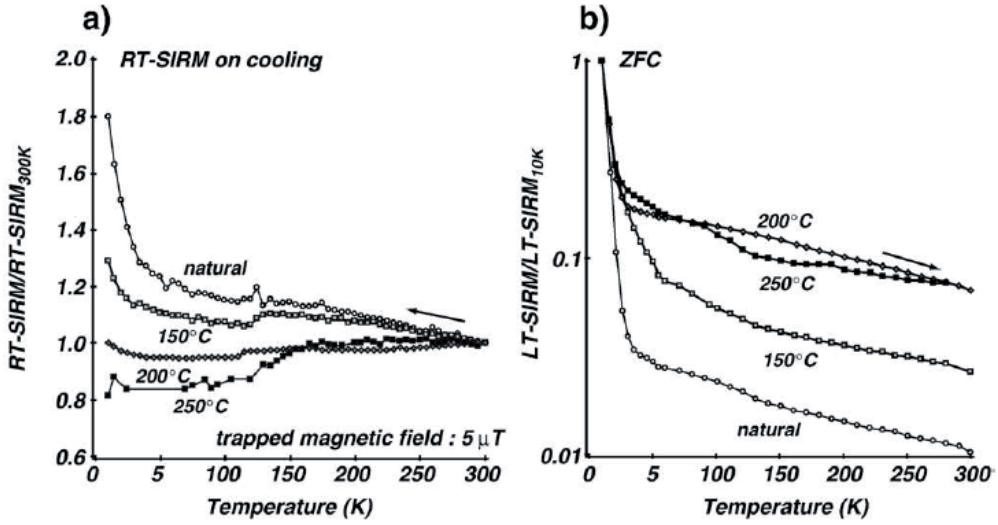

Figure IV.1 – Burial-like heating experiment results on Opalinus claystones BHE-D5-2C. A) RT-SIRM cooling curves. A magnetic field of 5 μT is applied upward during cooling. Note the progressive disappearance of the P-behavior. B) ZFC curves (Aubourg & Pozzi, 2010)

of magnetite and pyrrhotite, they derived from the ZFC [2] curve a parameter defined as :

$$PM = \frac{LTSIRM_{10K} - LTSIRM_{35K}}{LTSIRM_{10K}}$$

where LTSIRM stands for Low Temperature Saturation Isothermal Remanent Magnetization.

A PM [3] value near 1 suggests the predominance of pyrrhotite over magnetite. On the contrary, a value close to 0 implies an overwhelming abundance of magnetite over pyrrhotite. Note that this scenario was based on Aubourg & Pozzi (2010) preliminary results. Our heating experiments (chapter V, Kars *et al.*, in revision, appendix 2) seem to indicate that PM may be controlled by the relative amount of SP [4] grains versus >SD [5] grains.

Plotting all the PM values of their heating experiment against temperature (Figure IV.2), they suggested the existence of two different trends : a PM-UP (PM increase) branch and a PM-DOWN (PM decrease) branch, with a maximal PM value occurring at about 80°C. This illustrates that the PM parameter should evolve with burial (hence temperature) in natural sedimentary systems. The PM parameter, first defined as a proxy of the relative contributions of pyrrhotite and magnetite, is referred to as the so-called MagEval geothermometer.

2. Zero Field Cooling
3. Pyrrhotite-Magnetite
4. superparamagnetic
5. single domain

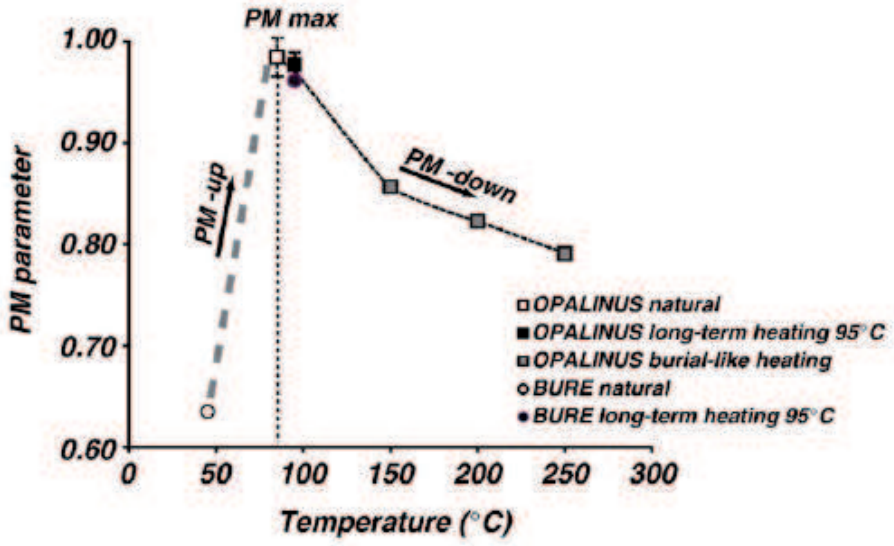

Figure IV.2 – Evolution of the PM parameter with temperature for natural and heated Opalinus and Bure samples (Aubourg & Pozzi, 2010)

1.2 Occurrence of the MagEval signal

It can be seen in the previous figures (e.g. Figure IV.6A) that the MagEval signature observed in ZFC curves shows a 2-step pattern (Aubourg *et al.*, 2008 ; Figure IV.3) :

- a decrease of the remanence from 10 K which permits the calculation of the PM parameter between 10 and 35 K ;
- a decrease of the remanence at ∼120 K which is the Verwey transition of magnetite.

This typical signal is present in most samples from wells and outcrops studied as part of this thesis work, but is also commonly encountered in samples studied in other R & D projects (Figure IV.4). It is found in many geological settings (Figure IV.5) including :

- Syn to post-orogenic sedimentary basins (e.g., SE France, Paris Basin...)
- Volcanic margin basin (e.g. Greenland) (Abdelmalak, 2010 ; Abdelmalak *et al.*, 2012)
- fold and thrust belts (e.g. Appalachians, Jura, Borneo)

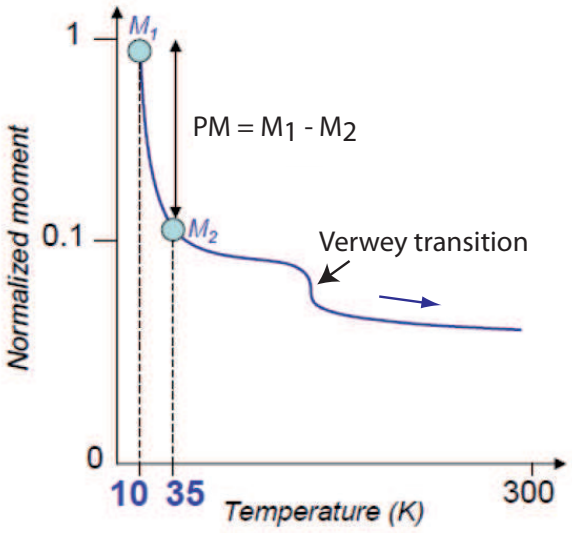

Figure IV.3 – Schematic 2-step pattern of ZFC curve

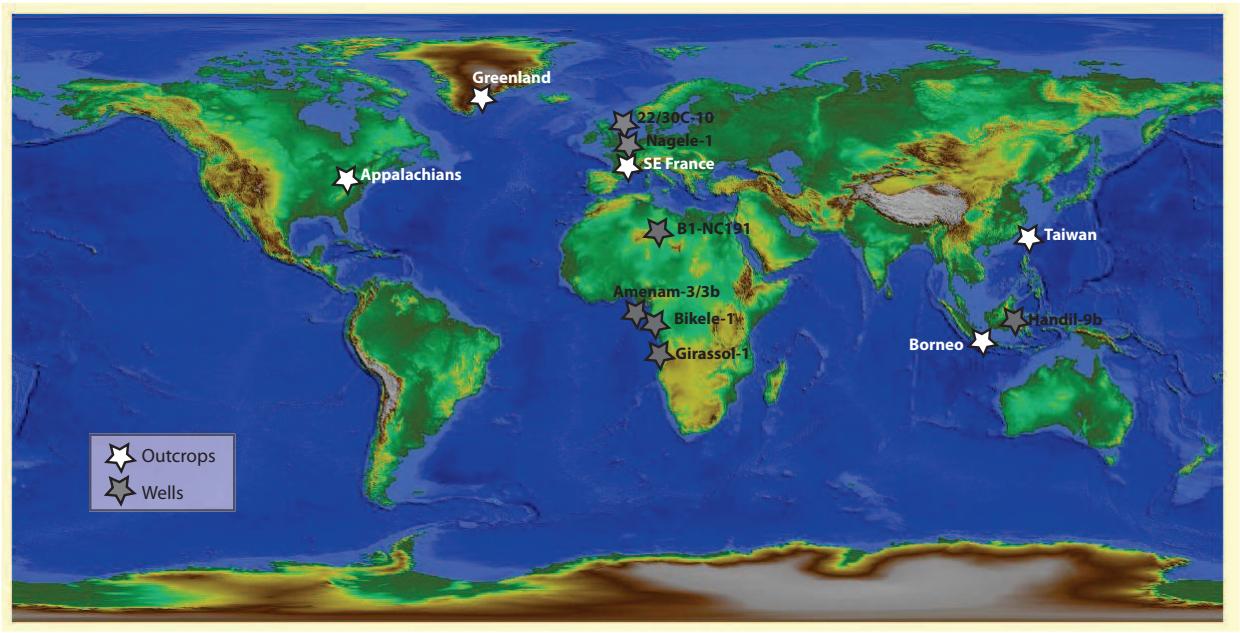

Figure IV.4 – Geographical locations of samples in which typical MagEval signal has been documented up to today

1.3 Significance of the PM parameter

Even though the mathematical formula of PM is not questioned (a starting point is needed), the significance of PM could be discussed.
In our heating experiments from 50 to 130°C performed on Bure claystones (chapter V, Kars *et al.*,

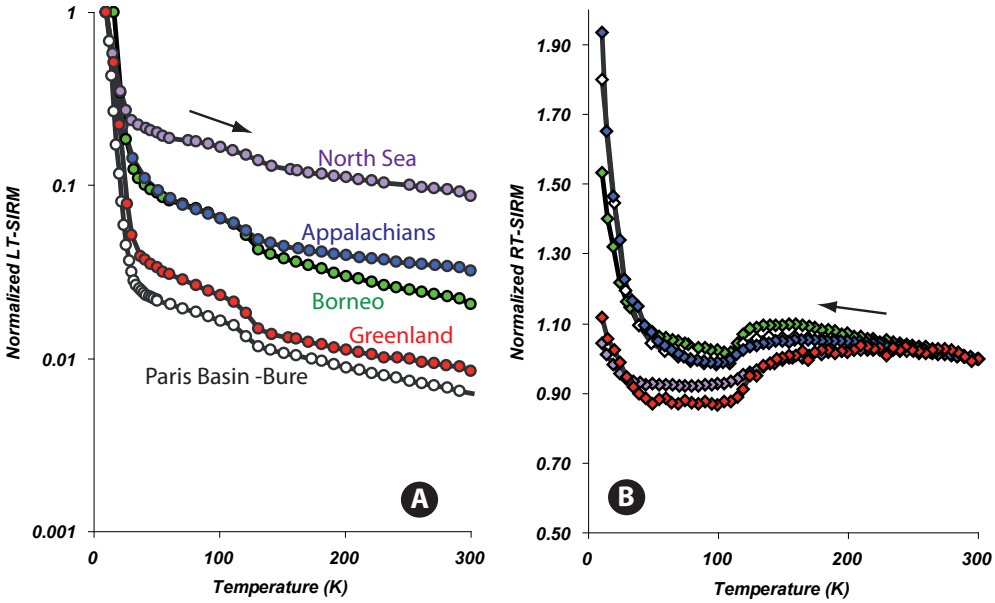

Figure IV.5 – MagEval signature in samples from different geological settings (Borneo, Paris Basin, North Sea, West Virginia, Greenland). A) ZFC and B) RT-SIRM curves

in rev., app. 2) similar to one used by Aubourg *et al.* (2008), we are able to distinguish grains distribution below and above the blocking volume (∼20 nm for magnetite) by studying the thermoviscous remanent magnetization (TVRM) and the chemical remanent magnetization (CRM) respectively. We assume that magnetite (not pyrrhotite) is the magnetic mineral formed during the experiment. In this case, the parameter PM does not describe the equilibrium between two different magnetic species but rather the quantitative contribution of superparamagnetic grains to the remanence. The MagEval geothermometer would therefore represent the relative proportion of SP over SD grains of one single magnetic mineral. However, in the previous heating experiment realized at 70 and 90°C on Boom and Bure claystones, significant breaks were observed in the slope of PM versus temperature trends (chapter V) which may indicate the occurrence/formation of two distinct mineral phases as early stated by Aubourg & Pozzi (2010).

To test the occurrence of SP grains, one can realize frequency-dependence of AC susceptibility at low temperature (< 300 K) because the susceptibility of SP grains is highly frequency-dependent. However, our samples are claystones and the paramagnetic clayish matrix can overwhelm the SP contribution. On the other hand, SP grains which acquire remanence at very low temperature unblock very rapidly at temperatures below 50 K. In this case, the SP contribution may be hidden by a possible Néel transition occurring at this temperature range. In Figure IV.6, AC susceptibility measurement on Mont Terri claystones shows a frequency-dependence at about ∼120 K and ∼230 K which corresponds to the Verwey transition (magnetite) and the Morin transition (hematite) respectively. Note that this

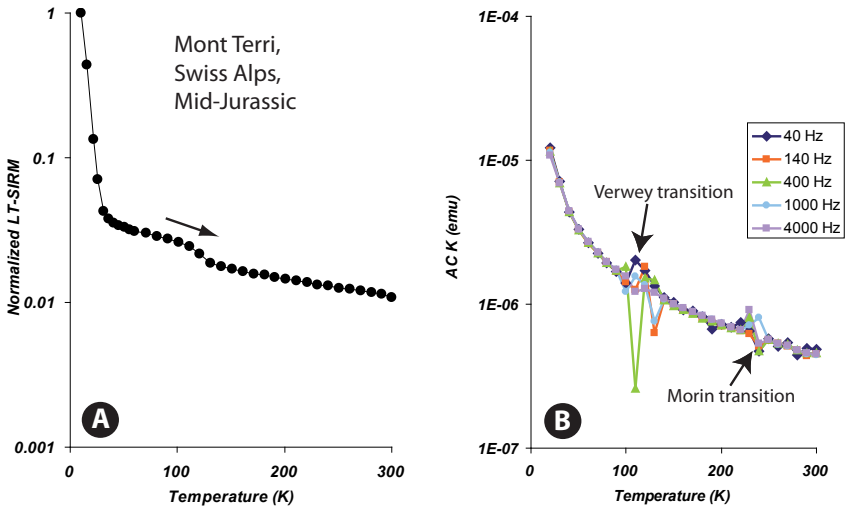

Figure IV.6 – A) ZFC curve of Opalinus claystone from Mont Terri (Swiss Alps) and B) the frequency-dependence of AC susceptibility corresponding to this site

measurement was realized down to 20 K. Another frequency-dependence of AC susceptibility was realized on a West Virginia sample from 30 to 5 K (Figure IV.7B). It is clear that there is a frequency-dependence of susceptibility for T < 10 K, showing the presence of SP grains. However the increase of the AC susceptibility with lowering temperature indicates an important contribution of paramagnetic grains. In this case, the AC susceptibility measurement may not be the appropriate way to prove occurrence of SP grains. It is the huge decrease of the remanence from 10 to 50 K that is characteristic of such grain size (Figure IV.7A, see chapter II). This drop, however, could represent a Néel transition.

On the other hand, it is interesting to document changes in magnetic behavior when a CBD [6] treatment is applied to remove ultra-fined iron oxides (chapter III for the protocol). This was done on a sample of Bure claystone (Figure IV.8). If SP grains are present, one should expect the disappearance or a significant drop of the PM value. In Figure IV.8, there is no significant difference between ZFC curves before and after CBD treatment. This can be explained in two ways : 1) the protocol utilized is inadequate for this type of samples (time, temperature, concentration...), or 2) the iron oxide grains are not accessible to the CBD treatment because they are engulfed within host minerals (such as pyrite framboid and calcite).

It is unlikely that the PM parameter characterizes a Néel transition (see Kars *et al.* (2011a) in appendix 1). The decrease of the remanence between 10 and 35 K is observed in many specimens : some samples show a Néel transition on the RT-SIRM curve, some not (inserts Figure IV.9). The ubiquity of its occurrence rules out the Néel character of such a decrease. Moreover, samples showing a

6. sodium Citrate-sodium Bicarbonate-sodium Dithionite

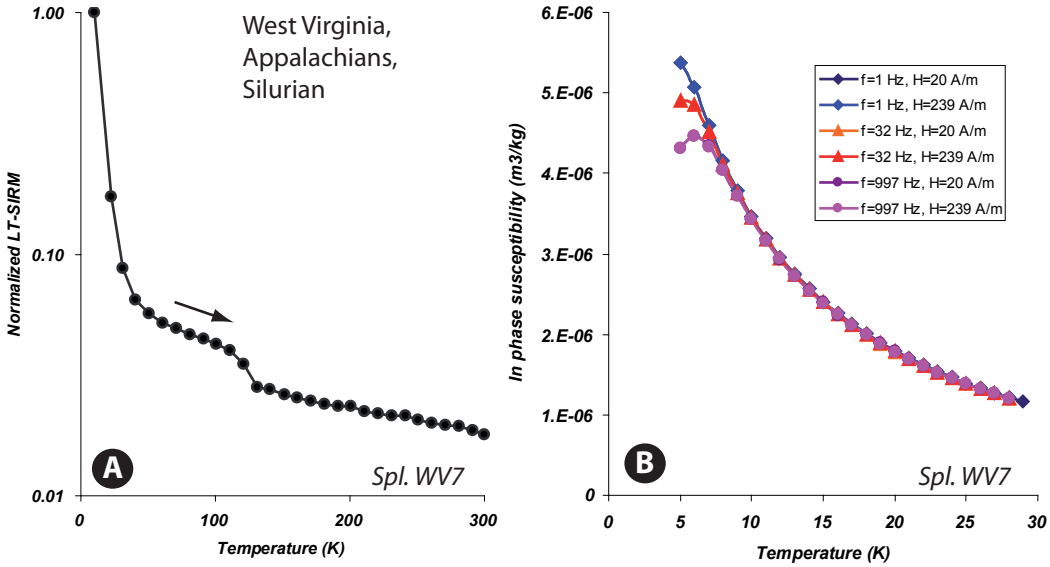

Figure IV.7 – A) ZFC curve of a West Virginia sample (10-300 K) and B) the corresponding frequency- and field- dependence of in-phase AC susceptibility. No field dependence is observed.

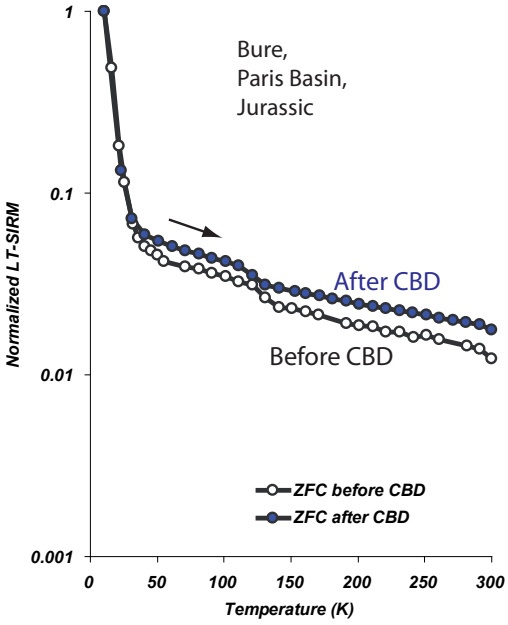

Figure IV.8 – Comparison of ZFC curves obtained before and after CBD treatment on a Callovo-Oxfordian Bure claystone sample. It is quite remarkable that chemical treatment leads to little, if any, alteration of magnetic properties, while moderate heating does.

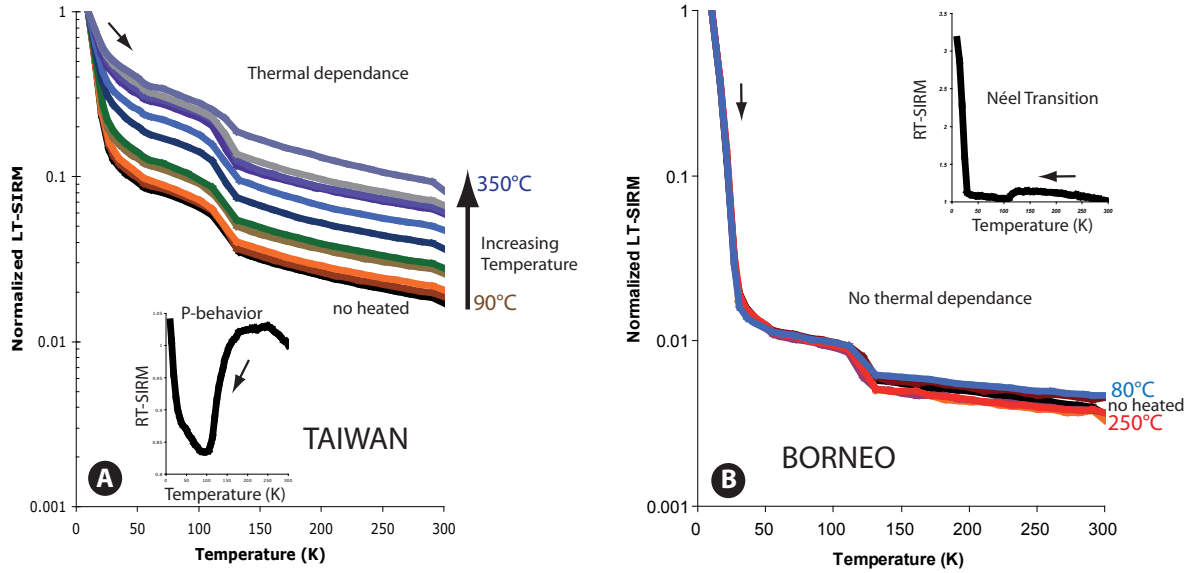

Figure IV.9 – Thermal dependence of ZFC curves for A) a sample from Taiwan (Chinshui claystone) showing no Néel transition and B) a sample from Borneo which displays a diagnostic Néel transition. RT-SIRM curve of the non heated (natural) sample is shown in insert. Data courtesy of Y-M. Chou and D. Janots.

clearly-documented Néel transition, when heated, do not display the previously described temperature dependence of the PM parameter (Figure IV.9B) which is the basis of the MagEval geothermometer.

2 Well study

2.1 Preliminary survey

The PM parameter used for MagEval geothermometry being defined at least, the objective of this part is to measure the characteristic magnetic signal over a selection of wells located in different basins with variable tectono-sedimentary histories (burial, lithology, temperature...). A total of 7 wells were investigated in this preliminary survey covering a wide geographical area. The wells are also very variable as far as age of sediments, present-day temperature and maturity ranges (Table IV.1). They are situated in well-known petroleum provinces including : the North Sea, Nigeria, Gabon, Indonesia, the Netherlands, Libya, and Angola (Figure IV.10).

A total of 135 samples, mostly cuttings, were collected for all wells (89% cuttings and 11% cores). Sample-spacing was defined for each well on the basis of the depth interval and available rock lithologies.

Country	Well	Drilling year	Total Depth TD (m)	Bottom Hole Age	Maximum in situ T (°C)	Ro(%)	Tectonic sedimentary context
Angola	Girassol-1	1996	4128	Oligocene	~140	~0.3-0.7	Simple
Gabon	Bikele-1	1975	4306.5	Cretaceous	~150	~0.4-2.3	Complex
Indonesia	Handil-9b	1979	3986	Mid Miocene	~160	~0.6-1.3	Simple
Libya	B1-NC191	2004	2082	Ordovician			Complex
Nigeria	Amenam-3/3bis	1992	4909	Miocene	~170	~0.4-1	Simple
The Netherlands	Nagele-1	1970	4304	Early Carboniferous	~160	~0.3-6.7	Complex
United Kingdom	22/30C-10	1992	6008	Mid Jurassic	~200	~0.3-2	Simple

Table IV.1 – Selected wells for the development of the MagEval geothermometer. Ro values indicated in table refer to the total range of values available for the well of interest

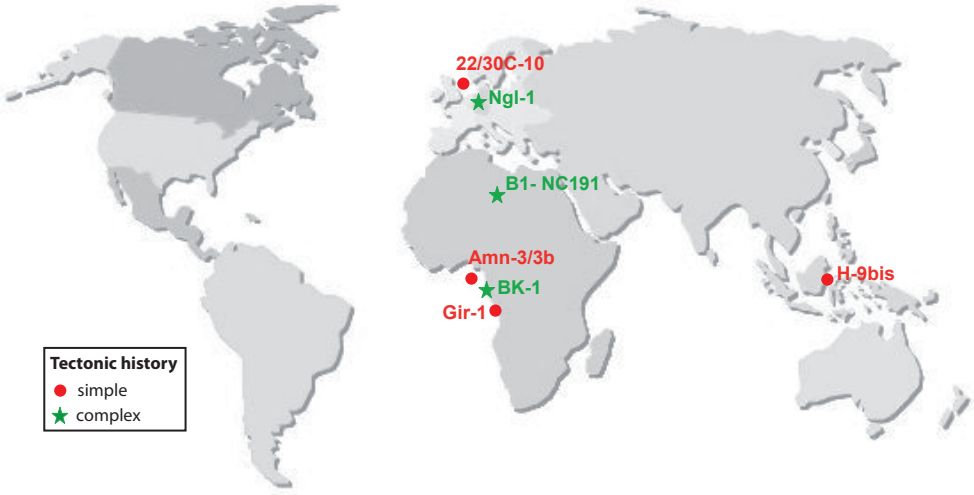

Figure IV.10 – Location of the selected wells

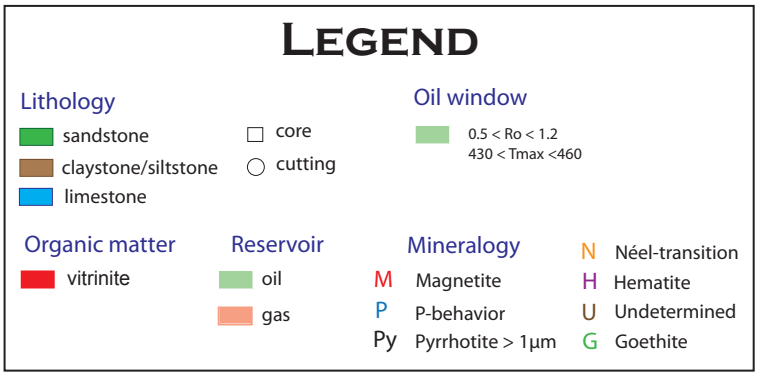

Figure IV.11 – Legend for Figures IV.12 to IV.34. All depths are measured depth MD, otherwise specified.

Data available and samples used for each well in this study are reported in appendix 4 and presented in Figures IV.11 to IV.18. The measured samples comprise argillites/shales, sandstones and limestones, of ages ranging from Miocene to Ordovician. They reflect temperatures (present or past) covering the complete diagenetic domain (60-350°C), and organic matter maturity range (Ro = 0.3-7%). This diversity permitted to test MagEval applicability in a wide range of situations.

The results of magnetic measurements performed on these samples are displayed in Figures IV.19 through IV.34. Firstly, the low field magnetic susceptibility χ was measured. Then low temperature MPMS measurements were performed according to the measurement sequence defined in chapter III. Detailed data are reported in appendix 4.

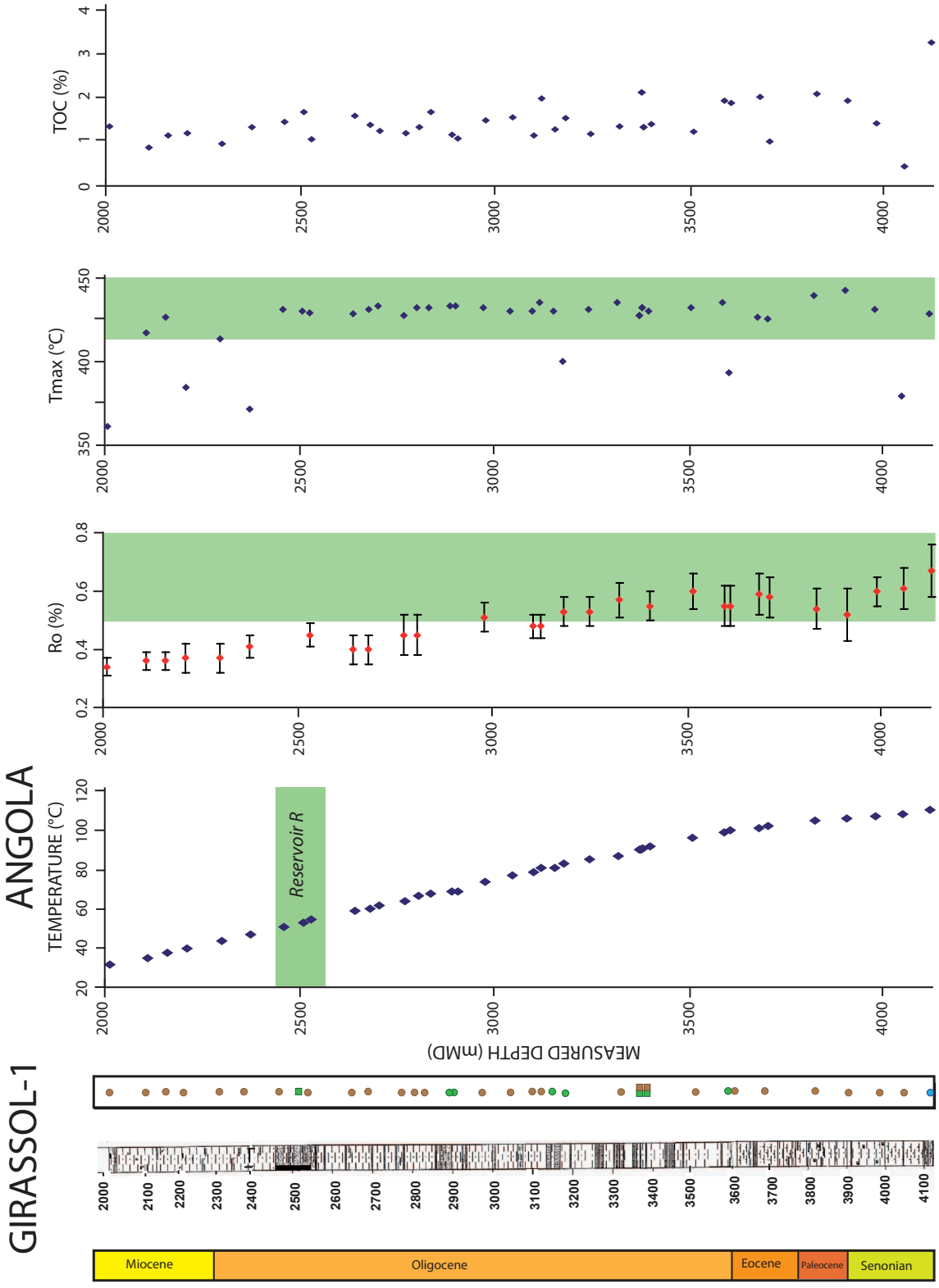

Figure IV.12 – Well Girassol-1, Angola : location and lithology of studied samples and available data. See Figure IV.11 for legend.

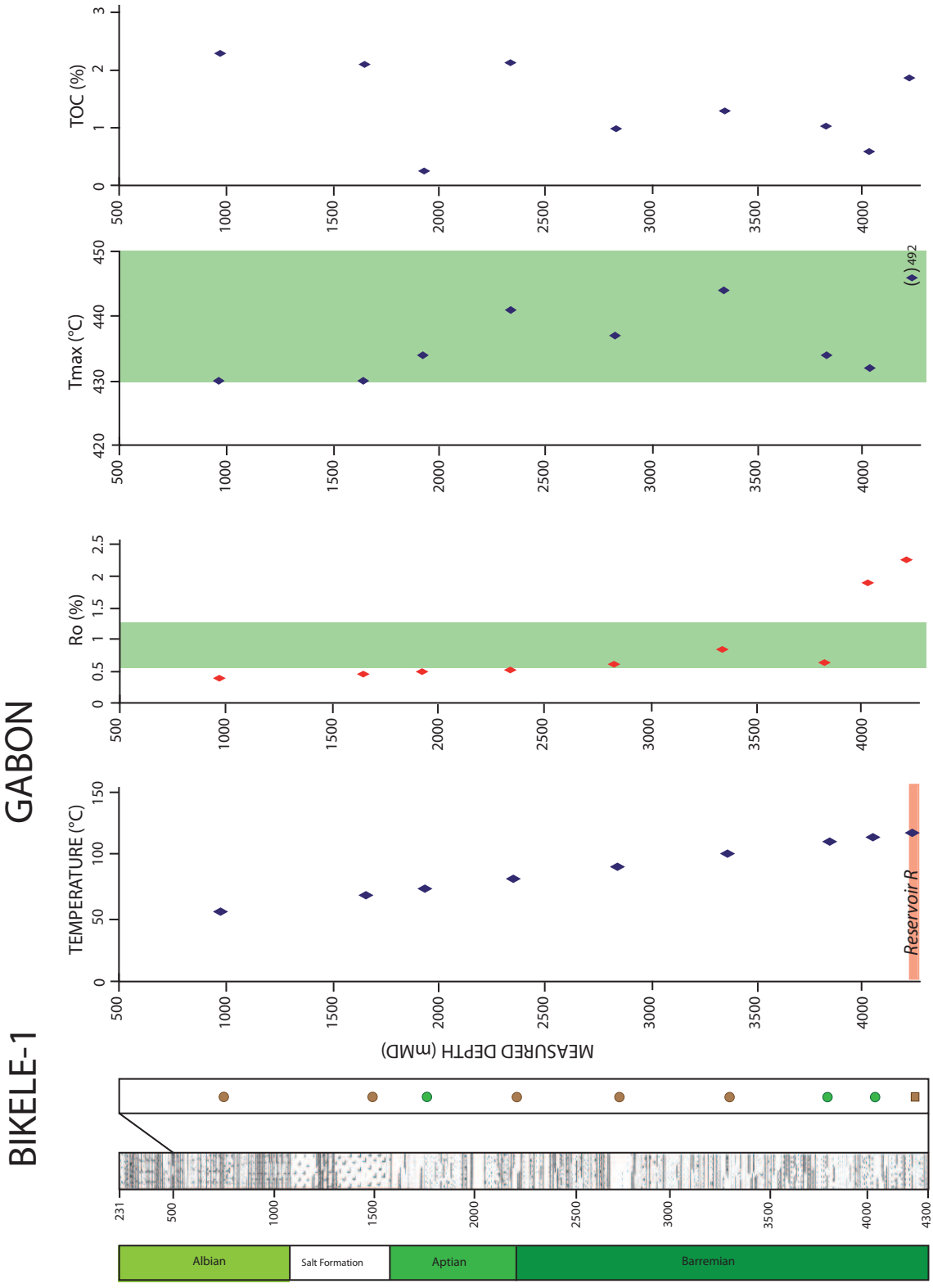

Figure IV.13 – Well Bikele-1, Gabon : location and lithology of studied samples and available data. See Figure IV.11 for legend.

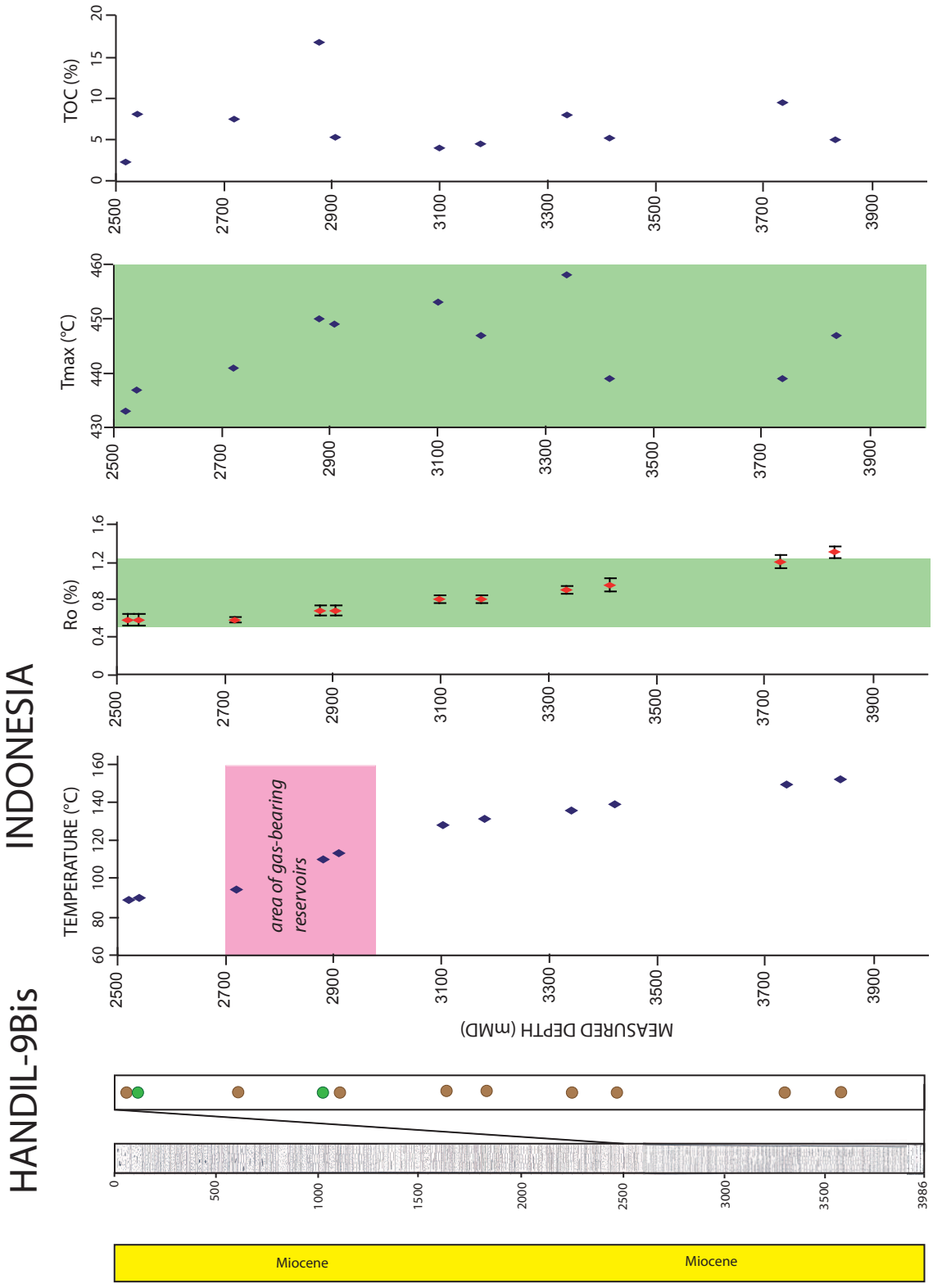

Figure IV.14 – Well Handil-9bis, Indonesia : location and lithology of studied samples and available data. See Figure IV.11 for legend.

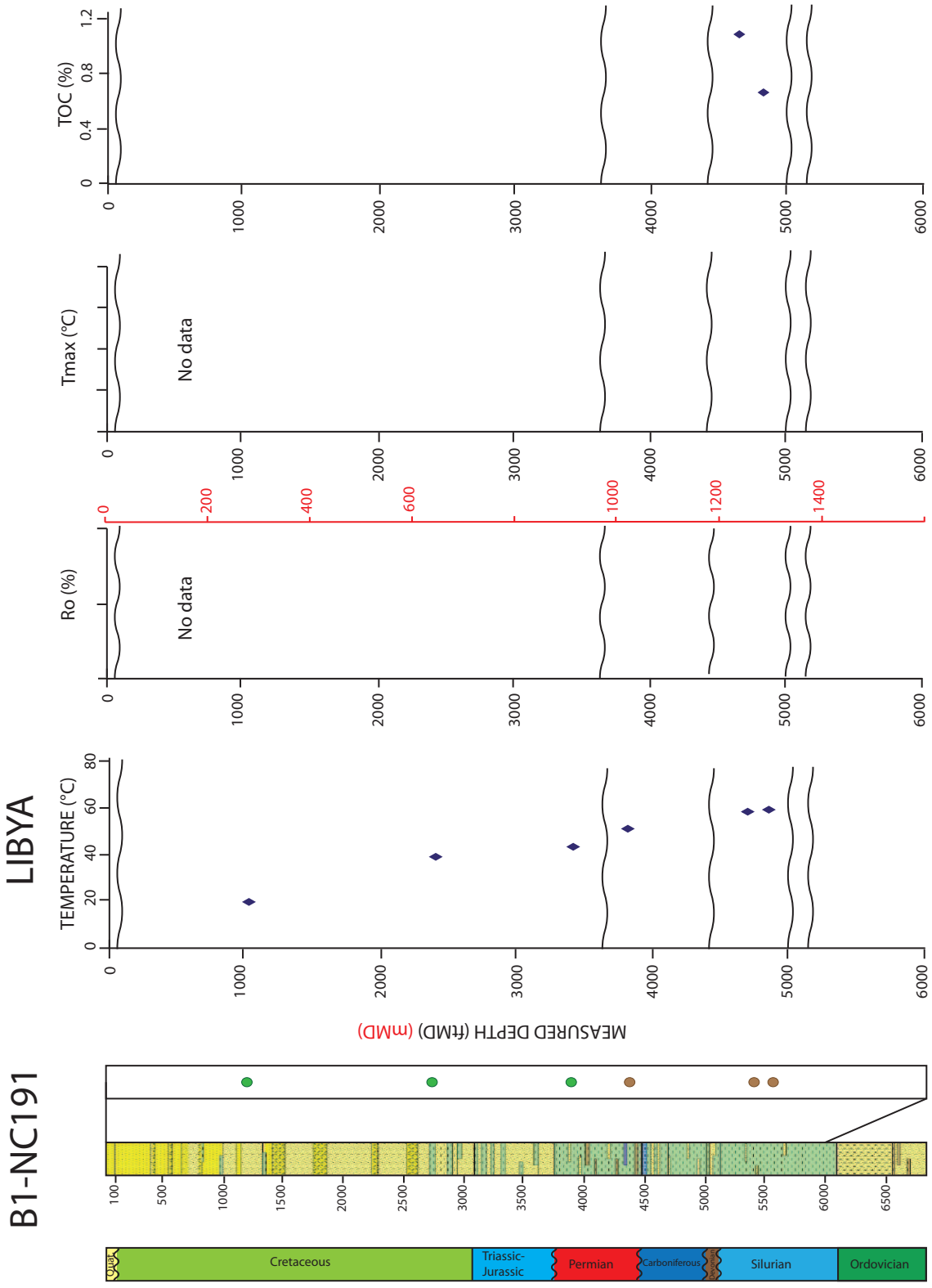

Figure IV.15 – Well B1-NC191, Libya : location and lithology of studied samples and available data. See Figure IV.11 for legend.

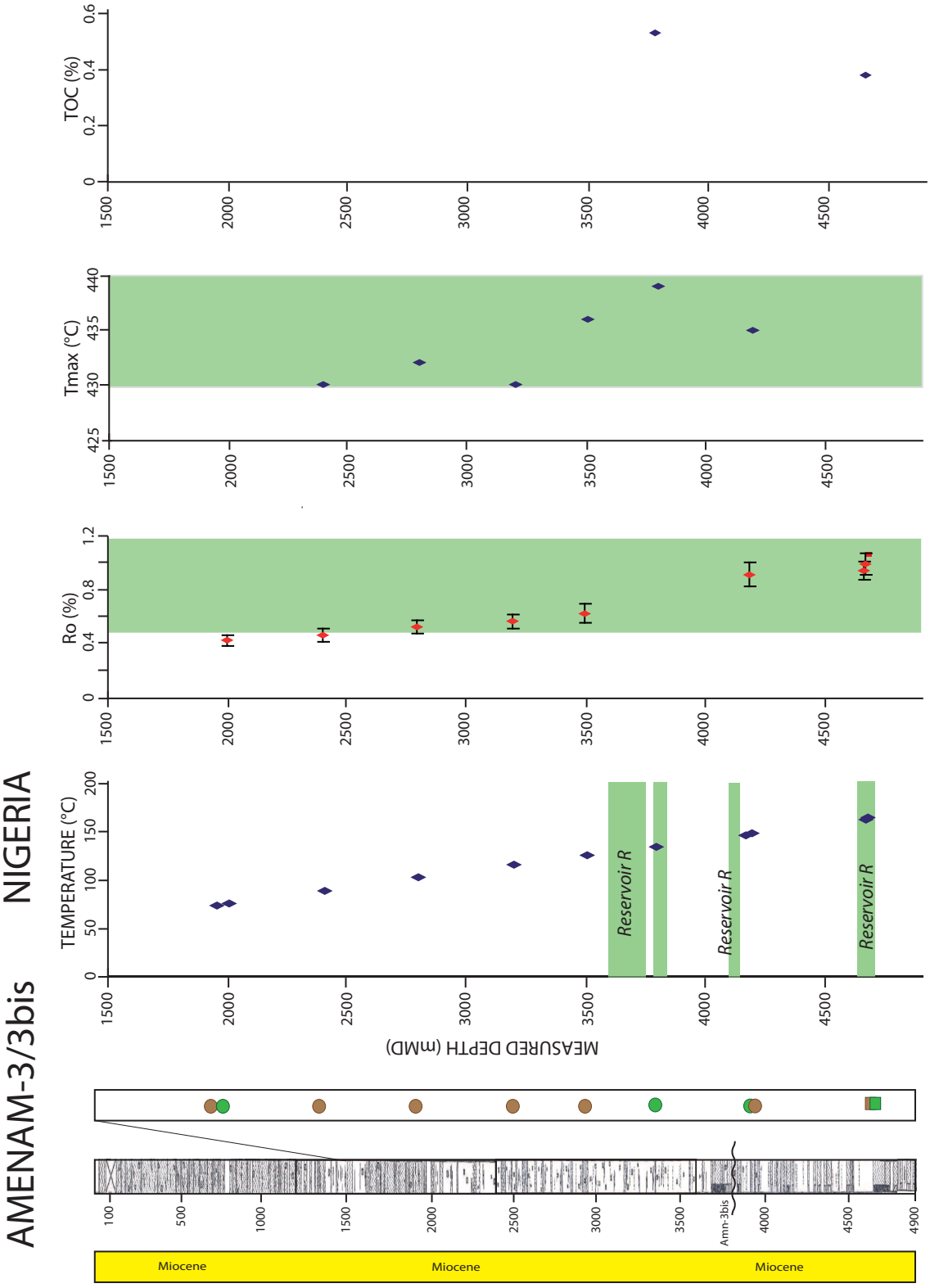

Figure IV.16 – Well Amenam-3/3bis, Nigeria : location and lithology of studied samples and available data. See Figure IV.11 for legend.

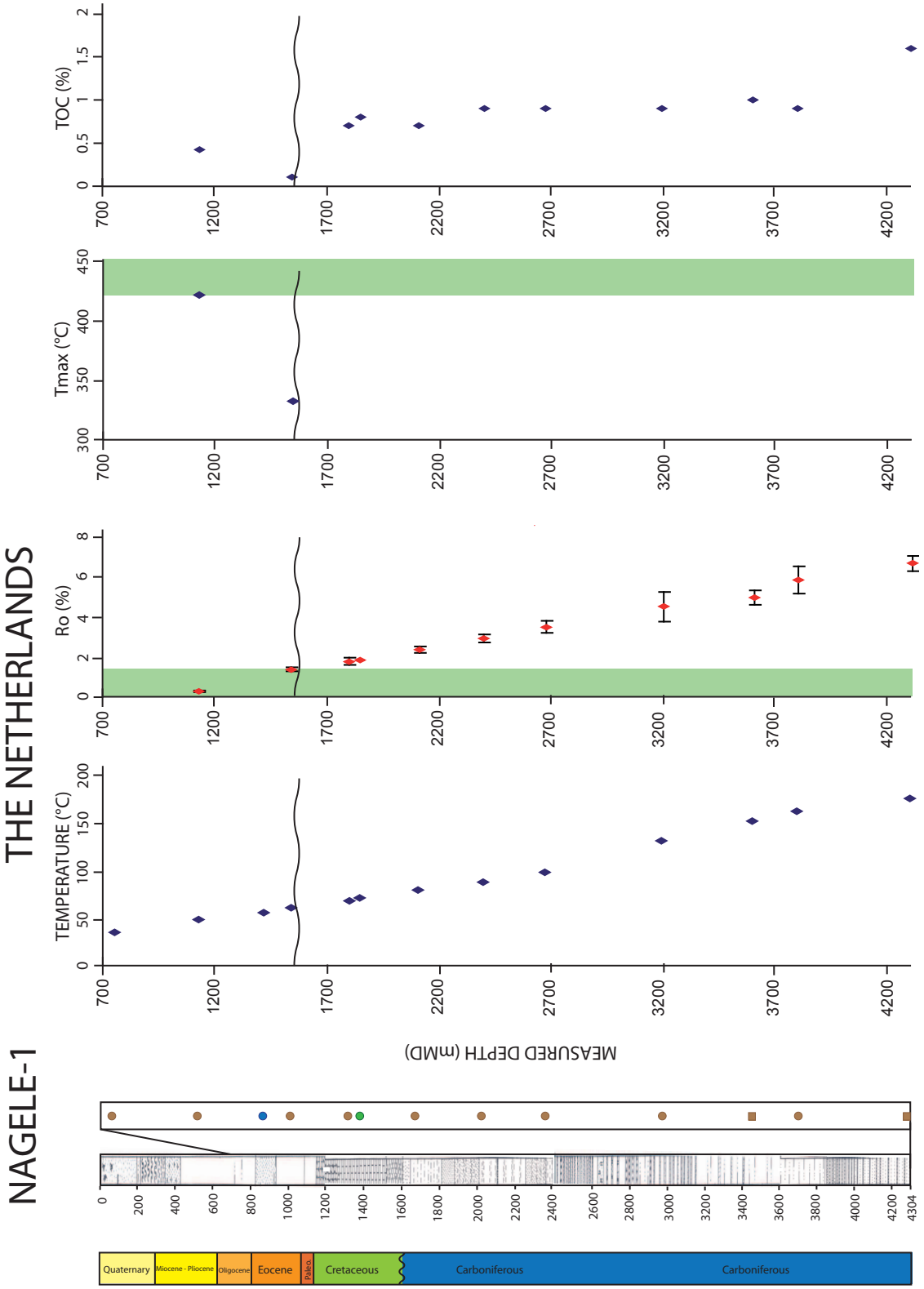

Figure IV.17 – Well Nagele-1, The Netherlands : location and lithology of studied samples and available data. See Figure IV.11 for legend.

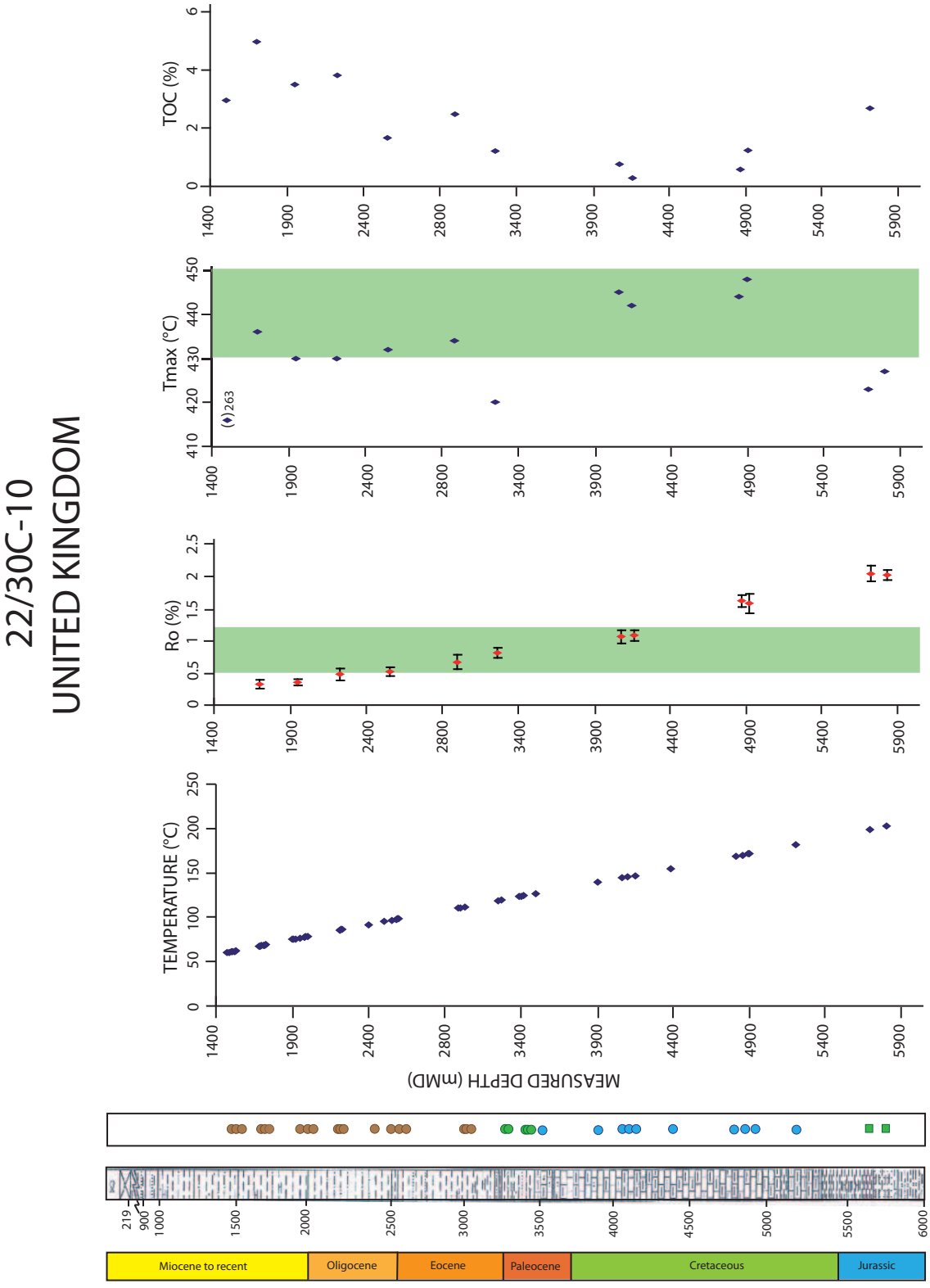

Figure IV.18 – Well 22/30C-10, United Kingdom : location and lithology of studied samples and available data. See Figure IV.11 for legend.

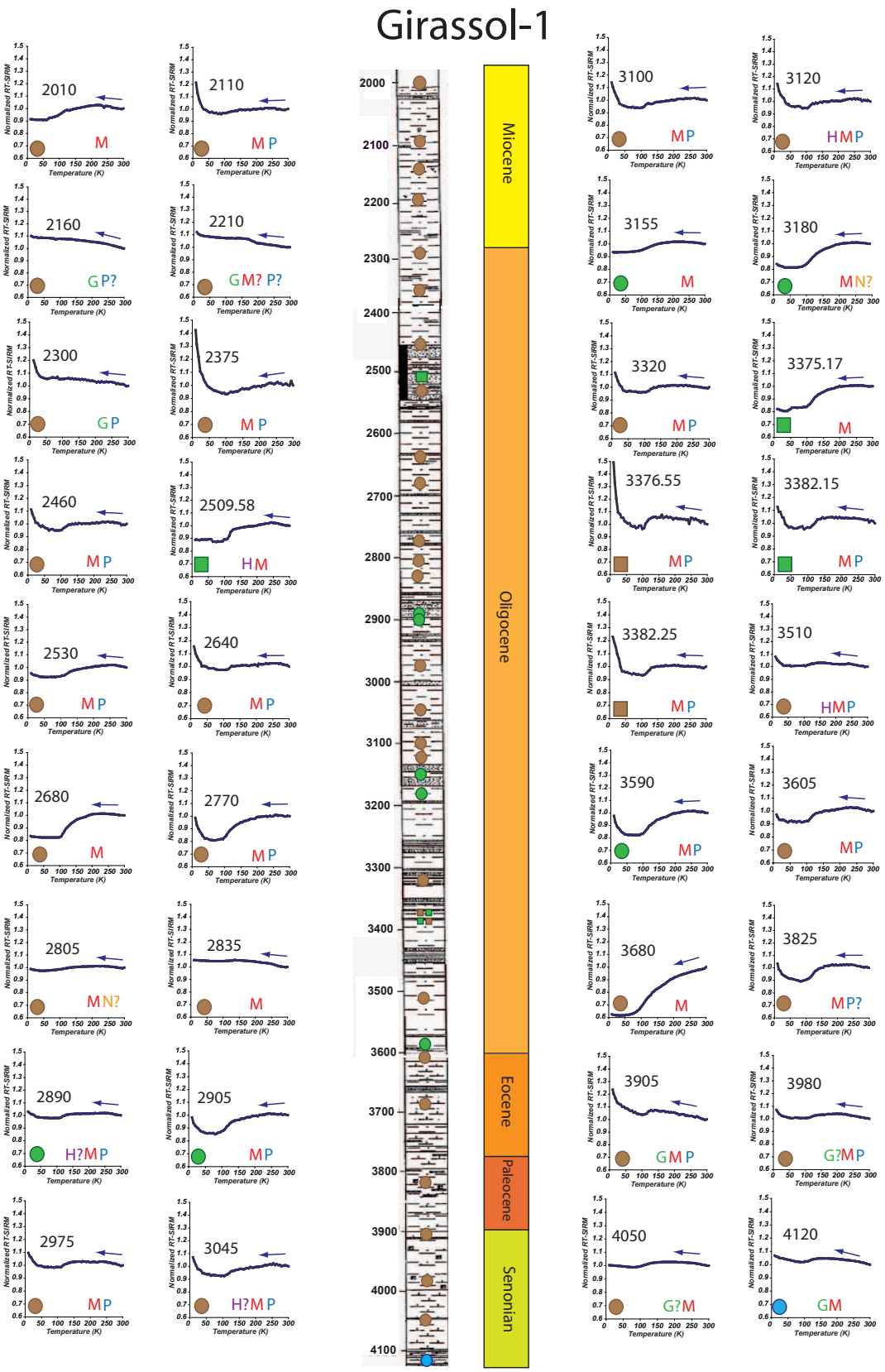

Figure IV.19 – RT-SIRM curves for Gir-1 samples. See Figure IV.11 for legend.

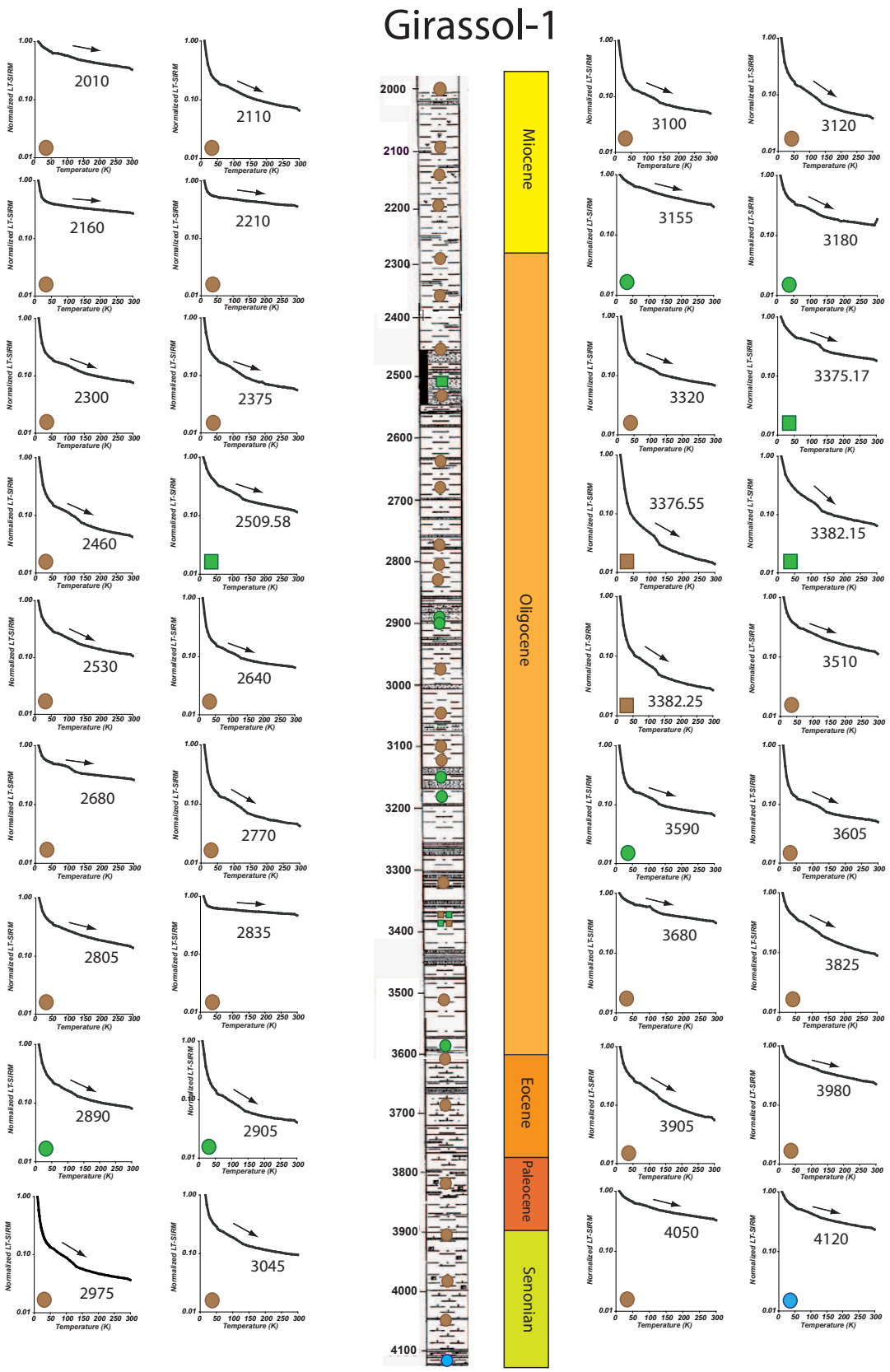

Figure IV.20 – ZFC curves for Gir-1 samples. See Figure IV.11 for legend.

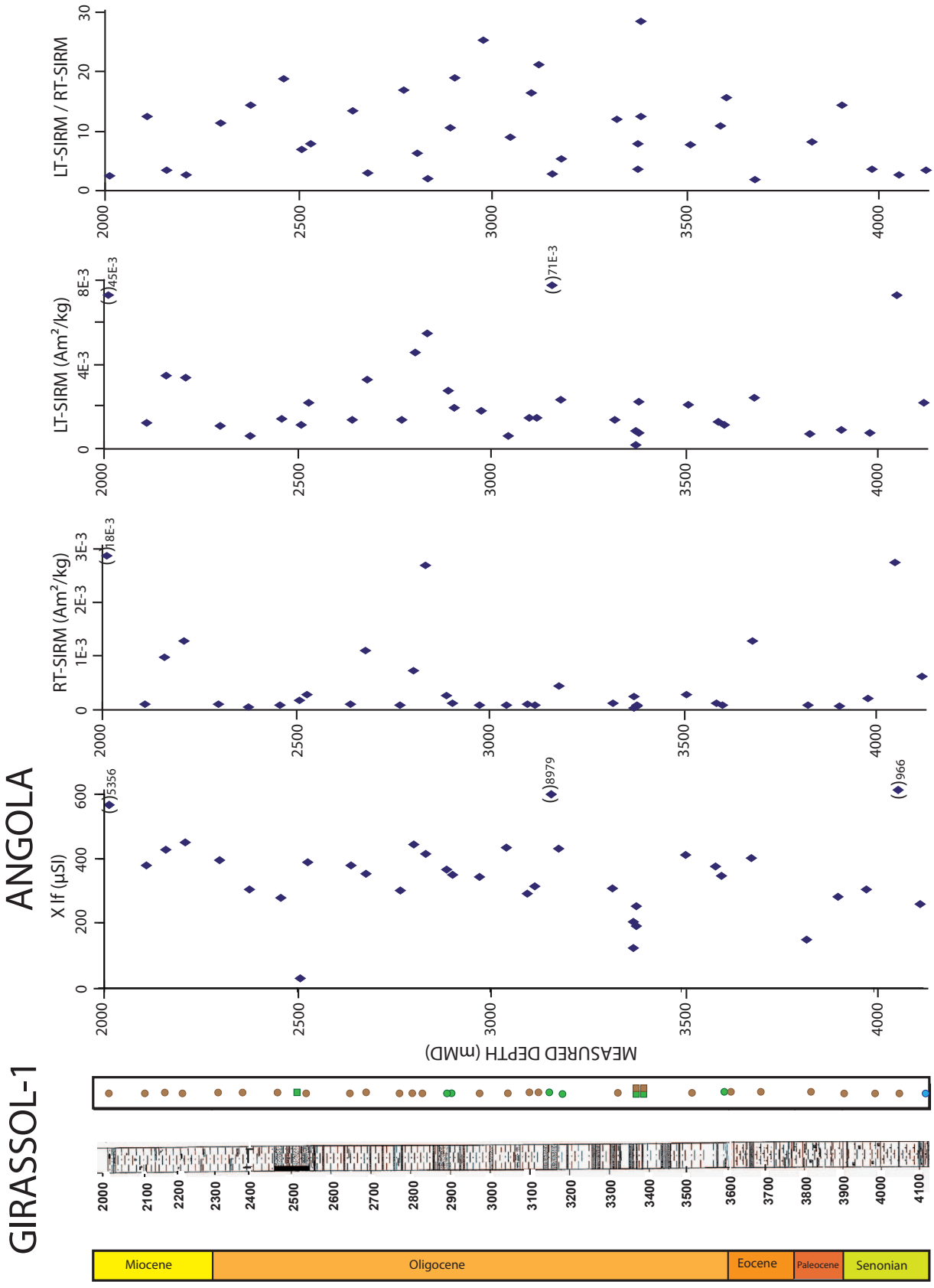

Figure IV.21 – Magnetic data for Gir-1 samples. See Figure IV.11 for legend and text for explanation.

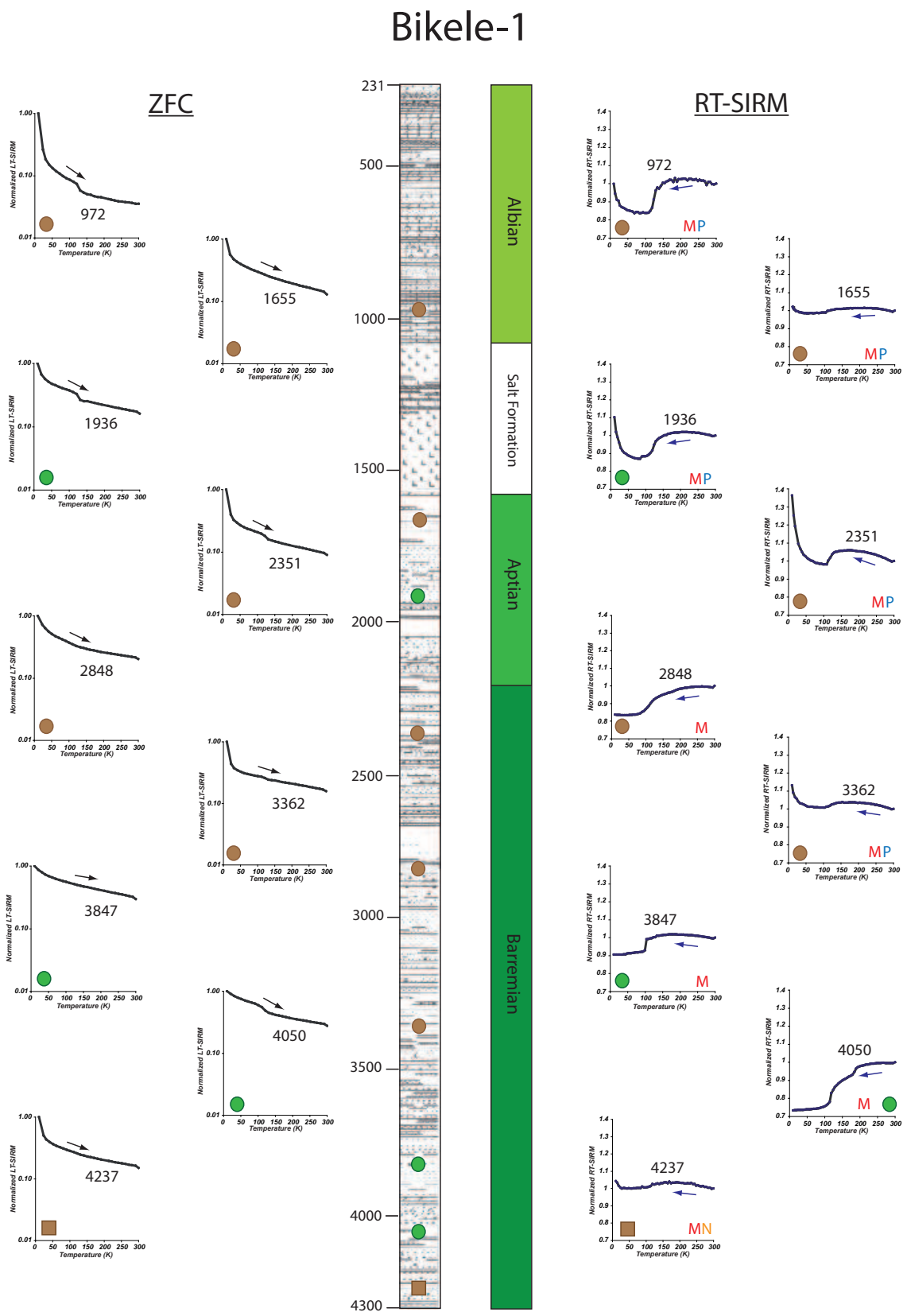

Figure IV.22 – ZFC and RT-SIRM curves for Bikele-1 samples. See Figure IV.11 for legend.

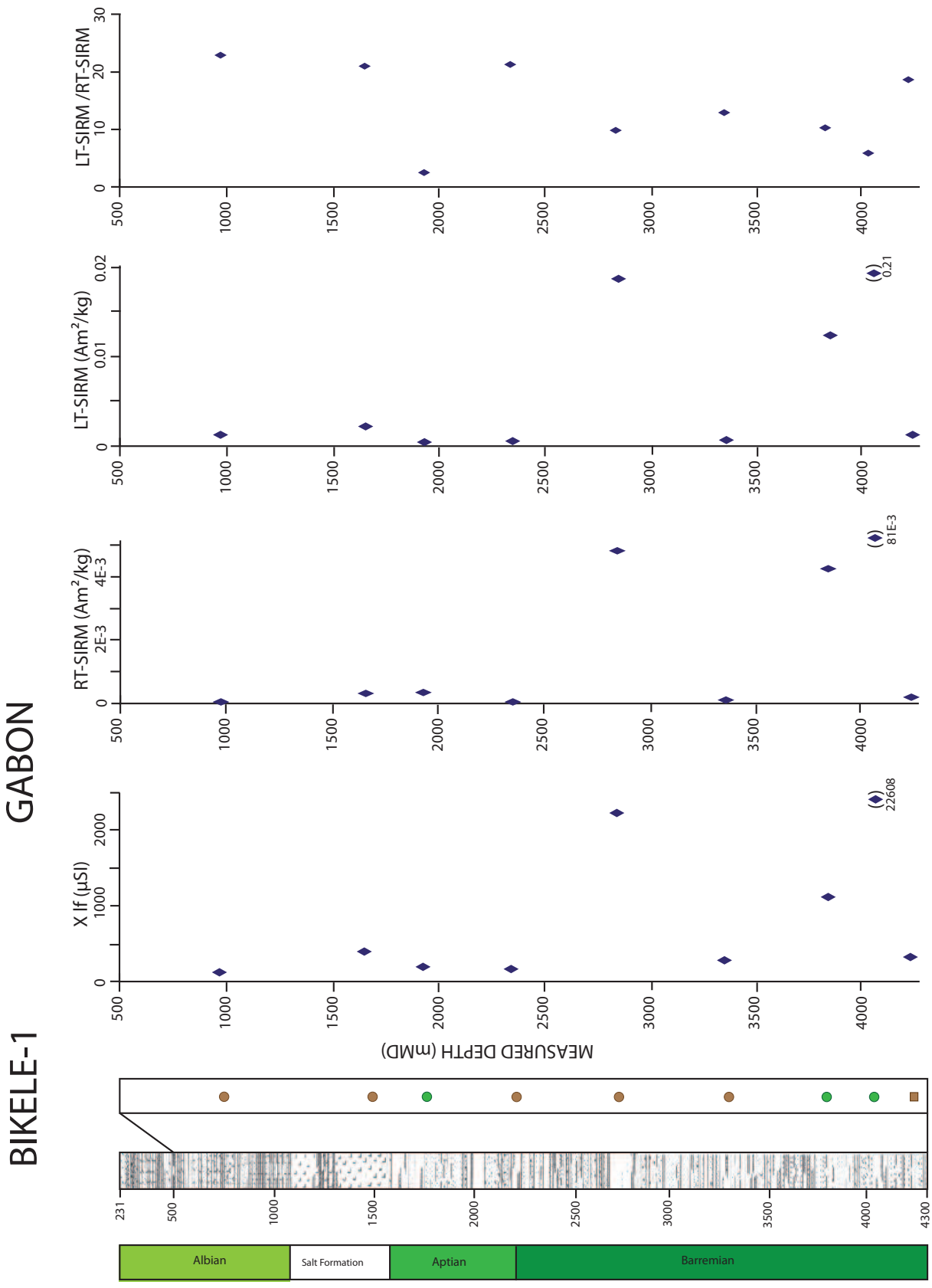

Figure IV.23 – Magnetic data for Bikele-1 samples. See Figure IV.11 for legend and text for explanation.

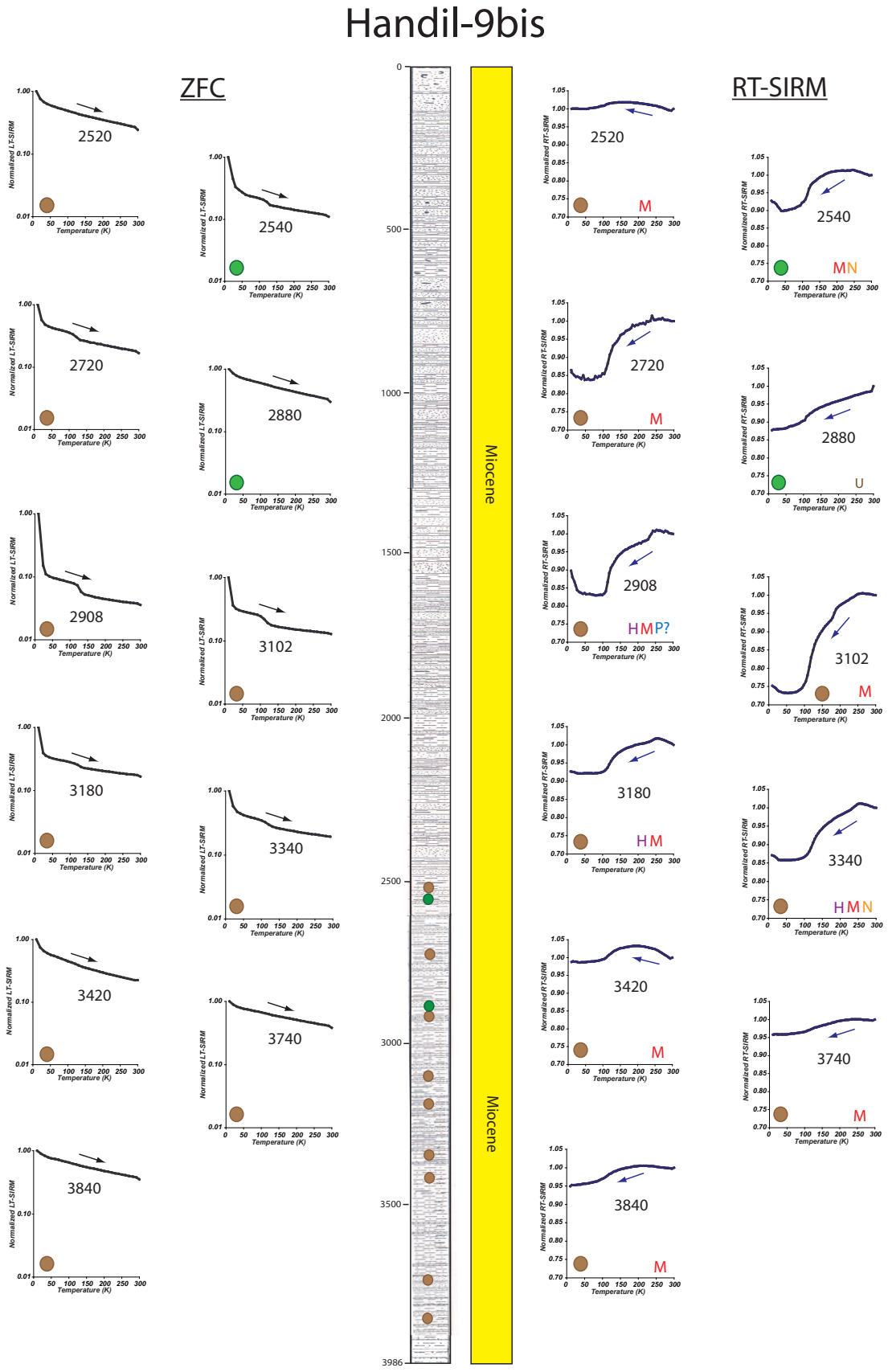

Figure IV.24 – ZFC and RT-SIRM curves for Handil-9bis samples. See Figure IV.11 for legend.

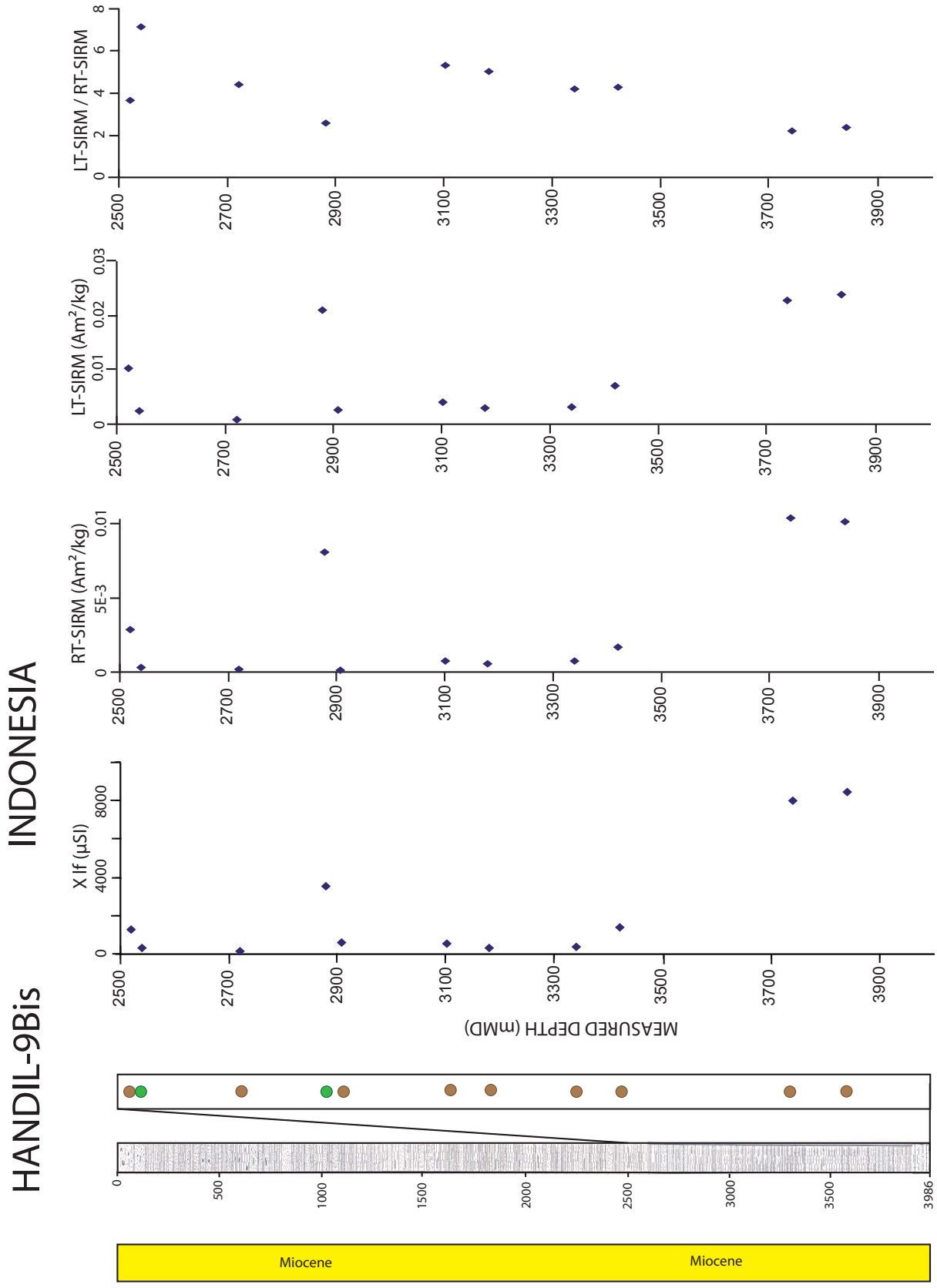

Figure IV.25 – Magnetic data for Handil-9bis samples. See Figure IV.11 for legend and text for explanation.

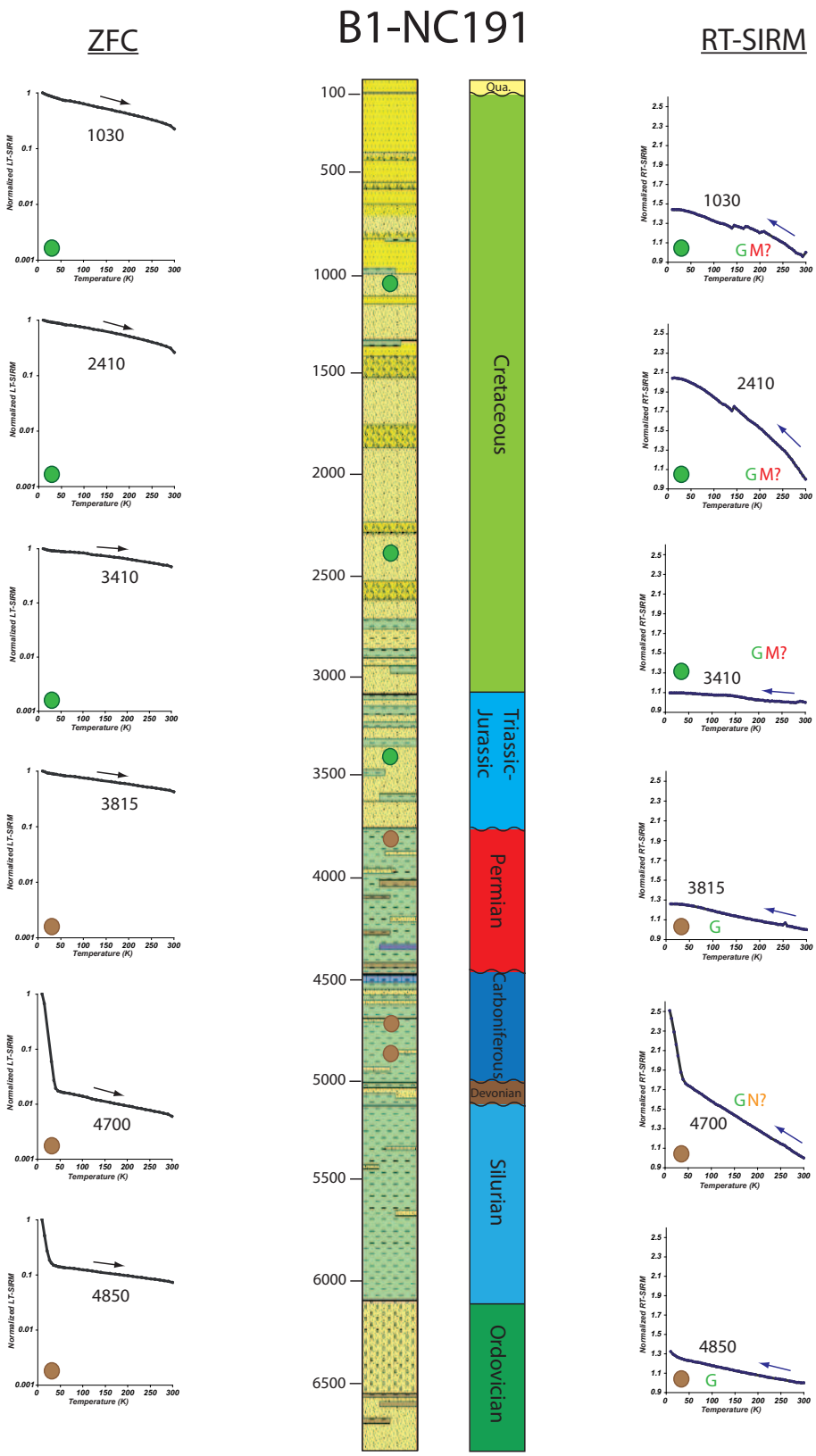

Figure IV.26 – ZFC and RT-SIRM curves for B1-NC191 samples. See Figure IV.11 for legend.

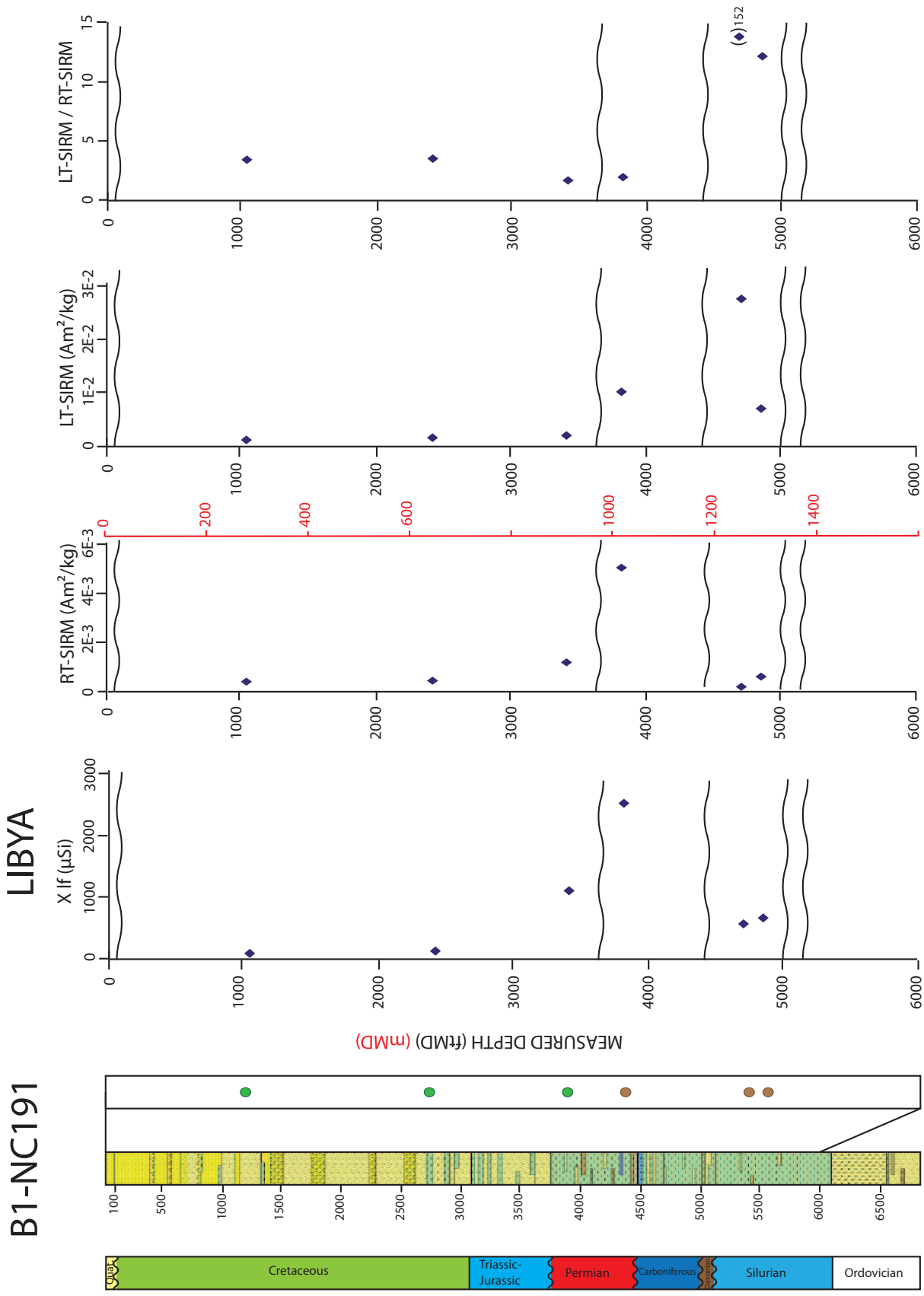

Figure IV.27 – Magnetic data for B1-NC191 samples. See Figure IV.11 for legend and text for explanation.

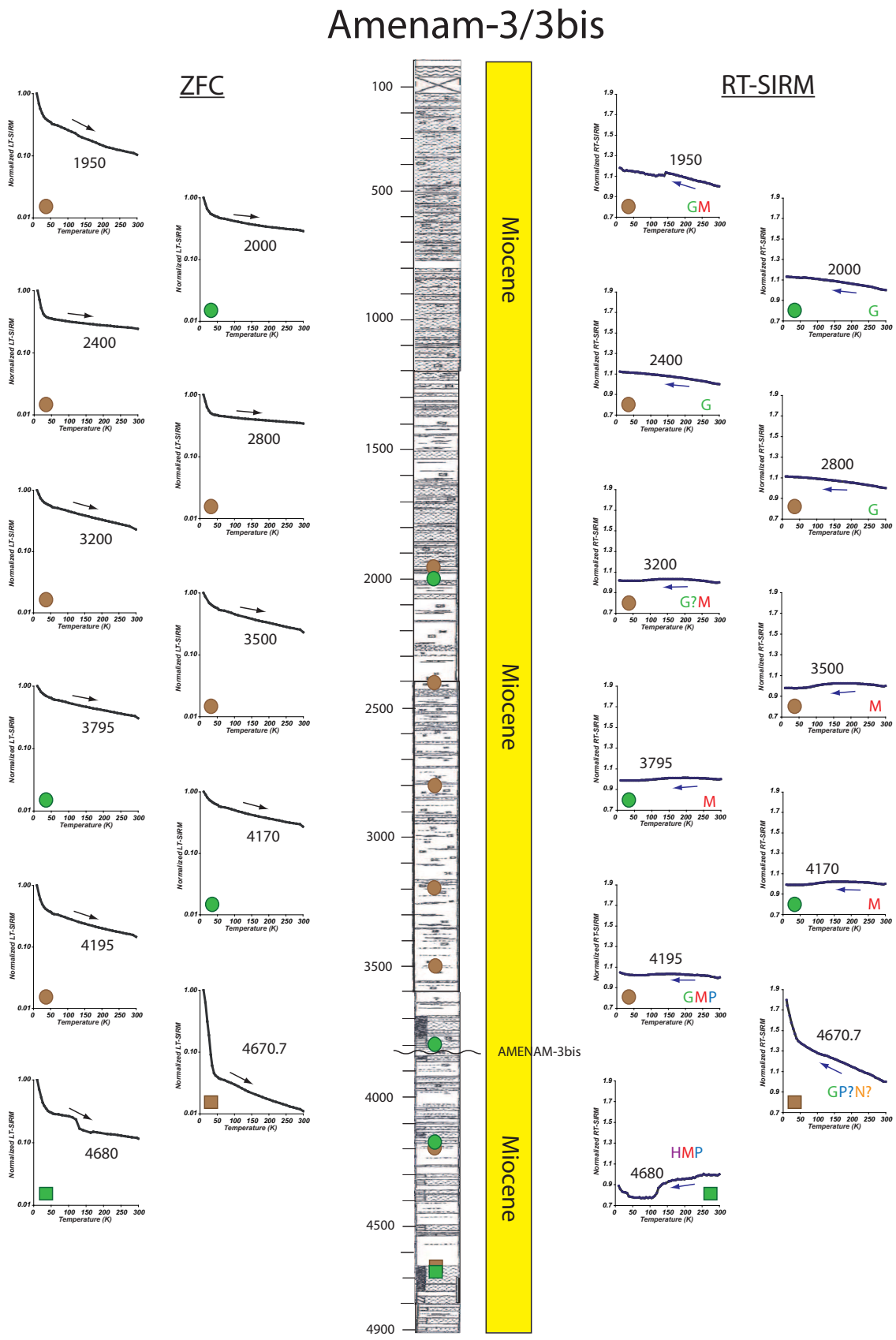

Figure IV.28 – ZFC and RT-SIRM curves for Amenam-3/3bis samples. See Figure IV.11 for legend.

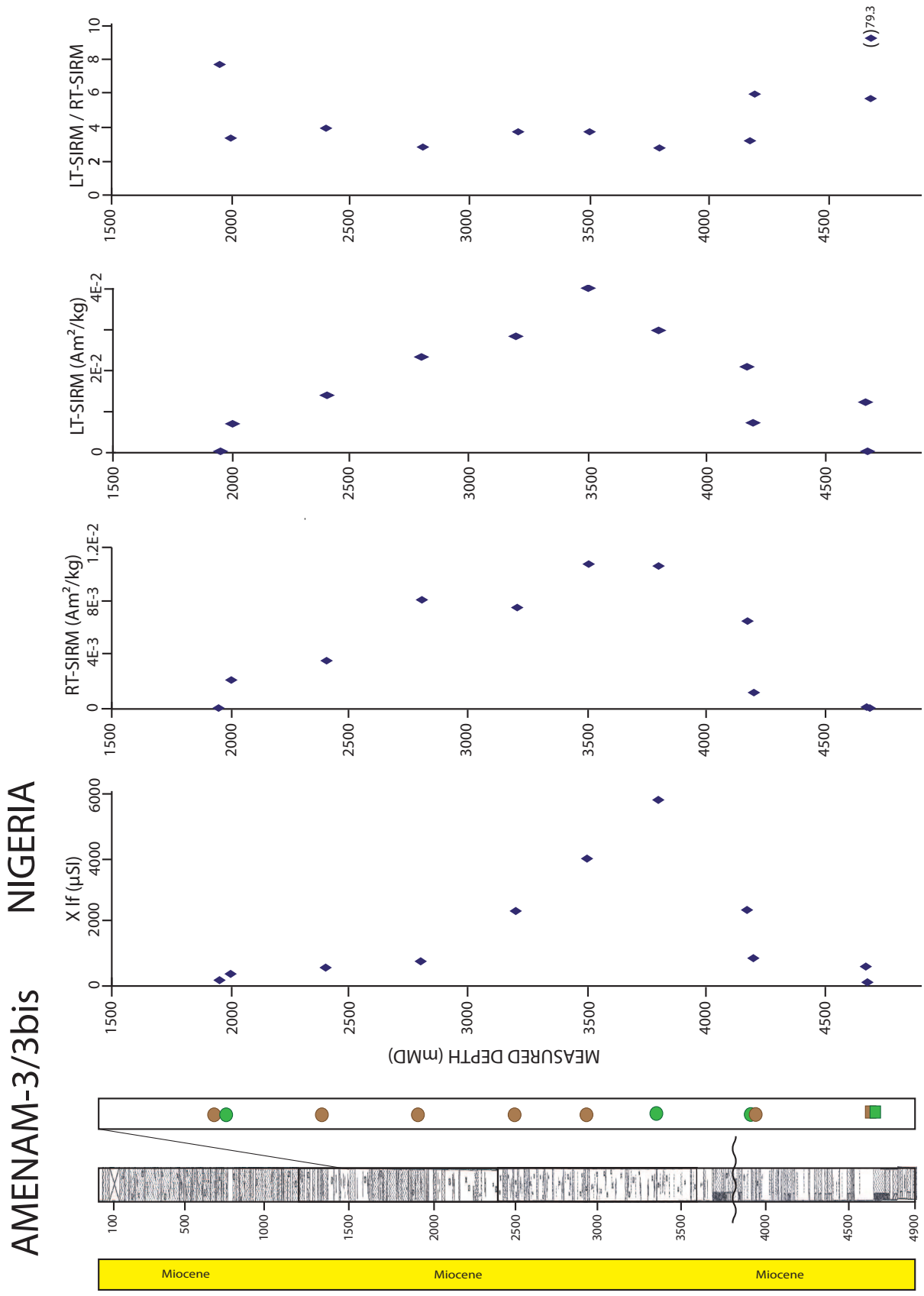

Figure IV.29 – Magnetic data for Amenam-3/3bis samples. See Figure IV.11 for legend and text for explanation.

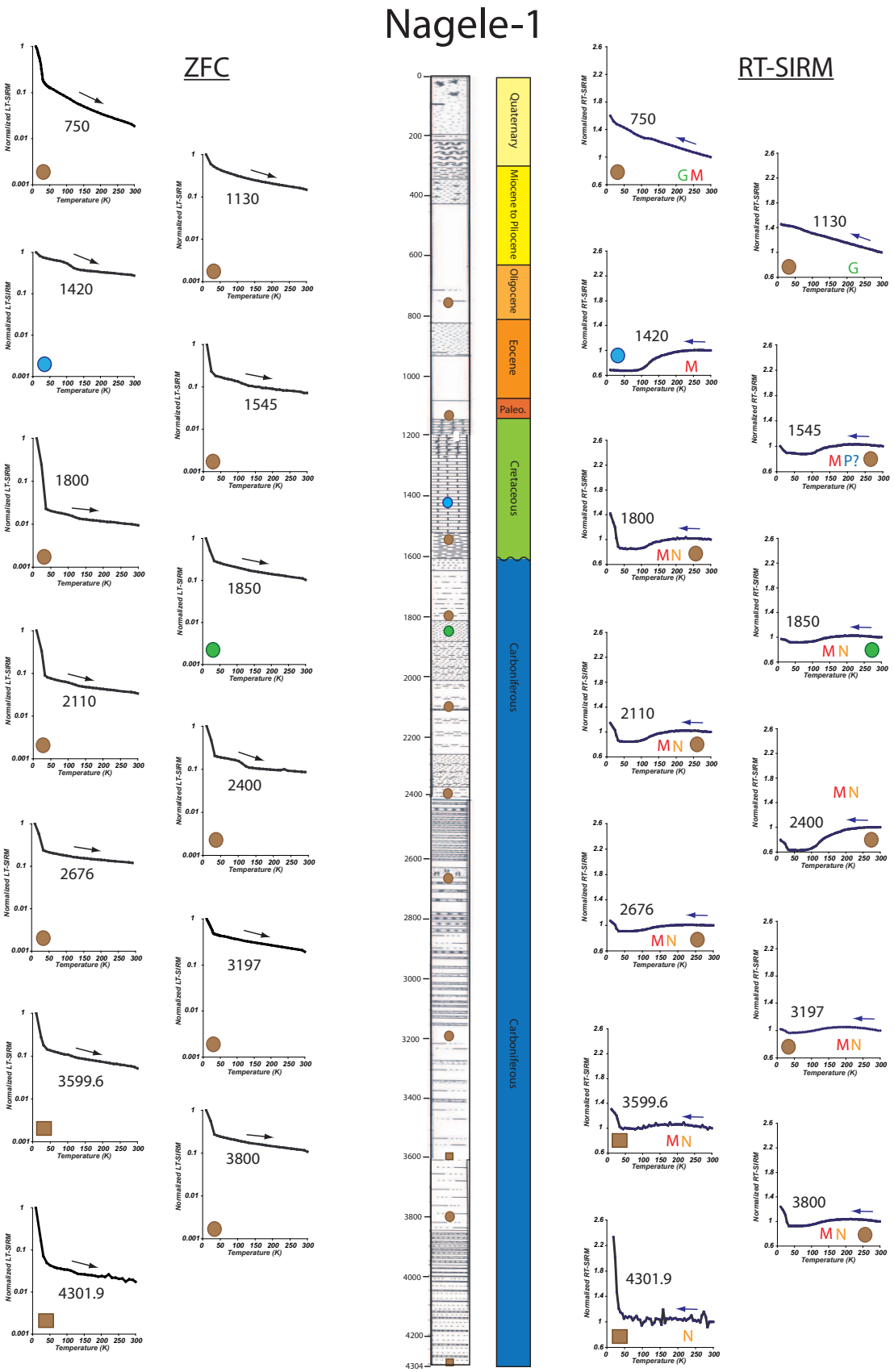

Figure IV.30 – ZFC and RT-SIRM curves for Nagele-1 samples. See Figure IV.11 for legend.

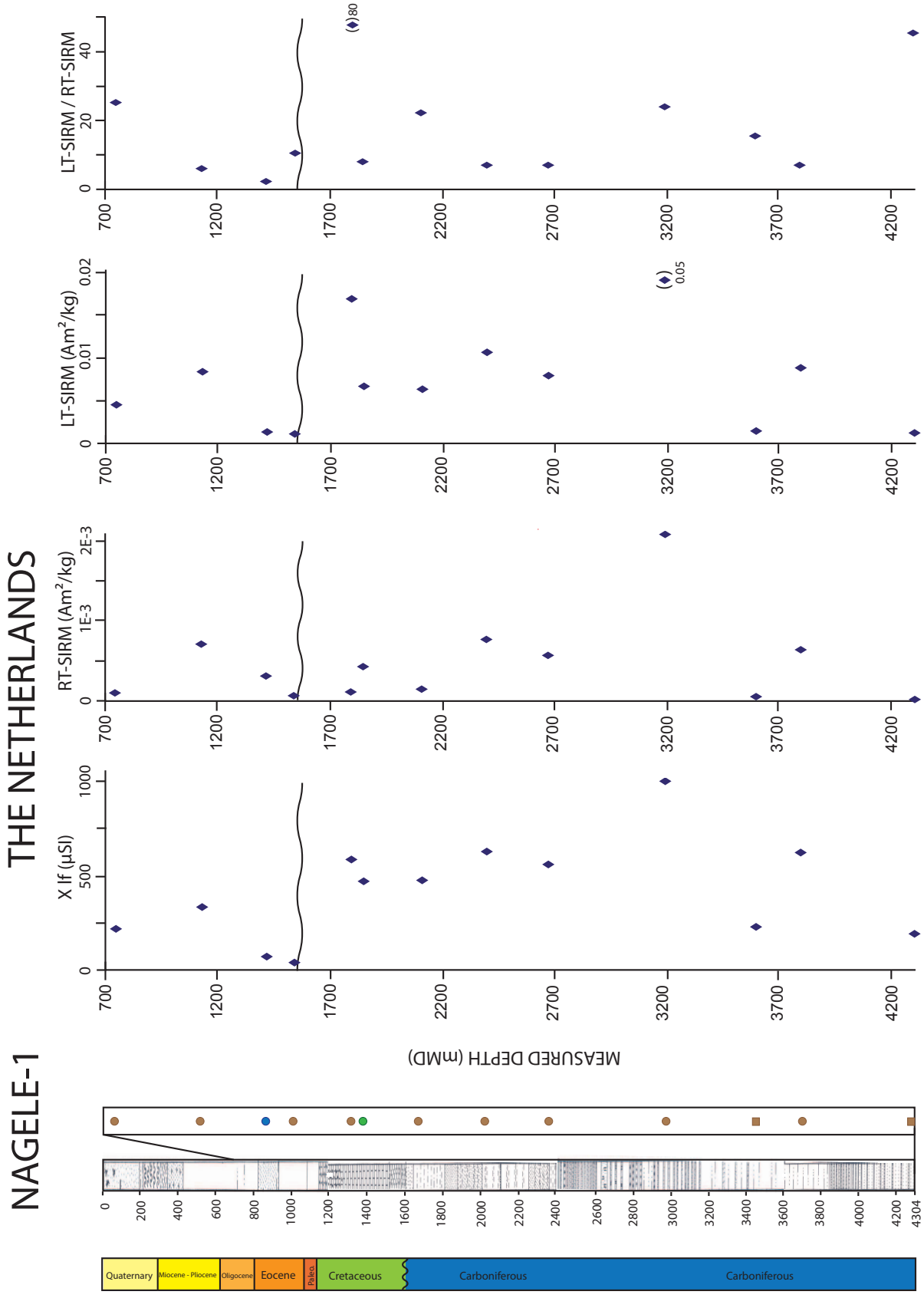

Figure IV.31 – Magnetic data for Nagele-1 samples. See Figure IV.11 for legend and text for explanation.

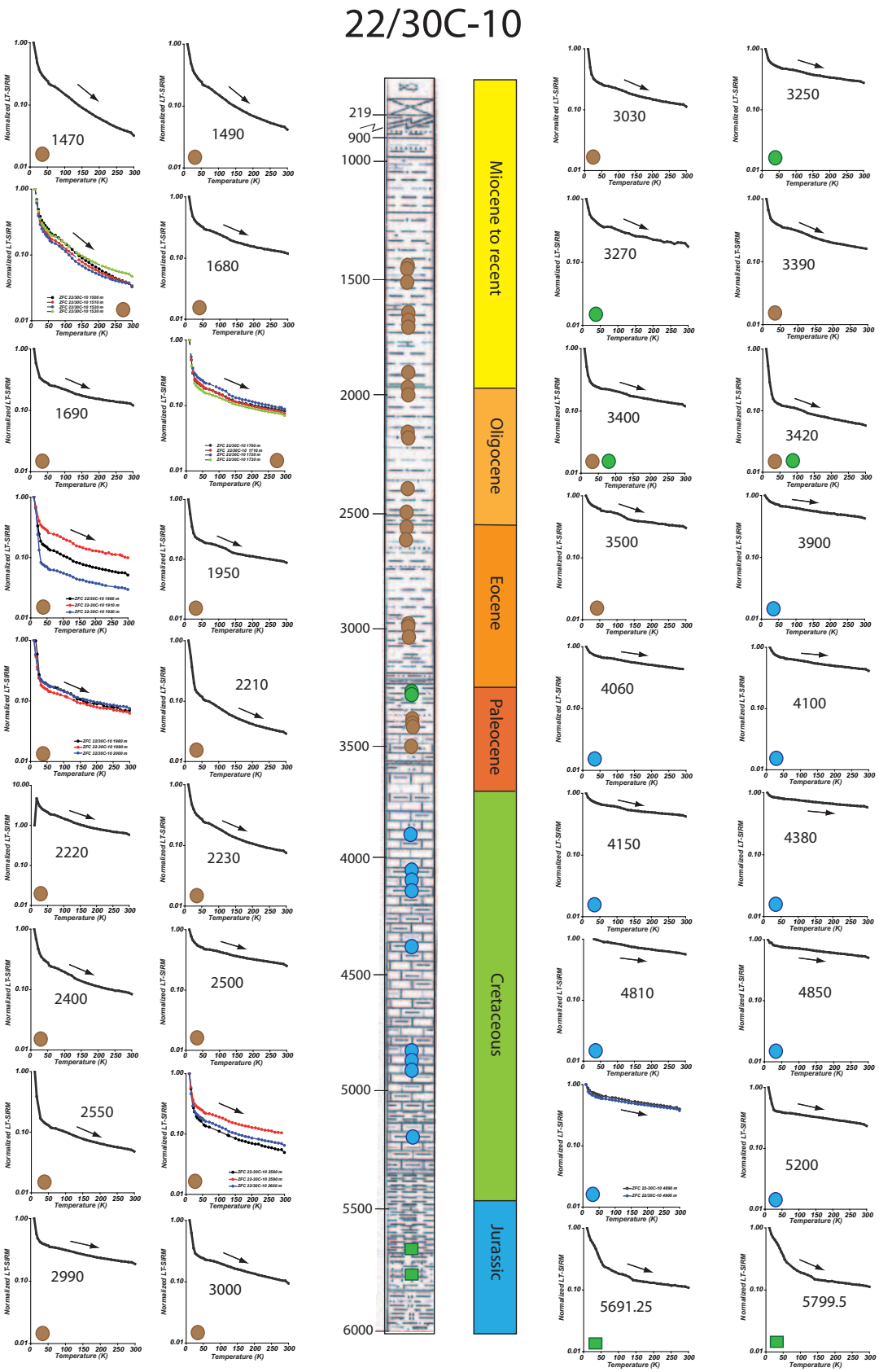

Figure IV.32 – ZFC curves for 22/30C-10 samples. See Figure IV.11 for legend.

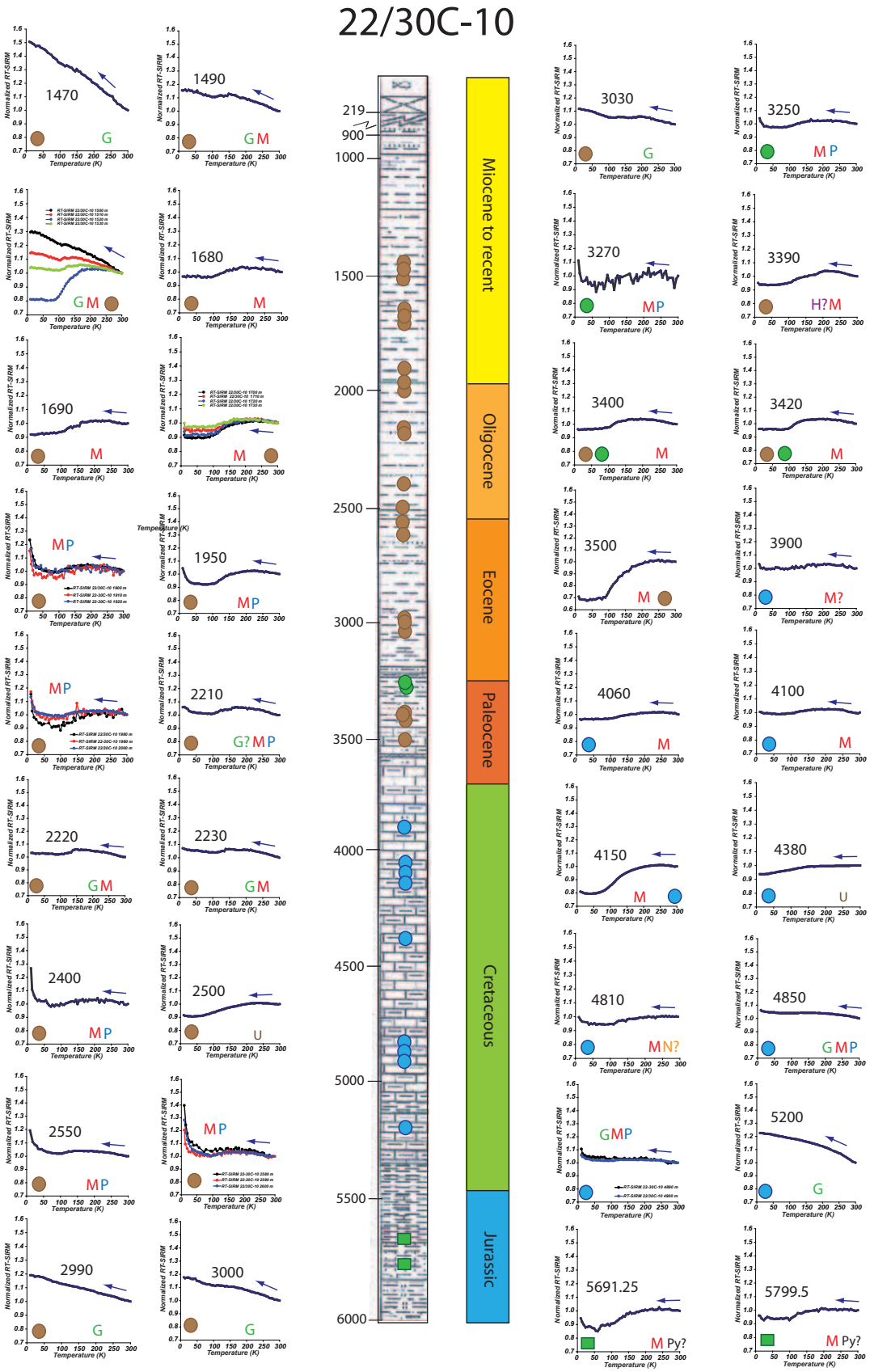

Figure IV.33 – RT-SIRM curves for 22/30C-10 samples. See Figure IV.11 for legend.

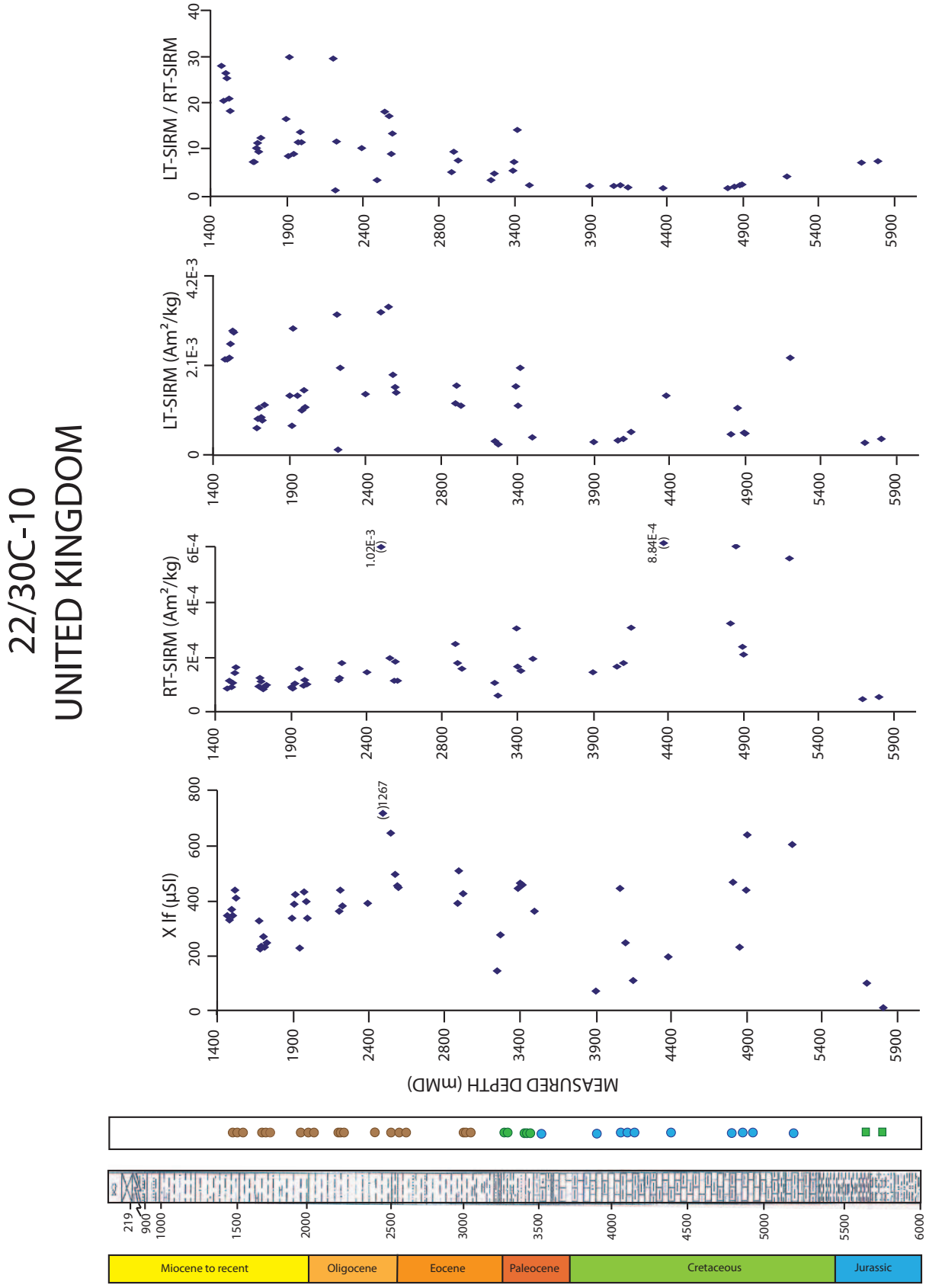

Figure IV.34 – Magnetic data for 22/30C-10 samples. See Figure IV.11 for legend and text for explanation.

2.2 Concentration in magnetic minerals

The application of the MagEval geothermometer requires the partial or the complete removal of the original detrital magnetic signal. The dissolution of detrital iron oxides in the sediment usually occurs in the first few meters of burial, or during later burial, according to a reaction involving magnetite, pyrite and organic matter (see Introduction, Rowan *et al.*, 2009). Any remaining high magnetic concentrations can be explained by several factors. Firstly, geological factors such as volcanic ashes and heavy minerals concentrated in sediments can explain a high magnetic minerals content. Secondly, drilling factors such as contamination by drill mud and/or mixing of different facies in cuttings samples can explain differences in magnetization. Then, the preservation conditions may oxidize small fragments of cuttings leading to an increase of the iron oxides content.

The magnetic susceptibility χ and saturation isothermal remanent magnetization at room temperature (RT-SIRM$_{300K}$) yield indication on magnetic concentration in rocks (e.g. Thompson & Oldfield, 1986). In the studied claystones, it was found that the MagEval signal is best observed in low-susceptibility rocks, typically < 500 μSI. However, due the limited set of samples studied, it is not sure whether MagEval signal exists or not in claystones with higher magnetic susceptibility. Considering the entire set of data, it is documented that MagEval magnetic behavior is well seen for low χ and RT-SIRM$_{300K}$ values (Figure IV.35). We estimated threshold values to be 500 μSI for χ and 500 μAm^2/kg for RT-SIRM$_{300K}$. The samples lying in the non applicability domain ($\chi > 500$ μSI and RT-SIRM$_{300K} > 500$ μAm^2/kg) of the MagEval geothermometer display a magnetic behavior different of that of the typical MagEval signal described previously. If considering magnetite as the main mineral responsible for the RT-SIRM$_{300K}$, then the magnetite content can be derived from the intrinsic value of magnetite (Mr $\sim$ 10 Am^2/kg for soft magnetite ; Maher & Thompson, 1999). This provides only an estimate of the order of magnitude of the magnetite concentration according to :

$$\text{concentration} = \text{Mr}/\text{RT-SIRM}_{300K}$$

An RT-SIRM$_{300K}$ threshold value at 500 μAm^2/kg corresponds to 50 ppmv of magnetite. This implies that samples exhibiting a typical MagEval signal are characterized by a very low content in magnetite, which would not be detected by many standard geochemical or physical techniques including XRD (concentration $> 1\%$).

Figure IV.36 shows an example of magnetic signals measured for two argillites from Bikele-1 : one is of the MagEval-type, the other is not, as explained thereafter. Regarding the RT-SIRM$_{300K}$ and χ values (Table IV.2), BK-1 2848m does not satisfy the selection criteria established previously. The 10-35 K drop of the remanence in the ZFC cooling curve for BK-1 2848m is not well marked, whereas it is well defined for BK-1 972m (Figure IV.36A). The PM values are 0.39 and 0.83 respectively. In addition, the BK-1 972m ZFC curve displays the Verwey transition of magnetite at $\sim$120 K, which does not appear for BK-1 2848m. On the RT-SIRM curves, the two samples show the Verwey transition,

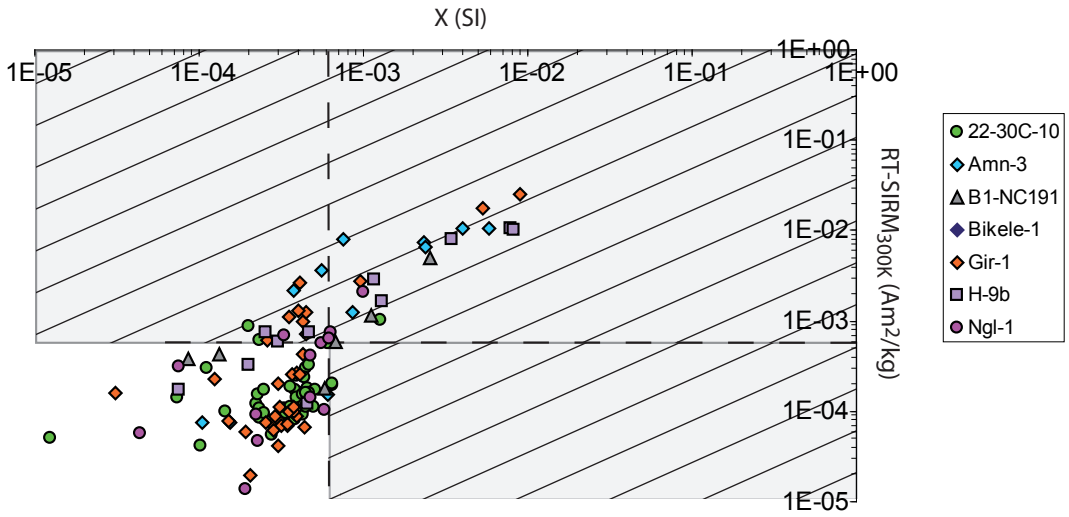

Figure IV.35 – Magnetic susceptibility χ vs. room temperature saturation magnetization (RT-SIRM) for all samples. The dashed area represents the non applicability domain of the MagEval geothermometer (see text). 27% of the samples fall beyond the applicability threshold limit.

even if the shape is slightly smoother for BK-1 2848m. The major difference between these two curves occurs below 50 K. BK-1 2848m does not show any P-behavior, whereas BK-1 972m shows a well developed one. The difference between the two samples is certainly due to the fact that BK-1 2848m is highly magnetic compared to the other claystone (Table IV.2).

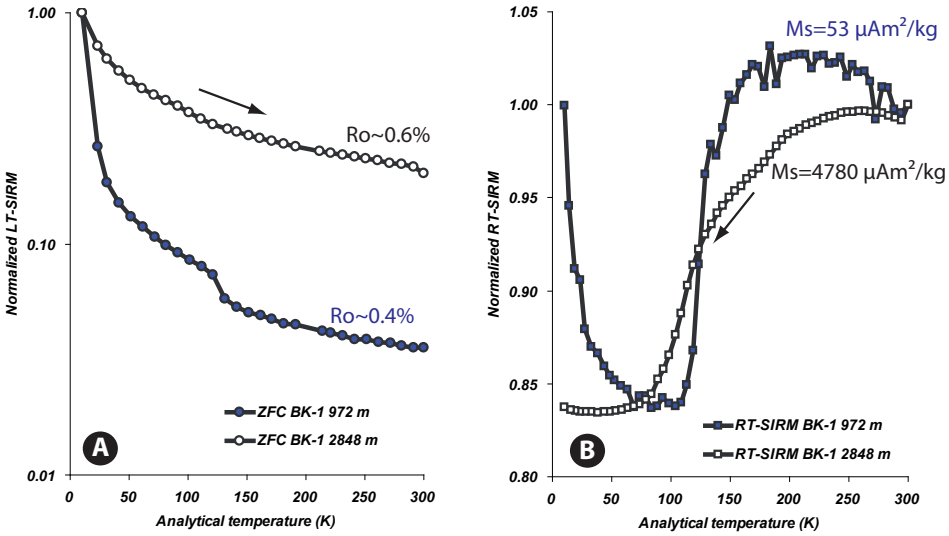

Figure IV.36 – A) ZFC and B) RT-SIRM curves for two argillites from BK-1. P-behavior and 2-step pattern are not observed for the higher magnetization at saturation.

Sample	χ (μSI)	RT-SIRM$_{300K}$ (μAm^2/kg)	Magnetite concentration (ppmv)	PM
BK-1 972m	120	53	∼5	0.83
BK-1 2848m	2240	4780	∼500	0.39

Table IV.2 – Magnetization of two argillites from Bikele-1. Magnetite concentration is calculated from the RT-SIRM$_{300K}$ value.

If only magnetite is considered, then the magnetite content (grain size > 20 nm) can be derived (Table IV.2). The magnetic parameters observation leads to the fact that superparamagnetic content is more important in BK-1 972m. The strong magnetization of BK-1 2848m may be explained by three factors : 1) the original detrital magnetic signal was not erased due to the strong magnetite content, 2) a different sedimentary source for this sample (for instance, volcanic or metamorphic rocks erosion) or 3) a possible contamination by drill mud. The later point is of significance because, in this preliminary well study, most available samples are cuttings which are characterized by important surface area (with drill mud, air).

2.3 Sample ageing

The small size of the analyzed cuttings fragments and the effect of reducing sample grains-size into powders raise the question of the potential impact of samples ageing. In particular, the question of whether the powdered samples could alter significantly as a result of prolonged contact with the atmosphere.

To further evaluate this question, two samples were re-measured several months after the original measurement. Gir-1 3100m powder was re-measured (in duplicates) 19 months later and Gir-1 3825m 21 months later (Figure IV.37).

For Gir-1 3825m, the ZFC curve is very different for the three measurements, including for the two different aliquots (subsamples) of this sample measured on two consecutive days (04/11 and 05/11/2010). This means that the ageing effect is not homogeneous within the powder of a single sample. For Gir-1 3100m, there is also an important difference in the ZFC curves. The PM value decreases from 0.81 to 0.56. That shows that a sample let in contact with the atmosphere during a significant period of time (almost two years in the present case) undergoes some transformations (e.g. oxidation, formation/growth of grains) which affect sample magnetization. Table IV.3 shows that the RT-SIRM$_{300K}$ increases up to two orders of magnitude for the aged samples, resulting in lowered (underestimated) PM values. Hence, we used a particular protocol to minimize the ageing effect. The biggest cuttings fragments (> 3 mm) were crushed and a quite great amount of powder (> 5 g) was obtained for representativeness. Then the powder sample was sealed in a gelatin capsule and measured by the next two days.

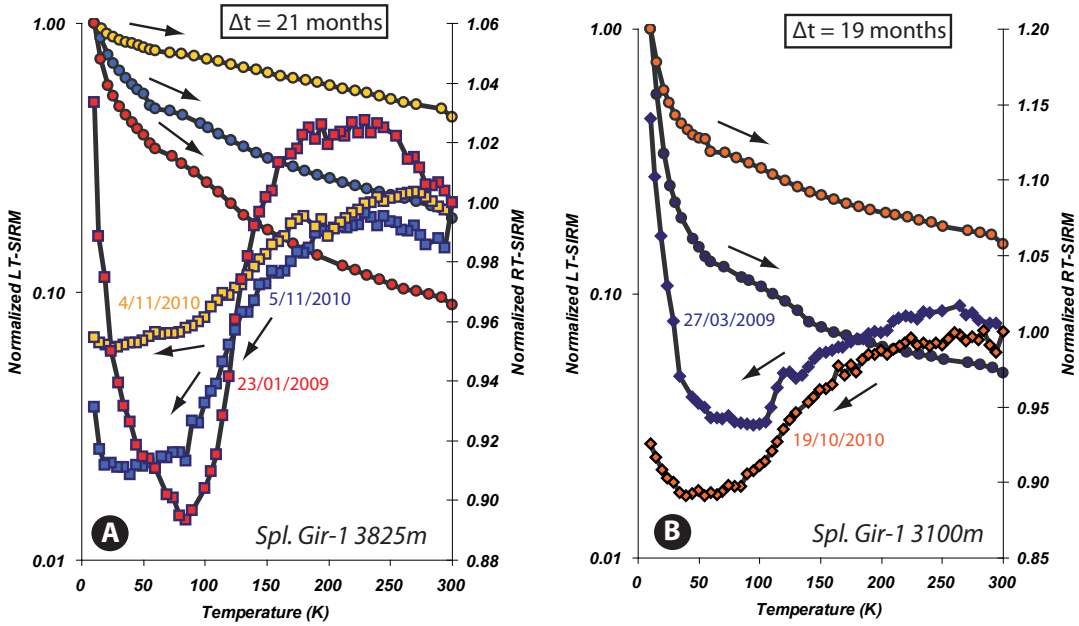

Figure IV.37 – Ageing effect on powders of two Gir-1 samples measured more than 1 year after the first measurement

Sample	Date	RT-SIRM$_{300K}$ (μAm^2/kg)	PM
Gir-1 3100m	27/03/2009	90	0.81
	19/10/2010	500	0.56
Gir-1 3825m	23/01/2009	80	0.54
	4/11/2010	3400	0.15
	5/11/2010	540	0.37

Table IV.3 – Evolution of the saturation magnetization RT-SIRM$_{300K}$ of two Gir-1 samples as a function of measured time

2.4 Lithologic/mineralogical parameters

In the boreholes study, the analyzed samples were collected from different lithologies classified in source rocks (claystones) and reservoir rocks (sandstones, limestones). These rocks differ by many factors including TOC, porosity and permeability. In the previous figures (e.g. Figure IV.37), the lithology of the samples is mainly claystones or siltstones. In the following, we focused on the occurrence (or not) of the MagEval signal in various lithologies.

2.4.1 MagEval signal in sandstones and limestones ?

Firstly, we are dealing with three different facies with similar maturity. The ZFC curves of three samples, one for each kind of lithology (Figure IV.38), display a 2-step pattern, even though the de-

crease of the remanent magnetization at ∼120 K is not well marked. The RT-SIRM curves show the Verwey transition of magnetite (∼120 K) and the P-behavior (increase from 70-80 K).

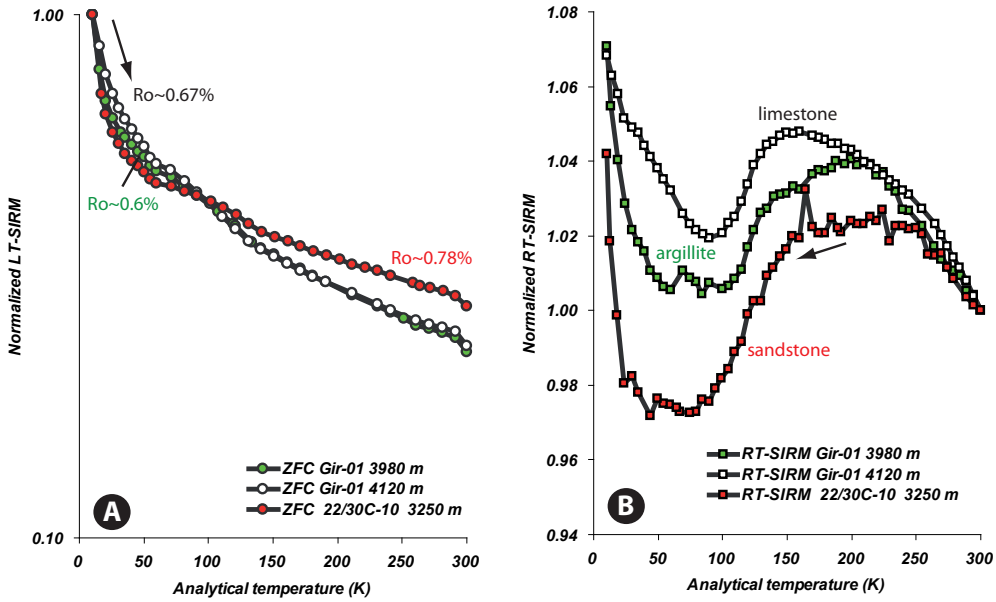

Figure IV.38 – Occurrence of the MagEval signal in three different lithologies (argillite, limestone, sandstone) with similar maturity. A) ZFC and B) RT-SIRM curves

Secondly, two samples, one claystone and one limestone, from the 22/30C-10 well are now compared. They are separated by 2 km depth but represent the closest sample pair of this type in our data set. Quantitative mineralogy analyses indicate that, except for clays and calcite, the two samples differ essentially by their siderite content which is 10%wt. in the claystone 22/30C-10 1950m and 0.7% in the limestone for 22/30C-10 4150m.

The ZFC curves for the two samples show a 2-step pattern even if the Verwey transition of magnetite is not well marked in the limestone 22/30C-10 4150m (Figure IV.39A). The RT-SIRM curves display the Verwey transition, well developed in the limestone 22/30C-10 4150m, and an increase of the magnetization from ∼40 K (Figure IV.39B). Even if the siderite content of the claystone 22/30C-10 1950m is rather high and despite the 5 μT magnetic field applied, the characteristic Néel transition of this mineral is not observed. The RT-SIRM$_{300K}$ and χ of these two samples are in the same order of magnitude (Table IV.4). Thus the two magnetic signals have quite similar patterns overall.

Our results indicate that the MagEval signal used for geothermometry is observed in many different geological settings and different lithologies, suggesting the approach could be applied in a very ubiquitous way.

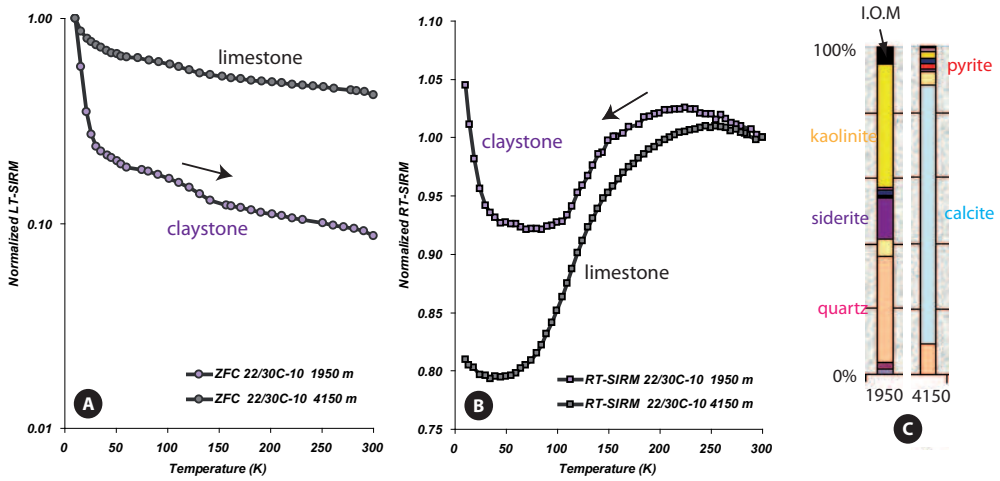

Figure IV.39 – A) ZFC and B) RT-SIRM curves for a claystone and a limestone from 22/30C-10 with C) their associated quantitative mineralogy

Sample	χ (μSI)	RT-SIRM$_{300K}$ (μAm^2/kg)	Magnetite concentration (ppmv)
22/30C-10 1950m	228	150	~15
22/30C-10 4150m	112	300	~30

Table IV.4 – Some magnetic values of two samples from 22/30C-10 : one is a claystone, the other one is a limestone. Magnetite concentration is calculated from the RT-SIRM$_{300K}$ value.

However, it is not quite true. Samples are not clearly identifiable as being composed of one single lithology. In the case of well cuttings, they are sometimes mixing of different lithologies from different depths (Figure IV.40A). In that case, it is preferable to first sort the fragments in the sample according to their different lithology in order to use an homogeneous facies for magnetic measurements. For one thing, visibly oxidized facies (reddish or yellowish) must be ruled out as they may contain abundant iron oxides/hydroxides (Figure IV.40B).

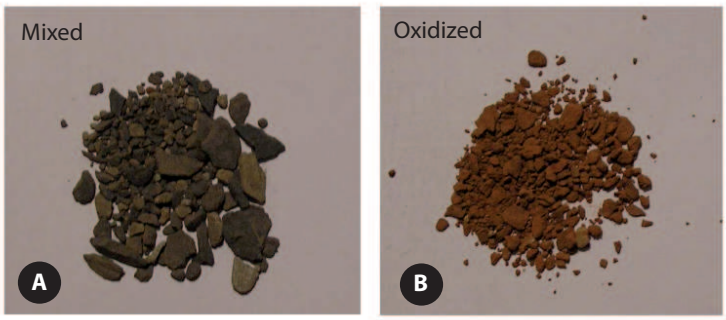

Figure IV.40 – Pictures of cuttings showing A) mixed facies and B) oxidized facies

2.4.2 Some variability

Siltstone vs. Sandstone Let's first compare a siltstone (Gir-1 3382.25m) and a sandstone (Gir-1 3382.15m), which are very close lithologies (clastics mainly composed of quartz). These two samples were removed from a core, so that no possible contamination from another lithology occurred. They are located 10 cm apart and so they experienced the same burial history precluding any temperature effect on the magnetic signal. Quantitative mineralogy analyzes were done on the two samples (Figure IV.41C). The two samples differ mainly by their quartz content, with the sandstone Gir-1 3382.15m being more quartz-rich (∼75%wt.), than the siltstone Gir-1 3382.25m (∼46%wt. quartz), which in turn contains more clays (40%wt.).

At first order, these two samples show the MagEval signature with a characteristic 2-step pattern ZFC curve and the Verwey and P-behaviors on the RT-SIRM curve (Figures IV.41A and B). They display a similar magnetic remanence evolution with the analytical temperature which indicates the existence of a same magnetic assemblage (Table IV.5). However, the drop of the remanence from 10 to 35 K on the ZFC curve is more marked for the siltstone Gir-1 3382.25m than for the sandstone Gir-1 3382.15m. The PM value is 0.84 for the siltstone while it is 0.64 for the sandstone. Thus, in terms of geothermometry, this means that these PM values would give different temperatures for a same given depth.

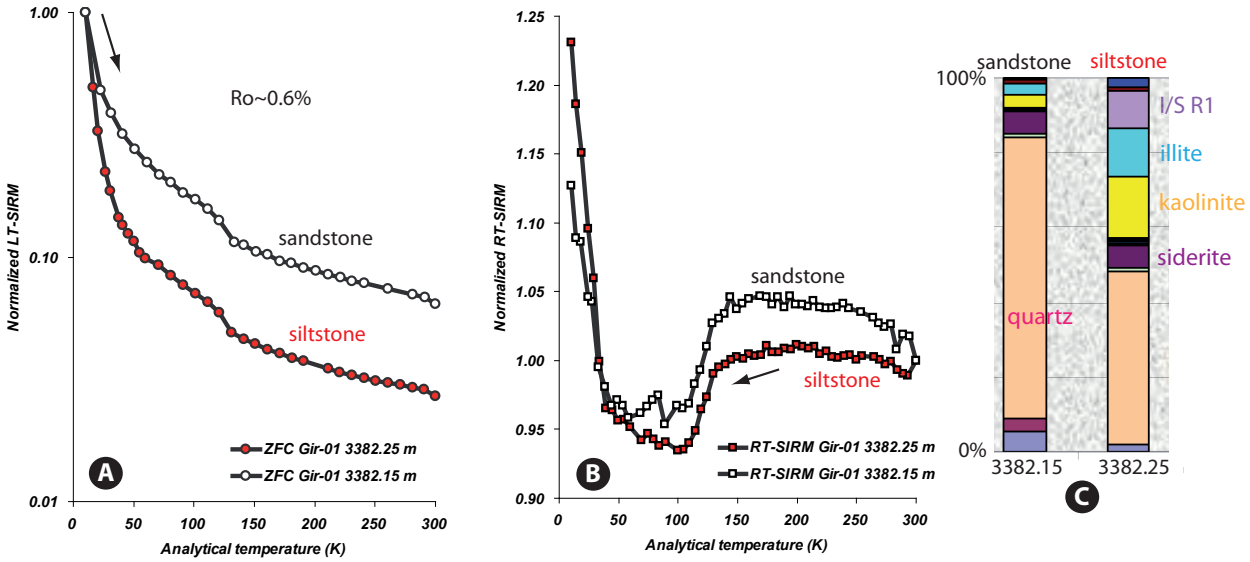

Figure IV.41 – A) ZFC and B) RT-SIRM curves for closed siltstone and sandstone from Gir-1 with C) their associated quantitative mineralogy

At this point of our knowledge, it is not easy to conclude about the origin of such a difference of PM values between these two samples. It is necessary to repeat comparisons between different lithologies from the same depth to check statistically the robustness of this variability. One may suggest

Sample	χ (μSI)	RT-SIRM$_{300K}$ (μAm^2/kg)	Magnetite concentration (ppmv)	PM
Gir-1 3382.15m	200	60	∼6	0.64
Gir-1 3382.25m	250	76	∼8	0.84

Table IV.5 – Some magnetic values of the two samples from Gir-1. Magnetite concentration is calculated from the RT-SIRM$_{300K}$ value.

a difference in clays content (40%wt. vs. 7.5%wt. for the siltstone and the sandstone respectively), porosity, permeability and hence in granulometry to explain the variability. Those may be important factors on the mineralogical transformations due to, for instance, fluid circulation. Thus it is important to use a homogeneous facies throughout a given study.

Particular magnetic behavior in sandstones (reservoirs) Two sandstones from Gir-1 (Gir-1 2509.58m and Gir-1 3375.17m) with a RT-SIRM$_{300K}$ of ∼200 μAm^2/kg were chosen on the basis of their low remanent magnetization in order to avoid possible problems with magnetic minerals concentration (Table IV.6). In addition, they are core samples and so pollution by another lithology is excluded. TOC content of these samples is 1.7% for Gir-1 2509.58m and 2.1% for Gir-1 3375.17m. Figure IV.42 shows the two samples exhibit different magnetic signals. On the ZFC curves, the 2-step pattern is found. The difference in PM value is attributed to difference in thermal history since the two samples come from very different depths. On the RT-SIRM curves, the Verwey transition at ∼120 K is well developed. Gir-1 2509.58m displays an increase of the magnetization at about 250 K which is the Morin transition of hematite. This latter transition is absent from Gir-1 3375.17m, but it does not mean necessarily that hematite is absent. Hematite can indicate an oxidized facies. These two samples do not display the P-behavior, as expected at those depths. By contrast, they show a particular magnetic behavior. Gir-1 2509.58m is coarser and oil impregnated compared to Gir-1 3375.17m. We concluded that impregnated samples and those showing an undetermined magnetic behavior must not be retained for MagEval application, though the 2-step patterned ZFC curves.

Sample	χ (μSI)	RT-SIRM$_{300K}$ (μAm^2/kg)	Magnetite concentration (ppmv)	PM
Gir-1 2509.58m	31	160	∼16	0.55
Gir-1 3375.17m	125	230	∼23	0.43

Table IV.6 – Values of some relevant magnetic parameters for two sandstones from Gir-1 with similar TOC content. Magnetite concentration is calculated from the RT-SIRM$_{300K}$ value.

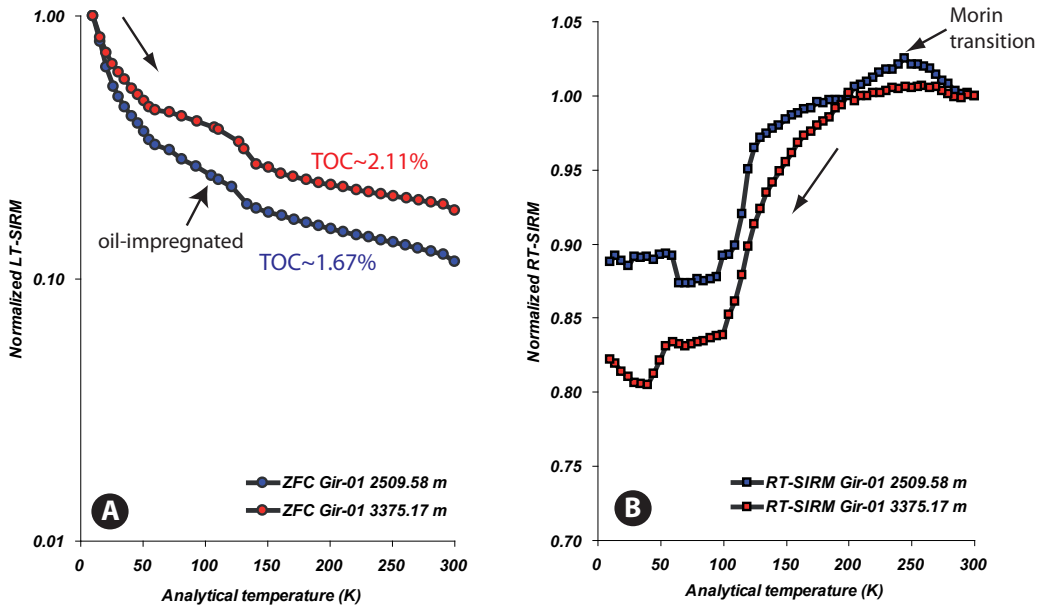

Figure IV.42 – A) ZFC and B) RT-SIRM curves of two sandstones from Gir-1. Gir-1 2509.58m is impregnated.

In summary, the same general magnetic signal typical of MagEval occurs in the three main lithologies :

- a 2-step pattern for the ZFC curve : drop of the remanence from 10 to 35 K and inflexion point at about 120 K (Verwey transition of magnetite) ;
- for the RT-SIRM curves, Verwey transition of magnetite (120 K) and increase of the magnetization from 70-80 K (P-behavior).

However, some differences may arise that are related to sample specificities. Lithologic and mineralogical parameters, hydrocarbons content, ageing effect and especially concentration of ferromagnetic minerals and pollution by others (issued of oxidation process for instance) may influence the MagEval signal which eventually might prevent its use for geothermometry. One must therefore defined criteria for selection of suitable samples.

2.5 Samples selection criteria

The results of the preliminary survey presented above illustrate that the application of the MagEval geothermometer is not straightforward and that several factors influence the PM value. Considering all data gathered in this survey of samples from variable settings, it appears that criteria for selection of best samples can be defined. They should be applied in the following order because the low temperature measurements are time-consuming and quite expensive. The criteria succession is the following :

- Samples lithology : essentially claystones. As inferred previously, claystones provide most satisfactory results. When selecting cuttings, one needs to focus preferentially on rather thick (>

10 m) claystones horizons, in which mixing of different lithologies is less likely. Sandstones and limestones can also provide a correct signal, but it is not guaranteed.

- Facies mixing has to be considered with attention. Selecting levels as homogenous and thick as possible seem to be the best way to avoid facies mixing.
- Among cuttings fragments, it is best to select coarser fragments to limit or avoid ageing effect (which essentially impacts fine-grained powder).
- Low field magnetic susceptibility, i.e. values of χ less than 500 μSI, is advisable. Beyond this value, the ferromagnetic concentration may be not as typical as one should expect from the cycle alteration-through-neoformed magnetic minerals in weakly-magnetized claystones.
- MPMS measurements :
  - RT-SIRM$_{300K} < 500\mu\text{Am}^2/\text{kg}$: higher values would reflect high concentration of ferromagnetic minerals
  - Morin transition of hematite (250 K) should not be too developed. This would reflect an oxidized state
  - No Néel transition
  - Goethite : the presence of goethite is difficult to deal with. Indeed, it may reflect an oxidized state (due to weathering, fluid circulation...), but goethite may also be present in very immature samples as an early diagenetic/detrital mineral
  - No unknown (exotic) magnetic transition distinctly visible

Applying these criteria to our sample set reveals that many samples and a number of wells are not suitable for MagEval geothermometry essentially because of their high magnetic parameters (see Appendix 4). Such samples are not considered in the following of the manuscript. Two wells stand out as containing a large proportion of suitable samples, i.e., Girassol-1 (Angola) and 22/30C-10 (United Kingdom). They were therefore selected as reference wells for the calibration of the MagEval geothermometer.

3 Calibration of the MagEval geothermometer

3.1 Comparison of MagEval signal measured in wells with that of Bure and Opalinus claystones

It is interesting to compare some magnetic signals of the two reference wells with those known of Bure (Paris Basin) and Opalinus (Swiss Alps) claystones. As inferred from the heating experiments results (chapter V), it was expected that samples from the wells would carry a similar magnetic assemblage.

The Bure claystones are immature and experienced burial temperature < 50°C. These claystones contain goethite. A similar magnetic signal is found in 22/30C-10 for samples experiencing $\sim$60°C

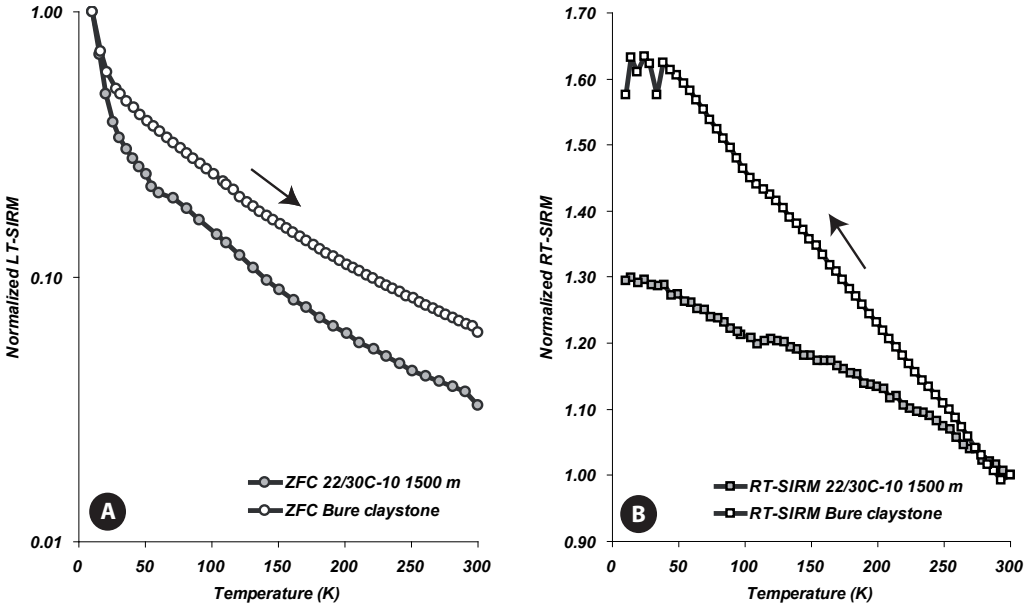

Figure IV.43 – A) ZFC and B) RT-SIRM curves of a sample from 22/30C-10 compared to those of Bure claystones showing similar burial depth and maturity

(Figure IV.43). The ZFC curves are quite similar, even parallel from 50 K, excepting the decrease of the remanence below 50 K (Figure IV.43A). Both RT-SIRM curves display an increase of the remanence from 300 to 50 K with a slight decrease at ∼115 K corresponding to the Verwey transition of magnetite (Figure IV.43B). Such signal is not found in Gir-1.

The Opalinus claystones present a magnetic assemblage representative of the PM max point at about 85-90°C (Mazurek *et al.*, 2006). As the two reference wells reach temperatures > 120°C, one would expect that some samples in those wells would shown an Opalinus-like magnetic signal. This is indeed observed. For Gir-1, the PM maximum type signal corresponds to sample Gir-1 3376.55 m (∼90°C burial) and for 22/30C-10 to sample 22/30C-10 2210m (∼80°C burial).
The ZFC curve of Gir-1 3376.55m (Figure IV.44) displays a 2-step pattern with an important decrease of the remanence between 10 and 35 K but not as ample as in the Opalinus claystone. The RT-SIRM curve shows the Verwey transition and a well marked P-behavior.
The ZFC curve of 22/30C-10 2210m (Figure IV.45) is almost parallel to that of Opalinus but does not display the Verwey transition. By contrast, the RT-SIRM shows the Verwey transition and a P-behavior.

3.2 Assessment of the uncertainty on PM calculation

Like all parameters used in calculations, it is necessary to estimate the related uncertainties of PM. The analytical uncertainties on PM estimation may be influenced by :

– errors emanating from interpolation of the raw data at 10 and 35 K ;

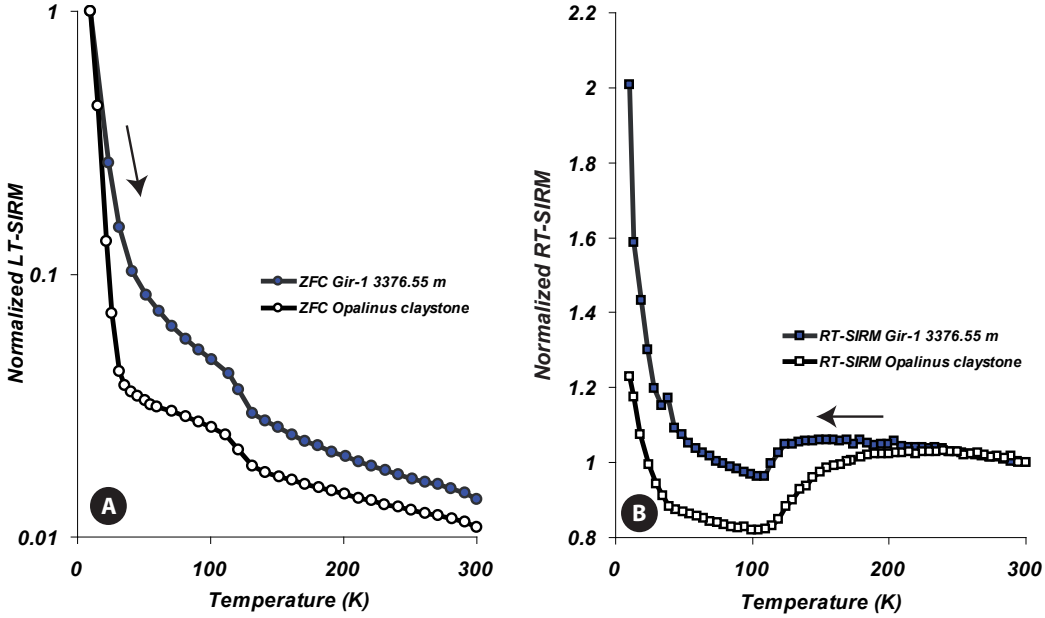

Figure IV.44 – A) ZFC and B) RT-SIRM curves of claystones from Gir-1 compared to those of Opalinus Claystone close to the PM max point

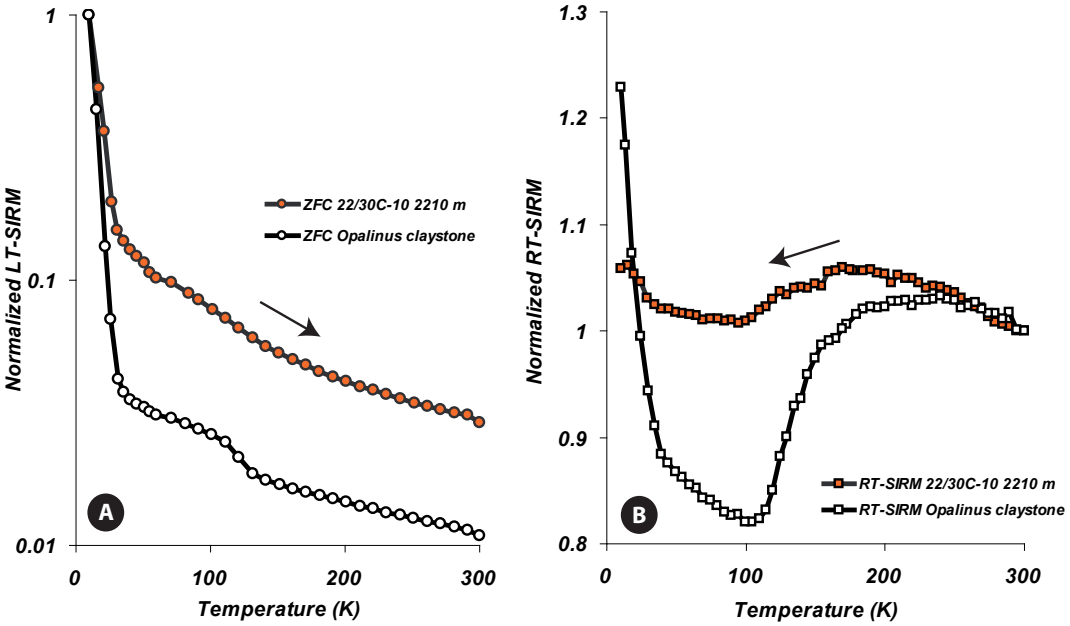

Figure IV.45 – A) ZFC and B) RT-SIRM curves of a claystone from 22/30C-10 compared to those of Opalinus Claystone close to the PM max point

– the repeatability of the measurement when performed on the same aliquot (subsample) of sample powder (internal reproducibility)
– the (in)homogeneity of the sample when measurements are performed on different aliquots (subsamples) of a single sample (external reproducibility).

3.2.1 Interpolation of the raw data

The magnetic measurements done on the MPMS (raw data) are not necessarily performed at the exact same fixed temperature steps for different samples. The suite of temperatures at which measurements are done to define the ZFC curve may vary from one sample to another, but also for a same sample when duplicated. As the PM parameter is defined as the drop of the remanence from 10 to 35 K, interpolation at 35 K is necessary. The point at 10 K is always measured as it is the first point in the sequence of temperature measurements. In contrast, a measurement is not necessarily always carried out at exactly 35K, but possibly at slightly higher and/or lower temperature. It is therefore necessary to interpolate along the ZFC curve in between the two closest measurements. The interpolation formula assumes a linear relationship because spread between points of measurements never exceed 10 K. Interpolation calculation is done as follows :

$$y = \frac{(y_{i+1} - y_i) \times (x - x_i)}{(x_{i+1} - x_i)} + y_i \quad for \quad x_i < x < x_{i+1}$$

3.2.2 Internal reproducibility

One source of error of the determination of a PM value is the analytical measurement itself. To estimate it, several measurements of the ZFC curve were repeated on the same aliquot of a sample using identical analytical conditions. This was done for three different samples : 22/30C-10 1900m, 22/30C-10 4900m and Gir-1 3120m. The ZFC curve was measured 20 times for each sample. The different ZFC curves were first interpolated at same temperature (from 10 to 300 K with a 5 K step) then averaged. The Figure IV.46 and the Table IV.7 show the obtained statistics. Confidence interval at 95% is represented.

The repeated MPMS measurements of a same gelatin capsule show that the PM parameter is quasi-constant over the whole series of measurements, attesting the excellent stability of the instrument and the reproducibility of the measurement protocole. The maximum variation on PM measurement for a given sample is ± 0.03. The very good internal reproducibility illustrates the excellent quality of MPMS measurements as long as laboratory conditions are well reproduced. The standard deviation calculated for PM for the three samples shows that PM value is defined at ± 0.01.

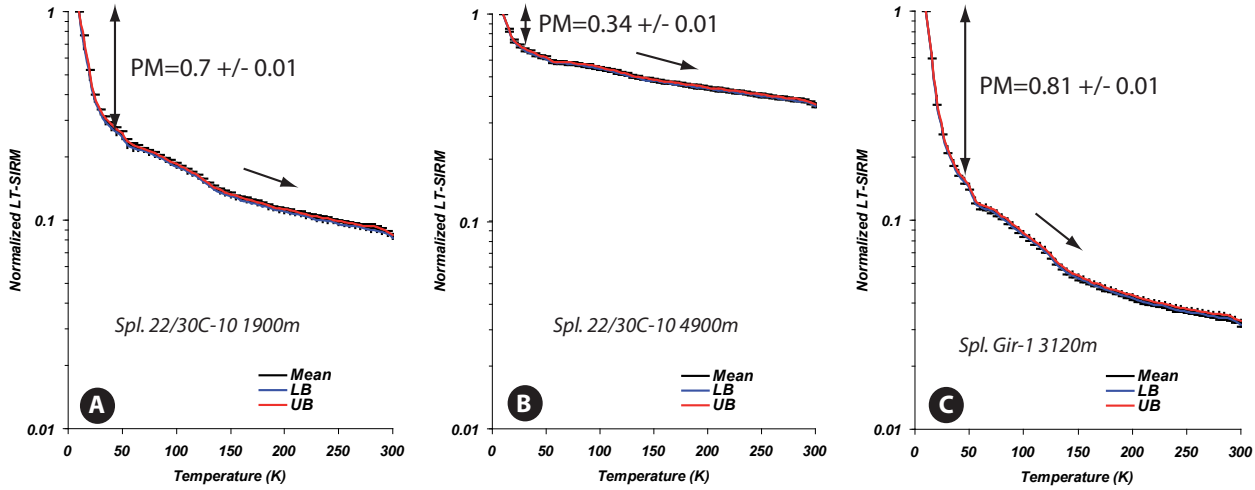

Figure IV.46 – Internal reproducibility : evolution of the 10 K saturation remanence over 20 measurements of the same powder aliquot for three samples (22/30C-10 1900m and 4900 m, Gir-1 3120 m). Standard deviation is ± 1σ.

	22/30C-10 1900m	22/30C-10 4900m	Gir-1 3120m
1	0.69	0.32	0.81
2	0.69	0.35	0.81
3	0.71	0.35	0.81
4	0.66	0.35	0.81
5	0.69	0.32	0.80
6	0.71	0.35	0.81
7	0.69	0.32	0.81
8	0.71	0.35	0.82
9	0.70	0.35	0.81
10	0.69	0.35	0.81
11	0.71	0.35	0.81
12	0.70	0.35	0.82
13	0.70	0.35	0.81
14	0.71	0.35	0.81
15	0.71	0.35	0.82
16	0.69	0.33	0.82
17	0.71	0.35	0.82
18	0.70	0.35	0.82
19	0.68	0.35	0.82
20		0.35	0.82
Mean	**0.70**	**0.34**	**0.81**
SD	**0.01**	**0.01**	**0.01**

Table IV.7 – Internal reproducibility : PM values for 3 samples measured 20 times

3.2.3 External reproducibility

Homogeneity of the measured sample is a key factor for the PM calculation.
Samples showing clearly facies mixing (for instance clays + carbonates) must be sorted out under binoculars in order to use an homogeneous fraction for measurement.
The question arises of knowing whether an homogeneous-looking facies under naked eyes is really magnetically homogeneous. Is the magnetic signal identical considering different fractions of a same sample ? To assess these questions, ∼5-10 g of a sample was crushed finely. 10 different aliquots of that single sample were randomly taken within the bulk powder (no mapping) and measured for PM. This approach was carried out for 2 different samples : 22/30C-10 1990m and 22/30C-10 4900m. The Figure IV.47 shows the averaged ZFC and the corresponding 1σ confidence interval. The PM values are reported in Table IV.8.

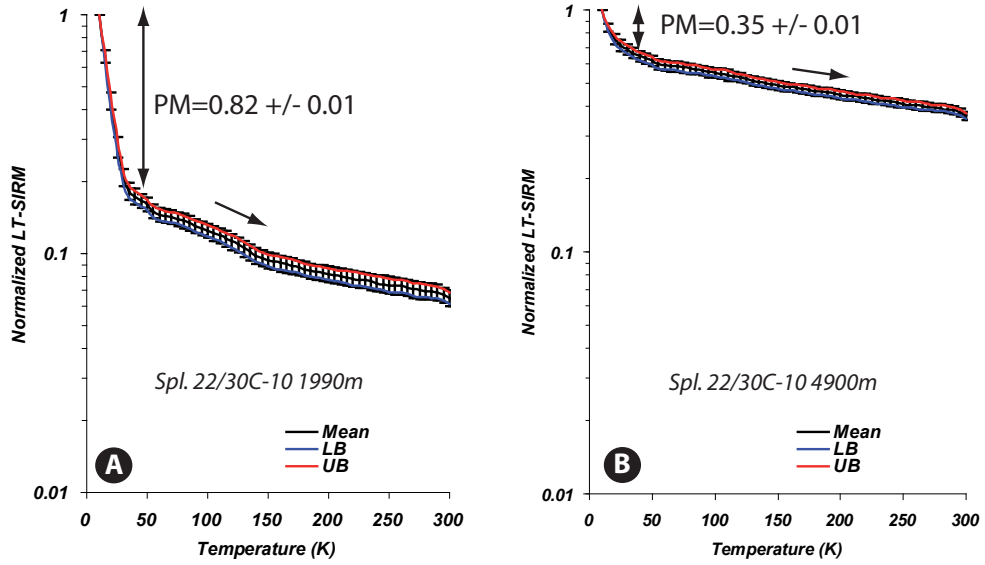

Figure IV.47 – External reproducibility : evolution of the 10 K saturation remanence of 8 different aliquots samples from bulk powder for two different samples (22/30C-10 1990m and 4900 m). Standard deviation is ± 1σ.

Due to unquestionable analytical artifacts related to the cryogenic head release and the pollution of one particular aliquot, two ZFC measurements for each sample were rejected from the statistics. The cryogenic head release is easily recognizable in the low temperature curves by a jump/drop in the magnetization (Figure IV.48). A a result, the average curve was calculated based on 8 measurements per sample. A good external reproducibility is observed. The standard deviation of the PM value is ± 0.01, similar to that of internal reproducibility. To comfirm the good external reproducibility of PM measurements, the value of RT-SIRM$_{300K}$ was also checked for all the measurements. The RT-SIRM$_{300K}$ is reproducible at ± 10% for 22/30C-10 4900m (121 ± 5 μAm^2/kg) and at ± 5% for

	22/30C-10 1990m	22/30C-10 4900m
1	0.83	0.35
2	0.82	0.35
3	0.83	0.35
4	0.82	0.34
5	0.83	0.35
6	0.83	0.36
7	0.80	0.36
8	0.83	0.32
Mean	**0.82**	**0.35**
SD	**0.01**	**0.01**

Table IV.8 – External reproducibility : PM values for 8 aliquots of a same sample for two specimens from well 22/30C-10

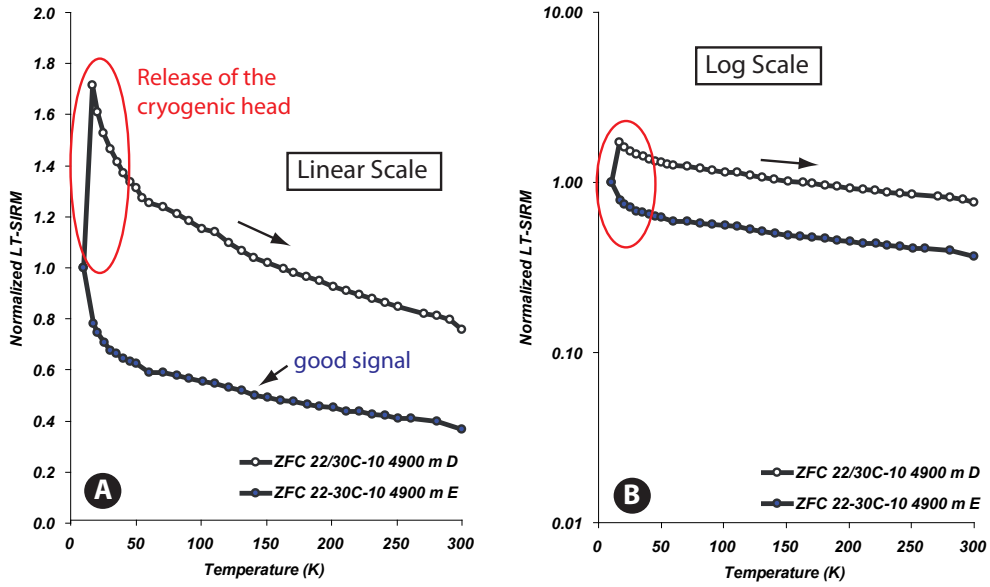

Figure IV.48 – ZFC curves for two aliquots of the same sample, one displaying a typical ZFC curve due to the cryogenic head release.

22/30C-10 1950m (243 ± 23 $\mu Am^2/kg$).

Cumulating the two types of uncertainty (internal and external) after interpolation, it can be stated that the error on determination of PM values is no greater that ± 0.02 according to our protocol.

3.3 MagEval calibration from Girassol-1 (AO) data

3.3.1 Geological setting

The well Girassol-1 (Girassol Field, Block 17) is situated in the Lower Congo Basin of offshore northern Angola (Figure IV.49). It is a deep water basin with high hydrocarbon potential developed

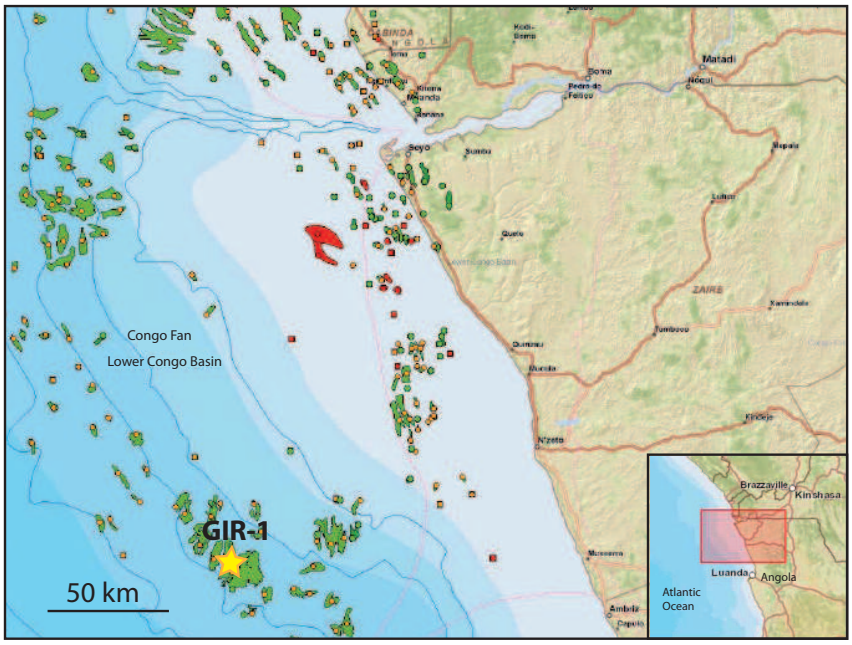

Figure IV.49 – Location map of the well Girassol-1

along the West African passive margin. This region has experienced a complex history of structural deformation during the Late Cretaceous and Tertiary post-rift thermal subsidence (Anderson *et al.*, 2000 and references therein). The Lower Congo Basin origin is related to the Early Cretaceous breakup of Gondwana : rift basins formed a thinned continental crust as Africa and South America rifted apart. In the Upper Cretaceous (Cenomanian-Maastrichtian time), anoxic basinal conditions developed periodically generating black shale source rocks (Iabe Formation, type II kerogen) (Figure IV.50). A phase of basin starvation occurs in the Early Tertiary prior to rejuvenation of clastic input in the Neogene. Oil reservoirs are found principally within the Oligocene-Miocene aged turbiditic sand Malembo Formation (Figure IV.50). The deposition of this formation is associated with the Congo fan, offshore of the delta of the Congo River. The stratigraphic signature of this formation is progradational with deltaic sediments prograding westwards with time. Then the depositional environments recorded by the Malembo Formation reflect the interaction between open marine sedimentation and deltaic conditions associated with fluvial discharge from the Congo River.

3.3.2 PM evolution with temperature in Girassol-1

Samples from well Gir-1 used to investigate the thermal dependence of the MagEval parameter PM range from 636 mTVD (2010 mMD) to 2746 mTVD (4120 mMD) and cover in-situ temperatures going from ∼30 to 110°C.

The geothermal gradient (GG) in Gir-1 is not well constrained. Rock Eval analyses exhibit a rather constant Tmax value of 430°C throughout the entire well. In contrast, a complete set of vitrinite re-

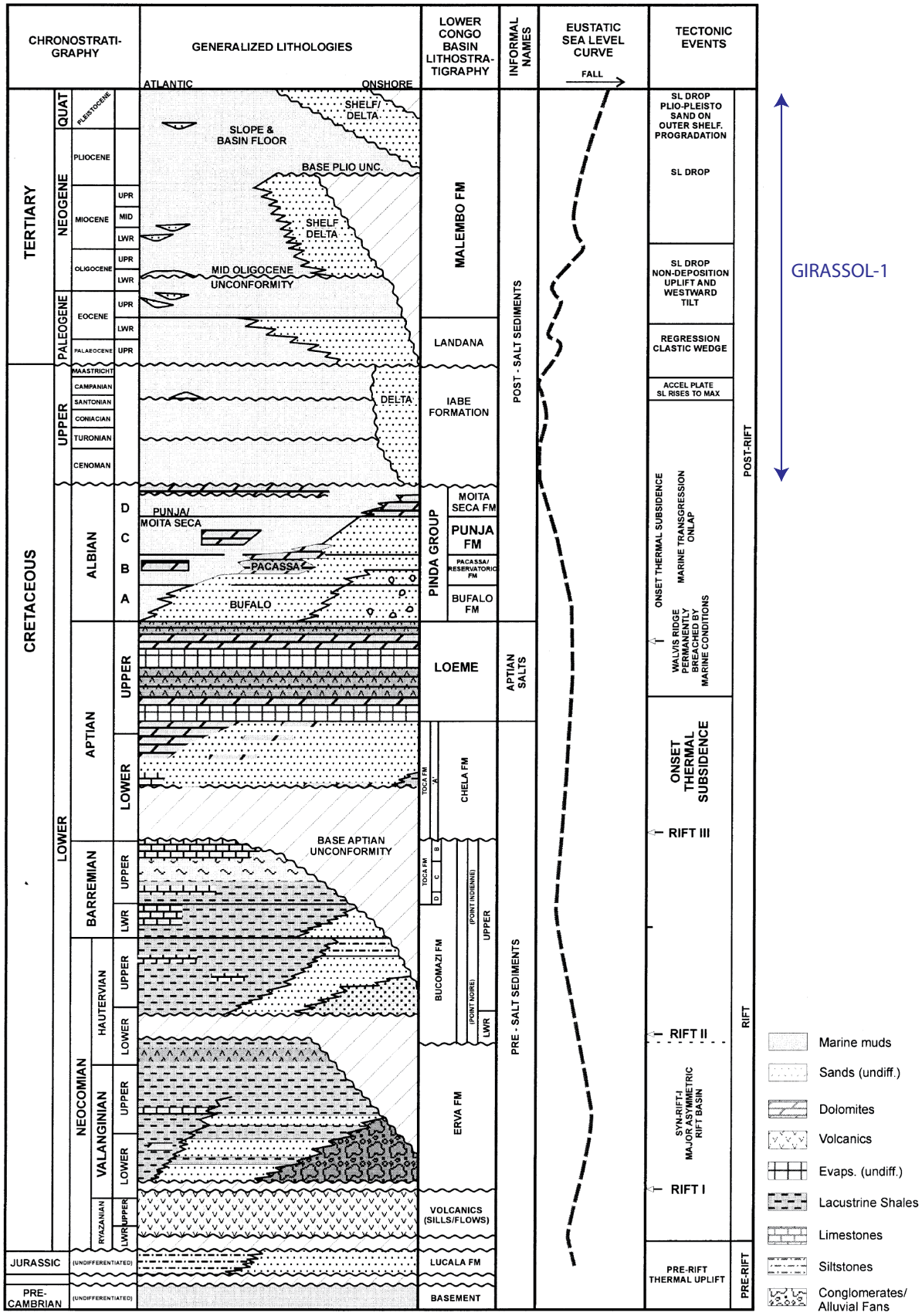

Figure IV.50 – Southern Lower Congo Basin stratigraphy (after Anderson *et al.*, 2000)

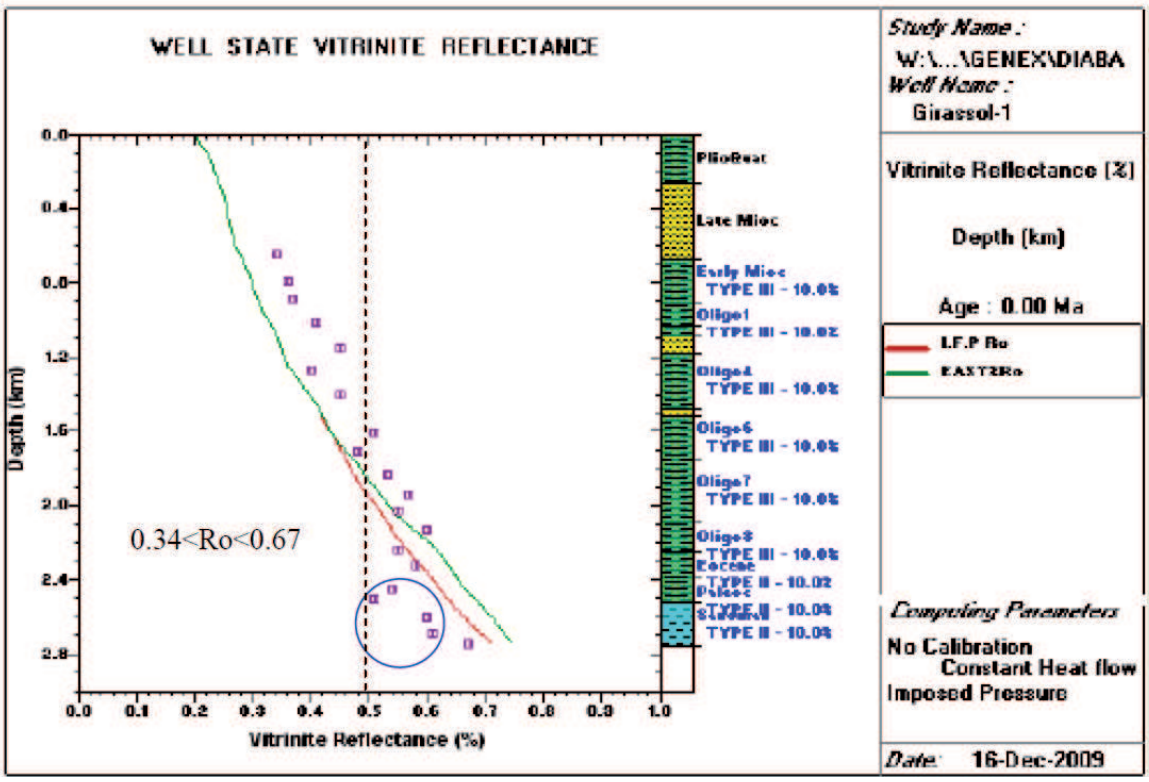

Figure IV.51 – Modeling of the evolution of the vitrinite reflectance as a function of depth (km) for well Gir-1 (E. Legendre, pers. com.)

flectance Ro data is available over the depth range of interest and was thus used to constrain GENEX 1D modeling (E. Legendre, pers. com.) (Figure IV.51).
GENEX modeling integrates several sources of temperature information to reconstruct the thermal history of sediments in a well (present-day temperatures, paleotemperatures, heat flux, vitrinite reflectance...). Two different models are available for the calculation of geothermal gradient in GENEX : 1) the IFP Ro model ; 2) the EASY%Ro model. Both models were run on Gir-1 and provide slightly diverging thermal curves at depth greater than about 1800 m.
The samples with Ro values lower than 0.5% (500 to 1700 m) and those coming from measurements on II organic matter (circled in blue in Figure IV.51) are considered less reliable because of the limitations of the vitrinite reflectance technique.

Consequently, the preferred model of Ro evolution with depth is the IFP model which best constrains the most representative data (see chapter I for a description of kinetic modeling). This model yields a geothermal gradient of 43°C/km.

Girassol-1 experienced a continuous burial history with a rapid subsidence episode in the Oligocene (Figure IV.52). Using the calculated geothermal gradient of 43°C/km, it is possible to calculate the

burial temperatures of the samples studied for MagEval.

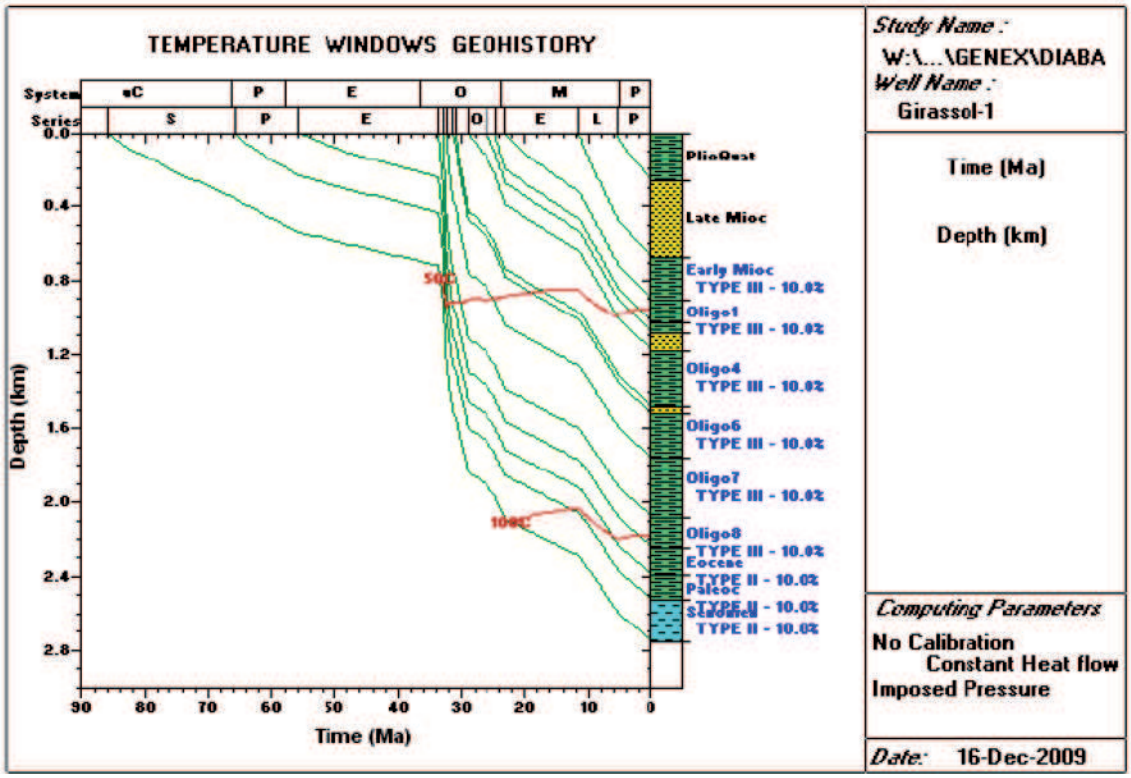

Figure IV.52 – Reconstructed burial history of Girassol-1 by GENEX (E. Legendre, pers. com.)

Measured PM values are plotted against modeled temperatures in Figure IV.53, thereby providing a temperature calibration of the MagEval geothermometer. The vocabulary used to describe the calibration is the same that proposed by Aubourg & Pozzi (2010).
This calibration is based on 15 samples (over 36) selected in homogenous clayish levels, except for the deepest sample (in blue on the Figure IV.53) which is rather marly.
The PM Up branch displays a rather weak slope with increasing temperature compared to that of PM Down branch. R^2 correlation coefficients of linear regression through the PM Up and PM Down branches are 0.9 and 0.87 respectively. PM max point is located at about 91°C considering GG = 43°C/km. In terms of depth, this sample is located at 3376.55 m MD, i.e., 2002.55 m burial depth. It is notable that the two branches do not exhibit symmetrical shape on each side of the PM max fixed point. The PM Up branch covers a very small, smaller than expected, range of PM values (0.7 to 0.9), while the PM Down branch reflects a much greater range of PM values (0.9 to 0.4), inducing a very steep slope of the thermal dependence over a rather narrow temperature range (100 to 120°C).

This calibration shows a PM evolution with temperature in agreement with the model initially

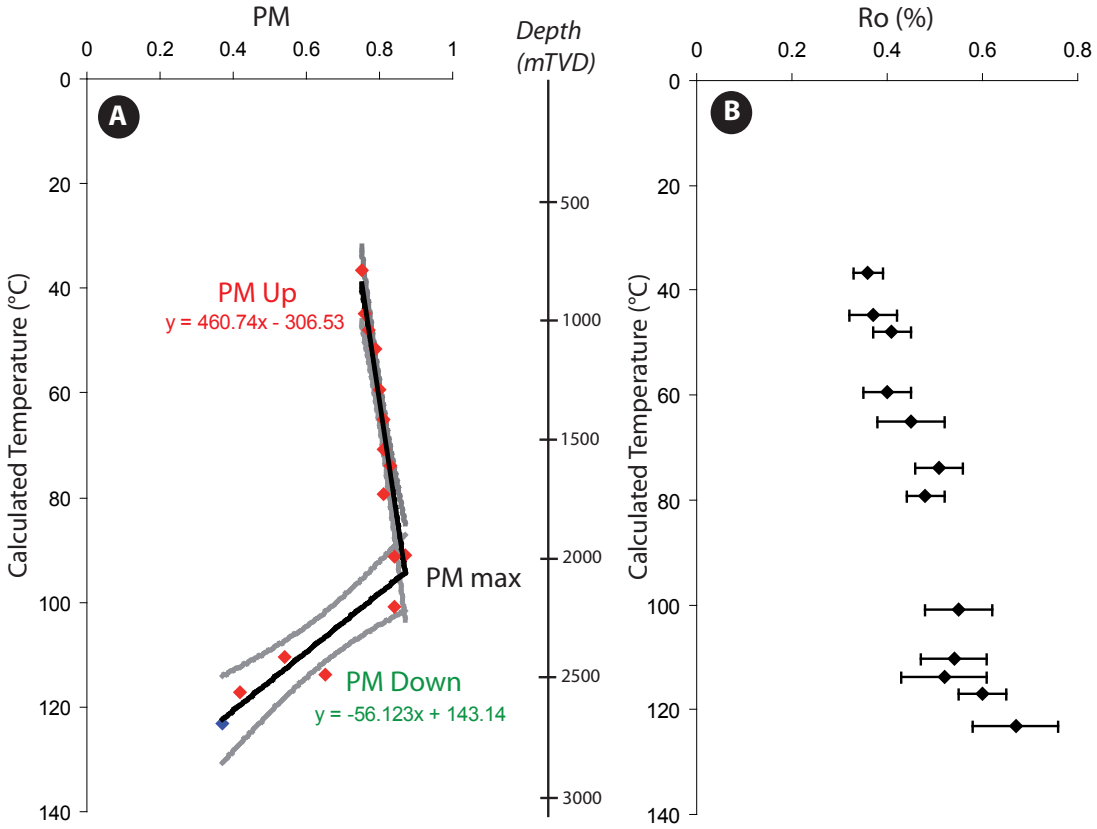

Figure IV.53 – Calibration based on Gir-1 well data. A) Evolution of the PM values with calculated temperature from GENEX modeling. Confidence interval is 95% (calculated with Origin software). Red points : claystones, blue point : marl. B) Evolution of Ro as a function of temperature calculated from GENEX modeling

proposed by Aubourg & Pozzi (2010), i.e., two branches (PM Up and PM Down) passing through a maximum (PM max) at about 90°C.
Using a least square linear regression, the following equations can be derived from Figure IV.53 :

PM UP : T in situ (°C) = 460.74 x PM -306.53

PM DOWN : T in situ (°C) = -56.123 x PM +143.14

As shown in the Figure IV.53, the PM values of the PM Up branch display a low thermal dependence with increasing depth/temperature. This behavior is rather particular compared to the PM Up trend proposed by Aubourg & Pozzi (2010). We tested the thermal dependence of the magnetic assemblage of Gir-1 samples. Heating experiments under Ar atmosphere were performed. The protocol is described in the chapter III. The Figure IV.54 shows the evolution of the ZFC curves for 2 samples

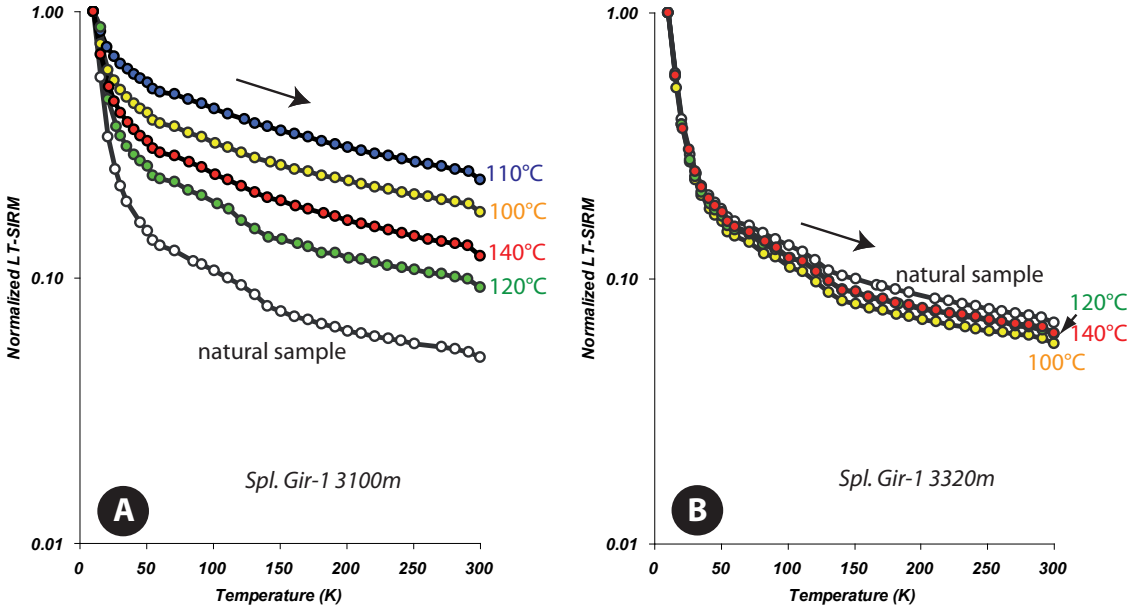

Figure IV.54 – Evolution of the ZFC curves for different heating temperatures under Ar atmosphere for two claystone samples from Gir-1

in the PM Up branch : Gir-1 3100m (T in situ ∼80°C) and Gir-1 3320m (T in situ ∼90°C). Their TOC value is quite similar (1.1% for Gir-1 3100m and 1.3% for Gir-1 3320m). For the sample Gir-1 3100m, the ZFC curves evolve with experimental temperature but do not describe a regular trend as it was observed in the case of the Taiwan sample for instance (Figure IV.9). The sample Gir-1 3320m does not display significant changes in the ZFC curves with increasing temperature. This behavior is quite similar to that of the previously discussed Borneo sample (Figure IV.9) except that there is no Néel transition in Gir-1 3320m. The thermal dependence of the magnetic assemblage of Gir-1 samples is difficult to characterize experimentally and our tests are not truly conclusive.

In order to further investigate the PM evolution with temperature the second reference well 22/30C-10 (UK) was studied in detail. As Gir-1, well 22/30C-10 is characterized by a simple tectonic history. However, it covers a wider range of burial temperature than Girassol-1, with in situ temperatures up to 200°C and Ro values up to 2%.

3.4 MagEval calibration for well 22/30C-10 (UK)

3.4.1 Geological setting

The well 22/30C-10 (Elgin Field, Block 22/30C) is situated in the Central Graben in the North Sea (UK) (Figure IV.55). This area is characterized by high pressure (1.1 MPa/1000 bars) - high

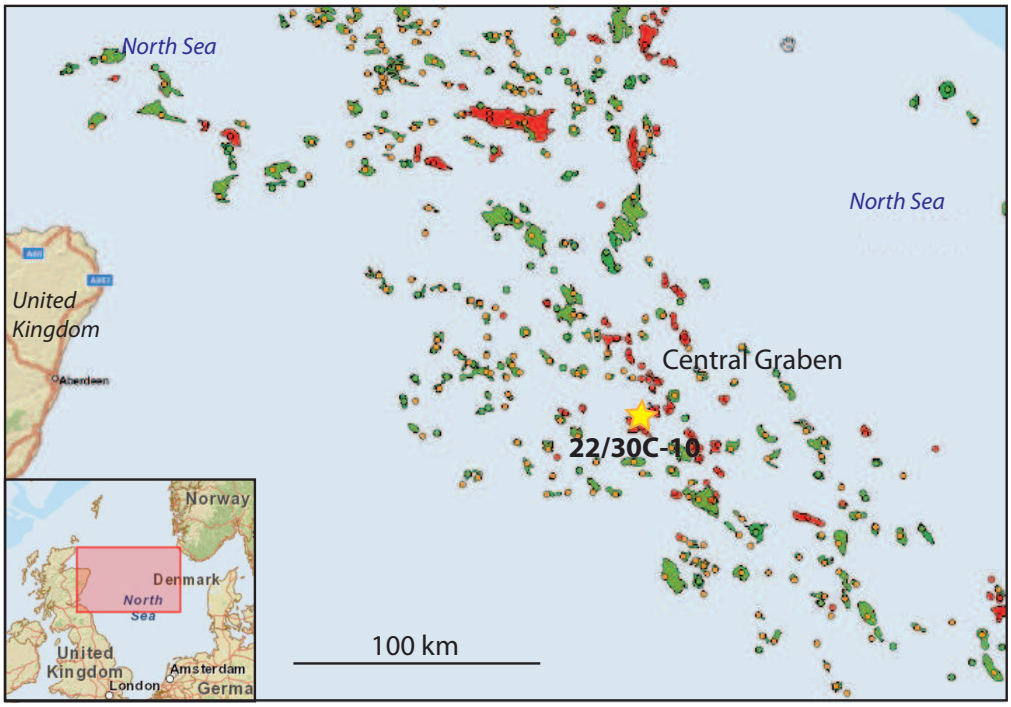

Figure IV.55 – Location map of the 22/30C-10 well

temperature (190°C) conditions (Vandenbroucke *et al.*, 1999). The graben is part of the passive North Sea rift system which failed during the breakup of Pangea in the Triassic-Mid Jurassic. The rifting stage of the North Sea lasted ∼175 Ma (from Early Triassic to Late Paleocene), with an accelerated phase during the Jurassic (Ziegler, 1992). During the Cretaceous and the Tertiary, this graben underwent a sag phase with the accumulation of significant sediment thicknesses (Isaksen, 2004 and references therein).

The principal source rocks for oil are the Late Jurassic Kimmeridge Clay, which is type II kerogen (marine algal organic matter), and to a lesser extent the Oxfordian Heather Shales dominated by mixtures of marine algal and herbaceous organic matter (types II and III kerogens). Reservoirs rocks are shoreface and mass-flow sandstones of the Middle Jurassic Fulmar Formation (also known as Franklin Sands), fluvial sandstones of the Triassic Skagerrak Formation and Tertiary-age submarine fan sandstones (Figure IV.56 ; Isaksen, 2004). The Upper Jurassic shales and Cretaceous shales and marls are the main seal rocks for the Mesozoic reservoirs.

3.4.2 PM evolution with temperature in 22/30C-10

The geological history of the borehole area suggests that the geothermal gradient was probably higher in the past. Consequently, as for Girassol-1, a GENEX modeling was performed (E. Legendre, pers. com.) based on available vitrinite reflectance data (Figure IV.57).

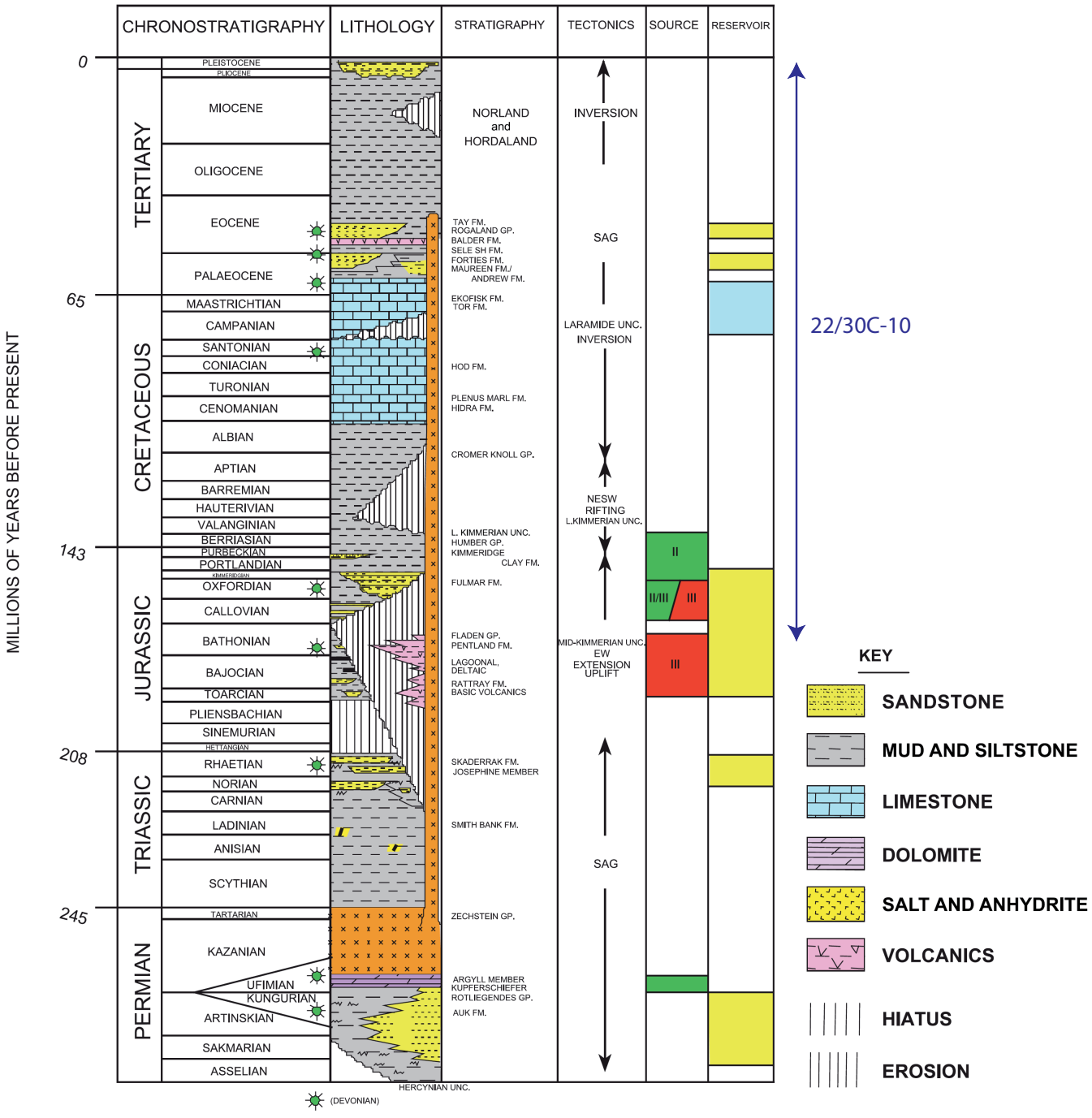

Figure IV.56 – Stratigraphic, tectonic event, source rocks and reservoirs chart for the Central North Sea (Isaksen, 2004)

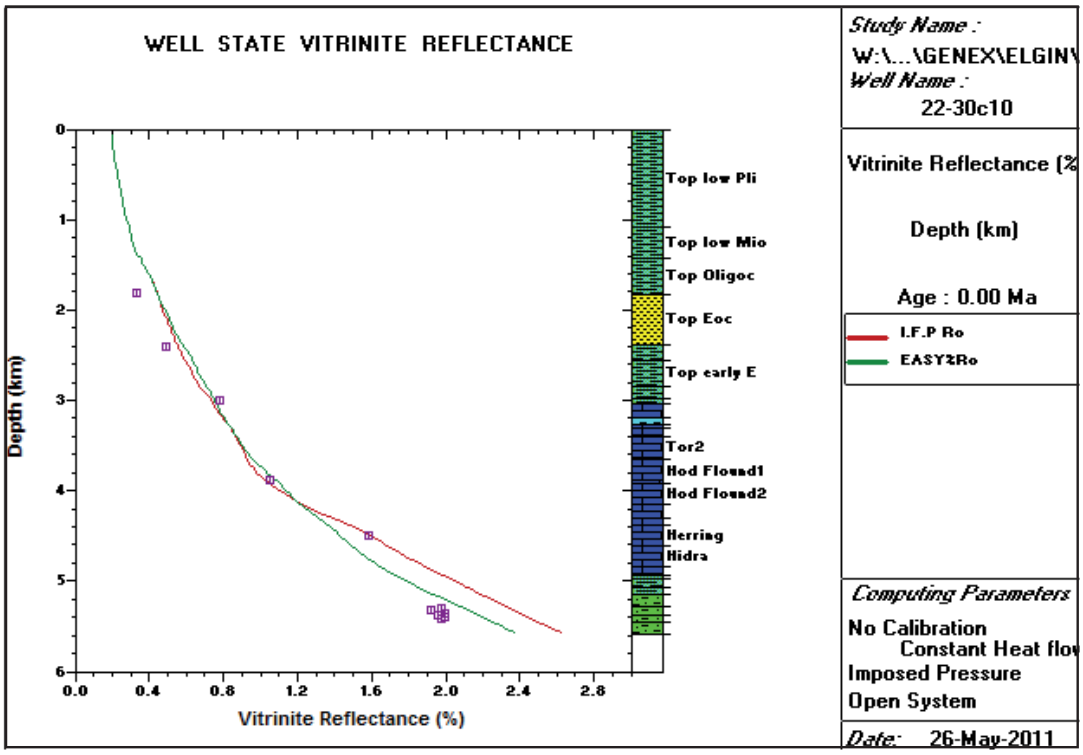

Figure IV.57 – Modeling of the evolution of vitrinite reflectance data Ro as a function of depth (km) for well 22/30C-10 (E. Legendre, pers. com.)

Results shown in Figure IV.57 illustrate that the Easy%Ro model (Sweeney & Burnham, 1990 ; see chapter I for kinetic modeling) provides the best fit of the Ro data. This model yields a geothermal gradient of ∼36°C/km, only slightly higher than the present gradient (34.5°C/km).

Well 22/30C-10 underwent a continuous burial history through time, no uplift episode is documented (Figure IV.58). However, there is an unconformity at the base of the Cretaceous which corresponds to a non-deposition period, going from the Late Jurassic through the mid-Lower Cretaceous (Kimmeridgian).

A total of 49 samples was measured and 23 samples were selected for the calibration presented on Figure IV.59. The burial temperatures are calculated using the modeled geothermal gradient (∼36°C/km).
The evolution of PM with temperature agrees with the model proposed by Aubourg & Pozzi (2010). PM-Up and PM-down trends are observed, that are similar to those observed in Girassol-1 but with different slopes. The PM Up branch ranges from ∼55 to 80°C and presents a stronger slope than in Gir-1. The PM max is situated at ∼80°C. The PM Down branch extends to ∼180°C and also integrates

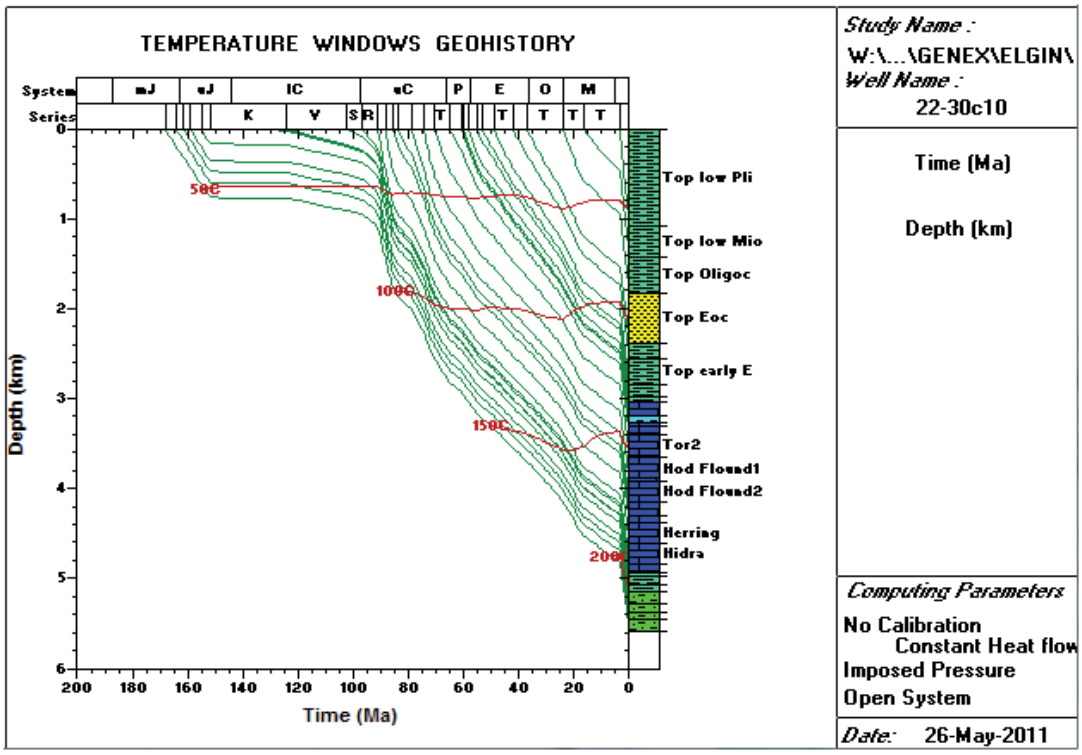

Figure IV.58 – Reconstructed burial history of 22/30C-10 well (UK) by GENEX modeling (E. Legendre, pers. com.)

sandstones and limestones. One can note a strong variability in the PM Up branch at ∼70°C essentially due to two close-by samples (10 m interval) showing very different PM values of 0.68 and 0.92 (see question marks in Figure IV.59). These two outliers (circled in Figure IV.59) strongly influence the linear regression of the PM Up branch. However, there is no magnetic and lithologic reason to exclude these two samples as they satisfy all quality criteria defined in section 2. Consequently, the PM Up branch is rather poorly correlated ($R^2 = 0.39$). The spread of 0.22 recorded by the PM values of the two close-by samples is significant as it is one order of magnitude greater than the uncertainty on PM measurement (±0.02, see above), but cannot be explained by any specificities of one or the other sample. It is considered to represent intrinsic variability in the MagEval technique as any other temperature indicators (see chapter I). The PM Down branch is more progressive than in Gir-1 and more conform to the Aubourg & Pozzi (2010) model. This branch is quite well correlated ($R^2 = 0.83$) but is associated to a wide 95% confidence interval due to low number of data points in the 80-110°C temperature range.

Using a least square linear regression, the following equations can be derived from the Figure IV.59 :

PM UP : T in situ (°C) = 78.585 x PM + 4.0474

PM DOWN : T in situ (°C) = -136.64 x PM + 188.65

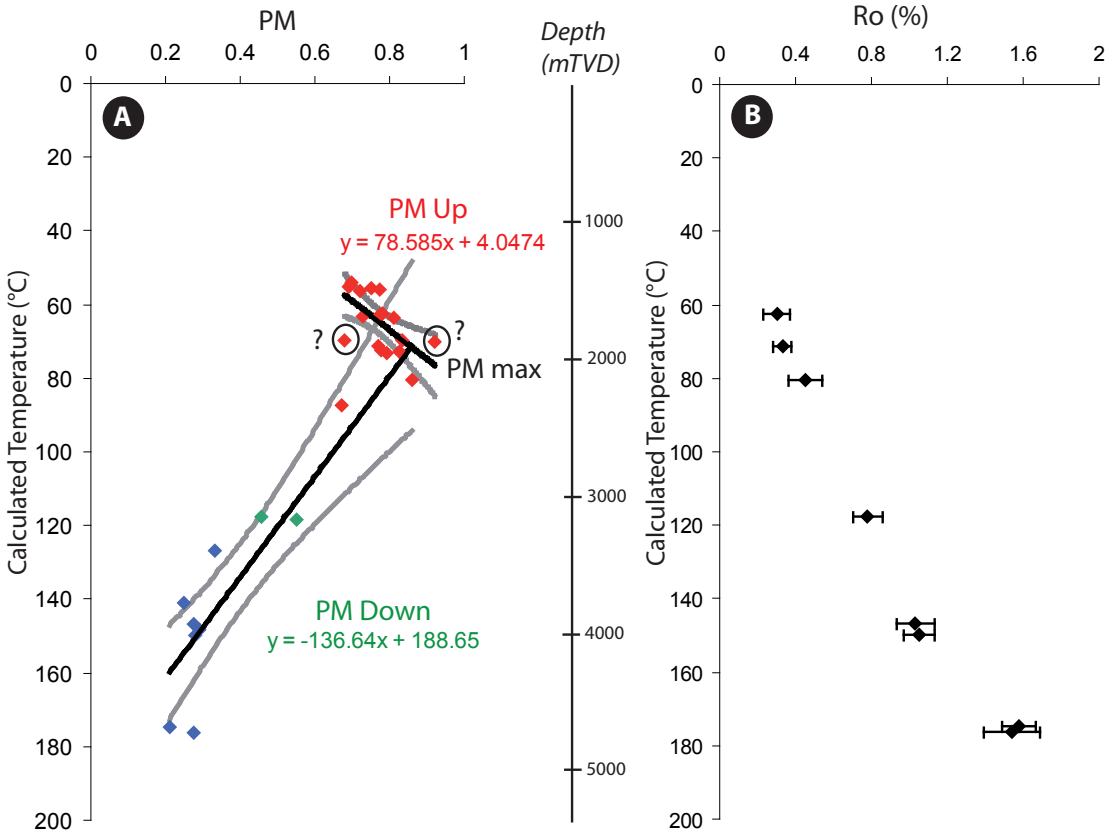

Figure IV.59 – Calibration based on 22/30C-10 well data. A) Evolution of the PM values with calculated temperature from GENEX modeling. Confidence interval is 95%. Red points : claystones, green : sandstones, blue : limestones. B) Evolution of vitrinite reflectance Ro as a function of temperature calculated from GENEX modeling

3.5 Application of the two calibrations

Now that two calibrations have been established showing somewhat different PM evolution with temperature, the question arises of which one should be used. For this reason a detailed comparison is presented on the following.

3.5.1 Girassol-1 and 22/30C-10

In this section, the calibration based on Gir-1 well is applied to 22/30C-10 well and reciprocally the calibration based on 22/30C-10 is applied to Gir-1 (Figure IV.60). This exercise permits to highlight the differences between the two calibrations.

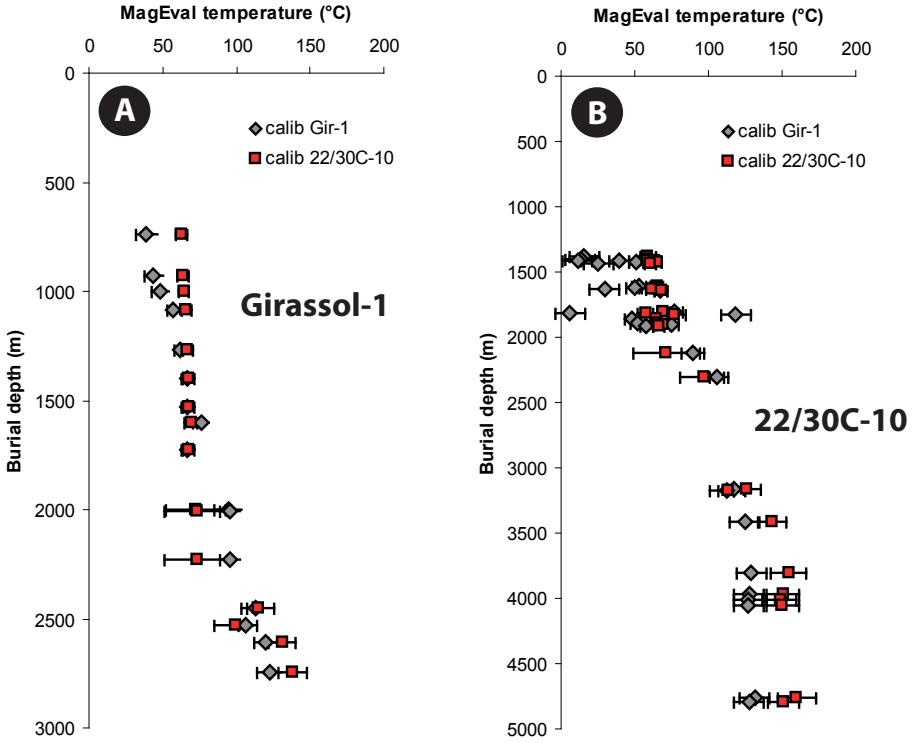

Figure IV.60 – MagEval temperature calculated from the two calibrations as a function of burial depth for A) Gir-1 and B) 22/30C-10

Indeed, although the two calibrations, for a given well, give relatively similar trends, there is some divergence locally.

For Gir-1 (Figure IV.60A), the major difference between the two calibrations is the temperature estimation below 1000 m and between 2000 and 2500 m which corresponds to the occurrence of PM Max. The quasi-linear trend of MagEval temperatures from 1700 m to the top of the well is due to the very low variability of PM values in this depth range.

For 22/30C-10, in the lower part of the well (below 3500m) the temperatures derived from the Gir-1 calibration are slightly lower than those derived from the 22/30C-10 calibration, but remain within error bars or close to. A greater spread is observed at the top of the well where the variability of MagEval temperatures derived from Gir-1 calibration is large. This dispersion is due to the measured PM values themselves which exhibit a wider range in 22/30C-10. This also explains the low estimated MagEval temperatures in the 1400-1700m depth interval. The calibration from Gir-1 does not appear

to be appropriate to describe temperature evolution in well 22/30C-10.

On the basis of the observations above, we conclude that there is a better consistency of MagEval temperatures when calculated with the 22/30C-10 calibration. In addition, the 22/30C-10 calibration displays a general shape and slopes in better agreement with the model of Aubourg & Pozzi (2010). However, the latter calibration also presents some inaccuracies due to the presence of two "outlier" data points (Figure IV.59). Consequently, we consider that the calibration defined on well 22/30C-10 may provide a better description of the thermal dependence of the MagEval parameter at this time.

3.5.2 Application of the calibration to the other investigated wells

In order to further evaluate the two calibrations, it is useful to apply them to the set of investigated wells of the section 2. Two wells (over seven) have samples presenting a magnetic signal suitable for the MagEval geothermometry : Nagele-1 (The Netherlands) and Bikele-1 (Gabon). Because very few samples are available for each well, it is difficult to determine which of the two calibrations branch should be considered. This is particularly true for Bikele-1 because of the lack of burial history information for this well. Consequently, MagEval temperatures are calculated using the two different branches of the calibrations.

Nagele-1 (The Netherlands) The burial history of Nagele-1 shows that the two analyzed samples (at 750 and 1545 mMD) come from the Tertiary part of the well and they are today at their maximum burial depth (Figure IV.61). They are situated in the temperature interval corresponding to the PM Up branch.

The MagEval temperatures calculated for these two samples give some interesting results (Figure IV.62). The two calibrations agree for the sample situated at ∼1550 m giving an estimated temperature close to the in situ temperature. But they totally disagree for the sample situated at the top of the well. The calibration based on Gir-1 underestimates the present temperature by ∼30°C and the calibration based on 22/30C-10 overestimates it by 12°C. It is probable that the temperature estimated by the Gir-1 calibration is out of the applicability domain of the MagEval geothermometer. If considering some errors on the estimation of the present temperature, 22/30C-10 calibration is probably the closest to the actual temperature. Due to the very limited data set for this well, it is difficult to conclude on the choice and validity of the two calibrations.

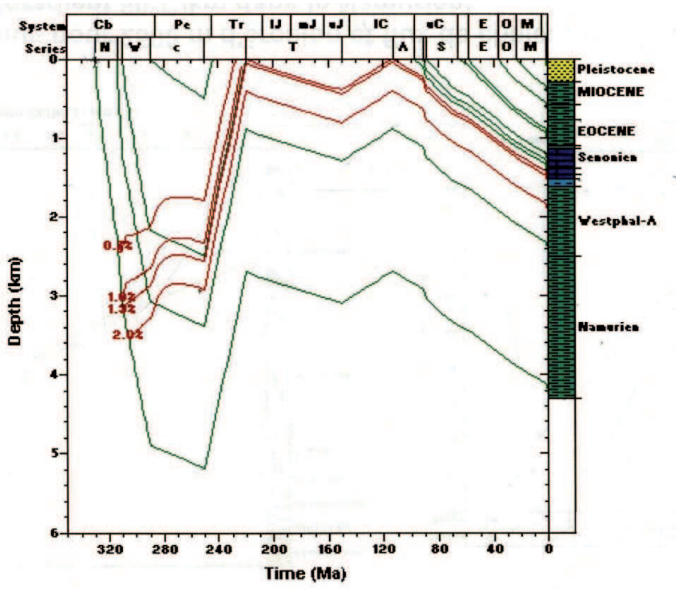

Figure IV.61 – Reconstructed burial history of Nagele-1 well (pers. com.)

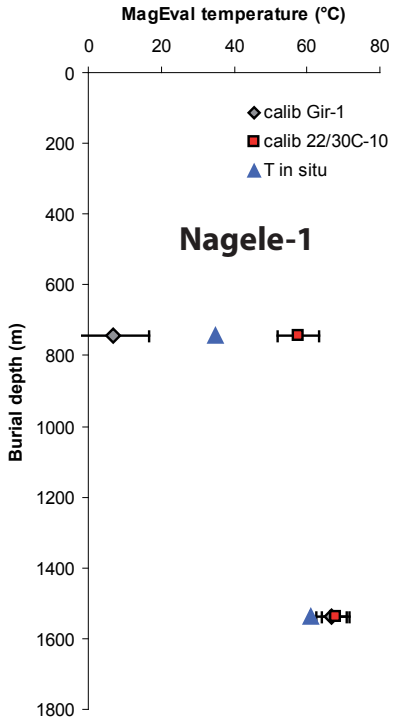

Figure IV.62 – In situ temperatures and MagEval temperatures calculated from the two calibrations for Nagele-1 (The Netherlands) by using the PM Up equations

Bikele-1 (Gabon) Bikele-1 is a well with a complex tectonic history which experienced burial and exhumation episodes. Only five samples samples were analyzed in this well. When calculating the MagEval temperatures with the equations of the two branches, some inconsistencies arise with the PM Up equations. Indeed, in the case of Gir-1 calibration, the PM Up equation gives negative values for the temperatures whereas temperatures are decreasing with depth by considering 22/30C-10 PM Up branch. Thus, the condition for using the right equation is that the calculated temperature should be equal or higher to the in situ temperature. The PM Down equations are then used. The MagEval temperatures calculated with the two calibrations give values similar or higher to the in situ temperatures, especially in the upper part of the well (1000-2000 m depth) (Figure IV.63). In contrast, they are in good agreement at the bottom (> 2000 m). The higher estimated MagEval temperatures in the 1650-1950 m interval depth cannot be explained by either an erosion episode at about 2200 m (no unconformity observed in this interval) nor by a blanketing effect due to the massive salt interval present between 1100 and 1600 m. Overall, the MagEval temperatures are partially consistent with the thermal history of the site. However, vitrinite data suggest that the latter remains complex for depth > 3500 m (Figure IV.64).

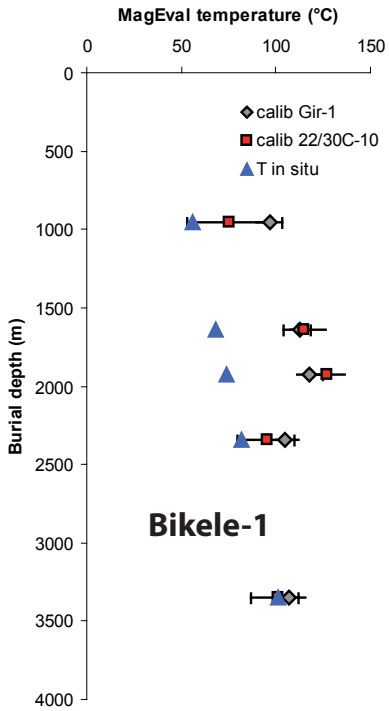

Figure IV.63 – In situ temperatures and MagEval temperatures calculated from the two calibrations for Bikele-1 (Gabon) by using the PM Down equations.

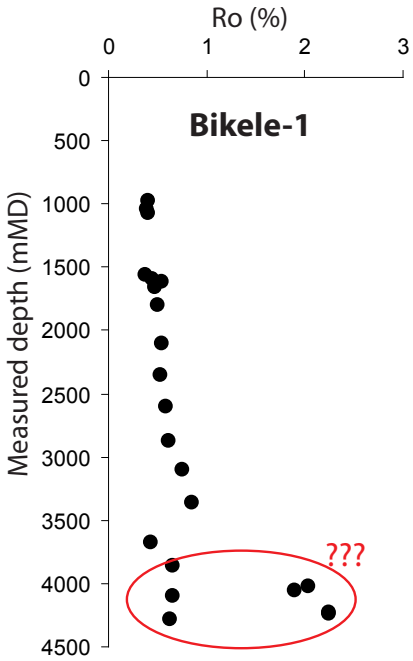

Figure IV.64 – Evolution of vitrinite reflectance data with measured depth for Bikele-1 (Gabon)

3.6 Conclusion

The extensive wells study carried out to develop the MagEval geothermometer highlights some important aspects.

The overall trend of the PM Up and PM Down branches with a maximum value PM max is verified in the two reference wells (Gir-1 and 22/30C-10). The measurement of the PM parameter is well reproducible with a maximum uncertainty of ±0.02 on the PM value.

Many factors such as magnetic pollution and lithological parameters influence the low temperature magnetic signal. However, to date, some questions are still unanswered. Specific selection criteria have been established to identify samples most suitable for the application of the MagEval geothermometer (Figure IV.65).

The detailed study of these wells showed that in the case of Gir-1, the magnetic signal is poorly thermal dependent, compared to that observed in 22/30C-10. The thermal dependence is a key criterion for the MagEval geothermometer. By sides, the PM evolution for close samples in 22/30C-10 shows some variability which is inherent to the technique (the two outliers in a linear trend).

The two calibrations could only be applied to two (Nagele-1 and Bikele-1) of the five other wells investigated in the preliminary survey. Variable results are obtained, with calculated MagEval temperatures in or out of agreement with in situ temperatures. To date, the discrepancies cannot be explained. Where MagEval temperatures fit well with other data, the MagEval calibration established by use of 22/30C-10 well data gives better results compared to that of Gir-1 well.

One major implication of the observations above is that the MagEval geothermometer will not be applicable to an isolated sample, devoid of temperature constraints. The approach requires to perform MagEval measurements on a suite of samples, to generate a well profile of PM values permitting to locate the present-day depth of PM max.

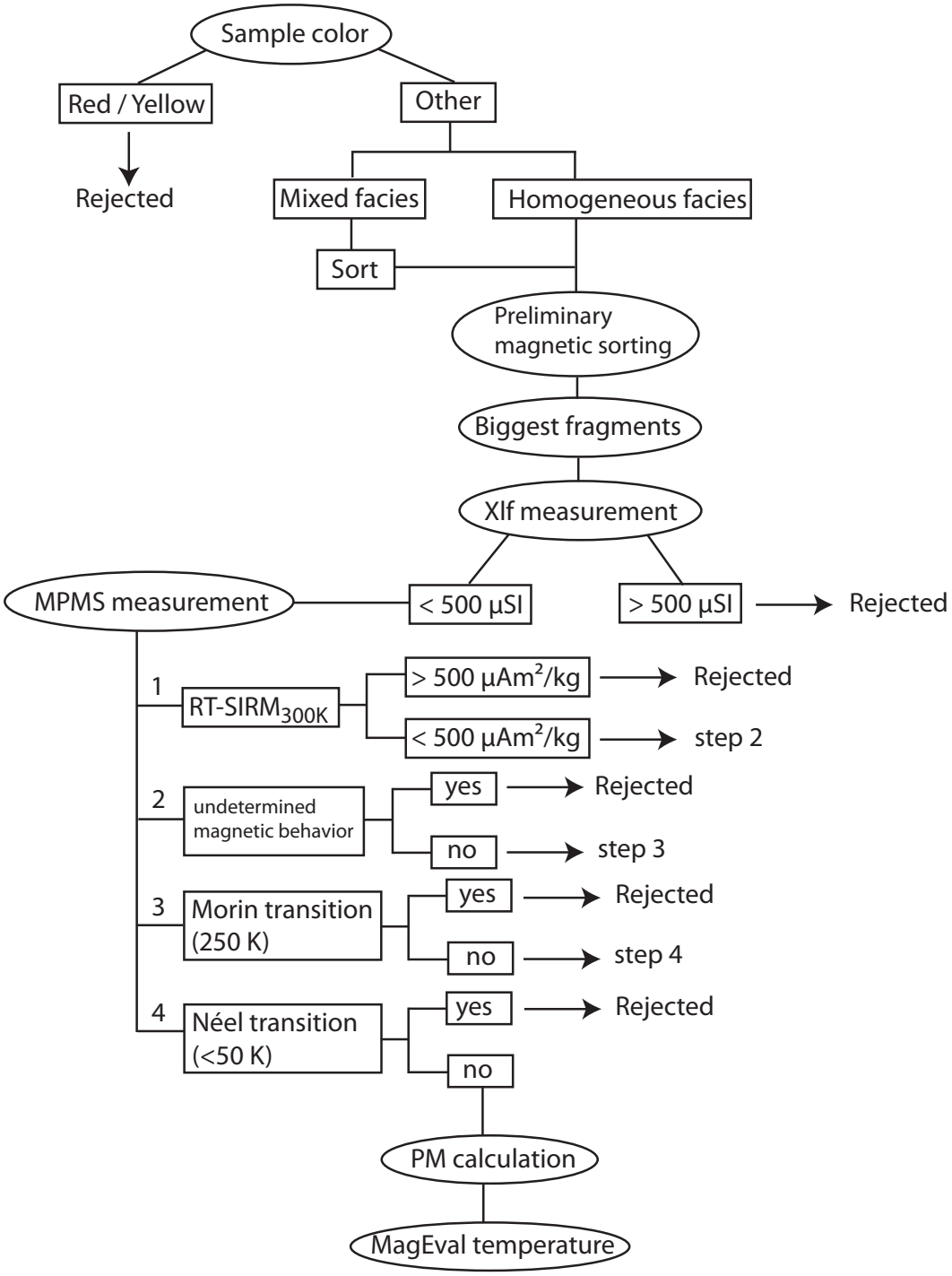

Figure IV.65 – Protocol and use of the MagEval geothermometer. Xlf is the magnetic susceptibility, RT-SIRM is the room temperature saturation isothermal remanent magnetization, MPMS is the Magnetic Properties Measurement System (cryogenic SQUID magnetometer).

Chapter V

LABORATORY HEATING EXPERIMENTS

1 Open-conditions heating experiments at 0.1 MPa

Laboratory heating experiments at temperatures ranging from 95 to 250°C under a magnetic field of 2 mT show that magnetic minerals, though in small amount, are rapidly formed and transformed in heated samples (Cairanne *et al.*, 2004 ; Moreau *et al.*, 2005 ; Aubourg *et al.*, 2008 ; Aubourg & Pozzi, 2010). When transposing to natural settings, it is likely that burial promotes the formation of magnetic minerals as a result of the temperature elevation.

Careful monitoring of the remanence during heating experiments (at regular time-steps) allows the detection of trace amount of neoformed magnetic minerals. The principle of this approach is simple : as a result of the growth initiated by heating, magnetic minerals will reach a blocking volume above which they acquire a remanence. Consequently, the measurement of the remanent magnetization may provide information about the fraction of neoformed magnetic minerals.

The primary aim of the performed experiments was to simulate in laboratory conditions the progressive temperature increase that prevails during burial in sedimentary basins. Two series of heating experiments were performed, whose results are presented below. The experimental protocols are described in chapter III.

1.1 Some background on the samples used for the experiments

Claystones from two origins were used for these experiments : the Boom Clay (Belgium) and the Bure claystones (Paris Basin, France). These two clay formations have been widely studied because of their possible use for radioactive waste storage. They are both characterized by a very low permeability (100-500 nD for the Boom Clay and <100 nD for the Bure claystones).

1.1.1 Boom Clay (Belgium)

The claystone formation was sampled in an underground gallery of the Belgian Nuclear Energy Research Center (SCK-CEN) laboratory HADES in Mol, Belgium (Figure V.1). It is situated at -223 m in the Mid-Oligocene (Rupelian, 30-36 Ma) Boom Formation. This 100-120 m thick Boom Clay

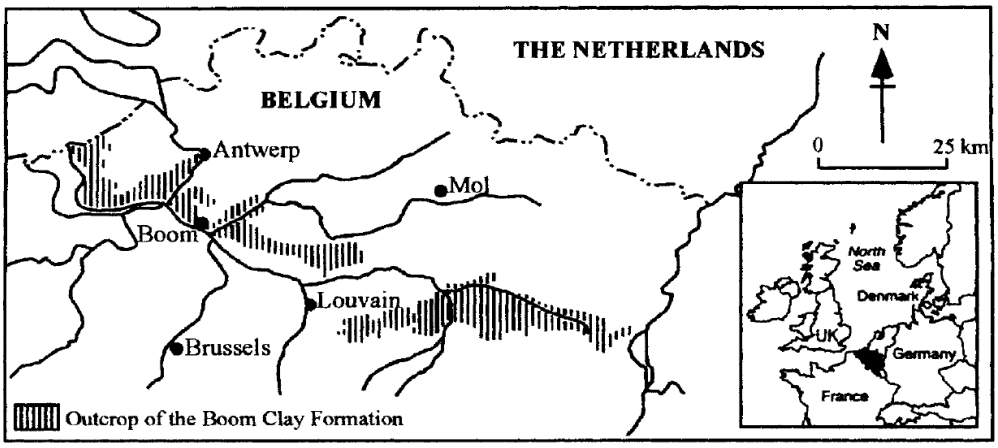

Figure V.1 – Location of Boom Clay Formation and Mol laboratory on the north of Belgium (Deniau *et al.*, 2001)

Clay components	Boom Clay	Bure claystones
Illite/Smectite mixed layers	40-50	15-26
Illite	25-35	2-20
Kaolinite	15-25	0-4.4
Chlorite	5-10	1-3
Calcite	∼1	21-41
Quartz	∼20	19-26
Feldspar	5-10	3-5
Pyrite	1-5	0.4-0.8
Organic matter	1-5	0.4-1.4

Table V.1 – Mineralogical composition and organic matter content (wt.%) of clay samples from the Boom Clay and the Bure claystones (Deniau *et al.*, 2008)

layer occurs in the Mol area at depths between 160 and 280 m. The Boom Clay Formation outcrops southern across Belgium.

The Boom Clay Formation (BCF) was deposited in an open marine environment (Wouters & Vandenberghe, 1994). It is an immature deposit that did not experience temperature higher than 50°C (Deniau *et al.*, 2005).

Clay content ranges from 37 to 71% and pyrite content is up to 5% (Table V.1 ; Decleer *et al.*, 1983). The organic matter content is rather high, up to 5%, average is 3%. Total Organic Carbon (TOC) is 1.7 ± 0.9%. The kerogen is type II with a major contribution of phytoplanktonic material (Deniau *et al.*, 2001). The organic matter is associated with framboidal pyrite and bioclasts. Rock Eval analysis yields a Tmax value of 425°C for a crude sample and of 414°C on isolated kerogen (Deniau *et al.*, 2001). Vitrinite reflectance values range from 0.25 to 0.4% for most wood fragments (type III kerogen) (Vandenberghe, 1978).

The magnetic properties of the Boom Clay Formation yield a natural remanent magnetization (NRM) intensity of ∼400 μA/m and a magnetic susceptibility of 80.10^{-9}m^3/kg (∼ 210 μSI) (Lagrou *et al.*, 2004). Magnetite is the most important remanence carrier. Iron sulfides are also present and may be candidates to carry a part of the remanence (Lagrou *et al.*, 2004).

1.1.2 Bure Claystone (Paris Basin, France)

Geological history of the Paris Basin The Paris Basin is a wide Meso-Cenozoic basin of ∼140 000 km^2 lying over a Carboniferous hercynian basement (Figure V.2).

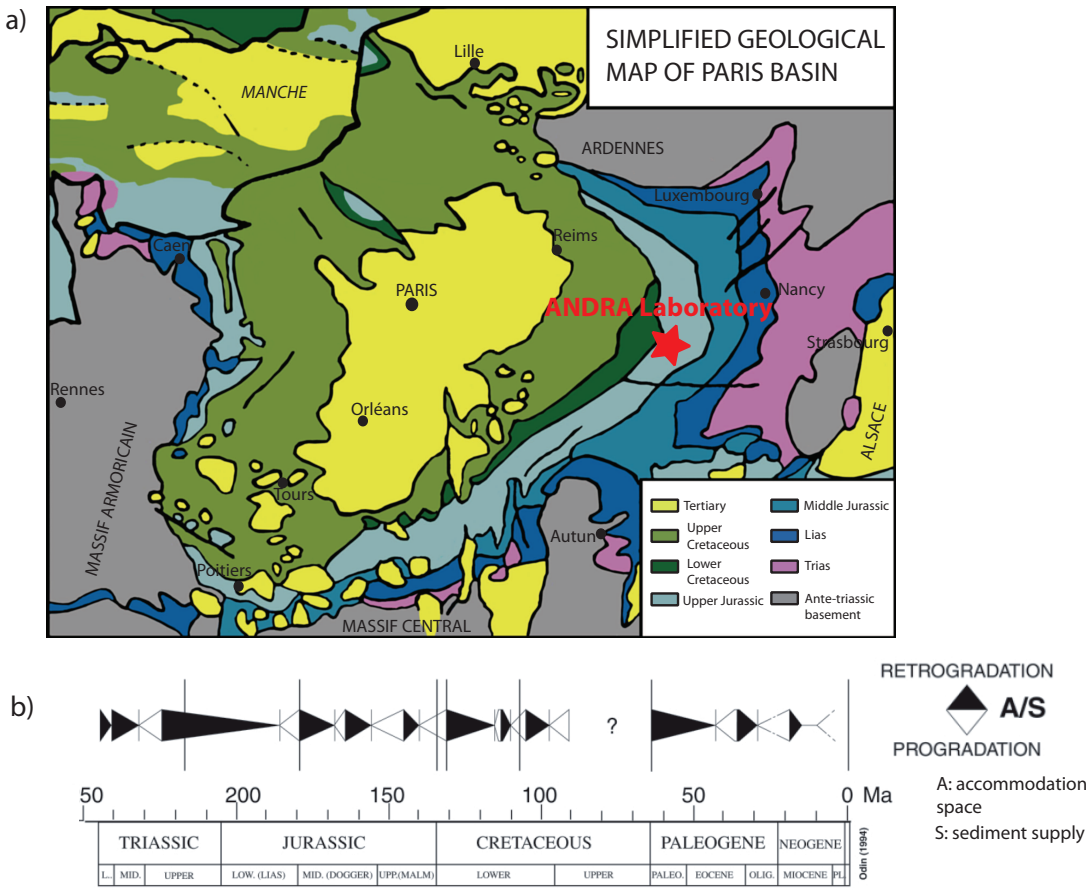

Figure V.2 – a) Simplified geological map of the Paris Basin and b) associated stratigraphic cycles (Guillocheau *et al.*, 2000)

In the Late Carboniferous, after the Hercynian orogeny, the Paris Basin was a high Tibet-like plateau. Then in the Permian, subsidence occurs. In the Early Triassic, the basin is filled with terrigenous sediments (sandstones) from surrounding erosive hercynian reliefs. Then flooding-emergence alternations occur leading to evaporatic deposit at the end of the Triassic, carbonates in the Jurassic

and chalk in the Cretaceous. A marine transgression-regression period follows from Eocene to Late Oligocene. From this time, the Paris Basin remains emerged and progressively acquires its present morphology (Figure V.2 ; Guillocheau *et al.*, 2000 and references therein).

If the geological conditions have been optimal, the Paris Basin would have been a large oil basin with a rather high petroleum potential. With the exception of the Toarcian black shales which constitute a good quality source rock (Tissot *et al.*, 1971 ; Bessereau & Guillocheau, 1994), the Paris Basin is now the object of attention for underground storage of radioactive waste. The targeted geological formation is the Jurassic Callovo-Oxfordian (COX) argillites owning to their low permeability.

Callovo-Oxfordian argillites The Bure claystones used for this study are from the Callovo-Oxfordian (COX) argillites (Figure V.3). They come from the oblique core EST-211 (849.19-849.69 mMD) drilled by ANDRA -(French National Radioactive Waste Management Agency) in the Eastern part of the Paris Basin near Bure, France.

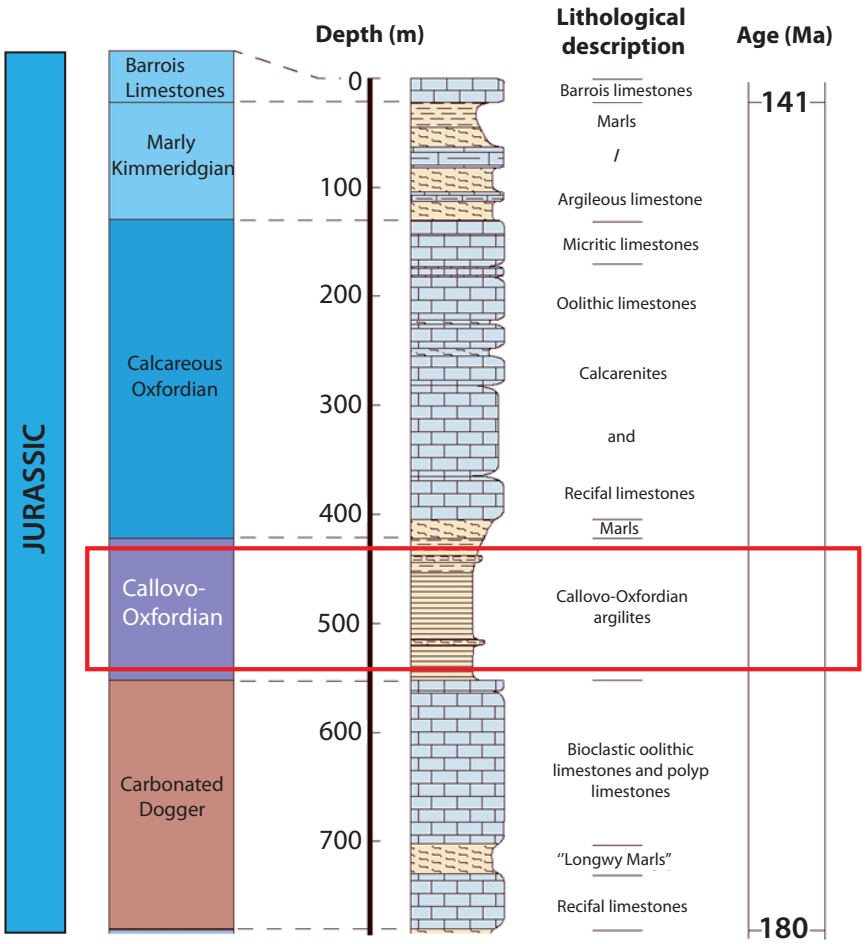

Figure V.3 – Jurassic litostratigraphic sequence in the Paris Basin (from ANDRA website)

The Bure argillites are a ∼130 m thick marine formation, deposited on sea bed far from the coast 150 Ma ago (Deniau *et al.*, 2008).
The clay content varies between 35 and 60% (Gaucher *et al.*, 2004). Remaining dominant phases are calcite and silt. These claystones contain less than 2% of pyrite and 0 to 0.9% of TOC. The organic matter (type III kerogen) is associated with framboidal pyrite and bioclasts. The mineralogical composition of Bure claystones is reported in Table V.1. The Bure claystones have undergone low burial temperatures < 50°C (Landais & Elie, 1999). Rock Eval pyrolysis yields a Tmax value of ∼420°C (Deniau *et al.*, 2008).
The magnetic properties of these claystones have also been studied. The low field magnetic susceptibility (χ) varies between 10 to 194 μSI and the natural remanent magnetization (NRM) between 61 and 1416 μA/m (Esteban *et al.*, 2006). Iron oxides ((titano)-maghemite or -magnetite) and iron sulfides (greigite, pyrite) occurrences have been documented (Esteban *et al.*, 2006 ; Aubourg & Pozzi, 2010).

1.2 Acquisition of a CRM in Bure and Boom claystones at 70 and 90°C

1.2.1 Single-step experiment at 70°C - 13 days

The first part of the experiment A, described in chapter III, consists of heating Bure and Boom claystones at 70°C during 13 days. Temperature is 25°C lower than that used in the heating experiments by Aubourg & Pozzi (2010). The remanence of the samples is regularly measured every 2 days (Figure V.4A).

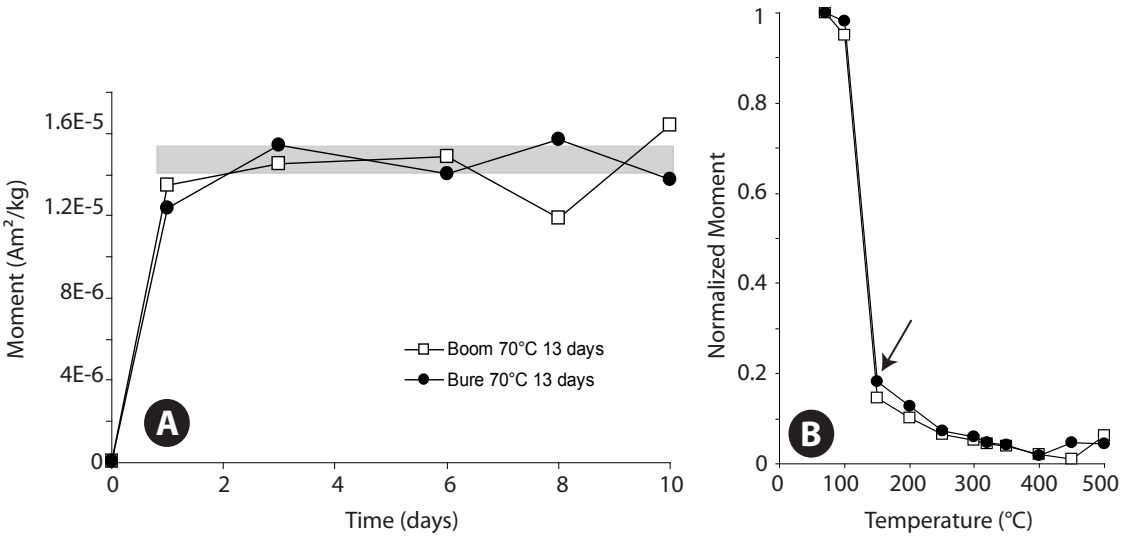

Figure V.4 – Heating experiment at 70°C, 13 days : A) Evolution of the remanent magnetization with time and B) Thermal demagnetization of the corresponding CRMs. The arrow shows the break-in-slope.

At 70°C, the remanence increases rapidly in the first days of the experiment. Then, the magnetization reached a plateau with no subsequent change. We note that the two claystone samples behave the same, even if the plateau for Boom Clay is not as flat as for the Bure claystone due to the TVRM instability. The TVRM (not represented on Figure V.4A) represents the largest contribution to the remanence (>60%). The CRM represents about 36% (6 $\mu Am^2/kg$) and 40% (5.5 $\mu Am^2/kg$) of the total remanent magnetization for Boom and Bure claystones respectively after 13 days heating. These values are remarkably similar.
The samples were then heated in nil field from 100 to 600°C to characterize the CRM (Figure V.4B). The remanent magnetization values between 500 and 600°C are not represented on Figure V.4B because the samples experienced remagnetization due to heating. The magnetic moment drops abruptly at 150°C where a break-in-slope occurs. At 150°C, about 85% of the remanence is lost. The maximum unblocking temperature of these samples is between 400 and 500°C. We observe the exact same behavior for the two samples. We can therefore postulate that the CRM is carried by the same magnetic phase in both claystones formations.

1.2.2 Two-step experiment at 70°C - 29 days and 90°C - 34 days

The second part of experiment A consists of heating Bure and Boom claystones in a two step manner, with a first step at 70°C during 29 days, followed by a second step at 90°C for 34 days. The remanence of the samples is regularly measured (Figure V.5A).

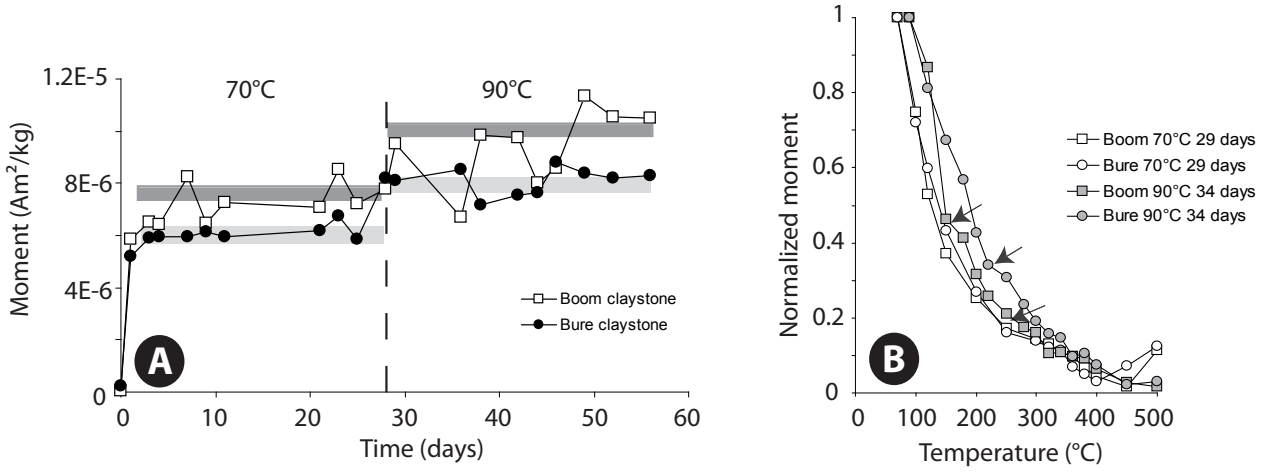

Figure V.5 – Results of the two-step heating experiment at 70°C, 29 days followed by 90°C, 34 days. A) Evolution of the remanent magnetization during the two-step heating experiment with time and B) Thermal demagnetization of the corresponding CRMs. The arrows indicate the break-in-slopes.

Figure V.5A represents the evolution of the remanence for Boom and Bure claystones at 70°C then 90°C. The behavior is similar for both claystones. As observed in the single-step experiment, the remanence increases abruptly and reaches rapidly a plateau at 70°C. When temperature is further increased at 90°C, the remanence increases further and reach a new plateau at a higher mean remanence value. It is noticeable that Boom claystone remanence exhibits a more pronounced dispersion. This may be due to the input of TVRM which is time-dependent. At the end of the heating at 70°C, we performed TVRM test to measure the CRM created during the first stage of this heating experiment (thereafter referred to as CRM1). CRM1 represents about 37% for the Boom claystones and 38% for the Bure claystones (respectively 2.6 and 2.4 $\mu Am^2/kg$). We note the remarkable similarity of the CRM magnitude of both claystones. One can notice also that the CRM1 is half the CRM acquired in 13 days (single-step experiment, Figure V.4). The CRM recorded at 90°C (CRM2) is about 51% for the Boom sample and 58% for the Bure sample (respectively 5.4 and 4.9 $\mu Am^2/kg$). CRM2 is significantly greater than CRM1. The fact that CRM produced at 90°C is much greater than at 70°C in spite of similar heating duration (CRM2-CRM1>CRM1) implies that temperature plays a role on the amount of CRM generated. We observe that the higher the temperature, the higher the CRM produced.

We performed thermal demagnetization for twinned Boom and Bure samples heated at 70°C and 90°C (Figure V.5B). At 70°C, the CRM1 evolves in the same way decreasing linearly to 250°C. At this temperature, a break-in-slope in the demagnetization curves occurs. From 250 to 400°C for the Bure sample and to 450°C for the Boom sample, CRM1 is still diminishing. At 400°C (450°C for Boom claystone), the samples undergo magnetic grains remagnetization under the effect of temperature. At 90°C, we can note differences in the evolution of the CRM2 during thermal treatment. The remanence decreases to 150-200°C (for Boom and Bure claystones respectively) where a break-in-slope occurs. Then, the magnetization still decreases to 500°C where the remanence is almost totally lost.

1.2.3 Discussion and preliminary conclusions

The two heating experiments at 70°C and 90°C conducted on two different claystones yielded remarkably similar behaviors, in particular : 1) a similar kinetics ; 2) a comparable CRM and TVRM and 3) a similar magnetic assemblage of neoformed magnetic minerals. This suggests that the process that leads to the formation of magnetic minerals in Boom and Bure claystones at temperature as low as 70°C is the same. This temperature would therefore occur in nature at burial depths of about 2 to 3 km in normal geothermal gradients. Note that the chemical composition of the two claystones is different (Table V.1). In particular the pyrite and organic matter contents are larger in the Boom claystones.

The process being discussed is probably fast at geological time scale because the remanence acquired during heating claystones attains rapidly a plateau (Figures V.4A and V.5A). Heating experiments we performed were not long enough to assess long-term stability of the plateau (e.g. Aubourg *et al.*,

2008), but we assume that most magnetic minerals are formed rapidly upon heating. The second experiment (two-step experiment) was intended to simulate the effect of an increasing burial temperature. Indeed we observed two distinct plateaus corresponding to each heating increment (70°C and 90°C, Figure V.5A). If we transpose this result to sedimentary burial, it implies that magnetic minerals are formed continuously with burial as long as temperature increases. The results further indicate that the formation of magnetic minerals stops when the temperature remains stable, suggesting that the primary factor of control on magnetic mineral growth during burial would be temperature rather than time.

Neoformation of magnetic minerals induces a remanence. The heating experiments show that the remanence is half carried by a TVRM and by a CRM for tens days heating. The intensity of CRM measured at 70°C and 90°C is remarkably similar for the Boom and Bure claystones ranging from 2 to 6 μAm^2/kg. Assuming CRM is proportional to the strength of the magnetic field (Stokking & Tauxe, 1990), we calculated the expected CRM$_{EMF}$ obtained at 50 μT, the local strength of the Earth's magnetic field (EMF). The CRM$_{EMF}$ is then ranging from 0.05 to 0.15 μAm^2/kg, which is about 1 : 10 of the NRM. We observe that the CRM obtained at 70°C for 29 days is about half of the CRM obtained at 90°C for 34 days. This suggests either a higher concentration of magnetic minerals formed at 90°C, or a different magnetic assemblage.

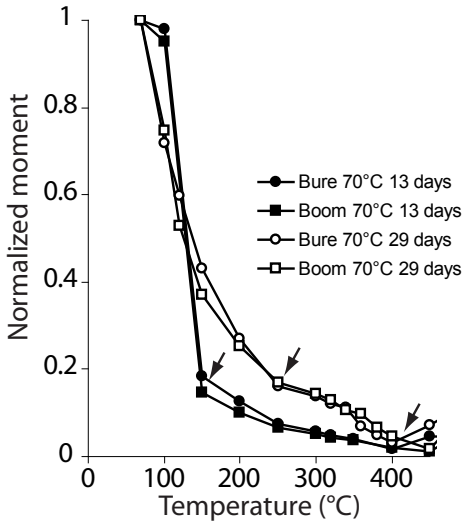

Figure V.6 – Thermal demagnetization of the CRM for Boom and Bure claystones created at 70°C for two heating durations. The arrows show the break-in-slopes.

It can be noticed that the CRM obtained in the single-step experiment at 70°C for 13 days is about two times higher that the CRM obtained in the two-step experiment at 70°C for 29 days. Thermal demagnetization of the CRM confirms that the magnetic assemblage differs partly in the two experiments (Figure V.6). In both cases, the maximum unblocking temperature is about the same

between 400°C and 500°C. This is consistent with fine-grained magnetite being the magnetic carrier. The data for the 13-day experiment show a sharp break-in-slope with 80% of CRM lost at 150°C. For the 29-day experiment, less than 60% of CRM is lost at 150°C with no evidence of break-in-slope. The lower loss of CRM at 150°C in the longer experiment (29 days) can be attributed to a coarser grain size of neoformed magnetic minerals ; the coarser the grain, the higher the unblocking temperature (Dunlop & Özdemir, 1997).

Two main hypotheses can be formulated to explain these observations. They are presented below. The first hypothesis relies on the neoformation of only one mineral specie, most likely magnetite given the maximum unblocking temperature T_{UB}, which grain size distribution evolves to larger grains during the heating experiment. Following Stokking & Tauxe (1987), we use the Néel equation which links the grains size and the blocking temperature :

$$V = \frac{(kT)}{K}\ ln(C\tau)$$

where V is the grain volume (cm^3), k is the Boltzmann's constant ($1.38.10^{-16}$ erg/K), T is the blocking temperature (Kelvin), K is the anisotropy constant of the magnetic mineral of interest, C is a frequency factor (1.10^9) and τ is the relaxation time. The grain diameter d can be expressed as :

$$d(cm) = \left[\frac{6kT}{\pi K} ln(C\tau)\right]^{1/3}$$

Using $K = -1.35.10^5$ erg/cm^3 (magnetocrystalline anisotropy of magnetite) and $\tau = 3600$ s, we calculate maximum grain sizes of magnetites ranging from 29 nanometers to 35 nanometers for T_{UB} ranging from 150 (423 K) to 500°C (773 K).

The second hypothesis brings into play different magnetic minerals. We discuss successively the possible occurrence of goethite and pyrrhotite, which could have formed in addition to magnetite.

Some goethite ? Goethite is a common iron oxyhydroxide in many soils and sediments and results from weathering of iron-bearing minerals (e.g. Maher, 1998). As Bure and Boom claystones were collected from boreholes, it is unlikely that goethite results from long-standing weathering processes. The low temperature measurements performed on natural Boom and Bure claystones show that the SIRM acquired at room temperature with a 2.5 T magnetic field increases regularly on cooling from 300 to 10 K, up to twice of its initial value (Figure V.7A). Such an increase is a good indication of the presence of goethite according to Maher *et al.* (2004). One can notice also a very slight Verwey transition of magnetite occurring at ∼110 K (Figure V.7B).

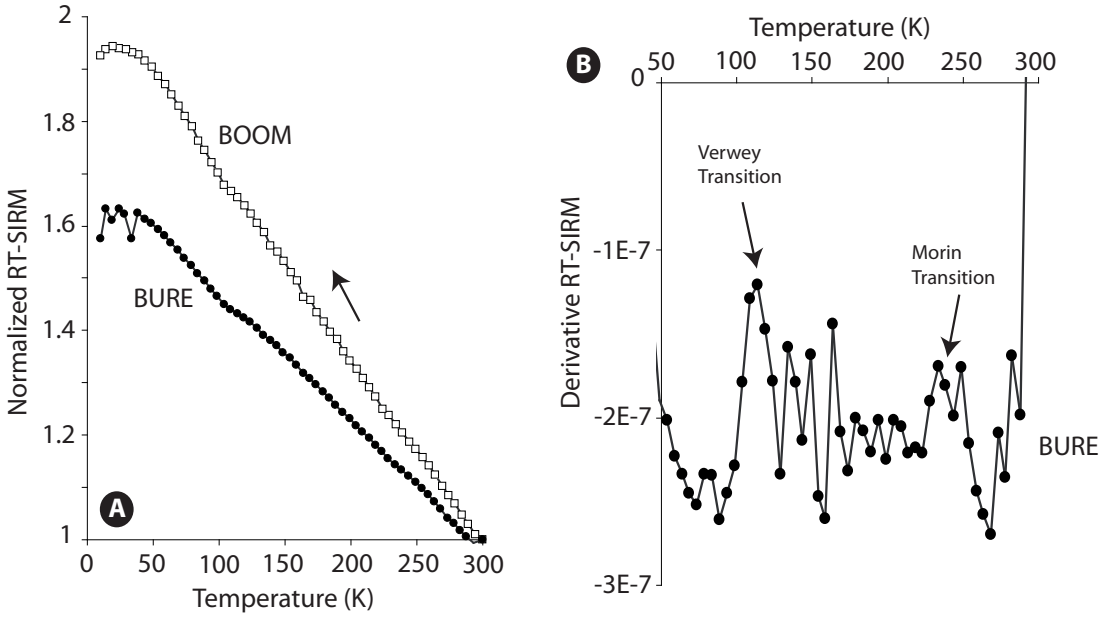

Figure V.7 – A) RT-SIRM curves for natural Boom and Bure claystones and B) the RT-SIRM derivative for natural Bure claystone sample. RT-SIRM increase is a diagnostic feature of goethite. Note that the Verwey and Morin transitions are better marked in the derivative.

The existence of a break-in-slope near 150°C (Figure V.4B) suggests that at least two types of magnetic minerals carry the CRM acquired at 70°C. The goethite (α-FeOOH), with a Néel temperature of 120°C (e.g. Özdemir & Dunlop, 1996), is the most likely candidate to explain the sharp drop near 150°C. The disappearance of this break-in-slope for 29-day heating at 70°C suggests that goethite, once formed, is probably unstable under our experimental conditions. The remanent magnetization at saturation of goethite is 0.05 Am^2/kg (Maher & Thompson, 1999), i.e., 1 : 200 with respect to magnetite. Consequently, it is conceivable that the degradation of goethite could explain the half-drop of CRM between 13 and 29 days. However, the presence of a plateau on one hand, with no evidence of remanence decay, and the same proportion of CRM (35%) on the other hand, are puzzling. At this time, we found nothing in our experimental procedure, or in the nature of the samples that could explain this intriguing result, and the question remains open.

Iron sulfide ? For the 29-day heating at 70°C and the 34-day heating at 90°C, the unblocking temperature spectra reveal the presence of an additional unblocking temperature between 200°C and 300°C, marked by a break-in-slope (Figure V.5B). In this range of temperature, about 80% of CRM is demagnetized. Aubourg *et al.* (2008) reported similar trends and proposed that these spectra are indicative of an assemblage of magnetite and pyrrhotite (Fe_7S_8). Evidence of stoichiometric magnetite

and fine-grained pyrrhotite is observed in Opalinus claystones from the Jura fold belt that experienced burial temperature near 90°C (Aubourg & Pozzi, 2010). Our results are consistent with this observation.

The results confirm prior conclusions emphasized by Cairanne *et al.* (2004) and Aubourg *et al.* (2008), i.e., the production of magnetic minerals is very fast at geological time scale and stabilizes shortly after each incremental elevation of temperature. The 2-step heating experiment suggests that magnetic minerals are continuously produced. Considering burial as a progressive elevation of temperature with depth, continuous production/removal of magnetic minerals means that chemical reactions involving iron are sustained during burial. One key result of this study is that two distinct claystones from two different sedimentary settings and different ages yield similar results upon heating in the laboratory under the same experimental conditions.

In order to better interpret the results obtained in experiment A, the following scenario is proposed. During early burial, goethite is formed. In parallel, magnetite is also formed, but in much lower concentration. The finding of goethite in natural Boom and Bure claystones (Figure V.7) suggests that a minimum burial temperature - as low as 40°C - permits goethite formation implying burial depth > 1 km. Upon further burial, goethite would then gradually disappear to the profit of magnetite and possibly pyrrhotite (Rowan *et al.*, 2009 ; Aubourg & Pozzi, 2010). This hypothetical scenario requires to be fully validated by thermodynamical modeling and/or more specifically targeted experiments, which were beyond the scope of the thesis.

According to our experiment, the magnitude of the CRM_{EMF} is about one tenth of the NRM but it is possible that CRM overwhelms NRM. We thus suggest that the CRM due to burial effect is rather common in claystones. If this is further confirmed in future research works, the preservation of the primary magnetization signal recorded in sediments may be questioned (Aubourg *et al.*, in revision, appendix 3).

1.3 Step-heating experiment from 50 to 130°C on Bure claystones

Kars *et al.* (in revision, appendix 2) report on the results of the heating experiment on the Bure claystones in a temperature range going from 50 to 130°C. A review of the most important results is presented below.

The evolution of mean remanence in the different experimental heating temperature T_{exp} shows a similar trend to the previous experiment on Boom and Bure claystones at 70 and 90°C. The remanence first increases rapidly and then stabilizes for each incremental temperature step (Figure V.8). The measured CRM_{2mT} displays a consistent increase from 5 ± 1 to 19 ± 6 $\mu Am^2/kg$ with increasing T_{exp} (Figure V.9). If we consider a regular increase, the increasing rate would be ~ 0.2 $\mu Am^2/kg/°C$. The $TVRM_{2mT}$ is on the same order of magnitude as the CRM_{2mT} and increases from 5 ± 1 to 14 ± 4

$\mu Am^2/kg$ (Figure V.9). The $TVRM_{2mT}$ is slightly higher than the CRM_{2mT} for T_{exp} from 50 to 70°C, and is lower at T_{exp} = 130°C. At the latter temperature, the CRM_{2mT} contribution is predominant in the total remanence measured.

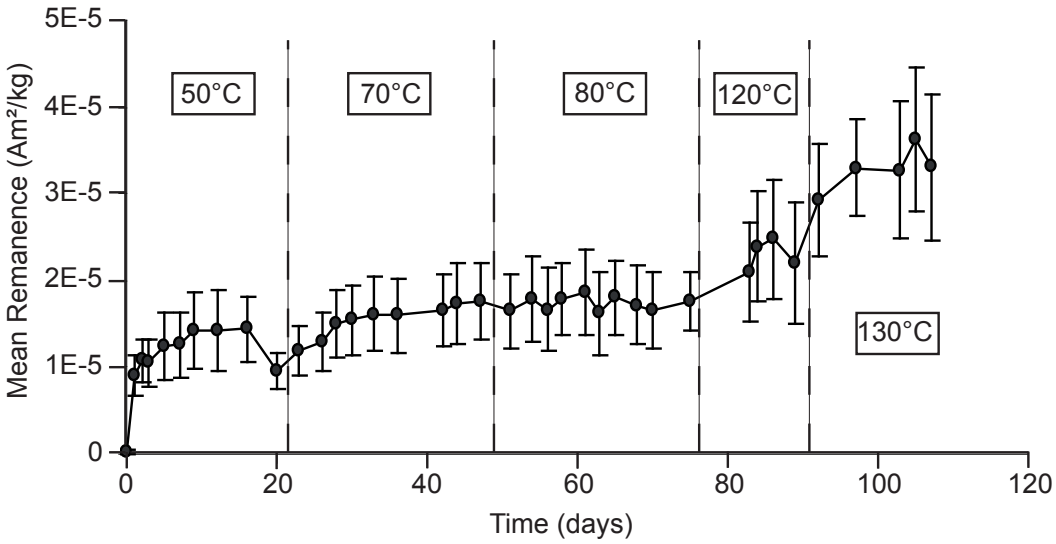

Figure V.8 – Evolution of the mean remanent magnetization with time during the step-heating experiment from 50 to 130°C. Standard deviation ($\pm 1\sigma$) is also reported.

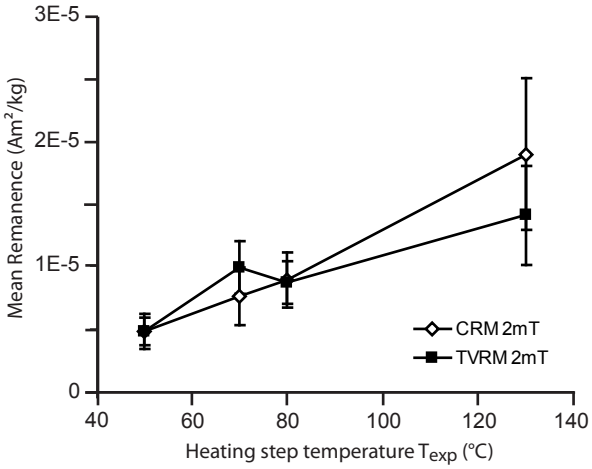

Figure V.9 – Evolution with heating temperature of the mean CRM_{2mT} and mean $TVRM_{2mT}$ created during the 50-130°C step-heating experiment. Standard deviation ($\pm 1\sigma$) is also reported.

These results demonstrate the formation of magnetic minerals in Bure claystones for temperatures as low as 50°C. The strength of the CRM_{2mT} at 130°C obtained is similar to the NRM (12 ± 26 $\mu Am^2/kg$) at the order of magnitude. This finding suggests either a higher concentration of one kind of neoformed magnetic mineral or an assemblage of different magnetic species. As we do not observe any distinct break-in-slope in the thermal demagnetization curves of the CRM_{2mT}, it is unlikely that the increase of CRM_{2mT} is due to an assemblage of different magnetic minerals (Figure V.10A). In contrast, we observe a regular shift in the maximum unblocking temperature T_{UB} ; the lowest T_{exp} showing the lowest T_{UB} (Figure V.10A). The shift can be attributed to variable grain size of magnetic minerals. We therefore favor the hypothesis according to which only one magnetic mineral is formed during the heating experiment, acquiring a distribution of grain sizes as reaction progresses. We assume that this mineral is magnetite as the maximum T_{UB} (extrapolated for T_{exp} = 130°C) is near 500°C. By using T_{UB} values (from 250 to 500°C) and the Néel equation, it is found that the maximum grain size for magnetite ranges from 30 to 35 nm (single domain SD size). On the other hand, the $TVRM_{2mT}$ is partly carried by neoformed ultra fined magnetic minerals and partly carried by former magnetic minerals. The observed increase of $TVRM_{2mT}$ can be attributed to a greater concentration of ultra fined magnetic minerals. This is confirmed by the evolution of parameter PM which may be used as a proxy for superparamagnetic SP minerals (Figure V.10B). The regular PM increase suggests that very small magnetic SP grains are formed continuously throughout temperature elevation.

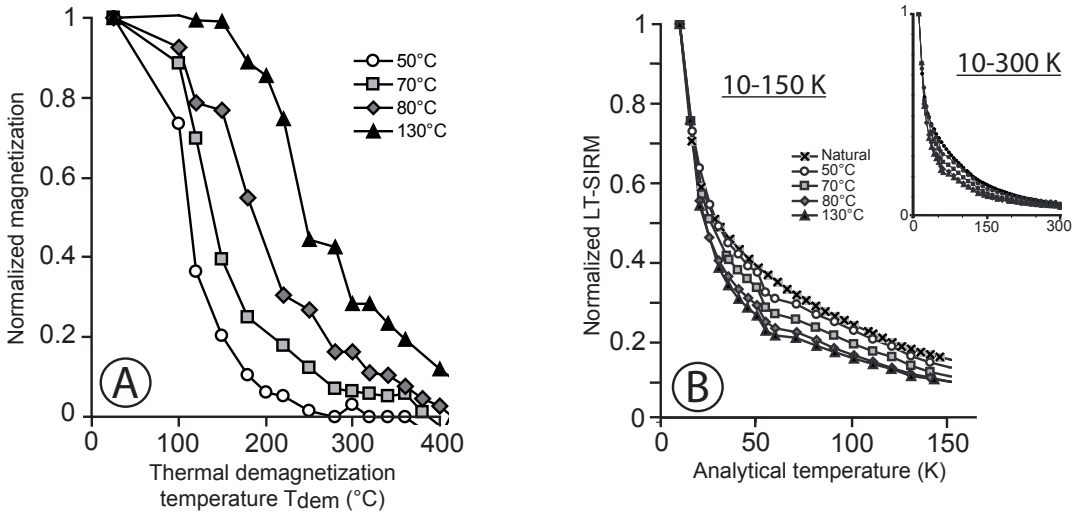

Figure V.10 – A) Thermal demagnetization of CRMs produced in the 50-130°C step-heating experiment, B) LT-SIRM curves for the "twin" samples. Natural sample LT-SIRM is shown for reference.

As inferred from the experiment A, the growth and neoformation of magnetite minerals in sedi-

mentary rocks during burial produce a secondary magnetization that may overprint the initial magnetization. Our results, transposed to the strength of the Earth's magnetic field, suggest that sediments with weak NRM on the order of ∼1 $\mu Am^2/kg$ experiencing temperature higher than 220°C should be remagnetized.

2 Confined-conditions heating experiments at 100 MPa

In the series of open-conditions heating experiments, pressure was not considered. Moreau *et al.* (2005) suggested that pressure has no effect on magnetite formation during experimental heating. However, in order to better simulate burial conditions it is interesting to perform heating experiments in confined-conditions and under pressure (Cairanne *et al.*, 2004). In the following experiments, the applied pressure is 100 MPa (= 1 kbar) which corresponds approximately to 3 km depth lithostatic pressure. In this series of experiments, the samples are sealed in gold capsules to create a confined environment and placed in autoclaves. We followed the procedure described in Aubourg & Pozzi (2010). The samples were maintained at stable temperature and pressure throughout the duration of the experiment. Two series of gold capsules experiments were done (Table V.2). In these experiments, remanence was not monitored as in the open-conditions experiments. Here, we compare the magnetic assemblage present in the samples before and after heating, corresponding to the initial magnetic minerals and the experimentally neoformed magnetic minerals. Of course, it cannot be excluded that initial magnetic minerals are altered during the heating experiments.

Experiment	Sample	Capsule name	Temperature (°C)	Duration (days)
1	A	E1 E2	80 110	80 80
	B	E3 E4	110 140	80 80
2	A	C1	80 110	110 101
		C2	90 120	110 101
		C3	130 160	110 101
		C4	110 140	110 101

Table V.2 – Temperature and duration of the 100 MPa experiment

2.1 80-day heating experiment

Two claystones from a borehole in offshore Angola were used for this experiment. The samples will be labeled A and B. Sample A (RT-SIRM$_{300K}$ ∼ 973 $\mu Am^2/kg$) experienced burial temperature of

∼40°C and sample B (RT-SIRM$_{300K}$ ∼ 128 μAm^2/kg) a temperature of ∼80°C. Four gold capsules were prepared. The two gold capsules of the sample A (E1 and E2) were heated to 80 and 110°C respectively, those of the sample B (E3 and E4) to 110 and 140°C.
At the end of the experiment, the gold capsules were cut open. The sediments were removed and dried in a oven (< 40°C) over one night. Then, they are put in gelatin capsules for the low temperature magnetic measurements (Table V.3).

Capsule name	T (°C)	RT-SIRM$_{300K}$ (μAm^2/kg)	LT-SIRM$_{10K}$ (μAm^2/kg)	PM
E1	80	354	3460	0.73
E2	110	527(?)	3460	0.64
E3	110	398	2460	0.6
E4	140	174	2200	0.72

Table V.3 – Some magnetic values of the 4 samples heated in gold capsules

Only the warming curves from 10 to 300 K (Zero Field Cooled ZFC) are of interest, especially the drop of the remanence between 10 and 35 K. This decrease can be quantified by using the concept of PM parameter, previously described (Aubourg & Pozzi, 2010, see chapter IV) which characterizes the SP particles.

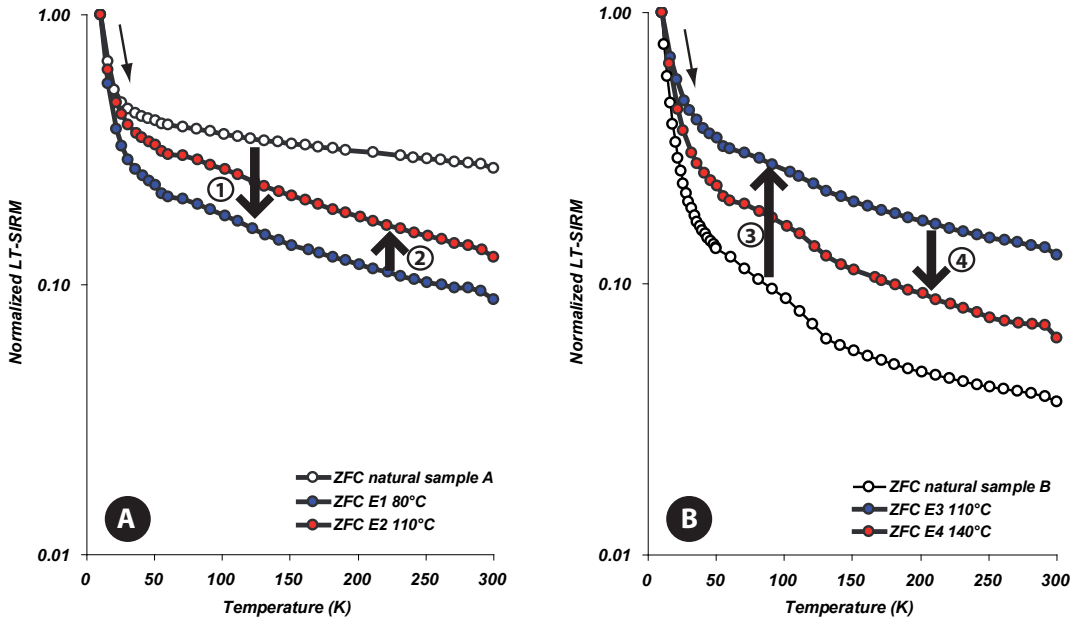

Figure V.11 – Evolution of the ZFC curves for the samples A) A and B) B obtained after heating in the autoclaves compared to their respective original magnetic signal

The initial PM value of the natural sample A is 0.57. When heated, the ZFC curve first moves downward at 80°C (1) and then goes back up at 110°C (2) (Figure V.11A). The PM values are 0.73 and 0.64 respectively. PM increases when considering the PM Up branch and decreases when situating in the PM Down branch (Figure V.11). The downward shift (1) can be explained by the formation of very small SP grains which lost rapidly their remanence acquired at 10 K. That leads to a more important decrease of the remanence between 10 and 35 K. The upward trend (2) is characterized by a lower PM value meaning that the SP grains amount is lower. Thus the SP grains formed at lower temperature (80°C) progressively grow, eventually passing through their blocking volume.

The initial PM value of the original sample B is 0.82, close to the PM max value of the model. Assuming that sample B corresponds to the PM max, heating this sample at higher temperature would induce lowering of the PM value with increasing temperature. The PM values are 0.6 and 0.72 for 110 and 140°C respectively. The upward shift of the ZFC curve at 110°C is higher than that at 140°C. One should expect the contrary by referring to the PM evolution curve of Aubourg & Pozzi (2010) (Figure V.12). The PM value of the 110°C heated sample should be higher than that of the 140°C heated sample. One should retain the overall trend of decreasing the PM value when heating at higher temperature a sample close to the PM max. It is possible that the samples can not be compared quantitatively due to the use of different aliquots of a same sample. Also the fact that samples are let dry out over night might have affected the PM value.

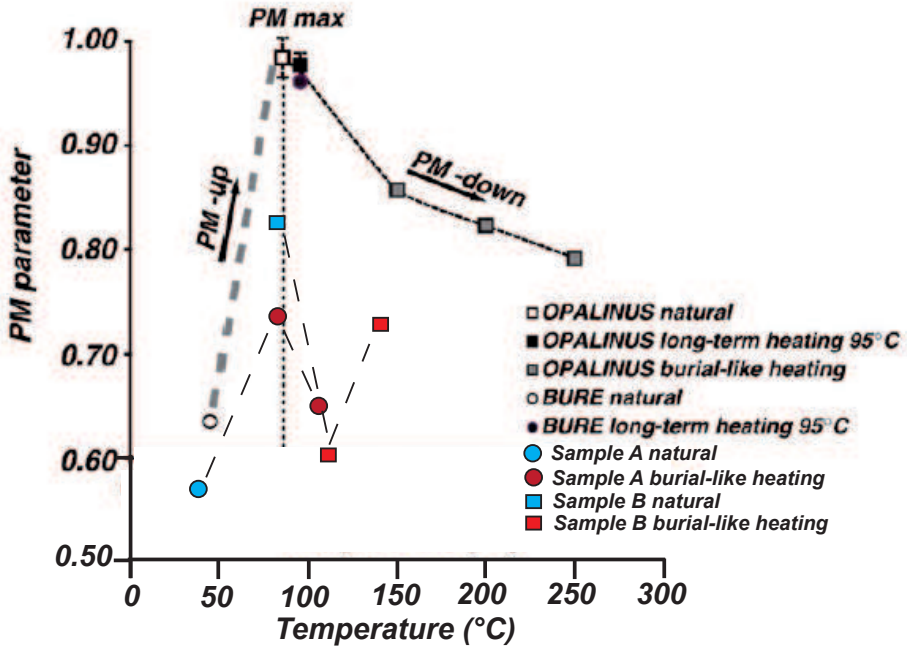

Figure V.12 – Evolution of the PM parameter measured after heating with temperature compared to the Aubourg & Pozzi (2010) model

2.2 ∼100-day heating experiments

To complete results obtained in the first series of gold capsules heating, a second experiment was performed. In this case, only the sample A is used. 4 aliquots (C1, C2, C3 and C4) are placed in the autoclaves. Two series of heating were done. The first series consists of heating the gold capsules at 80, 90, 110 and 130°C for 110 days. The low temperature measurements protocol changed compared to the 80-day heating experiment. In this case, the gold capsules are not opened after heating but rather, the MPMS measurements are performed on the gold capsule directly. Keeping the gold capsules closed is intended to prevent from possible oxidation and/or air pollution effect.
It should be pointed out that the measured remanence for capsule C3 heated to 130°C cannot be interpreted, most likely because of a probably asymmetrical distribution of the powder inside the gold capsule.

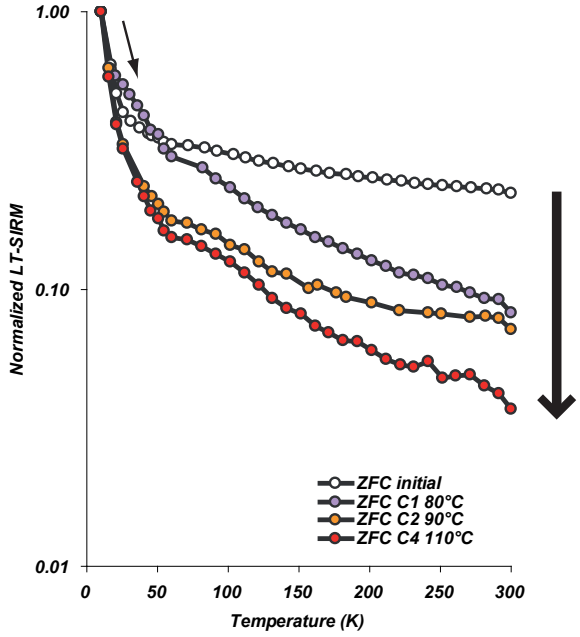

Figure V.13 – Evolution of ZFC curves for gold capsules heated at 80, 90 and 110°C compared to the original signal. The curves show a downward trend.

The evolution of the ZFC curves for this first series is represented in Figure V.13. The ZFC curves display an increasing downward shift with increasing heating temperature. The gold capsule C1 shows a slightly different behavior compared to the other capsules in the 10-50 K temperature range. To date, no explanation was found. The warming curve of the 110°C heated C4 capsule displays a downward shift more important than the one of the C2 capsule. These two capsules, C2 and C4, display a slight Verwey transition at ∼110-120 K suggesting that magnetite is formed. As it was the case for the 80-day heating experiment, one should retain the qualitative trend of increasing PM value with

increasing temperature in the case of the PM Up branch described by Aubourg & Pozzi (2010). The fact that the experimental results are slightly different to that of Aubourg & Pozzi (2010) could be due to the experimental conditions that are not those encountered in nature (duration, pressure...). Thus the experimental PM max value might occur at a temperature different of that occurring in natural conditions. The experimental heating rate is approximately 100°C/30 min. This is very different from natural heating rate of 10°C/Ma for a subsiding sedimentary basin.

A second series of heating was done on the same gold capsules by increasing temperature of 30°C compared to the initial experiment (Figure V.14). C1, C2, C3 and C4 were heated to 110, 120, 160 and 140°C respectively.

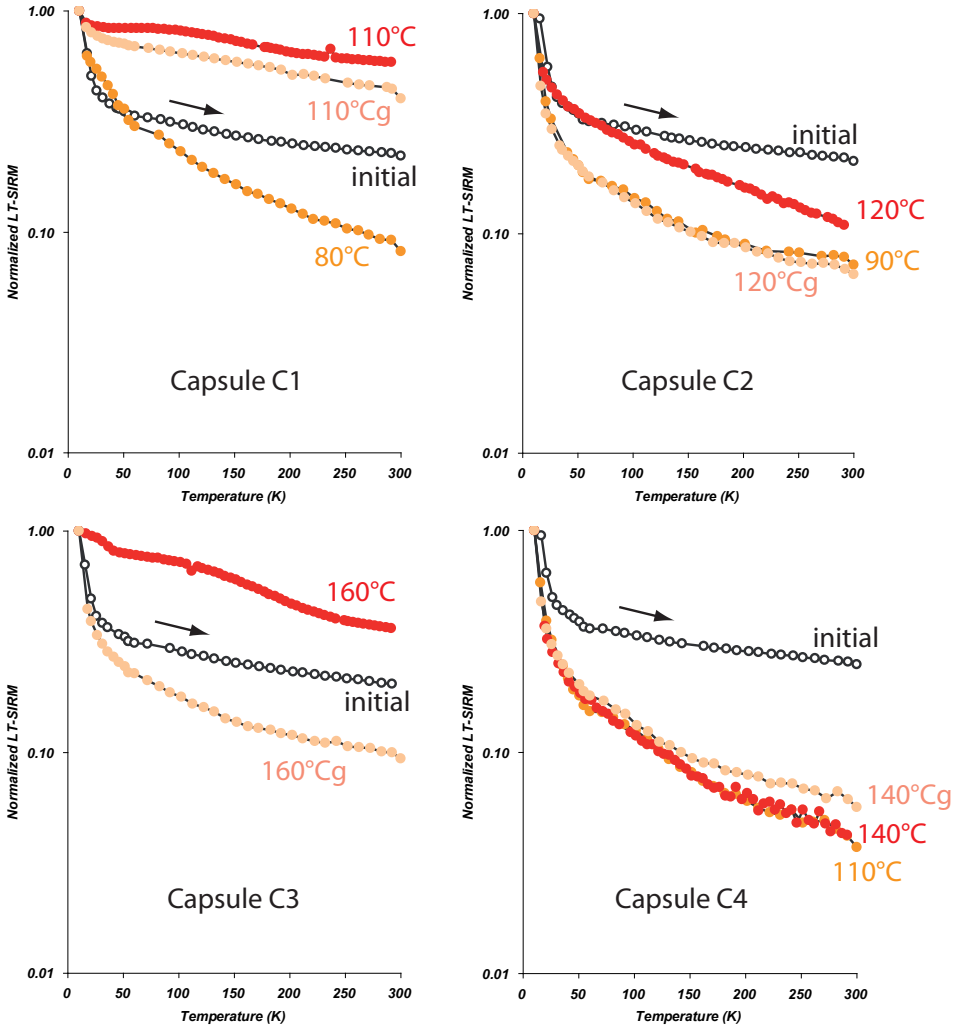

Figure V.14 – Evolution of the ZFC curves obtained for the 4 gold capsules in the two series of ∼100 day heating experiments. "g" stands for gelcap.

The low temperature measurements revealed evidence of some pollution effect (e.g. black residue incrusted in the gold capsule) and were therefore not interpretable for two capsules (C1 and C3). In order to circumvent this problem, the gold capsules were opened and the sample recovered and placed in a gelatin capsule. The different ZFC curves were measured for the four capsules, one day after the gold capsule opening, and are represented in the Figure V.14. The capsule C1 shows a downward shift followed by an upward trend. The capsule C2 displays the same pattern at 90 and 120°C but the ZFC curve for 90°C and for the gelcap are superimposed. C3, as a result of the uneven distribution of the sample inside the gold capsule, does not show any usable results, and the downward trend of the C3 gelcap ZFC curve is meaningless. C4 displays a downward trend and the ZFC curves for 110 and 140°C heating temperature are superimposed. The ZFC curve of the C4 gelcap is slightly upward compared to the 140°C heated C4 gold capsule. The magnetic values (Table V.4) do not show any distinct trend. However, it seems that the RT-SIRM$_{300K}$ value decreases by a factor of 2 to 8 after the first series of heating in the autoclaves. The LT-SIRM$_{10K}$ also decreases but less drastically. RT-SIRM$_{300K}$ and LT-SIRM$_{10K}$ seem to increase when heated again at a higher temperature.

Capsule	**Mass (mg)**	**T (°C)**	**RT-SIRM$_{300K}$ (μAm^2/kg)**	**LT-SIRM$_{10K}$ (μAm^2/kg)**	**PM**
C1	288	natural	265	1120	0.62
		80	122	1150	0.54
		110	ND	3520	0.16
	247	110	3190	6220	0.26
C2	250	natural	313	1410	0.61
		90	74	902	0.73
		120	ND	1110	0.6
	217	120	151	1930	0.76
C3	268	natural	290	1400	0.63
		130	ND	ND	ND
		160	ND	7280	0.15
	233	160	221	2040	0.72
C4	243	natural	344	1310	0.57
		110	47	947	0.76
		140	ND	890	0.77
	221	140	138	1770	0.75

Table V.4 – Magnetic values of the 4 gold capsules. The values represented in this table have to be taken with caution, as a result of the non homogenous distribution of the sample inside the capsule and of pollution effect.

The ∼100 day heating experiments in gold capsules therefore do not provide very conclusive results. This is largely due to pollution effect (e.g. C1) and non homogeneous distribution of the powder inside the capsule (e.g. C3).

3 Synthesis of the heating experiments

The aim of the heating experiments was to describe and quantify experimentally the evolution of parameter PM with increasing temperature (experiments under pressure) and to better understand the nature of the neoformed magnetic minerals (experiments under magnetic field). However, in doing so we must recognize that the heating experiments differ from natural conditions in several aspects. Nevertheless, beyond these limitations, the results of the heating experiments provide valuable information.

A very interesting result that we obtained is the quasi similarities of magnetic results while we are running in parallel two different immature claystones : the Jurassic Bure argillites and the Oligocene Boom Clay. This was observed for the two series of experiment A (Figures V.4 and V.5). The magnetization of the samples increases rapidly in the first hours/days of the experiment and then stabilizes. A wider temperature range (50-130°C) of the heating experiment performed only on Bure claystones leads to similar observations for each temperature step (Figure V.8). Similar kinetics and similar magnetic assemblage suggest that the different experiments reflect a single process. This has two main implications :

1. it reinforces the assumption that the processes leading to the establishment of the MagEval geothermometer is the same in argillites of different nature
2. the reaction site (incubator) is similar (pyrite ? calcite ?) and the reaction occurs in situ.

Our results indicate that production of magnetic minerals stops very rapidly at a given temperature. Though we do not exclude the formation of other magnetic minerals such as goethite and iron sulfides, the results of the 50-130°C experiment (Kars *et al.*, in revision, appendix 2) can be interpreted with a grain size evolution of magnetite. During heating, magnetic grains are formed (Figure V.15). We suggest that nano magnetite < 20 nm is responsible for the unstable TVRM observed. We do not exclude the participation of large > 1 μm magnetic minerals, but the whole evolution is consistent with the growth of nano minerals. They grow continuously as temperature increases, as suggested by the continuous drop of the remanence between 10 and 35 K (PM, Figure V.12). This is also observed in the results of confined heating experiments (gold capsules) in autoclaves under a pressure (100 MPa). Grains with size > 20 nm are responsible for the CRM which increases with increasing temperature. Eventually, these neoformed minerals may overcome the original magnetic record, possibly leading to a complete remagnetization of the sedimentary rocks (from 220°C by considering very weak NRM on the order of 1 $\mu Am^2/kg$) (Kars *et al.*, in revision, appendix 2).

The gold capsules experiments do illustrate that SP particles are produced, however results are not clear cut. The formation of magnetic minerals is on the order of a few ppb and it is likely that a part of magnetic fraction is altered, as it may be suggested by the decrease of the RT-SIRM$_{300K}$ after the first heating series. Quantifying neoformed magnetic minerals is not possible, contrary to the under magnetic field heating experiment.

The results of our experiments therefore do demonstrate that magnetic particles are produced and grow as a result of temperature increase, according to a distinct single reaction process which could not be fully characterized in our work. However, these results can be transposed to natural burial in sedimentary basin to state that continuous production/removal of magnetic minerals takes place in sediments being buried and that chemical reactions involving iron are maintained throughout increasing burial.

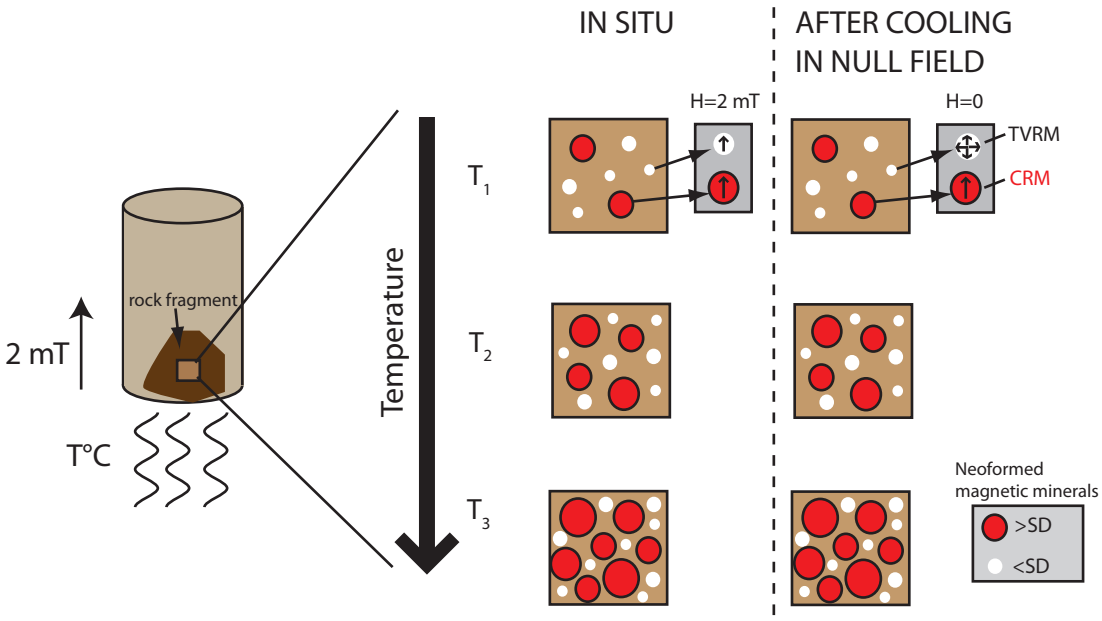

Figure V.15 – Interpretative sketch of formation/growth of the magnetic minerals during heating experiments. With increasing temperature (from T_1 to T_3), both >SD and <SD grains are neoformed. When applying a magnetic field, both are magnetized. When cooling in a null field, only >SD grains acquire a remanence (chemical remanent magnetization CRM) while <SD grains exhibit random moment and characterize in part the thermoviscous remanent magnetization (TVRM).

Part C

Field Case Studies

Chapter VI

MAGNETIC ASSEMBLAGE IN THE GRES D'ANNOT BASIN, SE FRANCE

The Grès d'Annot turbiditic basin in SE France has been the object of many sedimentary studies over the years (e.g. Joseph & Lomas, 2004) in academic as well as industrial spheres. It is still being studied today. One major interest relates to the architecture of the turbidite sandstones bodies, in order to improve the characterization of analogous deep-water subsurface hydrocarbon reservoirs, where topography has played a key role. The Grès d'Annot basin is now considered as a benchmark example of a sand-rich delta-fed turbidite system.

Recently, Labaume *et al.* (2008) integrated different techniques to estimate paleotemperatures in the Grès d'Annot area. Here, we used a magnetic approach to characterize diagenetic up to low-grade metamorphic episodes in the sedimentary rocks which underwent a burial gradient from west to east. It is expected to reach the "pyrrhotite window" ($T > 250°C$), where neoformed magnetites are progressively consumed to the benefit of pyrrhotite.

1 Presentation of the study area

The Western Alps describe a 90° arc which developed in the Cenozoic when the Apulian or Adriatic microplate collided with the European passive margin subducting toward the south (Ford & Lickorish, 2004). The Tertiary outer foreland basins recorded the northeastern advances of the Apulian plate on the European passive margin. In the southwestern part of the Alpine arc, the Tertiary depocenters of the subalpine chains, containing the Grès d'Annot and the Grès du Champsaur, were part of the foreland basins.

The Eocene-Oligocene Grès d'Annot outcrops are observed in an area between the eastern Maritime Alps and the Digne thrust front which represents the western margin, but also in the Devoluy and Champsaur sectors. Southwards the Grès d'Annot are limited by the Maures-Estérel crystalline massif and eastwards by the Argentera-Mercantour massif and the Embrunais-Ubaye Alpine nappes (Figure VI.1 ; Apps *et al.*, 2004).

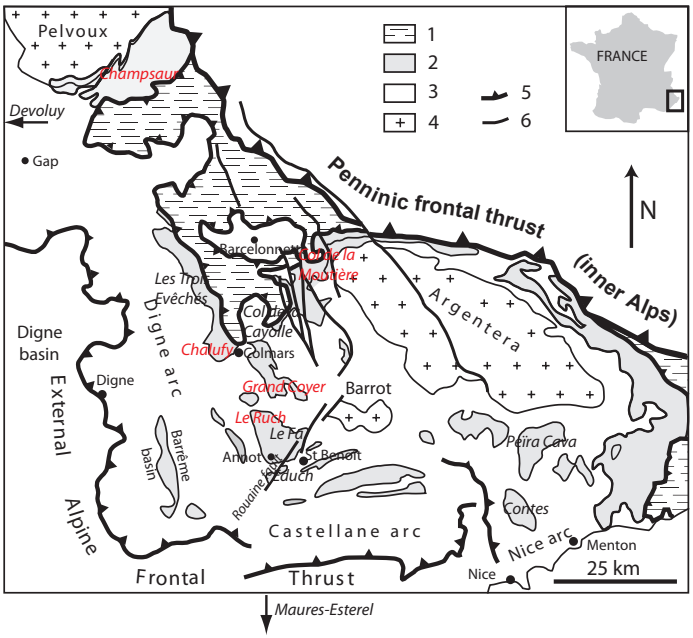

Figure VI.1 – Location map of the study area (modified from Labaume *et al.*, 2008). 1 : Embrunais-Ubaye nappes, 2 : Grès d'Annot formation and its shallow-water lateral equivalent, and underlying tertiary strata, 3 : Mesozoic, 4 : Paleozoic substratum (crystalline basement), 5 : base of allochthonous thrust units, 6 : normal and strike-slip faults

1.1 Geological history of the Grès d'Annot area

The SE France region underwent three different orogenic events (Apps *et al.*, 2004).

In the Late Cretaceous, the Greater Iberia block - consisted of Iberia, Corsica, Sardinia, Calabria and other fragments - anticlockwise rotated leading to the opening of the Bay of Biscay and the closing of the Pyrenean and Provençal basins (Figure VI.2A).

In the Paleocene, the completed collision with SW Europe produced the Pyreneo-Provençale mountain belt (Figure VI.2B). From Maastrichtian (Upper Cretaceous) to Paleocene-Eocene, the subduction of the Tethyan oceanic crust under the SE margin of Greater Iberia occurred. This created an orogen along that margin referred to as the East Iberian orogeny which is genetically separated from the Alpine orogeny sensu stricto (Figure VI.2B ; Apps *et al.*, 2004).

The evolution of the foreland basins system in the Tertiary reflected the changes in the flexural behavior of the European Plate during the collision, and the major geodynamical events related to the orogeny. In the Middle Eocene (50-35 Ma, Figure VI.2C), the SW compressive Alpine orogeny affected the study area producing local thrust and fold topography. Transgression and subsequent deepening of the Grès d'Annot basin were caused by the Alpine orogenic wedge loading on the European margin. The East Iberian orogen to the south of the basin was still active and resulted in uplift of the granitic massifs of Corsica-Sardinia and Maures-Estérel. The erosional derived products were clastic sediments

deposited as the turbidites of the Grès d'Annot formation.

In the Late Rupelian (Early Oligocene, 34-24 Ma), in the SE of France, the advance of the main Alpine thrust front toward the west filled the remaining accommodation space, first by a massive influx of products derived from the orogeny (Schistes à Blocs) and then by the Alpine thrust flysh nappes (Embrunais-Ubaye nappes for instance) that took place over the Eocene foreland basin (Figure VI.2D). At the same time, to the south of the basin, the rifting of a continental mass begun. The onset of the rifting of the Gulf of Lion is estimated at 30 Ma, and that of the Corsica at ∼32 Ma. The rifting diverted away the sediments supply from the Corsica-Sardinia massifs leading to the death of the Grès d'Annot basin.

Between 32 and 19 Ma, the orogeny was a post-collision phase. The major steps of thrusting occurred in the Alpine outer and inner zones.

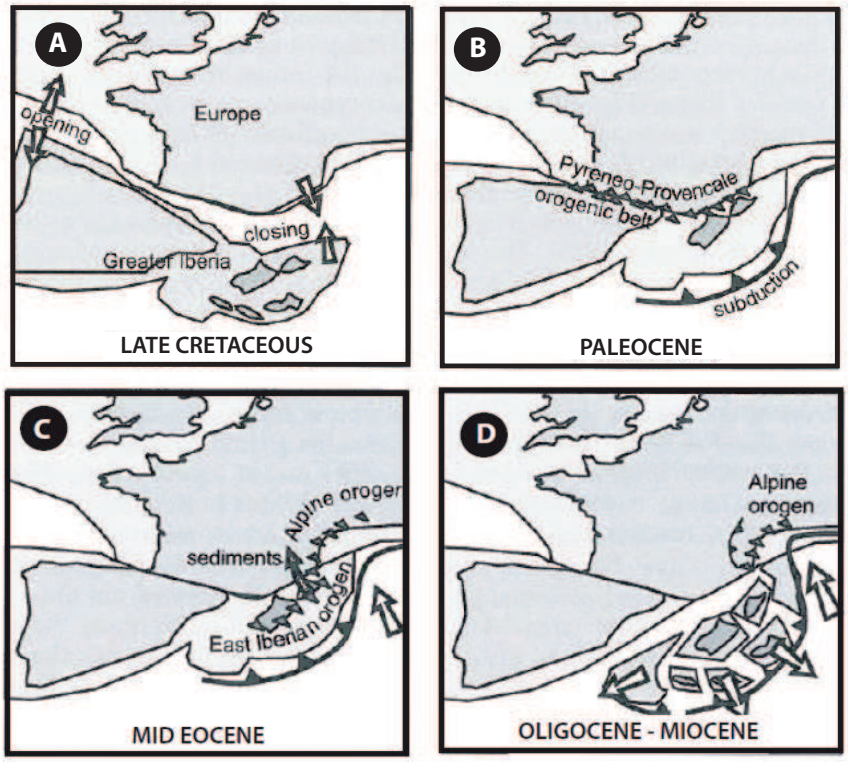

Figure VI.2 – Evolution of the plate motion from Late Cretaceous to Miocene (from Apps *et al.*, 2004)

1.2 Stratigraphy

The Eocene-Oligocene lithostratigraphic succession of the Annot area (Figure VI.3) lies unconformably over a Cretaceous substratum (Santonian limestones and Campanian calcareous marls) or even the basement, near the Champsaur locality. Locally, this substratum is affected by E-W Pyrenean

folds (Early Tertiary).

In the Educh and Le Ruch area (Figure VI.1), the alternation of bored-pebbles conglomerates and shells-rich limestones represents the first Paleogene deposits, called Conglomérats d'Argens or Poudingues d'Argens (Gubler, 1958). These are continental to littoral conglomerates locally associated with erosion surface paleoreliefs (Apps *et al.*, 2004). The pebbles content disappears progressively toward the top of the formation and the sedimentary content evolves progressively toward the Calcaires Nummulitiques. This formation is called Infra-Nummulitic Conglomerates (Conglomérats Infra-Nummulitiques ; Callec, 2004).

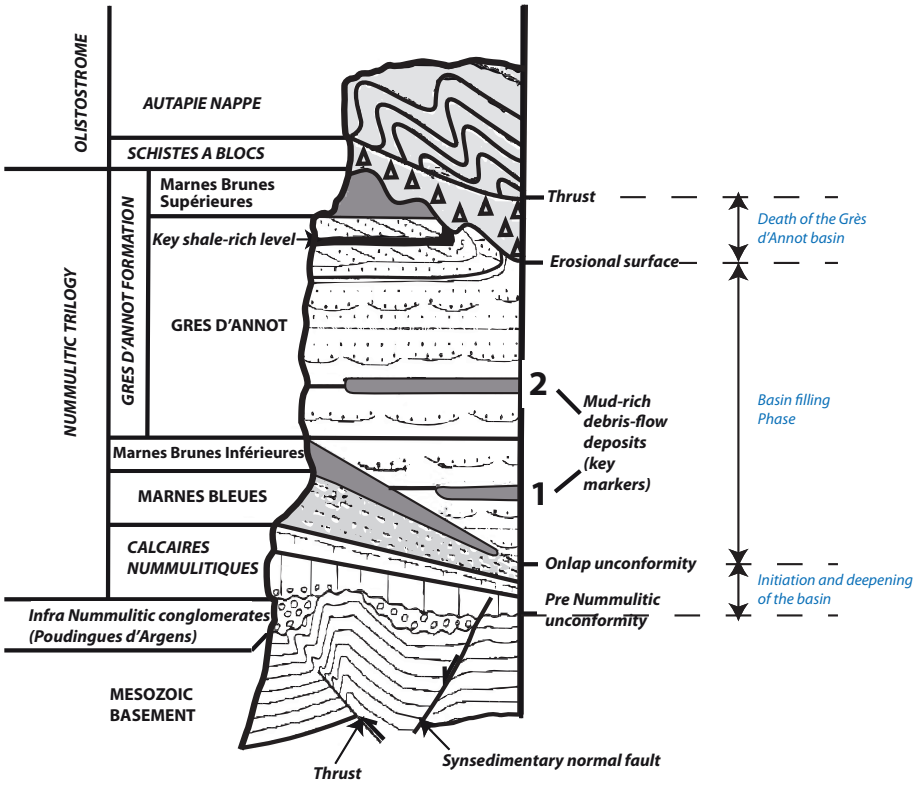

Figure VI.3 – Lithostratigraphic sequence of the Eocene-Oligocene Grès d'Annot basin (modified from Joseph & Lomas, 2004)

The Calcaires Nummulitiques in the Annot basin are characterized by a quite homogeneous range of bioclastic calcareous facies, with 5 m thick beds (Besson, 1972). These facies are interpreted as shallow marine platform deposits of the Tertiary basin transgressive phase. The transgression was induced by the flexural subsidence of the crust by the Alpine Orogeny (Allen *et al.*, 1991 ; Sinclair, 1997). Alternation of shell-rich calcarenites and calcareous marls, known as the Intermediate Limestones (Besson, 1972), constitutes the transitional formation toward the subjacent Marnes Bleues. These formations present strong thickness variations through the Rouaine fault zone, becoming thicker in the eastern

area of St Benoît (Besson *et al.*, 1970). The Calcaires Nummulitiques are also diachronous with the oldest beds in the East (Lutetian) and the youngest in the West (Campredon, 1977).

The Marnes Bleues (globigerina marls) are mudstones intercalated with claystones and calcarenites. The abundant planktonic fauna (benthic and planktonic foraminifera) records low sedimentation rates. These hemipelagic deposits show the progressive deepening of the basin during this time (Mougin, 1978 ; Apps *et al.*, 2004). The upper part of the Marnes Bleues in the northern areas (Le Ruch and Le Fa areas) often displays a silty marl interval which represents downhill deposits of several meters thick. This interval indicates the transition toward the Grès d'Annot formation and corresponds to the formation of the Marnes Brunes Inférieures (Lower Brown Marls) described in the north of the basin (Jean, 1985 ; Ravenne *et al.*, 1987). The shallower marls of the Marnes Bleues formation record the deepest water depths reached by the foreland basin and date the onset of siliciclastic turbidite deposits over the basin (Campredon, 1977 ; Callec, 2001). The Marnes Bleues thickness varies through the Rouaine fault zone, from 60 up to 400 m thick in the St Benoît area (Besson *et al.*, 1970).

The Infra-Nummulitic Conglomerates, the Calcaires Nummulitiques and the Marnes Bleues constitute the Bartonian-Priabonian (Late Eocene) marine transgression. This succession characterizes a general progressive deepening of the Annot basin from shoreface to bathyal environment (Mougin, 1978 ; Apps, 1987 ; Pairis, 1988). It is overlain by a sand-rich interval of Late Priabonian-Early Rupelian age as a result of an increasing supply of sediments inside the basin. This interval is the Grès d'Annot.

The Grès d'Annot are siliciclastic turbidites which are preserved in the Tertiary synclines of Col de la Cayolle, Trois Evêchés, Grand Coyer, Annot, Peïra Cava, Contes and Menton (Figures VI.1 and VI.4). They lie in onlap on the globigerina marls or on the Marnes Brunes. These turbidites represent a drastic increase in the sediments supply and in the sedimentation rate in the southwestern alpine foreland basin. They also indicate a progressive infill of the flexural topography. The Grès d'Annot turbidites originate from a granitic high relief mountain belt on the south, which the remains are now found in Corsica and in Sardinia (Keunen *et al.*, 1957). This is confirmed by regional paleocurrents data that show a dominant axial flux northward and westward from a southern source (Apps *et al.*, 2004). Globally, the Grès d'Annot display a cumulated sedimentary infill of more than 600 m thick in the Annot basin. They present a typical progradational lithology which thickens and becomes coarser toward the top of the sedimentary sequence (e.g. Mutti, 1992).

The Nummulitic Trilogy (Calcaires Nummulitiques, Marnes Bleues and Grès d'Annot) in the eastern area is affected by the Rouaine sinistral synsedimentary faults zone, with a differential development of the thickness for each formation. The Tertiary Trilogy is locally capped by the Oligocene Schistes à Blocs Formation. This latter constitutes a ∼100 m thick submarine olistostrom, lying immediately underneath the inner Alpine Embrunais-Ubaye nappes. This formation comprises a wide variety of deep water gravitational sedimentary deposits. It is interpreted as debris fed by in progressing Embrunais-Ubaye nappes and its deposit preceded the emplacement of the nappes themselves (Kerckhove, 1969). The Grès d'Annot constitute therefore the footwall of the nappes emplacement and are closed to the main detachment where fluid circulation is likely.

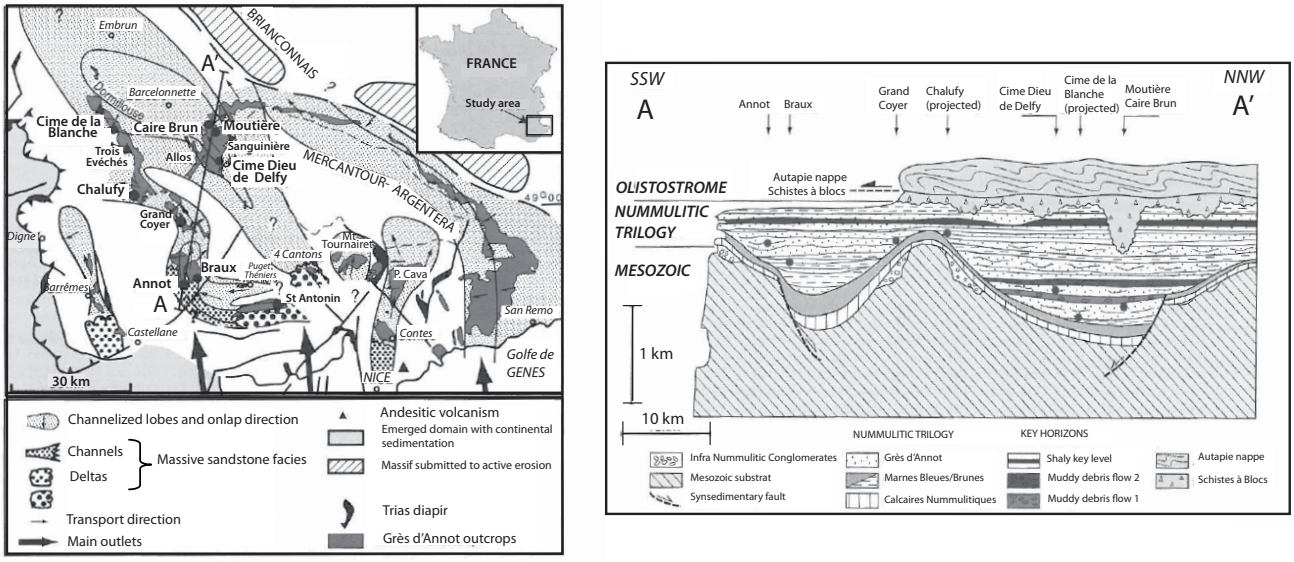

Figure VI.4 – Paleogeography of the Grès d'Annot area (after Garcia *et al.*, 2004)

1.3 Organization of the depositional system - Paleogeography

The basin deepening was accompanied by the formation of NNW-SSE folds, the anticlines forming the deep sea highs (Argentera, Barrot Massifs), the synclines forming the troughs within the Grès d'Annot were deposited (Figure VI.5 ; Apps *et al.*, 2004). The sediments at the origin of the Grès d'Annot came from the reliefs of the Corsica-Sardinia Massif uplifted by the Pyreneo-provençale Orogeny (Jean *et al.*, 1985 ; Garcia *et al.*, 2004). The deposition within the troughs was in their axis and formed turbiditic flows from SE to NW (Jean *et al.*, 1985 ; Ravenne *et al.*, 1987).

The different facies of the Nummulitic Trilogy display an important diachronism reflecting the westward shift of the sedimentary environments and of the depocenters (Sztrakos & Du Fornel, 2003 ; Du Fornel *et al.*, 2004 ; Joseph & Lomas, 2004). The Calcaires Nummulitiques, characterizing the progression of the marine transgression, and the Grès d'Annot, representing a successive infill of the different troughs, display ages going from Bartonian in the East to Priabonian in the West.

The organization of the Grès d'Annot facies forms a model of turbiditic ramp fed by prograding fan-deltas (Du Fornel *et al.*, 2004 ; Guillocheau *et al.*, 2004). Downhill the fan-deltas, the architecture of successive facies is constrained by the structural troughs. Firstly, there are transit channels strongly erosive, and then lobes of elongated deposits and finally distal turbiditic nappes (Figure VI.5). These deposits show lateral onlap geometry on the troughs flanks (Jean *et al.*, 1985). The infilling of these channels corresponds to hyperconcentrated coarser flow deposits. The lobes and the distal turbiditic nappes are organized sequentially into two superposed lithologic members (Du Fornel *et al.*, 2004 ; Guillocheau *et al.*, 2004) :

– The "heterolithic" lower member constituted of tabular alternations of centi-decimeter sandy layers and centimeter pelitic levels ;
– The "homolithic" upper member constituted of massive beds of coarser sandstones.

These sequences are interpreted as prograding bodies deposited by flows of low (lower member) and high (upper member) density during the 20 ka cycling variation of the sea level.

In the Late Rupelian, the Schistes à Blocs and then the Embrunais-Ubaye nappes (∼30-28 Ma) covered the eastern part of the basin (Kerckhove, 1969). The emplacement of the nappes, but also the aperture of the Ligurian Gulf (Séranne, 1999), suppressed the feeding zone of the turbiditic system and then ended the sedimentation of the Grès d'Annot.

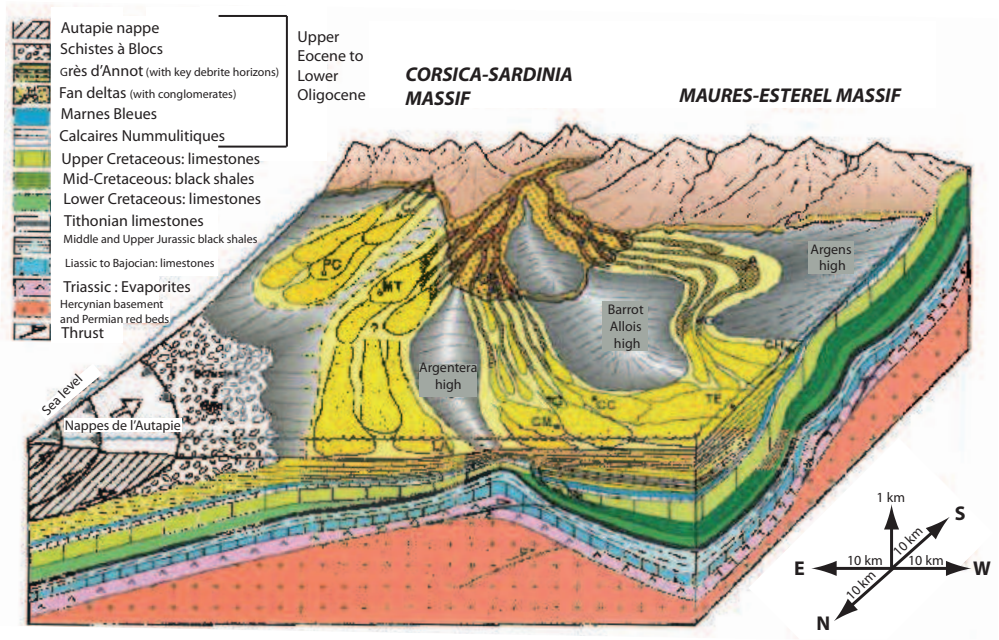

Figure VI.5 – Schematic tectono-sedimentary organization of the Grès d'Annot system in the Rupelian (Joseph & Lomas, 2004)

1.4 Burial history

The burial and diagenetic evolution of the Grès d'Annot is divided in two major steps :

– An early diagenesis as a result of a shallow sedimentary burial ;
– A late diagenesis related to deep burial underneath the Alpine nappes.

The Schistes à Blocs, intercalated between the Grès d'Annot formation and the Alpine nappes, have a low thickness on the order of a hundred meters. This implies that burial of the Grès d'Annot was essentially due to the nappes tectonic load which emplacement started in submarine domain just after the deposition of the Grès d'Annot. The Grès d'Annot were thus exhumed as a result of the uplifting

of the external crystalline massifs (Argentera, Pelvoux) and of the Barrot Dôme at the end of the Oligocene but essentially in the Miocene.
The studied cross-section (from Annot on the SW to Bersezio on the NE) is oriented parallel to the tectonic load following the lateral erosion fringe of the Embrunais-Ubaye nappes to underneath the Penninic Front. Petrologic and thermochronologic studies permitted to determine its burial and exhumation history (Souquière, 2005 ; Labaume *et al.*, 2008).
Based on Apatite Fission Tracks Analysis (AFTA), the section can be divided into 3 successive zones with maximum paleotemperature increasing from SW to NE (Figure VI.6) :

- In the SW, in the Annot region (A), the very low partial annealing of the fission tracks indicates that the temperature did not exceed 60°C. This zone is the outer area ;
- In the North of the Annot massif and in Grand Coyer (GC), the fission tracks were partially annealed. This indicates a temperature comprised between 60 and 110°C. This zone is called intermediate area ;
- In the NE of the Grand Coyer, the fission tracks are totally annealed leading to a temperature higher than 110°C. This zone constitutes the inner area.

The trend of increasing paleotemperature from SW to NE, revealed by AFTA, is confirmed and completed by the results of petrological studies (Souquière, 2005 ; Labaume *et al.*, 2008). Indeed, silica diagenesis is more developed from the SW to the NE. The silica transfer by pressure-solution is very low in the outer area and increases progressively toward the inner area. This allows to position the 80°C isotherm in the intermediate area, in agreement with the AFTA isotherms (Figure VI.6). The abundant presence of sericite (white mica) in the Bersezio area indicates that a temperature of about 200°C was reached at this site.

Vitrinite reflectance Ro data available in this study area (Barlier *et al.*, 1974 ; Pickering & Hilton, 1998 ; Labaume *et al.*, 2008 unpublished report) display an increasing value trend from SW to NE, from 0.3% in the Rouaine area up to $> 7\%$ underneath the Penninic Front (Gias Vallonetto area) (Figure VI.7). The increase of Ro is not constant through the study area. The evolution is rather low and progressive in the outer area (0.5-0.65%). In the intermediate area, Ro values range from 0.5% in Le Ruch area to a maximum of 1.1% in the Grand Coyer sector. By contrast, in the inner area, the values are higher and increase more rapidly (from $\sim$4% in La Moutière to more than 6% in Gias Vallonetto). Based on the calibration established by Vassoyevitch *et al.* (1970), and assuming a geothermal gradient of 30°C/km (Bigot-Cormier *et al.*, 2006) and a same age for the maximum burial, Labaume *et al.* (2008 unpublished report) reconstructed the burial and thermal history of the Grès d'Annot area :

- The outer area experienced burial temperature of 45°C in the Rouaine sector and 65°C in the Braux sector, and a maximum burial depth of 2-2.5 km ;
- The intermediate area underwent higher temperatures of about 65-70°C in Le Ruch up to 110°C in Grand Coyer ;

– The inner area, when approaching the Penninic Front, is characterized by paleotemperatures higher than 200°C, up to 270°C in Gias Vallonetto. The maximum burial depth varies from 3.5 to 4.5 km, up to 5-6 km underneath the inner part of the Embrunais-Ubaye nappes and about 8 km just below the Penninic Front.

From a chronologic point of view, AFTA showed that, in the intermediate and inner areas, the Grès d'Annot were exhumed during the Upper Miocene (Labaume *et al.*, 2008 unpublished report). The maximum burial was reached during the thrusting of the Penninic Front and the Parpaillon nappe, probably at ∼28 Ma.

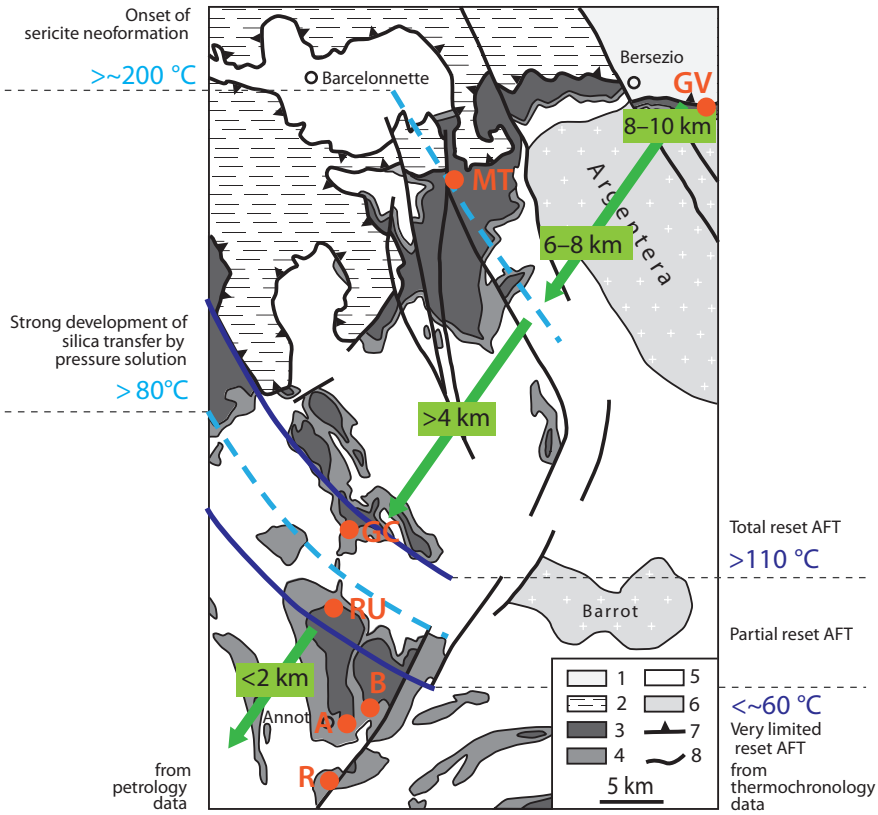

Figure VI.6 – Schematic structural map of the study area with the estimated paleotemperatures and burial depths (Labaume *et al.*, 2008). 1 : Penninic unit, 2 : Embrunais-Ubaye nappes, 3 : Grès d'Annot formation, 4 : pre-Grès d'Annot Tertiary strata, 5 : Mesozoic, 6 : Paleozoic substratum, 7 : base of allochtonous thrust units, 8 : normal and strike-slip faults, A : Annot, B : Braux, GC : Grand Coyer, GV : Gias Vallonetto, MT : La Moutière, R : Rouaine, RU : Le Ruch

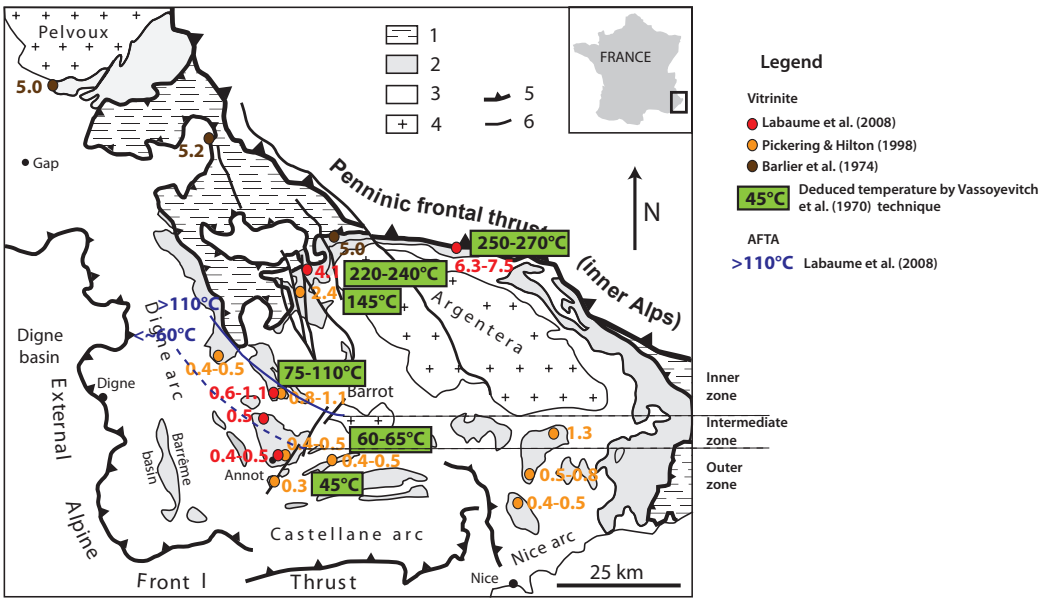

Figure VI.7 – Vitrinite reflectance data distribution and estimated paleotemperatures (Labaume *et al.*, 2008 ; unpublished report). Same legend as Figure VI.1.

The reconstruction of the thermal history shows 4 stages in the sedimentary evolution of the Grès d'Annot basin (Figure VI.8) :

- A weak sedimentary deepening of a few hundred meters in 32-36 Ma ;
- A very fast burial underneath the nappes for 4-6 Ma with a maximum burial at 28 Ma ;
- An uplift phase until 10-5 Ma with a mean rate of 8°C/Ma for the inner zone and a slower rate for the outer and intermediate areas ;
- A recent exhumation (since 5-10 Ma) more rapid for the inner area.

This interpretation however requires additional investigation to be confirmed.

2 Sampling and Methods

2.1 Sampling

Samples were collected at 13 different sites in October 2009. We collected a total of 27 samples to which 18 provided to us by P. Labaume were added (Table VI.1). The sampled area describes a SW-NE transect from the Rouaine area to the Gias Vallonetto sector (Figure VI.9). The temperature range and the burial depth cover the entire burial history of the Grès d'Annot formation. The samples are mainly claystones and are from the shale level occurring in the Nummulitic Trilogy (mainly Marnes Bleues).

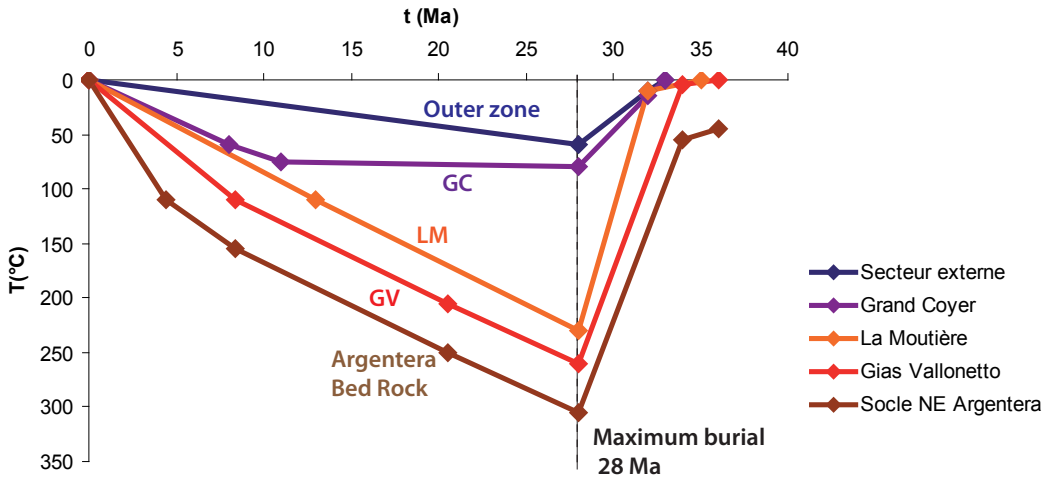

Figure VI.8 – Reconstitution of the thermal history of the Grès d'Annot area (Labaume *et al.*, 2008 ; unpublished report)

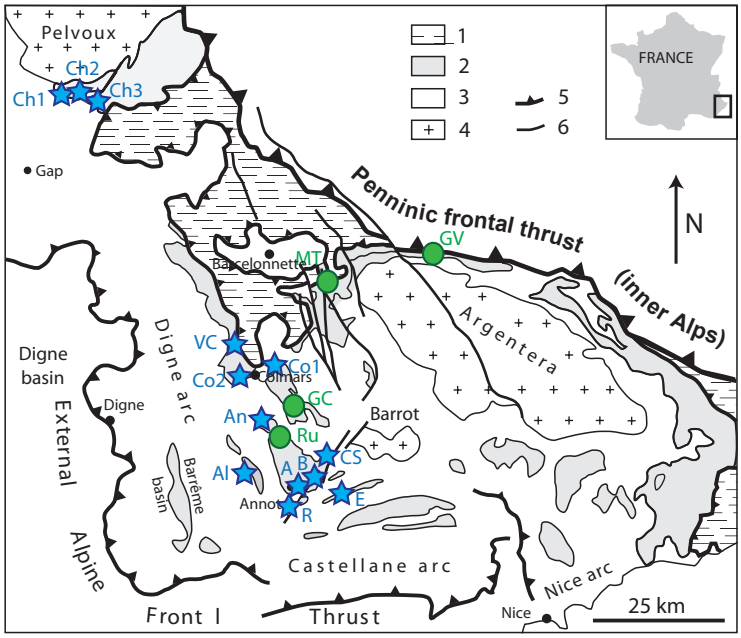

Figure VI.9 – Location map of the collected samples in the SE France (map from Labaume *et al.*, 2008). Stars : location of samples collected by us ; circles : location of samples provided by P. Labaume. Same legend as Figure VI.1. Sites names are given in Table VI.1.

Sampling site	Age	Sample	Latitute (°)	Longitude (°)	Altitude (m)	Facies
Allons (Al)	Eocene - Oligocene	1A	N43°59'05.9"	E 6°34'56.3"	1050	marl
		2A	N44°0'09.4"	E 6°34'11.1"	1014	conglomerates
		3A	N44°0'09.4"	E 6°34'11.1"	1014	graphite
Rouaine (R)		4A	N43°56'01.1"	E 6°40'12.9"	848	marl
		5A	N43°56'06.6"	E 6°40'29.4"	820	sandstones
Braux (B)		6A	N43°58'16"	E 6°42'17.2"	947	marl
		7A	N43°58'16"	E 6°42'17.2"	947	sandstones
Entrevaux (E)		8A	N43°56'47.0"	E 6°48'42.9"	755	marl
		9A	N43°56'47.0"	E 6°48'42.9"	755	sandstones
Castellet-les-Sausses (CS)		10A	N44°0'03.6"	E 6°45'12.7"	792	marl
Annot (A)		A0	N43°57'43.1"	E 6°40'34.6"	802	marl
		11A	NO GPS DATA			marl
		12A	NO GPS DATA			sandstones
Villars-Colmars (VC)		13A	NO GPS DATA			marl
		14A	NO GPS DATA			marl
		15A	NO GPS DATA			sandstones
Champsaur (Ch1)		16A	N44°41'27.2"	E6°09'44.0"	1636	marl
		17A	N44°41'27.2"	E6°09'44.0"	1637	marl
Champsaur (Ch3)		19A	N44°40'44.3"	E6°16'22.8"	1344	marl
Nord Annot (An)		20A	N44°02'12.0"	E6°36'25.6"	1302	marl
Colmars (Co1)		21A	N44°09'11.1"	E6°32'41.2"	1876	marl
		22A	N44°09'26.2"	E6°32'29.1"	1802	marl
		23A	N44°09'49.3"	E6°31'50.7"	1866	marl
Colmars (Co2)		25A	N44°09'07.7"	E6°40'28.7"	1795	marl
		26A	N44°09'26.9"	E6°39'19.0"	1648	marl
Le Ruch (Ru)		RUmg	N44°02'40.5"	E 6°40'28.1"		marl
		RUmb	N44°02'40.5"	E 6°40'28.1"		marl
Grand Coyer (GC)		CY1p	N44°05'09.1"	E 6°41'0"		marl
		CY3p	N44°05'09.1"	E 6°41'0"	265	marl
		CY5	N44°05'09.1"	E 6°41'0"	375	marl
		CY6	N44°05'09.1"	E 6°41'0"	358	marl
		CY7	N44°05'09.1"	E 6°41'0"	390	marl
		CY8	N44°05'09.1"	E 6°41'0"	317	marl
		CY10	N44°05'09.1"	E 6°41'0"		marl
		CY11	N44°05'09.1"	E 6°41'0"	315	marl
La Moutière (MT)		MT12	N44°18'58"	E 6°47'46"		marl
		MT17	N44°18'58"	E 6°47'46"		marl
		MT29	N44°18'58"	E 6°47'46"		marl
		MT120	N44°18'58"	E 6°47'46"		marl
		MTmg	N44°18'58"	E 6°47'46"		marl
Gias Vallonetto (GV)		GV1	N44°21'41.7"	E 7°03'32.4"	270	marl
		GV11	N44°21'41.7"	E 7°03'32.4"	302	marl
		GVmg	N44°21'41.7"	E 7°03'32.4"	386	marl
Colmars (Co2)	Cret.	24A	N44°08'54.8"	E6°40'21.3"	1818	marl
Champsaur (Ch2)	Jur.	18A	N44°39'52.4"	E6°10'33.7"	1262	marl

Table VI.1 – Samples from the Grès d'Annot basin used in this study

2.2 Methods

We performed a series of different magnetic measurements on the samples. First, the low field magnetic susceptibility χ was measured at Ecole Normale Supérieure (ENS). The room temperature hysteresis loops and FORCs and low temperature MPMS measurements were done at the Institute for Rock Magnetism. The routine measurements are described in chapter III. 23 samples were chosen for the Lowrie test (Lowrie, 1990). SEM examination was conducted on 8 samples at ENS. Finally, X-ray diffraction analyses were done on the clay fraction of 23 selected samples in order to identify clays. These results would be an additional contribution to the thermal history of the study area. Table VI.2 indicates the different measurements performed on the studied samples.

Sampling site	Age	Sample	Xlf (SI)	RT-SIRM 300 K (Am²/kg)	LT-SIRM 10 K (Am²/kg)	SEM Obs.	X-Ray	"Lowrie Test"
Allons (Al)	Eocene - Oligocene	1A	7.38E-05	1.83E-05	3.87E-04			
		2A	2.89E-05	2.95E-05	3.17E-04	X	X	X
		3A	-9.91E-06	5.70E-06	1.10E-04			
Rouaine (R)		4A	5.43E-05	1.76E-05	3.14E-04		X	X
		5A	2.77E-05	2.89E-05	1.48E-04			
Braux (B)		6A	1.71E-04	4.24E-05	5.72E-04	X	X	X
		7A	1.23E-04	4.08E-05	3.99E-04		X	X
Entrevaux (E)		8A	2.25E-05	1.08E-05	2.56E-04		X	X
		9A	1.80E-05	1.69E-05	2.71E-04			
Castellet-les-Sausses (CS)		10A	7.90E-05	1.18E-05	1.44E-04		X	X
Annot (A)		A0	1.01E-04	2.81E-05	3.78E-04	X	X	X
		11A	2.61E-04	1.11E-04	7.02E-04			
		12A	1.70E-04	9.19E-05	9.05E-04		X	X
Villars-Colmars (VC)		13A	1.94E-04	2.69E-05	7.83E-04			
		14A	1.28E-04	7.23E-05	9.81E-04	X	X	X
		15A	2.05E-04	2.20E-04	8.16E-04		X	X
Champsaur (Ch1)		16A	2.86E-04	3.64E-04	2.61E-03		X	X
		17A	1.74E-04	2.96E-05	5.47E-04			
Champsaur (Ch3)		19A	2.11E-04	3.09E-05	1.19E-03			
Nord Annot (An)		20A	4.48E-05	2.85E-05	4.22E-04		X	X
Colmars (Co1)		21A	4.98E-05	2.04E-05	2.38E-04			
		22A	5.97E-05	2.46E-05	2.05E-04			
		23A	4.13E-05	2.81E-05	3.11E-04		X	X
Colmars (Co2)		25A	1.21E-04	7.81E-05	1.21E-03		X	X
		26A	1.25E-04	1.08E-04	9.01E-04			
Le Ruch (Ru)		RUmg	1.52E-04	1.16E-04	6.42E-04			
		RUmb	1.85E-04	5.93E-05	2.89E-03	X	X	X
Grand Coyer (GC)		CY1p	2.01E-04	3.16E-05	1.37E-03	X	X	X
		CY3p	2.20E-04	3.73E-05	5.08E-03		X	X
		CY5	2.29E-04	3.72E-05	1.33E-03		X	X
		CY6	2.51E-04	2.23E-05	1.53E-03			
		CY7	2.31E-04	3.54E-05	1.98E-03			
		CY8	2.29E-04	5.07E-05	4.61E-03			
		CY10	1.68E-04	2.39E-05	3.29E-04		X	X
		CY11	1.33E-04	4.54E-05	3.53E-04			
La Moutière (MT)		MT12	3.07E-04	3.52E-05	2.25E-03			
		MT17	2.59E-04	5.87E-05	7.15E-03	X	X	X
		MT29	3.01E-04	3.40E-05	3.21E-03		X	X
		MT120	1.98E-04	3.91E-05	3.36E-03			
		MTmg	1.30E-04	1.66E-05	4.67E-04			
Gias Vallonetto (GV)		GV1	2.39E-04	2.28E-05	1.03E-02		X	X
		GV11	2.44E-04	3.89E-05	7.09E-04			
		GVmg	2.55E-05	1.13E-04	5.38E-04	X	X	X
Colmars (Co2)	Cret.	24A	1.11E-04	3.09E-05	3.92E-04			
Champsaur (Ch2)	Jur.	18A	3.12E-04	1.04E-04	1.75E-03		X	X

Table VI.2 – Some magnetic data and petrographic-mineralogical analyses performed on studied samples

3 Magnetic assemblage in the Grès d'Annot basin, SE France

All the samples have $\chi < 500$ μSI and a saturation isothermal remanent magnetization (SIRM) at room temperature RT-SIRM$_{300K}$ in the range of 6 to 36 μAm^2/kg.

The low temperature measurements done on all the samples show characteristic magnetic features which are summarized in Table VI.3.

Combining high and room temperature magnetic measurements, 4 distinct magnetic signal types can be recognized in our data set (Figure VI.10). They are presented with respect to the tectonic/diagenetic areas in Figure VI.10 and described in detail thereafter.

			RT-SIRM curve				ZFC curve	
Sampling site	Age	Sample	V	P-beh.	G	Pyrr.	2-step	200 K
Allons (Al)	Eocene - Oligocene	1A						
		2A				?		
		3A	ininterpretable					
Rouaine (R)		4A				?		
		5A	?	?				
Braux (B)		6A						?
		7A						
Entrevaux (E)		8A		?		?		
		9A		?		?		
Castellet-les-Sausses (CS)		10A				?		
Annot (A)		A0						
		11A						
		12A						?
Villars-Colmars (VC)		13A						
		14A						
		15A				?		
Champsaur (Ch1)		16A		?				
		17A						
Champsaur (Ch3)		19A						
Nord Annot (An)		20A						
Colmars (Co1)		21A		?		?		
		22A						
		23A						
Colmars (Co2)		25A						
		26A						
Le Ruch (Ru)		RUmg		?			?	
		RUmb		?				
Grand Coyer (GC)		CY1p		?				
		CY3p		?				
		CY5				?		
		CY6				?		
		CY7				?		
		CY8				?		
		CY10						
		CY11						
La Moutière (MT)		MT12						
		MT17				?		
		MT29		Néel?				
		MT120						
		MTmg						
Gias Vallonetto (GV)		GV1	?	?				
		GV11		?		?		
		GVmg						
Colmars (Co2)	Cret.	24A					?	
Champsaur (Ch2)	Jur.	18A						

Table VI.3 – Magnetic characteristics of studied samples of the Grès d'Annot basin (V : Verwey transition, P-beh. : P-behavior, G : Goethite, Pyrrh. : > 1 μm pyrrhotite, 2-step : 2-step pattern, 200 K : break-in-slope within 200-250 K)

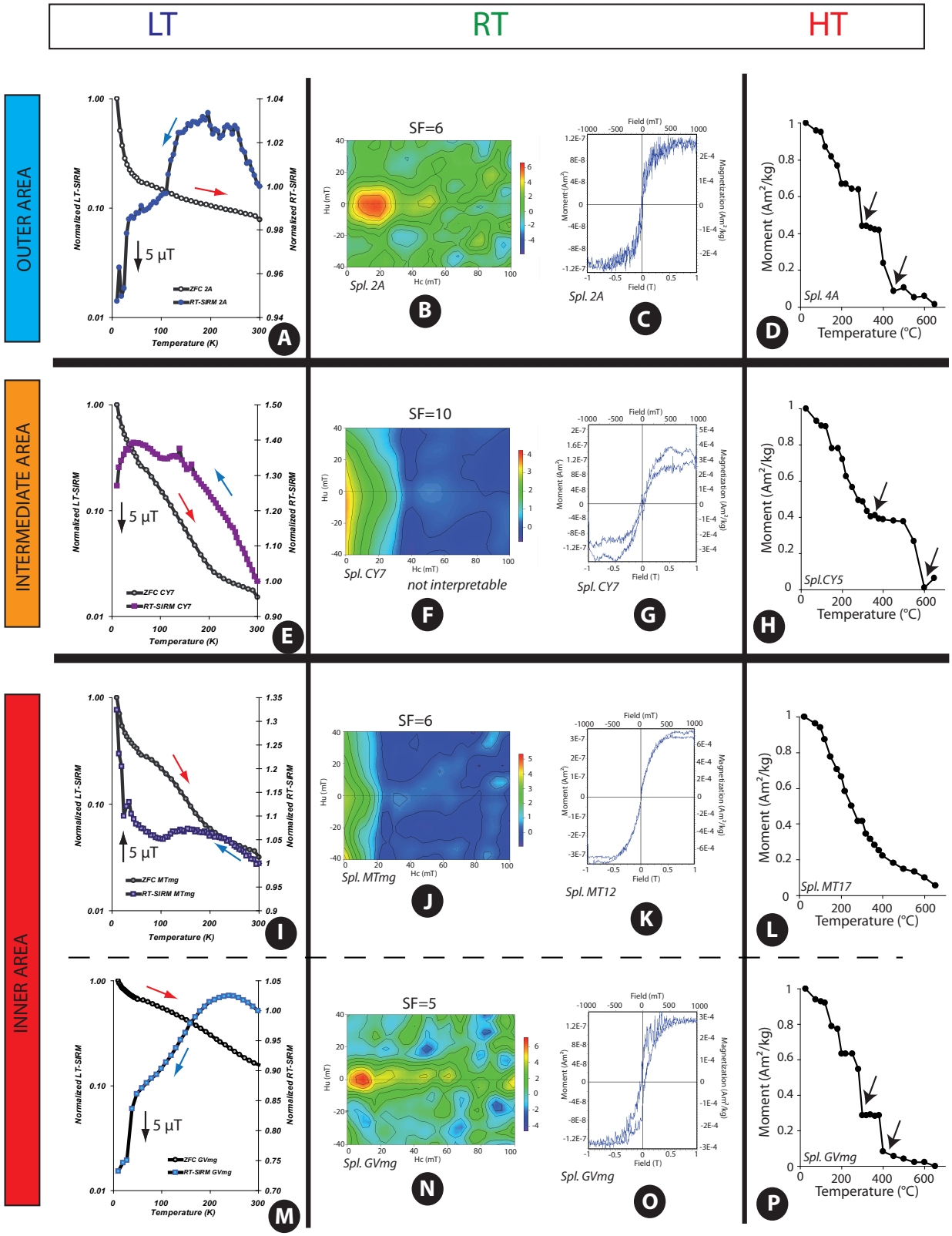

Figure VI.10 – Magnetic features of the three tectonic/diagenetic areas (LT : low temperature, RT : room temperature, HT : high temperature). SF : smoothing factor. The black arrows show break-in-slopes.

3.1 The outer area

The low temperature magnetic signal of the outer area is characterized by a warming curve (Zero Field Cooled ZFC) with a 2-step pattern (Aubourg & Pozzi, 2010 ; Kars *et al.*, 2011a). This pattern, as described in the chapter IV, is represented by a strong decrease of the Low Temperature SIRM (LT-SIRM) from 10 to 35 K and a slight decrease at ∼120 K (Figure VI.10A). This latter represents the well-known Verwey transition of magnetite, easily recognizable in the cooling curve (RT-SIRM curve) (Figure VI.10A). The magnetization on the RT-SIRM curve decreases from 35 to 10 K because it is actually an induced magnetization following the direction of the 5 μT magnetic field applied inside the MPMS. This magnetic setting is called P-behavior.

Room temperature FORCs diagrams and hysteresis loops performed on the samples from the outer area indicate that single domain magnetite is present over the study area (Figures VI.10B and VI.10C). No other magnetic mineral is detected.

High temperature IRM demagnetization decays to 650°C with two abrupt drops at 300°C and 450°C corresponding respectively to an iron sulfide (greigite or pyrrhotite) and magnetite (Figure VI.10D). From 450 to 650°C, the remanence slowly decreases and at 650°C, the IRM is totally removed.

In the Braux area (Figure VI.9), the RT-SIRM curves show an increase of the remanence from 300 to ∼35 K, similar to that found in the intermediate zone (Figure VI.10E). This is characteristic of goethite. To check the occurrence of goethite, we performed Mössbauer spectra at 300 and 4.2 K on a bulk sample with the cooperation of T. Berquò (Figure VI.11). At room temperature, the Mössbauer spectrum was fitted with three doublets corresponding to contributions of Fe^{2+} and Fe^{3+}. These components may be associated with paramagnetic iron silicates and, in addition, the Fe^{3+} doublet of smaller QS (Quadrupole Splitting) may also be related to the presence of superparamagnetic iron oxide. In order to observe the presence of superparamagnetic thermal relaxation at room temperature, the spectrum was taken at low temperature. At 4.2 K a small sextet contribution (∼8%) was observed and its hyperfine parameters reflect the presence of goethite. The B_{HF} (magnetic hyperfine field) has a small decrease as compared with a stoichiometric goethite of B_{HF} of 50.6 T (Murad & Cashion, 2004) and it can be associated with the presence of lattice defects (vacancies or isomorphic substitution) (T. Berquò, pers.com.).

Thus the outer area is characterized by a magnetic assemblage composed of an iron sulfide, goethite and magnetite.

3.2 The intermediate area

The intermediate area is characterized by a ZFC curve showing an inflexion point at about 200-250 K. The remanence monotonically decreases before that point and decreases more slightly after that (Figure VI.10E). The RT-SIRM curves of the samples from this zone show a regular increase from 300 to 10 K, with the occurrence of the Verwey transition of magnetite and an abrupt increase of the remanence from 35 to 10 K (P-behavior). This increase in the RT-SIRM curve is typical of goethite

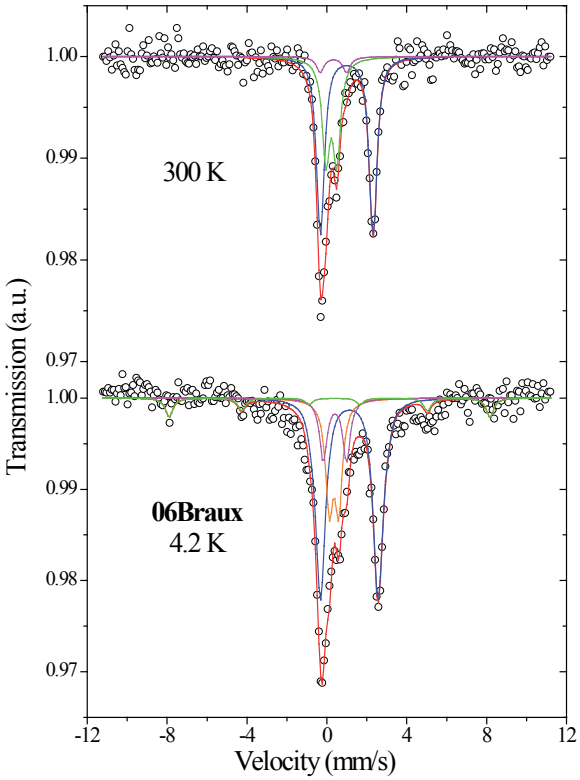

Figure VI.11 – Mössbauer spectra at 300 and 4.2 K of the 6A Braux sample (T. Berquò, pers. com.)

(Figure VI.10E ; Dekkers, 1989a).

The FORCs diagrams realized at room temperature are not interpretable due to a very bad smoothing factor (Figure VI.10F). Magnetite, which occurrence is attested on the low temperature measurements, is not seen on the FORCs diagrams. The hysteresis loop shown on Figure VI.10G is not saturated at 1 T, due to the presence of a high coercive magnetic mineral, probably goethite.

The IRM thermal demagnetization shows a decrease of the remanence up to 340°C. Then it decays slowly up to 500°C where a abrupt drop occurs (Figure VI.10H). The IRM is totally removed at 600°C. As for the outer zone, these two temperatures are characteristic of an iron sulfide (greigite/pyrrhotite) and of magnetite respectively. On the other hand, there is no evidence of a break-in-slope at about ∼120°C, corresponding to the unblocking temperature of goethite (e.g. Özdemir & Dunlop, 1996). This is concordant with the observation of the non saturation of the hysteresis loop. This finding is not surprising because in a recent study, Rochette *et al.* (2005) show that a very high magnetic field is sometimes necessary to saturate goethite (up to 57 T).

Thus, a magnetic assemblage of magnetite, goethite and iron sulfide characterizes the intermediate area. The typical feature of this zone is the inflexion point at ∼200-250 K of the ZFC curve, believed to be a marker of nanoparticles of goethite (e.g. Guyodo *et al.*, 2003).

3.3 The inner area

In the inner area, two different low temperature magnetic signals are found, both characterized by a particular behavior < 50 K : 1) a 24 K "transition" observed in the southern site (La Moutière) and 2) a pyrrhotite-type signal documented in the northern site (Gias Vallonetto).

3.3.1 The 24 K "transition" signal

The ZFC measurement performed on samples from the La Moutière area show an inflexion point at ~200-250 K (Figure VI.10I). The occurrence of goethite in these samples is attested by the increase (between 6 and 15%) of the RT-SIRM curve from 300 K (Figure VI.10I). The Verwey transition of magnetite is shown on all the samples from this area. One of the samples from this zone displays a particular magnetic behavior below 50 K. The RT-SIRM increases to 35 K, then decreases to 24 K before increasing again to 10 K (Figure VI.10I). The sharp increase from 10 K is probably a Néel transition. The change in the magnetization (reminding that actually the RT-SIRM curve represents an induced magnetization) at this temperature is believed to be related to micron-size pyrrhotite. This feature is also found in other rocks such as the Jurassic Terres Noires in the Alps and the Silurian Tonoloway Limestone in the Appalachians (Figure VI.12). The AC magnetic susceptibility conducted on this sample does not show any field-dependence at low temperature (Figure VI.13).

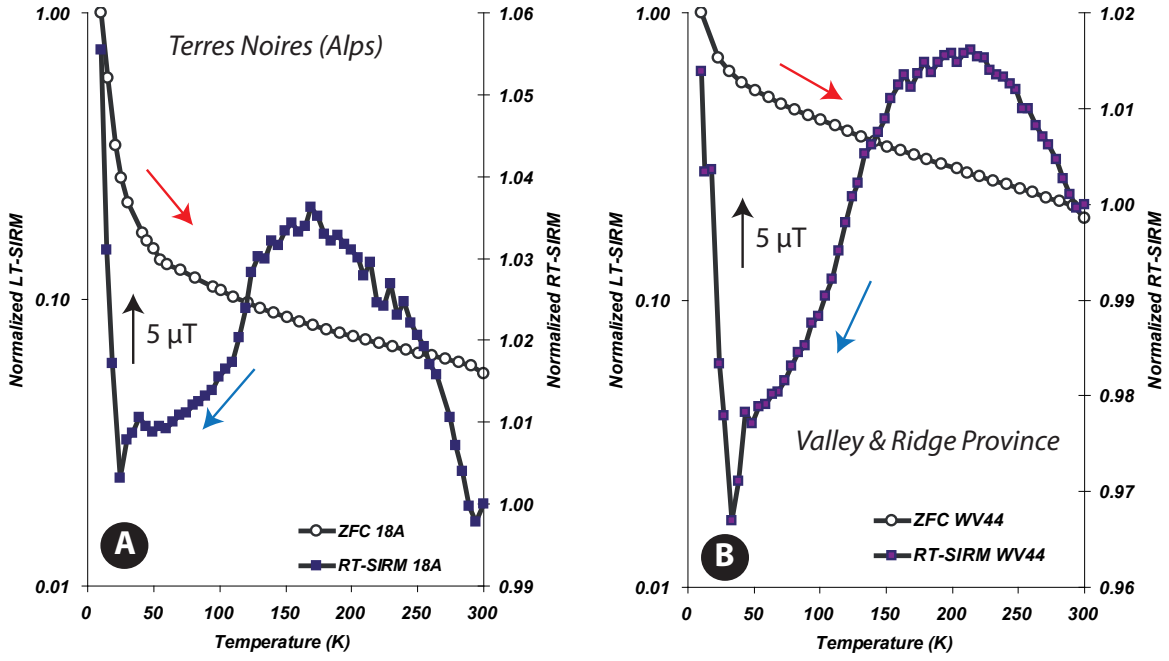

Figure VI.12 – Other occurrences of the 24 K "transition". A) Jurassic Terres Noires (Alps), B) Silurian Tonoloway Formation (Appalachians)

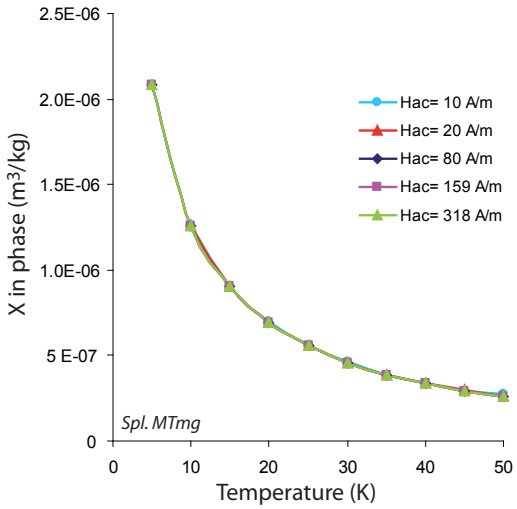

Figure VI.13 – Field-dependence of AC magnetic susceptibility of the sample displaying a 24 K "transition"

The poor quality of FORCs diagrams does not provide any useful information of the magnetic assemblage of the samples from this zone (Figure VI.10J). The hysteresis loops performed on the samples show magnetic saturation at 1 T indicating the presence of a low coercive mineral. The exception is the sample displaying the 24 K "transition" which is not saturated (Figure VI.10K).

The IRM thermal demagnetization does not carry more information. The IRM decays monotonically with increasing temperature, being quasi-removed at 650°C. A slight break-in-slope is observed at ∼450-500°C indicating occurrence of small magnetite grains (Figure VI.10L).

3.3.2 The pyrrhotite signal

The Gias Vallonetto area samples show also ZFC curves similar to those of the La Moutière area. Magnetite and goethite are thus present. One sample (GVmg) measured displays a typical magnetic signal. This is characteristic of > 1 μm pyrrhotite which the occurrence is attested in rocks which underwent temperature of ∼250°C (Figures VI.10M and VI.14 ; Rochette *et al.*, 1990).

The FORC diagram realized on this particular sample shows the occurrence of a low coercive SD magnetic mineral (Figure VI.10N) which is interpreted as magnetite which signal is masked in low temperature measurement. The hysteresis loops are saturated at 1 T, with a broad shape for GVmg sample (Figure VI.10O).

The IRM thermal demagnetization realized on this sample displays a steps pattern (Figure VI.10P). This reflects its noisy behavior. One may notice however two major decreases at 300 and 400°C suggesting the occurrence of an iron sulfide (pyrrhotite) and very small particles of magnetite.

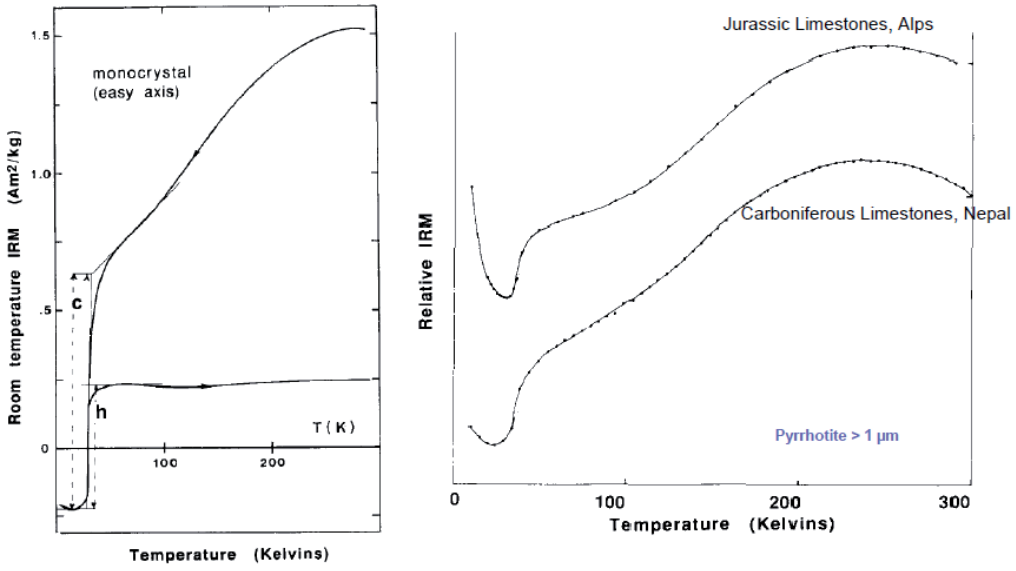

Figure VI.14 – Low temperature magnetic measurement of pyrrhotite samples (after Rochette *et al.*, 1990)

The inner area is then characterized by an assemblage of goethite, magnetite and pyrrhotite. This assemblage is a typical feature of the inner area and interpreted as indicating a high temperature zone.

4 Magnetic assemblage and thermal history

Our study is aiming to use magnetic properties of claystones to estimate the burial conditions. In the Grès d'Annot basin, we refer to the temperature isotherms established by Labaume *et al.* (2008) on the basis of apatite fission tracks analyses and silica polymorphism. Vitrinite reflectance data (Ro) from Pickering & Hilton (1998) are roughly consistent with the trends established by Labaume *et al.* (2008). The outer area is characterized by Ro $< 0.5\%$, the intermediate area by Ro values between 0.5 and 1.3%, and the inner area by Ro $> 1.3\%$ (up to 7%).
In order to add additional constraints on temperature estimates, X-ray diffraction analyses of the clay fraction were conducted on a selection of samples. Typical X-Ray diffractograms are shown in Figure VI.15. The peaks of chlorite, illite and kaolinite are clearly identified. The clays nature evolves from a S-N transect which characterizes an increasing burial to the North. The peaks corresponding to chlorite and kaolinite do not show any relevant change to the North. Besides, some interlayered illite/smectite (I/S) components are present. With increasing burial, I/S progressively dissappear and the illite peak becomes thinner. The interlayered I/S present in the outer zone are progressively transformed into illite. Despite this evolution, which would support a higher temperature towards the inner zone, it is not possible to extract more accurate temperature constraints for our study area.

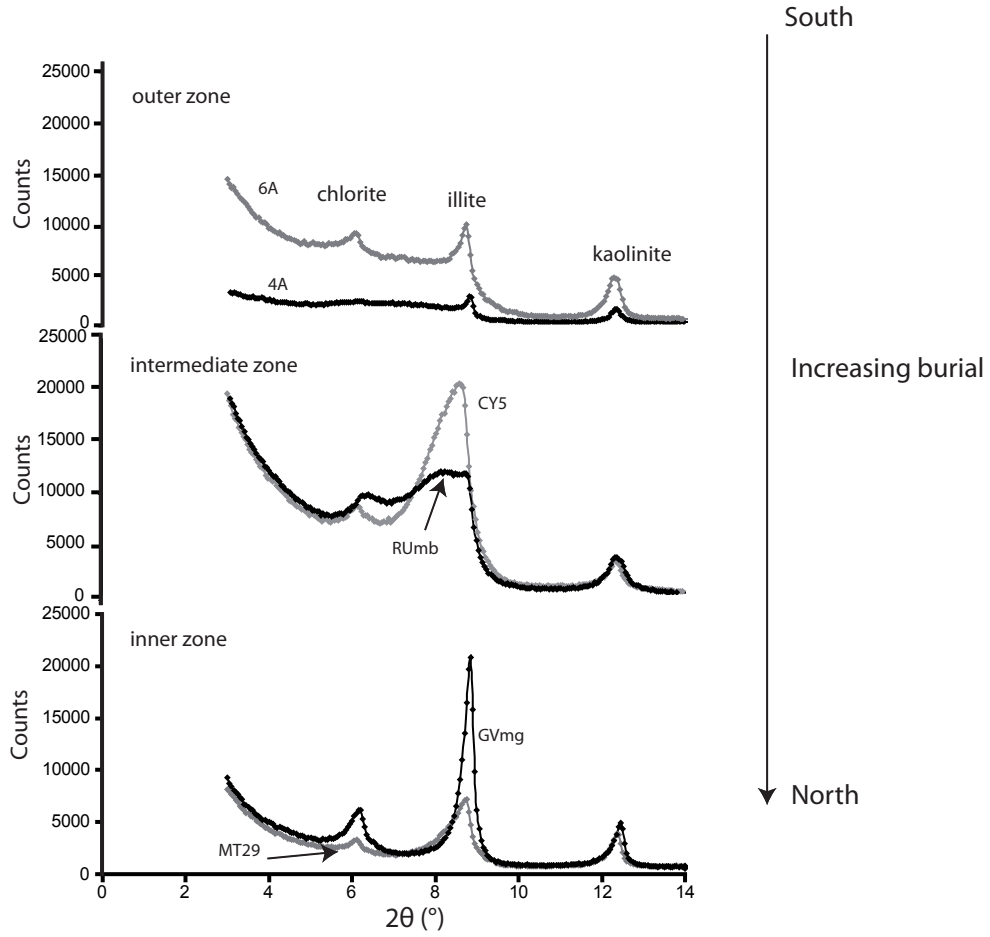

Figure VI.15 – X-ray diffraction on the clay fraction of selected samples from the Grès d'Annot basin. Note the progressive disappearance of the interlayered I/S and narrowing of the illite peak with increasing temperature.

It is clear that magnetite is present throughout the study transect from SW to NE (from ∼60 to > 200°C) (Figure VI.16). The 2-step pattern of the ZFC curves observed in the outer area may relate the onset of the oil window (Aubourg & Pozzi, 2010).

Goethite, occurring as nanoparticles, is present in the intermediate and inner areas (Figure VI.16). It is present in zones which experienced burial depth greater than 3 km (Ro ∼1.1% ; ∼100-120°C). The origin of these nanoparticles of goethite is not clear. They may represent an alteration product developed as a result of fluid circulation (Evans & Elmore, 2006). In the SE France basin, the main fluid migration episodes took place before the Eocene time (Guilhaumou *et al.*, 1996). As the tectonic contact of the nappes is not so far from the sampling site, this possibility can not be ruled out (Figure VI.17). Recent weathering may also lead to the formation of goethite. Finally, goethite could be an authigenic (diagenetic ?) mineral formed in certain environmental conditions. The occurrence of nanogoethite is also observed in West Virginia samples (see chapter VII).

Pyrrhotite in grain-size > 1 μm occurs in the inner area which is characterized by temperature > 200°C (burial depth ~8-10 km) (Figure VI.16). The presence of > 1 μm pyrrhotite is displayed near the Alpine nappes edge front and the Penninic Front. It is also found in Alps metamorphic units northward to our study area (e.g. Rochette, 1987; Rochette *et al.*, 1990; Crouzet *et al.*, 1999). It is typical of high temperature and corresponds to the entry of the greenschist facies.

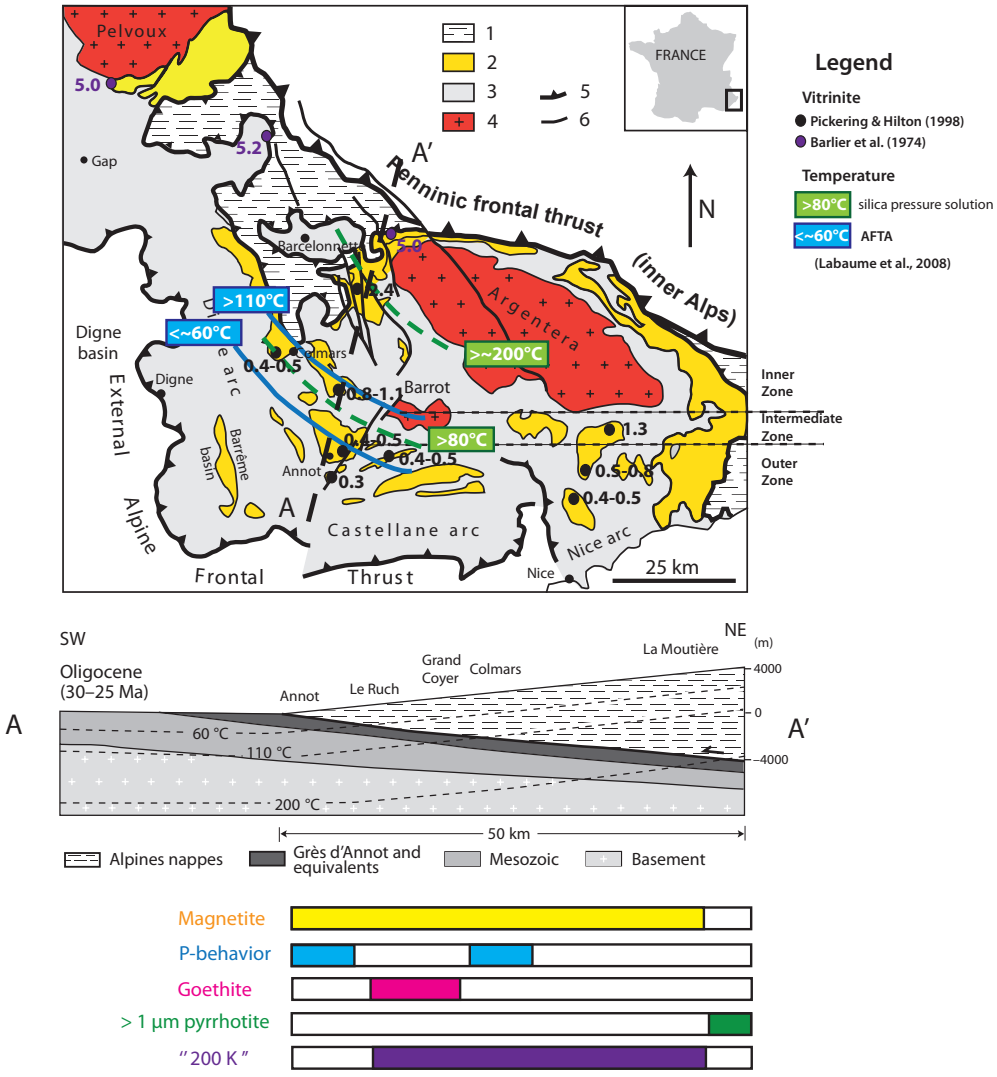

Figure VI.16 – Spatial distribution of the magnetic features in the study area (map from Labaume *et al.*, 2008). Same legend as Figure VI.1.

Figure VI.17 – A) Onlap structure of Montagne de Chalufy showing the progressive filling of the foreland basin and B) calcite veins on the footwall of Chalufy suggesting fluid circulation.

It was proposed that pyrrhotite can form by reaction of pyrite with magnetite and organic matter in metamorphic conditions (Rochette, 1987), even at low temperature ($< 200°C$; Gillett, 2003). Following this idea, we examined framboidal grains which are mainly composed of pyrite often associated with organic matter as a result of the bacterial activity (Wilkin & Barnes, 1997). The observed framboids in samples from the outer area are well shaped (Figure VI.18A) or replacing carbonate shells (Figure VI.18B). Their elementary analyses by X-ray spectra show that Fe and S are the main constituents of such framboids, with a Fe/S ratio of $\sim$0.5 which is pyrite FeS_2. In samples from the intermediate area, framboidal structures present a rim darker than the core (Figure VI.18C). A EDX transect done from the core to the outer zones revealed that the Fe/S ratio varies as a result of a decrease in S content in the rim. The oxidation rim is certainly magnetite. Replacement of pyrite by magnetite has been widely described in previous studies (e.g. Suk *et al.*, 1990). Some alteration features are also observed in euhedral grains (Figure VI.18D), which most likely represent dissolution features. In samples from the inner zone, framboidal structures look like grey and the main constituents are Fe and O. The former pyrite framboids are totally oxidized into magnetite. Thus, there is an evolution of S and Fe content from the outer to the inner areas. Reducing conditions are prevalent in the outer area, while oxidation effect occurs in the inner area. The increase of temperature experienced by the rocks and changes in redox conditions may be one possible mechanism explaining the SEM observations. Presence of pyrrhotite could not be documented in our SEM observations, most likely because of its extremely low concentration.

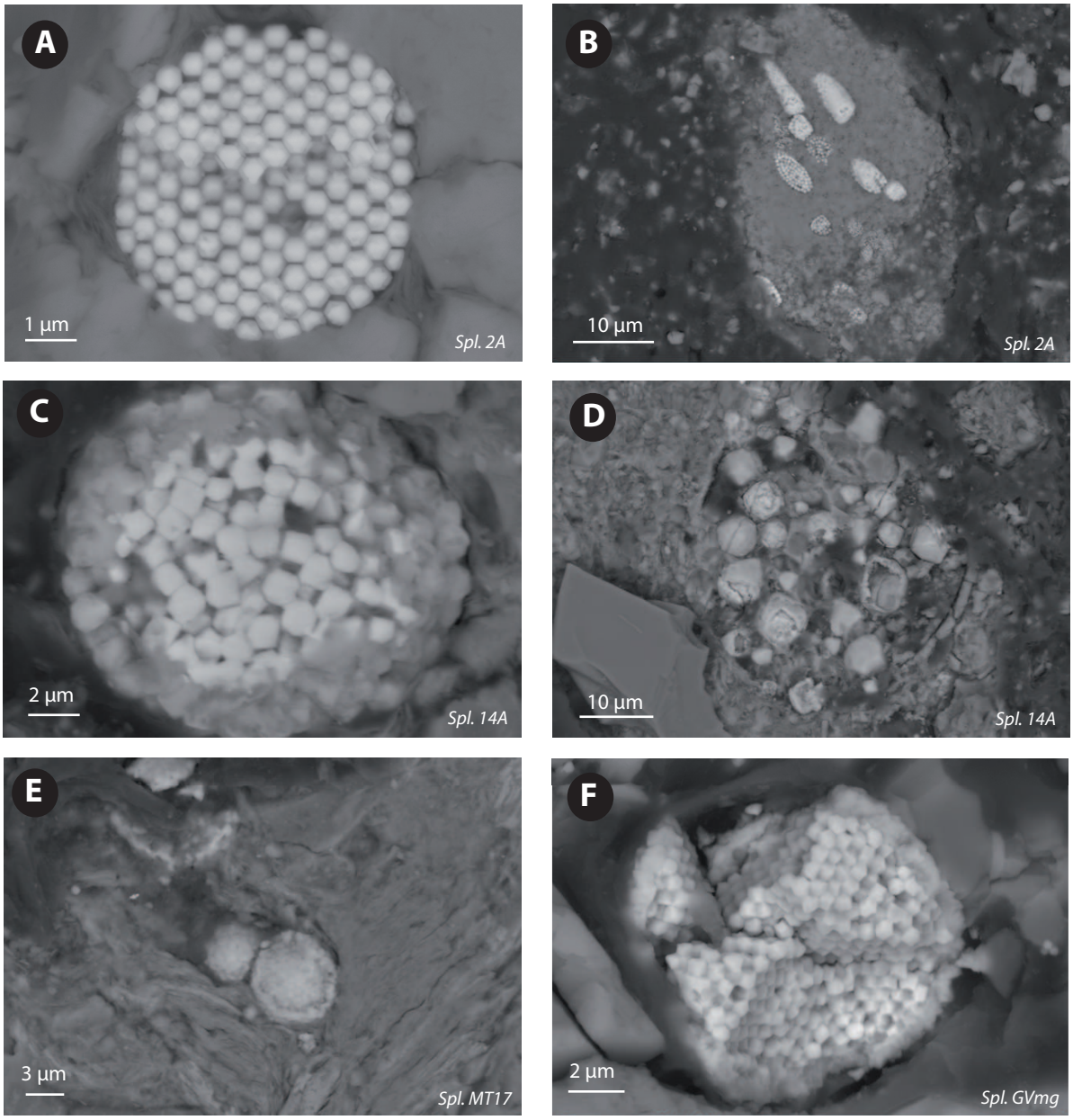

Figure VI.18 – SEM images of framboidal structures. A) Well crystallized pyrite framboids, B) shells replacement by pyrite, C) pyrite framboids with oxidation rim, D) altered framboids, E) oxidized framboids, F) altered Fe-rich framboids.

5 Application of the MagEval geothermometer

Some samples exhibit MagEval-type signals (see chapter IV) in the outer and intermediate zones of the study area. It is therefore possible to apply the MagEval geothermometer. The available thermal data on the study area suggest that the PM Up branch can be used in the outer area (Ro $< 0.6\%$) and the PM Down branch in the intermediate zone. The PM Up branch of the calibration based on Girassol-1 is not appropriate for the Grès d'Annot samples, the calculated temperatures being unrealistic. For samples located in the outer area, the MagEval temperatures calculated using the 22/30C-10 calibration do not exceed 75°C, range from ∼50 to 72°C, which is consistent with the paleotemperatures of $<$ 60 to 80°C derived from petrological and thermochronologic analyses (Labaume *et al.*, 2008 ; Figure VI.16). For samples displaying a MagEval signal located in the intermediate zone, the MagEval temperatures calculated from both Gir-1 and 22/30C-10 calibrations are greater than 85°C, ranging from ∼85 to 112°C, which is also consistent with the results of prior studies (80 to 110°C). We therefore conclude that the application of the MagEval geothermometer to the Grès d'Annot samples is satisfactory, in spite of the limited number of samples displaying a MagEval-type signal which did not allow application to the high temperature range.

6 Synthesis-Conclusion

This study was carried out to investigate the variation of magnetic properties, as well as the presence and evolution of the MagEval signal, in clastic rocks that had been submitted to a very wide range of paleotemperatures going from $<$ 60°C to $>$ 200°C in the Grès d'Annot basin. The results indicate that the magnetic assemblage evolves along a SW-NE transect in the basin, across the successive outer to inner tectonic/diagenetic zones. This is consistent with increasing vitrinite reflectance data and maximum burial temperatures. Magnetite, goethite and iron sulfides (greigite/pyrrhotite) are the main magnetic minerals identified in our study.

In the SW, where the maximum temperature experienced by the rocks is ∼60°C (burial depth ∼2-3 km), SD magnetite and iron sulfides are the main constituents. In the intermediate area, where temperatures are ∼110-120°C, the magnetic assemblage is composed of magnetite and goethite which occurs in nanoparticles. The diagnostic magnetic feature of this assemblage is the presence of an inflexion point at ∼200 K on the warming curve ZFC. This is characteristic of the presence of very small particles of goethite. This goethite may be neoformed as a result of burial and may be present up to ∼250°C (see also chapter VII). Fluid circulation caused by nearby Alpine thrusting may explain the formation of these nanoparticles. Alternatively, they may result from recent weathering. In the NE area (inner zone), the magnetic assemblage is mainly magnetite and coarse-grained (> 1 μm) pyrrhotite. The > 1 μm pyrrhotite indicates a temperature of ∼250°C and marks the entry of the greenschist facies (burial depth ∼8-10 km).

The magnetic assemblage varies with distance from the Alpine nappes and according to the tectonic

load. The greater the tectonic load, the higher the temperature experienced by the rocks. Magnetite and pyrite progressively disappear at the expense of pyrrhotite with increasing temperature. The recognition of this particular magnetic assemblage (magnetite, goethite, > 1 μm pyrrhotite) may be used as a marker for very low metamorphism (< 250°C). Geographically the western limit of the > 1 μm pyrrhotite is roughly located at the present edge of the Alpine nappes and by extrapolation may be an indicator of the advance of the thrust front.

The application of the MagEval geothermometer methodology to the Grès d'Annot samples yields temperatures < 75°C for the outer zone and > 85°C for the intermediate zone. This is consistent with the results of petrological and thermochronological studies conducted in the area (Labaume *et al.*, 2008). These results illustrate that the MagEval geothermometer can be successfully applied to sediments in a foreland basin context such as the Grès d'Annot basin.

Chapter VII

MAGNETIC ASSEMBLAGE IN THE APPALACHIANS, WEST VIRGINIA, USA

In order to further document the thermal dependence of the magnetic signal/assemblage found in boreholes and in the Grès d'Annot basin (chapters IV and VI), a study was conducted in the thrust-and-fold belts of the Appalachians, in West Virginia, USA. This site was chosen for several reasons. First, a number of paleomagnetic studies have been conducted in the Appalachians which documented a wide remagnetization of the area. Second, recent focus on the Marcellus gas shale play triggered a renewed interest for the Appalachians. Third, thermal indicators, such as vitrinite reflectance and fluid inclusions, show some disagreement in the study area. The identification of the magnetic minerals may therefore provide constrain to help unravel the temperature history of the area.

1 Study area

The Appalachians is one of the most important coal provinces in the USA and one of the biggest over the world. This 3 000 km long mountain belt extends upon nearly 20° in latitude and more than 30° in longitude from Newfoundland (Canada) to Alabama (SE USA). The narrowest part of the belt is situated to the west of New York City and represents a time barrier with older deformations on the north and younger ones on the south. The Appalachians are subdivided into 5 main physiographic provinces from East to West (Figure VII.1) :

- The Coastal Plain is mainly composed of Cretaceous to Quaternary sediments ;
- The Piedmont Province comprises of Precambrian to Late Paleozoic crystalline rocks (gneiss, granite). Mesozoic sedimentary and volcanic rocks are also present ;
- The Blue Ridge Province is composed of Cambrian to Ordovician sedimentary rocks ;
- The Valley and Ridge Province includes mainly Devonian sedimentary rocks, with some Cambrian rocks as well. This province is named after its characteristic topography represented by the anticline-syncline succession ;
- The Appalachian Plateau is composed of Carboniferous and Permian sedimentary rocks. It is the province richest in coal, oil and gas deposits.

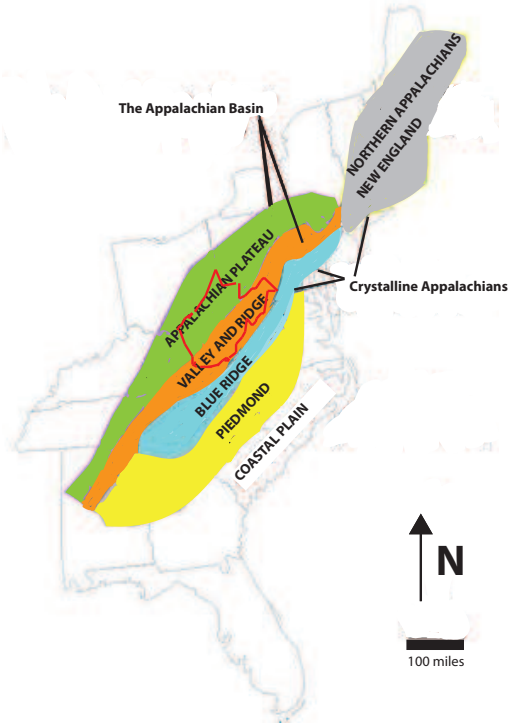

Figure VII.1 – The five main physiographic provinces of the Appalachians (USA) ; outline of West Virginia State shown in red (after USGS)

The Appalachian Plateau and the Valley and Ridge Province, separated by the Alleghanian Front, constitute the "Appalachian Basin" or the "Sedimentary Appalachians". The Piedmont and Blue Ridge Provinces are called the "Crystalline Appalachians".

1.1 Simplified geological history of the Appalachians

The actual Appalachians were formed by three main orogenies over 490 Ma characterizing a complete Wilson cycle between the breakup of the supercontinent Rodinia (end of the Proterozoic Grenvillian Wilson cycle) and the formation of the supercontinent Pangea (end of the Late Paleozoic Appalachian Wilson cycle) (Figure VII.2 ; Hatcher, 2010).
Each orogenic phase is characterized by an accumulation of marine sediments and volcanic deposits. Deformation and mountains elevation constitute the climax of the orogen, followed by a quiescent period dominated by relief erosion, clastic sediments deposits and marine transgressions in between the different orogenies.

At 750 Ma, the breakup of Rodinia leads to the formation of the Laurentian passive margin on the edge of the North America continent that is separating from the African continent Gondwana (e.g. Cawood *et al.*, 2001 ; Whitmeyer & Karlstrom, 2007). A period of riftings follows. At ∼565 Ma, the Iapetus Ocean aperture allows the distal deposit of clastic sediments and volcanic rocks. The rift to

drift transition occurs along the margin with the development of a carbonate platform in the Early Cambrian (e.g. Williams & Hiscott, 1987). From Late Cambrian to Early Ordovician, the most part of the North America continent, located at the time on the equator, is flooded. This strong marine transgression permitted deposition of carbonates well inside the continent. The Appalachians region then becomes a passive margin alternatively flooded and emerged. During the flooded periods, thick layers of sediments and carbonates are deposited. During emerged periods, the erosive phase is dominant with sediments deposits of continental origin. In the Mid-Ordovician (480-440 Ma), a change in plate motion starts the first orogeny called Taconic Orogeny. The Appalachian passive margin then becomes a subduction zone where the oceanic plate constituent the Iapetus Ocean subducted underneath the North American craton. The sediments deposited in the Central Appalachians reached their greatest thickness (∼5 km) in the Martinsburg Basin in the Late Ordovician (Hatcher, 2010). Diachronous foreland basins are filled in the first half of the Ordovician. Along the continental margin, a volcanic arc develops due to the subduction. The deformation due to the Taconic Orogeny is intense inside the chain and seems to be linked to the arc accretion between 496 and 428 Ma (e.g. Stanley & Ratcliffe, 1985). At ∼420 Ma, the Iapetus Ocean is closed.

Great quantities of clastic sediments forming wide alluvial plains are deposited within the Appalachians from Late Ordovician to Devonian (Rodgers, 1971). These deposits are diachronous from North East to South West and constitute the Chemung Group in the Central Appalachians and the Catskills in the Northern Appalachians (Ettensohn, 2004 ; Merschat & Hatcher, 2007).

In the Early Devonian (∼410 Ma), a second major orogenic phase occurs. This is the Acadian Orogeny that lasts about 50 Ma. This orogeny concerns essentially the northern part of the Appalachians centered on New England and South East of New York State (e.g. Osberg *et al.*, 1989). The maximum Acadian Orogeny is in Late Devonian but deformation, volcanic and metamorphic phases keep going to ∼345 Ma (Mississippian, Early Carboniferous). This orogen is the result of the junction of the superterrane Avalonia (Avalon and Carolina) with the North America continent, Laurentia, following the closure of the Rheic Ocean (Skehan & Rast, 1990). The Acadian Orogeny is contemporaneous of the Caledonian Orogeny affecting the British Islands, Greenland and Scandinavia in Europe.

In the Mid-Carboniferous around 320 Ma (Mississipian), the closure of the Theic Ocean (last remainder of the Iapetus Ocean) induces the collision of Laurentia (North America) and Gondwana (Africa) continents (e.g. Bradley, 1982). This is the beginning of the formation of the supercontinent Pangea. In North America, this corresponds to the third and last orogen affecting the Appalachians : the Alleghanian Orogeny. This orogen is associated to the formation of the great folds and the thrust faults through the Central and Southern Appalachians. On the East of the Appalachian Basin, the sedimentary rocks are squeezed and form large folds which axes are perpendicular to the maximum stress (e.g. Evans, 1989). The greatest deformation occurs in the Central Appalachians (North Carolina, Tennessee, Virginia and West Virginia) forming the Valley and Ridge Province. The Alleghanian Orogeny is contemporaneous of the Variscan (Hercynian) Orogeny in Europe (Matte, 2002).

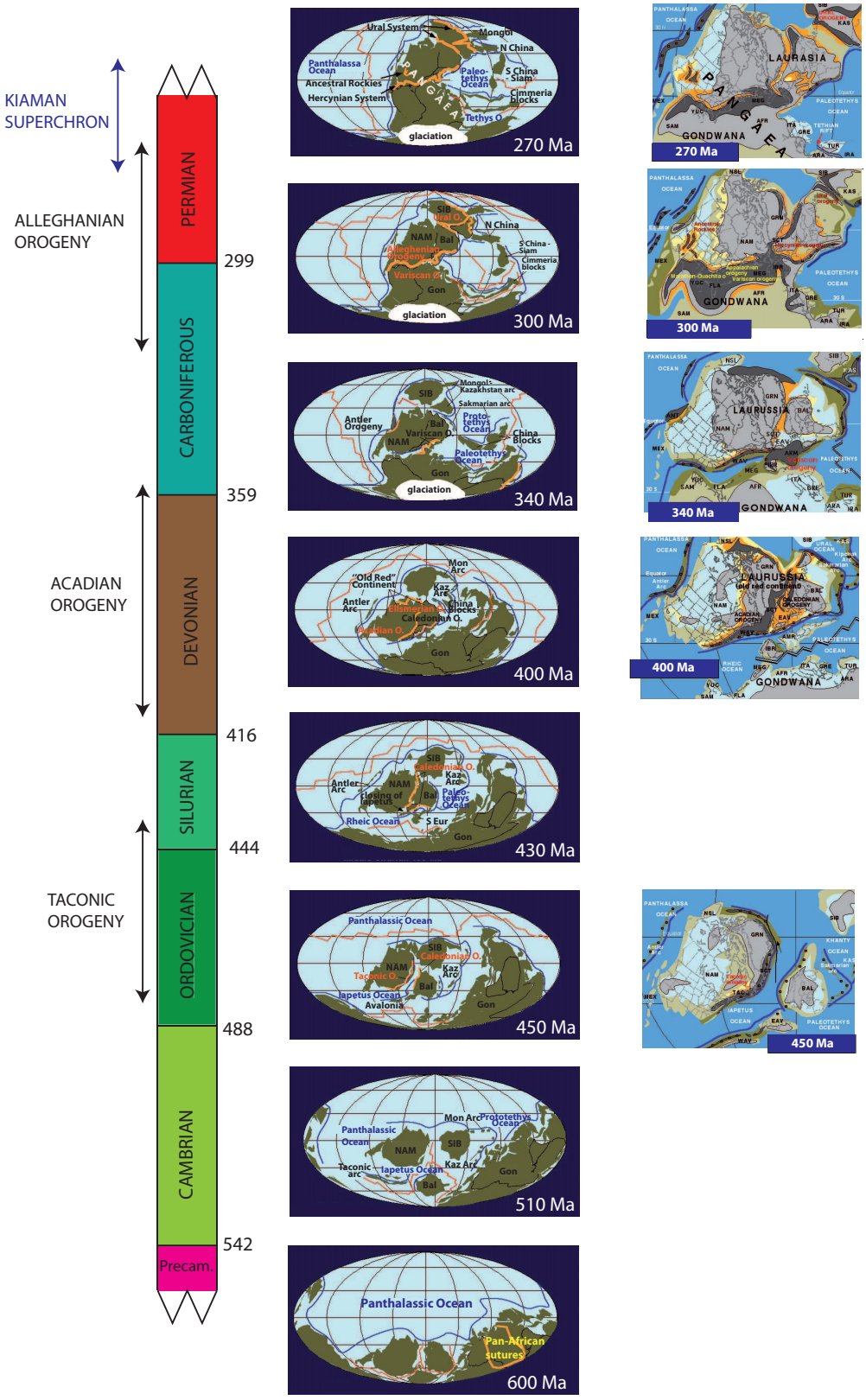

Figure VII.2 – Geological history of the Appalachians (maps from website http ://jan.ucc.nau.edu/~rcb7/index.html)

From Late Paleozoic to Permian, Pangea is complete and remains stable up to Triassic. In the Late Triassic (∼220 Ma), a series of rifts is developing in the Piedmont Province. Rifting and aperture of an oceanic floor begin in Jurassic and become more rapid in Cretaceous leading to the formation of the Atlantic Ocean. The continental margin progressively subsides and the sediments (clastic deposits) coming from the Appalachians are accumulating and forming the Coastal Plain.

1.2 The Valley and Ridge Province, West Virginia

1.2.1 Stratigraphy

The rocks constitutive of the Valley and Ridge Province are of Ordovician to Early Carboniferous age (Figure VII.3).
The stratigraphy is marked by orogenic phase/marine transgression alternations which follow the breakup of the supercontinent Rodinia to the formation of Pangea.

The stratigraphic sequence in the Valley and Ridge Province may be divided in several different distinct lithologic units (Evans, 2010). The lowermost unit is composed of the Ordovician limestones Black River and Trenton Formations. These limestones are separated from the overlying unit by a regional décollement located near the base of the Martinsburg Formation. The overlying lithologic unit, composed of the Ordovician Martinsburg Shales through the Silurian Tuscarora and Clinton sandstones, is a coarsening-upward clastic sequence. Above this section, a second limestone interval, mainly constituted of the Silurian McKenzie, Wills Creek and Tonoloway Formations and the Lower Devonian Helderberg Group, occurs. Just above the Helderberg Group, the Devonian Oriskany sandstone is a poorly to well-cemented quartz arenite. This sandstone is overlain by a thick coarsening-upward sequence through the Devonian Needmore shale to the Upper Devonian Chemung Formation siltstone. At the base of this sequence, the Middle Devonian Marcellus shale is a well known gas shale formation (Harper, 2008). Toward the top of this sequence, the different formations grade into interbedded siltstones and shales for the Braillier Formation and interbedded siltstones and sandstones for the Chemung Formation. Above the Chemung Formation, the Upper Devonian Hamsphire through the Mississippian Pocono Formations represent a massive thick sandstones unit.
In the Appalachian Plateau, the overlying formations are preserved up to the Pennsylvanian Monongahela Group.

1.2.2 Structural context

The great folds of the Valley and Ridge Province formed during the Alleghanian Orogeny in a compressive context where the maximum stress is perpendicular to the fold axis (Evans, 1989, 2010). On the West, the Valley and Ridge Province is separated from the Appalachian Plateau by a structural front called the Alleghany (or Alleghanian) Front. This front represents the western limit of large-scale thrusting in the underlying duplex. On the East, the Valley and Ridge Province is bounded by the North Mountain thrust (Evans, 1989).

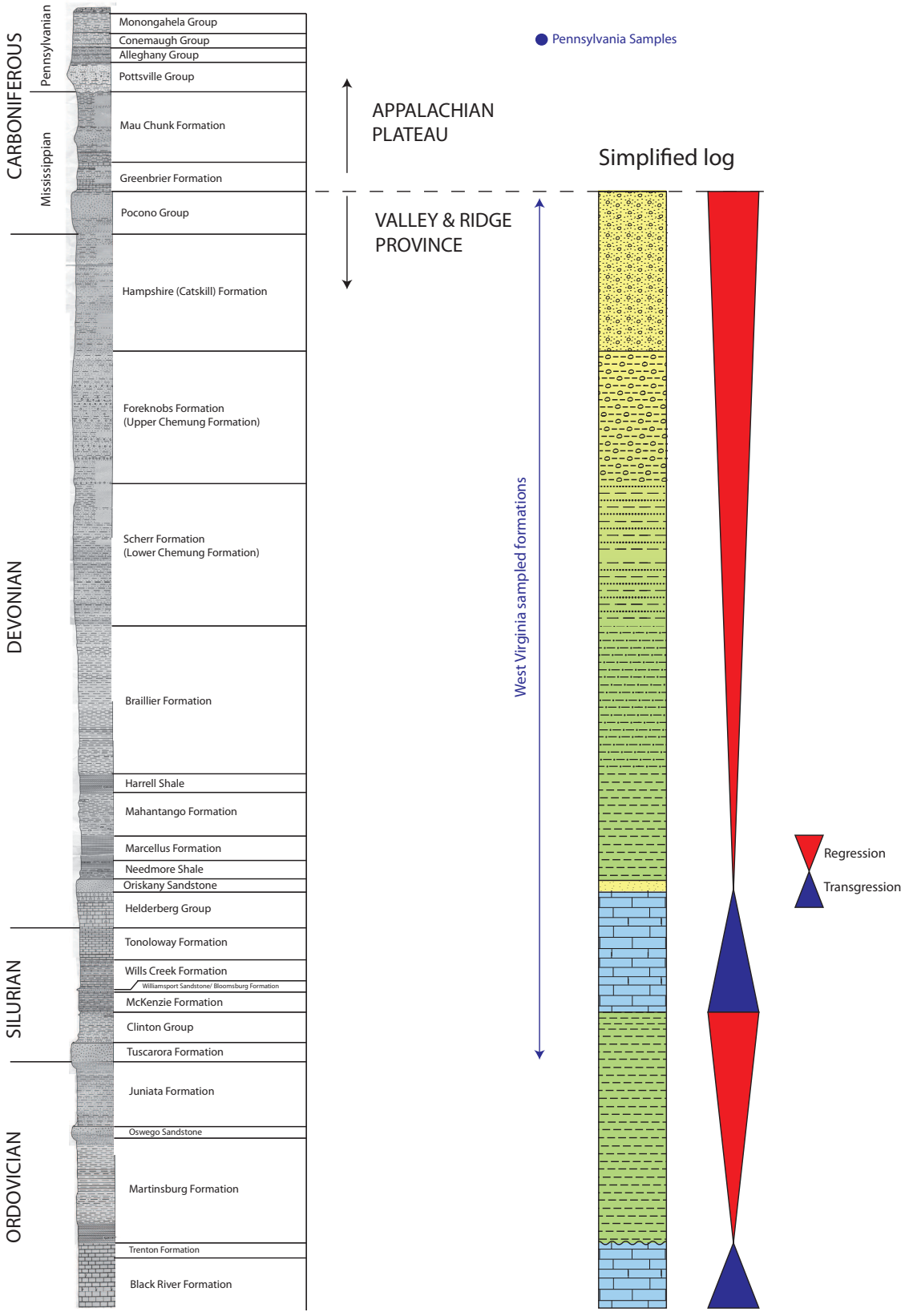

Figure VII.3 – Stratigraphy of the Valley and Ridge Province in West Virginia (after M. Evans, pers. com.)

The geometrical complexity of the Valley and Ridge Province is illustrated in its subdivision into four units (Figure VII.4 ; Evans, 1989, 2010 and references therein) :

- The Nittany Anticlinorium defined by a complete duplication of the Cambrian-Ordovician, lithotectonic unit for over 17 km ;
- The Broadtop Synclinorium distinguished by a regional structural low formed by partial duplication of the Cambrian-Ordovician lithotectonic unit in the blind duplex ;
- The Adams Run-Cacapon Mountain Anticlinorium defined by an antiformal stack duplex of the Cambrian-Ordovician lithotectonic unit in the blind duplex section ;
- The Meadow Branch Synclinorium characterized by rocks, adjacent to the North Mountain thrust ramp, deformed into a footwall syncline with an overturned southeast limb.

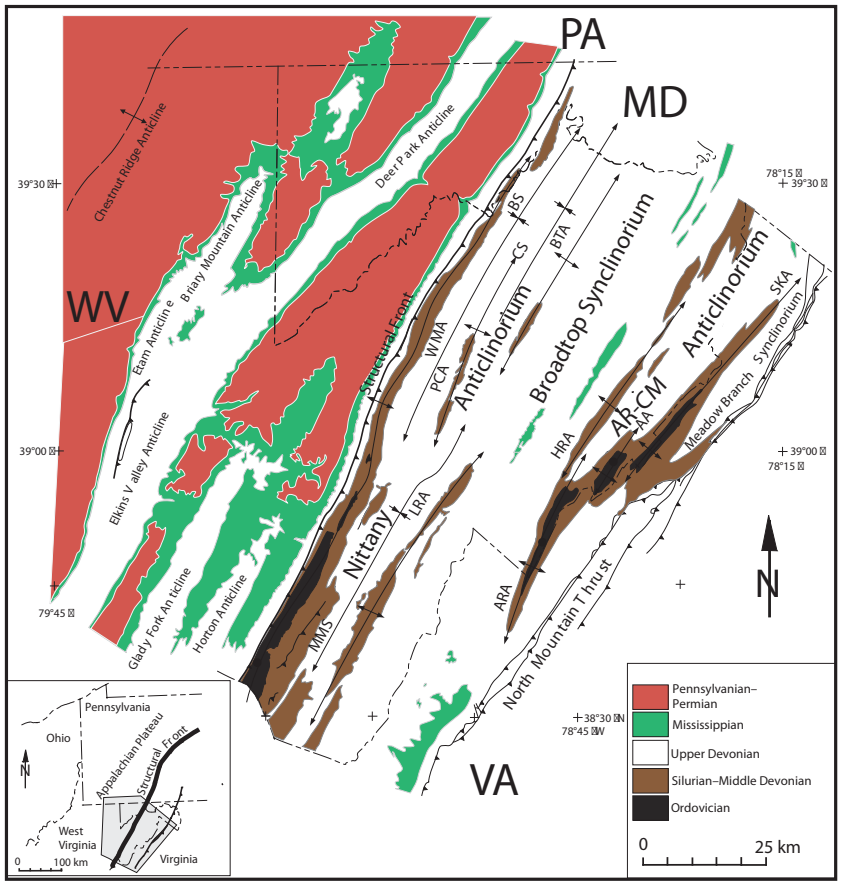

Figure VII.4 – Geological map of the study area with the main structural features (after Evans, 2010). AA : Anderson Ridge anticline, ARA : Adams Run anticline, AR-CM : Adams Run-Cacapon Mountain, BS : Bedford syncline, BTA : Broadtop anticline Cacapon Mountain, CS : Clearville syncline, HRA : Hanging Rock anticline, LRA : Long Ridge anticline, MMS : Middle Mountain syncline, PCA : Patterson Creek anticline, SKA : Sugar Knob anticline, WMA : Wills Mountain anticline.

1.2.3 Burial history

The stratigraphic interval we studied covers two of the main stratigraphic groups which burial histories are described below.

Using fluid inclusions data (Evans & Battles, 1999 ; Evans & Hobbs, 2003) and considering a geothermal gradient of 20°C/km, Evans & Elmore (2006) reconstructed the burial history of the Tonoloway and Helderberg limestones formations in West Virginia (Figure VII.5). Following deposition at about 400 Ma, these two formations undergo rapid burial as a result of the Acadian Orogeny, down to 3.5 km in 20 Ma (∼175 m/Ma). Following this rapid subsidence phase, burial becomes monotonous and stabilizes at a slower burial rate (15 m/Ma) until Early Permian. In the Carboniferous (340-290 Ma), hydrocarbons generation occurs and ends when burial temperature reaches ∼120°C (∼5 km depth) (step A in Figure VII.5). In the Early Permian (285 Ma), the Siluro-Devonian Tonoloway and Helderberg Formations undergo again a rapid burial (200 m/Ma) as a result of the Alleghanian Orogeny (step B in Figure VII.5). They reach 7 km depth at ∼265 Ma. At this time the great folds of the Valley and Ridge Province formed. Hot fluids, with temperature up to ∼200°C, circulate through the Devonian layers (Marcellus Formation to Chemung Group) (Evans & Battles, 1999). Later, synfolding uplift occurs associated with the emergence of the Wills Mountain and Patterson Creek anticlines (step C in Figure VII.5).

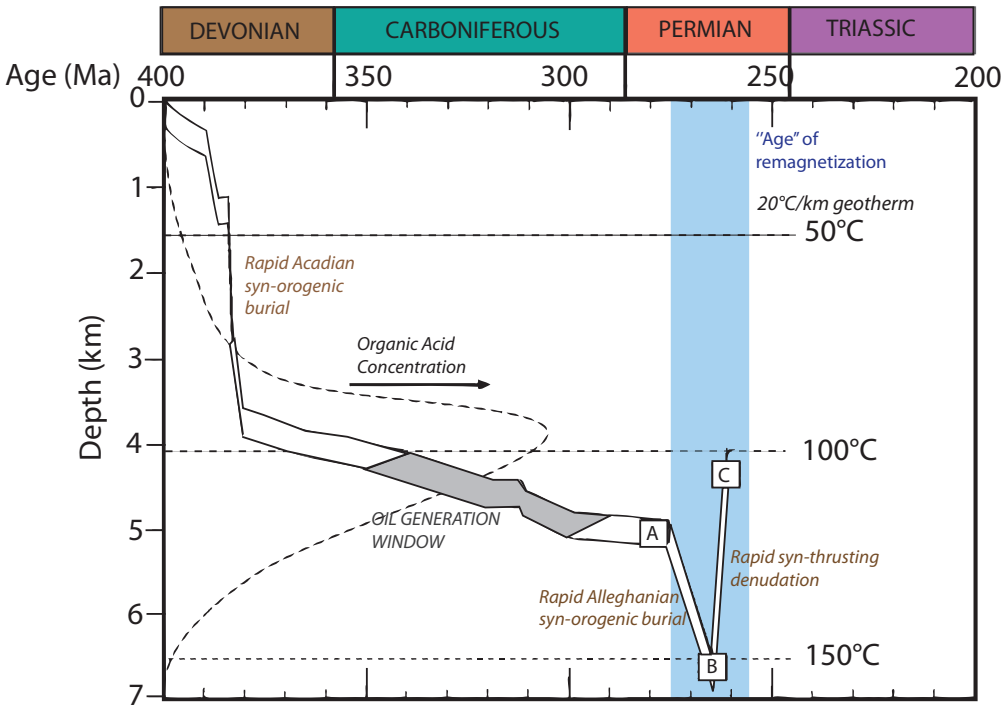

Figure VII.5 – Burial history of the Tonoloway and Helderberg Formations (after Evans & Elmore, 2006)

The three last geological steps A, B and C experienced by these formations are found to be characterized by typical magnetic assemblages. These assemblages are controlled by the redox conditions during burial and deformation (Evans & Elmore, 2006). Chronologically, at the onset of burial, the reductive conditions in the environment lead to the alteration of biogenic or detrital magnetite into pyrite (step A). The deformation related to the Alleghanian Orogeny causes fractures opening and warm fluids circulation. These fluids alter pyrite into authigenic magnetite (step B) (e.g. Suk *et al.*, 1990, 1991). Then during folding event and ramp unit transport, rock seal breaches permitting oxygen-rich meteoric water infiltration. This leads to the formation of goethite (step C) which may also be a recent weathering product (Lu *et al.*, 1990 ; Jackson *et al.*, 1992).

Based on fluid inclusions and vitrinite reflectance data, Evans (1995) also reconstructed the burial history of the Devonian Shales in the Appalachian Plateau (Figure VII.6). A constant geothermal gradient of 28°C/km was used with a surface temperature of 20°C. Indeed at this time, North America was at an equatorial latitude (Van der Voo, 1983) and the climate was tropical. The surface temperature decreased through time at a constant rate to take into consideration the present position of North America at 10° latitude. Apatite fission tracks analysis suggested that uplift in northern West Virginia was initiated during the Triassic to Early Jurassic (Roden, 1991). Maximum burial is therefore considered to have occurred in the latest Permian.
The reconstructed burial curves are different in Pennsylvania (central Appalachian Plateau) and in southwestern West Virginia (Western Plateau) (Figure VII.6). The maximum burial of the Devonian shales occurs between 4 and 5.2 km thus in terms of temperature between 132 and 165°C for West Virginia and Pennsylvania respectively. In West Virginia, the maximum temperature experienced by the shales corresponds to the so-called oil window (< 120°C), whereas in Pennsylvania, the shales reached the dry gas zone (>120°C) (Figure VII.6 ; Evans, 1995).

1.2.4 Remagnetization of the Late Paleozoic sedimentary rocks

Under certain conditions sedimentary rocks may be affected by significant remagnetization overwhelming the original paleomagnetic signal. This phenomenon is typically encountered in the Late Paleozoic rocks of North America (McCabe & Elmore, 1989) and of Europe (Weil & Van der Voo, 2002). In the following, we consider the Appalachians Paleozoic rocks only due to our sampling limitations. Originally, the remagnetization of these rocks was highlighted by paleomagnetic studies on red beds and limestones from North America (McCabe & Elmore, 1989 for a review). These studies showed that the Upper Paleozoic magnetic paleopole was identical to that of the Lower Paleozoic with an inverse polarity characteristic of the Kiaman superchron (e.g. Irving & Opdyke, 1965 ; Roy *et al.*, 1967) 255-275 Ma ago (Stamatakos *et al.*, 1996).

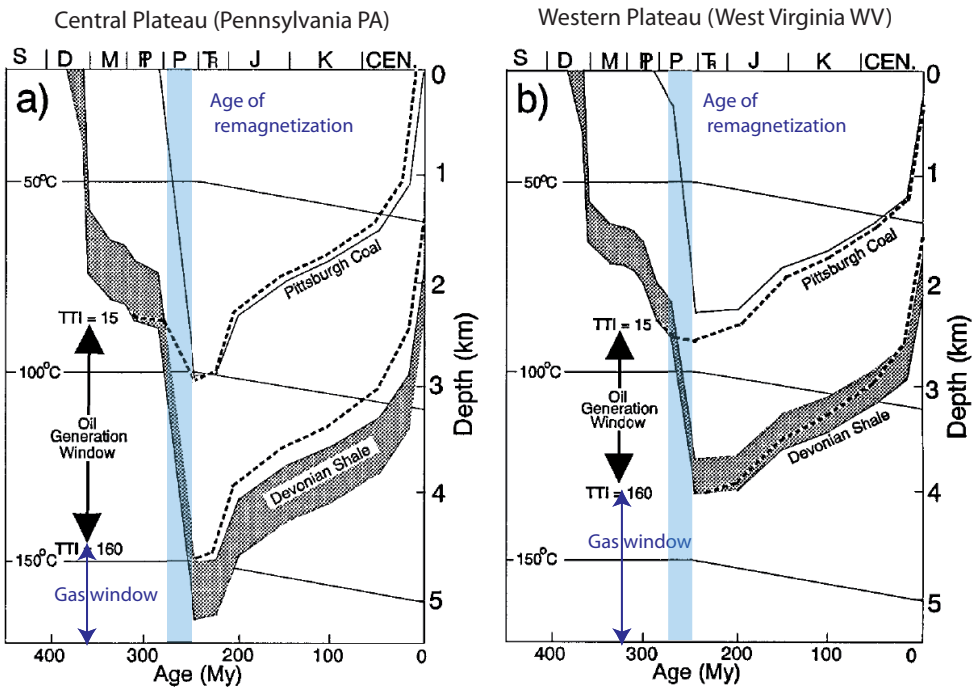

Figure VII.6 – Burial history curves for the Middle Devonian shales and the Pittsburgh coal for a) the central Appalachian Plateau (Pennsylvania) and b) the western Plateau (West Virginia) (modified after Evans, 1995)

Two principal mechanisms are evoked to explain the remagnetization of these rocks :

- A CRM [1] acquisition by the formation and/or growth of authigenic magnetic minerals passing through their blocking volume. CRM may originate from a variety of processes but in the Appalachians, the CRM is mainly due to orogenic fluid circulation (Oliver, 1986 ; Evans *et al.*, 2000 ; Elmore *et al.*, 2001) ;
- A TVRM [2] acquisition by heat conduction during burial or a prolonged exposition to high temperatures below the Curie temperature of the magnetic carrier of the remagnetization (Kent, 1985).

In most Paleozoic limestones from North America, authigenic magnetite carries the remagnetization (e.g. Lu *et al.*, 1990). This magnetite displays very small SP [3] to SD [4] particles (Jackson, 1990 ; Jackson *et al.*, 1992 ; Jackson & Worm, 2001). Two classical tests allow the identification of these magnetites : 1) the Hcr/Hc vs. Mrs/Ms diagram (also called Day diagram) where hysteresis data are aligned along specific "remagnetized" slopes (Figure VII.7) ; 2) an unblocking temperature near or below 500°C which is an indication of fine magnetites.

1. Chemical Remanent Magnetization
2. Thermoviscous Remanent Magnetization
3. Superparamagnetic
4. Single domain

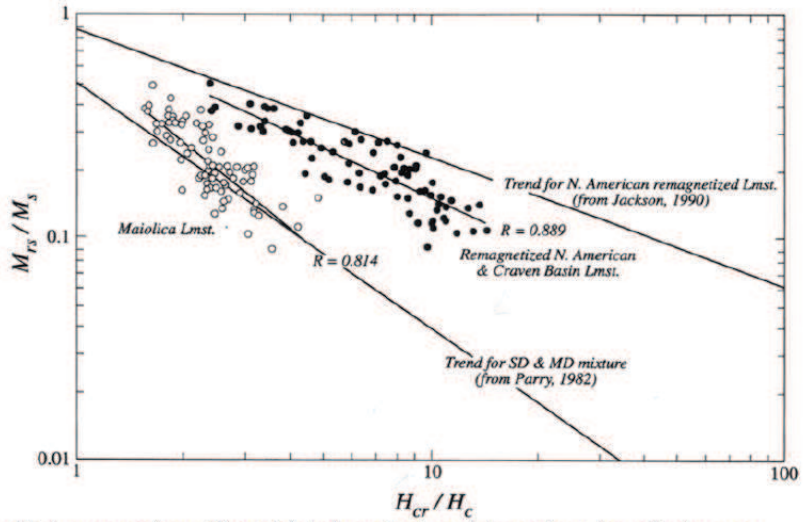

Figure VII.7 – Hysteresis parameters of the remagnetized and non remagnetized limestones (Channell & McCabe, 1994)

In the Trenton limestones, the absence of the Verwey transition of magnetite suggests that the authigenic magnetite is either maghemitized (e.g. Muxworthy & McClelland, 2000) or slightly to moderately cation-deficient (Jackson & Worm, 2001). Much evidence is in favor of the CRM hypothesis being responsible for this remagnetization. Magnetite observed in the North America limestones presents spherule or framboid shapes formed respectively by authigenesis or by oxidation of a precursor mineral such as pyrite (Suk *et al.*, 1990, 1991). On the other hand, by studying a carbonate transect on the north of the New York State, Jackson et al. (1988) observed a narrow relationship between authigenic magnetite and interlayered illitization. Besides these mechanisms, penetration of K-rich brines (McCabe *et al.*, 1989), presence of hydrocarbons (Elmore *et al.*, 1987 ; McCabe *et al.*, 1987) and orogenic fluid circulation (McCabe *et al.*, 1989) are also evoked to explain the formation of the authigenic magnetite.

The Siluro-Devonian Tonoloway and Helderberg Formations limestones were remagnetized during the Permian Kiaman superchron (Elmore *et al.*, 2001 ; Lewchuk *et al.*, 2002). Even though the remagnetization carrier is well identified to be magnetite (e.g. Elmore *et al.*, 2006), the formation of this authigenic magnetite and the origin of the remagnetization are debated. By considering a maximum burial temperature of 150°C (Figure VII.5 ; Evans & Battles, 1999), Elmore *et al.* (2006) ruled out the TVRM hypothesis because the unblocking temperatures of 500-525°C are too high compared to the time-unblocking temperature relationship determined by Pullaiah *et al.* (1975). Then this is a CRM. Their study and that of Lewchuk *et al.* (2003) show a link between deformation and remagnetization, especially between deformation and the degree of folding. It is unlikely that this remagnetization is related to orogenic fluids which occurrence is attested (Evans *et al.*, 2000). Indeed, Evans & Battles (1999) reported a distinct stratification of the fluid inclusions and isotopic data indicating that during

the Alleghanian orogeny the regional hydrologic system was connected at the formation scale. Each formation was isolated from the adjacent rocks. On the other hand, there is no evident correlation between warm fluids circulation and remagnetization. Magnetite which carries the CRM was probably formed by diagenetic processes related to burial (Dorobek, 1987 ; Brothers *et al.*, 1996 ; Elmore *et al.*, 2006). This is supported by $^{87}Sr/^{86}Sr$ isotopic data which showed that external fluids could not alter in large scale the Tonoloway and Helderberg Formations (Dorobek, 1989 ; Evans & Battles, 1999 ; Elmore *et al.*, 2001 ; Elmore *et al.*, 2006).
In the Southern Appalachians, McCabe *et al.* (1989) showed that the remagnetization carried by magnetite could not be a TVRM as a result of the low thermal maturity of the studied rocks (CAI $<$ 1.5). However, the TVRM hypothesis can not be completely ruled out, notably on the north of the New York State (Hudson Valley) where the CAI values of about 4.5 indicate a rather high maturity (deeper burial or warm fluid circulation) (e.g. Dorobek, 1989 ; McCabe *et al.*, 1989). Remagnetizations of chemical or thermoviscous origin are not incompatible but it is the CRM hypothesis which is widely accepted.

2 Sampling and Methods

2.1 Sampling

We collected our samples in clays-rich rocks in order to check whether the magnetic assemblage diagnostic of burial can be identified. If positive, then the wide remagnetization observed in the Appalachians belt could be attributed to burial occurring during folding event.
Sampling was done in March 2010. We collected 61 samples : 56 in West Virginia, 2 in Maryland and 3 in Pennsylvania (Table VII.1). Maryland and Pennsylvania samples comfort the results provided by the large number of samples from West Virginia. Only results obtained on West Virginia samples are presented below (Figure VII.8).

The samples analyzed in our study cover the stratigraphic interval going from the Silurian Clinton Group to the Upper Devonian Chemung Formation including the gas shale Marcellus Formation. This interval represents a cumulated 3 km thickness at maximum and 80 km wide sampling zone. Samples were taken from fresh road cuts whenever possible to ensure minimum weathering alteration. Care was taken to sample away from mineral veins (quartz, calcite) to avoid zones impacted by the effect of fluid circulation. Some samples, especially within limestones, are recognized as clearly weathered. The weathering aspect indicated in the Table VII.1 is based on the naked eye observation (e.g. sample color after crushing).

The Figure VII.9 shows some sampled outcrops. We did not observe any pencil or slaty cleavage in our samples suggesting that the paleotemperatures experienced by the rocks did not exceed ∼200-250°C, in agreement with evidence from fluid inclusions microthermometry data.

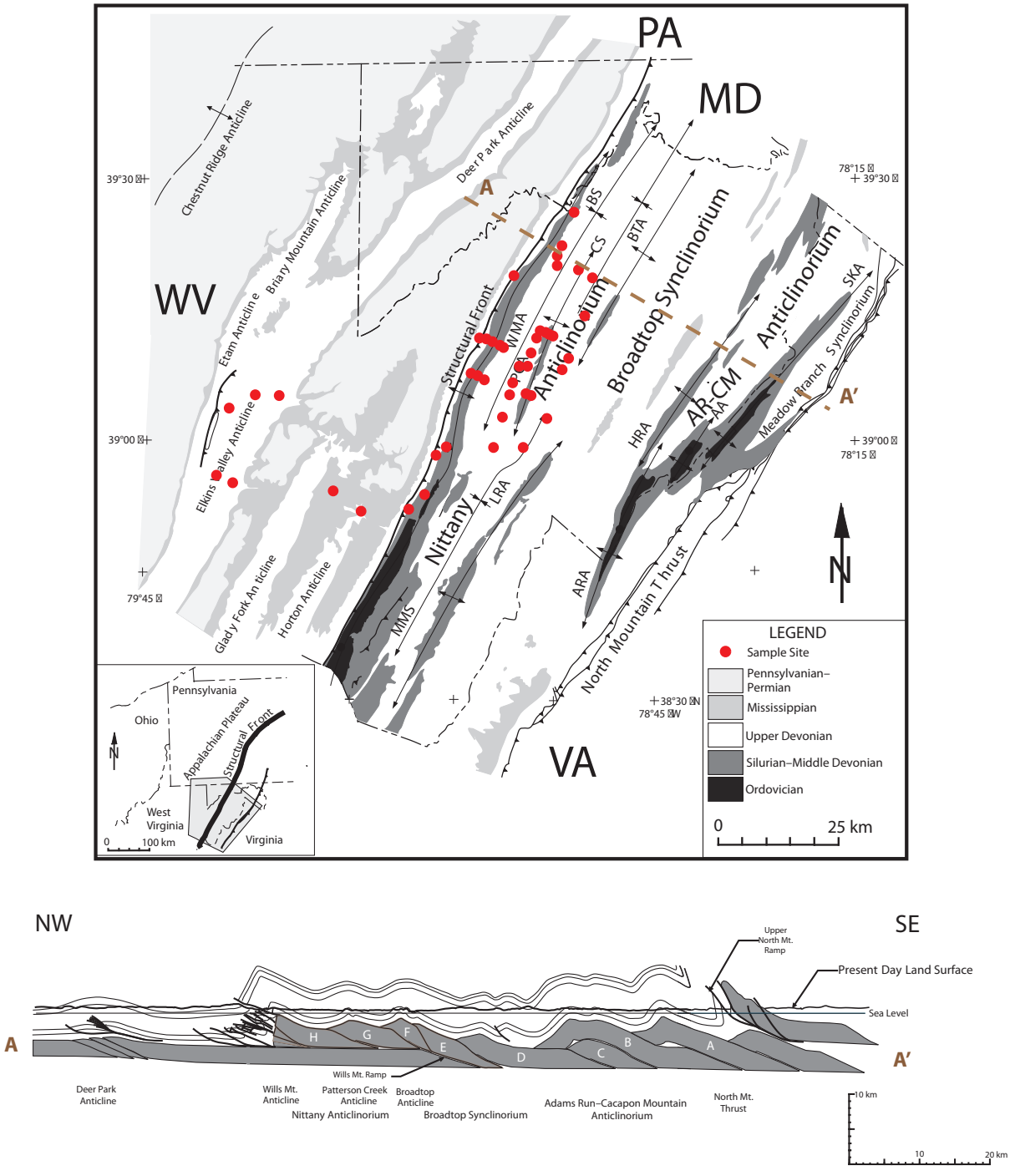

Figure VII.8 – Location map of samples collected in West Virginia (map and cross section from Evans, 2010). One red dot can represent several nearby samples collected in a same sampling site. Same legend as Figure VII.4.

Formation	Age	Sample	State	Latitute (°)	Longitude (°)	Altitude (m)	Alteration
Conemaugh	Carbon	WV60	PA	N 40°18'10.4"	W 79°30'04.7"	347	
		WV61	PA	N 40°18'12.9"	W 79°30'39.9"	379	
Pocono		WV49	WV	N 38°54'55.3"	W 79°30'37.7"	816	
Hamsphire	Devonian	WV48	WV	N 38°52'30.0"	W 79°27'32.9"	491	
Chemung		WV37	WV	N 39°11'54.8"	W 79°11'11.1"	625	
		WV38	WV	N 39°11'56.0"	W 79°11'13.3"	651	X
		WV47	WV	N 38°51'39.2"	W 79°22'04.2"	428	
		WV50	WV	N 38°54'58.8"	W 79°47'07.1"	787	
		WV51	WV	N 38°54'58.8"	W 79°47'07.1"	787	
		WV54	WV	N 39°05'42.0"	W 79°45'19.7"	612	
		WV55	WV	N 39°05'17.6"	W 79°41'16.8"	519	X
		WV56	WV	N 39°20'04.1"	W 79°05'26.6"	488	X
		WV58	MD	N 39°41'55.2"	W 78°42'25.6"	231	
Braillier		WV26	WV	N 39°18'07.3"	W 78°52'29.6"	243	
		WV42	WV	N 38°59'35.4"	W 79°02'44.5"	323	X
		WV52	WV	N 38°57'16.8"	W 79°51'18.5"	595	
		WV53	WV	N 39°04'09.8"	W 79°48'37.0"	628	
Harrell-Braillier		WV10	WV	NO GPS DATA			
		WV11	WV	NO GPS DATA			
		WV24	WV	N 39°20'45.2"	W 78°59'17.8"	282	
		WV45	WV	N 38°57'24.4"	W 79°17'38.9"	428	
		WV59	PA	N 40°02'32.3"	W 78°34'21.1"	363	X
Mahantango		WV12	WV	NO GPS DATA			
		WV15	WV	NO GPS DATA			
		WV21	WV	NO GPS DATA			X
		WV27	WV	N 39°13'48.5"	W 78°55'02.4"	265	
		WV28	WV	N 39°05"44.6"	W 79°06'18.0"	375	
		WV29	WV	N 39°03'18.5"	W 79°06'49.2"	358	
		WV30	WV	N 39°06'48.0"	W 79°09'53.6"	390	
		WV40	WV	N 39°21'09.4"	W 78°59'13.7"	317	X
		WV41	WV	N 39°21'38.0"	W 78°58'53.8"	315	X
Marcellus-Needmore		WV2	WV	NO GPS DATA			
		WV13	WV	NO GPS DATA			
		WV14	WV	NO GPS DATA			
		WV22	WV	NO GPS DATA			
		WV23	WV	NO GPS DATA			
		WV25	WV	N 39°19'44.7"	W 78°53'12.5"	270	
		WV43	WV	N 39°00'13.0"	W 79°09'26.8"	302	
Needmore/Oriskany		WV33	WV	N 39°10'33.9"	W 79°07'04.0"	386	
Oriskany		WV1	WV	NO GPS DATA			
		WV3	WV	NO GPS DATA			
Oriskany/Helderberg		WV34	WV	N 39°10'37"	W 79°07'13.4"	412	
		WV35	WV	N 39°10'37"	W 79°07'13.4"	412	
Helderberg		WV9	WV	NO GPS DATA			
		WV16	WV	NO GPS DATA			X
		WV32	WV	N 39°07'53.6"	W 79°12'14.3"	484	
		WV36	WV	N 39°11'30.2"	W 79°09'47.7"	447	
Tonoloway	Silurian	WV4	WV	NO GPS DATA			
		WV5	WV	NO GPS DATA			X
		WV8	WV	NO GPS DATA			
		WV17	WV	NO GPS DATA			
		WV18	WV	NO GPS DATA			
		WV19	WV	NO GPS DATA			
		WV20	WV	NO GPS DATA			
		WV39	WV	N 39°26'03.6"	W 78°57'16.1"	293	X
		WV44	WV	N 38°59'10.4"	W 79°15'52.2"	343	
		WV46	*WV*	N 38°54'18.0"	W 79°18'54.5"	437	
McKenzie/Clinton		WV6	WV	NO GPS DATA			
		WV7	WV	NO GPS DATA			
Clinton		WV31	WV	N 39°07'33.3"	W 79°10'51.7"	455	
		WV39	WV	N 39°26'03.6"	W 78°57'16.1"	293	X
		WV46	*WV*	N 38°54'18.0"	W 79°18'54.5"	437	
		WV57	*MD*	N 39°38'28.8"	W 78°47'36.3"	365	
Tuscarora		*WV57*	*MD*	N 39°38'28.8"	W 78°47'36.3"	365	

Table VII.1 – Samples collected in West Virginia (WV), Pennsylvania (PA) and Maryland (MD). The exact stratigraphic attribution of sample 46 and 57 (in italic) was not possible, thus these two samples are listed in two formations.

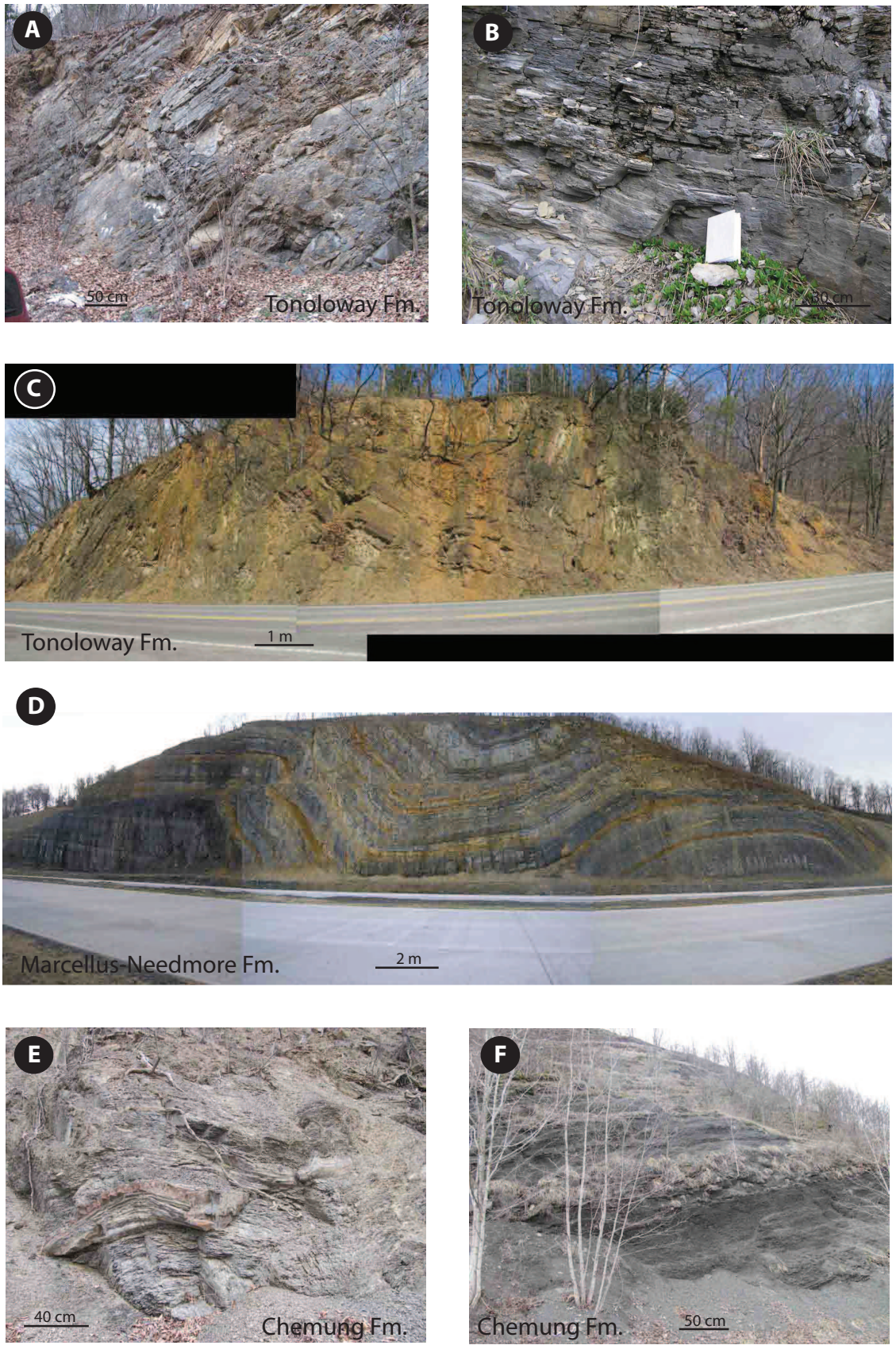

Figure VII.9 – Outcrops pictures in West Virginia

2.2 Methods

We performed a series of magnetic measurements on the samples. Low field magnetic susceptibility χ was measured at the Ecole Normale Supérieure (ENS), while room temperature hysteresis loops and FORCs and low temperature MPMS measurements were done at the Institute for Rock Magnetism. These routine measurements are described in chapter III. 12 samples were chosen for the Lowrie test (Lowrie, 1990). A few SEM observations were also realized at the ENS (Figure VII.10). Table VII.2 reports the different measurements performed on the samples.

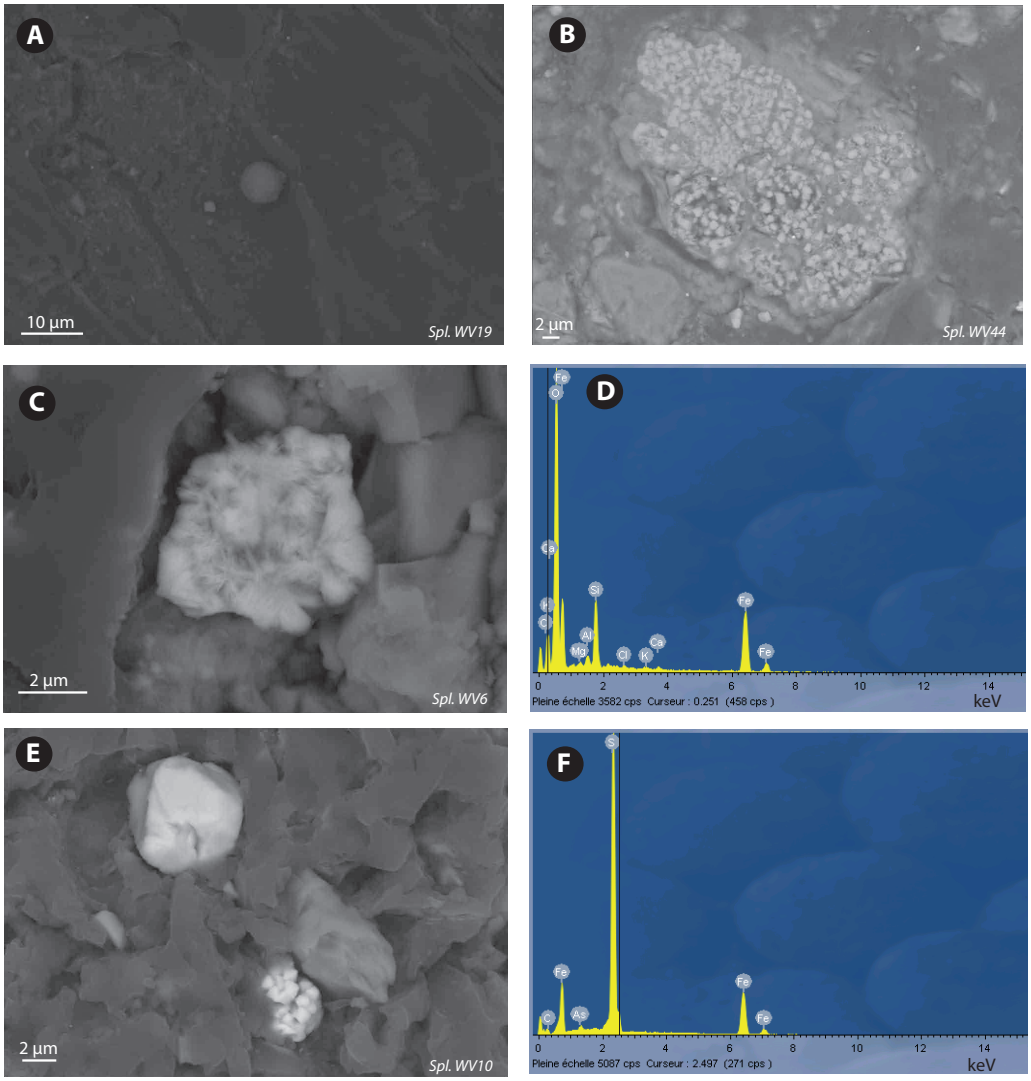

Figure VII.10 – SEM observations : A) magnetite spherule comforting the neoformation feature and B) oxidized framboids in the Tonoloway Formation, C) goethite in the Clinton Formation with D) the associated XRD spectrum and E) pyrite in the Harrell-Braillier Formation with F) the associated XRD spectrum

Formation	Age	Sample	Xlf (SI)	RT-SIRM 300K (Am^2/kg)	LT-SIRM 10 K (Am^2/kg)	Altera-tion	SEM Obs.	X-ray	"Lowrie test"
Conemaugh	Carbon	WV60	3.33E-04	1.97E-04	1.42E-03				
		WV61	1.93E-04	2.35E-05	6.82E-04				
Pocono		WV49	1.67E-04	5.63E-05	3.05E-03				X
Hamsphire	Devonian	WV48	2.43E-04	6.08E-05	3.89E-04				X
Chemung		WV37	3.54E-04	1.60E-03	3.97E-03				
		WV38	3.14E-04	3.24E-05	2.07E-02	X			
		WV47	3.63E-04	5.44E-05	3.49E-03				
		WV50	3.31E-04	2.77E-05	1.89E-03				
		WV51	3.95E-04	4.21E-05	3.19E-03				
		WV54	3.16E-04	3.56E-05	1.85E-02				
		WV55	2.79E-04	4.06E-05	1.69E-02	X			
		WV56	3.99E-04	2.74E-04	1.29E-02	X			
		WV58	2.54E-04	3.21E-05	4.07E-04				X
Braillier		WV26	3.28E-04	2.44E-05	9.72E-04				
		WV42	3.14E-04	3.49E-05	6.11E-03	X			
		WV52	2.83E-04	1.87E-05	2.54E-03				
		WV53	2.78E-04	4.99E-05	2.75E-03				X
Harrell-Braillier		WV10	4.13E-04	4.48E-05	1.13E-03		X	X	
		WV11	4.33E-04	2.87E-05	1.07E-03				
		WV24	2.90E-04	2.69E-05	3.32E-04				
		WV45	2.72E-04	3.17E-05	5.68E-04				
		WV59	2.09E-04	1.97E-05	1.61E-02	X	X	X	
Mahantango		WV12	1.05E-04	2.29E-05	3.02E-04				
		WV15	2.63E-04	1.13E-04	2.09E-03				
		WV21	3.70E-04	1.05E-04	2.66E-02	X			
		WV27	2.67E-04	1.85E-05	6.54E-04				
		WV28	4.08E-04	2.63E-05	1.51E-03				
		WV29	2.92E-04	3.04E-05	1.87E-03				
		WV30	1.38E-04	1.12E-05	2.77E-04				
		WV40	2.94E-04	9.77E-05	2.27E-02	X			
		WV41	2.63E-04	5.58E-05	4.96E-03	X			
Marcellus-Needmore		WV2	8.34E-05	2.87E-05	3.35E-04				
		WV13	3.00E-04	1.97E-05	5.55E-04				X
		WV14	1.41E-04	1.82E-05	9.18E-04				X
		WV22	1.52E-04	7.46E-05	5.35E-04				X
		WV23	2.15E-04	1.15E-04	1.01E-03				X
		WV25	3.15E-04	3.20E-05	1.04E-03				X
		WV43	3.35E-04	1.71E-05	6.95E-04				X
Needmore/Oriskany		WV33	2.01E-04	3.39E-05	5.04E-03		X	X	
Oriskany		WV1	6.37E-05	4.96E-05	3.49E-04				
		WV3	1.67E-04	7.55E-05	1.30E-02				
Oriskany/Helderberg		WV34	3.47E-04	3.17E-05	8.88E-04			X	
		WV35	3.69E-04	2.90E-05	1.18E-03				
Helderberg		WV9	1.45E-04	1.14E-04	6.22E-03				
		WV16	2.29E-04	9.04E-05	2.57E-02	X			
		WV32	2.27E-05	5.37E-05	3.26E-04				
		WV36	1.03E-04	7.79E-05	4.05E-04				
Tonoloway	Silurian	WV4	5.51E-04	4.37E-04	1.93E-03		X		
		WV5	1.72E-04	4.32E-05	9.77E-03	X			
		WV8	5.08E-04	2.17E-04	1.26E-03				
		WV17	2.47E-04	1.87E-04	7.61E-04				
		WV18	2.19E-04	8.07E-05	7.59E-03			X	
		WV19	1.16E-04	7.79E-05	3.91E-04		X	X	
		WV20	1.20E-04	3.77E-04	3.11E-03				
		WV39	3.48E-04	1.34E-04	1.28E-02	X			
		WV44	2.81E-04	1.40E-04	6.45E-04		X	X	X
		WV46	3.23E-04	1.34E-04	8.35E-04				
McKenzie/Clinton		WV6	2.23E-04	5.82E-05	2.14E-02		X	X	
		WV7	2.87E-04	2.43E-05	1.00E-03		X	X	
Clinton		WV31	3.49E-04	6.00E-04	1.10E-03		X	X	X
		WV39	3.48E-04	1.34E-04	1.28E-02	X			
		WV46	3.23E-04	1.34E-04	8.35E-04				
		WV57	4.26E-04	1.61E-03	2.24E-03				
Tuscarora		*WV57*	4.26E-04	1.61E-03	2.24E-03				

Table VII.2 – Some magnetic properties and analyses of the samples

3 Magnetic assemblage in West Virginia

The stratigraphic section of West Virginia samples can be divided in two parts : a sandstone-limestone section (section A ; from the Tonoloway Formation to the Oriskany Sandstone) and a shale-to-silt section (section B ; from the Needmore Shale to the Chemung Group). Paleomagnetic studies that revealed a pervasive Kiaman remagnetization were performed in section A. This remagnetization has been dated during the Alleghanian orogeny (syn-tilting remagnetization) (e.g. Lewchuk *et al.*, 2003).

Our measurements indicate that the low magnetic susceptibility χ ranges from 23 to 551 μSI with a mean value of 241 $\pm$ 146 μSI for the section A and from 83 to 433 μSI (287 $\pm$ 88 μSI) for the section B. The two sections cannot be distinguished on the basis of magnetic susceptibility. The saturation isothermal remanent magnetization at room temperature RT-SIRM$_{300K}$ ranges from 29 to 437 μAm^2/kg (131 $\pm$ 113 μAm^2/kg) and from 11 to 1610 μAm^2/kg (95 $\pm$ 272 μAm^2/kg) for section A and B respectively. One sample presenting a very elevated value of RT-SIRM$_{300K}$ in section B strongly influences standard deviation. If one does not consider this sample, RT-SIRM$_{300K}$ values in section B (shaly facies) are generally lower than those in section A (carbonate facies).

The low temperature measurements performed on the samples show characteristic magnetic signals, similar to those identified in the Grès d'Annot basin (see chapter VI). The Table VII.3 shows the occurrence of the different magnetic features identified in the West Virginia samples. A detailed description follows.

3.1 From the Tonoloway Formation to the Oriskany Sandstone

The section A is predominantly characterized by a particular low temperature magnetic signal called S1 (S stands for signal). Representative samples of such a signal are shown in Figure VII.11. The cooling curve RT-SIRM increases from 300 to 10 K in both specimens of more than 25% of the RT-SIRM$_{300K}$. In Figure VII.11B, the sample shows a slight Verwey transition of magnetite and a more rapid increase of the magnetization from ∼34 K. The warming curve ZFC decays monotonically to ∼150-170 K, and then decreases very rapidly to ∼250 K where a break-in-slope occurs (Figure VII.11). The remanence is quasi-stable to 300 K. This break-in-slope at ∼250 K may also occur at ∼200 K.

This signal is considered characteristic of goethite based on the increase of the RT-SIRM curve (Dekkers, 1989a) and the similarity with those found in the Grès d'Annot basin in the Le Ruch and Grand Coyer areas (Figure 10E in chapter VI).

A second type of magnetic signal named S2 can be found in the Tonoloway Formation (Figure VII.12A). The interesting feature of this signal is the shape of the RT-SIRM curve. The remanence decreases in the temperature range of magnetite Verwey transition and displays a abrupt drop between 40 and 33 K. It is typical of micron-size pyrrhotite (Dekkers, 1989b ; Dekkers *et al.*, 1989 ; Rochette

			RT-SIRM curve				ZFC curve		
Formation	Age	Sample	V	P-beh.	G	Pyrr.	2-step	200 K	Remark
Conemaugh	Carbon	WV60							
		WV61							
Pocono		WV49							
Hamsphire	Devonian	WV48				?			
Chemung		WV37							E
		WV38	?						A
		WV47					?		
		WV50							
		WV51							
		WV54		Néel?					
		WV55							A
		WV56							A
		WV58							
Braillier		WV26							
		WV42	?		?				A
		WV52							
		WV53							
Harrell-Braillier		WV10							
		WV11							
		WV24							
		WV45							
		WV59							A
Mahantango		WV12		?					
		WV15		?					
		WV21				?			A
		WV27							
		WV28							
		WV29				?			
		WV30							
		WV40							A
		WV41							A
Marcellus-Needmore		WV2		?					
		WV13		?					
		WV14							
		WV22		?					
		WV23		?			?		
		WV25							
		WV43							
Needmore/Oriskany		WV33							
Oriskany		WV1							
		WV3							
Oriskany/Helderberg		WV34							
		WV35							
Helderberg		WV9							
		WV16							A
		WV32				?			
		WV36				?	?		
Tonoloway	Silurian	WV4						?	
		WV5		?					A
		WV8	?				?		
		WV17					?		
		WV18							
		WV19					?		
		WV20						?	
		WV39		?					A
		WV44					?		
		WV46					?		
McKenzie/Clinton		WV6							
		WV7							
Clinton		WV31							E
		WV39		?					A
		WV46					?		
		WV57							E
Tuscarora		*WV57*							E

Table VII.3 – Magnetic features distribution through the stratigraphic column (A : altered, E : undetermined). V : Verwey transition, P-beh. : P-behavior, G : goethite, Pyrr : pyrrhotite $> 1\mu$m, 2-step : 2-step pattern„ 200 K : inflexion point within 200-250 K

et al., 1990). As the result of the 5 μT upward magnetic field applied inside the MPMS, the remanence, which is actually an induced magnetization, increases to 10 K. This sharp increase is probably a Néel transition (see also chapter VI).

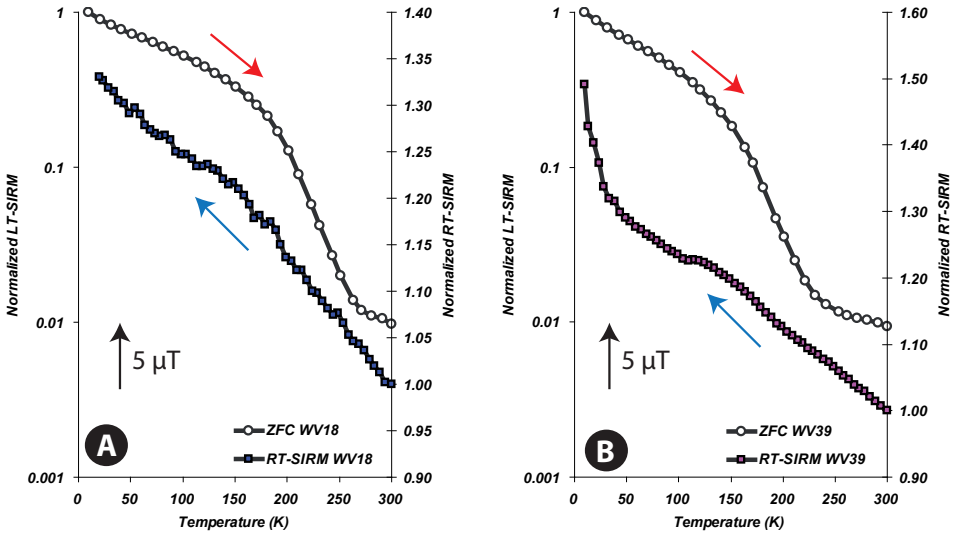

Figure VII.11 – Low temperature magnetic signal S1 found from the Tonoloway Formation to the Oriskany Sandstone stratigraphic section (the two samples are from the Tonoloway Formation)

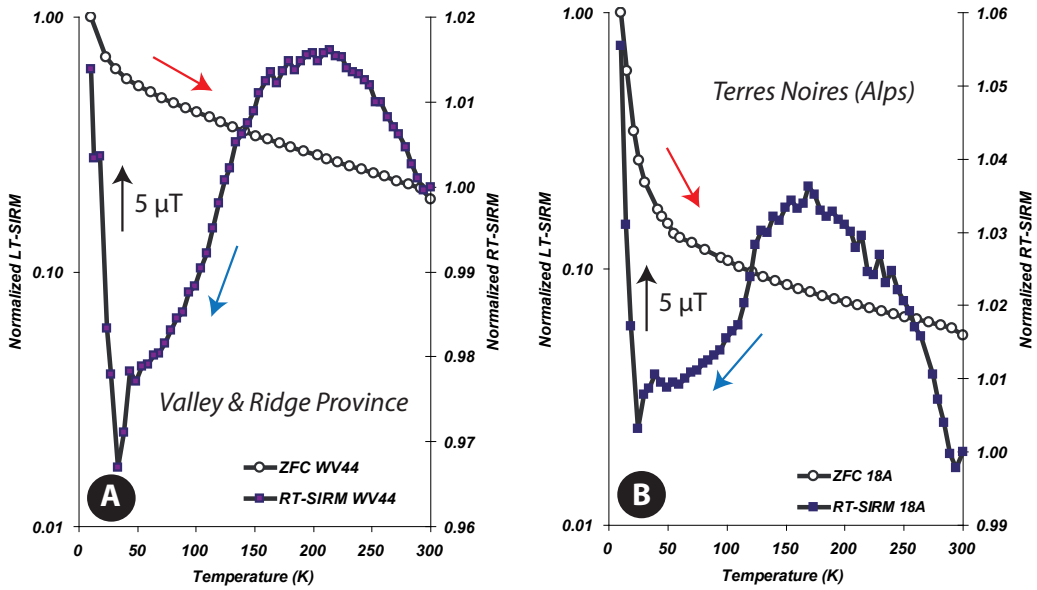

Figure VII.12 – Low temperature S2 signal for a sample from A) the Tonoloway Formation and B) the Jurassic Terres Noires from the Vocontian trough.

A magnetic signal similar to this S2 signal is found in other geological settings such as the Jurassic Terres Noires in the Alps (Figure VII.12B) and the Marnes Bleues in the La Moutière area (Figure 10I in chapter VI). Besides, Jackson *et al.* (1993) suggested that pyrrhotite is present in samples from the Trenton and Onondaga Limestones of New York State, even though the 34 K magnetic transition of pyrrhotite is not displayed.

Hysteresis loops and FORC diagrams were done on samples from section A. FORC diagrams (Figure VII.13A) show a soft SD magnetic mineral. The coercive field Hc is pretty low of ∼10 mT. These room temperature observations lead that non-interacting SD magnetite is probably present in these samples even if the characteristic transition of magnetite at 120 K is not always present in the low temperature magnetic measurements. Previous studies (Jackson, 1990 ; Jackson *et al.*, 1992 ; Jackson & Worm, 2001) on the magnetic properties of remagnetized carbonates from North America showed that authigenic stoichiometric magnetite occurs in very small grain-sizes (SP to SD). This magnetite is responsible for the Late Paleozoic pervasive chemical remanent magnetization identified in this geographical area (McCabe & Elmore, 1989). In addition the hysteresis loops (Figure VII.13B) are wasp-waisted meaning that different coercive magnetic minerals are present and/or two different grain-sizes. Saturation at 1 T is completed indicating that a low coercive magnetic mineral is present. The wasp-waisted feature is characteristic of the remagnetized limestones in North America (Jackson, 1990). The hysteresis parameters plotted on a Day plot (Figure VII.14) of selected (valid) samples from section A fall between a mixture of SD + MD particles and remagnetized samples. The goethite identified at low temperature is not seen in these hysteresis loops and FORC diagrams. It is probably not saturated because it needs a higher magnetic field (Rochette *et al.*, 2005).

3.2 From the Needmore Shale to the Chemung Group (including Marcellus Fm.)

In the upper part of the stratigraphic sequence, section B is characterized by two distinct magnetic signals. A few samples display S1 magnetic signal. 16% of them reflect surface alteration (yellowish at naked eye). By side, a majority of samples (56%) shows a third additional magnetic signal S3 (Figure VII.15).

The S3 signal is characterized by a ZFC curve displaying a 2-step pattern as described by Aubourg & Pozzi (2010). The remanence acquired at 10 K drops rapidly between 10 and 35 K then regularly decreases to 300 K with another sharp drop occurring at ∼120 K. The RT-SIRM curve is quasi-stable from 300 to ∼120 K, temperature at which a slight decrease occurs, then the remanent magnetization (actually an induced magnetization) increases from 100 to 10 K. The increase of RT-SIRM is more rapid below 50 K. The decrease of the remanence, both in ZFC and RT-SIRM curves, at about 120 K corresponds to the well known Verwey transition of stoichiometric SD magnetite (e.g. Muxworthy & McClelland, 2000). This magnetite is authigenic (e.g. Jackson *et al.*, 1988 ; Jackson *et al.*, 1992). The increase of the magnetization from ∼100 to 10 K in this signal has a debated origin (Kars *et al.*,

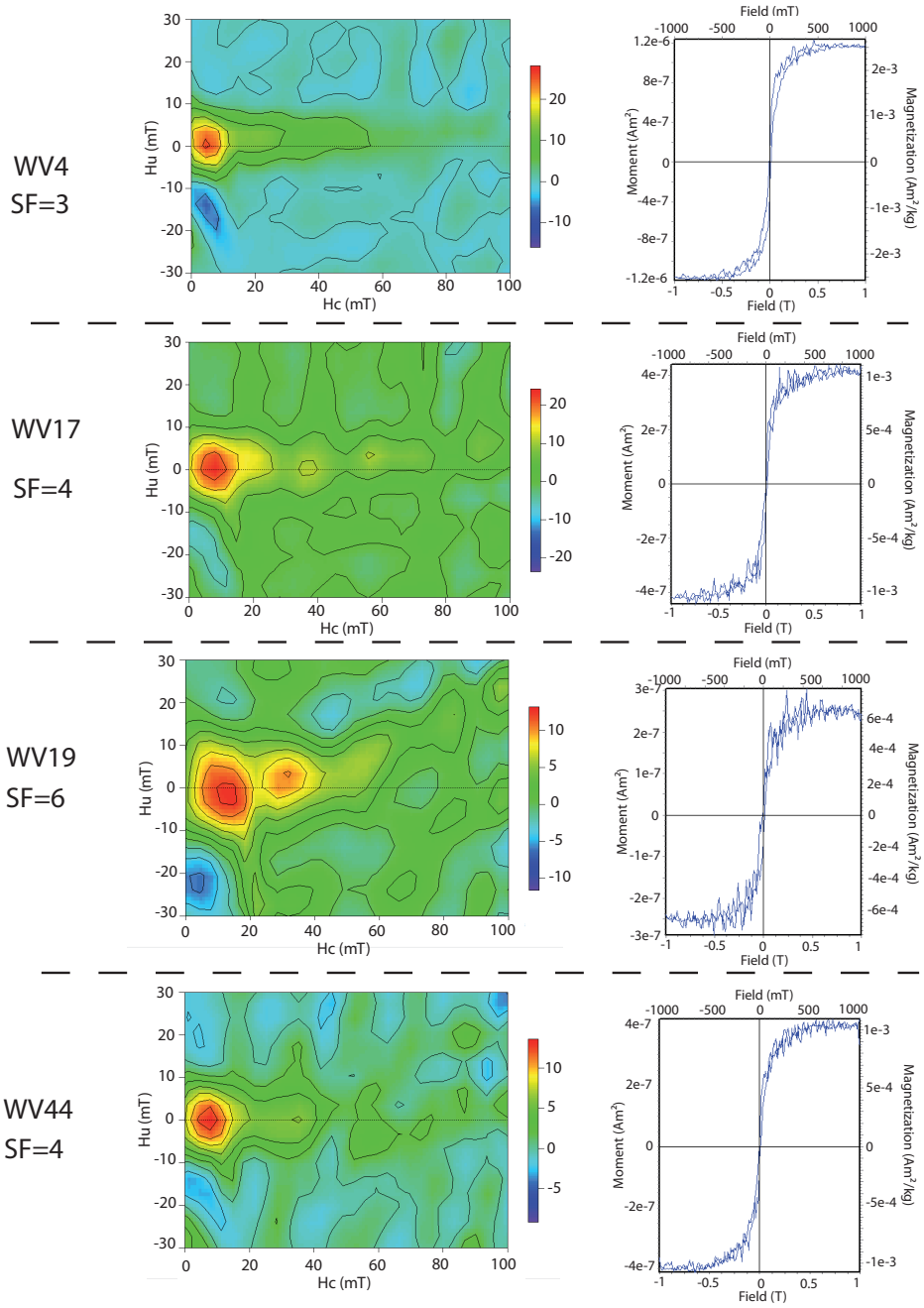

Figure VII.13 – A) FORC diagrams (SF : smoothing factor) and B) wasp-waisted hysteresis loops at room temperature for four samples from the Tonoloway Formation supporting the presence of SD magnetite. See Figure VII.10A for a SEM image of this magnetite.

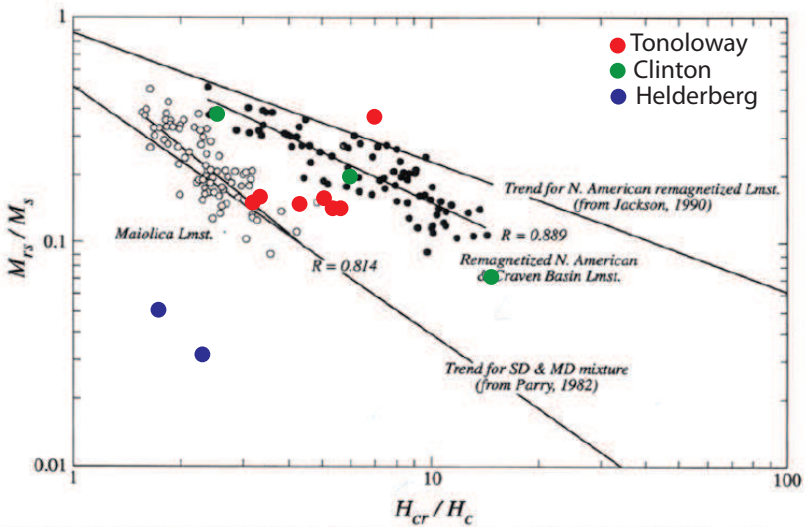

Figure VII.14 – Hysteresis parameters of section A samples in Day plot with "remagnetized" slopes (after Channell & McCabe, 1994)

2011a). Aubourg & Pozzi (2010) suggested that this increase is due to < 1 μm pyrrhotite. In the following, the general term of iron sulfides will be used. From SEM observations, it seems that iron sulfides are present in higher content compared to S1 signals. However, this is not proof that the S3 signal is characteristic of iron sulfides, as magnetite is the dominant magnetic mineral. The important decrease of the ZFC curve between 10 and 35 K represents more than 85% of the SIRM acquired at 10 K. This represents a large proportion of very small grains (< 20 nm in the case of magnetite).

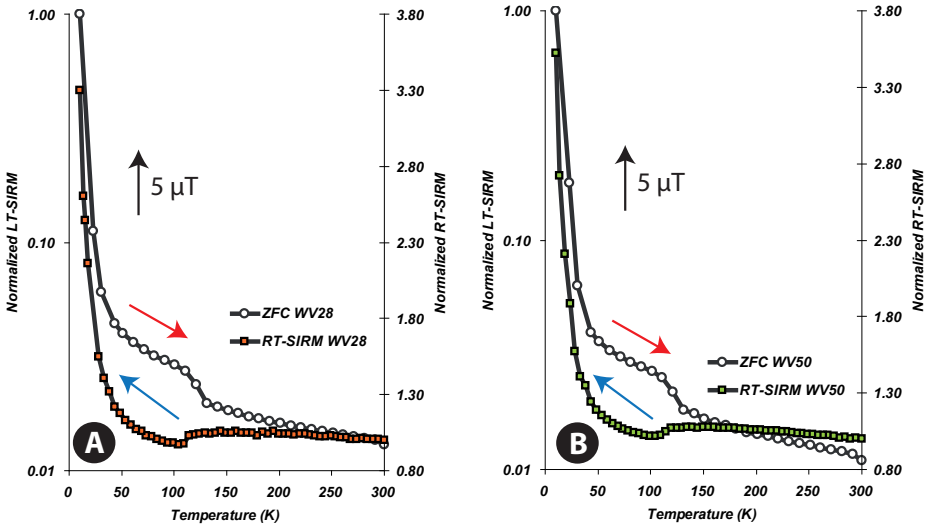

Figure VII.15 – Low temperature magnetic signal S3 found in A) the Mahantango Formation and B) the Chemung Group

Contrary to the samples from the Tonoloway-Oriskany interval, the room temperature hysteresis loops and FORC diagrams of samples displaying S3 signal are poorly defined and hardly interpretable. This could be due to a higher paramagnetic input (e.g. clays) and a lower magnetization.

Figures VII.16 and VII.17 represent the spatial distribution of the three magnetic signals identified in the study area. Altered samples and undetermined magnetic signals are also reported. No geographical trend appears as it was the case for the samples from the Grès d'Annot basin. However the definition of the different magnetic signals in the study area clearly shows a distinct pattern. Based on low temperature data, samples displaying S1 and S2 signals are found in the lower interval from the Tonoloway Formation to the Oriskany Sandstone. Samples displaying S3 signal are found in the upper part of the stratigraphic section from the Needmore Shale to the Chemung Group. Stoichiometric neoformed magnetite is found in the whole stratigraphic sequence.

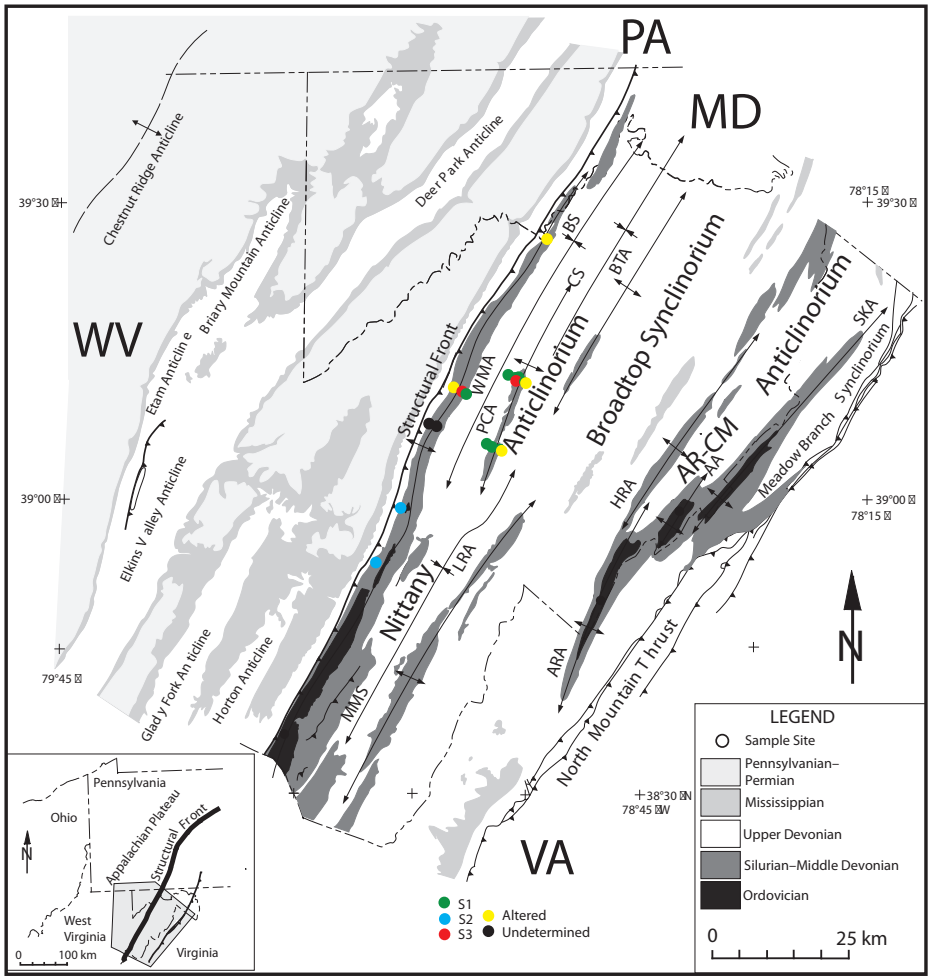

Figure VII.16 – Location map of the magnetic signals identified in West Virginia for section A. Same legend as Figure VII.4.

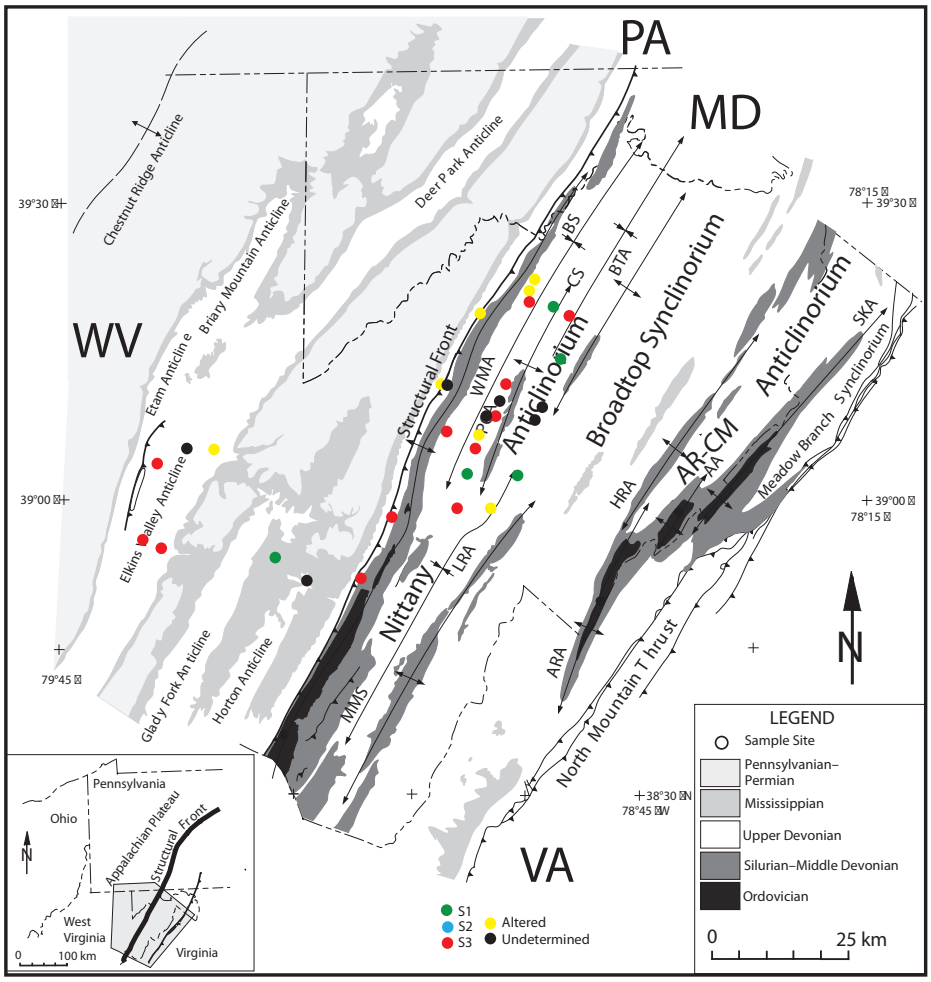

Figure VII.17 – Location map of the magnetic signals identified in West Virginia for section B. Same legend as Figure VII.4

4 Magnetic assemblage and thermal history

In the Grès d'Annot basin, the magnetic assemblage of the argillaceous samples is related to the burial/thermal history of the basin (chapter VI). As stated above, the different magnetic signals identified in West Virginia are stratigraphically distributed suggesting that lithologic and/or burial/thermal control may occur.

4.1 From the Tonoloway to the Oriskany Formations

The S1 magnetic signal is mainly observed in the Tonoloway-Oriskany interval. Based on fluid inclusions analyses, Evans & Elmore (2006) suggested that these formations underwent burial temperature of ∼150°C. In their reconstructed thermal history (Figure VII.5), they used a geothermal gradient of 20°C/km (present value) which may be low for Paleozoic time (Reed *et al.*, 2005). A value

of 25°C/km would be more realistic, although some authors suggest using a value of 30°C/km (Reed *et al.*, 2005). Evans & Elmore (2006) provided a well documented study of the different magnetic assemblages found in these formations in relation to tectonic history. They suggested that goethite found in the Tonoloway and Helderberg formations results from the oxidation of magnetite due to meteoric water circulations. During uplift (post-folding event) breaching of folds by fracturing occurred. This allowed penetration of such oxidizing fluids in fracture zones.
However, goethite could also be regarded as resulting from recent/present-day weathering (Lu *et al.*, 1990 ; Jackson *et al.*, 1992). Because all studied samples were collected at the surface, this possibility cannot be ruled out.

When comparing with the results of the Grès d'Annot basin study (chapter VI), such a magnetic assemblage would correspond to temperatures higher than 110-120°C in absence of fluids influence. One may conclude that this signal is characteristic of temperatures above the oil window. Oil generation in the Tonoloway and Helderberg Formations occurred in the Carboniferous when they were buried to 4-5 km depth (100-120°C ; Figure VII.5). Hence, the observations done in France and in the Appalachians are concordant. The upper boundary of this signal is not well defined. The occurrence of micron pyrrhotite in the Tonoloway Formation suggests that temperature reached locally 250°C. The S1 magnetic signal could therefore be a marker of temperature higher than 110-120 up to 250°C in carbonate-bearing rocks.

4.2 From the Needmore to the Chemung Formations

The S3 magnetic signal is particularly interesting because it is present in a stratigraphic interval which comprises the well known Marcellus Formation. This gas-shale formation is of a major interest because of its great petroleum potential as a major natural gas resource. The Marcellus Formation is characterized by high organic matter content (TOC∼10%) and high pyrite content (5-13%) (Harper, 2008).

The occurrence of the S3 signal corresponds to the zone where "warm" CH_4-saturated NaCl-$CaCl_2$ brines circulated in the Central Appalachians during the Late Paleozoic Alleghanian Orogeny (e.g. Dorobek, 1989 ; Evans & Battles, 1999). They were probably syn-orogenic and were expelled from the hinterland (Evans & Battles, 1999). Evans & Hobbs (2003) stated that these "warm" fluids did not significantly infiltrate the Appalachian Plateau Province, but rather migrated into the overlying strata along open fractures by forming hot springs at the paleosurface. The "warm" migrating fluids had circulated in the Oriskany-Lower Chemung interval prior to and during the Late Permian folding event. Based on fluid inclusions microthermometry data in mineral veins, Evans (1995, 2010) and Evans & Elmore (2006) stated that these "warm" migrating fluids ranged from 160 to > 200°C in temperature. Such high temperatures are only reported in late quartz veins (M. Evans pers. com.), and are unlikely to represent the ambient temperatures experienced by the host rocks which show no evident cleavage

(T < 200°C). Indeed it is possible that elevated temperatures and fluid circulations were restricted to fractures and fracture wall, and did not affect rock mass (M. Evans, pers. com.). Fluids inclusions analyses in the Middle Devonian Marcellus shale (Evans, 1995, pers. com.) show that the sedimentary rocks experienced maximum burial temperatures of 120 to 145°C. Oil generation window occurred during burial probably from Late Devonian to Early Carboniferous (M. Evans pers. com.).

Other maturity indicators are available for the Marcellus shale. The study area of the Valley & Ridge Province is situated to the east of the Alleghanian Structural Front. In relation to oil and gas exploitation history in the Appalachian Plateau, a few vitrinite reflectance Ro and Conodont Alteration Index (CAI) measurements were done in this part of West Virginia. Ro and CAI isograds are well defined in the west of the Alleghanian Structural Front in the Plateau where most of oil and gas wells are situated (Repetski *et al.*, 2005). In West Virginia, CAI and Ro values increase eastward. In the study area, CAI varies between 3.5 and 4, and Ro between 2 and 3% for the Devonian rocks. In terms of maturity of sedimentary rocks, these values correspond to a post-mature stage that is dry gas for hydrocarbons with temperatures higher than 180-200°C. Indeed, Evans & Battles (1999) report hydrocarbon inclusions of post-mature gas in the Oriskany-Marcellus interval.

The information reported above highlights some contradiction between temperatures derived from fluid inclusions microthermometry and organic indicators. Evans & Battles (1999) suggested that the "warm" migrating fluids caused the elevated thermal maturation indicators in the Valley & Ridge and Appalachian Plateau Provinces. These "warm" fluids may be also responsible for hydrocarbons flushing from the Valley & Ridge into the Appalachian Plateau. Another speculative explanation for the high thermal maturity is done by Cercone *et al.* (1996). They suggested that low thermal conductivity of coal- and carbonaceous shale-bearing Carboniferous strata acting as an insulator induced an abnormally elevated temperature in the underlying layers. This may also be valid for Devonian black shales.

Because the S3 magnetic signal is also found in the Appalachian Plateau (Figure VII.17), it seems unlikely that "warm" fluid circulations are responsible for the magnetic assemblage of S3 signal. However, it is found in the Helderberg/Oriskany boundary where a zone of fluid mixing was identified (Evans & Battles, 1999).

Such a magnetic signal displaying an important drop of the remanence between 10 and 35 K is not found in the Grès d'Annot basin. However, it is present in samples from the Borneo prism with similar Ro values (Figure VII.18). These samples experienced burial temperatures in the 200-250°C range (C. Aubourg pers. com).

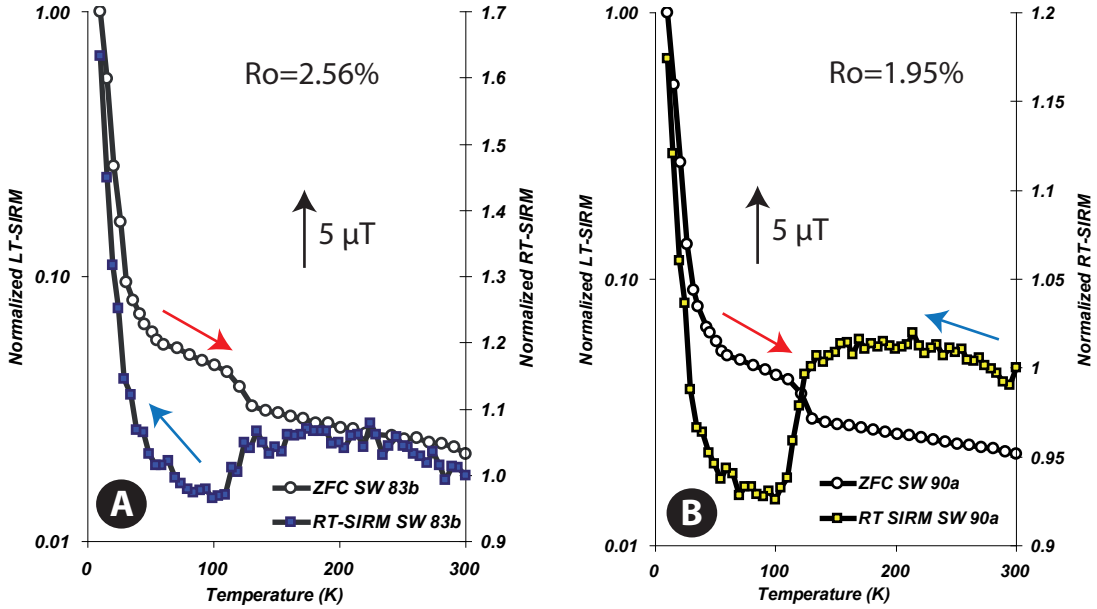

Figure VII.18 – Magnetic signal for two claystones from the Borneo Prism (data courtesy from D. Janots)

5 Application of the MagEval geothermometer

Only a few occurrences of MagEval-type signals, identified as S3 signal, are found in West Virginia. This S3 signal is stratigraphically constrained to the claystone/siltstone interval (from Needmore to Chemung Formations). The PM values are quite high, close to the theoretical PM max, for the most part of these samples (> 0.8). According to the model and the established calibrations (chapter IV), such PM values would correspond to a temperature around 90°C. As discussed previously, the Needmore-Chemung interval displays some discrepancies when considering different thermal indicators. Vitrinite reflectance and fluid inclusions data suggest that the study area underwent a temperature of at least 150°C (value commonly admitted). This is significantly higher that temperatures derived from the MagEval approach. For a temperature of ∼150°C, the MagEval PM values should be much lower (∼0.3-0.4). Considering the geological history of the studied area, a maximum temperature of 90°C seems unrealistic. A possible explanation for the non-application of the MagEval geothermometer in this geological site is that the magnetic signal S3 is not a true MagEval-type signal of the type defined in Aubourg & Pozzi (2010) and above. It may not be strongly dependant on temperature, or its relation to temperature may be modified by the presence of abundant organic matter. It appears as a marker of high maturity sedimentary rocks (Ro $> 2\%$) as documented by its common occurrence in other rocks of high maturity (e.g. Borneo).

6 Synthesis-Conclusion

The results of this study show that the magnetic assemblages identified in the West Virginia samples are stratigraphically distributed. The goethite-magnetite assemblage samples are mostly located within the lower part of the stratigraphic section from the Tonoloway Formation to the Oriskany Sandstone (section A). Samples displaying the S3 signal are located in the upper part of the section from the Needmore Shale to the Chemung Group (section B). This stratigraphic distribution is probably influenced by lithologic parameters, as section A is mainly composed of limestones and section B mainly shales-siltstones.

The different magnetic assemblage may also be related to fluid circulation history, even if care was taken to sample away from veins. Section A signal may be related to meteoric water circulation forming goethite at the expense of magnetite. Section B signal may represent hydrocarbons migration pathway by tectonically driven fluids leading to an environment favoring the formation/preservation of magnetite and iron sulfides.

The S3 signal may be an indicator of deep burial conditions or at least of high maturity with high Ro ($> 2\%$) and high organic matter content. In this case, the S1 signal occurring stratigraphically below may then represent burial temperature up to 250°C, characterized by the occurrence of nanoparticles of goethite. This nanogoethite is not the carrier of the Kiaman remagnetization in the Late Paleozoic limestones. Stoichiometric magnetite observed to be present in both signals is neoformed (e.g. Jackson *et al.*, 1992).

From a thermal point of view, fluid inclusions microthermometry yields a maximum burial temperature of ∼150°C for the Devonian shales and probably < 180°C for the Silurian limestones. Occurrence of neoformed stoichiometric magnetite and absence of micron pyrrhotite in most of the collected samples lead to the conclusion that rocks did not undergo burial temperatures higher than 250°C, except locally near the Alleghanian Structural Front (Rochette *et al.*, 1990 ; Crouzet *et al.*, 1999). This neoformed magnetite is the magnetic carrier of the widespread remagnetization of the Late Paleozoic sedimentary rocks in North America recording the inverse Kiaman Superchron (McCabe & Elmore, 1989).

At this stage, it remains quite difficult to conclude on the origin of the magnetic assemblages identified in this part of West Virginia. The main magnetic features of this study are the specific magnetic signal S3 which seems to characterize high mature and high organic matter-rich shales and the evidence of nanogoethite which does not carry the Kiaman remagnetization.

As a result of the very particular nature of magnetic signal S3, it was not possible to apply the MagEval geothermometer in the investigated zone. Consequently, no distinct information can be extracted from these results to further validate the MagEval geothermometer.

Chapter VII. MAGNETIC ASSEMBLAGE IN THE APPALACHIANS, WEST VIRGINIA, USA

Synthesis

In their investigation on the effects of burial on magnetic properties of claystones, Aubourg & Pozzi (2010) found a particular magnetic assemblage composed of magnetite and possibly pyrrhotite for temperature less than 150°C. On the other hand, Rochette (1987) documented the existence of a magnetic "isograde" corresponding to the formation of micron pyrrhotite at 250°C. This suggests the existence of magnetic windows related to burial processes.

In this thesis work, various magnetic properties of sedimentary rocks in a context of increasing burial temperature were studied and lead to the recognition of typical magnetic assemblage as a function of temperature and rock maturity. In this chapter, we propose a synthesis based on the comparison between a standard geothermometer - vitrinite reflectance - and the magnetic assemblage (Figure S.4).

The magnetic mineralogy of natural claystones

During early diagenesis (below tens of meters), under anoxic conditions, two main processes occur : 1) the dissolution of the detrital iron-bearing minerals (mainly iron oxides) and 2) the formation of iron sulfides (for a review, Larrasoana *et al.*, 2007 ; Roberts *et al.*, 2011). Iron-bearing minerals will react with H_2S produced by bacterial activity to produce iron sulfides. Not all the detrital Fe-bearing minerals may be dissolved : the coarser detrital fraction may still be present (Horng *et al.*, 1998). In the first meters of the sedimentary column, at the onset of the methanogenic zone, iron sulfides such as greigite and pyrrhotite form and may reach grain-sizes of $\sim$10 μm (e.g. Larrasoana *et al.*, 2007). The dominant iron sulfides species will depend on the amount of reactants (e.g. Kao *et al.*, 2004).
The samples we studied are mainly representative of deeper conditions, corresponding approximately to 1 km depth and more. Therefore, we could not investigate the magnetic evolution of sedimentary rocks in the first $\sim$1 km depth. Our results however provide insights on the evolution of magnetic properties of sedimentary rocks occurring at depths greater than about 1 km. In the following, we attempt to summarize and discuss what we learnt and highlight what remains unanswered or unexplained.

The immature domain (Ro < 0.5%)

Greigite and pyrrhotite ? Are still greigite and pyrrhotite, precursors of pyrite, present in the shallowest immature samples ? Our magnetic investigation was appropriate for the recognition of pyrrhotite (through the 34 K transition) but not for greigite (no low-temperature magnetic transition). Horng & Roberts (2006) reported the occurrence of monoclinic pyrrhotite in immature sediments from Taiwan. However, these pyrrhotites may be detrital. In our study, many immature claystones do not display relevant pyrrhotite 34 K transition (Bure, Boom, boreholes and Cretaceous claystones from Greenland). This suggests that the occurrence of pyrrhotite is rather scarce in immature claystones. Unlike pyrrhotite, the occurrence of greigite is better documented (Roberts *et al.*, 2011). In the Bure claystones, Esteban (2006) reported the occurrence of greigite based on abundant magnetic data. In Gir-1 borehole, the sample Gir-1 2160m (Figure S.1) displays a FORC diagram that suggests the occurrence of greigite, though this mineral has generally higher coercivity (∼80 mT) (Roberts *et al.*, 2006). In addition, sample Gir-1 2160m exhibits a remanence at saturation that is one to two orders of magnitude higher than the underlying samples and out of our selection criteria for the MagEval geothermometer.

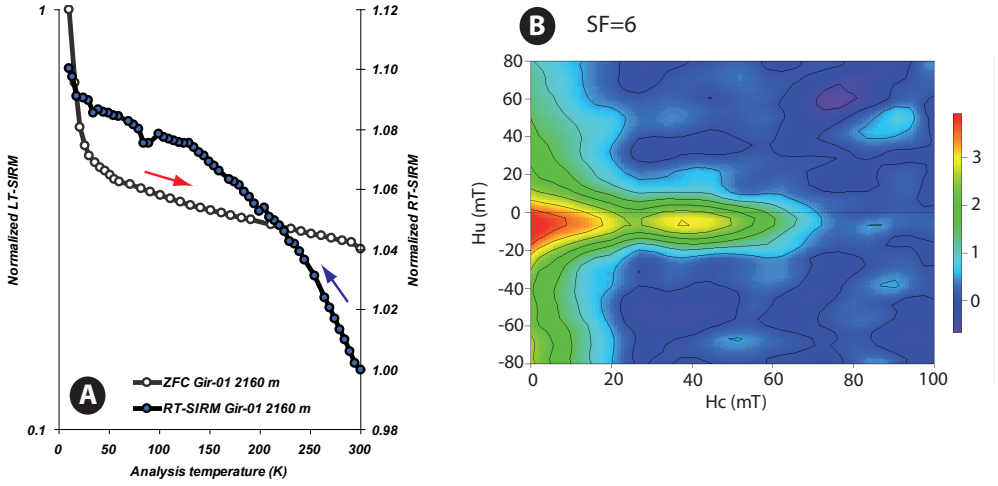

Figure S.1 – A) Evolution of the saturation magnetization (10-300 K) showing occurrence of goethite and magnetite and B) FORC diagram for Gir-1 2160m displaying the probable occurrence of greigite

Neoformed goethite ? Based on our low-temperature measurements, we were able to document the common occurrence of goethite in immature claystones. The goethite is not easy to detect, especially if goethite is in ultra-fine grain-size and does not carry a distinct remanence (superparamagnetic domain state). Rochette *et al.* (2005) suggested that the identification of goethite may be missed in sedimentary rocks because of its extreme coercivity (no saturation up to 57 T). For example, the rock

magnetic study conducted by Esteban (2006), though very detailed, missed the occurrence of goethite in Bure claystones.
An increase of up to 20% of the remanence acquired at room temperature from 300 to 10 K indicates the presence of fine-grained goethite (Figure S.4-1). The monitoring of room temperature remanence from 300 to 10 K is then a good test to identify this mineral. Mössbauer spectrum at 4.2 K (see chapter VI) is also a good indication of the presence of nanogoethite. The origin of goethite was beyond the scope of this work. However, because depositional goethite is altered during anoxic early diagenesis, we postulate that nanogoethite is probably neoformed during burial. Neoformed goethite is probably related to the degradation of pyrite (e.g. Herbert, 1997) in oxidizing conditions. The recognition of goethite in immature claystones from Greenland leads Abdelmalak *et al.* (2012) to suggest that goethite may be an indicator of < 3 km burial.

Neoformed magnetite ? Another common observation in immature claystones is the Verwey transition which indicates the occurrence of stoichiometric magnetite. Whether this magnetite is detrital or neoformed remains questionable. We obtained some consistent FORC diagrams that suggest that magnetite is single domain (SD) magnetite (see chapter VI). The narrow distribution of magnetite grain size suggests that magnetite is not of detrital origin but neoformed (< 1 μm). This hypothesis is comforted by our heating experiments which show that small grains of magnetite (nanomagnetite) can be formed at temperature as low as 50°C ($\sim$1 km depth). We propose that the identification of SD magnetite is characteristic of the magnetite window (Aubourg *et al.*, in press, appendix 3) which the onset corresponds approximately to the entry of the oil window.

Our observations in immature claystones (absence of pyrrhotite, presence of goethite and stoichiometric magnetite) are comparable to those of Abdelmalak *et al.* (2012).

The low to moderate maturity domain (Ro = 0.5-1.2%)

At the entry of the oil window, we observed that claystones are particularly weakly magnetized ($\sim 10^{-5}$ Am^2/kg) suggesting that the concentration of the magnetic minerals is of a few ppm. For this reason, the rock magnetic investigation is rather difficult, and even the analysis of the natural remanent magnetization (NRM) can fail (Moreau *et al.*, 2002). It turns out that FORC diagrams at room temperature are mostly non interpretable and the magnetic signal is dominated by paramagnetism. This is in this kind of rocks that the so-called MagEval signal is found. This signal is at the origin of the same named geothermometer. This thermal dependent signal shows a 2-step pattern on the ZFC curve and a P-behavior the more often associated with the Verwey transition of magnetite on the RT-SIRM curve (Figure S.4-2). The most typical example of the MagEval signal is that of the Opalinus Claystones in the Alps (Ro$\sim$0.6-0.7% ; Mazurek *et al.*, 2006) (Figure S.4-2). The occurrence of this signal is documented worldwide (see chapter IV).

Neoformed magnetite ? The common occurrence of non-reversible Verwey transition indicates that magnetite is stoichiometric, with a rather large grain size distribution, from SP to MD. Following the lines of our proposed model, that is 1) dissolution of magnetite during early diagenesis, then 2) formation of fine-grained magnetite in immature claystones, we propose that the stoichiometric magnetite evidenced by the Verwey transition is essentially neoformed. If our assumption is correct, this would have profound implications on the understanding of magnetostratigraphy record and remagnetization processes (e.g. Aubourg *et al.*, appendix 3). However, it is likely that detrital magnetite can survive and carry primary magnetostratigraphy signals. Our heating experiments suggest that a minimum temperature of 200°C is required to overwhelm the NRM (Kars *et al.*, in revision, appendix 2).
In addition to the above considerations, the large occurrence of magnetite in early mature claystones leads us to propose the existence of a "low-concentration magnetite" window.

The P-behavior and the presence of pyrrhotite The observed so-called P-behavior is still questioned : is it a feature of submicron pyrrhotite (Aubourg & Pozzi, 2010) ? Or something more complex (Kars *et al.*, 2011a) ? In their study, Aubourg & Pozzi (2010) measured successively the magnetic properties of a single Opalinus claystone using similar intensity but opposite magnetic fields. When subtracting two remanence curves with similar opposite fields, they observed the transition of pyrrhotite at 34 K (Figure S.2). In a nill magnetic field, this transition is hardly visible (Figure S.2). We conclude that the application of a magnetic field amplifies it, but also the paramagnetic component. We did a low temperature study on different claystones to better characterize the magnetic behavior below 50 K. We found that the P-behavior is complex and not necessarily associated to submicron pyrrhotite (Kars *et al.*, 2011a). We could not document, by use of other non magnetic techniques, the presence of significant pyrrhotite in our samples, although the burial conditions are a priori reducing. The reason is unclear : is it due to a very weak concentration of magnetic minerals ? Or to very small grain-sizes ? Or else, to the fact that pyrrhotite is encapsulated in other minerals ? We deal with claystones having a small content of magnetic minerals (∼ppm-ppb) which makes difficult their observation by non magnetic ways. X-ray diffraction and SEM were not conclusive. As the magnetic minerals are neoformed, it is likely they are of very fine grain-size (< 1 μm) and hence difficult to observe. However a few microscopic observations (see below) allow us to suggest that these neoformed minerals are probably related to other ones, such as pyrite or calcite. If it is correct, magnetic separation would be inadequate. Nevertheless, the recognition of this MagEval signal/assemblage could be used as a complementary tool with respect to the routine thermal indicators. This constitutes the MagEval geothermometer (Aubourg & Pozzi, 2010).

An occurrence of nano-goethite or -hematite ? Some mature samples, with Ro∼1.1%, exhibit a particular magnetic feature. This consists in the occurrence of a break-in-slope within the 200-250 K range on the ZFC curve (Figures S.3 and S.4-3). We interpret this transition as representing the

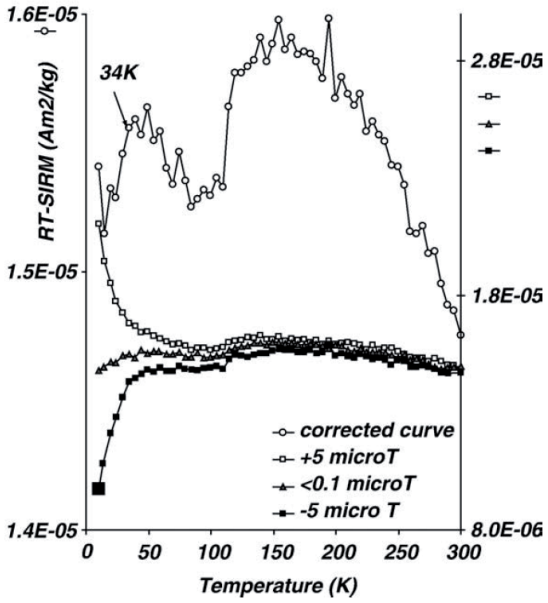

Figure S.2 – RT-SIRM cooling curves of natural Opalinus claystone measured with different magnetic field values (Aubourg & Pozzi, 2010). The corrected curve corresponds to the difference between $+5\mu$T magnetization and -5μT magnetization.

occurrence of nanoparticles of goethite or possibly hematite (Guyodo *et al.*, 2003). Though we cannot rule out surficial weathering processes (as goethite is an easy by-product of alteration), we believe that nanogoethite is linked either to burial processes, or, more likely, to fluid circulation. In the Grès d'Annot, the tectonic setting is particular in that the unit is the footwall of the internal alpine nappes. The fault zone acted possibly as a fluid conduit. We noticed diverging results between the evolution of the magnetic assemblage and vitrinite data. For instance, in Le Grand Coyer area, the vitrinite data suggest burial temperature of ∼110-120°C while we do not observe the MagEval magnetic assemblage. A similar break-in-slope at ∼200-250 K was observed in other geological settings, such as Borneo or Vocontian trough (C. Aubourg, pers. com.) with similar Ro (Ro∼1.1-1.2%). This Ro value corresponds to the end of the oil window. Hence, this particular magnetic signal may be associated to burial history. However, no such signal was identified in the boreholes investigation. The causes may be the prevailing reductive conditions as a result of the petroleum context.

The high maturity to overmature domain (Ro > 1.2%)

The high maturity to overmature rocks showed the widest variety of magnetic assemblage but are easily recognized. First, we identified a Néel transition at very low temperature (< 50 K) corresponding to siderite (∼38 K) and/or rhodochrosite (∼32 K) (Kars *et al.*, 2011a). The Néel transitions are well known (e.g. Frederichs *et al.*, 2003; Kosterov *et al.*, 2006), and they are amplified by the analytical procedure of our measurements. This magnetic feature is found in limestones from Nagele-1

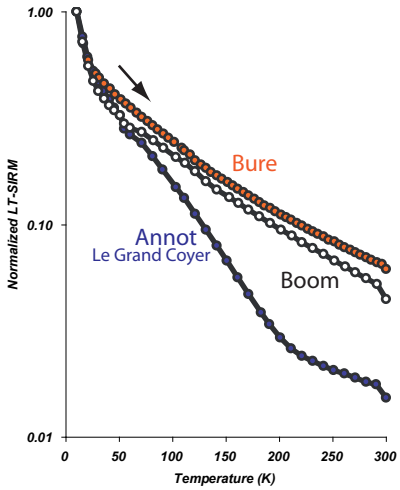

Figure S.3 – ZFC curves of two immature (Boom and Bure) and one early mature (Annot) claystones. The latter displays the 200 K break-in-slope.

(The Netherlands) and is largely represented in overmature claystones from Borneo (Figure S.4-6) (Aubourg *et al.*, 2011). This Néel transition is apparently associated with a low grade metamorphism (for Ro > 1.2%, T > 200°C).

We identified an unknown Néel-like transition at ∼24 K (Figure S.4-4). This is observed in sedimentary rocks which experienced a rather high burial temperature (> 200°C) with Ro > 2%, such as the Jurassic Terres Noires and the Liassic marls in the Alps, but also in the Valley & Ridge Province (Appalachians) when approaching the Alleghanian Structural Front. The link between burial and the occurrence of 24 K transition is strengthened by the absence of this 24 K transition in the boreholes study where claystones have Ro < 2%. The origin and the nature of this particular transition type remain unresolved.

We also identified the pyrrhotite (> 1 μm) transition such as determined by Rochette *et al.* (1990) (Figure S.4-7). It characterizes temperature higher than 250°C corresponding to the entry of the greenschist facies. The SD neoformed magnetite which characterizes the cooler samples is removed, being totally consumed to the benefit of pyrrhotite. This marks the end of the magnetite window and the onset of the pyrrhotite window. We observed the pyrrhotite occurrence in Annot claystones, and near the Alleghanian Front.

Finally, another magnetic assemblage, similar to the MagEval one, was identified in a few claystones from Valley & Ridge Province and Borneo (Figure S.4-5). These samples are characterized by a high Ro value (> 2%). The Valley & Ridge claystones display similar characteristics like : low remanence (generally < 50 $\mu Am^2/kg$), 2-step pattern of ZFC, a P-behavior, and the prevalence of a Verwey transition. The magnetic mineral(s), except magnetite, responsible for this behavior are not known.

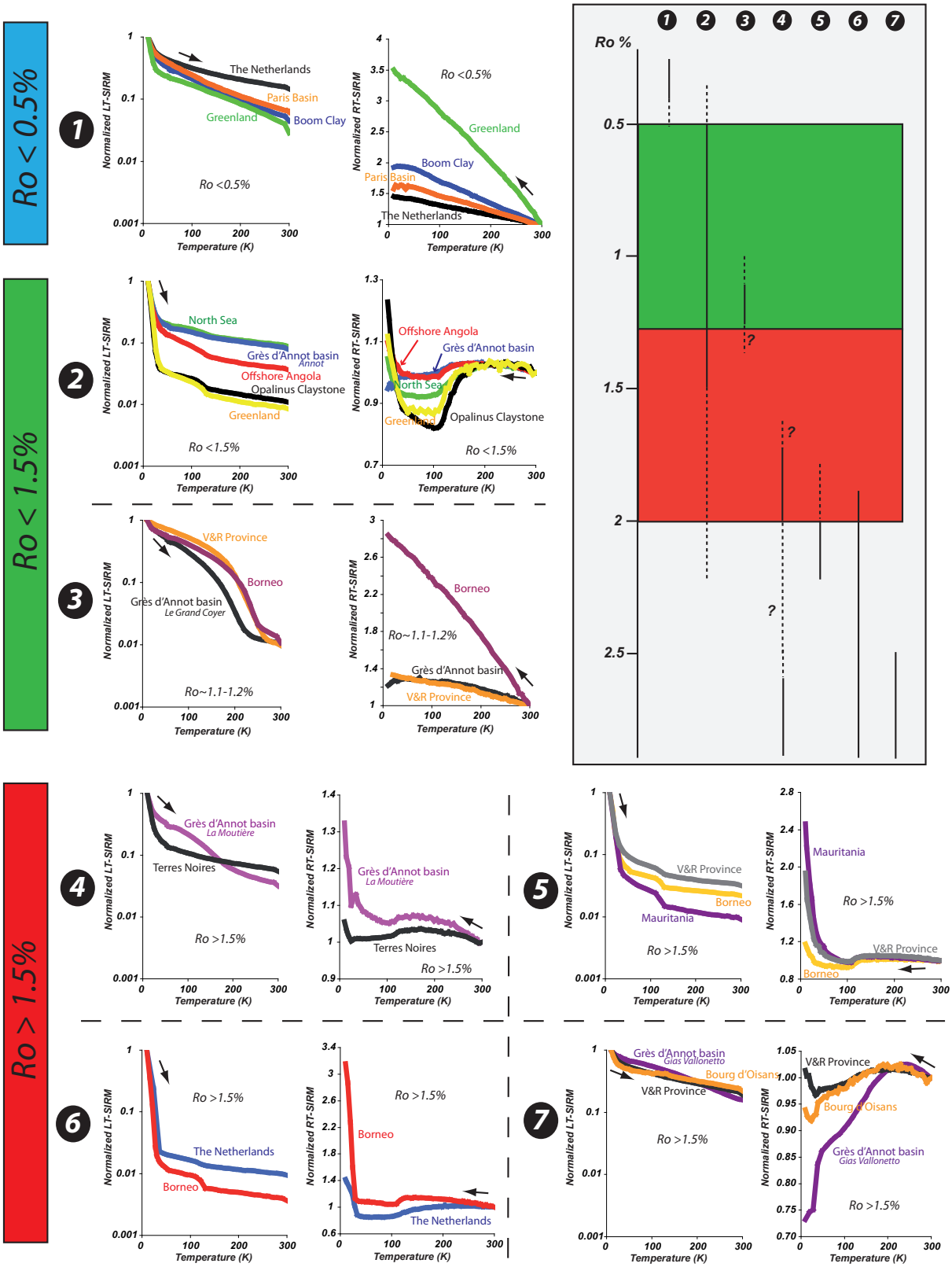

Figure S.4 – Magnetic assemblage as a function of temperature and maturity of the rocks. Greenland data from courtesy of M. Abdelmalak. Borneo data from courtesy of F. Sapin and D. Janots

Origin of the observed signals

Our heating experiments aimed to document the neoformation of magnetic minerals with temperature. The CRM-experiments show that grains are continuously formed with increasing temperature (< 20 nm and > 20 nm). In the meantime, magnetic minerals are also removed/transformed. A very intriguing result is the quasi similarities of magnetic behaviors while we are running in parallel two immature claystones (Boom Clay and Bure argillites). Such similar kinetics and magnetic assemblage suggest a common process.

Prior observations reported by C. Aubourg on pyrite framboids from Bure claystones (Callovo-Oxfordian, well ANDRA EST-211) suggested that these were the locus of chemical reactions leading to the formation of pyrrhotite by interacting pyrite with organic matter and iron oxides. It is well documented that framboidal pyrites can be completely oxidized into magnetite during burial (e.g. Suk *et al.*, 1990). Brothers *et al.* (1996) showed that this process may start from 90°C, when bacteria are no longer active. We did a SEM observation of that oxidation in the Grès d'Annot basin (Figure S.5). We performed an EDX transect from in to out : the sulfur content decreases in the rim.

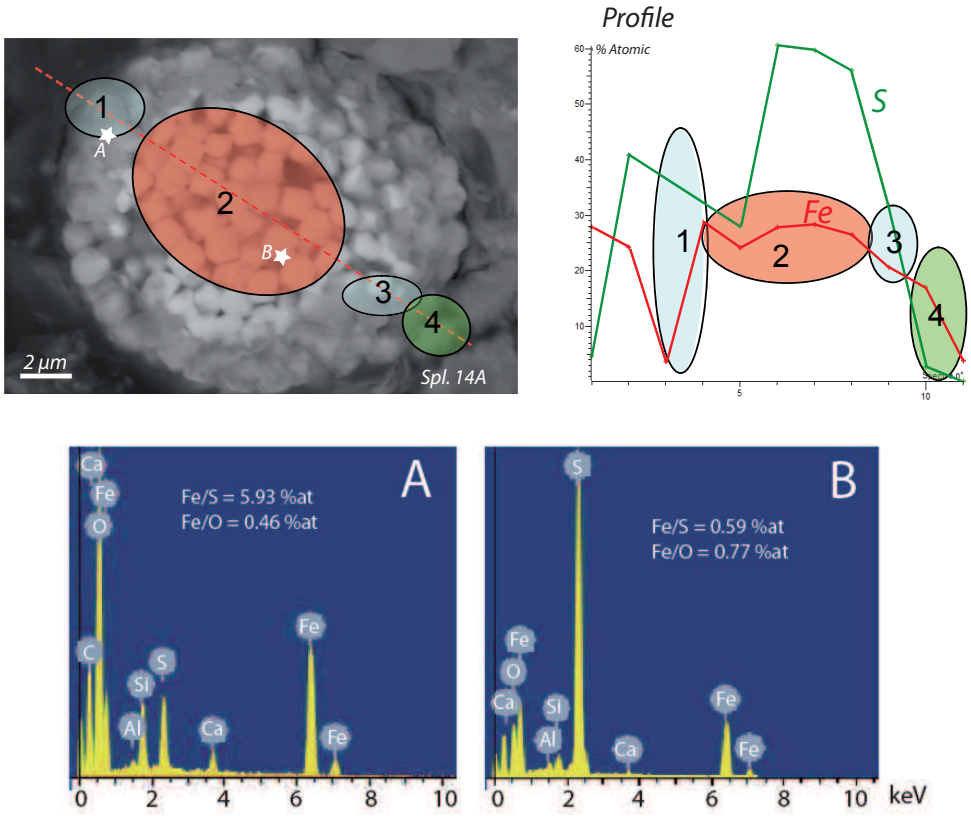

Figure S.5 – SEM observation of a pyrite framboid showing an oxidation rim and EDX measurement throughout the framboid for sample 14A from the Grès d'Annot basin. S content decreases outwards.

From this observation, 4 FIB (Focused Ion Beam) sections were realized through pyrite framboids at the CP2M in Marseille. The samples analyzed are from well Girassol-1 at 2160, 2375 and 3905 mMD (2 sections for the latter). They represent a burial temperature range going from ~35 to 110°C. The different TEM observations on the clay matrix/pyrite framboid interface of Gir-1 (Figure S.6) do not show any transitional zone where possible chemical reactions might occur. However, in the sample Gir-1 3905 m which is the deeper one, a cluster of very small grains situated on the edge of the pyrite framboid is observed and displays a Fe/S ratio different from that of the framboid (Figure S.7). Nevertheless, it is very difficult to identify these iron sulfides. On the other hand, SEM observations of the grains constituting the framboids revealed a granular aspect which may reflect presence of smaller grains. This is also comforted by X-ray diffraction images (Figure S.8) which show concentric circles suggesting that pyrite is an aggregate of fine-grained minerals. The nature of these small grains could not be determined.

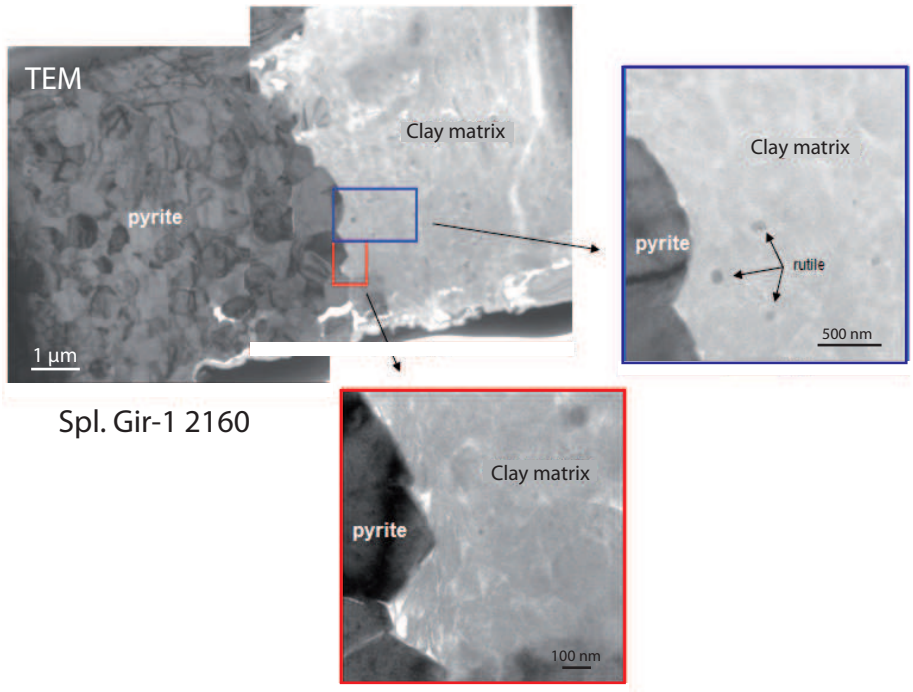

Figure S.6 – TEM observation of the pyrite framboid/matrix interface for Gir-1 2160m. No transitional zone between the framboid and the matrix was observed.

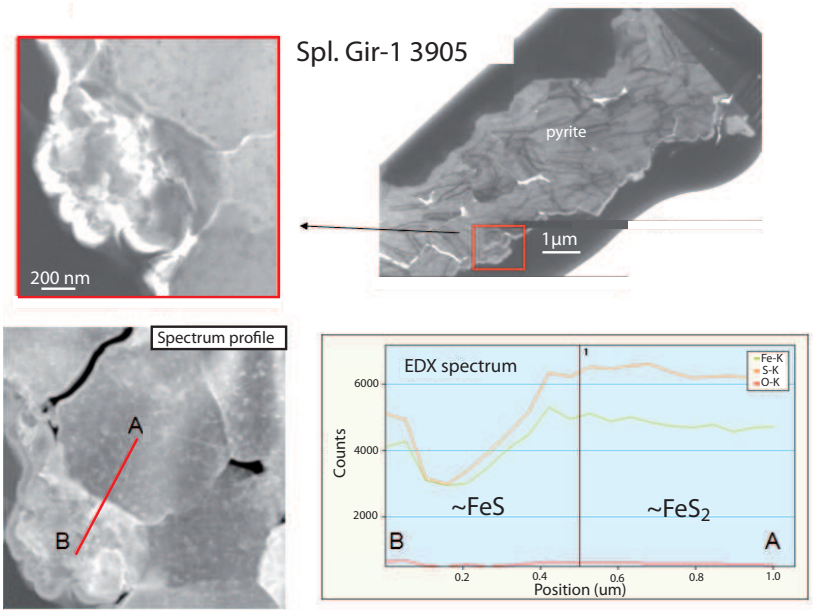

Figure S.7 – TEM observation of a granular cluster on the edge of a pyrite framboid and EDX spectrum of a transect through them for Gir-1 3905m. Fe/S ratio is different between the granular cluster and pyrite.

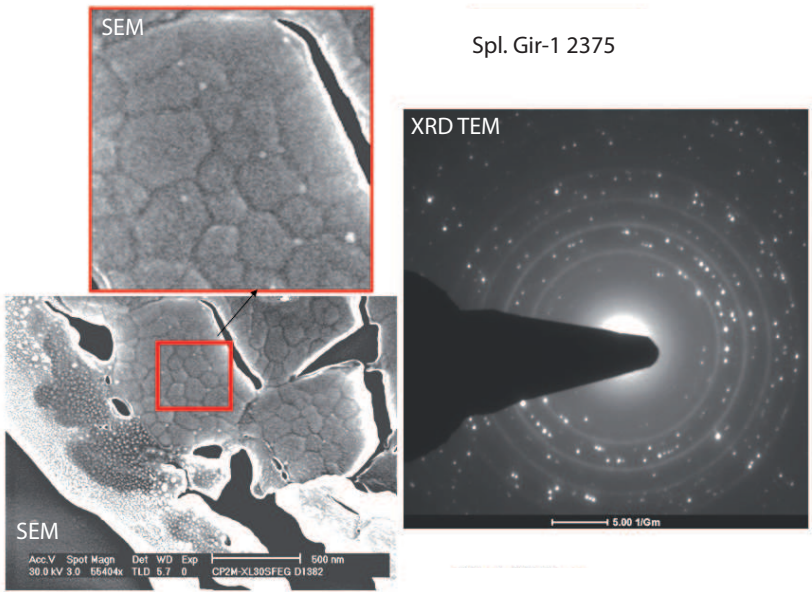

Figure S.8 – SEM observations of granular pyrite framboid with a XRD spectrum for Gir-1 2375m. The granular aspect may correspond to smaller grains which presence is further documented by concentric circles in the XRD spectrum.

Generally, in our samples, we did a few or no observations of euhedral iron oxides grains and no observation of pyrrhotite suggesting that these grains are present in very low content (< ppmv) and/or in very small grain-size.

One of the key observations of our heating experiments is the identification of the growth of nano magnetic minerals that are superparamagnetic. In order to detect the occurrence of superparamagnetic grains, we performed a CBD treatment on Bure claystones (see chapter IV) that revealed non conclusive. This implies that either the CBD treatment was not appropriated for our samples or the superparamagnetic grains are engulfed in other grains (and not accessible to CBD solution).

We have tested one magnetic extraction on an early mature Borneo claystone that displays a diagnostic MagEval magnetic assemblage. The magnetic extraction, in principle, is designed to pick up the SD to MD magnetic minerals from a rock powder. The comparison between natural claystones and the magnetic extraction shows that the hyper-fined magnetic fraction (SP) has been removed successfully (Figure S.9). It results that the PM parameter is considerably reduced, the P-behavior removed, and also the goethite input reduced as RT-SIRM does not show an increase from 300 K to 200 K. This comparison means that SP minerals are not encaged within SD to MD magnetic minerals.

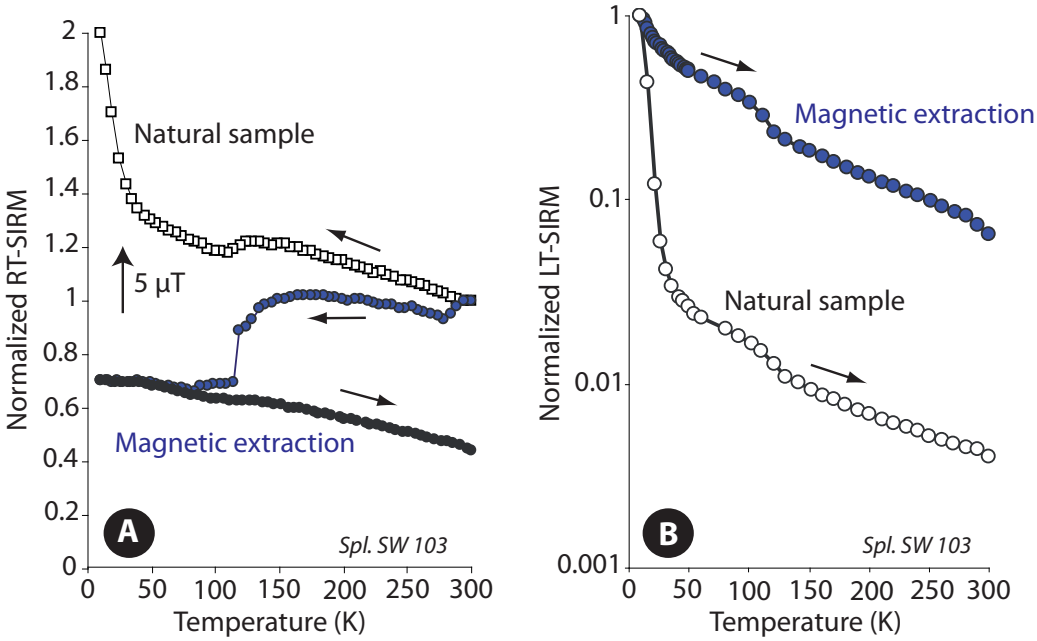

Figure S.9 – A) RT-SIRM curves on cooling and warming and B) ZFC curves for a natural claystone from Borneo and its magnetic extraction. SP grains were removed from magnetic extraction.

Nano minerals can be included deep in pyrite framboid as possibly illustrated by our FIB sections (Figure S.10). However, as show in Figure S.10, iron oxides and sulfides seem to form inside a calcite

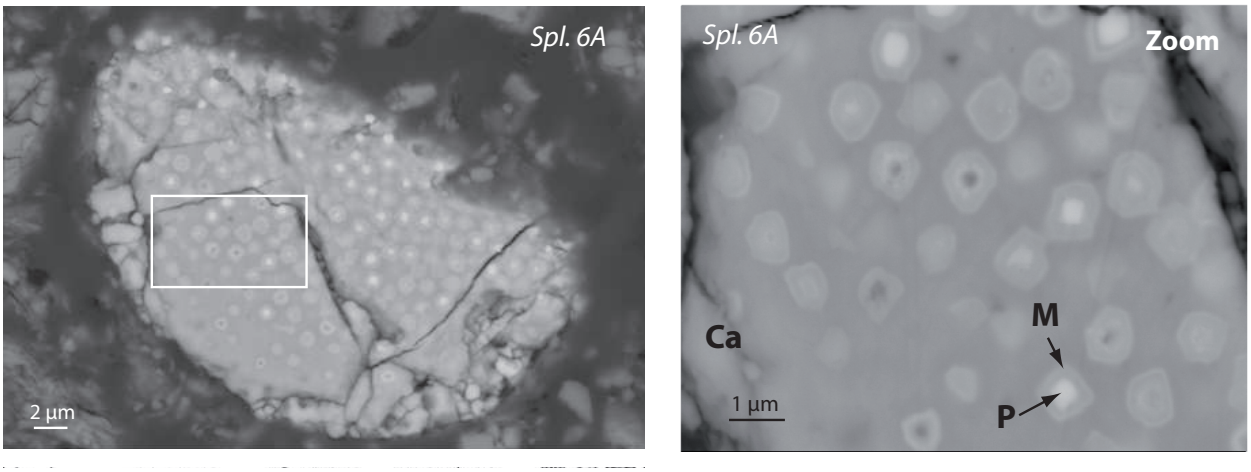

Figure S.10 – Iron oxides (magnetite M) and iron sulfides (pyrite P) within a calcite (Ca) grain in the sample 6A from the Grès d'Annot basin (Ro∼0.5%)

grain.

This summary points out a number of key observations. First of all, our results confirm the evolution, with burial and temperature, of the magnetic assemblage constitutive of sedimentary rocks. Different claystones, placed under similar conditions, develop the same magnetic assemblage. It seems that nanogoethite characterizes early mature rocks. Neoformed magnetite constitutes a magnetic window from ∼50 to 250°C. The ratio of SP/SD magnetite is thermally dependent and is therefore a burial indicator. The siderite-rhodochrosite solid solution appears as a marker of low-grade metamorphism (Ro > 1.5%). The development of a 24 K "transition" is diagnostic of low-grade metamorphism (Ro > 1.5-2%). The similarities of the observations suggest that same chemical process(es) lie(s) behind. An attempt to locate reactive sites for such a mechanism was conducted by making SEM and TEM observations of FIB sections in pyrite framboids.

The applicability of the MagEval geothermometer

The different studies performed on petroleum boreholes and field outcrops permitted the calibration and application of the MagEval geothermometer. Although some limitations are identified, the MagEval geothermometer is potentially applicable to a broad range of cases. The MagEval-type signal has been identified in a variety of geological settings such as sedimentary basins and fold-and-thrust belts. Although the application of the MagEval geothermometer was not possible in the Valley & Ridge Province, it has been applied in a similar geological setting (e.g. Borneo, Taiwan) (Aubourg *et al.*, 2011).

Our wells study suggests that the MagEval geothermometer can be applied in a temperature range

from ∼50 to ∼180°C, and maybe to a higher temperature (∼250°C). To date, the uncertainty of the estimated temperature by the use of the MagEval geothermometer is, at most, 15-20°C. As MagEval signal has been found in Paleozoic rocks, we suggest that this geothermometer has no limitation on age, by contrast to the vitrinite reflectance for instance. With respect to other geothermometers, the influence of time is less significant on the evolution of PM with temperature. In other words, MagEval has the potential to record the effect of short-term heating. Shear heating is one of the possible geological process. Chou *et al.* (pers. com.) applied successfully MagEval to a fault gouge framed by early mature siltstones.

Suitable samples for the use of this geothermometer have to satisfy a suite of criteria that have been defined in chapter IV. Clayish samples are the best suited for MagEval geothermometry. Some problems (pollution, oxidation, aging) have risen when dealing with cuttings. Cores or side-well cores (SWC) are preferable, as it is the case for the most techniques.

To improve the use of the MagEval geothermometer, we suggest two approaches : 1) averaging PM values for close samples in order to minimize samples variability, implying that complementary sampling is needed ; 2) we suggest to perform further experimental heating experiments on natural samples, and monitor the PM evolution upon increasing temperature. We anticipate that changes in PM value experimentally documented will reflect the temperature dependence of the magnetic signal in natural systems. This work could be done by using selected samples from the two boreholes used for our calibration.

Conclusion and perspectives

Different techniques are commonly used to estimate the maximum temperatures experienced by sedimentary rocks. In addition to the methods routinely applied, such as vitrinite reflectance or fluid inclusion microthermometry, we explored the use of magnetic properties measured in specific conditions.

It is known for decades that magnetic minerals have characteristic temperature ranges of stability. In anoxic low temperature environment affected by early diagenesis, detrital magnetic minerals are dissolved to form iron sulfides. At high temperature ($> 250°C$), micron pyrrhotite is the feature mineral. Between these two temperature ranges, little is known. This work investigated the magnetic properties of sedimentary rocks especially claystones.

Our approach used essentially low temperature magnetic measurements (below room temperature). This kind of analytical procedure was important to prevent chemical and mineralogical transformations induced when heating samples. The low temperature technique allowed the identification of the magnetic minerals by their characteristic magnetic behavior at a certain temperature with no change on the mineralogy.

We analyzed 135 samples from 7 boreholes in 7 different basins. This study had two main goals :

1. the evolution/recognition of the magnetic assemblage throughout the borehole ;
2. the calibration of the MagEval geothermometer through the evolution of the parameter PM derived from magnetic measurement (Aubourg & Pozzi, 2010).

zThe first goal was satisfied as typical magnetic signals, comparable to the signals from Bure and Opalinus claystones, were identified in the wells. The evolution of the magnetic signals was consistent with expectations. The second goal was achieved by the establishment of two calibrations curves. Both are based on selected samples (essentially claystones) which satisfy the established selection criteria. One is from the well 22/30C-10 (Elgin field, North Sea), the other from the well Girassol-1 (Angola).

We carried out heating experiments for 1) a better comprehension and 2) a possible calibration

of the MagEval signal. To better characterize the process(es) responsible for the MagEval behavior, we performed heating experiments on immature claystones (Jurassic Bure claystones and Oligocene Boom Clay) under magnetic field from 50 to 130°C. This was done to record neoformation of the magnetic minerals. We showed that the production/growth of magnetic minerals, mainly magnetite, is continuous with burial/temperature. The content of small magnetic grains (superparamagnetic) and single domain grains increase with burial. The equilibrium between these two grain sizes seems to characterize the PM parameter. To further improve the calibration of the MagEval geothermometer based on naturally-occurring samples, we realized heating experiments with gold capsules in autoclaves. We found the same trends identified by Aubourg & Pozzi (2010). An immature claystone, heated at a higher temperature than the maximum burial temperature experienced, displayed an increase of the PM value (PM Up branch). An early mature claystone, heated at a higher temperature than that experienced, displayed a decrease of the PM value (PM Down branch). However, establishing a specific calibration curve from the results of our experiment was not possible. The cause may be diverse but likely resides in the experimental conditions (oxidation of the sample ? Pollution of the autoclaves ? Anoxic conditions not fully satisfied ?...).

A major contribution of this work was to investigate the presence of such magnetic assemblage in sedimentary rocks in two different geological settings of petroleum interest :

- The Eocene-Oligocene turbiditic Grès d'Annot basin in SE France (burial temperature from ∼60°C to > 250°C)
- The Late Paleozoic fold and thrust belts of the Valley and Ridge Province in the Appalachians, West Virginia, USA (burial temperature > 150°C)

In the Grès d'Annot basin, the magnetic assemblage evolved in a SW-NE transect from the outer (Rouaine area, France) to inner (Bersezio, Italy) tectonic/diagenetic zones. The application of the MagEval geothermometer in this study area was successful. The calculated MagEval temperatures were consistent with other thermal indicators. In the Appalachians, the magnetic assemblage identified was stratigraphically distributed. In the West Virginia limestones interval, a particular magnetic signal, same as that found in the Grès d'Annot basin, was found. It is probably due to the occurrence of nanogoethite or nanohematite. However its origin remains unknown : alteration ? Fluid circulation ? Burial effect ? Further studies are needed to answer these questions. For rocks which underwent a higher temperature (200°C), we identified a 24 K "transition" (new magnetic mineral ?) which is also found in the Jurassic Terres Noires and Liassic marls of the Alpine chains. In the claystones interval of the Appalachians, the more interesting feature is the occurrence of a MagEval-like signal at high temperature (Ro > 2 %) which is not MagEval-proof. As a result of the very peculiar magnetic signals identified in this part of West Virginia, it was not possible to apply the MagEval geothermometer.

The results from this thesis combined with previous heating studies allow us to suggest a burial model of the magnetic minerals (Figure C.1). Three successive magnetic windows are defined based

on the main occurrence of a magnetic mineral : the greigite window, the magnetite window and the pyrrhotite window (Aubourg *et al.*, in press, appendix 3). At this stage, the presented model is intended to be simple and focused on magnetic minerals of interest. In nature other magnetic minerals can occur such as goethite and other Fe-bearing magnetic minerals. Greigite forms during early burial within the first tens of centimeters as a result of the dissolution of the detrital iron oxides (e.g. Rowan *et al.*, 2009). Magnetite forms by 2 km depth at least and finally pyrrhotite forms at the expense of magnetite for a temperature of about 250°C (∼8-10 km).

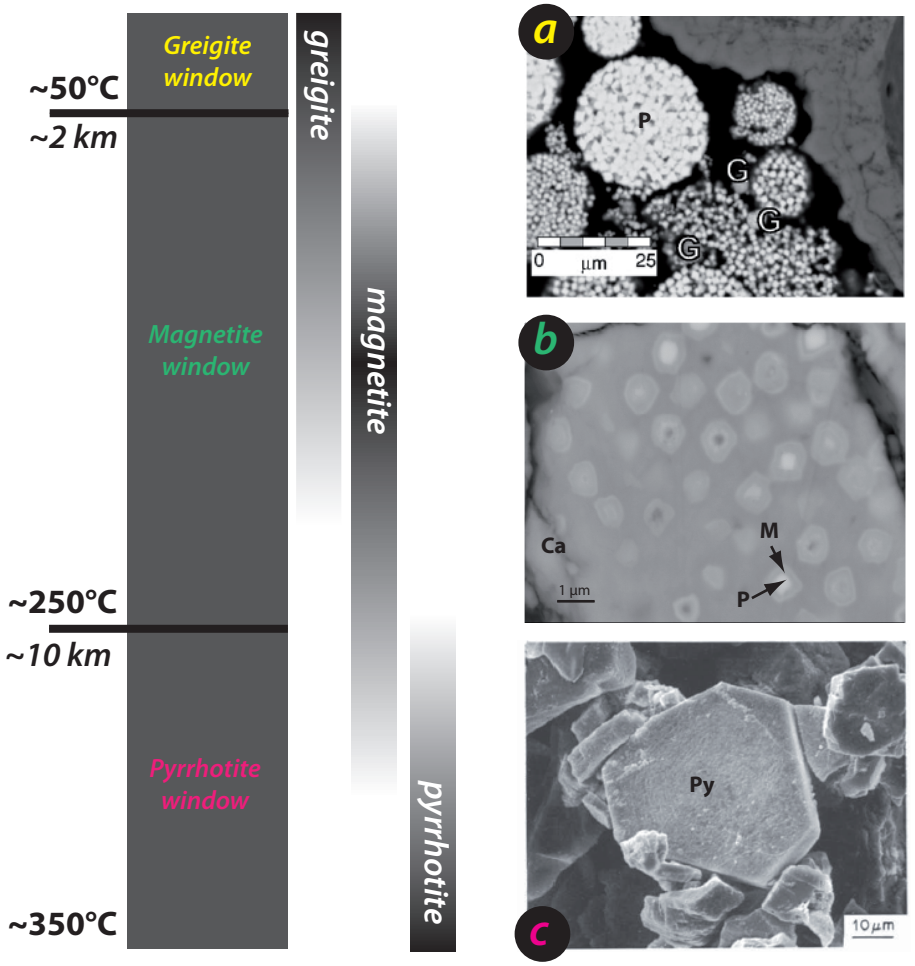

Figure C.1 – Three magnetic windows burial model of the magnetic minerals (after Aubourg *et al.*, in press, appendix 3). SEM images : a) extracted from Horng *et al.* (1998), b) Spl. 6A from our Grès d'Annot basin study, and c) extracted from Sassen *et al.* (1989) (P : pyrite, G : greigite, M : magnetite, Ca : calcite, Py : pyrrhotite)

Perspectives This thesis brings new magnetic elements for the recognition of the burial conditions. Nevertheless, further studies are needed. To better characterize the formation (and also destruction) of magnetic minerals during diagenesis, we propose to keep going time-constant heating experiments under magnetic field with a wider temperature range up to 250°C and by considering different lithologies (claystones, limestones). One may also monitor the neoformation of magnetic minerals at a given temperature with varying heating duration. As we deal with very small amounts of magnetic minerals (∼ppb-ppm), it would be useful to consider chemical or magnetic separations to concentrate the magnetic minerals present in samples. Microscopic (SEM, TEM) observations and X-ray diffraction spectra thus would be more satisfying and accurate. Synthetic samples could also be prepared. One may create his own mixture of synthetic magnetic and non magnetic minerals, associated or not with organic matter (bacteria, hydrocarbons), to monitor the changes in magnetic mineralogy with temperature. Thermodynamic modeling could be also considered to help to the understanding of the chemical processes controlling the mineral reactions at stake.

The MagEval geothermometer developed in this thesis gives interesting and valuable results. The potential of this new geothermometer was demonstrated, but a number of limitations were also discovered. Further work is needed to improve the calibration and the understanding of controlling factors. Averaging PM values for close samples in order to minimize samples variability could be envisaged. Monitoring of the PM evolution with increasing temperature could be useful to comfort the dependence of the magnetic signal with temperature. It might be necessary to redefine the PM parameter as it may be too global to date. Validation examples showing well constrained thermal history may be also envisaged. Comparison with other geothermometers could also be useful.

Bibliography

Abdelmalak, M. (2010), Transition spatio-temporelle entre rift sédimentaire et marge passive volcanique : l'exemple de la Baie de Baffin, Centre Ouest, Groenland, Ph.D. thesis, Université du Maine, France.

Abdelmalak, M., Aubourg, C., Geoffroy, L. & Laggoun-Defarge, F. (2012), A new oil window indicator ? The magnetic assemblage of claystones from the Baffin Bay volcanic margin (Greenland), *AAPG Bulletin*, 96(2), 205–215.

Allen, P., Crampton, S. & Sinclair, H. (1991), The inception and evolution iof the North Alpine Foreland Basin, Switzerland, *Basin Research*, 3, 143–163.

Anderson, J., Cartwright, J., Drysdall, S. & Vivian, N. (2000), Controls on turbidite sand deposition during gravity-driven extension of a passive margin : examples from Miocene sediments in Block 4, Angola, *Marine and Petroleum Geology*, 17, 1165–1203.

Apps, G., Peel, F. & Elliott, T. (2004), Deep-water sedimentation in the Alpine Basin of SE France : new perspectives on the Grès d'Annot and related systems, volume 221, chapter The structural setting and palaeogeographical evolution of the Grès d'Annot basin, 65–96, Geological Society Special Publication, London.

Apps, G. (1987), Evolution of the Grès d'Annot Basin, SW Alps, Ph.D. thesis, University of Liverpool, UK.

Aragòn, R., Buttrey, D., Shepherd, J. & Honig, J. (1985), Influence of non stoichiometry on the Verwey transition, *Physical Review*, B31, 430–436.

Aubourg, C. & Pozzi, J.P. (2010), Toward a new < 250°C pyrrhotite-magnetite geothermometer for claystones, *Earth and Planetary Science Letters*, 294(1-2), 47–57.

Aubourg, C., Pozzi, J.P., Janots, D. & Sahraoui, L. (2008), Imprinting chemical remanent magnetization in claystones at 95°C, *Earth and Planetary Science Letters*, 272, 172–180.

Aubourg, C., Sapin, F., Pubellier, M., Janots, D., Lahfid, A. & Ringenbach, J.C. (2011), Toward the use and fast maturity indicator in very-low grade metamorphic claystones from the NW Borneo wedge, in Geophysical Research Abstracts, volume 13, EGU2011–3817, EGU.

Banerjee, S., Elmore, R. & Engel, M. (1997), Chemical remagnetization and burial diagenesis in the Pennsylvanian Belden Formation, Colorado, *Journal of Geophysical Research*, 102, 24 825–24 842.

Barbarand, J., Hurford, T. & Carter, A. (2003), Variation in apatite fission track length measurement : implications for thermal history modelling, *Chemical Geology*, 198(1-2), 77–106.

Barker, C. & Pawlewicz, M. (1986), Paleogeothermics, *Lecture Notes in Earth Sciences*, volume 5, chapter The correlation of vitrinite reflectance with maximum temperature in humic organic matter, 79–93, Springer-Verlag.

Barker, W. & Parks, T. (1986), The thermodynamic properties of pyrrhotite and pyrite : a re-evaluation, *Geochimica et Cosmochimica Acta*, 50, 2185–2194.

Barlier, J., Ragot, J.P. & Thouray, J.C. (1974), L'évolution des Terres Noires subalpines méridionales d'après l'analyse minéralogique des argiles et la réflectance des particules carbonées, *Bulletin du BRGM (2ème série)*, 6(section II), 533–548.

Barnard, P., Cooper, B. & Fisher, M. (1976), Organic maturation and hydrocarbon generation in the mesozoic sediments of the Sverdrup basin, Arctic Canada, 581–588, 4th Int. Palynol. Conf., Lucknow.

Beardsmore, G. & Cull, J., editors (2001), Crustal heat flow : a guide to measurement and modelling, Cambridge University Press.

Beaufort, D., Cassagnabere, A., Petit, S., Lanson, B., Berger, G., Lacharpagne, J.C. & Johansen, H. (1998), Kaolinite-to-dickite reaction in sandstone reservoirs, *Clay Minerals*, 33, 297–316.

Beaufort, D., Patrier, P., Quirt, D., Morichon, E., Rigault, C., Gaboreau, S., Laverret, E. & Vieillard, P. (2009), Clay minerals and associated phases related to the deposition of unconformity-type uranium deposits, Keynote speach of the Clays in Geological Processes session, 14th International Clay Conference, Italy (Castellanata Marina).

Belzile, N., Chen, Y.W., Cai, M.F. & Li, Y. (2004), A review on pyrrhotite oxidation, *Journal of Geochemical Exploration*, 84, 65–76.

Berner, R.A. (1984), Sedimentary pyrite formation : an update, *Geochimica et Cosmochima Acta*, 48, 605–615.

Berquò, T.S., Imbernon, R., Blot, A., Franco, D., Toledo, M. & Partiti, C. (2007), Low temperature magnetism and Mössbauer spectroscopy study from natural goethite, *Physics and Chemistry of Minerals*, 34, 287–294.

Bertrand, R. (1990), Correlations among the reflectances of vitrinite, chitinozoans, graptolites and scolecodonts, *Organic Geochemistry*, 15(6), 565–574.

Besnus, M.J. (1966), Propriétés magnétiques de la pyrrhotine naturelle, Ph.D. thesis, Université de Strasbourg, France.

Besnus, M. & Meyer, A. (1964), Nouvelles données expérimentales sur le magnétisme de la pyrrhotine naturelle, 507–511, Proc. Int. Conf. Mag., Nottingham.

Bessereau, G. & Guillocheau, F. (1994), Hydrocarbon and petroleum geology of France, chapter Sequence stratigraphy and organic matter distribution of the Lias of the Paris Basin, 107–119, Spec. Publ. European Assoc. Petroleum Geoscientists.

Besson, L. (1972), Contributions à l'étude micropaléontologique et géochimique du Tertiaire du synclinal d'Annot (Alpes de Haute Provence), Ph.D. thesis, Université de Grenoble, France.

Besson, L., Grosso, F., Pairis, J.L. & Uselle, J.P. (1970), Etudes préliminaires sur les microfaunes et les carbonates des Marnes Bleues du synclinal d'Annot (Basses Alpes), *Géologie Alpine*, 46, 29–42.

Bigot-Cormier, F., Sosson, M., Poupeau, G., Stéphan, J.F. & Labrin, E. (2006), The denudation history of the Argentera Alpine external crystalline massif (Western Alps, France-Italy) : an overview from the analysis of fission tracks in apatites and zircons, *Geodynamica Acta*, 19, 455–473.

Biju-Duval, B. (1999), Géologie sédimentaire : bassins, environnements de dépôts, formation du pétrole, Institut Français du Pétrole, technip edition.

Bina, M. & Daly, L. (1994), Mineralogical change and self-reversed magnetizations in pyrrhotite resulting from partial oxidation : geophysical implications, *Physics of the Earth and Planetary Interiors*, 85, 83–99.

Bloemendal, J., King, J., Hunt, A., DeMenocal, P. & Hayashida, A. (1993), Origin of the sedimentary magnetic record at Ocean Drilling Program sites on the Owen Ridge, western Arabian Sea, *Journal of Geophysical Research*, 98, 4199–4219.

Bocquet, S. & Kennedy, S. (1992), The Néel temperature of fine particle goethite, *Journal of Magnetism and Magnetic Materials*, 109, 260–264.

Bodker, F., Hansen, M.F., Koch, C.B., Lefmann, K. & Morup, S. (2000), Magnetic properties of hematite nanoparticles, *Physical Review*, B61(10), 6826–6837.

Bordenave, M. (1993), Applied Petroleum Geochemistry, technip edition.

Borradaile, G.J. & Jackson, M. (1993), Changes in magnetic remanence during simulated deep sedimentary burial, *Physics of the Earth and Planetary Interiors*, 77, 315–327.

Bowles, J., Jackson, M., Chen, A. & Solheid, P. (2009), Interpretation of low-temperature data Part 1 : Superparamagnetism and Paramagnetism, *The IRM Quarterly*, 19(3).

Bradley, D. (1982), Subsidence in Late Paleozoic basins in the northern Appalachians, *Tectonics*, 1, 107–123.

Brothers, L., Engel, M. & Elmore, R. (1996), The late diagenetic conversion of pyrite to magnetite by organically complexed ferric iron, *Chemical Geology*, 130, 1–14.

Burnham, A. & Sweeney, J. (1989), A chemical kinetic model of vitrinite maturation and reflectance, *Geochimica et Cosmochimica Acta*, 53, 2649–2657.

Burton, E.A., Machel, H.G. & Qi, J. (1993), Applications of Paleomagnetism to Sedimentary Geology, volume 49, chapter Thermodynamic constraints on anomalous magnetization in shallow and deep hydrocarbon seepage environments, 193–207.

Butler, R.F. (1992), Paleomagnetism : Magnetic domains to geologic terranes.

Cairanne, G., Aubourg, C., Pozzi, J.P., Moreau, M.G., Decamps, T. & Marolleau, G. (2004), Laboratory chemical remanent magnetization in a natural claystones : a record of two polarities, *Geophysical Journal International*, 159, 909–916.

Callec, Y. (2001), La déformation synsédimentaire des bassins paléogènes de l'arc de Castellane (Annot, Barrême, St Antonin), Ph.D. thesis, Ecole des Mines de Paris, France.

Callec, Y. (2004), Deep-water sedimentation in the Alpine Basin of SE France : new perspectives on the Grès d'Annot and related systems, volume 221, chapter The turbidite fill of the Annot sub-basin (SE France) : a sequence-stratigraphy approach, 111–135, Geological Society Special Publication, London.

Campredon, P. (1977), Les Formations Paléogènes des Alpes Maritimes franco-italiennes, *Mémoire Hors Série de la Société Géologique de France*, volume 9.

Canfield, D.E. & Berner, R.A. (1987), Dissolution and pyritization of magnetite in anoxic marine sediments, *Geochimica et Cosmochima Acta*, 51, 645–659.

Carr, A. (1999), A vitrinite reflectance kinetic model incorporating overpressure retardation, *Marine and Petroleum Geology*, 16, 355–377.

Carvallo, C. (2004), Paleointensity determinations on basalts from the Emperor seamounts and testing the properties of FORC diagrams using micromagnetic modelling and measurements, Ph.D. thesis, University of Toronto, Canada.

Cathelineau, M. & Nieva, D. (1985), A chlorite solid solution geothermometer. The Los Azufres geothermal system (Mexico), *Contributions to Mineral Petrology*, 91, 235–244.

Cawood, P., McCausland, P. & Dunning, G. (2001), Opening Iapetus : constraints from the Laurentian margin in Newfoundland, *Geological Society of America Bulletin*, 113, 443–453.

Cercone, K., Deming, D. & Pollack, H. (1996), Insulating effect of coals and black shales in the Appalachian basin, western Pennsylvania, *Organic Geochemistry*, 24(2), 243–249.

Chang, L., Roberts, A.P., Rowan, C.J., Tang, Y., Pruner, P., Chen, Q. & Horng, C.S. (2009), Low-temperature magnetic properties of greigite (Fe_3S_4), *Geochemistry, Geophysics, Geosystems*, 10(1), Q01 704, doi :10.1029\2008GC002276.

Channell, J. & McCabe, C. (1994), Comparison of magnetic hysteresis parameters of unremagnetized and remagnetized limestones, *Journal of Geophysical Research*, 99(B3), 4613–4623.

Clark, D. (1984), Hysteresis properties of sized dispersed monoclinic pyrrhotite grains, *Geophysical Research Letters*, 11(3), 173–176.

Cornell, R. & Schwertmann, U. (1996), The Iron oxides - structure, properties, reactions, occurrence and uses, Weinheim, New York.

Crerar, D., Susak, N., Borsik, M. & Schwarz, S. (1978), Solubility of the buffer assemblage pyrite+magnetite in NaCl solutions from 200 to 350°C, *Geochemica et Cosmochima Acta*, 42, 1247–1437.

Crouzet, C., Ménard, G. & Rochette, P. (1999), High-precision three-dimensional paleothermometry derived from paleomagnetic data in an Alpine metamorphic unit, *Geology*, 27(6), 503–506.

Crouzet, C., Ménard, G. & Rochette, P. (2001), Cooling history of the Dauphinoise Zone (Western Alps, France) deduced from the thermopaleomagnetic record : geodynamic implications, *Tectonophysics*, 340, 79–93.

Crouzet, C., Rochette, P., Ménard, G. & Prévot, M. (1997), Acquisition d'aimantations thermorémanentes partielles successives portées par la pyrrhotite monodomaine lors du refroidissement de la zone dauphinoise interne (Alpes occidentales, France), *Comptes Rendus de l'Académie des Sciences, Paris*, 325, 643–649.

Dalla Torre, M., Mahlmann, R. & Ernst, W. (1997), Experimental study on the pressure dependence of vitrinite maturation, *Geochimica et Cosmochimica Acta*, 61, 2921–2928.

Day, R., Fuller, M. & Schmidt, V. (1977), Hysteresis properties of titanomagnetites : grain-size and compositional dependence, *Physics of the Earth and Planetary Interiors*, 13, 260–267.

de Boer, C.B., Mullender, T.A. & Dekkers, M.J. (2001), Low-temperature behaviour of haematite : susceptibility and magnetization increase on cycling through the Mori transition, *Geophysical Journal International*, 146, 201–216.

De Caritat, P., Hutcheon, I. & Walshe, J.L. (1993), Chlorite goethermometry : a review, *Clays and Clay Minerals*, 41(2), 219–239.

De Grave, E., Bowen, L., Vochten, R. & Vandenberghe, R. (1988), The effet of crystallinity and Al substitution on the magnetic structure and Morin transition in hematite, *Journal of Magnetism and Magnetic Materials*, 72, 141–151.

Decleer, J., Viaene, W. & Vandenberghe, N. (1983), Relationships between chemical, physical and mineralogical characteristics of the Rupelian Boom Clay, Belgium, *Clay Minerals*, 18, 1–10.

Dekkers, M. (1989a), Magnetic properties of natural goethite. II. TRM behaviour during thermal and alternating field demagnetization and low-temperature treatment, *Geophysical Journal International*, 97, 341–355.

Dekkers, M. (1989b), Magnetic properties of natural pyrrhotite. II : High-and low-temperature behaviour of Jrs and TRM as function of grain size, *Physics of the Earth and Planetary Interiors*, 57, 266–283.

Dekkers, M. (1990), Magnetic monitoring of pyrrhotite alteration during thermal demagnetization, *Geophysical Research Letters*, 17(6), 779–782.

Dekkers, M. & Linssen, J. (1989), Rock magnetic properties of fine-grained natural low-temperature haematite with reference to remanence acquisition mechanisms in red beds, *Geophysical Journal International*, 99, 1–18.

Dekkers, M., Mattéi, J.L., Fillion, G. & Rochette, P. (1989), Grain-size dependence of the magnetic behavior of pyrrhotite during its low-temperature transition at 34 K, *Geophysical Research Letters*, 16(8), 855–858.

Deniau, I., Derenne, S., Beaucaire, C., Pitsch, H. & Largeau, C. (2001), Morphological and chemical features of a kerogen from the underground Mol Laboratory (Boom Clay Formation, Oligocene, Belgium) : structure, source organisms and formation pathways, *Organic Geochemistry*, 32, 1343–1356.

Deniau, I., Derenne, S., Beaucaire, C., Pitsch, H. & Largeau, C. (2005), Simulation of thermal stress influence on the Boom Clay kerogen (Oligocene, Belgium) in relation to long-term storage of high activity nuclear waste. I : study of generater soluble compounds, *Applied Geochemistry*, 20, 587–597.

Deniau, I., Devol-Brown, I., Derenne, S., Behar, F. & Largeau, C. (2008), Comparison of the bulk geochemical features and thermal reactivity of kerogens from Mol (Boom Clay), Bure (Callovo-Oxfordian argillite) and Tournemire (Toarcian shales) underground research laboratories, *Science of the Total Environment*, 389, 475–485.

Deville, E. & Sassi, W. (2006), Contrasting thermal evolution of thrust systems : an analytical and modeling approach in the front of the western Alps, *AAPG Bulletin*, 90(6), 887–907.

Dorobek, S. (1987), Petrography, geochemistry, and origin of burial diagenetic facies, Siluro-Devonian Helderberg Group (carbonate rocks), Central Appalachians, *AAPG Bulletin*, 71, 492–514.

Dorobek, S. (1989), Migration of orogenic fluids through the Siluro-Devonian Helderberg Group during Late Paleozoic deformation : constraints on fluid sources and implications for thermal histories of sedimentary basins, *Tectonophysics*, 159, 24–45.

Du Fornel, E., Joseph, P., Desaubliaux, G., Eschard, R., Guillocheau, F., Lerat, O., Muller, C., Ravenne, C. & Sztrakos, K. (2004), Deep-water sedimentation in the Alpine Basin of SE France : new perspectives on the Grès d'Annot and related systems, volume 221, chapter The southern Grès d'Annot outcrops (French Alps) : an attempt at regional correlation, 137–160, Geological Society Special Publication, London.

Dunlop, D. & Arkani-Hamed, J. (2005), Magnetic minerals in the Martian crust, *Journal of Geophysical Research*, 110, E12S04, doi :10.1029/2005JE002404.

Dunlop, D. & Kletetschka, G. (2000), Multidomain hematite : a source for planetary magnetic anomalies ?, *Geophysical Research Letters*, 28, 3345–3348.

Dunlop, D. & Özdemir, O. (1997), Rock Magnetism : Fundamentals and Frontiers, Cambridge University Press, New York, 573 .

Dunlop, D. & Özdemir, O. (2007), Geomagnetism, Treatise on Geophysics, volume 5, chapter Magnetizations in rocks and minerals, 277–336, Elsevier, Amsterdam, the Netherlands.

Dunlop, D., Özdemir, O., Clark, D. & Schmidt, P. (2000), Time-temperature relations for the remagnetization of pyrrhotite (Fe_7S_8) and their use in estimating paleotemperatures, *Earth and Planetary Science Letters*, 176, 107–116.

Elmore, R.D., Imbus, S.W., Engel, M.H. & Fruit, D. (1993), Applications of Paleomagnetism to Sedimentary Geology, volume 49, chapter Hydrocarbons and magnetizations in magnetite, 181–191, SEPM Special Publication.

Elmore, R., Engel, M., Crawford, L., Nick, K., Imbus, S. & Sofer, Z. (1987), Evidence for a relationship between hydrocarbons and authigenic magnetite, *Nature*, 325, 428–430.

Elmore, R., Foucher, J., Evans, M. & Lewchuk, M. (2006), Remagnetization of the Tonoloway Formation and the Helderberg Group in the Central Appalachians : testing the origin of syntilting magnetizations, *Geophysical Journal International*, 166, 1062–1076.

Elmore, R., Kelley, J., Evans, M. & Lewchuk, M. (2001), Remagnetization and orogenic fluids : testing the hypothesis in the Central Appalachians, *Geophysical Journal International*, 144, 568–576.

Elwood, B., Chrzanowski, T., Hrouda, F., Long, G. & Buhl, M. (1988), Siderite formation in anoxic deep-sea sediments : a synergetic bacterially controlled process with important implications in paleomagnetism, *Geology*, 16, 980–982.

Epstein, A., Epstein, J. & Harris, L. (1977), Conodont color alteration : an index to organic metamorphism, *USGS Professional Paper*, 995, 1–27.

Espitalié, J., Laporte, J.L., Madec, M., Marquis, F., Leplat, P., Paulet, J. & Boutefeu, A. (1977), Méthodes rapides de caractérisation des roches mères, de leur potentiel pétrolier et de leur degré d'évolution, *Revue de l'Institut Français du Pétrole*, 32, 23–42.

Esteban, L., Bouchez, J.L. & Trouillier, A. (2006), The Callovo-Oxfordian argillites from the eastern Paris Basin : magnetic data and petrofabrics, *Comptes Rendus Géosciences*, 338, 867–881.

Esteban, L. (2006), Anisotropies magnétiques et de porosité des argilites du Callovo-Oxfordien du laboratoire souterrain de l'ANDRA, Ph.D. thesis, Université de Toulouse, France.

Ettensohn, F. (2004), Modeling the nature and development of major Paleozoic clastic wedges in the Appalachian Basin, USA, *Journal of Geodynamics*, 37, 657–681.

Evans, M. (1995), Fluid inclusions in veins from the Middle Devonian shales : a record of deformation conditions and fluid evolution in the Appalachian Plateau, *Geological Society of America Bulletin*, 107(3), 327–339.

Evans, M., Elmore, R. & Lewchuk, M. (2000), Examining the relationship between remagnetization and orogenic fluids : central Appalachians, *Journal of Geochemical Exploration*, 69-70, 139–142.

Evans, M. (1989), The structural geometry and evolution of foreland thrust systems, northern Virginia, *Geological Society of America Bulletin*, 101, 339–354.

Evans, M. (2010), From Rodinia to Pangea : the lithotectonic record of the Appalachian Region, *Geological Society of America Memoir*, volume 206, chapter Temporal and spatial changes in deformation conditions during the formation of the Central Appalachian fold-and-thrust belt : evidence from joints, vein mineral paragenesis, and fluid inclusions, 477–552.

Evans, M. & Battles, D. (1999), Fluid inclusion and stable isotope analyses of veins from the Central Appalachian Valley and Ridge Province : implications for regional synorogenic structure and fluid migration, *Geological Society of America Bulletin*, 111(12), 1841–1860.

Evans, M. & Elmore, R. (2006), Fluid control of localized mineral domains in limestone pressure solution structures, *Journal of Structural Geology*, 28, 284–301.

Evans, M. & Hobbs, G. (2003), Fate of "warm" migrating fluids in the Central Appalachians during the Late Paleozoic Alleghanian orogeny, *Journal of Geochemical Exploration*, 78-79, 327–331.

Ford, M. & Lickorish, H. (2004), Deep-water sedimentation in the Alpine Basin of SE France : new

perspectives on the Grès d'Annot and related systems, volume 221, chapter Foreland basin evolution around the western Alpine arc, 39–63, Geological Society Special Publication, London.

France, D. & Oldfield, F. (2000), Identifying goethite and hematite from rock magnetic measurements of soils and sediments, *Journal of Geophysical Research*, 105(B2), 2781–2795.

Frederichs, T., von Dobenek, T., Bleil, U. & Dekkers, M. (2003), Towards the identification of siderite, rhodochrosite and vivianite in sediments by their low-temperature magnetic properties, *Physics and Chemistry of the Earth*, 28, 669–679.

Gallagher, K., Brown, R. & Johnson, C. (1998), Fission track analysis and its applications to geological problems, *Annu. Rev. Earth Planet. Sci.*, 26, 519–572.

Garcia, D., Joseph, P., Maréchal, B. & Moutte, J. (2004), Deep-water sedimentation in the Alpine Basin of SE France : new perspectives on the Grès d'Annot and related systems, volume 221, chapter Patterns of geochemical variability in relation to turbidite facies in the Grès d'Annot Formation, 349–365, Geological Society Special Publication, London.

Gaucher, E., Robelin, C., Matray, J.M., Négrel, G., Gros, Y., Heitz, J.F., Vinsot, A., Rebours, H., Cassagnabère, A. & Bouchet, A. (2004), ANDRA underground research laboratory : interpretation of the mineralogical and geochemical data acquired in the Callovo-Oxfordian formation by investigative drilling, *Physics and Chemistry of the Earth*, 29, 55–77.

Gehring, A. & Hofmeister, A. (1994), The transformation of lepidocrocite during heating : a magnetic and spectroscopic study, *Clays and Clay Minerals*, 42(4), 409–415.

Gillett, S.L. (2003), Paleomagnetism of the Notch Peak contact metamorphic aureole revisited : Pyrrhotite form magnetite+pyrite under sbmetamorphic conditions, *Journal of Geophysical Research*, 108(B9), 2446, doi :10.1029/2002JB002386.

Girard, J.P. & Fouillac, A.M. (1995), Structure et transformation des argiles dans les champs pétroliers et géochimiques, chapter Géochimie isotopique de l'oxygène et de l'hydrogène des argiles : exemples d'application aux domaines diagénétique et géothermique, 167–195, Bulletin des centres de recherche EP Elf Aquitaine.

Gleadow, A., Duddy, I., Green, P. & Lovering, J. (1986), Confined fission track lenghts in apatite : a diagnostic tool for thermal history analysis, *Contributions to Mineral Petrology*, 94, 405–415.

Goldstein, R. & Reynolds, T. (1994), Systematics of fluid inclusions in diagenetic minerals, *SEPM Short course*, volume 31, Tulso, 199 .

Goldstein, R.H. (2001), Fluid inclusions in sedimentary and diagenetic systems, *Lithos*, 55(1-4), 159–193.

Green, P. (1986), On the thermo-tectonic evolution of Northern England : evidence from fission track analysis, *Geological Magazine*, 123, 493–506.

Green, P., Duddy, I., Gleadow, A. & Lovering, J. (1989), Thermal history of sedimentary basins : methods and case histories, chapter Apatite fission track analysis as a paleotemperature indicator for hydrocarbon exploration, Springer-Verlag, New York.

Green, P., Duddy, I., Gleadow, A., Tingate, P. & Laslett, G. (1986), Thermal annealing of fission tracks in apatite : 1. a qualitative description, *Chemical Geology*, 59, 237–253.

Gubler, Y. (1958), Etude critique des sources du matériel constituant certaines séries détritiques dans le Tertiaire des Alpes françaises du Sud : formations détritiques de Barrême, flysh "Grès d'Annot", *Eclogae Geologicae Helvetica*, 51, 942–977.

Guilhaumou, N., Thouray, J.C., Perthuisot, V. & Roure, F. (1996), Palaeocirculation in the basin of southeastern France sub-alpine range : a synthesis from fluid circulations studies, *Marine and Petroleum Geology*, 13(6), 695–706.

Guillocheau, F., Quéméner, J.M., Robin, C., Joseph, P. & Brouck, O. (2004), Deep-water sedimentation in the Alpine Basin of SE France : new perspectives on the Grès d'Annot and related systems, volume 221, chapter Genetic units : parasequences of the Grès d'Annot turbidite system, SE France, 181–202, Geological Society Special Publication, London.

Guillocheau, F., Robin, C., Allemand, P., Bourquin, S., Brault, N., Dromart, G., Friedenberg, R., Garcia, J.P., Gaulier, J.M., Gaumet, F., Grosdoy, G., Hanot, F., LeStrat, P., Mettraux, M., Nalpas, T., Prijac, C., Rigollet, C., Serrano, O. & Grandjean, G. (2000), Meso-Cenozoic geodynamic evolution of

the Paris Basin : 3D stratigraphic constraints, *Geodinamica Acta*, 13, 189–246.

Guyodo, Y., LaPara, T.M., Anschutz, A.J., Penn, R.L., Banerjee, S.K., Geiss, C.E. & Zanner, W. (2006), Rock magnetic, chemical and bacterial community analysis of a modern soil from Nebraska, *Earth and Planetary Science Letters*, 251, 168–178.

Guyodo, Y., Mostrom, A., Penn, R.L. & Banerjee, S.K. (2003), From nanodots to nanorods : oriented aggregation and magnetic evolution of nanocrystalline goethite, *Geophysical Research Letters*, 30(10), 1512, doi :10.1029/2003GL017021.

Halgedahl, S.L. & Jarrard, R.D. (1995), Low-temperature behavior of single-domain through multidomain magnetite, *Earth and Planetary Science Letters*, 130, 127–139.

Harper, J. (2008), The Marcellus Shale : an "old" new gas reservoir in Pennsylvania, *Pennsylvania Geology*, 38(1), 2–13.

Harrison, R. & Feinberg, J. (2008), FORCInel : an improved algorithm for calculating first-order reversal curve distributions using locally weighted regression smoothing, *Geochemistry, Geophysics, Geosystems*, 9, doi :10.1029/2008GC001987.

Hatcher, R. (2010), From Rodinia to Pangea : the lithotectonic record of the Appalachian Region, chapter The Appalachian orogen : a brief summary, 1–19, number 206 in Geological Society of America Memoir.

Heider, F., Dunlop, D. & Soffel, H. (1992), Low-temperature and alternating field demagnetization of saturation remanence and thermoremanence in magnetite grains (0.037 μm to 5 mm), *Journal of Geophysical Research*, 97, 9371–9381.

Helsen, S., David, P. & Fremont, W. (1995), Calibration of conodont color alteration using color image analysis, *Journal of Geology*, 103(3), 257–267.

Herbert, R.B. (1997), Properties of goethite and jarosite precipitated from acidic groundwater, Dalarna, Sweden, *Clays and Clay Minerals*, 45(2), 261–273.

Hillier, S., Matyas, J., Matter, A. & Vasseur, G. (1995), Illite/Smectite diagenesis and its variable correlation with vitrinite reflectance in the Pannonian Basin, *Clays and Clay Minerals*, 43(2), 174–183.

Hirt, A., Lanci, L., Dobson, J., Weidler, P. & Gehring, A. (2002), Low-temperature magnetic properties of lepidocrocite, *Journal of Geophysical Research*, 107(B1), 2011, doi :10.1029/2001JB000242.

Hoffmann, J. & Hower, J. (1979), Aspects of diagenesis, *SEPM Special Publication*, volume 26, chapter Clay mineral assemblages as low grade metamorphic geothermometers : application to the thrust faulted disturbed belt of Montana, 55–79.

Hoffmann, V. (1992), Greigite (Fe_3S_4) : magnetic properties and first domain observations, *Physics of the Earth and Planetary Interiors*, 70, 288–301.

Horng, C.S. & Roberts, A.P. (2006), Authigenic or detrital origin of pyrrhotite in sediments ? : resolving a paleomagnetic conumdrum, *Earth and Planetary Science Letters*, 241, 750–762.

Horng, C.S., Torii, M., Shea, K.S. & Kao, S.J. (1998), Inconsistent magnetic polarities between greigite and pyrrhotite/magnetite-bearing marine sediments from the Tsailiao-chi section, *Earth and Planetary Science Letters*, 164, 467–481.

Housen, B., Banerjee, S. & Moskowitz, B. (1996), Low-temperature magnetic properties of siderite and magnetite in marine sediments, *Geophysical Research Letters*, 23(20), 2843–2846.

Irving, E. & Opdyke, N. (1965), The paleomagnetism of the Bloomsburg red beds and its possible application to the tectonic history of the Appalachians, *Geophys. J. R. Astron. Soc.*, 9, 153–167.

Isaksen, G.H. (2004), Central North Sea hydrocarbon systems : Generation, migration, entrapment and therma degradation of oil and gas, *AAPG Bulletin*, 88(2), 1545–1572.

Jackson, M. (1990), Diagenetic sources of stable remanence in remagnetized Paleozoic cratonic carbonates : a rock magnetic study, *Journal of Geophysical Research*, 95, 2753–2762.

Jackson, M., McCabe, C., Ballard, M. & Van der Voo, R. (1988), Magnetite authigenesis and diagenetic paleotemperatures across the northern Appalachian basin, *Geology*, 16, 592–595.

Jackson, M., Rochette, P., Fillion, G., Banerjee, S. & Marvin, J. (1993), Rock magnetism of remagnetized Paleozoic carbonates : low-temperature behavior and susceptibility characteristics, *Journal of Geophysical Research*, 98(B4), 6217–6225.

Jackson, M., Sun, W.W. & Craddock, J. (1992), The rock magnetic fingerprint of chemical remagnetization in midcontinental paleozoic carbonates, *Geophysical Research Letters*, 19(8), 781–784.

Jackson, M. & Worm, H.U. (2001), Anomalous unblocking temperatures, viscosity and frequency-dependent susceptibility in the chemically-remagnetized Trenton limestone, *Physics of the Earth and Planetary Interiors*, 126, 27–42.

Jacob, H. (1985), Disperse, feste Erdölbitumina als migrations - und maturitätsindikatoren im rahmen der erdöl - erdags - Prospektion Eine Modellstudies in NW-Deutschland, *Dtsh Ges. Mineraloelwiss. Kohlechem. e. V.*, Projekt 267, english summary p4–6.

Jean, S. (1985), Les Grès d'Annot au NW du Massif de l'Argentera-Mercantour, Ph.D. thesis, Université de Grenoble, France.

Jean, S., Kerckhove, C., Perriaux, J. & Ravenne, C. (1985), Un modèle Paléogène de bassin à turbidites : les Grès d'Annot du NW du massif de l'Argentera-Mercantour, *Géologie Alpine*, 61, 115–143.

Joseph, P. & Lomas, S. (2004), Deep-water sedimentation in the Alpine basin of SE France : new perspectives on the Grès d'Annot and related systems, volume 221, chapter Deep-water sedimentation in the Alpine Foreland Basin of SE France : a new perspective on the Grès d'Annot and related systems : an introduction, 1–16, Geological Society Special Publication, London.

Kakol, Z., ans J. Stickler, J.S. & Honig, J. (1992), Effect of low level titanium (IV) doping on the resistivity of magnetite near the Verwey transition, *Physical Review*, B46, 1975–1978.

Kao, S.J., Horng, C.S., Roberts, A.P. & Liu, K.L. (2004), Carbon-Sulfur-Iron relationships in sedimentary rocks from southwestern Taiwan : influence of geochemical environment on greigite and pyrrhotite formation, *Chemical Geology*, 203, 153–168.

Karlin, R. (1990), Magnetite diagenesis in marine sediments from the Oregon continental margin, *Journal of Geophysical Research*, 95, 4405–4419.

Karlin, R., Lyle, M. & Ross Heath, G. (1987), Authigenic magnetite formation in suboxic marine sediments, *Nature*, 326, 490–493.

Kars, M., Aubourg, C. & Pozzi, J.P. (2011a), Low temperature magnetic behaviour near 35 K in unmetamorphosed claystones, *Geophysical Journal International*, 186, 1029–1035.

Kars, M., Aubourg, C., Pozzi, J.P., Labaume, P. & Girard, J.P. (2011b), Diagenesis to low grade metamorphism in the Grès d'Annot basin : a magnetic approach, EGU2011-5404, EGU General Assembly, Vienna.

Kelso, P. & Banerjee, S. (1994), Elevated temperature viscous remanent magnetizaion of natural and synthetic multidomain magnetite, *Earth and Planetary Science Letters*, 122, 43–56.

Kent, D. (1985), Thermoviscous remagnetization in some Appalachian limestones, *Geophysical Research Letters*, 12(12), 805–808.

Kerckhove, C. (1969), La "zone du Flysh" dans les nappes de l'Embrunais-Ubaye (Alpes Occidentales), *Géologie Alpine*, 45, 5–204.

Keunen, P., Fauret-Muret, A., Lanteaume, N. & Fallot, P. (1957), Observation sur les flyshs des Alpes Maritimes françaises et italiennes, *Bulletin de la Sociètè Géologique des France*, 6(VII), 4–26.

Kilgore, B. & Elmore, R. (1989), A study of the relationship between hydrocarbon migration and precipitation of authigenic magnetic minerals in the Triassic Chugwater formation, southern Montana, *Geological Society of America Bulletin*, 101, 1280–1288.

Kontny, A., de Wall, H., Sharp, T.G. & Pósfai, M. (2000), Mineralogy and magnetic behavior of pyrrhotite from a 260°C section of the KTB drilling site, Germany, *American Mineralogist*, 85, 1416–1427.

Kosterov, A., Frederichs, T. & von Dobenek, T. (2006), Low-temperature magnetic properties of rhodochrosite ($MnCO_3$), *Physics of the Earth and Planetary Interiors*, 154, 234–242.

Kübler, B. & Jaboyedoff, M. (2000), Illite crystallinity, *Comptes Rendus de l'Académie des Sciences, Paris*, 331, 75–89.

Labaume, P., Jolivet, M., Souquière, F. & Chauvet, A. (2008), Tectonic control on diagenesis in a foreland basin : combined petrologic and thermochronologic approaches in the Grès d'Annot sub-basin (Late Eocene-Early Oligocene, French-Italian external Alps), *Terra Nova*, 20, 95–101.

Lafargue, E., Marquis, F. & Pillot, D. (1998), RockEval 6 applications in hydrocarbon exploration, production and soil contamination studies, *Revue de l'Institut Français du Pétrole*, 53(4), 421–437.

Lagroix, F., Banerjee, S.K. & Berquò, T.S. (2005), Isolating the alteration by-products from the detrital component in Alaskan loess by chemical extraction : a feasibility study for paleoclimate reconstruction, *EOS Transactions AGU Fall Meeting*, 86(52), GP13A–0019.

Lagrou, D., Vandenberghe, N., Van Simaeys, S. & Hus, J. (2004), Magnetostratigraphy and rock magnetism of the Boom Clay (Rupelian stratotype) in Belgium, *Netherlands Journal of Geosciences/Geologie en Mijnbouw*, 83(3), 209–225.

Landais, P. & Elie, M. (1999), Utilisation de la géochimie organique pour la détermination du paléoenvironnement et de la paléothermicité dans la Callovo-Oxfordien du site de l'Est de la France, in E. Paris, editor, Acte des Journés Scientifiques CNRS-ANDRA.

Landau, L. & Lifschitz, E. (1935), On the theory of the dispersion of magnetic permeability in ferromagnetic bodies, *Phys. Z. Sowjetunion*, 8, 153–169.

Larrasoana, J.C., Roberts, A.P., Musgrave, R.J., Gràcia, E., Pinero, E., Vega, M. & Martínez-Ruiz, F. (2007), Diagenetic formation of greigite and pyrrhotite in gas hydrate marine sedimentary systems, *Earth and Planetary Science Letters*, 261, 350–366.

Larson, E., Walker, T., Patterson, P., Hobbit, R. & Rosenbaum, J. (1982), Paleomagnetism of the Moenkopi Formation, Colorado Plateau : basis for long-term model of acquisition of chemical remanent magnetism in red beds, *Journal of Geophysical Research*, 87, 1081–1106.

Laslett, G., Gleadow, A. & Duddy, I. (1984), The relationship between fission track length and density in apatite, *Nucl. Tracks*, 9, 29–38.

Leslie, B.W., Lund, S.P. & Hammond, D.E. (1990), Rock magnetic evidence for the dissolution and authigenic growth of magnetic minerals within anoxic marine sediments of the California continental borderland, *Journal of Geophysical Research*, 95(B4), 4437–4452.

Lewchuk, M., Elmore, R. & Evans, M. (2002), Remagnetization signature of Paleozoic sedimentary rocks from the Patterson Creek Mountain Anticline in West Virginia, *Physics and Chemistry of the Earth*, 27, 1141–1150.

Lewchuk, M., Evans, M. & Elmore, R. (2003), Synfolding remagnetization and deformation : results from Paleozoic sedimentary rocks in Western Virginia, *Geophysical Journal International*, 152, 266–279.

Lin, S. (1959), Magnetic properties of hematite single crystals. I. Magnetization isotherms, antiferromagnetic susceptibility, and weak ferromagnetism of a natural crystal, *Physical Review*, 116(6), 1447–1452.

Lopatin, N. (1971), Temperature and geologic time as a factor in coalification, *Izveotiya Akademii, Nauk SSSR, Seryia Geolichestkya*, 3, 95–106.

Lopatin, N. (1976), Study of organic matter in recent and old sediments, chapter The influence of temperature and geologic time on the catagenetic processes of coalification and petroleum and gas formation, 361–366, Nauka Press, Moscow.

Lowrie, W. (1990), Identification of ferromagnetic minerals in a rock by coercivity and unblocking temperature prop, *Geophysical Research Letters*, 17(2), 159–162.

Lu, G., Marshak, S. & Kent, D. (1990), Characteristics of magnetic carriers responsible for Late Paleozoic remagnetization in carbonate strata of the mid-continent, USA, *Earth and Planetary Science Letters*, 99, 351–361.

Machel, H.G. (1995), Palaeomagnetic Applications in Hydrocarbon exploration and production, volume 98, chapter Magnetic minerals assemblages and magnetic contrasts in diagenetic environments - with implications for studies of palaeomagnetism, hydrocarbon migration and exploration, 9–29, Geological Society Special Publication.

Machel, H. & Burton, E. (1991), Chemical and microbial processes causing anomalous magnetizaion in environments affected by hydrocarbon seepage, *Geophysics*, 56(5), 598–605.

Maher, B. (1998), Magnetic properties of modern soils and quaternary loessic paleosols : paleoclimatic implications, *Palaeogeography, Palaeoclimatology, Palaeoecology*, 137, 25–54.

Maher, B., Karloukovski, V. & Mutch, T. (2004), High-field remanence properties of synthetic and natural submicrometre haematites and goethites : significance for environmental contexts, *Earth and Planetary Science Letters*, 226, 491–505.

Maher, B. & Taylor, R. (1988), Formation of ultrafine-grained magnetite in soils, *Nature*, 336, 368–370.

Maher, B. & Thompson, R. (1999), Quaternary Climates, Environments and Magnetism, Cambridge University Press.

Matte, P. (2002), Variscan-Appalachian dynamics : the building of the Late Paleozoic basement, *Geological Society of America Special Paper*, volume 394, chapter Variscides between the Appalachians and Urals : similarities and differences between Paleozoic subduction and collision belts, 239–251.

Mayergoyz, I. (1986), Mathematical models of hysteresis, *IEEE. Trans. Mag*, MAG22, 603–608.

Mazurek, M., Hurford, A.J. & Leu, W. (2006), Unravelling the multi-stage burial history of the Swiss Molasse Basin : integration of apatite fission track, vitrinite reflectance and biomarker isomerisation analysis, *Basin Research*, 18, 27–50.

McCabe, C. & Elmore, R. (1989), The occurrence and origin of Late Paleozoic remagnetization in the sedimentary rocks of North America, *Review of Geophysics*, 27(4), 471–494.

McCabe, C., Jackson, M. & Saffer, B. (1989), Regional patterns of magnetite authigenesis in the Appalachian basin : implications for the mechanism of Late Paleozoic remagnetization, *Journal of Geophysical Research*, 94(B8), 10 429–10 443.

McCabe, C., Sassen, R. & Saffer, B. (1987), Occurence of secondary magnetite within biodegraded oil, *Geology*, 15, 7–10.

Mehra, O. & Jackson, M. (1960), Iron oxide removal from soils and clays by a dithionite-citrate system buffered with sodium bicarbonate, *Clays and Clay Minerals*, 5, 317–327.

Merriman, R.J. (2005), Clay minerals and sedimentary basin history, *European Journal of Mineralogy*, 17, 7–20.

Merschat, A. & Hatcher, R. (2007), The 4-D Framework of Continental crust, *Geological Society of America Memoir*, volume 200, chapter The Cat Square terrane : possible Siluro-Devonian remnant ocean basin in the Inner Piedmont, southern Appalachians, 553–566.

Meunier, A. & Velde, B. (1989), Solid solutions in I/S mixed-layer minerals and illite, *American Mineralogist*, 74, 1106–1112.

Moore, D. & Reynolds, R. (1997), X-ray diffraction and the identification and analysis of clay minerals, Oxford University Press, New York.

Moreau, M.G., Ader, M. & Enkin, R. (2005), The remagnetization of clay-rich rocks in sedimentary basins : low-temperature experimental formation of magnetic carriers in natural sample, *Earth and Planetary Science Letters*, 230, 193–210.

Moreau, M.G., Bucher, H., Bodergat, A.M. & Guex, J. (2002), Pliensbachian magnetostratigraphy : new data from Paris Basin (France), *Earth and Planetary Science Letters*, 203, 755–767.

Morin, F. (1950), Magnetic susceptibility of $\alpha - Fe_2O_3$ with added titanium, *Physical Review*, 78, 819–820.

Morse, J.W. & Wang, Q. (1997), Pyrite formation under conditions approximating those in anoxic sediments : II. Influence of precursor iron minerals and organic matter, *Marine Chemistry*, 57, 187–193.

Moskowitz, B. (1992), Rock magnetism Laboratory notes, Technical report, University of Minnesota, Minneapolis.

Moskowitz, B., Jackson, M. & Kissel, C. (1998), Low-temperature magnetic behavior of titanomagnetites, *Earth and Planetary Science Letters*, 157, 141–149.

Moskowitz, B., Frankel, R.B. & Bazylinski, D.A. (1993), Rock magnetic criteria for the detection of biogenic magnetite, *Earth and Planetary Science Letters*, 120, 283–300.

Mougin, F. (1978), Contribution à l'étude des sédiments tertiaires de la partie orientale du synclinal d'Annot, Ph.D. thesis, Université de Grenoble, France.

Murad, E. & Cashion, J. (2004), Mössbauer spectroscopy of environmental materials and their industrial utilization, Kluwer Academic Publishers, Boston, Dordrecht, New York, London.

Mutti, E. (1992), Turbidite sandstones, Technical report, AGIP and Instituto di Geologia, Università di Parma, Italy.

Muxworthy, A.R. & McClelland, E. (2000), Review of the low-temperature magnetic properties of magnetite from a rock magnetic perspective, *Geophysical Journal International*, 140, 101–114.

Muxworthy, A. (1999), Low-temperature susceptibility and hysteresis of magnetite, *Earth and Planetary Science Letters*, 169, 51–58.

Muxworthy, A. & Dunlop, D. (2002), First-order reversal curve (FORC) diagrams for pseudo-single domain magnetites at high temperature, *Earth and Planetary Science Letters*, 203, 369–382.

Naeser, N.D. & McCulloh, T.H. (1989), Thermal history of sedimentary basins : methods and case histories, AAPG, society of economic paleontologists and mineralogists edition.

Néel, L. (1949), Théorie du traînage magnétique des ferromagnétiques en grains fins avec applications aux terres cuites, *Ann. Géophys.*, 5, 99–136.

Néel, L. (1955), Some theoritical aspects of rock magnetism, *Adv. Phys.*, 4, 191–243.

Oliver, J. (1986), Fluids expelled tectonically from orogenic belts : their role in hydrocarbon migration and other geologic phenomena, *Geology*, 14, 99–102.

Osberg, P., Tull, J., Robinson, P. & Butler, J. (1989), The Appalachian-Ouachita orogen in the United States : Boulder, Colorado, *Geological Society of America, Geology of North America*, volume F-2, chapter The Acadian orogen, 179–232.

Özdemir, O., Dunlop, D. & Moskowitz, B. (2002), Changes in remanence, coercivity and domain state at low-temperature in magnetite, *Earth and Planetary Science Letters*, 194, 343–358.

Özdemir, O. & Dunlop, D.J. (2000), Intermediate magnetite formation during dehydration of goethite, *Earth and Planetary Science Letters*, 177, 59–67.

Özdemir, O., Dunlop, D.J. & Moskowitz, B.M. (1993), The effect of oxidation on the Verwey transition in magnetite, *Geophysical Research Letters*, 20(16), 1671–1674.

Özdemir, O. & Dunlop, D. (1996), Thermoremanence and Néel temperature of goethite, *Geophysical Research Letters*, 23(9), 921–924.

Özdemir, O. & Dunlop, D. (1999), Low-temperature properties of a single crystal of magnetite oriented along principal magnetic axes, *Earth and Planetary Science Letters*, 165, 229–239.

Özdemir, O. & Dunlop, D. (2002), Thermoremanence and stable memory of single-domain hematites, *Geophysical Research Letters*, 29(18), 1877, doi :10.1029/2002GL015597.

Özdemir, O. & Dunlop, D. (2010), Hallmarks of maghemitization in low-temperature remanence cycling of partially oxidized magnetite nanoparticles, *Journal of Geophysical Research*, 115(B02101), doi :10.1029/2009JB006756.

Özdemir, O., Dunlop, D. & Berquó, T. (2008), Morin transition in hematite : size dependence and thermal hysteresis, *Geochemistry, Geophysics, Geosystems*, 9(10, Q10Z01), doi :10.1029\2008GG002110.

Pairis, J.L. (1988), Paléogène marin et structuration des Alpes Occidentales Françaises (domaine externe et confins sud-occidentaux du Sub-Briançonnais), Ph.D. thesis, Université de Grenoble, France.

Peters, K.E., Clifford, C.W. & Moldowan, J.M. (2005), The biomarker guides : biomarkers and isotopes in the environment and human history, volume 1, Cambridge University Press, 1155 .

Pick, T. & Tauxe, L. (1991), Chemical Remanent Magnetization in synthetic magnetite, *Journal of Geophysical Research*, 96(B6), 9925–9936.

Pick, T. & Tauxe, L. (1994), Characteristics of magnetite in submarine basaltic glass, *Geophysical Journal International*, 119, 116–128.

Pickering, K. & Hilton, V. (1998), Turbidite systems of southern France : application to hydrocarbon prospectivity, Vallis Press, London.

Pokhil, T. & Moskowitz, B. (1997), Magnetic domains and domain walls in pseudo-single domain magnetite studied with magnetic force microscopy, *Journal of Geophysical Research*, 102, 22 681–22 694.

Pollastro, R.M. (1993), Considerations and applications of the illite/smectite geothermometer in hydrocarbon-bearing rocks of Miocene to Missippian age, *Clays and Clay Minerals*, 41(2), 119–133.

Pósfai, M., Sharp, T.G. & Kontny, A. (2000), Pyrrhotite varieties from the 9.1 km deep borehole of the KTB project, *American Mineralogist*, 85, 1406–1415.

Pozzi, J.P. & Dubuisson, G. (1992), High temperature viscous magnetization of oceanic deep crustal- and mantle- rocks as a partial source for Magsat magnetic anomalies, *Geophysical Research Letters*, 19, 21–24.

Pullaiah, G., Irving, E., Buchan, K. & Dunlop, D. (1975), Magnetization changes caused by burial and uplift, *Earth and Planetary Science Letters*, 28, 133–143.

Ravenne, C., Vially, R., Riche, P. & Trémolières, P. (1987), Sédimentation et tectonique dans le bassin éocène sup-oligocène des Alpes du Sud, *Revue de l'Institut Français du Pétrole*, 42, 529–553.

Reed, J.S., Spotila, J.A., Eriksson, K.A. & Bodnar, R.J. (2005), Burial and exhumation history of Pennsylvanian strata, central Appalachian basin : an integrated study, *Basin Research*, 17, 259–268.

Repetski, J., Ryder, R., Lee Avary, K. & Trippi, M. (2005), Thermal maturity patterns (CAI and % Ro) in the Ordovician and Devonian rocks of the Appalachian Basin in West Virginia, Technical Report open-file report 2005-1078, USGS.

Reynolds, R.L., Goldhaber, M.B. & Tuttle, M.L. (1993), Applications of Paleomagnetism to Sedimentary Geology, volume 49, chapter Sulfidization and magnetization above hydrocarbon reservoirs, 167–179, SEPM Special Publication.

Reynolds, R., Fishman, N. & Hudson, M. (1991), Sources of aeromagnetic anomalies over Cement oil field (Oklahoma), Simpson oil field (Alaska) and the Wyoming-idaho-Utah thrust belt, *Geophysics*, 56(5), 606–617.

Roberts, A.P., Chang, L., Rowan, C.J., Horng, C.S. & Florindo, F. (2011), Magnetic properties of sedimentary greigite (Fe_3S_4) : an update, *Review of Geophysics*, 49, RG1002, doi :10.1029/2010RG000336.

Roberts, A.P., Liu, Q., Rowan, C.J., Chang, L., Carvallo, C., Torrent, J. & Horng, C.S. (2006), Characterization of hematite ($\alpha - Fe_2O_3$), goethite ($\alpha -$ FeOOH), greigite (Fe_3S_4), and pyrrhotite (Fe_7S_8) using first-order reversal curve diagrams, *Journal of Geophysical Research*, 111(B12S35), doi :10.1029/2006JB004715.

Roberts, A.P. & Turner, G.M. (1993), Diagenetic formation of ferromagnetic iron sulphides minerals in rapidly deposited marine sediments, South Island, New Zealand, *Earth and Planetary Science Letters*, 115, 257–273.

Roberts, A. (1995), Magnetic characteristics of sedimentary greigite (Fe_3S_4), *Earth and Planetary Science Letters*, 134, 227–236.

Rochette, P., Fillion, G., Mattéi, J.L. & Dekkers, M.J. (1990), Magnetic transition at 30-34 Kelvin in pyrrhotite : insight into a widespread occurrence of this mineral in rocks, *Earth and Planetary Science Letters*, 98, 319–328.

Rochette, P. (1987), Metamorphic control of the magnetic mineralogy of black shales in the Swiss Alps : toward the use of "magnetic isograds", *Earth and Planetary Science Letters*, 84, 446–456.

Rochette, P., Mathé, P.E., Esteban, L., Rakoto, H., Bouchez, J.L., Liu, Q. & Torrent, J. (2005), Non-saturation of the defect moment of goethite and fine-grained hematite up to 57 T, *Geophysical Research Letters*, 32(L22309), doi :10.1029/2005GL024196.

Rochette, P., Ménard, G. & Dunn, R. (1992), Thermochronometry and cooling rates deduced from single sample records of successive magnetic polarities during uplift of metamorphic rocks in the Alps (France), *Geophysical Journal International*, 108, 491–501.

Roden, M. (1991), Apatite fission-track thermochronology of the southern Appalachian basin : Maryland, West Virginia and Virginia, *Journal of Geology*, 99, 41–53.

Rodgers, J. (1971), The Taconic orogeny, *Geological Society of America Bulletin*, 82, 1141–1178.

Roedder, E. (1984), Fluid inclusions, *Reviews in Mineralogy*, volume 12, 644 .

Rowan, C.J. & Roberts, A.P. (2005), Tectonic and geochronological implications of variability timed magnetizations carried by authigenic greigite in marine sediments from New Zealand, *Geology*, 33(7), 553–556.

Rowan, C.J. & Roberts, A.P. (2006), Magnetite dissolution, diachronous greigite formation, and secondary magnetizations from pyrite oxidation : unravelling complex magnetizations in Neogene marine

sediments from New Zealand, *Earth and Planetary Science Letters*, 241, 119–137.

Rowan, C.J., Roberts, A.P. & Broadbent, T. (2009), Reductive diagenesis, magnetite dissolution, greigite growth and paleomagnetic smoothing in marine sediments : a new view, *Earth and Planetary Science Letters*, 277, 223–235.

Roy, J., Opdyke, N. & Irving, E. (1967), Further paleomagnetic results from the Bloomsburg Formation, *Journal of Geophysical Research*, 72, 5075–5086.

Sassen, R. (1980), Biodegradation of crude oil and mineral deposition in a shallow Gulf Coast salt dome, *Organic Geochemistry*, 2, 153–166.

Sassen, R., McCabe, C., Kyle, J.R. & Chinn, E.W. (1989), Deposition of magnetic pyrrhotite during alteration of crude oil and reduction of sulfate, *Organic Geochemistry*, 14(4), 381–392.

Schill, E., Appel, E. & Gautam, P. (2002), Towards pyrrhotite/magnetite geothermometry in low-grade metamorphic carbonates of the Thethyan Himalayas (Shiar Khola, Central Nepal), *Journal of Asian Earth Sciences*, 20, 195–201.

Schwarz, E. (1975), Magntic properties of pyrrhotite and their use in applied geology and geophysics, *Geol. Surv. Can. Pap.*, 74–79.

Schwarz, E. & Harris, D. (1970), Phases in natural pyrrhotite and the effect of heatin on their magnetic properties and composition, *Journal of Geomagnetism and Geoelectricity*, 22(4), 463–470.

Schwarz, E. & Vaughan, D. (1972), Magnetic phase relations of pyrrhotite, *Journal of Geomagnetism and Geoelectricity*, 24, 441–458.

Senftle, F.E., Thorpe, A.N., Briggs, C., Alexander, C., Minkin, J. & Griscom, D.L. (1975), The Néel transition and magnetic properties of terrestrial, synthetic and lunar ilmenites, *Earth and Planetary Science Letters*, 26, 377–386.

Senftle, J. & Landis, C.R. (1991), Source rock and migration processes and evaluation techniques, chapter Vitrinite reflectance as a tool to assess thermal maturity, 119–125, Treatise of petroleum geology - Handbook of Petroleum Geology, American Association of Petroleum Geologists.

Séranne, M. (1999), The Mediterranean Basins : Tertiary extension within the Alpine orogen, volume 156, chapter The Gulf of Lion continental margin (NW Mediterranean) revisited by IBS : an overview, 15–36, Geological Society Special Publication.

Sinclair, H. (1997), Tectonostratigraphic model for underfilled peripheral foreland basins : an Alpine perspective, *Geological Society of America Bulletin*, 109, 324–346.

Skehan, J. & Rast, N. (1990), Geology of the composite Avalon Terrane of southern New England, *Geological Society of America Special Paper*, volume 245, chapter Pre-Mesozoic evolution of Avalon terranes of southern New England, 13–53.

Smith, G. & Banerjee, S. (1986), Magnetic structure of the upper kilometer of the marine crust at Deep Sea Drilling Project Hole 504B, eastern Pacific Ocean, *Journal of Geophysical Research*, 91, 10 337–10 354.

Souquière, F. (2005), Relations tectonique/diagenèse dans un bassin d'avant-chaîne, exemple des Grès d'Annot : approche pétrologique et thermochronologique, Master's thesis, Université de Montpellier, France.

Srodon, J., Elsass, F., McHardy, W. & Morgan, D. (1992), Chemistry of illite-smectite inferred from TEM measurements of fundamental particles, *Clay Minerals*, 27, 137–158.

Stacey, F. & Banerjee, S.K. (1974), The physical principles of Rock Magnetism, Elsevier, Amsterdam, 195 .

Stamatakos, J., Hirt, A. & Lowrie, W. (1996), The age and timing of folding in the central Appalachians from paleomagnetic results, *Geological Society of America Bulletin*, 108(7), 815–829.

Stanley, R. & Ratcliffe, N. (1985), Tectonic synthesis of the Taconic orogeny in western New England, *Geological Society of America Bulletin*, 96, 1227–1250.

Staplin, F. (1969), Sedimentary organic matter, organic metamorphism and oil and gas occurrence, *Bulletin of Canadian Petroleum Geology*, 17(1), 47–66.

Stokking, L. & Tauxe, L. (1987), Acquisition of chemical remanent magnetization by synthetic iron oxides, *Nature*, 327, 610–612.

Stokking, L. & Tauxe, L. (1990), Properties of chemical remanence in synthetic hematite : testing theoretical predictions, *Journal of Geophysical Research*, 95(B8), 12 639–12 652.

Suk, D., Peacor, D. & Van der Voo, R. (1990), Replacement of pyrite framboids by magnetite in limestone and implications for paleomagnetism, *Nature*, 345, 611–613.

Suk, D., Van der Voo, R. & Peacor, D. (1991), SEM/STEM observations of magnetite in carbonates of eastern North America : evidence for chemical remagnetization during the Alleghenian orogeny, *Geophysical Research Letters*, 18(5), 939–942.

Suk, D., Van der Voo, R. & Peacor, R. (1993), Origin of magnetite responsible for remagnetization of Early Paleozoic limestones of New York State, *Journal of Geophysical Research*, 98, 419–434.

Sweeney, J.J. & Burnham, A.K. (1990), Evaluation of a simple model of vitrinite reflectance based on chemical kinetics, *AAPG Bulletin*, 74(10), 1559–1570.

Sztrakos, K. & Du Fornel, E. (2003), Stratigraphie, paléoécologie et foraminifères du Paléogène des Alpes Maritimes et des Alpes de Haute-Provence (SE de la France), *Revue de Micropaléontologie*, 46, 229–267.

Tauxe, L. (2007), Lectures in Paleomagnetism.

Tauxe, L. (2008), Essentials of Rocks and Paleomagnetism.

Tauxe, L., Mullender, T. & Pick, T. (1996), Potbellies, wasp-waists, and superparamagnetism in magnetic hysteresis, *Journal of Geophysical Research*, 101(B1), 571–583.

Thompson, R. & Oldfield, F. (1986), Environmental Magnetism, Allen and Unwin.

Tissot, B. (1984), Recent advances in petroleum geochemistry applied to hydrocarbon exploration, *AAPG Bulletin*, 68(5), 545–563.

Tissot, B., Califet-Debyser, Y., Deroo, G. & Oudin, J.L. (1971), Origin and evolution of hydrocarbons in Early Toarcian shales, Paris Basin, France, *AAPG Bulletin*, 55(12), 2177–2193.

Tissot, B., Durand, B., Espitalié, J. & Combaz, A. (1974), Influence of nature and diagenesis of organic matter in formation of petroleum, *AAPG Bulletin*, 58(3), 499–506.

Tissot, B., Pelet, R. & Ungerer, P. (1987), Thermal history of sedimentary basins, maturation indexes, and kinetics of oil and gas generation, *AAPG Bulletin*, 71, 1445–1466.

Tobin, R.C. & Claxton, B.L. (2000), Multidisciplinary thermal maturity studies using vitrinite reflectance and fluid inclusion microthermometry : a new calibration of old techniques, *AAPG Bulletin*, 84(10), 1647–1665.

Tyson, R. (1995), Sedimentary organic matter : organic facies and palynofacies, Chapman and Hall, London.

Van der Voo, R. (1983), Contributions to the tectonics and geophysics of Mountain Chains, *Geological Society of America Memoir*, volume 158, chapter A plate tectonics model for the Paleozoic assembly of Pange based on paleomagnetic data, 19–23.

Van der Zee, C., Roberts, D.R., Rancourt, D.G. & Slomp, C.P. (2003), Nanogoethite is the dominant reactive oxyhydroxide phase in lake and marine sediments, *Geology*, 31(11), 993–996.

Van Krevelen, D. (1961), Coal : typology, chemistry, physics, constitution, Elsevier, Amsterdam.

Van Velzen, A. & Zijderveld, J. (1992), A method to study alterations of magnetic minerals during thermal demagnetization applied to a fine-grained marine marl (Trubi formation, Sicily), *Geophysical Journal International*, 110(1), 79–90.

Vandenberghe, N. (1978), Sedimentology of the Boom Clay (Rupelian) in Belgium, Verhandeling Koninklijke Academie voor Wetenschappen, Letteren en Schone Kunsten van België, Klass Wetenschappen XL.

Vandenbroucke, M., Behar, F. & Rudkiewicz, J.L. (1999), Kinetic modelling of petroleum formation and cracking : implications from the high pressure/high temperature Elgin field (UK, North Sea), *Organic Geochemistry*, 30(9), 1105–1125.

Vassoyevitch, N., Yu, I., Korchagina, N. & Chernyshev, V. (1970), Principal phase of oil formation, *International Geology Review*, 12(11), 1276–1296.

Velde, B. & Vasseur, G. (1992), Estimation of the diagenetic smectite to illite transformation in time-temperature space, *American Mineralogist*, 77, 967–976.

Verwey, E. (1935), The crystal structure of $\gamma - Fe_2O_3$ and $\gamma - Al_2O_3$, *Z. Krist.*, 91, 65–69.

Wagner, G. & Van den Haute, P. (1992), Fission track dating, *Solid Earth Sciences library*, volume 6, Kluwer Academic Publishers.

Walz, F. (2002), The Verwey transition - a topical review, *Phys. Condens. Matter*, 14, R285–R340.

Wang, Q. & Morse, J.W. (1996), Pyrite formation under conditions approximating those in anoxic sediments : I. Pathway and morphology, *Marine Chemistry*, 52, 99–121.

Waples, D.W. (1980), Time and temperature in Petroleum Formation : applications of Lopatin's method to petroleum exploration, *AAPG Bulletin*, 64(6), 916–926.

Waples, D.W. & Marzi, R.W. (1998), The universality of the relationship between vitrinite reflectance and transformation ratio, *Organic Geochemistry*, 28(6), 383–388.

Waples, D.W., Masahiro, S. & Kamata, H. (1992), The art of maturity modeling. Part 2 : alternative models and sensitivity analysis, *AAPG Bulletin*, 76(1), 47–66.

Weil, A. & Van der Voo, R. (2002), Insights into the mechanism for orogen related carbonate remagnetization from growth of authigenic Fe-oxide : a scanning electron microscopy and rock magnetic study of Devonian carbonates from northern Spain, *Journal of Geophysical Research*, 107(B4), 2063, doi : 10.1029/2001JB000200.

Whitmeyer, S. & Karlstrom, K. (2007), Tectonic model for the Proterozoic growth of North America, *Geosphere*, 3, 220–259.

Wilkin, R. & Barnes, H. (1997), Formation processes of framboidal pyrite, *Geochimica et Cosmochimica Acta*, 61(2), 323–339.

Williams, H. & Hiscott, R. (1987), Definition of the Iapetus rift-to-drift transition in Newfoundland, *Geology*, 15, 1044–1047.

Wolfers, P., Fillion, G., Ouladdiaf, B., Ballou, R. & Rochette, P. (2011), The pyrrhotite 32 K magnetic transition, *Solid State Phenomena*, 170, 174–179.

Worden, R.H. & Morad, S. (2003), Clay Mineral Cement in sandstones, *International Association of Sedimentologists Special Publication*, volume 34, chapter Clay minerals in sandstones : controls on formation, distribution and evolution, 509, Blackwell Publishing.

Wouters, L. & Vandenberghe, N. (1994), Géologie de la Campine, Essai de synthèse, ONDRAF, Bruxelles.

Zapletal, K. (1993), Effect of intergrowths of the ferrimagnetic and antiferromagnetic phases on the rock magnetic properties of natural pyrrhotites, *Physics of the Earth and Planetary Interiors*, 76, 151–162.

Ziegler, P. (1992), North Sea rift system, *Tectonophysics*, 208, 55–75.

LIST OF FREQUENTLY USED SYMBOLS AND ABBREVIATIONS

X, Xlf	(low-field) magnetic susceptibility, *susceptibilité magnétique (à champ faible)*
Ms	Saturation Magnetization, *Aimantation à saturation*
Mrs	Saturation Remanent Magnetization, *Aimantation rémanente à saturation*
Hc	Coercive Field, *Champ Coercitif*
Hcr	Coercivity of remanence, *Coercivité de la rémanence*
NRM	Natural Remanent Magnetization, *Aimantation Rémanente Naturelle*
CRM	Chemical Remanent Magnetization, *Aimantation Rémanente Chimique*
TRM	Thermal Remanent Magnetization, *Aimantation Rémanente Thermique*
VRM	Viscous Remanent Magnetization, *Aimantation Rémanente Visqueuse*
TVRM	Thermo Viscous Remanent Magnetization, *Aimantation Rémanente Thermo Visqueuse*
(S)IRM	(Saturation) Isothermal Remanent Magnetization, *Aimantation Rémanente Isotherme (à Saturation)*
RT-SIRM	Room temperature –SIRM, *ARI à saturation à temperature ambiante*
LT-SIRM	Low temperature –SIRM, *ARI à saturation à basse temperature*
ZFC	Zero Field Cooling,*"Refroidissement en champ nul"*
T_N	Néel Temperature, *Température de Néel*
T_C	Curie Temperature, *Température de Curie*
T_{UB}	Unblocking Temperature, *Température de déblocage*
SP	SuperParamagnetic, *Superparamagnétique*
SD	Single Domain, *Monodomaine*
PSD	Pseudo-Single Domain, *Pseudo-monodomaine*
MD	MultiDomain, *Polydomaine*
FORC	First-Order Reversal Curve
TOC	Total Organic Carbon, *Carbone Organique Total*
Ro	Vitrinite reflectance, *Réflectance de la vitrinite*
Tmax	RockEval parameter, *paramètre du RockEval*
CAI	Conodont Alteration Index, *Indice d'Altération des Conodontes*

Appendix

1 Low temperature magnetic behaviour near 35 K in unmetamorphosed claystones

Geophys. J. Int. (2011) **186,** 1029–1035 doi: 10.1111/j.1365-246X.2011.05121.x

Low temperature magnetic behaviour near 35 K in unmetamorphosed claystones

Myriam Kars,[1,2] Charles Aubourg[1] and Jean-Pierre Pozzi[2]

[1]*Laboratoire des Fluides Complexes et leurs Réservoirs* (UMR 5150)*, Université de Pau et des Pays de l'Adour, Avenue de l'Université,* 64013 *Pau cedex, France. E-mail: kars@geologie.ens.fr*
[2]*Laboratoire de Géologie, CNRS* (UMR 8538)*, Ecole Normale Supérieure,* 24 *rue Lhomond,* 75231 *Paris cedex* 05*, France*

Accepted 2011 June 22. Received 2011 May 20; in original form 2010 July 27

SUMMARY

There is growing evidence that the magnetic assemblage of claystones, illustrated by low-temperature magnetic transitions at ∼120 K and ∼35 K, may be representative of the peak burial temperature in the so-called oil-window (60–150°C). In previous studies, it was proposed that this magnetic assemblage is characterized by fine-grained pyrrhotite (Fe_7S_8) and magnetite (Fe_3O_4). However, evidence of pyrrhotite was not so obvious and the magnetic transition near 35 K of fine-grained pyrrhotite has similarities with those of siderite ($FeCO_3$) or rhodochrosite ($MnCO_3$). Here, we propose some diagnostic tests to distinct <50 K behaviours by studying claystones from Netherlands borehole and Borneo Prism that experienced different peak burial temperatures. We perform magnetic susceptibility, temperature dependency of SIRM (ZFC, RT-SIRM) and field cooled hysteresis loops. On cooling of RT-SIRM (300 K to 10 K), we applied a magnetic field of 5 μT to enhance Néel type magnetic transition. It is found that our samples can be classified in two categories based on the shape of the RT-SIRM curve: one displaying an abrupt break-in-slope in the remanence at ∼30 K, called *N*-behaviour, and the other one characterized by a progressive increase of the remanent magnetization by 80 K, named *P*-behaviour. The first category contains essentially magnetite and Fe–Mn carbonates, the second one magnetite and probably iron sulphides.

Key words: Magnetic and electrical properties; Rock and mineral magnetism; Phase transitions.

1 INTRODUCTION

Claystones are potentially oil source rocks in sedimentary basins and thrust belts. Aubourg & Pozzi (2010) proposed recently that a given magnetic assemblage of claystones may be diagnostic of burial within the oil window from 60°C to 150°C (Sweeney & Burnham 1990). More precisely, they proposed that fine-grained pyrrhotite (Fe_7S_8) and magnetite (Fe_3O_4) formed from 2 km depth and more. Thus, the occurrence of these two magnetic minerals may inform on the maturity of claystones. To define the magnetic assemblage in rocks where organic matter coexists with iron sulphides, the best way is certainly low temperature investigation (<300 K; <27°C) because it prevents the chemical transformation, which arises from heating higher than room temperature usually used in palaeomagnetic studies (Van Velzen & Zijderveld 1992). Stoichiometric magnetite is firmly identified by a magnetic transition at 120 K, named Verwey transition (e.g. Ozdemir *et al*. 2002). This transition results from a solid-state phase change from cubic above 120 K to monoclinic below 120 K (e.g. Muxworthy & McClelland 2000; Walz 2002). Pyrrhotite is characterized by a magnetic transition at 35 K and its origin remains unknown (Dekkers *et al*. 1989; Rochette *et al*. 1990). When the saturation isothermal remanent magnetization (SIRM) is cooled down from 300 K to 10 K, the pyrrhotite transition for grains larger than 1 μm is marked by a loss of remanence. Its recovery on warming is an indication of domain state, and therefore grain size (Dekkers *et al*. 1989). Instead of a regular pyrrhotite transition, Aubourg & Pozzi (2010) reported a peculiar magnetic behaviour at ∼35 K during the cooling of RT-SIRM, named hereafter the *P*-behaviour. More precisely, they showed that the *P*-behaviour of Opalinus claystones from the Jura fold belt is a combination of an induced magnetization and a pyrrhotite transition. Both are detected at ∼35 K, which led Aubourg & Pozzi (2010) to propose that the *P*-behaviour is due to the input of fine-grained pyrrhotite. However, evidence of pyrrhotite in the samples is not so clear. Besides, rhodochrosite ($MnCO_3$, Néel temperature $T_N = 32$ K; Kosterov *et al*. 2006), siderite ($FeCO_3$, $T_N = 38$ K; Housen *et al*. 1996) and lepidocrocite (γ-FeOOH, $T_N = 52$ K; Hirt *et al*. 2002) are likewise candidates to explain the origin of this behaviour. Rhodochrosite and siderite (Frederichs *et al*. 2003) can occur in solid solution because Fe^{2+} and Mn^{2+} can easily substitute each other, leading to Néel temperatures ranging from 32 to 38 K. In this study, our aim was to add new low temperature data to characterize the nature of the *P*-behaviour. The different magnetic measurements, performed on four samples coming from two different sites, permitted to classify these specimens in two categories: one shows a characteristic Néel transition and the other one displays a *P*-behaviour.

2 SAMPLES AND METHODS

Work in progress of claystones from different boreholes and the Borneo accretion prism reveals a homogenous pattern of low-temperature rock magnetic properties. We have selected four representative claystones from a set of tens of samples. We studied two claystones from a borehole in the Netherlands (samples A and B) and two claystones from the Borneo Eocene prism (samples C and D). Sample A is a calcareous claystone. The samples A and B are located at 1538 m and 1793 m depth, respectively (depth interval 255 m). There is a Cretaceous–Carboniferous unconformity at 1597 m depth between sample A (Cretaceous) and sample B (Carboniferous). This involves different burial history for sample B. Maturity parameters from vitrinite reflectance are Ro = 1.4 per cent and Ro = 1.8 per cent for A and B, respectively (unpublished report). However, regarding the basin history, it is likely that the sample A vitrinite reflectance is <1 per cent. The samples C and D are taken in the Crocker formation from the Sarawak prism from two road-cut fresh outcrops (Sapin *et al*. 2011). The maturity parameters of sample C and D are Ro = 0.7 per cent and Ro = 1.2 per cent, respectively. Regarding vitrinite data, Borneo and Netherlands samples are early mature (A, C; burial temperature $T_{bu} < 120^{\circ}$C) to overmature (B, D; $T_{bu} > 150^{\circ}$C; Sweeney & Burnham 1990).

We measured the magnetic properties of the four claystones at the Institute for Rock Magnetism, University of Minnesota, Minneapolis, USA. We studied the temperature dependency in the range 300 K-10 K of SIRM. For this purpose, we used the following measurement cycle:

(1) a 2.5 T field was applied at 300 K to impart an Isothermal Remanent Magnetization (IRM) and then switched off. The samples were cooled down to 10 K within an upward magnetic field of 5 μT (∼1/10 of the Earth's magnetic field) at about 5 K steps. This part of the measurement cycle is called RT-SIRM (RT for Room Temperature). The application of a magnetic field of 5 μT inside the MPMS (controlled by a fluxgate) was proposed by Aubourg & Pozzi (2010) with the aim to exacerbate the amplitude of the *P*-behaviour below 100 K. Generally, the cooling of a RT-SIRM is performed under a trapped magnetic field lower than 0.1 μT. For convenience, we will talk about remanence monitoring, while in fact, this is a monitoring of a RT-SIRM and a small induced magnetization, which parallels the magnetic field of 5 μT. We have now the practice of tens of measurements in claystones using this procedure. Despite the paramagnetic input of clays, this procedure allows the detection of Néel transitions that are not visible using the zero-field cooling of a RT-SIRM.

(2) at 10 K, LT-SIRM was imparted with a 2.5 T magnetic field. Then, the magnetic field is switched off. The samples were warmed back to 300 K in zero field at 10 K steps. This is called Zero Field Cooled (ZFC).

We studied the temperature dependency of AC magnetic susceptibility from 300 K to 10 K. We obtained from this measurement the in-phase magnetic susceptibility (K') and the quadrature (out-of-phase) magnetic susceptibility (K''). Magnetic susceptibility was measured at different magnetic field strength (from 16 to 240 A m^{-1}) at 100 Hz. RT-SIRM, ZFC, K′ and K″ were measured using two Quantum Design Magnetic Properties Measurement System (MPMS). We studied the hysteresis loops using a Princeton Vibrating Sample Magnetometer (VSM). We ran hysteresis loops at room temperature and at low temperature (<100 K). The samples were cooled from 300 K to 10 K in a field of 1 T to impart a field-cooled remanence (FC). All magnetic measurements (MPMS and VSM) were done on samples powders of about 400 mg sealed in a gel capsule.

3 RESULTS

At room temperature, the low field magnetic susceptibilities (K_{lf}) for samples A, B, C and D are 120, 641, 349 and 309 μSI, respectively (Table 1). The ferromagnetic susceptibility ($K_{ferro} = K_{lf} - K_{hf}$), inferred from the high-field magnetic susceptibility (K_{hf}), represents 30–40 per cent of the low-field magnetic susceptibility (Table 1). SIRM are 56, 105, 140 and 42 μAm^2 kg^{-1} for samples A, B, C and D, respectively. SIRM and K_{ferro} values indicate a weak concentration of ferromagnetic minerals. ZFC and RT-SIRM demagnetization curves are shown in Fig. 1, together with the derivatives from 10 to 50 K shown in inset. ZFC demagnetization curves (Fig. 1a, c), when plotted in a log-scale, are characterized by a 2-step pattern, with: (1) a large drop of LT-SIRM between 10 and 35 K (a minimum of 80 and a maximum of 99 per cent of the remanence are lost), and (2) a change-in-slope at 120 K which is characteristic of stoichiometric magnetite.

RT-SIRM demagnetization curves (Fig. 1b, d) show that all claystones display the Verwey transition at 120 K, in agreement with the ZFC demagnetization curves. Below 120 K, the behaviour of the magnetization is different. For claystone C, the magnetization increases regularly from ∼100 K to 10 K (see inset Fig. 1d). The claystone A presents also an increase in the same range of temperature, but a break-in-slope is apparent at ∼30 K (see inset Fig. 1b). The claystones B and D display an abrupt magnetic transition at ∼40 K and ∼30 K, respectively (see inset Fig. 1b, d). The magnetization parallels the 5 μT magnetic field applied upward. Samples A and C present a regular increase of RT-SIRM from 70–80 K to 10 K. Sample C is also characterized by a progressive rise of the magnetization from 300 K to the Verwey transition temperature. Sample B reveals a slightly concave curve around 40–50 K and then a sharp increase from 38 K, before being convex from 25 to 10 K. Sample D magnetization is quasi-constant from room temperature to 120 K, where a drop is observed, and again remains constant to 30 K. At this temperature, a sharp upward break-in-slope is observed with a slight decrease at very low temperature.

We show FC hysteresis loops after slope correction obtained between 10 and 50 K (Fig. 2). Claystones A and C display hysteresis

Table 1. Some rock magnetic properties at room temperature for the four claystones. X_{lf}: low field magnetic susceptibility. X_{hf}: high-field magnetic susceptibility. X_{ferro}: ferromagnetic susceptibility ($X_{ferro} = X_{lf} - X_{hf}$). M_s and M_{rs}: magnetization at saturation and remanence at saturation. H_c and H_{cr} coercive magnetic field and back remanence coercive field. All parameters, but X_{lf}, are measured with a vibrating sample magnetometer.

Sample	X_{lf} (μSI)	X_{hf} (μSI)	X_{ferro} (μSI)	M_s (μAm^2 kg^{-1})	M_{rs} (μAm^2 kg^{-1})	H_c (mT)	H_{cr} (mT)
A	120	71	49	485	68	10	39
B	641	430	211	2460	135	17	39
C	349	214	135	1267	124	13	34
D	309	216	93	574		8	36

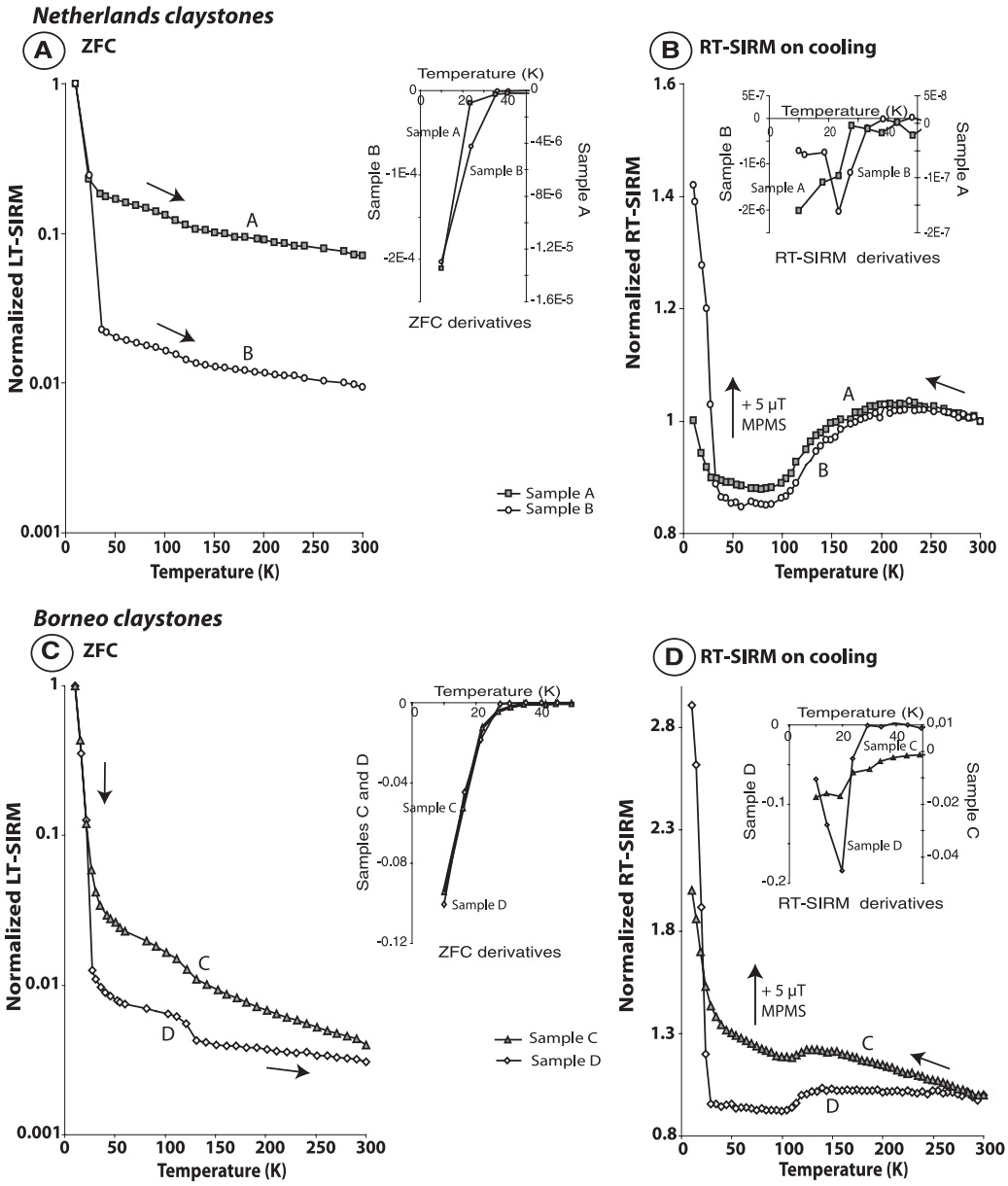

Figure 1. MPMS measurements in the 10–300 K temperature range. For the Netherlands samples: (a) Zero Field Cooled (ZFC) curve from 10 K to 300 K and (b) RT-SIRM on cooling from 300 K to 10 K and for Borneo samples: (c) Zero Field Cooled curve from 10 K to 300 K and (d) RT-SIRM on cooling from 300 K to 10 K.

loops with weak coercivity (Fig. 2a, c) less than 15 mT at 10 K. The behaviour of claystones B and D is markedly different (Fig. 2b, d), coercivity at 10 K for samples B and D are higher (>60 mT). These latter show open hysteresis loops but magnetic saturation is attained. Hysteresis loops are slightly wasp waisted which is an indication of a mixture of coercivity (Tauxe *et al*. 1996). But the most important feature of these specimens is the shift of hysteresis loop centre along the $+Y$ axis from 10 to 40 K. This shift is parallel to the applied field during the cooling of the sample.

We report in Fig. 3(a) the magnetization at saturation (M_s) inferred from hysteresis loops. M_s evolves differently for the two sets of claystones. M_s increases of more than 90 per cent for claystones A and C from 40 to 10 K. By contrast, the increase of M_s is less marked for claystones B and D. About 78 per cent of increase is observed. The same trends are observed for high field susceptibilities

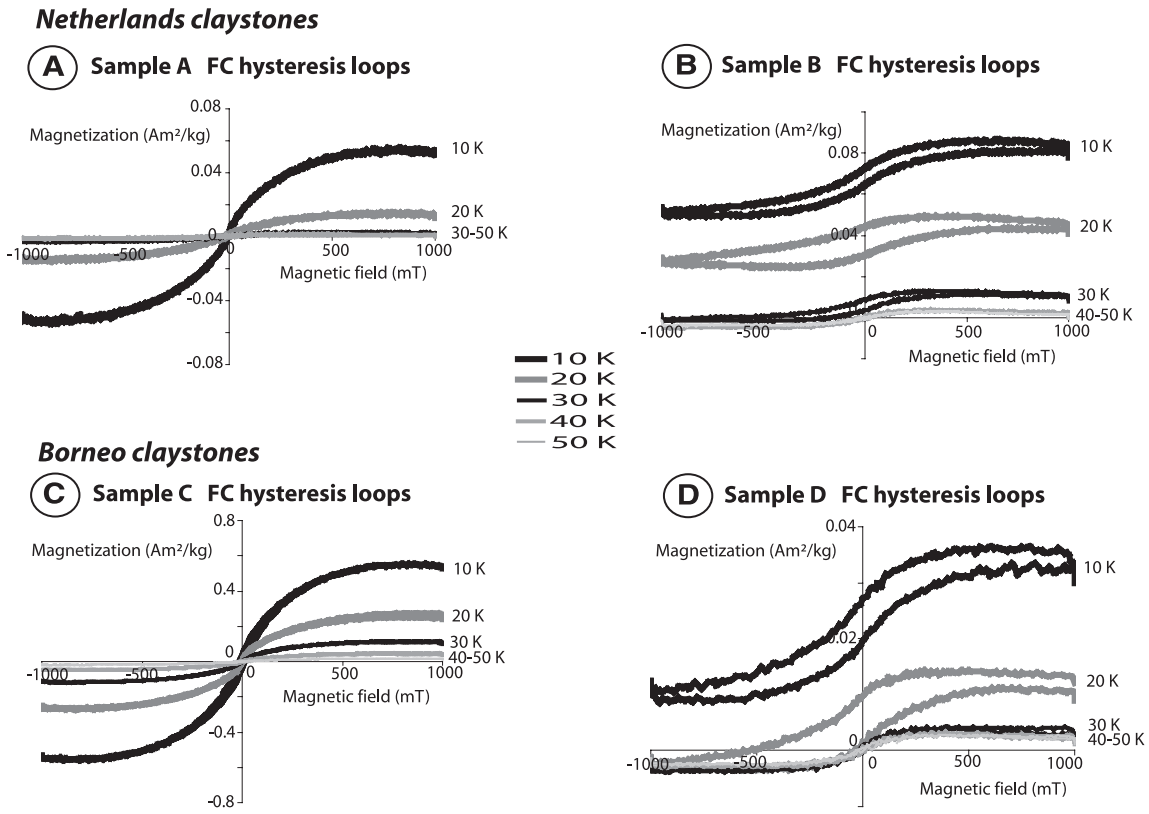

Figure 2. Field Cooled hysteresis loops from 50 K to 10 K for (a) sample A, (b) sample B from the Netherlands, and (c) sample C and (d) sample D from Borneo.

(X_{hf}; Fig. 3b). The X_{hf} of samples A and C increase of almost 70 per cent from 50 to 10 K, whereas the X_{hf} increase of sample D is smoother (45 per cent). The X_{hf} of sample B is quasi-stable.

We show in-phase (K') and out-out-phase (K'') AC susceptibility measurements in the 5–50 K temperature range (Fig. 3c, d). For the four claystones, we do not observe any field-dependency of K' and K''. In-phase K' shows different behaviour for the Netherlands claystones A and B (Fig. 3d). While K' regularly decreases from 10 to 50 K for sample A, a bump of K' is observed at ∼35 K for sample B. Out-of-phase K'' decreases in the same proportion from 10 to 50 K for both claystones A and B. It should be noted for sample A that (1) K'' is larger by one order of magnitude at 10 K compared to sample B, (2) there is a break-in-slope of K'' at ∼20 K. For Borneo claystones C and D, K' is decreasing from 10 to 50 K and it shows two break-in-slopes at ∼10 K and ∼20 K (Fig. 3d). The quadrature K'' of sample C displays a bump at ∼16 K. The magnitude of K'' is two times larger than that of sample D at 10 K.

4 DISCUSSION

Claystones A and C from the Netherlands borehole and the Borneo accretionary prism, respectively showed similar patterns as reported by Aubourg & Pozzi (2010). That consists in the recognition of *P*-behaviour, as well as the two-step pattern of ZFC curve, marked by a magnetic transition at ∼35 K and ∼120 K (Fig. 1). Both claystones experienced burial temperature T_{bu} less than 120°C, with respect to their vitrinite reflectance. However, the two other claystones, B and D, that both underwent $T_{bu} > 150$°C, do not show the *P*-behaviour. Instead, we observed Néel transition with a Néel temperature between 30 and 40 K. In the following, we attempt to distinguish the two types of samples.

4.1 Magnetite concentration

The concentration of magnetic grains can be approximated by using the SIRM value at room temperature. More precisely, the SIRM provides the concentration of ferromagnetic minerals capable to retain a remanence, that is, all grains above the blocking volume. The four samples present the Verwey transition at 120 K (Fig. 1), which is characteristic of the stoichiometric low coercive magnetite (Özdemir *et al*. 2002). The magnetic transition <50 K is carried by minerals that are paramagnetic or superparamagnetic at room temperature (e.g. Fe–Mn carbonates, iron sulphides). We assume therefore that magnetite constitutes the main magnetic mineral that carries the SIRM. To estimate the maximum magnetite concentration of the samples, we compare the SIRM to the half value of SIRM value of magnetite because magnetite minerals are not perfectly oriented (Aubourg *et al*. 2008). Using half value of magnetite SIRM at ∼10 $Am^2\ kg^{-1}$ (Maher *et al*. 1999) and the value of SIRM at room temperature (∼100 $\mu Am^2\ kg^{-1}$ to simplify), it

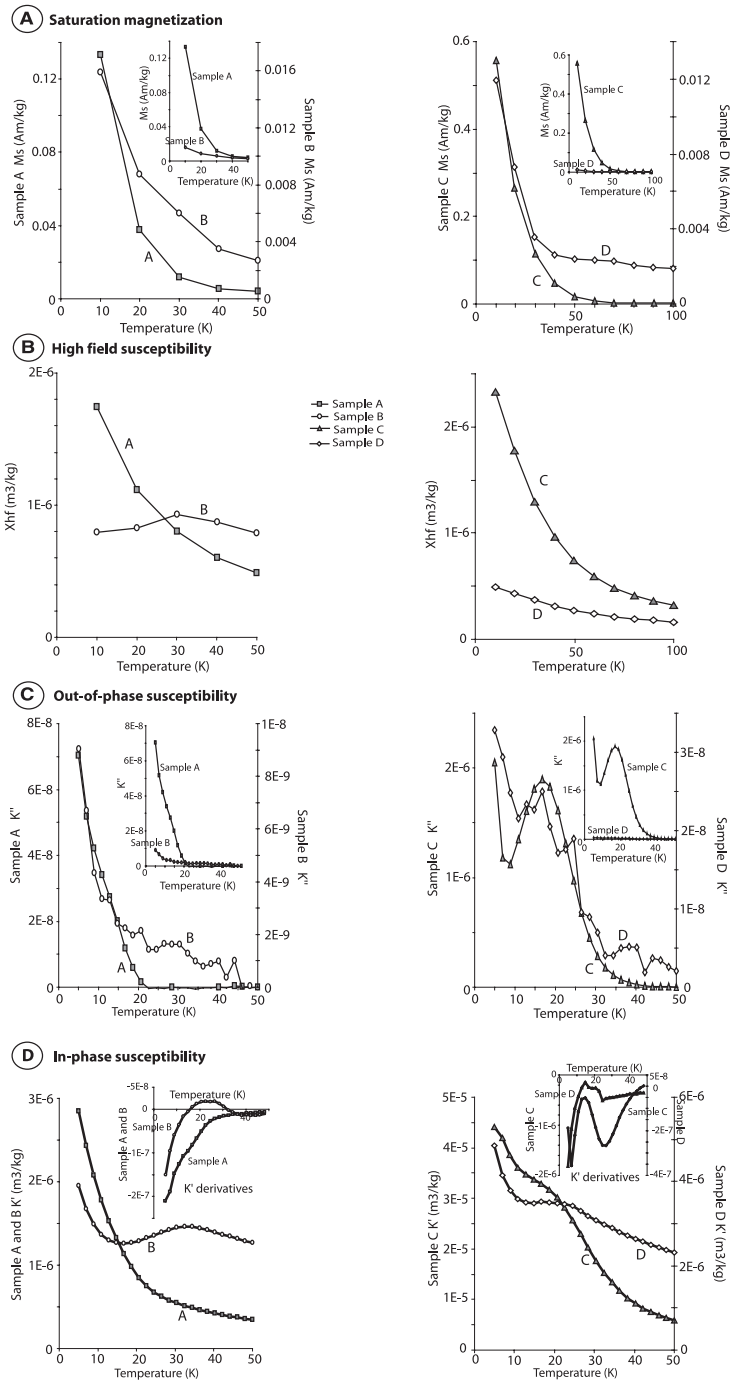

Figure 3. Evolution of (a) saturation magnetization, (b) high field susceptibility, 394 (c) Out-of-phase susceptibility and (d) in-phase susceptibility from 10 K to 50 K for the four claystones.

is found that the magnetite concentration is less than 10 ppm. The claystones contain therefore trace amount of magnetite above the blocking volume, that is, >20 nm. This low concentration of ferromagnetic mineral can be due to magnetite dissolution processes during burial (Rowan *et al*. 2009).

4.2 <50 K behaviours

In this study, we emphasized the <50 K magnetization evolution. In our protocol of RT-SIRM on cooling, the upward applied magnetic field of 5 μT inside the MPMS was found to be very useful to highlight the <50 K magnetic behaviour (Fig. 1b, d). In the following, we distinguished two classes: the *P*-class (samples A and C) and the *N*-class (samples B and D). Samples from the *P*-class display the *P*-behaviour, with progressive increase of an induced magnetization during the cooling of the RT-SIRM from ∼100 K (Fig. 1b, d). The slope of the derivative is regularly increasing down to 10 K. Samples from the *N*-class display abrupt Néel transition at 30 K and 38 K (Fig. 1b, d). The slope of the derivative is decreasing for temperature lower than 30 K.

For *P*-class and *N*-class samples, ZFC curves display the same 2-step pattern (Fig. 1a, c) and thus are not useful to distinguish between the two types of classes. Housen *et al*. (1996) noted already that ZFC curves of pyrrhotite, siderite and rhodochrosite displayed similar behaviours. Those are not so different from greigite SIRM warming curves (Chang *et al*. 2009). The best magnetic parameters to distinguish between *P*-class and *N*-class are the low-temperature hysteresis loops and the low temperature properties of magnetic susceptibility.

N-class samples display open FC hysteresis loops for T < 30 K (Fig. 2b, d). By contrast, the hysteresis loops of *P*-class samples remain narrow at low temperature (Fig. 2a, c). The most remarkable feature of *N*-class samples, however, is the observation of an offset of the hysteresis loops at 10 K and 20 K, characterized by a positive shift of the hysteresis loop along the axis of remanence (parallel to the field applied during cooling). By contrast, samples from the *P*-class do not show offset of hysteresis loops (Fig. 2a, c). The hysteresis loop offset was first reported by Housen *et al*. (1996) for siderite mineral. Kosterov *et al*. (2006) showed also offset of hysteresis loops for rhodochrosite.

Hysteresis parameters M_s (magnetization at saturation) and X_{hf} (high-field magnetic susceptibilities) show distinguishable differences (Fig. 3a, b). For the *P*-class samples, we observed an increase of more than 90 per cent of these parameters below 50 K. By contrast, the increase of M_s and X_{hf} is less marked for the *N*-class samples.

The low-temperature dependency of the in-phase (K') and out-of-phase (K'') AC magnetic susceptibilities provided additional information. Samples from the *N*-class displayed bumps of K' at ∼34 K for sample B and ∼22 K for sample D (Fig. 3d). Similar observations on siderite and rhodochrosite minerals are reported by Frederichs *et al*. (2003). Samples from the *P*-class displayed either no distinguishable bump during the decrease of K' (sample A) or break-in-slope for sample C (Fig. 3d). Out-of-phase K'' of *P*-class samples is one to two orders of magnitude larger than K'' of *N*-class samples. One way to explain the increase of K'' is the apparition of Foucault current in the mineral.

4.3 The nature of *P*-behaviour

Aubourg & Pozzi (2010) proposed that the *P*-behaviour observed during cooling of a RT-SIRM is carried by fine-grained pyrrhotite. However occurrence of this mineral needs further analysis and the *P*-behaviour can be a form of Néel transition of siderite ($T_N = 38$ K) and/or rhodochrosite ($T_N = 32$ K). Unlike *P*-class samples which exhibit *P*-behaviour, the *N*-class samples displayed unambiguous Néel temperature of ∼38 K for sample B and ∼30 K for sample D. These temperatures correspond respectively to siderite and rhodochrosite Néel transitions. Recognition of hysteresis loops offset (Fig. 2b, d) is an additional evidence of the occurrence of siderite and rhodochrosite (Housen *et al*. 1996; Kosterov *et al*. 2006).

It is possible that the *P*-behaviour is a combination of rhodochrosite/siderite transition and an input of an additional magnetic mineral. Sample A is possibly the illustration of this combination. From the derivative of the RT-SIRM on cooling, we observed a break-in-slope at ∼30 K (Fig. 1b). Thus the *P*-behaviour in this case is possibly triggered by the input of rhodochrosite. However, hysteresis loops do not show any offset nor opening at low-temperature (Fig. 2a, c). The sample C does not show evidence of Néel temperature between 30 and 38 K (Fig. 1d). We do not think that sample C *P*-behaviour is due to rhodochrosite/siderite for additional reasons. The *P*-behaviour is not abrupt, as it should be for a Néel transition (e.g. sample D in Fig. 1d). We do not observe shift of hysteresis loops at low temperature (Fig. 2c). There is a large increase by one to two orders of magnitude of the remanence at saturation, the high-field magnetic susceptibility and the out-of-phase magnetic susceptibility for the *P*-class samples.

4.4 <50 K behaviours and maturity of rocks

Aubourg & Pozzi (2010) proposed that *P*-behaviour develops at ∼60°C from the basis of experimental studies and natural observation. Ongoing studies by our group demonstrate the large occurrence of *P*-behaviour in immature to early mature claystones ($T_{bu} < 120$°C). The early mature claystone C from Borneo is an additional evidence for the development of the *P*-behaviour. However, for overmature claystones B and D ($T_{bu} > 150$°C; Ro > 1.2 per cent), we observed the development of a Néel transition of siderite and rhodochrosite. For calcareous claystone A, the *P*-behaviour is probably carried by rhodochrosite. Rhodochrosite and siderite occur in rapidly accumulating, fine-grained, organic rich sediment (Glasby & Schulz 1999). Rhodochrosite is observed at very low-grade metamorphic condition and is stable at higher grade (Peters *et al*. 1973). Further work is necessary to see if the Néel transitions of overmature claystones ($T_{bu} > 150$°C) is a marker of low-grade metamorphism or if it is related to the sedimentary conditions.

5 CONCLUSION

We performed magnetic measurements to characterize the magnetic assemblage of four early mature to overmature claystones from a borehole in the Netherlands and from Borneo prism. We focused on the <50 K magnetic behaviour. To evidence Néel transition, we applied a magnetic field of 5 μT inside the SQUID MPMS during the cooling of a SIRM. We proposed two classes of samples: the *P*-class and the *N*-class. Both classes contain magnetite in trace amount (<10 ppm). In the *P*-class, during the cooling of a SIRM, we observed an increase of induced magnetization at ∼100 K, named *P*-behaviour. The *P*-behaviour may be a fingerprint of early mature claystones ($T_{bu} < 120$°C) and might be carried by iron sulphides and possibly by the contribution of Néel-type mineral like siderite or rhodochrosite. In addition, the *P*-class samples showed enhancement below 50 K by one to two orders of magnitude of the

Appendix

magnetization at saturation, the high-field magnetic susceptibility and the out-of-phase magnetic susceptibility. The *N*-class samples, where claystones are overmature ($T_{bu} > 150°C$), showed Néel transitions at 30 K and 38 K that suggest the occurrence of rhodochrosite and siderite. The offset of field-cooled hysteresis loops and the increase of the coercivity for T < 30 K comforted the hypothesis of the occurrence of rhodochrosite and siderite. Further work is necessary to confirm our hypothesis that the *P*-class and *N*-class claystones are correlated to the index maturity of claystones; immature to mature for the *P*-class (T_{bu}∼60–<120°C), and overmature ($T_{bu} > 150°C$) for the *N*-class. If correct, the low-temperature magnetic investigation will constitute a valuable tool to precise very low-grade metamorphism of claystones.

ACKNOWLEDGMENTS

This work was conducted as a part of M. Kars PhD. Thesis supported by Total S.A./Université de Pau et des Pays de l'Adour, France.
We are grateful to IRM for providing us instrumental facilities and for invaluable discussions. F. Sapin and M. Pubellier provided us claystones from Borneo. We benefited from a grant from the University of Minnesota for our 10-day visit at the IRM in 2009.
We would like to thank reviewers Andrei Kosterov and Pierre Rochette, and editor Cor Langereis for their accurate comments.

REFERENCES

Aubourg, C. & Pozzi, J-P., 2010. Toward a new <250°C pyrrhotite-magnetite geothermometer for claystones, *Earth planet. Sci. Lett.*, **294**(1–2), 47–57.

Aubourg, C., Pozzi, J-P. Janots, D., & Sahraoui, L., 2008. Imprinting chemical remanent magnetization in claystones at 95°C, *Earth planet. Sci. Lett.*, **272**, 172–180.

Chang, L., Roberts, A.P., Rowan, C. J., Tang, Y. Pruner, P. Chen, Q., & Horng, C-S., 2009. Low-temperature magnetic properties of greigite (Fe_3S_4), *Geochem. Geophys. Geosyst.*, **10**(1), Q01Y04, doi:10.1029/2008GC002276.

Dekkers, M.J., Mattei, J-L. Fillion, G., & Rochette, P., 1989. Grain size dependence of magnetic behavior of pyrrhotite during its low-temperature transition at 34 K, *Geophys. Res. Lett.*, **16**, 855–858.

Frederichs, T., von Dobeneck, T. Bleil, U. & Dekkers, M.J., 2003. Towards the identification of siderite, rhodochrosite and vivianite in sediments by their low-temperature magnetic properties, *Phys. Chem. Earth*, **28**, 669–679.

Glasby, G.P. & Schulz, H.D., 1999. E_H, pH diagrams for Mn, Fe, Co, Ni, Cu and As under seawater conditions: application of two new types of E_H, pH diagrams to the study of specific problems in marine geochemistry, *Aqua. Geochem.*, **5**, 227–248.

Hirt, A.M., Lanci, L., Dobson, J. Weidler, P. & Gehring, A.U., 2002. Low-temperature magnetic properties of lepidocrocite, *J. geophys. Res.*, **107**(B1), 2011, doi:10.1029/2001JB000242.

Housen, B.A., Banerjee, S.K. & Moskowitz, B.M., 1996. Low-temperature magnetic properties of siderite and magnetite in marine sediments, *Geophys. Res. Lett.*, **23**(20), 2843–2846.

Kosterov, A., Frederichs, T. & von Dobeneck, T., 2006. Low-temperature magnetic properties of rhodochrosite (MnCO3), *Phys. Earth planet. Inter.*, **154**, 234–242.

Maher, B.A., Thompson, R. & Hounslow, M.W., 1999. Introduction to quaternary climates, environments and magnetism, in *Quaternary Climates, Environments and Magnetism*, pp. 1–48, eds Maher, B.A. & Thompson, R., Cambridge University Press, Cambridge.

Muxworthy, A.R. & McClelland, E. 2000. Review of the low-temperature magnetic properties of magnetite from a rock magnetic perspective, *Geophys. J. Int.*, **140**, 101–114.

Ozdemir, O., Dunlop, D.J. & Moskowitz, B.M., 2002. Changes in remanence, coercivity and domain state at low temperature in magnetite, *Earth planet. Sci. Lett.*, **194**(3–4), 343–358.

Peters, T., Schwander, H. & Trommsdorff, V., 1973. Assemblages among tephroite, pyroxmangite, rhodochrosite, quartz: experimental data and occurrences in the Rhetic Alps, *Contrib. Mineral. Pet.*, **42**, 325–332.

Rochette, P., Fillion, G. Mattei, J-L. & Dekkers,M.J., 1990. Magnetic transition at 30–40 Kelvin in pyrrhotite insight into a widespread occurrence of this mineral in rocks, *Earth planet. Sci. Lett.*, **98**, 319–328.

Rowan, C.J., Roberts, A.P. & Broadbent, T., 2009. Reductive diagenesis, magnetite dissolution, greigite growth and paleomagnetic smoothing in marine sediments: a new view, *Earth planet. Sci. Lett.*, **277**, 223–235.

Sapin, F., Pubellier, M., Lahfid, A., Janots, D. Aubourg, C. & Ringenbach, J.C., 2011. Onshore record of the subduction of a crustal salient : example of the NW Borneo Wedge, *Terra Nova*, **23,** 232–240.

Sweeney, J.J & Burnham, A.K., 1990. Evaluation of a simple model of vitrinite reflectance based on chemical kinetics, *AAPG Bull.*, **74**(10), 1559–1570.

Tauxe, L., Mullender, T.A.T. & Pick, T. 1996. Potbellies, wasp-waists and superparamagnetism in magnetic hysteresis, *J. geophys. Res.*, **101**(B1), 571–583.

Van Velzen, A.J. & Zijderveld, J.D.A., 1992. A method to study alterations of magnetic minerals during thermal demagnetization applied to a fine-grained marine marl (Trubi formation, Sicily), *Geophys. J. Int.*, **110**(1), 79–90.

Walz, F., 2002. The Verwey transition – a topical review, *J. Phys. Condens. Matter*, **14**, R285–R340.

2 The continuous production of nano magnetite through low grade burial, <4 km

This paper is in revision at G3.

THE CONTINUOUS PRODUCTION OF NANO MAGNETITE THROUGH LOW GRADE BURIAL, < 4 KM

Myriam Kars[1,2], Charles Aubourg[2], Jean-Pierre Pozzi[1], Dominik Janots[1]

1. Ecole Normale Supérieure, Laboratoire de Géologie, UMR8538 CNRS, 24 Rue Lhomond, 75231 Paris cedex 05, France
2. Université de Pau et des Pays de l'Adour, Laboratoire des Fluides Complexes et leurs Réservoirs, UMR5150 CNRS TOTAL, Avenue de l'Université, 64013 Pau cedex, France

Abstract

Geological processes, such as burial, can lead to remagnetization in rocks due to neoformed magnetic minerals that have passed a critical volume. In this study, we designed heating experiments for claystones obtained from the Paris Basin, in the 50-130°C temperature range, in order to simulate < 4 km burial remagnetization. Heating experiments were performed under a magnetic field of 2 mT, and the remanence acquired in the claystones was monitored repeatedly. Remanence was determined to be carried equally by stable chemical remanent magnetization and thermo-viscous remanent magnetization, which were carried, respectively, by neoformed magnetic grains above and below the critical volume. At a given temperature, remanence increased rapidly within a couple of days and stabilized afterward -the higher the experimental temperature, the higher the determined remanence. By assuming that magnetite formed during the experiment, we interpreted the increase of chemical remanent magnetization and the increase of thermo-viscous remanent magnetization as the continuous growth of the > 20 nm and < 20 nm minerals. Chemical remanent magnetization that formed during our heating experiments may represent 10%, at most, of the natural remanent magnetization when transposed to natural conditions. However, for temperatures < 250°C, natural examples suggest that burial remagnetization can totally overlap the remanent magnetization acquired soon after sediment deposition.

1. Introduction

Diagenetic and authigenic processes may lead to the formation of magnetic grains (e.g., *Karlin et al.*, 1987). As a result, new magnetization in rocks, called CRM (Chemical Remanent Magnetization), has been observed in different geological settings. CRMs are widely recognized in unmetamorphosed sedimentary rocks in basins and thrust-and-fold belts (e.g., *McElhinny & Opdyke*, 1973; *McCabe & Elmore*, 1989; *Weil & Van der Voo*, 2002). However, the origin of these CRMs is still debated. Classically evoked mechanisms are early diagenesis (*Rowan & Roberts*, 2005; *Roberts & Weaver*, 2005), geochemical degradation along methane horizons (*Larrasoaña et al.*, 2007), smectite-to-illite transformation (*Lu et al*., 1990; *Lu et al*., 1991; *Katz et al*., 2000), pyrite alteration (*Brothers et al*.,1996; *Gillett*, 2003), fluid circulation (*Oliver*, 1986; *Katz et al*., 1998; *Evans et al*., 2000; *Elmore et al*., 2001), deformation (*Lewchuk et al.,* 2003), and the maturation of organic matter (*Banerjee et al*., 1997).

Laboratory experiments from 25 to 250°C on claystones (*Cairanne et al.,* 2004; *Moreau et al.*, 2005, *Aubourg et al.*, 2008; *Aubourg & Pozzi*, 2010) have demonstrated that temperature alone leads to the rapid formation of minute amounts of magnetite. When transposing the results of these experiments to natural settings, it is likely that burial promotes the formation of magnetic minerals as a result of temperature elevation. Therefore, temperature elevation may be a simple explanation for the creation of CRMs. For this study, we repeated the experimental procedure proposed by *Aubourg et al.* (2008), from 50 to 130°C, in order to simulate the effect of stepwise burial on remanent magnetization in claystones from the Bure locality, in France.

2. Samples and methods

2.1. Samples description

The samples utilized for this work were claystones, widely studied as a result of their possible use for radioactive waste storage. The claystones came from the oblique core EST-211 (841–846 m

MD, drilled by the Agence Nationale pour la gestion des Déchets Radioactifs (the French National Radioactive Waste Management Agency), in the Jurassic (Callovo-Oxfordian) Formation of the Paris Basin near the Bure locality, in France.

The clay content of the core varies between 35 and 60% for Bure claystones (*Gaucher et al*., 2004). Remaining core components are calcite and silt. The claystones contains less than 2% pyrite, and 0 to 0.5% TOC (Total Organic Carbon). The organic matter is associated with framboidal pyrite and bioclasts.

Bure claystones undergo low burial temperatures < 50°C (*Landais & Elie*, 1999). The magnetic properties of these claystones have also been studied. Low field magnetic susceptibility (χ) varies between 10 to 154 (SI, and natural remanent magnetization (NRM) varies between 61 and 1416 (A/m (*Esteban et al*., 2006). Iron oxides (titano-maghemite or -magnetite) and iron sulfide (greigite, pyrite) occurrences have been confirmed (*Esteban et al*., 2006; *Aubourg & Pozzi*, 2010).

2.2. Methods

Prior to the heating experiment, we measured the χ and NRM of the claystones. Fragments of Bure claystones (1-2 g) were glued into small glass flasks (one fragment per flask). The bottles were then filled with glass wool and plugged in order to create a quasi-confined atmosphere. A total of 14 bottles were prepared, and separated into two sets (A and B). We focused on the remnant magnetization created by newly formed grains. To highlight this phenomenon, the NRM of the samples was initially demagnetized using an 80 mT alternating field. We performed heating experiments with progressively increasing temperatures of T_{exp} (50, 70, 80, 120, and 130°C in order to reproduce stepwise burial. The bottles were placed in an oven at a given temperature for approximately 25 days (20 days for 50°C, and 10 days for 120 and 130°C). During heating, the Earth's magnetic field was removed and an upward magnetic field of 2 mT was applied. The resulting remanence, R, was measured repeatedly at room temperature and is expressed, as follows: $R = NRM_{AF80} + IRM_{2mT} + CRM_{2mT} + TRM_{2mT}$ where NRM_{AF80} is the NRM after 80 mT of AF demagnetization, IRM_{2mT} is the isothermal remanent magnetization imparted at 2 mT, CRM_{2mT} is the chemical remanent magnetization acquired by neoformed magnetic minerals above their blocking volume at 2 mT, and TRM_{2mT} is a thermoviscous

remanent magnetization carried by former and neoformed magnetic minerals at 2 mT. NRM_{AF80} and IRM_{2mT} are one to two orders in magnitude less than CRM_{2mT} and TRM_{2mT}, and are, therefore, neglected (*Aubourg et al.*, 2008). The TRM is by essence time-dependent and unstable. Given the duration of the laboratory experiment (tens of days), it is likely that TRM is essentially carried by ultra-fined neoformed grains. Finally, the measured remanence can be expressed as: $R = CRM_{2mT} + TRM_{2mT}$. At the end of the heating step, we left the samples at temperature in a null magnetic field for a few days in order to remove TRM_{2mT}. The procedure constitutes what we refer to as the TRM test (*Aubourg et al.*, 2008). Therefore, the measured magnetization is a CRM_{2mT} for a given T_{exp} temperature. The samples were then again placed in the oven at a higher temperature, and so on. For each temperature step, a few samples (one from set A and one from set B) were removed from the experiment after the TRM test and left in a null field. At the end of the experiment, we obtained several CRM_{2mT} values corresponding to the various steps. The TRM tests were only performed for T_{exp}: 50, 70, 80, and 130°C.

The laboratory series of heating steps were distinct from natural conditions. Indeed, burial conditions were not satisfied. In our experiments, the heating rate (1°C/min) is very different from the natural heating rate which is on the order of 10°C/My (*Sweeney & Burnham*, 1990). Pressure was not considered and the experiments were performed at atmospheric pressure (0.1 MPa).

The sample remanence was measured with a 2G cryogenic SQUID magnetometer at Ecole Normale Supérieure, Paris, France. In order to identify the mineral responsible for the CRM_{2mT}, the set B samples were thermally demagnetized from T_{dem} = 100°C to 600°C using 20 or 50°C steps, depending on the investigated temperatures (the temperature steps were closer between 300 and 350°C). Set A samples were crushed and sealed in a gelcap and were measured with a Magnetic Properties Measurement System (MPMS) at the Institut de Physique du Globe de Paris, France. An initial low-temperature saturation isothermal remanent magnetization (LT-SIRM) was acquired at 10K using a magnetic field of 2.5 T. We then monitored the LT-SIRM demagnetization curve from 10 to 300 K.

3. Results

Bure claystones have low magnetic susceptibility (≤ 200 μSI) and their NRM are weak (~10^{-6} Am^{-1}kg^{-1}). However, one Bure sample presented higher NRM (~10^{-4} Am^{-1}kg^{-1}), likely due to surface alteration (Table 1). The NRM after demagnetization at 80 mT was very weak and was on the order of 10^{-7} Am^{-1}kg. However, one sample presented a higher value, by one order of magnitude (at approximately 10^{-6} Am^{-1}kg^{-1}).

Figure 1 represents the evolution of the mean remanence R for the different T_{exp} temperatures, for reproducing stepwise burial. At T_{exp} = 50°C, we observed (in the first days) that remanence increased rapidly by two orders of magnitude. The remanence then progressively reached a quasi-plateau with a mean moment of 12 ± 2 μAm^{-1}kg. No significant changes occurred in the plateau. The last remanence (t = 20 days) at T_{exp} = 50°C was less than expected. We do not have any explanation for this particular finding. When the temperature was increased to T_{exp} = 70°C, remanence again, very rapidly, reached a quasi-plateau at a higher mean value (16 ± 3 μAm^{-1}kg) than that of the previous heating step. The general pattern was the same for the other heating steps. The mean moments were 17 ± 1, 21 ± 6, and 31 ± 4 μAm^{-1}kg for T_{exp} = 80, 120, and 130°C, respectively. The difference between the remanence acquired between the 70 and 80°C steps (a 10°C difference) was not very distinct (16 versus 18 μAm^{-1}kg for 70 and 80°C, respectively).

The CRM_{2mT} displayed a consistent increase, from 5 ± 1 to 1 ± 6 μAm^{-1}kg, with an increasing T_{exp} temperature (Figure 2, Table 1). The T-RM_{2mT} was on the same order of magnitude as the CRM_{2mT}, and increased from 5 ± 1 to 14 ± 4 μAm^{-1}kg (Figure 2, Table 1). The T-RM_{2mT} was slightly higher than the CRM_{2mT} for T_{exp} from 50 to 70°C, and was lower at T_{exp} = 130°C. At the latter temperature, the CRM_{2mT} portion, was predominant in the total remanence of the samples.

Samples from set B were then heated from T_{dem} = 100 to 650°C in order to characterize the CRM_{2mT} (Figure 3a). Remanent magnetization values from T_{dem} = 400°C are not represented on the figure, as a result of remagnetization due to heating. Since several samples heated at T_{exp}=130°C were available, one representative example is shown in Figure 3A. Evolution of the thermal demagnetization of

CRM_{2mT} was observed. We focused on the following two proxies: the percentage of CRM_{2mT} loss at the thermal demagnetization temperature of T_{dem}: 150°C (higher than the maximum heating step temperature (T_{exp}) utilized and the maximum unblocking temperature (T_{UB}). At T_{dem} = 150°C: 80, 60, 23, and 1% of the CRM_{2mT} was lost for samples heated at a T_{exp} = 50, 70, 80, and 130°C, respectively (Figure 3a). T_{UB} evolved toward higher values, as follows: 280, 380, 400, and > 400°C for a T_{exp} = 50, 70, 80, and 130°C, respectively. At T_{exp} = 130°C, an interpolation of the demagnetization curve provided a T_{UB} near 500°C.

We measured the Low Temperature SIRM for set A samples (Figure 3b) from 10 to 300 K. We observed a decrease of LT-SIRM from 10 to 300 K, with a more abrupt decrease from 10 to 50 K. LT-SIRM curves were shifted downward with an increasing heating step temperature. Here, again, we could use a proxy to characterize the evolution of LT-SIRM, if PM was expressed as PM = (LT-$SIRM_{10K}$ - LT-$SIRM_{35K}$)/LT-$SIRM_{10K}$ (*Aubourg & Pozzi*, 2010). Values increased from 0.55 to 0.66 for T_{exp} = 50 to 130°C in heated samples, respectively, and was 0.34 for natural samples (Figure 3b).

4. Discussion

4.1. The nature of neoformed magnetic minerals

Our study demonstrates the formation of magnetic minerals in Bure claystones for temperatures as low as 50°C, which corresponds to the burial temperature encountered at approximately 2 km. Stepwise burial-like heating experiments revealed the following: 1) an increase in the CRM_{2mT} and the TRM_{2mT} consistent with an increasing T_{exp} temperature, and 2) an evolution of rock magnetism proxies.

The process behind neoformed magnetic grains was likely fast on the geological time scale since the remanence acquired during heating claystones rapidly attained a quasi-plateau (Figure 1). Our heating steps experiment was not long-lasting enough to determine the long-term trend of the plateau (e.g. *Aubourg et al*., 2008). However, we assumed that most of the magnetic minerals were rapidly formed upon heating. One motivation of our work was to simulate the effect of an increasing burial temperature. In this respect, we observed different plateaus for stepwise heating from T_{exp} = 50 to

Appendix

130°C (Figure 1). Extending this result to burial suggests that magnetic minerals form continuously and rapidly attain a steady state when the burial temperature increases.

During burial, neoformed magnetic minerals carry a remanence. Heating experiments indicate that remanence (R) is partly carried by a T(RM$_{2mT}$ and by a CRM$_{2mT}$ for ten days of heating. The strength of the CRM$_{2mT}$ obtained between T_{exp} = 50 and 130°C increases from 5 to 1 (Am(kg, which is the strength of the NRM (Figure 2, Table 1). The finding suggests either a higher concentration of one kind of neoformed magnetic mineral at 130°C, or an assemblage of different magnetic species.

(hen thermally demagnetizing the CRM$_{2mT}$, we did not observe any clear break-in-slope in the curves (Figure 3a). So, it is unlikely that the increase of the CRM$_{2mT}$ is due to an assemblage of magnetic minerals.

In contrast, we observed a regular shift in the maximum unblocking temperature (T_{UB}) the lowest burial-like T_{exp} temperature, with the lowest being T_{UB} (Figure 3a). The shift can be attributed to the grain size distribution of magnetic minerals(the coarser the grain, the higher the T_{UB} (*tokking & (au(e*, 1(87)(*unlop & Ozdemir*, 1((7). Magnetic grains become harder to thermally demagnetize as the T_{exp} increases. The simplest, and the more likely hypothesis, is that only one magnetic mineral is formed during the heating experiment. The maximum unblocking temperature (T_{UB}) near 500°C supports the occurrence of fine magnetite (Figure 3a). The presence of neoformed magnetite is found in accordance with conclusions from other heating experiments, in claystones at temperature from (5 to 250°C (*Cairanne et al.,* 2004(*Moreau et al.*, 2005(*Aubourg et al*., 2008). Therefore, we assume that magnetite formed continuously during our heating experiments. The boundary between superparamagnetic (SP) and single domain (SD) magnetite grains has been estimated to be 20 nm ((*unlop & Ozdemir*, 1((7). The CRM$_{2mT}$ may be a proxy for grains > 20 nm, while the T(RM$_{2mT}$ essentially marks the contribution of hyperfined grains < 20 nm. The evolution of CRM$_{2mT}$ demagnetization curves (Figure 3a) suggests that grain size distribution evolves to larger grains. According to (*tokking & (au(e* (1(87), we used the Néel equation, which links grain size and the blocking temperature as follows(

(((kT(K(ln ((Cτ(

where □ is the grain volume □cm^3□, k is the Boltzmann's constant □1.38 x 10^{-16} erg□K□, T is the blocking temperature □Kelvin□, K is the anisotropy constant of the magnetic mineral of interest, C is a frequency factor □1 x 10$^{-□}$□, and τ is the relaxation time □the duration of sample demagnetization□. The grain diameter □d□can be expressed as d□cm□□ □ln□Cτ□□6k□ΠK□T□$^{1/3}$. Using K □-1.35x10^5 erg□cm^3 □the magnetocrystalline anisotropy of magnetite□, and τ □ 3600s, we obtained different grain sizes for magnetites ranging from 30 to 35 nanometers, for T_{UB} from 250 □526 K□to 500°C □723 K□.

On the other hand, the intensity of T□RM_{2mT} increased three fold from 50 to 130°C, respectively □Figure 2, Table 1□. The T□RM_{2mT} is partly carried by neoformed ultra fined magnetic minerals and partly carried by former magnetic minerals. Assuming that magnetite is produced during the heating experiments, the increase of T□RM_{2mT} is likely attributable to the larger concentration of < 20 nm grains, an observation confirmed by the evolution of the parameter PM, as deduced from the low-temperature analysis □Figure 3b□. The parameter may be a proxy for a SP mineral that acquired a remanence at a low temperature, but not at room temperature □*Carter□□tiglitz et al*., 2002□. The regular PM increased from T_{exp}□ 50 to 130°C suggesting that very small magnetite SP grains are formed continuously throughout the burial-like T_{exp} temperature elevation □Figure 3b□.

4.2. The CRM_{2mT} and the magnetic overprint

The magnetic field imparted during the experiment was 2 mT, which is 40□1 of the Earth's magnetic field. By assuming that chemical remanent magnetization is proportional to the strength of the magnetic field □□*tokking & □au□e*, 1□□0□, we calculated the expected CRM_{EMF} obtained at 50 μT, the strength of the Earth's magnetic field □EMF□. Therefore, the CRM_{EMF} ranged from 0.1 to 0.5 μAm^2□kg, which is approximately 1□100 to 1□10 of the NRM of our samples □Table 1□.

From our heating experiments, which aimed to simulate maximum burial up to 4 km, we observed that the CRM_{EMF} << NRM, suggesting a maximum magnetic overprint of 10%, at most. However, assuming that the CRM_{EMF} evolution linearly increased with increasing temperature, as suggested from our experiments □Figure 2□, would lead to a temperature where $CRM_{EMF} \geq$ NRM. □hen extrapolating our results □Figure 2□, this temperature would be > 220°C with a weak NRM □□1 □Am□kg□. Beyond 220°C, the neoformed magnetic grain remanence would be predominant over the

preexisting grain remanence (*Aubourg & Pozzi*, 200). Our experimental data are corroborated by natural examples from mid-Jurassic claystones from the ocontian trough in the occidental French Alps. In the French Alps a pervasive remagnetization has been documented (*Aubourg & Chabert* *Pelline*, 1 *Katz et al.*, 2000 *Cairanne et al*., 2002). Mid-Jurassic claystones witnessed burial temperatures between 200 and 250°C during the late Cretaceous (*Guilhaumou et al*., 16). Interestingly, this pervasive remagnetization, with a magnitude on the order of 1 $\mu Am^2/kg$, completely overlapped the primary NRM likely indicating that long-term burial heating promotes larger magnetic overprints in claystones than our experimental results indicate.

Our experimental conditions were far from natural conditions. The heating experiments indicated the fast production of magnetite within the first days, followed by a quasi-plateau. That this trend is valid for the duration of natural heating, on the order of a million years, is not certain. In addition, we did not consider pressure which is likely an important parameter. However, two observations led us to the conclusion that our heating experiments produced similar magnetic minerals as those obtained during burial. First, we monitored the increase of hyperfine magnetite < 20 nm, as revealed both by the TRM and the PM factor. The development of hyperfine magnetic minerals throughout burial was envisaged by (*ackson et al.* 3) and *Aubourg & Pozzi* (2010). Second, the low unblocking temperature (≤500°C) of magnetite is also diagnostic of remagnetized claystones and carbonates (*ackson et al*., 3 *Katz et al*., 2000 *Cairanne et al.*, 2002).

Based on our experimental results, we suggest that moderate burial < 7 km triggers the formation of fine magnetites, and, in turn, produces CRM that could significantly overlap primary magnetization. The process could have important consequences for the interpretation of remanence in sedimentary rocks, and, in particular, for magnetostratigraphy. The latter has been discussed by *Aubourg & Pozzi* (200) and will be explored further in a forthcoming paper.

5. Conclusion

For the first time, we have shown that laboratory heating by 50°C triggers the formation of hyperfine magnetite. From 50 to 130°C, the heating steps experiment suggested that two populations of magnetite grains sizes, < 20 nm and > 20 nm, are continuously formed by the elevation of

temperature, reaching a maximum size of 35 nm. The growth and neoformation of magnetite minerals in sedimentary rocks during burial produces a secondary magnetization that may overprint initial magnetization. Therefore, sediments with a weak NRM □□1 □Am□kg□, experiencing temperature higher than 220°C, will be remagnetized.

Acknowledgments

This work was conducted as a part of M. Kars PhD. thesis supported by Total S.A. □Université de Pau et des Pays de l'Adour, France. □ e would like to thank France Lagroix from IPGP for her help when running low temperature measurements and ANDRA for providing us samples. The MPMS □L5EverCool used in this study was financed by the Conseil Régional d'Ile de France □No. I-06-206□R□, INSU-CNRS, IPGP and ANR.

Appendix

References

Aubourg, C. and C. Chabert-Pelline (1□□□), Neogene remagnetization of normal polarity in the Late Jurassic black shales from the southern Subalpine Chains (French Alps): Evidence for late anticlockwise rotations, *□ectonophysics,* □□□, 473-486.

Aubourg, C., J-P. Pozzi, D. Janots, and L. Sahraoui (2008), Imprinting chemical remanent magnetization in claystones at □5°C, *Earth and Planetary □cience Letters*, □□□,172-180.

Aubourg, C. and J-P. Pozzi, 200□, Burial and consequences to magnetostratigraphy, EGU General Assembly 200□, Geophysical Research Abstracts, □□, EGU200□-5687.

Aubourg, C. and J-P. Pozzi, 2010, Toward a new < 250°C pyrrhotite-magnetite geothermometer for claystones, *Earth and Planetary □cience Letters*, □□□□□□□, 47-57.

Baner□ee, S., R.D. Elmore and M.H. Engel, 1□□7, Chemical remagnetization and burial diagenesis in the Pennsylvanian Belden Formation, Colorado, *□ournal o□Geophysical Research,* □□□, 24825-24842.

Brothers, L.A., M.H. Engel and R.D. Elmore, 1□□6, The late diagenetic conversion of pyrite to magnetite by organically complexed ferric iron, *Chemical Geology,* □□□, 1-14.

Cairanne, G., C. Aubourg and J-P. Pozzi, 2002, Syn-folding remagnetization and the significance of the small circle test, Examples from the □ocontian trough (SE France), *Physics and Chemistry o□the Earth,* □□, 1151-115□.

Cairanne, G., C. Aubourg, J-P. Pozzi, M-G. Moreau, T. Decamps and G. Marolleau, 2004, Laboratory chemical remanent magnetization in a natural claystone□a record of 2 magnetic polarities, *Geophysical □ournal □nternational,* □□□, □0□-□16.

Carter-Stiglitz, B., M. Jackson and B. Moskowitz, 2002, Low-temperature remanence on stable single domain magnetite, *Geophysical Research Letters,* □□7, 112□.

Dunlop, D. and O. Ozdemir, 1□□7, *Rock magnetism□□undamentals and □rontiers,* Cambridge University Press, 573 pp.

Elmore, R.D., J. Kelley, M. Evans, M.T. Lewchuk, 2001, Remagnetization and orogenic fluids□testing the hypothesis in the Central Appalachians, *Geophysical □ournal □nternational,* □□□, 568-576.

Esteban, L., J-L. Bouchez and A. Trouillier, 2006, The Callovo-Oxfordian argillites from the eastern Paris Basin□magnetic data and petrofabrics, *Comptes Rendus G□oscience,* □□□, 867-881.

Evans, M., R.D. Elmore and M.T. Lewchuk, 2000, Examining the relationship between remagnetization and orogenic fluids□central Appalachians, *□ournal o□Geochemical E□ploration,* □□□ □□, 13□-142.

Gaucher, E., C. Robelin, J.M. Matray, G. Négrel, □. Gros, J.F. Heitz, A. □inso□, H. Rebours, A. Cassagnab□re and A. Bouchet, 2004, ANDRA underground research laboratory□interpretation of the mineralogical and geochemical data acquired in the Callovo-Oxfordian formation by investigative drilling, *Physics and Chemistry o□the Earth,* □□, 55-77.

Gillett, S.L., 2003, Paleomagnetism of the Notch Peak contact-metamorphic aureole, revisited□ pyrrhotite from magnetite □pyrite under submetamorphic conditions, *□ournal o□Geophysical Research B,* □□□, 2446.

Guilhaumou, N., J.C. Thouray, □. Perthuisot and F. Roure, 1□□6, Palaeocirculation in the basin of southeastern France sub-alpine range□a synthesis from fluid inclusions studies, *Marine and Petroleum Geology,* □□6□, 6□5-706.

Guyodo, □., T.M. LaPara, A.J. Anschutz, R. Lee Penn, S.K. Baner□ee, C.E. Geiss and □ . □anner, 2006, Rock magnetic, chemical and bacterial community analysis of a modern soil from Nebraska, *Earth and Planetary □cience Letters,* □□□, 168-178.

Jackson, M., P. Rochette, G. Fillion, S. Baner□ee and J. Marvin, 1□□3, Rock Magnetism of Remagnetized Paleozoic Carbonates□Low-Temperature Behavior and Susceptibility Characteristics, □*ournal o*□*Geophysical Research,* □□B4□, 6217-6225.

Karlin, R., M. Lyle and G. Ross Heath, 1□87, Authigenic magnetite formation in suboxic marine sediments, □*ature,* □□□, 4□0-4□3.

Katz, B., R.D. Elmore, M. Cogoini and S. Ferry, 1□□8, □ idespread chemical remagnetization orogenic fluids or burial diagenesis of clays□*Geology,* □□, 603-606.

Katz, B., R.D. Elmore, M. Cogoini, M.H. Engel and S. Ferry, 2000, Associations between burial diagenesis of smectite, chemical remagnetization and magnetite authigenesis in the □ocontian trough, SE France, □*ournal o*□*Geophysical Research,* □□□B1□, 851-868.

Landais, P. and M. Elie, 1□□□, Utilisation de la géochimie organique pour la détermination du paléoenvironnement et de la paléothermicité dans le Callovo-Oxfordien du site de l'Est de la France. In □E.S.E. Paris □Editor□, Acte des □ournées scientifiques CNRS-ANDRA.

Larrasoa□a, J.C., A. P. Roberts, R.J. Musgrave, E. Gr□cia, E. Pi□ero, M. □ega and F. Martinez-Ruiz, 2007, Diagenetic formation of greigite and pyrrhotite in gas hydrate marine sedimentary systems, *Earth and Planetary □cience Letters,* □□□3-4□, 350-366.

Lewchuk, M.T., M. Evans and R.D. Elmore, 2003, Synfolding remagnetization and deformation□ results from Palaezoic sedimentary rocks in □ estern □irginia, *Geophysical □ournal □nternational,* □□□, 266-27□.

Lu, G., S. Marshak and D.□. Kent, 1□□0, Characteristics of magnetic carriers responsible for Late Paleozoic remagnetization in carbonate strata of the mid-continent, USA, *Earth and Planetary □cience Letters,* □□, 351-361.

Lu, G., C. McCabe, J.S. Hanor and R.E. Ferrell, 1□□1, A genetic link between remagnetization and potassic metasomatism in the Devonian Onondaga formation, northern Appalachian basin, *Geophysical o*□*Research Letters,* □□11□, 2047-2050.

Maher, B.A., □.□. Karloukovski and T.J. Mutch, 2004, High field remanence properties of synthetic and natural submicrometre haematites and goethites□significance for environmental contexts, *Earth and Planetary □cience Letters,* □□□, 4□1-505.

McCabe, C. and R.D. Elmore, 1□8□, The occurrence and origin of Late Paleozoic remagnetization in the sedimentary rocks of North America, *Reviews o*□*Geophysics,* □□4□, 471-4□4.

McElhinny, M.□ . and N.D. Opdyke, 1□73, Remagnetization hypothesis discounted□a paleomagnetic study of the Trenton limestone, New □ork State, *G*□*A Bulletin,* □□, 3□67-3708.

Moreau, M-G., M. Ader and R.J. Enkin, 2005, The magnetization of clay-rich rocks in sedimentary basins□low-temperature experimental formation of magnetic carriers in natural samples, *Earth and Planetary □cience Letters,* □□□, 1□3-210.

Appendix

Oliver, J., 1□86, Fluids expelled tectonically from orogenic belts□their role in hydrocarbon migration and other geologic phenomena, *Geology,* □□, □□-102.

Ozdemir, O. and D.J. Dunlop, 1□□6, Thermoremanence and Néel temperature of goethite, *Geophysical Research Letters,* □□□□, □21-□24.

Roberts, A.P. and R. □ eaver, 2005, Multiple mechanisms of remagnetization involving sedimentary greigite □Fe_3S_4□, *Earth and Planetary □cience Letters,* □□□, 263-277.

Rochette, P., P-E. Mathé, L. Esteban, H. Rakoto, J-L. Bouchez, □. Liu and J. Torrent, 2005, Non-saturation of the defect moment of goethite and fine-grained hematite up to 57 Teslas, *Geophysical Research Letters,* □□, doi□10.102□2005GL0241□6.

Rowan, C.J. and A.P. Roberts, 2005, Tectonic and geochronological implications of variability timed magnetizations carried by authigenic greigite in marine sediments from New □ealand, *Geology,* □□7□, 553-556.

Stokking, L. and L. Tauxe, 1□87, Acquisition of chemical remanent magnetization by synthetic iron oxide, □*ature,* □□□, 610-612.

Stokking, L. and L. Tauxe, 1□□0, Properties of chemical remanence in synthetic hematite□testing theoretical predictions, □*ournal o*□*Geophysical Research,* □□B8□, 12,63□-12,652.

Suk, D., D.R. Peacor and R. □an der □oo, 1□□0, Replacement of pyrite framboids by magnetite in limestone and implications for palaeomagnetism, □*ature,* □□□, 611-613.

Sweeney J.J, and A.K. Burnham, 1□□0, Evaluation of a simple model of vitrinite reflectance based on chemical kinetics, *AAPG Bulletin,* □□□10□, 155□-1570.

□ eil, A.B. and R. □an der □oo, 2002, Insights into the mechanism for orogen-related carbonate remagnetization from growth of authigenic Fe-oxide□a scanning electron microscopy and rock magnetic study of Devonian carbonates from northern Spain, □*ournal o*□*Geophysical Research,* □□□B4□, 2063, doi□10.102□2001JB000200.

Figures captions

Figure 1 Evolution of the mean remanent magnetization R during heating steps experiment from T_{exp} 50 to 130°C. Standard deviation 1σ is also reported. One representative sample BU 0B is shown.

Figure 2 Evolution of the mean CRM_{2mT} and mean T RM_{2mT} created during the experiment. Standard deviation 1σ is also shown.

Figure 3 a thermal demagnetization of CRMs produced in the experiment, b LT SIRM for the set A samples. Natural sample LT-SIRM is represented on the figure for reference.

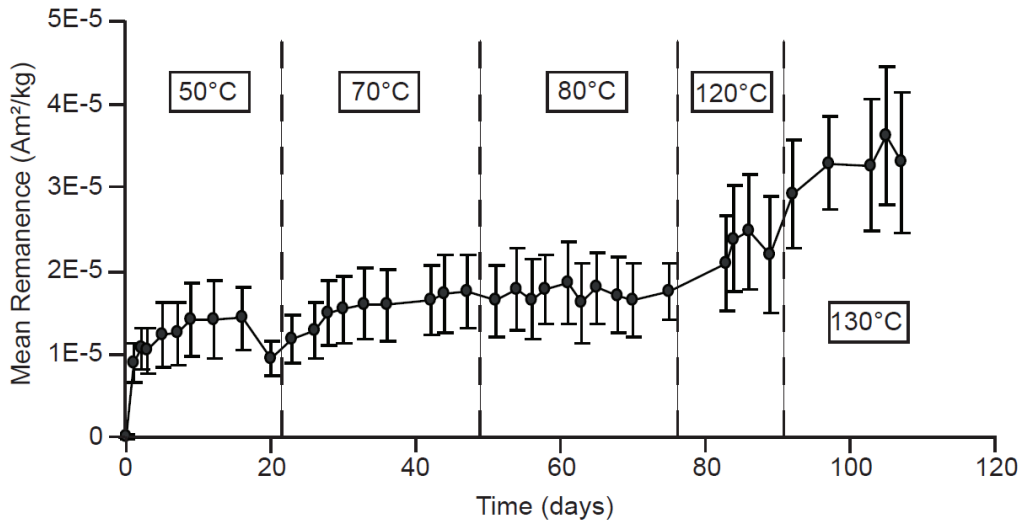

Figure 1 Evolution of the mean remanent magnetization R during heating steps experiment from T_{exp} 50 to 130°C. Standard deviation 1σ is also reported. One representative sample BU 0B is shown.

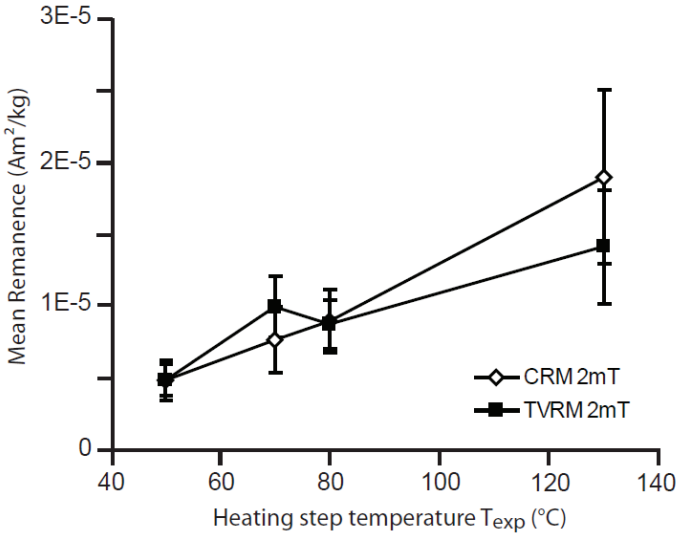

Figure 2 Evolution of the mean CRM_{2mT} and mean TRM_{2mT} created during the experiment. Standard deviation (1σ) is also shown.

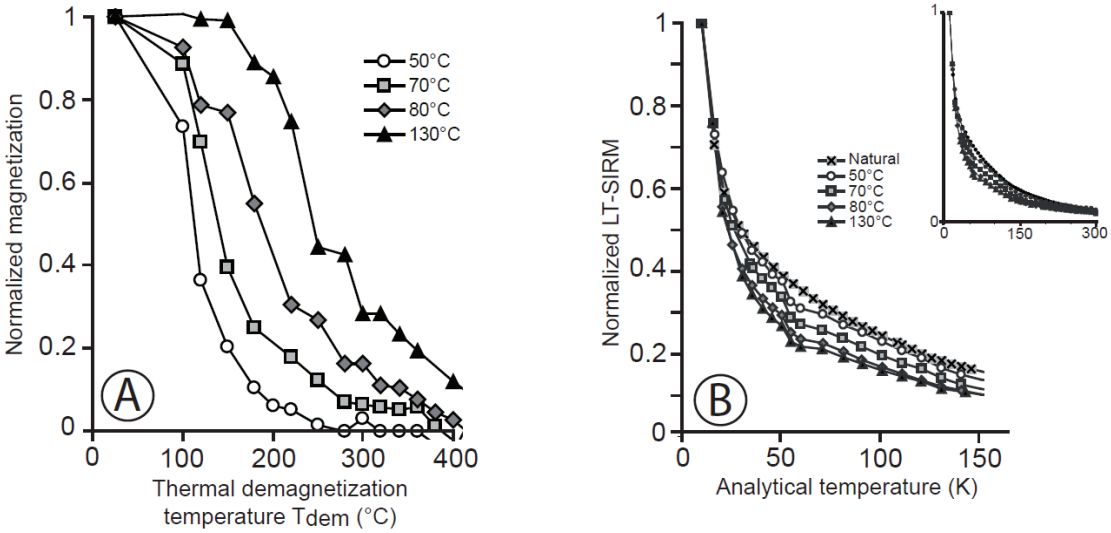

Figure 3 a) thermal demagnetization of CRMs produced in the experiment, b) LT SIRM for the set A samples. Natural sample LT-SIRM is represented on the figure for reference.

Sample	Mass (g)	NRM (μAm²/kg)	CRM_{2mT} (μAm²/kg)				$TVRM_{2mT}$ (μAm²/kg)			
			50	**70**	**80**	**130**	**50**	**70**	**80**	**130**
1	1.0□7	□8	6.□				6.5			
2	0.□□0	2.1	3.□				4.4			
3	1.144	1.4	3.□	6.3			4.7	7.6		
4	1.613	1.3	3.7	5.6			4.4	8.6		
5	1.1□7	5.2	4	6.2	7.3		4.5	8.7	7.□	
6	1.156	2.5	4.3	6.□	8.2		5	10	8.6	
7	1.7□1	1.8	4	6.4	7.2	12	3.5	8.5	8	15
8	1.262	0.07	3.8	6.2	6.8	23	4.8	□4	7.7	13
□	1.038	1.3	3.4	5.8	11	22	4.6	7.□	7.6	20
10	1.370	44	7.4	11	11	1□	4.3	13	13	14
11	0.8□2	2	6.7	10	10	16	3.3	12	□2	17
12	1.200	2.2	3.8	5.3	7.1	21	4.4	□1	7.7	14
13	0.□55	2.4	5.□	11	14	11	7.6	14	7.3	5.8
14	1.022	1.5	5.□	10	11	2□	5.6	11	11	14
Mean		**12**	**4.8**	**7.6**	**8.9**	**19**	**4.8**	**10**	**8.8**	**14**
SD		**26**	**1.4**	**2.3**	**2.2**	**6**	**1.1**	**2.1**	**1.7**	**3.9**

Table 1 □NRM, CRM_{2mT} and T□RM_{2mT} for samples used in heating steps experiment

3 Burial, claystones remagnetization and some consequences for magnetostratigraphy

Burial, claystones remagnetization and some consequences for magnetostratigraphy.

Charles Aubourg[1] , Jean-Pierre Pozzi[2] and Myriam Kars[1,2]

1 Laboratoire des Fluides Complexes et leurs Réservoirs. Université de Pau. CNRS (UMR5150). 64000. Pau. France.

2 Laboratoire de Géologie, Ecole Normale Supérieure, CNRS (UMR 8538). 24 rue Lhomond, 75231 Paris cedex 05, France.

Abstract

We investigate the broad lines of magnetic mineral formation for non-metamorphic claystones. More particularly, we focus on the formation of magnetite from tens-day experiments aiming to reproduce burial conditions. It is shown that the sole action of temperature from 25°C to 250°C drive to the formation of magnetite. The neoformed magnetites carry a chemical remanent magnetization which equates at least the natural remanent magnetization. We propose a schematic of burial with 3 magnetic windows where a chemical remanent magnetization superimposed the natural remanent magnetization. These are the greigite window (subsurface), the magnetite window (depth > 2km) and the pyrrhotite window (depth >6 km). The formation of magnetic minerals has profound consequence for the magnetostratigraphy record. We propose a conceptual model that shows that the continuous production of magnetite during burial may result in magnetozones that have no relation with the age of the sediment.

Introduction

Widespread remagnetization is a common process in sedimentary rocks (*Kligfield and Channell*, 1981; *McCabe and Elmore*, 1989; *Lu et al.*, 1990; *Morris and Robertson*, 1993; *Plattzman*, 1994). We focus here on the relationship between remagnetization and burial in claystones. The claystones are common targets for paleomagnetic applications, and especially the magnetostratigraphy. In addition, the claystones are potentially source rocks for oil and gas for burial conditions ranging approximately between 2 km and 10 km depth. So the elucidation of remagnetization processes during burial in claystones may have importance for academic and industrial applications.

During the early digenesis, many studies report on the dissolution of detrital iron oxides in the first meter of the sediments and the formation of iron sulfides such as greigite (Fe_3S_4) (*Roberts and Turner*, 1993). The greigite forms within anoxic sedimentary environments that support active bacterial sulfate reduction. Formation of iron sulfides follows in a specific order: mackinawite ($FeS_{0.9}$), greigite or pyrrhotite (Fe_7S_8, Fe_3S_{10}) and finally pyrite (FeS_2) (e.g. *Berner*, 1984). This process has some critical importance for dating sediments using magnetostratigraphy (*Rowan and Roberts*, 2005). The prerequisite of magnetostratigraphy is that natural remanent magnetization (NRM) is properly isolated and is contemporaneous of deposit. The combined effect of iron oxide dissolution and greigite formation implies a magnetic reset of the primary NRM. In addition, an early burial remagnetization carried by greigite delays the magnetostratigraphy record of tens to hundreds of thousand years (*Rowan et al.*, 2000). Larrasoana et al. (2007) demonstrated that the offset of magnetostratigraphy is possibly larger, from a few (≤40) thousand years to a few (≤3) millions years. This early burial remagnetization is by essence a chemical remanent magnetization (CRM).

Jumping now to a depth >6 km, when approaching 200°C (with a geothermal gradient 30°/km, that is used throughout the text), several studies report on formation of pyrrhotite (Fe_7S_8) at the expense of magnetite (Fe_3O_4) and pyrite (*Rochette and Lamarche*, 1986; *Crouzet et al.*, 2001; *Schill et al.*, 2002). More precisely, Rochette (1987) determined two isograds based on the breakdown of magnetite (~250°) and the breakdown of pyrite (>320°C) into monoclinic pyrrhotite. For burial temperature >300°C, the

neoformed pyrrhotite replaces completely the magnetite, leading to a remagnetization which consists in an assemblage of CRM and a thermo remanent magnetization (TRM). The previous magnetic record, acquired at temperature lower than 250°C, is then completely removed. At this depth (~10 km), there is no longer primary magnetization contemporaneous of the deposit of the sediments.

Between these two end-members, limited by the formation of greigite within the first tens of meter and the formation of high-temperature pyrrhotite for depth >6km, there should be another magnetic horizon that we focus on. We will use results from laboratory heating (50° to 250°C) to better understand the nature of neoformed magnetic minerals.

Experimental evidence for the formation of magnetite

For depth >2 km, widespread evidences pointed for the formation of magnetite. Illite-to-smectite transformation and alteration of pyrite are surely the most evoked processes to produce magnetite. Lu et al. (1990) first proposed that the Fe-smectite to illite transformation during burial leads to the formation of magnetite. Since this work, many authors envisaged a link between authigenic magnetite, smectite to illite transformation and remagnetization at depth >2 km (*Banerjee et al.*, 1997; *Katz et al.*, 2000; *Lohver et al.*, 2008). Besides, Brothers et al. (1996) showed experimentally the development of a magnetite rim on pyrite at 0°C in association with organic matter. It is common to observe an oxidation rim around pyrite grains (*Duk et al.*, 1990).

Although the exact mechanism of formation of magnetite is not fully understood (*Elmore et al.*, 2001), experimental heating studies in claystones aiming to reproduce burial confirmed that magnetite is produced on the sole action of heating. Cairanne et al. (2004), Moreau et al. (2005) and Aubourg et al. (2008) imparted a laboratory CRM at 250°C, 150°C and 5°C respectively. In these experiments, the production of magnetic minerals is monitored through the record of remanence acquired within an imposed magnetic field <5 mT. This remanence is by essence a CRM and a thermo viscous remanent magnetization (TVRM). The CRM is carried by neoformed grains with size larger than the blocking volume. The TVRM is carried essentially by former and neoformed magnetic grains below the blocking

volume. The thermal demagnetization of CRM provides an unblocking temperature spectrum. The maximum unblocking temperature is then a good indication of the nature of neoformed magnetic minerals. For all experiments described hereafter, the maximum unblocking temperature ranked between 400 and 580°C, which is consistent with magnetite. After heating for 60 hours at 250°C in an argon atmosphere, Cairanne et al. (2004) reported the production of magnetite and some hematite. At 150°C, Moreau et al. (2005) documented the production of magnetite after heating for at least one week in argon atmosphere. In these two experiments, the claystones come from the same stratigraphic horizon from the Basin of Paris (Toarcian). These claystones are characterized by low NRM (≤0.5 $\mu Am^2/kg$). At the end of the heating experiment, Moreau et al. (2005) reported the production of a CRM that is in average (14 $\mu Am^2/kg$ at 150°C for 7 days. Cairanne et al. (2004) reported a CRM of about 8 $\mu Am^2/kg$ at 250°C for 60h. Assuming that CRM is proportional to the strength of the magnetic field (*Stokking and Tauxe*, 1990), we calculate the expected CRM_{EMF} obtained at 50 µT, the value of the Earth's magnetic field (EMF). We obtain CRM_{EMF} (0.4 $\mu Am^2/kg$ at 250°C for 60 hours and CRM_{EMF} (4.5 $\mu Am^2/kg$ at 150°C for 7 days. The CRM_{EMF} obtained at 150°C and 250°C are not directly comparable because the heating time is different. We notice however that $CRM_{EMF} \geq NRM$.

At (5°C, Aubourg et al. (2008) and Aubourg and Pozzi (2010) reported the production of magnetite and some fine grained pyrrhotite during heating in an open environment for 15 days or more. Here, we present a new set of results at (5°C using the same claystones of these two studies.

New results for laboratory heating at 95°C

Two Bure and Opalinus claystones are studied. The Bure claystones (Callovo-Oxfordian) are from the borehole EST211 at 675 m depth from the Basin of Paris (*ANDRA*, 2000). They experienced a peak burial temperature near 40°C (*Landais and Elie*, 1999). The Opalinus claystones (Aalenian) are from the Jura fold belt (Mont Terri laboratory, core BHE-D5). Opalinus claystones experienced a burial temperature near 85°C (*Mazurek et al.*, 2006). The NRM of Bure and Opalinus claystones are low (≤0.5

μAm^2/kg). We operated laboratory heating as described in Aubourg et al. (2008). Claystones fragments (few grams) are placed in a nylon holder where fresh air is slowly renewed. We used a home-made furnace, shielded against the earth magnetic field. The heating rate is about 2 °C/minute, and the target temperature is reached within 20 mn. During heating at 75°C, the claystones are submitted to a vertical magnetic field of 2 mT. The remanence is monitored every few days for several weeks. To measure the remanence, we first cool down the sample to room temperature in a null magnetic field (residual field <100 nT). By doing this, we do not impart a thermo remanent magnetization in the sample. Then the sample is measured using a Squid magnetometer 2G. Note that the sample is not removed from the holder during the measurement Aubourg et al. (2008) showed that the residual NRM and isothermal remanent magnetization (IRM) acquired at 2 mT are negligible. The natural remanent magnetization of the samples is <0.1 μAm^2/kg after AF demagnetization at 100 mT. The IRM imparted by the application of a magnetic field of 2 mT is <0.5 μAm^2/kg The remanence is essentiallythe sum of a CRM and a T-RM. To remove the T-RM, the sample was heated for at least 2 days within a null magnetic field.

Standard curves are shown in Figure 1. They are comparable to the curves obtained by Aubourg et al. (2008). Opalinus claystones (5 samples) and Bure claystones (4 samples) show the development of a plateau after 10 days of heating. The CRM is 52 μAm^2/kg at 1 days for Opalinus claystones and 356 μAm^2/kg at 27 days for Bure claystones. The T-RM represents about half of the remanence. We calculate CRM_{EMF} 0.1 μAm^2/kg for Opalinus claystones and CRM_{EMF} 0. μAm^2/kg for Bure claystones. We notice that CRM_{EMF} equates NRM in both claystones.

Toward a burial model

We define three magnetic windows, each characterized by a CRM related to the formation of greigite, magnetite and pyrrhotite respectively (Figure 2). This model is simplified because additional magnetic minerals can formed under specific conditions, like the pyrrhotite (*Gillett*, 2003; *Wehland et al.*, 2005; *Larrasoana et al.*, 2007; *Aubourg and Pozzi*, 2010) or hematite and goethite (*Evans and Elmore*,

2006□. The participation of hematite and goethite can be neglected as magnetite, greigite and pyrrhotite have a stronger remanence by 1□100 □*Maher and* □*hompson*, 1999].

Greigite, magnetite and pyrrhotite have distinct magnetic properties making the CRM distinguishable. Their Curie temperatures (Tc) are ~340°C, 585°C, and 320°C respectively [*Hunt et al.*, 1995]. It turns out that the unblocking temperature (Tub) spectrum of the CRM is distinct, as Tub≤Tc. A CRM carried by magnetite has unblocking temperature ranging between room temperature and 580°C. A CRM carried by either greigite or pyrrhotite has an unblocking temperature between room temperature and ~340°C. The unblocking temperature spectrum of the CRM may be therefore a burial indicator. In our conceptual model represented in Figure 2, we plot the CRM unblocking spectra of neoformed magnetic minerals according to our proposed magnetic windows. When temperature increases, a thermo visquous remanent magnetization (TVRM) overlaps partially the CRM. The unblocking temperature of TVRM is larger than the burial temperature, from few °C up to 200°C depending on the time exposure to the temperature [*Pullaiah et al.*, 1975; *Dunlop and Özdemir*, 1997]. We plot the TVRM to show its correspondence with the CRM. In our model, we follow equation of Pullaiah et al. (1975) for magnetite for a time exposure at temperature of 1 Ma to illustrate the unblocking spectra of the TVRM.

The greigite forms from the first centimeters to tens of meters, implying the delay of magnetostratigraphy [*Rowan et al.*, 2009], the record of inconsistent polarities [*Horng et al.*, 1998] or pervasive remagnetization several millions years after sediment deposition [*Rowan and Roberts*, 2006]. Within the greigite window, the CRM overlaps the primary magnetization contemporaneous of the deposit of the sediments. Depending on how much is the dissolution of iron oxides driven by bacterial activity, there is the potential to erase the primary magnetization [*Rowan and Roberts*, 2006]. However, the original magnetostratigraphy can be preserved if some iron oxides (generally > 10 μm) survive to dissolution [*Roberts et al.*, 2010].

The boundary between the greigite and the magnetite windows is diffused, but it is well known that greigite is unstable for temperature >200°C [see *Dekkers et al.*, 2000]. It is generally assumed that the formation of magnetite starts for burial >2 km [*Suk et al.*, 1993]. Recent heating experiments (Kars et al.,

AG 2010, submitted) show that magnetite formed by temperature as low as 50°C. Taken this, we propose that magnetite window starts for depth >2 km. We suggest that the CRM carried by greigite is disappearing progressively. For depth > 7km, the CRM carried by greigite may be no longer present (Figure 2). The heating experiments on claystones suggest that the magnetite concentration is increasing with burial temperature. Taken comparable experiments at 95°C (this study) and 150°C (Moreau et al., 2005), we observe that CRM_{MF} (150°C)> CRM_{MF} (95°C). Kars et al. (2011, submitted) observed the same trend from 50°C to 130°C using ure claystones. This leads us to propose that the magnetite forms continuously from depth >2km. ur figure 2 illustrates the continuous production of magnetite, making a tie shape (Figure 2). The CRM within the magnetite window can be carried by greigite and magnetite. ecause those minerals form at different depths, it is possible that CRM reveals distinct polarities in the course of thermal demagnetization. .

The pyrrhotite window starts at about 200°C, for depth >6 km. The pyrrhotite forms at the expense of magnetite, and for temperature > 300°C, it is generally accepted that only neoformed pyrrhotite carries the RM [*Ro hette*, 1987]. The progressive replacement of remanence carried by magnetite and pyrrhotite has been well observed by chill et al. [2002]. For burial temperature >320°C, which is above the Curie temperature of pyrrhotite, the remanence is essentially a TRM that may record the successive change of magnetic polarities during cooling [*rouzet et al.*, 2001]. nlike magnetostratigraphy where the oldest polarity is found in the oldest part of the sediment, the youngest polarity may be found at the lowest part of a metamorphic pile.

The magnetostratigraphy in the magnetite window

Here we would like to focus on the consequence of magnetostratigraphy within the magnetite window as we suggest a continuous production of magnetite through burial > 2 km. As a hypothesis, we envisage the case where the CRM overwhelms the RM and what may be the consequence for magnetostratigraphy record. We make one additional assumption about magnetite formation. We assume that during grain growth through the critical single domain blocking volume, the magnetic minerals record the magnetic

polarity of the ambient field and that this record is retained even after subsequent mineral growth. The resulting polarity is then the sum of all polarities recorded by the neoformed grains [*rouzet et al.*, 2001]. Cairanne et al. [2003; 2004] demonstrated this additive behavior of magnetic polarities in a laboratory induced CRM carried by magnetite.

We present 2 scenarios to illustrate the evolution of an initial magnetostratigraphy record through burial (Figure 3). The initial sedimentary column has a three part polarity zonation, with a normal polarity zone in the middle of the column. In the first scenario, the magnetic field has the same polarity throughout the simulated burial period. During burial, the reversed polarity magnetozone located in the lower part of the hypothesized sediment column is progressively remagnetized (Figure 3A). At the end of the simulation, this magnetozone is completely remagnetized with normal polarity. The upper part of the stratigraphic column has preserved the initial polarity record. The final record is therefore a composite with an initial preserved polarity record and a later burial CRM. Misinterpretation of the polarity zonation will occur if the burial CRM carried by magnetite is not detected. In a second scenario, we impose a magnetic reversal sequence during the burial period (Figure 2). According to our second assumption above, the neoformed grains record the ambient magnetic polarity when they grow through their blocking volume. The resulting burial CRM at the end of the simulation is a sequence of normal and reversed polarities that has no correspondence with the initial record. uch a record of reversals during burial can be misinterpreted with respect to the primary record of magnetic reversals. Generally, the recognition of a sequence of magnetic reversals in a sedimentary record is considered as a good evidence of a primary magnetization, particularly if a reversal test is satisfied. ur model perturbs this assumption because the continuous production of magnetic minerals during burial will disrupt the magnetic reversals record.

The experimental data showed that CRM imparted during laboratory heating can be about the same order of RM. It remains to demonstrate if burial conditions for depth >2 km triggers any substantial CRM in claystones. In this regard, it is interesting to look at the paleomagnetic record of claystones that underwent burial >2 km. The urassic claystones from the western French ubalpine chains represent the >4 km buried counterpart of ure and palinus claystones. Along the eastern boarder of the Chartreuse

massif, the Jurassic claystones experienced a maximum burial near 4 km [*Deville and Sassi*, 2006]. There, Aubourg and Rochette [1992] proposed that these claystones have been fully remagnetized before the Alpine Miocene folding. This remagnetization overlaps the primary magnetization and is characterized by an absence of reverse polarity. Southward to this area, within the Vocontian trough, the burial of Jurassic claystones exceeded 5 km [*Guilhaumou et al.*, 1996] . There, Katz et al. [2000] documented a pervasive pre-Miocene folding remagnetization that they linked to peak burial during the long chrone of normal polarity 24 (83-124 Ma). Similarly to the remagnetization observed in Chartreuse massif, the remagnetization within the Vocontian tough overlaps the primary magnetization and is characterized by an absence of reverse polarity. Both examples suggest therefore that CRM took place before alpine folding and are likely related to a > 4km burial which lasted essentially during the long chrone 24. These burial CRMs constitute probably a good analog of our burial model of remagnetization represented in Figure 3A. The lack of reverse polarity in the Jurassic claystones clearly rules out any magnetostratigraphy interpretation. However, we believe that the pattern of magnetic reversals may have been more complex if burial took place during reversal chrones. Within a sedimentary column, where various rocks alternate, we think likely the coexistence of primary magnetization in some rocks and burial CRMs in others, like claystones. The recognition of burial CRMs carried by magnetite is difficult because the unblocking range of temperature overlaps largely the burial temperature. To prevent wrong interpretation of magnetostratigraphy in claystones, we recommend evaluating the burial temperature of claystones by using routine geothermometers like the reflectance of vitrinite or the pyrolysis of organic matter (Rock-Eval). For burial temperature >100°C, some detailed rock magnetism studies should be carried out. The identification of stoichiometric magnetite, through the identification of Verwey transition at 120K (~ 153°C), may be a good indication that magnetite is neoformed [*Aubourg and Pozzi*, 2010; *Abdelmalak et al.*, in revision] and then a CRM must be envisaged.

Conclusion

We propose the existence of 3 magnetic windows, where greigite, magnetite, and pyrrhotite form successively. Greigite forms within the first tens cm of the sedimentary column. Magnetite starts forming by 2 km at least, and pyrrhotite forms at the expense of neoformed magnetite for depth> 6 km. This leads to a continuous process of burial remagnetization that is by essence a chemical remanent magnetization. We investigate more specifically the consequence of the magnetostratigraphy record within the magnetite window, and propose that burial remagnetization may result in an alternation of normal and reverse polarities that has no correspondence with the age of the sediment.

Acknowledgments

We wish to thank D. □lmore for his solicitation to contribute to this volume. □arly drafts have benefited from attentive reading of A. Roberts and P. Rochette. This manuscript has benefited from constructive reviews of A. Weil and □. Appel.

FIGURE CAPTION

Figure 1 □aboratory heating experiments at 95°C. □ure claystones (□□T□211□675m) □4 samples. □palinus claystones (□H□□D5) □5 samples. □rror bars at 95□ confidence.

Figure 2 □urial model for the formation of magnetic mineral in claystones. The central box represents a sedimentary column from the surface to 10 km depth. □n left, is indicated the concentration of neoformed magnetic mineral. □n right, is indicated the unblocking temperature spectra of chemical remanent magnetization (CRM) and thermo viscous remanent magnetization (TVRM).

Figure 3 Conceptual model of burial CRM. Horizontal scale is time. Vertical scale is depth. □ine □in□ corresponds to the horizon where magnetite forms. Grey zone corresponds to the buried part of the sediment column below the line □in□. □lack (open) circles indicate a normal (reverse) polarity burial CRM. In the final record, we indicate the initial record of magnetostratigraphy (I.R.) and the burial CRM. A) □cenario of mineral formation with one polarity. □) □ame scenario as A, but with a magnetic reversal occurring during the burial of the sediments. □ew magnetic grains record the reversed polarity magnetic field, while magnetic grains formed before the magnetic reversal retains a normal polarity magnetization.

BIBLIOGRAPHY

A□DRA (2000), Thermicit□du Callovo□□xfordien du site de □□□st. D□termination d'un pal□oenfouissement maximum. □tude compl□mentaire.*Rep. D RP □□R□ □□□□□□*, A□DRA

Abdelmalak, M. M., C. Aubourg, □. Geoffroy, and F. □aggoun□Deffarge (in press), A new oil window indicator □The magnetic assemblage of claystones from the □affin □ay volcanic margin (Greenland), □□*P*□.

Aubourg, C., and P. Rochette (1992), Mise en □vidence d'□ne aimantation pr□tectonique dans les Terres □oires subalpines (Callovien□□xfordien), □.*R.* □□*ad. S*□ *Paris*, □(II), 591□594.

Aubourg, C., and □ P. Pozzi (2010), Toward a new □250°C pyrrhotite□magnetite geothermometer for claystones, □*arth and Planetar*□*S*□*ien*□*e* □*etters*, □□□, 47□57.

Aubourg, C., □□P. Pozzi, D. □anots, and □. □arahoui (2008), Imprinting chemical remanent magnetization in claystones at 95°C., □*arth and Planetar*□*S*□*ien*□*e* □*etters*, □□□, 172□180.

□aner□ee, □, R. D. □lmore, and M. H. □ngel (1997), Chemical remagnetization and burial diagenesis□ Testing the hypothesis in the Pennsylvanian □elden Formation, Colorado., □*ournal o*□□*eoph*□*si*□*al Resear*□*h*, □□□(□□. □11), 24,825□824,842.

□erner, R. A. (1984), □edimentary pyrite formation□An update, □*eo*□*himi*□*a et* □*osmo*□*himi*□*a* □□*ta*, □*ol.* □□, 605□615.

□rothers, □. A., M. H. □ngel, and R. D. □lmore (1996), The late diagenetic conversion of pyrite to magnetite by organically complexed ferric iron., □*hemi*□*al* □*eolog*□, □□□, 1□14.

Cairanne, G. (2003), □es r□aimantations chimiques et le filtrage des polarit□s du champ magn□tique terrestre. □xp□riences pressions□temp□rature et comparaisons avec des r□aimantations naturelles., 247 pp, □niversity of Cergy Pontoise, Cergy Pontoise.

Cairanne, G., C. Aubourg, □□P. Pozzi, M. G. Moreau, T. Decamps, and G. Marolleau (2004), □xperimental Chemical Remanent Magnetization in a natural claystone□a record of two magnetic polarities, □*eoph*□*s.* □ □*nt.*, □□□(doi□10.1111□□1365□246□.2004.02439x), 907□916.

Crouzet, C., P. Rochette, and G. M□nard (2001), □xperimental evaluation of thermal recording of polarity reversals during metasediments uplift., □*eoph*□*si*□*al* □*ournal* □*nternational*, □□□, 771□785.

Dekkers, M. □, H. F. Passier, and M. A. A. □choonen (2000), Magnetic properties of hydrothermally synthesized greigite (Fe3□4)□II High and low□temperature characteristics, □*eoph*□*s.* □ □*nt.*, □□□, 809□819.

Deville, □., and W. □assi (2006), Contrasting thermal evolution of thrust systems; An analytical and modeling approach in the fron of the western Alps, □□*P*□, □. □□(□□. 6), 887□907.

Dunlop, D. □, and □. □zdemir (1997), *Ro*□*k* □*agnetism*□□*undamentals and* □*rontiers*, 573 pp., Cambridge □niversity Press, Cambridge.

□lmore, R. D., □ Kelley, M. □vans, and M. T. □ewchuk (2001), Remagnetization and orogenic fluids□ testing the hypothesis in the central Appalachians, □*eoph*□*si*□*al* □*ournal* □*nternational*, □□□(3), 568□576.

□vans, M., and R. D. □lmore (2006), Fluid control of localized mineral domains in limestone pressure solution structures, □*ournal o*□*Stru*□*tural* □*eolog*□, □□, 284□301.

Gillett, □ □. (2003), Paleomagnetism of the □otch Peak contact metamorphic aureole, revisited□pyrrhotite from magnetite □pyrite under submetamorphic conditions. , □ □*eoph*□*s. Res.*, □□□(□9), 2446.

Guilhaumou, □., T. □C., V. Perthuisot, and F. Roure (1996), Paleocirculation in the basin of southeastern France sub□alpine range□a synthesis from fluid inclusion studies, □*arine and Petroleum* □*eolog*□, □□(6), 695□706.

Horng, C. □, M. Torii, K. □. □hea, and □. □ Kao (1998), Inconsistent magnetic polarities between greigite□and pyrrhotite□magnetite□bearing marine sediments from the Tsailiaochi section, southwestern Taiwan., □*arth Planet. S*□*i. □ett.*, □□□, 467□481.

Appendix

Hunt, C. P., □. K. □aner□ee, □. Han, P. A. □olheid, □. □ches, W. □un, and T. □iu (1995), Rock□magnetic proxies of climate change in the loess□palaeosol sequences of the western □oess Plateau of China, □*eoph□si□al □ournal □nterior*, □□□, 232□244.

Kars, M., C. Aubourg, and □ P. Pozzi (submitted), The continuous production of nano magnetites through low□grade burial □4 km, □*eoph□si□al Resear□h □etters*.

Kars, M., C. Aubourg, □P. Pozzi, and G. □P. (2010), □eoformation of magnetic minerals in claystones during burial (□3km) paper presented at AG□ Fall Meeting □an□Francisco. GP11A□0753

Katz, □., R. D. □lmore, M. Cogoini, M. H. □ngel, and □. Ferry (2000), Associations between burial diagenesis of smectite, chemical remagnetization, and magnetite authigenesis in the Vocontian trough, □□ France., □*ournal o□□eoph□si□al Reasear□h*, □□□(□□. □1), 851□868.

Kligfield, R., and □. □. T. Channell (1981), Widespread remagnetization of Helvetic limestones, □ □*eoph□s. Res.*, □□, 1888□1900.

□andais, P., and M. □lie (1999), □tilisation de la g□ochimie organique pour la d□termination du pal□oenvironement et de la pal□othermicit□dans le Callovo□□xfordien du site de l□□st de la France., Acte des □ourn□es scientifiques C□R□□A□DRA.

□arrasoana, □ C., A. P. Roberts, R. Musgrave, □. Gracia, □. Pinero, M. Vega, and F. Martnez□Ruiz (2007), Diagenetic formation of greigite and pyrrhotite in gaz hydrate marine sedimentary systems, □*arth and Planetar□S□ien□e □etters*, □□□, 350□366.

□u, G., □ Marshak, and D. V. Kent (1990), Characteristics of magnetic carriers responsible for late Paleozoic remagnetization in carbonate strata of the Mid□continent, □.□A., □*arth and Planetar□ S□ien□e □etters*, □□(4), 351□361.

Maher, □. A., and R. Thompson (1999), □*uaternar□□limates□n□ironments and □agnetism*, 390 pp., Cambridge □niversity Press.

Mazurek, M., A. □ Hurfordw, and W. □euz (2006), □nravelling themulti□stage burial history of the □wiss Molasse □asin□integration of apatite fission track, vitrinite reflectance and biomarker isomerisation analysis, □*asin Resear□h*, □□, 27□50.

McCabe, C., and R. D. □lmore (1989), The occurrence and origin of □ate Paleozoic remagnetization in the sedimentary rocks of □orth America, *Re□iews o□□eoph□si□s*, □□, 471□494.

Moreau, M. G., M. Ader, and R. □ □nkin (2005), The magnetization of clay□rich rocks in sedimentary basins□low□temperature experimental formation of magnetic carriers in natural samples., □*arth and Planetar□S□ien□e □etters*, □□□, 193□210.

Morris, A., and A. H. F. Robertson (1993), Miocene remagnetization of carbonate platform and Antalya Complex units within the Isparta angle, □W Turkey, □*e□tonoph□si□s*, □□□, 243□266.

Plattzman (1994), Widespread □eogene remagnetization in □urassic limestones of the □outh Iberian paleomargin (Western □etics, Gibraltar Arc), *Ph□si□s o□the □arth and Planetar□□nteriors*, □□(1□ 2), 3□15.

Pullaiah, G., □. Irving, K. □. □uchan, and D. □ Dunlop (1975), Magnetization changes caused by burial and uplift, □*arth and Planetar□S□ien□e □etters*, □□, 133□143.

Roberts, A. P., and G. M. Turner (1993), Diagenetic formation of ferrimagnetic iron sulphide minerals in rapidly deposited marine sediments, □outh Island, □ew □ealand. , □*arth and Planetar□S□ien□e □etters*, □□□, 257□273.

Roberts, A. P., F. Florindo, □ C. □arrasoana, M. A. □Regan, and □. □hao (2010), Complex polarity pattern at the former Plio□Pleistocene global stratotype section at Vrica (Italy)□Remagnetization by magnetic iron sulphides, □*arth and Planetar□S□ien□e □etters*, □□□, 98□111.

Rochette, P. (1987), Metamorphic control of the magnetic mineralogy of black shales in the □wiss Alps□ toward the use of □magnetic isograde□, □*arth Planet. S□i. □ett.*, □□, 446□456.

Rochette, P., and G. □amarche (1986), □volution des propri□t□s magn□tiques lors des transformations min□rales dans les roches □exemple du □urassique Dauphinois (Alpes fran□aises), □*ull. □in□ral.*, □□□, 687□696.

Rowan, C. □, and A. P. Roberts (2005), Tectonic and geochronological implications of variably timed magnetizations carried by authigenic greigite in marine sediments from □ew □ealand., □*eolog*□, □□, 553□556.

Rowan, C. □, and A. P. Roberts (2006), Magnetite dissolution, diachronous greigite formation, and secondary magnetizations from pyrite oxidation□unravelling complex magnetizations in □eogene marine sediments from □ew □ealand., □*arth and Planetar*□*S*□*ien*□*e* □*etters*, □□□, 119□137.

Rowan, C. □, A. P. Roberts, and T. □roadbent (2009), Reductive diagenesis, magnetite dissolution, greigite growth and paleomagnetic smoothing in marine sediments□A new view, □*arth and Planetar*□*S*□*ien*□*e* □*etters*, □□□, 223□235.

□chill, □., □. Appel, and P. Gautam (2002), Towards pyrrhotite□magnetite geothermometry in low grade metamorphic carbonates of the Tethyan Himalayas (□hiar Khola, Central □epal), □*ournal o*□□*sian* □*arth S*□*ien*□*es*, □□, 195□201.

□tokking, □. □., and □. Tauxe (1990), Properties of chemical remanence in synthetic hematite□testing theoretical predictions, □*ournal o*□□*eoph*□*si*□*al Resear*□*h* □□*Solid* □*arth*, □□, 12,639□612,652.

□uk, D.□W., R. Van der Voo, and D. R. Peacor (1993), □rigin of magnetite responsible for remagnetization of early Paleozoic limestones of □ew □ork □tate, □*ournal o*□□*eoph*□*si*□*al Resear*□*h* □□*Solid* □*arth*, □□, 419□434.

□uk, D., R. D. Peacor, and R. Van der Voo (1990), Replacement of pyrite framboid by magnetite in limestones and implication for paleomagnetism., □*ature*, □□□, 611□613.

Tohver, □., A. □. Weilb, □ G. □olumc, and C. M. Halld (2008), Direct dating of carbonate remagnetization by 40Ar□39Ar analysis of the smectite□illite transformation, □*arth and Planetar*□ *S*□*ien*□*e* □*etters*, □□□(3□4), 524□530.

Wehland, F., □. □ibl, □ Kotthoff, □. Alt□□pping, and □. Appel (2005), Pyrrhotite pTRM acquisition in metamorphic limestones in the light of microscopic observations, *Ph*□*si*□*s o*□*the* □*arth and Planetar*□□*nteriors*, □□□(1□2), 107□114.

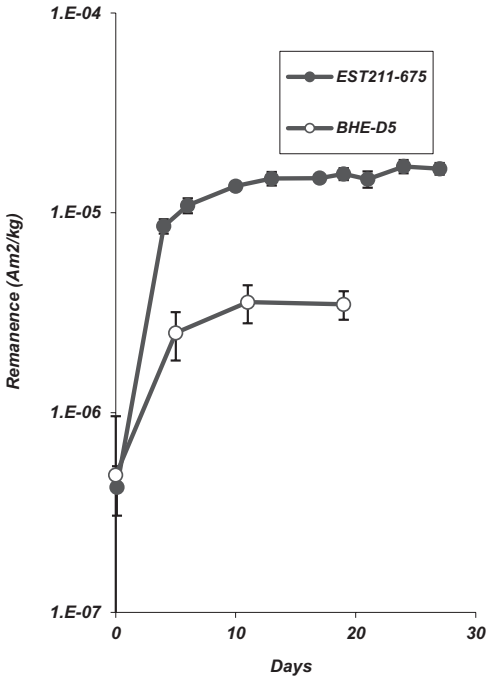

Figure 1 Laboratory heating experiments at 95°C. Bure claystones (EST-211-675m) :4 samples. Opalinus claystones (BHE-D5) : 5 samples. The remanence is the sum of a chemical remanent magnetization and a thermo viscous remanent magnetization. Error bars at 95% confidence.

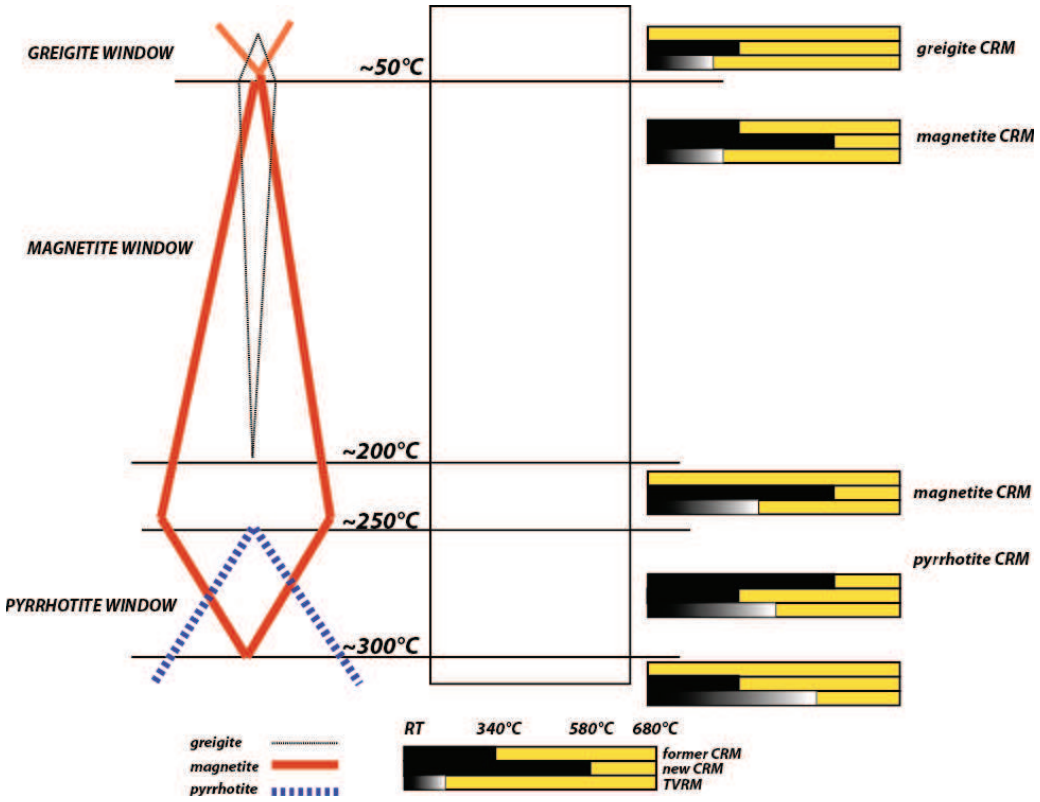

Figure 2 Burial model for the formation of magnetic mineral in claystones. On left, is indicated the concentration of neoformed magnetic mineral. On right, is indicated the unblocking temperature spectra of chemical remanent magnetization (CRM) and thermo viscous remanent magnetization (TVRM).

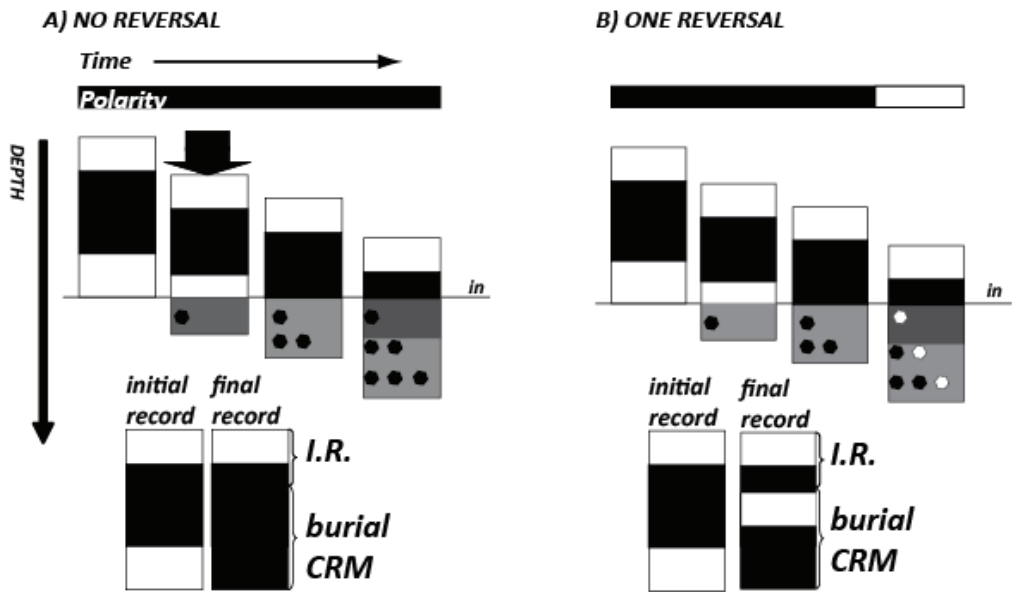

Figure 3 Conceptual model of burial CRM. Horizontal scale is time. Vertical scale is depth. Line 'in' corresponds to the horizon where magnetite forms. Grey zone corresponds to the buried part of the sediment column below the line 'in'. Black (open) circles indicate a normal (reverse) polarity burial CRM. In the final record, we indicate the initial record of magnetostratigraphy (I.R.) and the burial CRM. A) Scenario of mineral formation with one polarity. B) Same scenario as A, but with a magnetic reversal occurring during the burial of the sediments. New magnetic grains record the reversed polarity magnetic field, while magnetic grains formed before the magnetic reversal retains a normal polarity magnetization.

4 Boreholes data

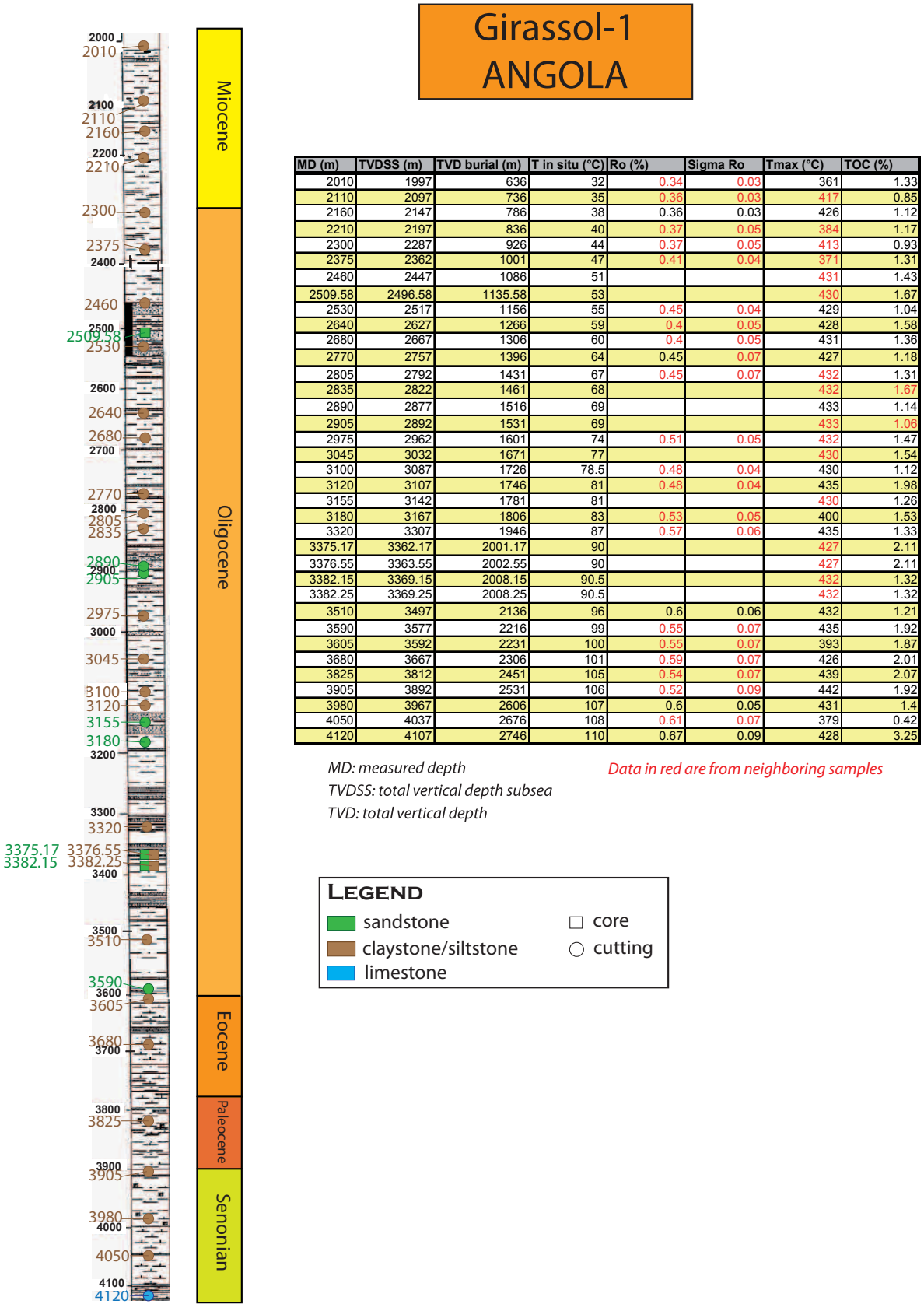

MD (m)	TVDSS (m)	TVD burial (m)	T in situ (°C)	Ro (%)	Sigma Ro	Tmax (°C)	TOC (%)
2010	1997	636	32	0.34	0.03	361	1.33
2110	2097	736	35	0.36	0.03	417	0.85
2160	2147	786	38	0.36	0.03	426	1.12
2210	2197	836	40	0.37	0.05	384	1.17
2300	2287	926	44	0.37	0.05	413	0.93
2375	2362	1001	47	0.41	0.04	371	1.31
2460	2447	1086	51			431	1.43
2509.58	2496.58	1135.58	53			430	1.67
2530	2517	1156	55	0.45	0.04	429	1.04
2640	2627	1266	59	0.4	0.05	428	1.58
2680	2667	1306	60	0.4	0.05	431	1.36
2770	2757	1396	64	0.45	0.07	427	1.18
2805	2792	1431	67	0.45	0.07	432	1.31
2835	2822	1461	68			432	1.67
2890	2877	1516	69			433	1.14
2905	2892	1531	69			433	1.06
2975	2962	1601	74	0.51	0.05	432	1.47
3045	3032	1671	77			430	1.54
3100	3087	1726	78.5	0.48	0.04	430	1.12
3120	3107	1746	81	0.48	0.04	435	1.98
3155	3142	1781	81			430	1.26
3180	3167	1806	83	0.53	0.05	400	1.53
3320	3307	1946	87	0.57	0.06	435	1.33
3375.17	3362.17	2001.17	90			427	2.11
3376.55	3363.55	2002.55	90			427	2.11
3382.15	3369.15	2008.15	90.5			432	1.32
3382.25	3369.25	2008.25	90.5			432	1.32
3510	3497	2136	96	0.6	0.06	432	1.21
3590	3577	2216	99	0.55	0.07	435	1.92
3605	3592	2231	100	0.55	0.07	393	1.87
3680	3667	2306	101	0.59	0.07	426	2.01
3825	3812	2451	105	0.54	0.07	439	2.07
3905	3892	2531	106	0.52	0.09	442	1.92
3980	3967	2606	107	0.6	0.05	431	1.4
4050	4037	2676	108	0.61	0.07	379	0.42
4120	4107	2746	110	0.67	0.09	428	3.25

MD: measured depth
TVDSS: total vertical depth subsea
TVD: total vertical depth

Data in red are from neighboring samples

LEGEND
sandstone
claystone/siltstone
limestone
core
cutting

Figure A.1 – Lithologic log of Girassol-1 (Angola)

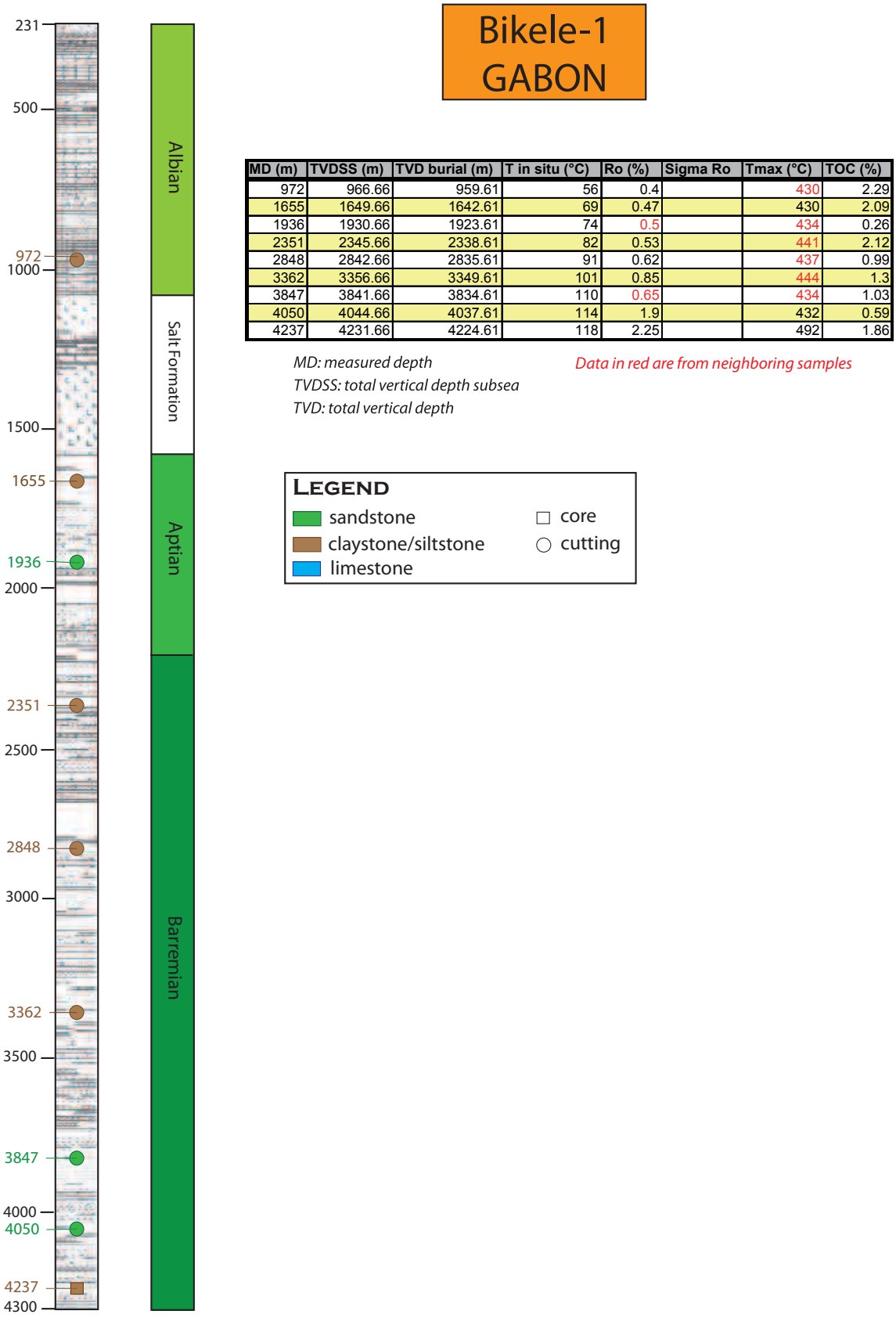

MD (m)	TVDSS (m)	TVD burial (m)	T in situ (°C)	Ro (%)	Sigma Ro	Tmax (°C)	TOC (%)
972	966.66	959.61	56	0.4		430	2.29
1655	1649.66	1642.61	69	0.47		430	2.09
1936	1930.66	1923.61	74	0.5		434	0.26
2351	2345.66	2338.61	82	0.53		441	2.12
2848	2842.66	2835.61	91	0.62		437	0.99
3362	3356.66	3349.61	101	0.85		444	1.3
3847	3841.66	3834.61	110	0.65		434	1.03
4050	4044.66	4037.61	114	1.9		432	0.59
4237	4231.66	4224.61	118	2.25		492	1.86

MD: measured depth
TVDSS: total vertical depth subsea
TVD: total vertical depth

Data in red are from neighboring samples

Figure A.2 – Lithologic log of Bikele-1 (Gabon)

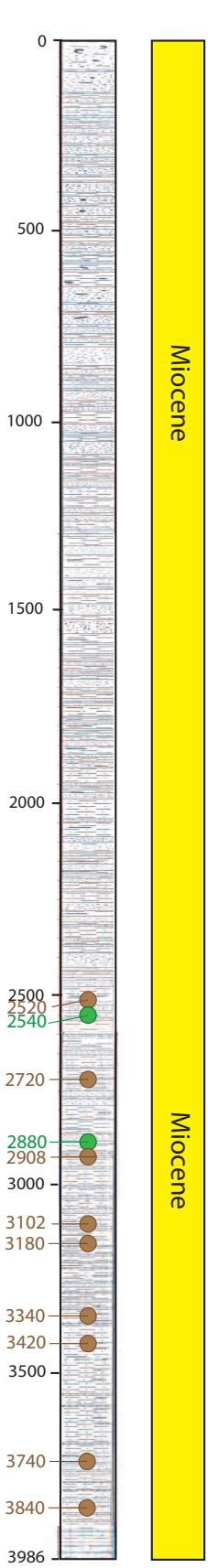

Handil-9bis
INDONESIA

MD (m)	TVDSS (m)	TVD burial (m)	T in situ (°C)	Ro (%)	Sigma Ro	Tmax (°C)	TOC (%)
2520	2507	2505	89	0.58	0.06	433	2.37
2540	2527	2525	90	0.58	0.06	437	8.12
2720	2707	2705	94.5	0.58	0.03	441	7.55
2880	2867	2865	110	0.68	0.05	450	16.77
2908	2895	2893	113	0.68	0.05	449	5.35
3102	3089	3087	128	0.8	0.04	453	4.01
3180	3167	3165	131	0.8	0.04	447	4.53
3340	3327	3325	135.5	0.9	0.04	458	8.02
3420	3407	3405	139	0.95	0.07	439	5.28
3740	3727	3725	149	1.2	0.07	439	9.5
3840	3827	3825	152	1.3	0.06	447	5.06

MD: measured depth
TVDSS: total vertical depth subsea
TVD: total vertical depth

Data in red are from neighboring samples

LEGEND

- sandstone
- claystone/siltstone
- limestone
- □ core
- ○ cutting

Figure A.3 – Lithologic log of Handil-9b (Indonesia)

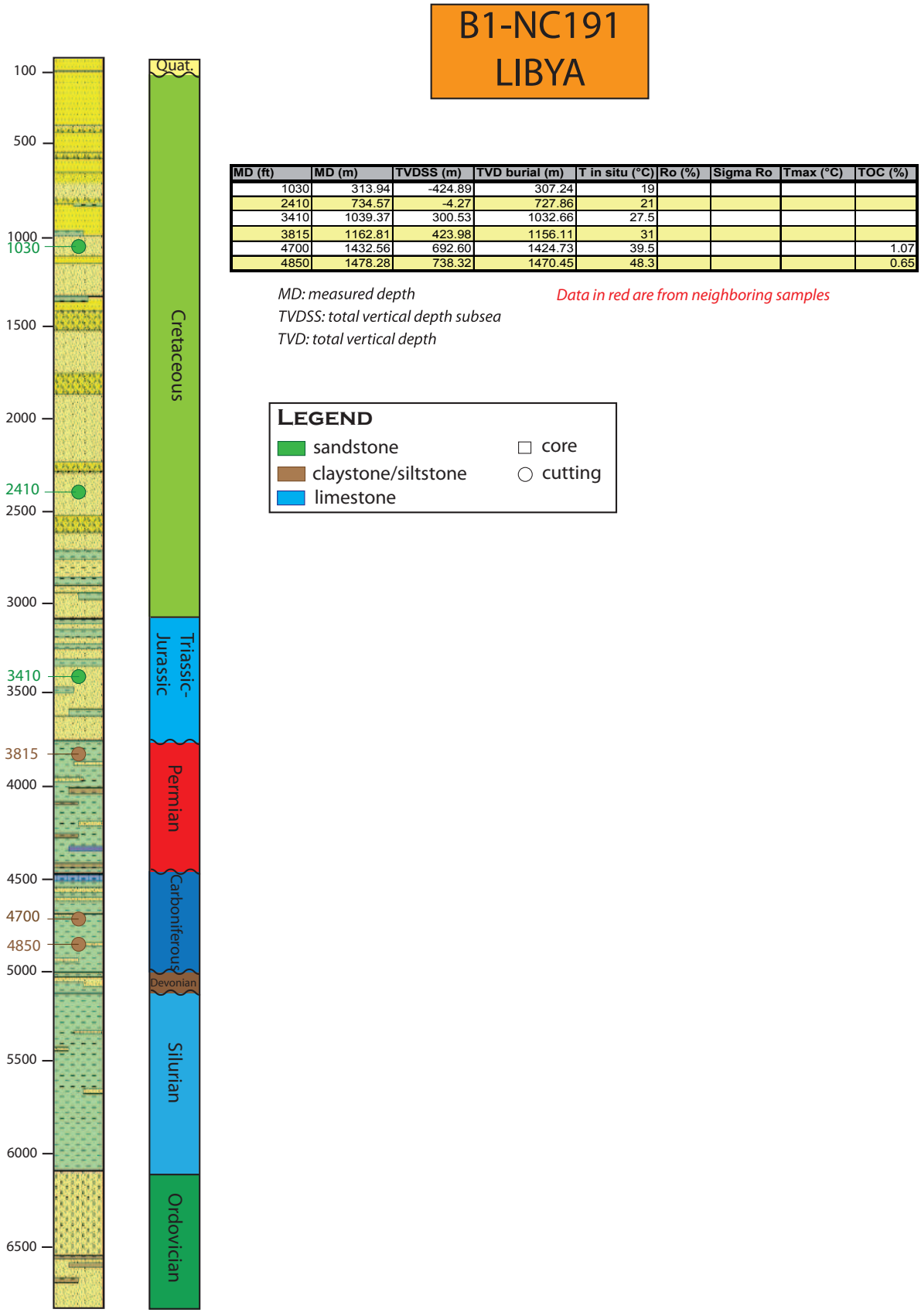

MD (ft)	MD (m)	TVDSS (m)	TVD burial (m)	T in situ (°C)	Ro (%)	Sigma Ro	Tmax (°C)	TOC (%)
1030	313.94	-424.89	307.24	19				
2410	734.57	-4.27	727.86	21				
3410	1039.37	300.53	1032.66	27.5				
3815	1162.81	423.98	1156.11	31				
4700	1432.56	692.60	1424.73	39.5				1.07
4850	1478.28	738.32	1470.45	48.3				0.65

MD: measured depth
TVDSS: total vertical depth subsea
TVD: total vertical depth

Data in red are from neighboring samples

Figure A.4 – Lithologic log of B1-NC191 (Libya)

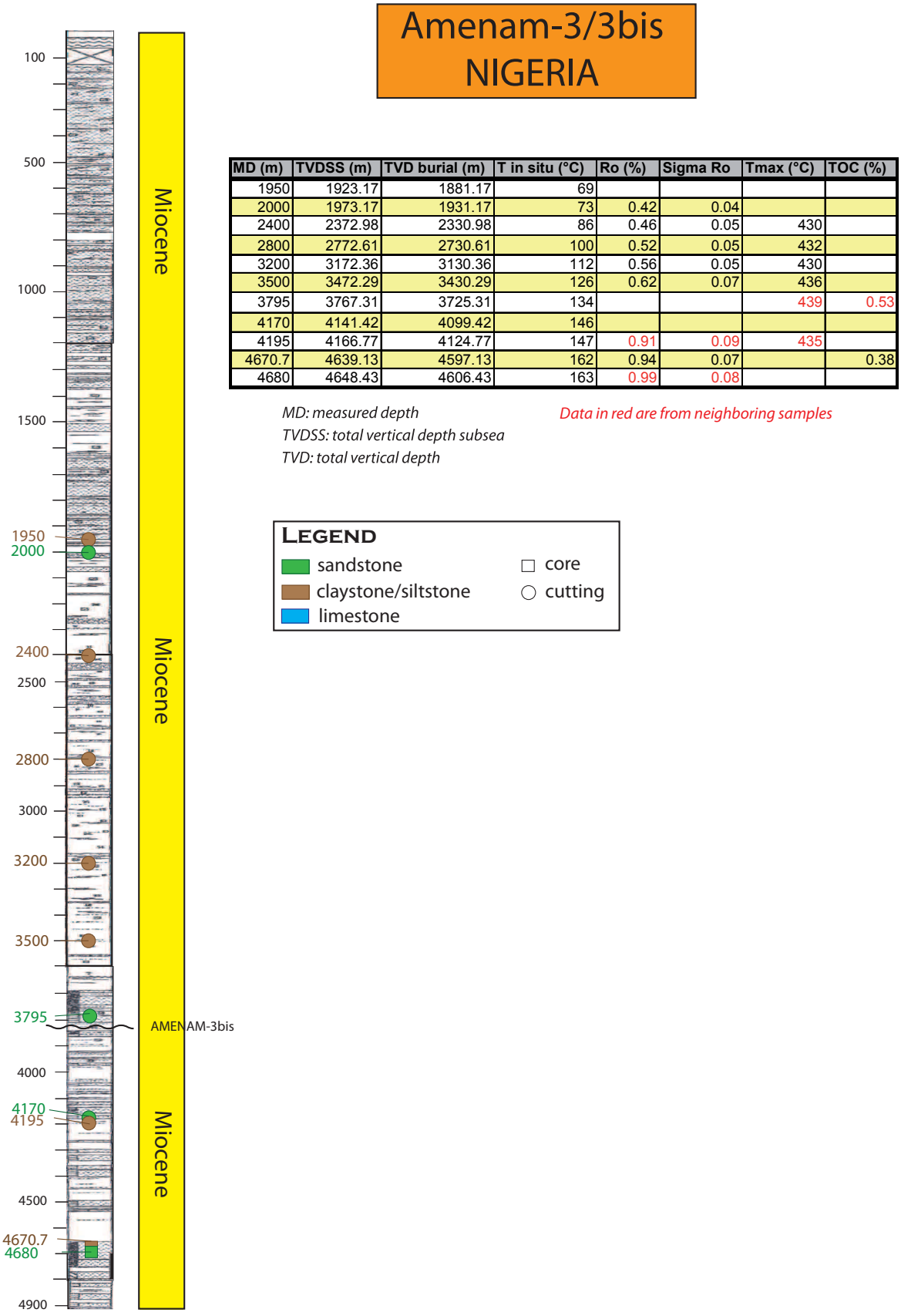

MD (m)	TVDSS (m)	TVD burial (m)	T in situ (°C)	Ro (%)	Sigma Ro	Tmax (°C)	TOC (%)
1950	1923.17	1881.17	69				
2000	1973.17	1931.17	73	0.42	0.04		
2400	2372.98	2330.98	86	0.46	0.05	430	
2800	2772.61	2730.61	100	0.52	0.05	432	
3200	3172.36	3130.36	112	0.56	0.05	430	
3500	3472.29	3430.29	126	0.62	0.07	436	
3795	3767.31	3725.31	134			439	0.53
4170	4141.42	4099.42	146				
4195	4166.77	4124.77	147	0.91	0.09	435	
4670.7	4639.13	4597.13	162	0.94	0.07		0.38
4680	4648.43	4606.43	163	0.99	0.08		

MD: measured depth
TVDSS: total vertical depth subsea
TVD: total vertical depth

Data in red are from neighboring samples

Figure A.5 – Lithologic log of Amenam-3/3b (Nigeria)

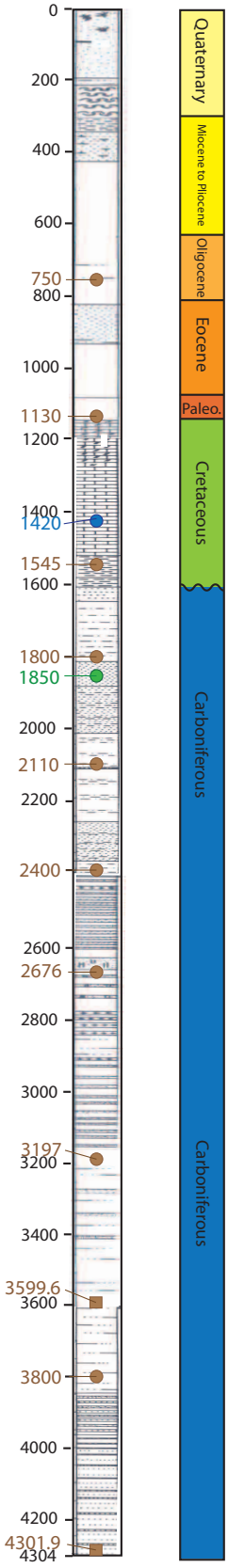

Nagele-1
THE NETHERLANDS

MD (m)	TVDSS (m)	TVD burial (m)	T in situ (°C)	Ro (%)	Sigma Ro	Tmax (°C)	TOC (%)
750	746	742.83	35				
1130	1126	1122.83	48	0.28	0.03	422	0.42
1420	1416	1412.83	56				
1545	1541	1537.83	61	1.37	0.09	333	0.1
1800	1796	1792.83	68	1.78	0.17		0.7
1850	1846	1842.83	71	1.85			0.8
2110	2106	2102.83	79	2.36	0.17		0.7
2400	2396	2392.83	88	2.91	0.2		0.9
2676	2672	2668.83	98	3.5	0.29		0.9
3197	3193	3189.83	131	4.52	0.74		0.9
3599.6	3595.6	3592.43	152	5.89	0.36		1
3800	3796	3792.83	162	5.84	0.69		0.9
4301.9	4297.9	4294.73	175	6.67	0.37		1.6

MD: measured depth
TVDSS: total vertical depth subsea
TVD: total vertical depth

Data in red are from neighboring samples

LEGEND

- sandstone
- claystone/siltstone
- limestone
- core
- cutting

Figure A.6 – Lithologic log of Nagele-1 (The Netherlands)

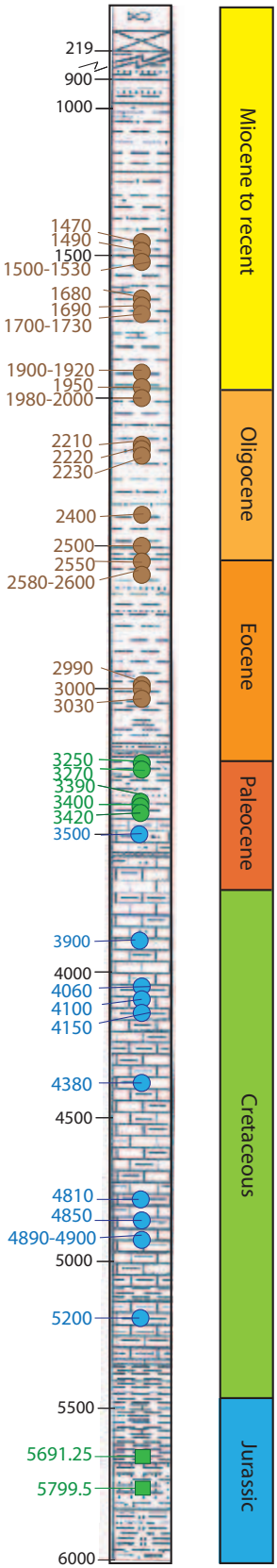

22/30C-10
UNITED KINGDOM

MD (m)	TVDSS (m)	TVD burial (m)	T in situ (°C)	Ro (%)	Sigma Ro	Tmax (°C)	TOC (%)
1470	1432	1340	59.9				
1490	1452	1360	60.6				
1500	1462	1370	61			263	2.96
1510	1472	1380	61.3				
1520	1482	1390	61.7				
1530	1492	1400	62				
1680	1641.9	1549.9	67.3				
1690	1651.9	1559.9	67.6				
1700	1661.86	1569.86	68	0.3	0.07	436	4.99
1710	1671.84	1579.84	68.3				
1720	1681.81	1589.81	68.7				
1730	1691.77	1599.77	69				
1900	1860.5	1768.5	75				
1910	1870.1	1778.1	75.2				
1920	1879.95	1787.95	75.6				
1950	1909.4	1817.4	76.7	0.33	0.05	430	3.52
1980	1938.83	1846.83	77.7				
1990	1948.6	1856.6	78.1				
2000	1958.5	1866.5	78.4				
2210	2161.32	2069.32	85.5				
2220	2170.88	2078.88	85.9	0.45	0.09	430	3.82
2230	2180.42	2088.42	86.2				
2400	2340.45	2248.45	91.8				
2500	2432.8	2340.8	95				
2550	2478.5	2386.5	96.7	0.49	0.07	432	1.68
2580	2505.55	2413.55	97.6				
2590	2514.67	2422.67	98				
2600	2523.75	2431.75	98.2				
2990	2873.25	2781.25	110.5	0.64	0.11	434	2.49
3000	2882.22	2790.22	110.8				
3030	2902.15	2810.15	111.5				
3250	3110	3018	118.8	0.78	0.08	420	1.22
3270	3125.99	3033.99	119.4				
3390	3234.26	3142.26	123.2				
3400	3241.12	3149.12	123.4				
3420	3261.12	3169.12	124				
3500	3331.92	3239.92	126.6				
3900	3690.17	3598.17	139.2				
4060	3834.08	3742.08	144.2	1.03	0.1	445	0.77
4100	3868.5	3776.5	145.4				
4150	3914	3822	147	1.05	0.08	442	0.3
4380	4120.5	4028.5	154.2				
4810	4526.5	4434.5	168.5				
4850	4564	4472	169.9	1.58	0.09	444	0.59
4890	4603.16	4511.16	171.2				
4900	4613	4521	171.6	1.54	0.15	448	1.25
5200	4908.24	4816.24	182				
5691.25	5395.5	5303.5	199	2	0.12	423	2.7
5799.5	5503	5411	203	1.98	0.08	427	2.58

MD: measured depth
TVDSS: total vertical depth subsea
TVD: total vertical depth

Data in red are from neighboring samples

LEGEND

- sandstone
- claystone/siltstone
- limestone
- □ core
- ○ cutting

Figure A.7 – Lithologic log of 22/30C-10 (United Kingdom)

Table A.1 – Magnetic data of the samples from Girassol-1

MD (m)	TVD burial (m)	Xlf (µSI)	RT-SIRM (µAm²/kg)	LT-SIRM (µAm²/kg)	LT/RT	PM
2010	649	5356	17833	45201	2.53	0.26
2110	749	380	95	1194	12.56	0.76
2160	799	429	973	3472	3.57	0.57
2210	849	451	1269	3349	2.64	0.44
2300	939	394	90	1030	11.48	0.78
2375	1014	304	41	593	14.37	0.77
2460	1099	280	74	1391	18.92	0.79
2509.58	1148.58	31	159	1110	7.00	0.55
2530	1169	390	272	2146	7.90	0.63
2640	1279	378	99	1335	13.53	0.81
2680	1319	352	1096	3280	2.99	0.45
2770	1409	302	80	1358	17.01	0.81
2805	1444	444	716	4561	6.37	0.57
2835	1474	415	2693	5474	2.03	0.36
2890	1529	368	258	2728	10.58	0.70
2905	1544	350	100	1912	19.12	0.81
2975	1614	344	69	1751	25.33	0.82
3045	1684	435	67	598	8.98	0.64
3100	1739	292	88	1451	16.49	0.81
3120	1759	314	68	1450	21.20	0.78
3155	1794	8979	24950	71121	2.85	0.25
3180	1819	432	432	2321	5.37	0.58
3320	1959	307	110	1329	12.09	0.78
3375.17	2014.17	125	226	838	3.71	0.43
3376.55	2015.55	206	20	159	8.00	0.87
3382.15	2021.15	192	58	727	12.49	0.61
3382.25	2021.25	254	76	2186	28.64	0.86
3510	2149	411	261	2047	7.84	0.61
3590	2229	375	112	1229	10.98	0.79
3605	2244	347	72	1125	15.73	0.84
3680	2319	402	1280	2383	1.86	0.26
3825	2464	150	79	648	8.18	0.55
3905	2544	284	61	871	14.39	0.66
3980	2619	304	202	728	3.60	0.42
4050	2689	966	2752	7282	2.65	0.27
4120	2759	260	608	2162	3.56	0.37

Table A.2 – Magnetic data of the samples from Bikele-1

MD (m)	TVD burial (m)	Xlf (µSI)	RT-SIRM (µAm²/kg)	LT-SIRM (µAm²/kg)	LT/RT	PM
972	964.95	120	53	1133	21.48	0.82
1655	1647.95	398	329	2066	6.27	0.52
1936	1928.95	182	365	365	1.00	0.75
2351	2343.95	165	59	523	8.87	0.67
2848	2840.95	2236	4780	18658	3.90	0.37
3362	3354.95	275	117	604	5.18	0.62
3847	3839.95	1120	4229	12393	2.93	0.21
4050	4042.95	22608	80691	206894	2.56	0.16
4237	4229.95	318	194	1160	5.99	0.56

Table A.3 – Magnetic data of the samples from Handil-9b

MD (m)	TVD burial (m)	Xlf (µSI)	RT-SIRM (µAm²/kg)	LT-SIRM (µAm²/kg)	LT/RT	PM
2520	2518	1295	2838	10324	3.64	0.33
2540	2538	321	327	2337	7.15	0.67
2720	2718	193	175	771	4.40	0.52
2880	2878	3549	8099	20938	2.59	0.21
2908	2906	592	120	2493	20.76	0.89
3102	3100	586	752	3999	5.32	0.68
3180	3178	347	584	2921	5.00	0.65
3340	3338	376	732	3066	4.19	0.53
3420	3418	1386	1655	7047	4.26	0.35
3740	3738	7999	10379	22759	2.19	0.17
3840	3838	8414	10172	23857	2.35	0.17

Table A.4 – Magnetic data of the samples from B1-NC191

MD (ft)	MD (m)	TVD burial (m)	Xlf (µSI)	RT-SIRM (µAm²/kg)	LT-SIRM (µAm²/kg)	LT/RT	PM
1030	313.9	307.2	87	385	1346	3.49	0.17
2410	734.6	727.9	131	436	1565	3.59	0.10
3410	1039.4	1032.7	1110	1170	2063	1.76	0.09
3815	1162.8	1156.1	2545	5042	10174	2.02	0.12
4700	1432.6	1424.7	577	181	27463	151.95	0.97
4850	1478.3	1470.4	682	579	7041	12.17	0.85

Table A.5 – Magnetic data of the samples from Amenam-3-3b

MD (m)	TVD burial (m)	Xlf (µSI)	RT-SIRM (µAm²/kg)	LT-SIRM (µAm²/kg)	LT/RT	PM
1950	1908	154	76	585	7.69	0.60
2000	1958	378	2138	7196	3.36	0.47
2400	2358	557	3576	14102	3.94	0.62
2800	2758	753	8148	23231	2.85	0.51
3200	3158	2352	7516	28265	3.76	0.39
3500	3458	4005	10757	39957	3.71	0.37
3795	3753	5829	10647	29773	2.80	0.30
4170	4128	2386	6522	20960	3.21	0.32
4195	4153	851	1229	7302	5.94	0.58
4670.7	4628.7	601	155	12267	79.25	0.94
4680	4638	103	74	419	5.67	0.65

Table A.6 – Magnetic data of the samples from Nagele-1

MD (m)	TVD burial (m)	Xlf (µSI)	RT-SIRM (µAm²/kg)	LT-SIRM (µAm²/kg)	LT/RT	PM
750	746.83	222	90	2264	25.15	0.67
1130	1126.83	334	700	4204	6.00	0.48
1420	1416.83	75	309	698	2.26	0.25
1545	1541.83	44	56	587	10.50	0.82
1800	1796.83	585	105	8409	80.15	0.98
1850	1846.83	473	418	3354	8.02	0.71
2110	2106.83	476	144	3187	22.19	0.91
2400	2396.83	628	755	5297	7.02	0.79
2676	2672.83	562	556	3938	7.08	0.76
3197	3193.83	1001	2070	49612	23.97	0.53
3599.6	3596.43	229	46	713	15.41	0.82
3800	3796.83	621	629	4430	7.04	0.73
4301.9	4298.73	191	14	627	45.42	0.93

Table A.7 – Magnetic data of the samples from 22-30C-10

MD (m)	TVD burial (m)	Xlf (µSI)	RT-SIRM (µAm²/kg)	LT-SIRM (µAm²/kg)	LT/RT	PM
1470	1378	348	80	2239	27.85	0.70
1490	1398	333	109	2229	20.44	0.69
1500	1408	369	87	2279	26.30	0.70
1510	1418	346	102	2587	25.25	0.75
1520	1428	439	139	2896	20.82	0.78
1530	1438	413	158	2873	18.22	0.72
1680	1588	328	88	633	7.22	0.63
1690	1598	225	119	848	7.14	0.69
1700	1608	236	108	1100	10.21	0.78
1710	1618	272	78	875	11.27	0.77
1720	1628	234	86	804	9.34	0.73
1730	1638	248	94	1167	12.46	0.81
1900	1808	337	85	1393	16.41	0.83
1910	1818	387	81	684	8.41	0.68
1920	1828	424	99	2959	29.76	0.92
1950	1858	228	154	1387	9.01	0.78
1980	1888	432	90	1042	11.53	0.78
1990	1898	399	112	1522	13.65	0.83
2000	1908	338	97	1118	11.53	0.79
2210	2118	362	111	3283	29.52	0.86
2220	2128	440	121	131	1.08	
2230	2138	382	175	2032	11.61	0.68
2400	2308	392	140	1426	10.18	0.69
2500	2408	1267	1022	3340	3.27	0.46
2550	2458	648	192	3456	17.96	0.85
2580	2488	498	110	1881	17.06	0.82
2590	2498	457	180	1594	8.88	0.73
2600	2508	449	110	1457	13.29	0.79
2990	2898	392	244	1208	4.96	0.61
3000	2908	508	174	1623	9.34	0.74
3030	2938	428	155	1158	7.49	0.71
3250	3158	146	101	324	3.22	0.46
3270	3178	277	55	254	4.64	0.55
3390	3298	446	303	1605	5.30	0.59
3400	3308	464	162	1160	7.18	0.74
3420	3328	458	145	2041	14.10	0.86
3500	3408	362	190	415	2.19	0.33
3900	3808	74	142	299	2.11	0.25
4060	3968	448	161	338	2.09	0.27
4100	4008	249	174	372	2.14	0.29
4150	4058	112	305	538	1.76	0.28
4380	4288	199	884	1388	1.57	0.17
4810	4718	467	320	479	1.50	
4850	4758	231	604	1102	1.82	0.21
4890	4798	441	235	527	2.24	0.28
4900	4808	641	206	497	2.41	0.36
5200	5108	607	560	2278	4.07	0.59
5691.25	5599.25	103	42	297	7.10	0.54
5799.5	5707.5	13	50	370	7.45	0.47